

NASA Conference Publication 2409

Instability in Rotating Machinery

(NASA-CP-2409) INSTABILITY IN ROTATING
MACHINERY (NASA) 458 F CSCL 13I

N86-30160

THRU

N86-30204

Unclas

G3/37 42955

*Proceedings of a symposium held in
Carson City, Nevada
June 10-14, 1985*

NASA

NASA Conference Publication 2409

Instability in Rotating Machinery

Proceedings of a symposium sponsored
by Bently Rotor Dynamics Research
Corporation and held in
Carson City, Nevada
June 10-14, 1985

NASA
National Aeronautics
and Space Administration
**Scientific and Technical
Information Branch**

1985

PREFACE

Excellent progress has been and is being made on the basic understanding and control of rotating machinery instability problems. A small group of researchers have been plugging away at the causes of instabilities and the cures for them, and machinery manufacturers and end users have recently joined the effort. Instead of the usual "quick fix" or "shotgun fix" when an instability problem crops up, problems are being cured directly in the field. Also several manufacturers have unveiled antiwhirl devices that are engineered cures aimed at and hitting the source of the problem.

Every 2 years Texas A&M holds an excellent and highly recommended Rotating Machinery Stability Workshop. Their next workshop will be held in 1986. Since their last workshop, however, there have been many important developments and achievements in the area of instability. Therefore, the Bently Rotor Dynamics Research Corporation called a symposium to assist in disseminating this new information.

The international Symposium on Instability in Rotating Machinery was held in Carson City, Nevada, June 10-14, 1985. This proceedings contains 45 papers presented at the symposium covering a wide range of subjects, including

- Rotor/seal and rotor/fluid lubricated-bearing-system instabilities
- Flow-generated instabilities in fluid flow machines
- Internal friction and rub-related instabilities
- Simulation and estimation of destabilizing forces in rotating machines
- Computational techniques for predicting the dynamic behavior of rotating machines
- Instability phenomena in compressors, turbines, and pumps: case histories
- Cracked-shaft detection
- Vibration control in turbomachinery, including "antiwhirl" techniques and magnetic bearings for active control

At the exhibit following the symposium a dozen working models of rotating machines equipped with modern computerized instrumentation demonstrated various machinery instability malfunctions as well as measures to correct them. The demonstrations are described at the end of the proceedings.

Nearly 100 participants from North and South America, Europe, Asia, Africa, and Australia attended the symposium. They represented research and educational organizations as well as manufacturers and users of rotating machinery. The symposium was also attended by maintenance engineers from refineries, chemical plants, and powerplants. The wide interest in the symposium reflects a considerable need to enhance knowledge in this relatively new but rapidly developing area of engineering.

PRECEDING PAGE BLANK NOT FILMED

We would appreciate receiving comments, corrections, data, and research disiderata.

Donald E. Bently
Agnes Muszynska
Bently Rotor Dynamics Research Corp.

Robert C. Hendricks
NASA Lewis Research Center

CONTENTS

	Page
FULL LOAD SHOP TESTING OF 18 000-hp GAS TURBINE DRIVEN CENTRIFUGAL COMPRESSOR FOR OFFSHORE PLATFORM SERVICE: EVALUATION OF ROTOR DYNAMICS PERFORMANCE R. Gordon Kirk and Mark Simpson, Ingersoll-Rand Company	1
INSTABILITY ANALYSIS PROCEDURE FOR THREE-LEVEL MULTI-BEARING ROTOR-FOUNDATION SYSTEMS Shixiang Zhou and Neville F. Rieger, Stress Technology Incorporated	15
SIMULATION OF NON-LINEAR BEARING FORCES FOR POST-STABILITY INVESTIGATION Z.A. Parszewski, J.M. Krodkiewski, K. Krynicky, and A.E. Salek, University of Melbourne	37
MEASUREMENT OF ROTOR SYSTEM DYNAMIC STIFFNESS BY PERTURBATION TESTING Donald E. Bently and Agnes Muszynska, Bently Rotor Dynamics Research Corporation	47
WHY HAVE HYDROSTATIC BEARINGS BEEN AVOIDED AS A STABILIZING ELEMENT FOR ROTATING MACHINES? Donald E. Bently and Agnes Muszynska, Bently Rotor Dynamics Research Corporation	59
TURBINE INSTABILITIES - CASE HISTORIES C.W. Laws, Bently Nevada (UK) Limited	65
TWO-PHASE FLOWS WITHIN SYSTEMS WITH AMBIENT PRESSURE ABOVE THE THERMODYNAMIC CRITICAL PRESSURE R.C. Hendricks, National Aeronautics and Space Administration, M.J. Braun and R.L. Wheeler III, University of Akron, and R.L. Mullen, Case Western Reserve University	83
MODELING OF ELASTICALLY MOUNTED VERTICAL ROTOR Seyyed Said Dana, Federal University of Paraiba, and Hans Ingo Weber, State University of Campinas	97
EXPERIMENTAL VERIFICATION AND PRACTICAL APPLICATION OF TORQUEWHIRL THEORY OF ROTORDYNAMIC INSTABILITY J.M. Vance and S.T. Noah, Texas A&M University, and K.B. Yim, Sunstrand Aviation	107
CO ₂ COMPRESSOR VIBRATION AND CAUSE ANALYSIS Ying Yin Lin, Liaohe Chemical Fertilizer Plant	125
INFLUENCE OF DESIGN PARAMETERS ON OCCURRENCE OF OIL WHIRL IN ROTOR-BEARING SYSTEMS Peter J. Ogrodnik and Michael J. Goodwin, North Staffordshire Polytechnic, and John E.T. Penny, University of Aston in Birmingham	135

BACKWARD WHIRL IN A SIMPLE ROTOR SUPPORTED ON HYDRODYNAMIC BEARINGS R. Subbiah, R.B. Bhat, and T.S. Sankar, Concordia University, and J.S. Rao, Indian Embassy	145
WHIRL AND WHIP - ROTOR/BEARING STABILITY PROBLEMS Agnes Muszynska, Bently Rotor Dynamics Research Corporation	155
SOME NEW RESULTS CONCERNING THE DYNAMIC BEHAVIOR OF ANNULAR TURBULENT SEALS H. Massmann and R. Nordmann, University of Kaiserslautern	179
ANALYTICAL PREDICTION OF LABYRINTH-SEAL-FLOW-INDUCED ROTOR EXCITATION FORCES C. Rajakumar and E. Sisto, Stevens Institute of Technology	195
OIL SEAL EFFECTS AND SUBSYNCHRONOUS VIBRATIONS IN HIGH-SPEED COMPRESSORS Paul E. Allaire and John A. Kocur, Jr., University of Virginia	205
EFFECT OF COULOMB SPLINE ON ROTOR DYNAMIC RESPONSE C. Nataraj, H.D. Nelson, and N. Arakere, Arizona State University	225
ROTOR-TO-STATOR RUB VIBRATION IN CENTRIFUGAL COMPRESSOR Gao Jin Ji and Qi Qi Min, Liaoyang Petrochemical Fiber Company	235
MEASURING DYNAMIC OIL FILM COEFFICIENTS OF SLIDING BEARING Guan-ping Feng and Xi-kuan Tang, Qinghua University	245
CRACKED SHAFT DETECTION ON LARGE VERTICAL NUCLEAR REACTOR COOLANT PUMP L. Stanley Jenkins, Westinghouse Electric Corporation	253
PUMP INSTABILITY PHENOMENA GENERATED BY FLUID FORCES S. Gopalakrishnan, Borg Warner Industrial Products, Inc.	267
VERTICAL REACTOR COOLANT PUMP INSTABILITIES Robert M. Jones, Tennessee Valley Authority	277
PREDICTION OF DESTABILIZING BLADE TIP FORCES FOR SHROUDED AND UNSHROUDED TURBINES Yuan J. Qiu and M. Martinez-Sanchez, Massachusetts Institute of Technology	287
IDENTIFICATION OF BEARING AND SEAL DYNAMIC STIFFNESS PARAMETERS BY STEADY STATE LOAD AND SQUEEZE FILM TESTS Donald E. Bently and Agnes Muszynska, Bently Rotor Dynamics Research Corporation	301
MAGNETIC BEARINGS FOR VIBRATION CONTROL G. Schweitzer, Swiss Federal Institute of Technology (ETH)	317
ACTIVE MAGNETIC BEARINGS FOR OPTIMUM TURBOMACHINERY DESIGN Jerry Hustak, R. Gordon Kirk, and Kenneth A. Schoeneck, Ingersoll-Rand Company	327

ROTOR INTERNAL FRICTION INSTABILITY Donald E. Bently and Agnes Muszynska, Bently Rotor Dynamics Research Corporation	337
TOPPING TURBINE (103-JAT) ROTOR INSTABILITY IN 1150-STPD KELLOGG AMMONIA PLANTS Richard Thomas, Agrico Chemical Company	349
HYDRAULIC INDUCED INSTABILITY ON A VERTICAL SERVICE WATER PUMP: CASE HISTORY R.F. Bosmans, Bently Rotor Dynamics Research Corporation	361
AERODYNAMIC INSTABILITY: A CASE HISTORY Robert C. Eisenmann, Machinery Diagnostics, Inc.	369
REMARKS ON ROTOR STABILITY (A CONTRIBUTION TO DISCUSSION DURING SYMPOSIUM ON INSTABILITY IN ROTATING MACHINERY) E. Kramer, Technical University of Darmstadt	379
EIGENVALUES AND STABILITY PROBLEMS OF ROTORS Zbigniew Walczyk, Polish Academy of Sciences	385
CHANGES OF INSTABILITY THRESHOLDS OF ROTOR DUE TO BEARING MISALIGNMENTS Helmut Springer and Horst Ecker, Technical University of Vienna, and Edgar J. Gunter, University of Virginia	399
DEMONSTRATION OF VARIOUS ROTOR INSTABILITIES (EXHIBIT OF BENTLY ROTOR DYNAMICS RESEARCH CORPORATION LABORATORY RIGS AT SYMPOSIUM ON INSTABILITY IN ROTATING MACHINERY) Agnes Muszynska, Bently Rotor Dynamics Research Corporation	409
WHIRL/WHIP DEMONSTRATION Robert Grissom, Bently Nevada Corporation	415
ANTI-SWIRLING DEMONSTRATION Agnes Muszynska, Bently Rotor Dynamics Research Corporation	423
PARTIAL ROTOR-TO-STATOR RUB DEMONSTRATION Robert Grissom, Bently Nevada Corporation	427
ROTOR INSTABILITY DUE TO LOOSE ROTATING PART Agnes Muszynska, Bently Rotor Dynamics Research Corporation	431
INSTABILITY IN HYDRAULIC MACHINES DEMONSTRATION RIG Agnes Muszynska, Bently Rotor Dynamics Research Corporation, and M.J. Braun, University of Akron	439
CRACKED ROTOR DEMONSTRATION R.F. Bosmans, Bently Rotor Dynamics Research Corporation	443
ROTOR/BEARING SYSTEM DYNAMIC STIFFNESS MEASUREMENTS BY NONSYNCHRONOUS PERTURBATION Agnes Muszynska, Bently Rotor Dynamics Research Corporation	447

SHAFT MODE SHAPE DEMONSTRATION	
Robert Grissom, Bently Nevada Corporation	457
ORBITS - COMPUTER SIMULATION	
Agnes Muszynska, Bently Rotor Dynamics Research Corporation	459
DATA PRESENTATION TECHNIQUES FOR ROTATING MACHINERY MALFUNCTION DIAGNOSIS	
Thomas Spettel, Bently Rotor Dynamics Research Corporation	465

FULL LOAD SHOP TESTING OF 18 000-hp GAS TURBINE DRIVEN
CENTRIFUGAL COMPRESSOR FOR OFFSHORE PLATFORM SERVICE:
EVALUATION OF ROTOR DYNAMICS PERFORMANCE

R. Gordon Kirk
Ingersoll-Rand Company
Phillipsburg, New Jersey 08865

Mark Simpson
Ingersoll-Rand Company, Ltd.
Wythenshawe, England

The results for in-plant full load testing of a 13.4 MW (18000 HP) gas turbine driven centrifugal compressor are presented and compared to analytical predictions of compressor rotor stability. Unique problems from both oil seals and labyrinth gas seals were encountered during the testing. The successful resolution of these problems are summarized.

SYMBOLS

Values are given in both SI and U.S. Customary Units. The measurements and calculations were made in U.S. Customary Units.

a, A	real part of eigenvalue, growth factor (sec^{-1})
N	rotor speed, Hz (RPM)
N_{cr}	rotor 1st critical speed (CPM)
N_d	rotor damped critical speed (CPM)
P_2	compressor discharge pressure, N/m^2 (lb/in^2)
P	pressure rise across compressor, N/m^2 (lb/in^2)
Q	aerodynamic cross-coupling, N/m (lb/in)

INTRODUCTION

The design and testing of centrifugal compressors have demanded increased interest and concern as a result of documented cases of compressor vibration instability when actual startup conditions are first encountered (1,2,3,4).

For this reason, two 13.4 MW (18000 HP) aircraft derivative gas turbine driven compressor trains for North Sea platform service were recently purchased with requirements for standard four-hour mechanical shop tests and full load performance testing. Actual contract gas composition was required to satisfy the customer specifications. The facility for this full load testing was constructed in the United Kingdom. Figure 1 shows this test facility with one of the two enclosures and associated hardware.

The contract gas moleweight was 18.3 and consisted mainly of methane. The discharge pressure was 7585 kPa (1100 psig) and the suction pressure was varied from 4137 kPa (600 psig) at 70% speed to 1724 kPa (250 psig) at 100% rated speed to simulate field conditions for year 1 through year 6 operation as the gas field pressure decays. This paper is concerned specifically with the rotor dynamics evaluation of the mechanical and full load tests of the two seven stage series flow centrifugal compressors for the year six, 100% speed condition. The relative position of this design to past experience at the authors' company is shown in Figure 2. The log decrement for the compressor supported on its bearings and without any other destabilizing element was 0.144 which was similar to numerous other units running without vibration problems.

EVALUATION OF OIL SEAL PERFORMANCE

One of the major components known to cause instability in high pressure compressors is the oil ring type seal. The original design of the seal for the subject compressor is shown in Figure 3. The predicted worst case stability parameters for this design are shown in Table 1 as growth factor for various operating speeds considering both soft start and hard start conditions (3). The year six condition is used for stability work since this condition had the highest speed and the highest pressure rise across the compressor. The initial year 6 design speed was 194.2 Hz (11650 RPM). A growth factor greater than +50 has been found to cause unbounded vibration. The authors' company has used a value of +15 as the upper limit of acceptance if seal and aerodynamic instability mechanisms are included in the analysis.

The mechanical testing of the compressors revealed unexpected problems from the oil seals. The outer seal lapped surface that contacts and seals to the housing was fretted after a short running time as illustrated by the typical ring shown in Figure 4. The vibration characteristic for this ring failure mode is shown in Figure 5. The low frequency oil ring whirl instability would typically start when compressor speed was just over 100 Hz (6000 RPM) and track with compressor speed. This sub-synchronous vibration would vary in magnitude and frequency with typical frequencies from 0 to 30 Hz.

Re-evaluation of the oil seal ring resulted in reducing the sealing length and width of the lapped face, and increasing the steady holding force of the springs to attempt to both stop the low frequency ring whirl and to improve the locked ring rotor stability. Table 2 summarizes this re-design condition which has much better stability for both soft and hard start conditions. Table 3 indicates that even with 1751 N/mm (10,000 lb/in) cross-coupling at midspan the design had acceptable stability for normal seal ring holding force. Further operation produced unacceptable results due to fretting damage and the outer seal was further modified to the final configuration shown in Figure 6. The predicted stability for three seal designs versus rotor speed are plotted in Figure 7 and compared to the condition without the influence of oil seals. The interaction of the aerodynamic excitation is plotted in Figure 8 for the re-design and final oil seal design as compared to the condition without oil seal ring influence. The final modification was made to the seal assembly procedure to assure that the casing end plate that mates to the oil ring lapped face was not distorting upon assembly. This combination of oil ring seal design and modified assembly procedure produced results that did not experience either fretting damage or oil seal re-excitation of the compressor 1st bending critical.

RESULTS OF FULL LOAD TESTING - AERODYNAMIC EXCITATION

The full load test facility was constructed during the same time period that the mechanical tests were being conducted. The first run up for the full load facility using inert gas with a moleweight of approximately 14 was made on June 24, 1984. The entire test facility was functional and the vibration looked very promising as indicated by all the vibration frequency scans. The thrust end horizontal spectrum plot given in Figure 9 was typical and indicated the absence of nonsynchronous vibration at the oil seal whirl frequency and very small components at or near the first rotor critical speed frequency. The entire project was considered to be satisfactory at that time.

The first run on contract "live" gas with a moleweight of 18.3 occurred on July 3, 1984. As indicated by Figure 10, a compressor speed of only 170 Hz (10,200 CPM) was possible before the vibration grew in excess of the overall acceptance level with re-excitation at the first critical frequency going as high as .038 mm (1.5 mils). Upon disassembly, no damage was found on the rotor. These results prompted the use of a standard balance piston shunt line modification to essentially reverse the flow on the back of the disk of the last stage impeller. A single feed line and circumferential groove was used to distribute the flow into the leading edge of the balance piston. This modification allowed maximum continuous speed to be obtained. The vibration had sub-synchronous pulsations with the steady levels at just over 0.6 mil and occasional spikes to 0.9 mil (see Fig. 11). The vibration was bounded and sustained operation was possible but the contract specification of .01 mm (0.4 mil) sub-synchronous was not satisfied. At that time and without bringing the unit down in speed, the loop gas was reduced in moleweight from 18.4 to 15.5. The compressor vibration reduced to acceptable levels indicating without doubt the aerodynamic origin of the excitation. These results gave increased evidence of the possibility that the balance piston labyrinth swirl excitation was a major contributor to the sub-synchronous instability. A unique modification was designed to produce a uniform swirl in the leading teeth of the balance piston. The orifice jets were directed against rotation to further negate or reduce any forward swirl of the balance piston gas. This modification was installed and on August 8, 1984, the compressor was capable of full speed operation with acceptable nonsynchronous vibration (see Fig. 12). A cross-section of this particular balance piston modification is given in Figure 13. This design is now referred to as the NEGASWIRL Insert (patent pending).

The results for the thrust end probes for year six design point are shown in Figure 14 where the average sub-synchronous levels are indicated to be less than .005 mm (0.2 mil). The compressor aerodynamic performance mandated that a new lower design speed be selected to match the field required flow and pressure condition. The results for the second unit for its new year six design point ($N = 10622$ CPM = 177 Hz) is shown in Figure 15. The nonsynchronous vibration levels are indicated to be only slightly higher than the unit one levels, while the synchronous component was lower indicating a slightly better dynamic balance condition for unit two. The overall vibration levels were within contract specification.

EVALUATION OF DESIGN STANDARDS FOR CENTRIFUGAL COMPRESSORS

The design standard from reference (5) has been overplotted with the inert gas run, the run limit without NEGASWIRL, and the operation with NEGASWIRL. It is evident that operation less than the unacceptable line can only be achieved by the incorporation of 1) stabilized oil seal designs and 2) balance piston and other labyrinth seal designs that enhance stable operation. The general slope of this standard

is believed to be valid and the region to the left of the design limit bandwidth is considered to be fully achievable with standard design features.

Upon completion of the unit one testing on this order, a new computer analysis for labyrinth seals was developed following the theory and general analysis of Iwatsubo (6) and Childs (7). The results of the stability of the compressor using each labyrinth seal stiffness and damping characteristic as calculated from this new program is given in Table 4. The influence of the moleweight reduction from 18.3 to 14 drops the growth factor from 7.3 to 5.5. Removing the balance piston influence results in a growth factor of 2.4 for the 18.3 moleweight condition.

The vibration spectrum from these units and other high pressure gas compressor units operating in the field have common characteristics. The nonsynchronous vibration pulses in a nonsteady fashion with occasional larger spikes that are quickly suppressed. To reject a machine for an occasional rise over the specification which is proven to be bounded and harmless is not realistic. To standardize the acceptance of units in the field and machines on full load test, the following standard has been developed to judge the acceptance of nonsteady sub-synchronous vibration.

The magnitude of any discrete nonsynchronous vibration shall not exceed 40% of the standard overall vibration acceptance limit (with N_{mcos} = RPM):

Compressors:

$$R_{\text{non-syn}} \text{ (mil peak to peak)} \leq 0.4 \sqrt{12000/N_{mcos}}$$

Turbines and Expanders:

$$R_{\text{non-syn}} \text{ (mil peak to peak)} \leq 0.4 \times 1.15 \times \sqrt{12000/N_{mcos}}$$

The magnitude of the discrete frequency component shall be measured using eight (8) or more exponential averages. A frequency range of 0-250 Hz shall be used for units with design speeds less than 7500 RPM, 0-500 Hz shall be used for units with design speeds greater than 7,500 but less than 15,000 RPM, and 0-1000 Hz shall be used for units having design speeds greater than 15,000 but less than 40,000 RPM. The frequency spectrum shall be monitored at the maximum continuous operating speed. If the nonsynchronous vibration is consistent to the point that the average level is above 40% of the acceptable overall level, alternate designs should be considered to enhance the rotor stability.

RECOMMENDATIONS

The following recommendations can be given as a result of the analysis and results of the full load testing reported in this paper.

1. It is essential to test under the actual gas moleweight condition to verify compressor stability.
2. The analysis of labyrinth seal characteristics are required to predict the aerodynamic excitation of the impeller labyrinth seals and the balance piston.
3. The stability analysis should consider locked seal excitation for rotor stability. Oil seal holding force must be adequate to prevent seal whirl which can result from low compressor suction pressure or seal element distortion.

4. The upper design limit for growth factor is considered to be +15 (log decrement of -.07) when oil seal and aerodynamic excitations are accounted for. The value of zero growth factor should remain the design limit for new machinery.
5. Acceptance specification for nonsynchronous vibration under field or simulated field conditions should be based on an average level as proposed in this paper. The overall vibration limit, warning limit, and trip level are not altered by these considerations.

REFERENCES

1. Booth, D., "Phillips Landmark Injection Project," *Petroleum Engineer*, October 1975, pp. 105-109 (Ekofisk).
2. Smith, K. J., "An Operating History of Fractional Frequency Whirl," *Proceedings of the Fourth Turbomachinery Symposium*, Texas A & M University, College Station, Texas, 1974, pp. 115-125.
3. Kirk, R. G. and Miller, W. H., "The Influence of High Pressure Oil Seals on Turbo-Rotor Stability," *ASLE Trans.*, Vol. 22, No. 1, January 1979, pp. 14-24.
4. Fulton, J. W., "The Decision to Full Load Test a High Pressure Centrifugal Compressor in Its Module Prior to Tow-Out," Conference Paper C45/84, I MECH E Conference Publication 1984-2.
5. Kirk, R. G. and Donald, G. H., "Design Criteria for Improved Stability of Centrifugal Compressor, ROTOR DYNAMICAL INSTABILITY, AMD - Vol. 55, 1983, pp. 59-72.
6. Iwatsubo, T., Matooka, N., and Kawai, R., "Spring and Damping Coefficients of the Labyrinth Seal," *NASA CP 2250*, 1982, pp. 205-222.
7. Childs, D. W. and Scharrer, J.K., "An Iwatsubo-Based Solution for Labyrinth Seals - Comparison to Experimental Results," *Rotordynamic Instability Problems in High Performance Turbomachinery - 1984*, Texas A & M University, College Station, Texas, May 28-30, 1984.

	C-radial (in.)	N(RPM) = 5000	7500	10000	12500
TEST 70 PSI	.003	-45.8	-13.5	1.5	10.2
FIELD 250 PSI	.005	-55	-10	-2.65	12.8

TABLE 1 - STABILITY GROWTH FACTORS WITH SEALS AT PREDICTED OPERATING CLEARANCE FOR TEST AND FIELD CONDITIONS
ORIGINAL SEALS: 1.25 IN. OUTER SEALS

	C-radial (in.)	N(RPM) = 5000	7500	10000	12500
TEST 70 PSI	.003 .004 .005	-35.2 -31.9 -30.2	-15.3 -15.7 -15.4	-4.95 -7.15 -7.58	1.17 -1.83 -3.2
FIELD 250 PSI	.003 .004 .005	-54.5 -46 -39.9	-11.6 -15.8 -17.9	10.0 2.07 -3.5	22.6 13.5 6.4

TABLE 2 - STABILITY GROWTH FACTORS FOR TEST AND FIELD CONDITIONS FOR THREE SEAL CLEARANCE CONDITIONS
REDESIGN SEALS: REDUCED SEAL LIP O.D.; 1.0 IN. OUTER SEAL

	Q(lb/in)	100	1000	10000	50000
Worst Case		3.38	4.22	12.3	45.5
Normal Conditions for Seals		-.3	.5	8.39	40.8

TABLE 3 - STABILITY GROWTH FACTORS FOR WORST CASE AND NORMAL SEAL LOADING CONDITIONS
REDESIGN SEALS: INFLUENCE OF Q - AERODYNAMIC CROSS-COUPLING

----Condition----		Total	W/O Bal. P.	W/O B.P. or Oil Seals
Baseline	Aero=0.0	-2.6	-2.6	-6.5
Labyrinth Analysis	MW=14 MW=18.3	5.5 7.3	1.59 2.37	-2.4 -1.7

TABLE 4 - RESULTS OF GROWTH FACTOR AT N = 194.17 HZ (11650 RPM)
NOTE: 1.0 LB/IN = 0.175 N/mm

ORIGINAL PAGE IS
OF POOR QUALITY

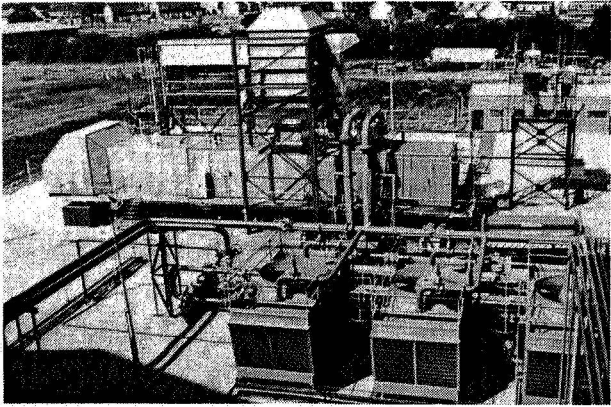


Figure 1. - Full-load test facility.

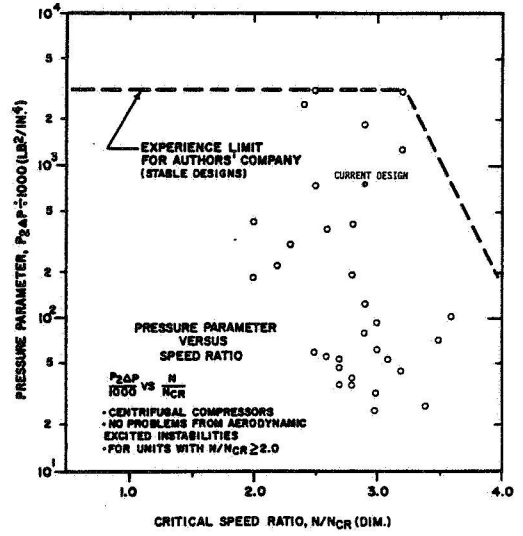


Figure 2. - Current design conditions.

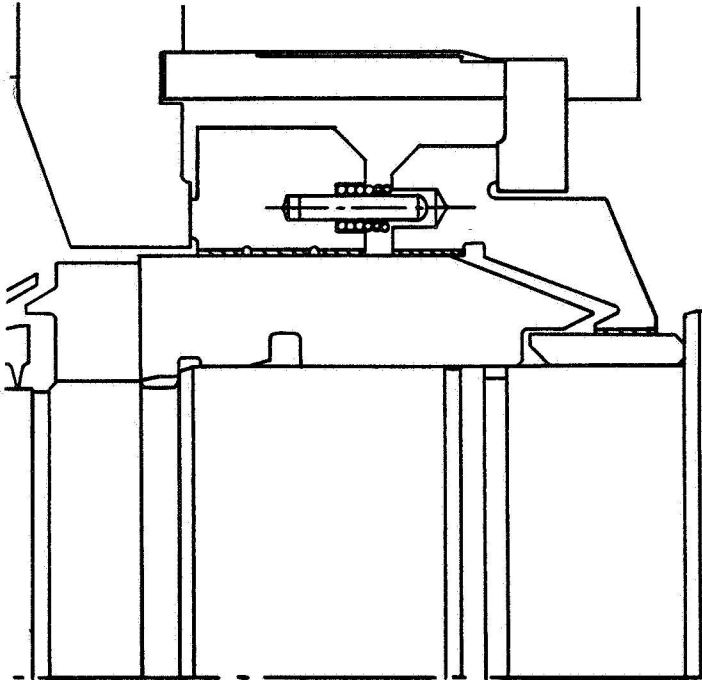


Figure 3. - Typical cone seal.

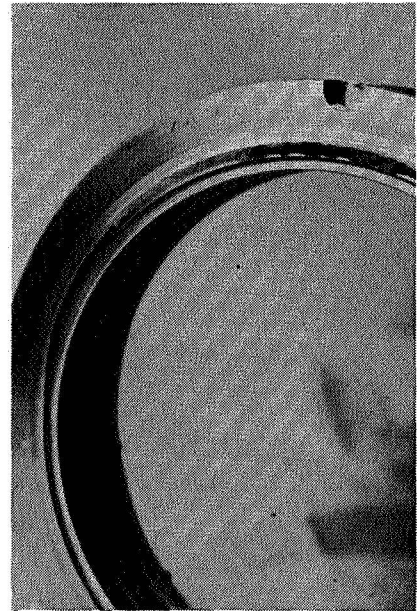


Figure 4. - Damaged seal ring.

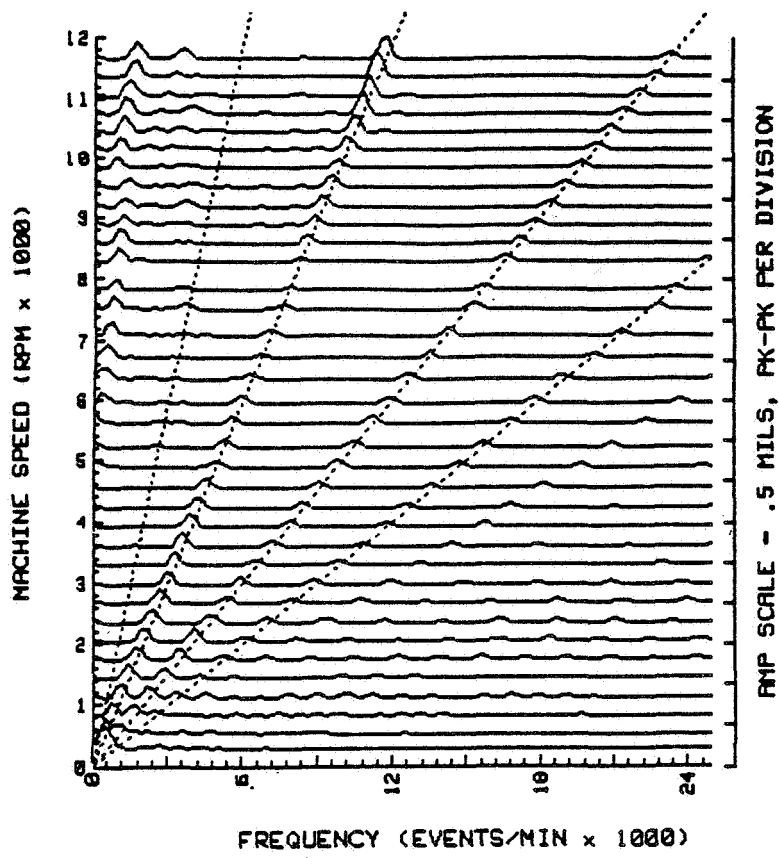


Figure 5. - Vibration resulting from oil ring seal whirl.

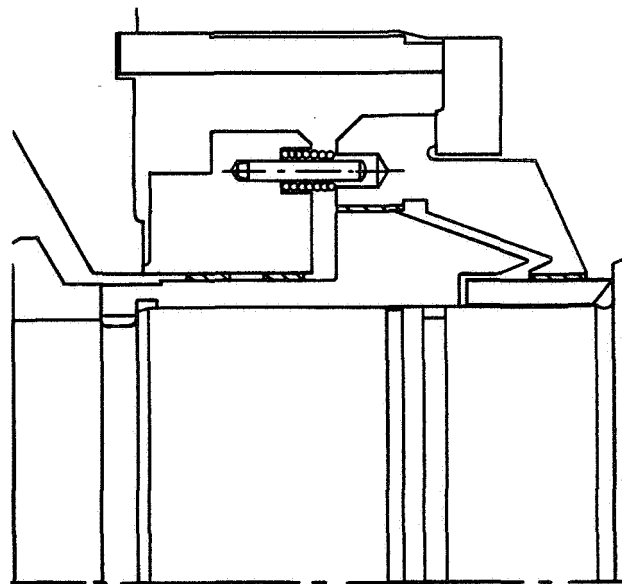


Figure 6. - Pressure balanced seal.

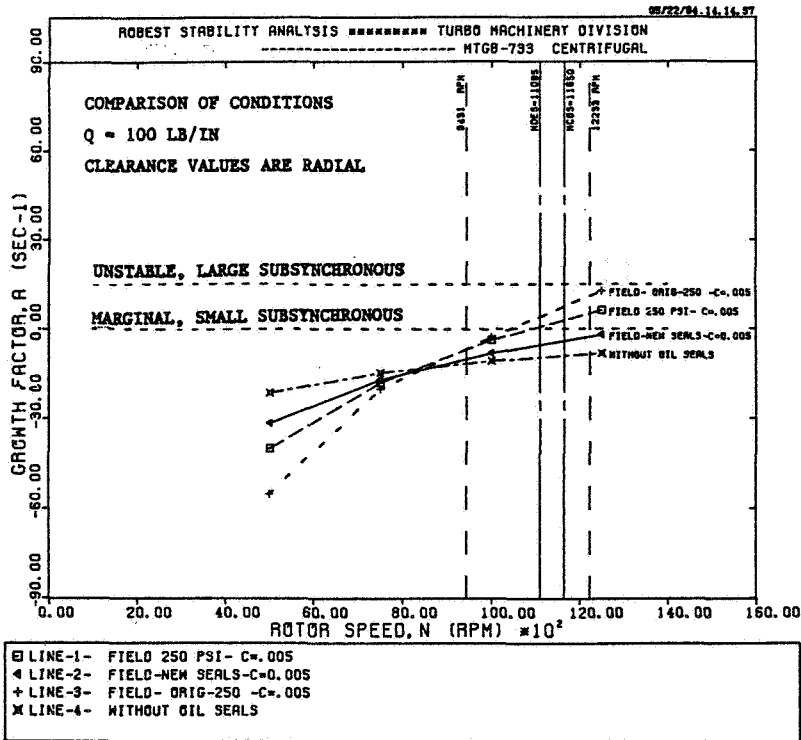


Figure 7. - Comparison of seal type versus rotor speed.

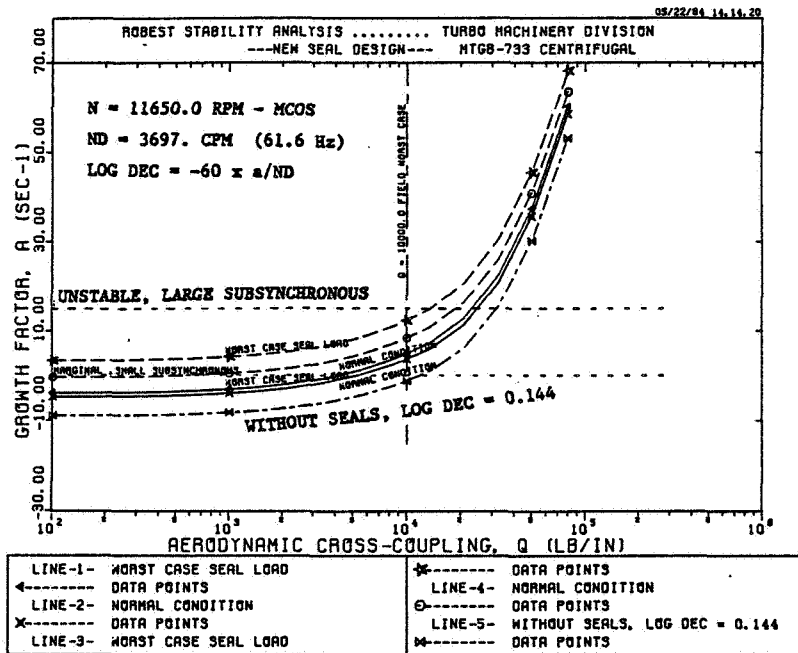


Figure 8. - Influence of aerodynamic excitation at M.C.O.S.

RUNDOWN
 RUN: 5
 MACHINE ID:
 PROBE ID:
 DATE: 3 JULY 84
 COMPRESSOR
 COMP AFT HORZ

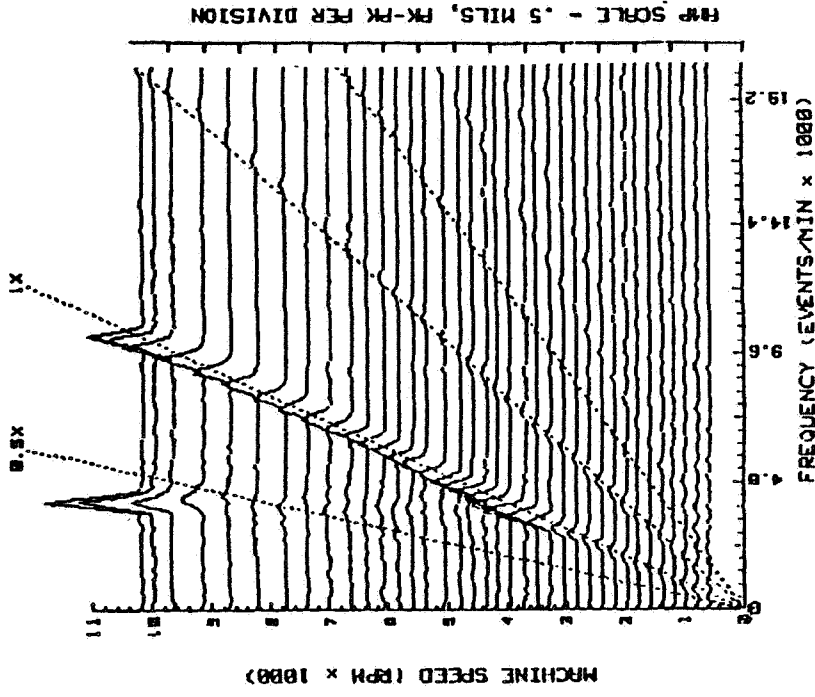


Figure 10. - Shutdown with live gas.

RUNDOWN
 RUN: 2
 MACHINE ID:
 PROBE ID:
 DATE: 24 JUNE 84
 COMPRESSOR
 AFT END HORZ

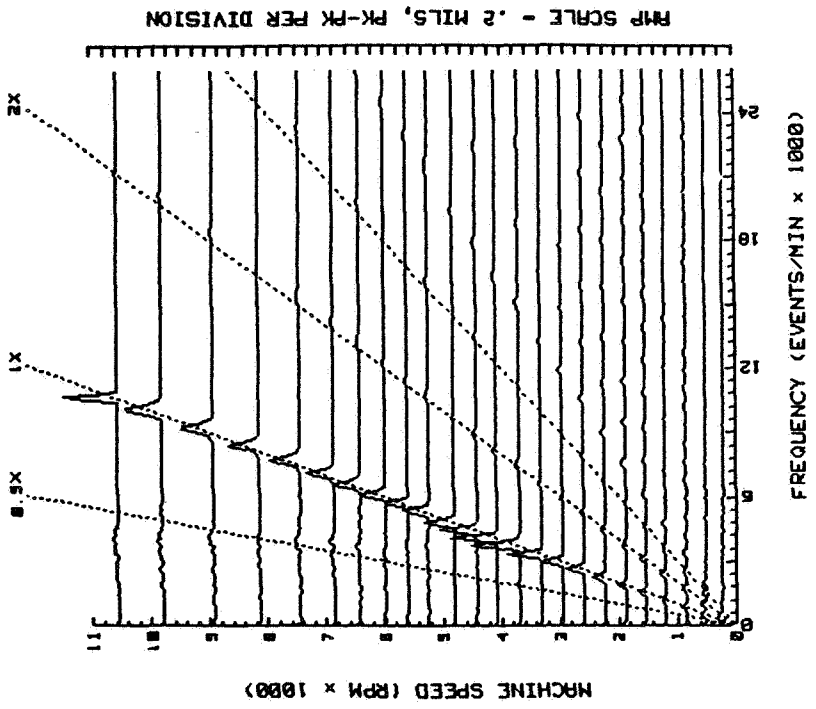


Figure 9. - Shutdown with inert gas.

TRAIN ID: 90560 UNIT 1
 MACHINE ID: COMPRESSOR K200
 PROBE ID: COMP AFT HORZ
 DATE: 8-AUG-84
 RUNUP
 RUN: 15

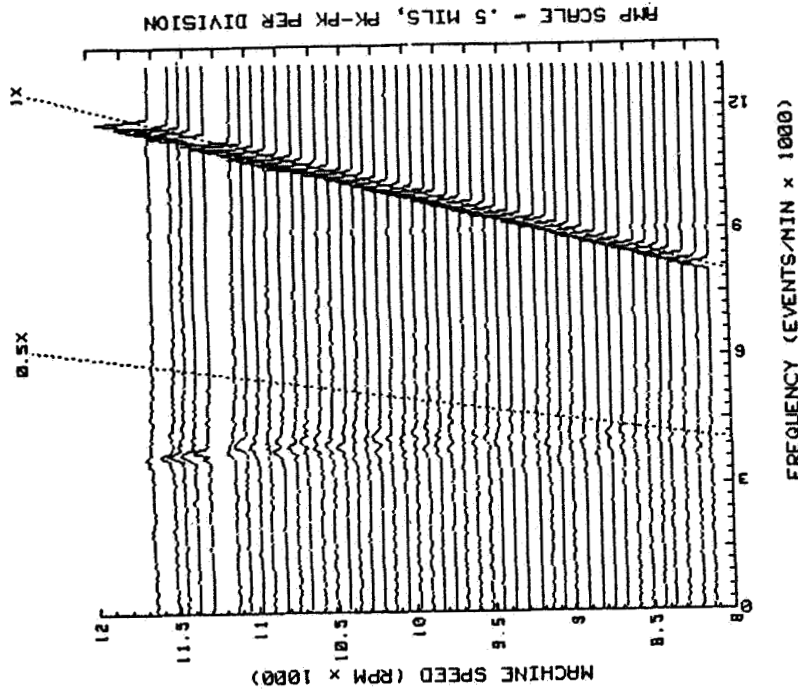


Figure 12. - Runup with negaswirl.

MACHINE ID: COMPRESSOR
 PROBE ID: AFT HORZ
 DATE: 17 JULY 84
 RUNDOWN
 RUN: 8

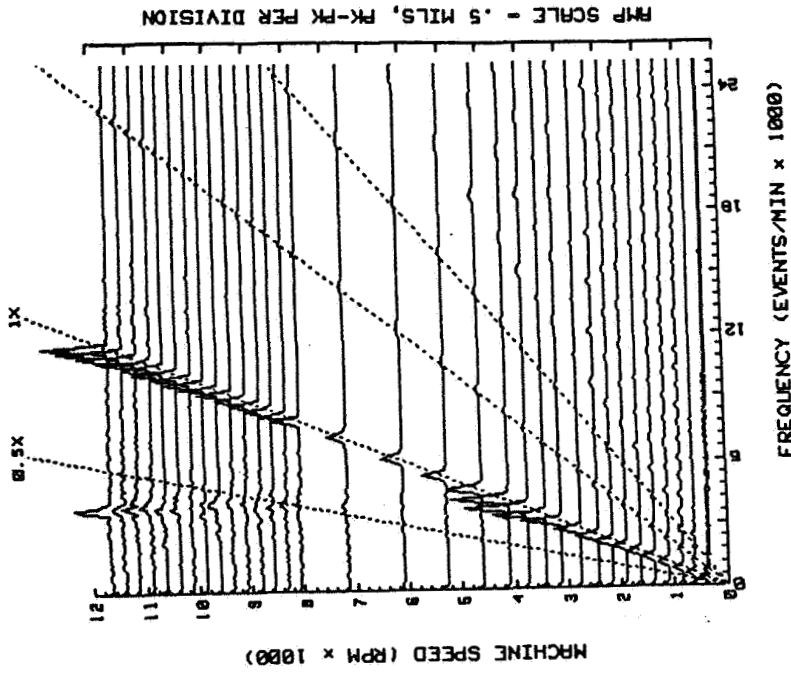


Figure 11. - Rundown with balance piston shunt line.

ORIGINAL PAGE IS
OF POOR QUALITY

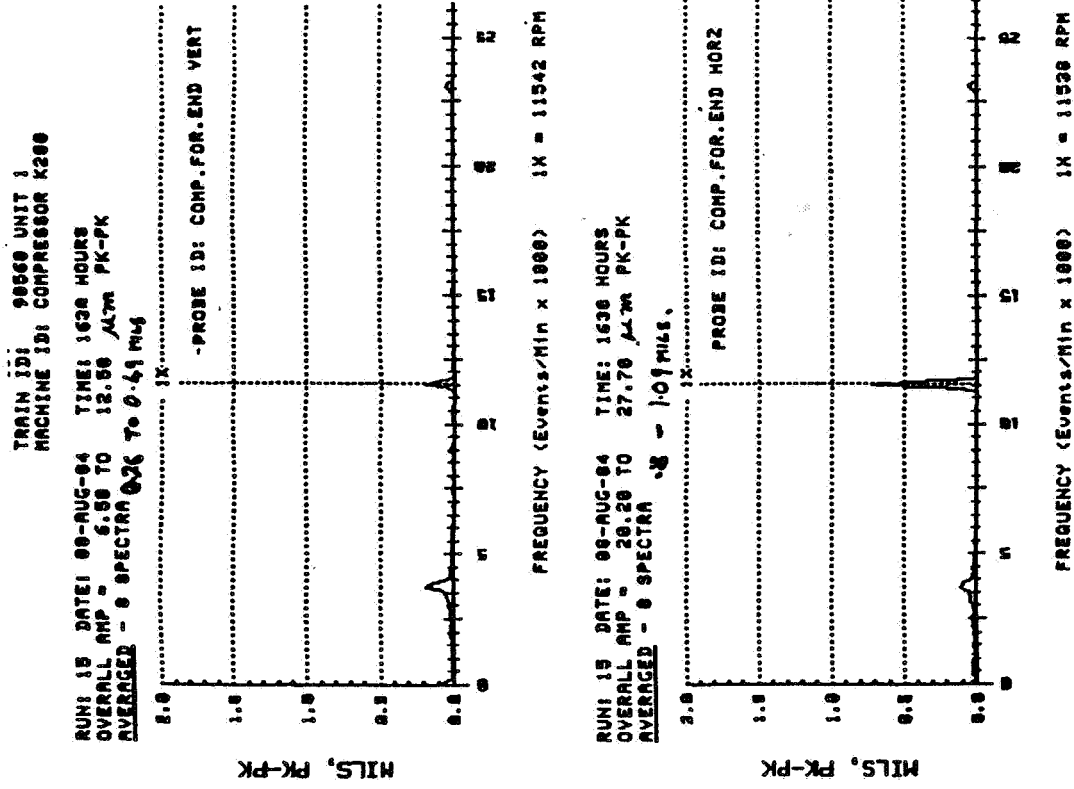


Figure 14. - Unit one.

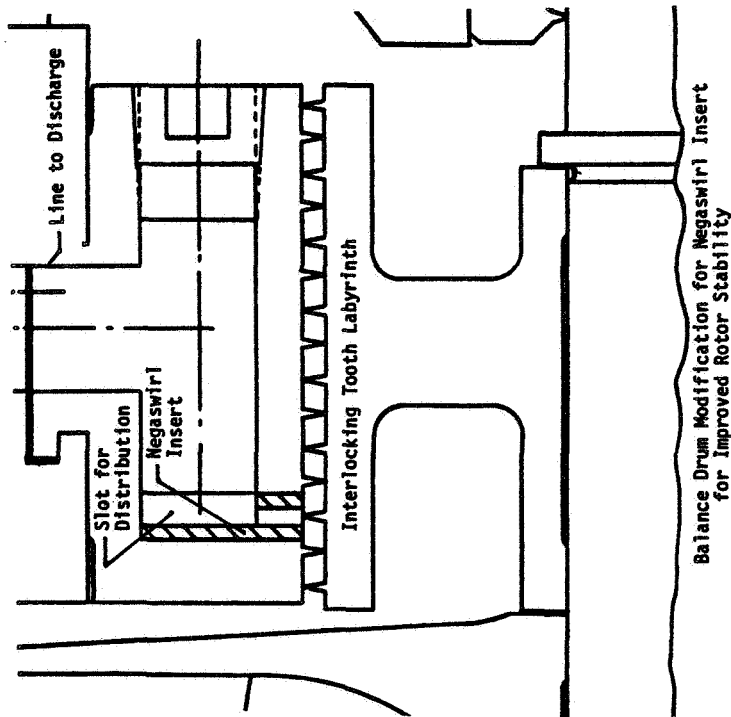
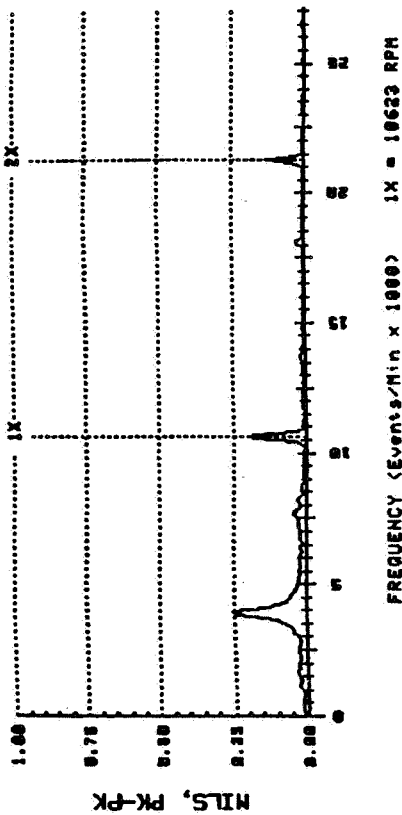


Figure 13. - Typical balance piston.

TRAIN ID: 9060-UNIT 2
 MACHINE ID: COMPRESSOR

RUN: 12 DATE: 24-OCT-84 TIME: 1523 HRS PROBE ID: APT VERT
 OVERALL AMP = 0.45 TO 0.94 MILS, PK-PK
 AVERAGED - 6 SPECTRA



RUN: 12 DATE: 24-OCT-84 TIME: 1523 HRS PROBE ID: APT HORZ
 OVERALL AMP = 0.39 TO 0.94 MILS, PK-PK
 AVERAGED - 6 SPECTRA

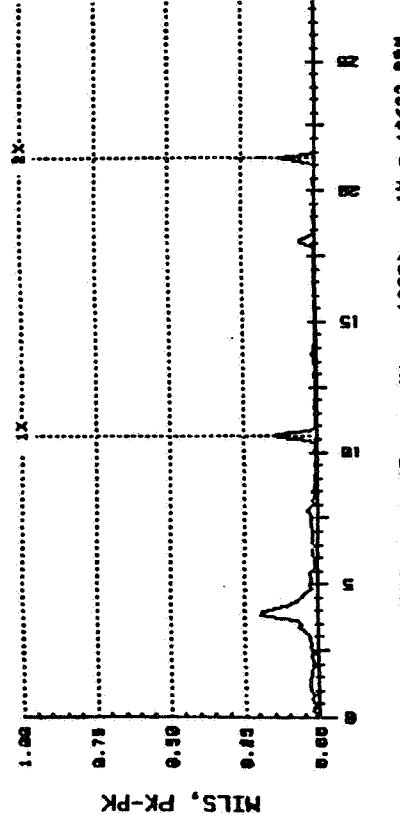


Figure 15. - Unit two.

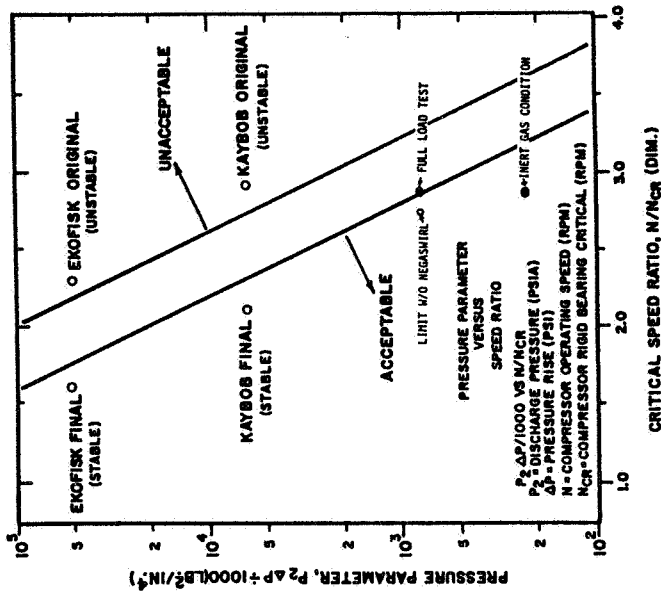


Figure 16. - Compressor design map showing full load test conditions of interest.

INSTABILITY ANALYSIS PROCEDURE FOR THREE-LEVEL
MULTI-BEARING ROTOR-FOUNDATION SYSTEMS

Shixiang Zhou and Neville F. Rieger
Stress Technology Incorporated
Rochester, New York 14623

A procedure for the instability analysis of three-level multi-span rotor systems is described. This procedure is based on a distributed mass-elastic representation of the rotor system in several eight-coefficient bearings. Each bearing is supported from an elastic foundation on damped, elastic pedestals. The foundation is represented as a general distributed mass-elastic structure on discrete supports, which may have different stiffnesses and damping properties in the horizontal and vertical directions. This system model is suited to studies of instability threshold conditions for multi-rotor turbomachines on either massive or flexible foundations. The instability condition is found by obtaining the eigenvalues of the system determinant, which is obtained by the transfer matrix method from the three-level system model. The stability determinant is solved for the lowest rotational speed at which the system damping becomes zero in the complex eigenvalue, and for the whirl frequency corresponding to the natural frequency of the unstable mode. An efficient algorithm for achieving this is described. Application of this procedure to a rigid rotor in two damped-elastic bearings and flexible supports is described. A second example discusses a flexible rotor with four damped-elastic bearings. The third case compares the stability of a six-bearing 300 Mw turbine generator unit, using two different bearing types. These applications validate the computer program and various aspects of the analysis.

INTRODUCTION

Problems of rotor instability continue to occur in modern turbomachinery as stability limits for speed, power, and flexibility are pressed more closely by advanced rotating equipment. Established methods for raising the instability threshold speed, such as flexible supports, stable bearing types, etc., are sometimes unable to accommodate operational requirements imposed by such designs. At the same time, demands for simpler and less costly support structures can introduce additional vibration problems to the turbomachine-foundation structure, which may further influence the instability threshold speed of the rotor system.

The purpose of the paper is to describe a general-purpose multi-bearing rotordynamics computer code for the calculation of instability whirl threshold speeds for three-level rotor systems, of the type shown in figure 1. The rotor has distributed mass-elastic properties, and may carry massive disks at the end of each shaft section. The usual linear eight-coefficient representation of bearing dynamic

properties is employed at each support location, and each bearing may be mounted upon a massive pedestal which is flexibly supported with damping from the foundation structure. The foundation also has distributed mass-elastic properties with allowance for concentrated masses at the ends of each foundation section. The foundation is mounted on discrete, damped, flexible supports which attach it to ground. The pedestal supports and the foundation supports both attach to the foundation, but not necessarily at the same locations: see figure 1. In this manner the influence of massive pedestals, and of a flexible, tuned foundation on the instability threshold of a multi-bearing rotor may be obtained.

NOMENCLATURE

A	Cross sectional area of shaft
c	Radial bearing clearance
C_{px}, C_{py}	Pedestal damping coefficient
$C_{xx}, C_{xy}, C_{yx}, C_{yy}$	Bearing damping coefficient
E	Young's modulus
F_x, F_y	Bearing reaction forces
I_x, I_y	Cross sectional moment of inertia
I_p	Polar mass moment of Inertia
I_T	Transverse mass moment of inertia
K_{px}, K_{py}	Pedestal stiffness coefficient
$K_{xx}, K_{xy}, K_{yx}, K_{yy}$	Bearing stiffness coefficients
L_n	Length of shaft section between station n and $n+1$
M_n	Bending moment to the left of station n
M'_n	Bending moment to the right of station n
M_{px}, M_{py}	Pedestal mass components
m_n	Mass at rotor station n
t	Time
V_n	Shear force to the left of station n
V'_n	Shear force to the right of station n
W	Bearing static load
x, y	Components of rotor whirl displacement
z	Axial coordinate along rotor
θ_x, θ_y	Components of deflected rotor slope
ω	Angular frequency of rotor
ω_n	Critical frequency of rotor
f_{rth}	Frequency ratio = ω_w / ω_{th}
Δ	Determinant of matrix
Δ_c	Real part of determinant

Δ_s	Imaginary part of determinant
ω_{th}, N_{th}	Threshold frequency, threshold speed
ω_w	Whirl frequency ($= \omega_{th} \times f_{rth}$)

PREVIOUS WORK

Studies of the instability properties of multi-bearing rotor systems are comparatively rare in the open literature. The earliest rotordynamic analysis of such systems appears to date back to Borowicz [1] in 1915, while numerical procedures for multi-rotor systems were initiated by Prohl [2] in 1945 for critical speeds, and by Koenig [3] in 1961 for multi-rotor system unbalance response studies with damped flexible bearings. More advanced multi-bearing rotor system procedures and codes were developed by Lund and others, for unbalance response and instability analysis of discrete rotor models [4], and for analysis of distributed mass-elastic rotors [5] and [6]. Critical speeds of multi-rotor systems with flexible bearing were also studied by Crook and Grantham [7]. Other multi-bearing rotordynamic codes were developed by Shapiro and Reddi [8], Zorzi and Nelson [9] using the finite element method, and by Gunter [10]. Most of these studies have included the influence of massive flexible pedestals, but there do not appear to have been any published studies in which the influence of pedestals and a general mass-elastic foundation on flexible supports is included. Most studies have concentrated on the influence of multiple spans on critical speeds and unbalance response, or on the influence of massive flexible supports on such properties. The only previous multi-bearing flexible support study which deals with instability threshold speed appears to be that by Lund [6]. The code upon which Lund's study is based includes pedestal effects, but not distributed foundation effects. Lund's study is noteworthy for the experimental confirmation of the theoretical threshold speed predictions which it includes.

SYSTEM MODEL

The system model used in this analysis is shown in figure 1. This model allows details of the rotor, bearings, pedestals, distributed foundation, and foundation supports to be included in the system response results. The number of rotor stations and the number of bearing and foundation supports, is limited only by the computer space available. Rotor stations and foundation stations are independent, and may be included as required within the system model.

The rotor is massive and elastic and its internal damping is small enough to be neglected. As the rotor is symmetric about its axis of rotation, it is modeled using circular cylindrical sections having mass, elasticity, rotatory and polar inertia properties distributed along their length. Both transverse bending and shear effects contribute to the rotor stiffness. The rotor is referred to as the first level of the system. For analysis a rotor is divided into uniform shaft sections, and large disks with concentrated mass and inertia properties are included at rotor stations at the ends of the shaft sections, i.e., at the stations designated 1, 2, 3, etc., in figure 1. For instability studies the rotor unbalance is omitted for this model.

The bearings which support the rotor at specified stations are represented by the well-known eight stiffness and damping coefficient procedure, which includes

both direct and cross-coupled relative displacement and relative velocity effects, between the journal and the pedestal motions. The bearing properties are therefore linear for small displacements, in keeping with the rest of the structural components. The pedestals which support the bearings are represented by mass properties in the x- and y- directions (no inertia properties), and they are supported by elastic, damped members in these directions. This model allows two-dimensional transverse pedestal dynamics (without support coupling) to be included. The pedestals are the second level of the system model.

The foundation is a continuous structural member which has different mass-elastic properties in the x- and y- directions. It is modeled in a similar manner to the rotor, using prismatic shear-beam members with distributed properties between stations. Discrete mass effects such as casing mass, generator stator, gearbox, etc., are incorporated at the end stations. The foundation supports are represented by concentrated elastic-damping elements at the ends of the beam sections, as required, in a similar manner to the rotor bearing-pedestal supports. The foundation supports possess different stiffness and damping properties in the x- and y- directions. The foundation is the third level of the system model.

FORCES AND MOMENTS ON ROTOR STATIONS

The convention and notation used in this analysis are shown in figure 2, for the x-z plane. Similar expressions apply for the y-z plane. The forces and moments which act on the n-th rotor station are shown in figure 3. They are considered in the following manner.

- a. Inertia forces. The inertia forces which act on the concentrated mass of the rotor station at angular frequency ω are given by:

$$\begin{aligned}\Delta V_{xM} &= -m \frac{\partial^2 x}{\partial t^2} = m\omega^2 x \\ \Delta V_{yM} &= -m \frac{\partial^2 y}{\partial t^2} = m\omega^2 y\end{aligned}\tag{1}$$

- b. Inertia moments. The inertia moments which act on the concentrated translatory and polar inertias at the rotor station at angular frequency ω are given by:

$$\begin{aligned}\Delta M_{xM} &= (I_p - I_T)\omega^2 \theta_x \\ \Delta M_{yM} &= (I_p - I_T)\omega^2 \theta_y\end{aligned}\tag{2}$$

- c. Bearing reactions. Each bearing is represented by eight stiffness and damping coefficients in the customary manner. The bearing forces are given by:

$$\begin{aligned}\Delta V_{xB} &= -K_{xx}(x - x_p) - C_{xx}(\dot{x} - \dot{x}_p) - K_{xy}(y - y_p) - C_{xy}(\dot{y} - \dot{y}_p) \\ \Delta V_{yB} &= -K_{yx}(x - x_p) - C_{yx}(\dot{x} - \dot{x}_p) - K_{yy}(y - y_p) - C_{yy}(\dot{y} - \dot{y}_p)\end{aligned}\tag{3}$$

Here x_p and y_p are the pedestal displacements, and \dot{x}_p and \dot{y}_p are the pedestal velocities. The cross-coupling terms in these expressions couple the bearing and pedestal displacements and velocity. The bearing coefficients are functions of Sommerfeld number, bearing type, and Reynolds number if turbulent flow is involved. The influence of bearing moments on the rotor is usually small and is neglected in this analysis.

FORCES AND MOMENTS ON SHAFT SECTIONS

The analysis procedure for the shaft follows the distributed mass-elastic method described by Lund and Orcutt [5], with the difference that the harmonic unbalance components are zero in the fourth-order equations of motion. This procedure is not repeated here, but is similar to that given in the next section for the foundation analysis.

FORCES AND MOMENTS ON FOUNDATION SECTIONS

A section of the foundation between stations r and $r+1$ is shown in figure 4. The foundation analysis is performed by developing a transfer matrix for each section, in a similar manner to the rotor analysis. The structure is sub-divided into uniform shear-beam sections. All speed-dependent terms in the foundation equations are zero, and the foundation is allowed to have different stiffness properties in the horizontal and vertical directions. The equations of motion for a uniform foundation beam section between end stations in the x - and y -directions are.

$$EI_x \frac{\partial^4 x_f}{\partial z^4} - \rho I_x \left\{ \frac{E}{\alpha_x G} + \frac{I_{Tx}}{\rho I_x} \right\} \frac{\partial^4 x_f}{\partial z^2 \partial t^2} + \rho A \frac{\partial^2 x}{\partial t^2} + \frac{\rho I_{Tx}}{\alpha_x G} \frac{\partial^4 x_f}{\partial t^4} = 0 \quad (4a)$$

$$EI_y \frac{\partial^4 y_f}{\partial z^4} - \rho I_y \left\{ \frac{E}{\alpha_y G} + \frac{I_{Ty}}{\rho I_y} \right\} \frac{\partial^4 y_f}{\partial z^2 \partial t^2} + \rho A \frac{\partial^2 y}{\partial t^2} + \frac{\rho I_{Ty}}{\alpha_y G} \frac{\partial^4 y_f}{\partial t^4} = 0 \quad (4b)$$

To solve these expressions set

$$x_f = \bar{x}_f e^{i\omega t} \quad (5)$$

$$y_f = \bar{y}_f e^{i\omega t}$$

Substituting gives the expressions

$$EI_x \frac{d^4 \bar{x}_f}{dz^4} + \rho I_x \omega^2 \left\{ \frac{E}{\alpha_x G} + \frac{I_{Tx}}{\rho I_x} \right\} \frac{d^2 \bar{x}_f}{dz^2} - \rho A \omega^2 \left\{ 1 - \frac{\omega^2 I_{Tx}}{\alpha_x GA} \right\} \bar{x}_f = 0 \quad (6a)$$

$$EI_y \frac{d^4 \bar{y}_f}{dz^4} + \rho I_y \omega^2 \left\{ \frac{E}{\alpha_y G} + \frac{I_{Ty}}{\rho I_y} \right\} \frac{d^2 \bar{y}_f}{dz^2} - \rho A \omega^2 \left\{ 1 - \frac{\omega^2 I_{Ty}}{\alpha_y GA} \right\} \bar{y}_f = 0 \quad (6b)$$

The form of these equations is identical, and they are uncoupled because of the coordinate symmetry. Where $I_x \neq I_y$, the x- and y- equations must be solved separately. To demonstrate the solution procedure for the x- direction, write

$$2\sigma^2 \lambda^2 = \omega^2 \left\{ \frac{\rho}{\alpha G} + \frac{I_T}{EI} \right\}; \quad \lambda^4 = \frac{\rho A \omega^2}{EI} \left\{ 1 - \frac{\omega^2 I_T}{\sigma GA} \right\} \quad (7)$$

Substitution in equation 6a gives

$$\frac{d^4 \bar{x}_f}{dz^4} + 2\sigma^2 \lambda^2 \frac{d^2 \bar{x}_f}{dz^2} - \lambda^4 \bar{x}_f = 0 \quad (8)$$

The solution to this expression is

$$\bar{x}_f = D_1 \cosh \lambda_1 z + D_2 \sinh \lambda_1 z + D_3 \cos \lambda_2 z + D_4 \sin \lambda_2 z \quad (9)$$

where $D_1, D_2, D_3,$ and D_4 are integration constants to be determined from the boundary conditions. The eigenvalues of these expressions are given by

$$\lambda_1 L_f = \lambda L_f \left\{ \sqrt{1 + (\sigma \lambda)^4} - (\sigma \lambda)^2 \right\}^{\frac{1}{2}} \quad (10)$$

$$\lambda_2 L_f = \lambda L_f \left\{ \sqrt{1 + (\sigma \lambda)^4} + (\sigma \lambda)^2 \right\}^{\frac{1}{2}}$$

The boundary conditions for the foundation section are:

$$z = 0; \quad x_f = x_{fn}, \quad \theta = \theta_{fn}, \quad M_f = M_{fn}, \quad V_f = V_{fn}$$

At the other end of the section $z = L_{fn}$; $x_f = x_{f,n+1}$, $\theta_f = \theta_{f,n+1}$, $M_f = M_{f,n+1}$, $V_f = V_{f,n+1}$.¹ Upon substitution the required transfer matrix expressions for the foundation become:

¹The simplest procedure is to eliminate the distributed rotary inertia effects I_{Tx} , I_{Ty} and to account for these terms by using lumped inertia where necessary at the end of the foundation section. Thus we will neglect I_{Tx} and I_{Ty} .

$$\begin{aligned}
x_{f,n+1} &= b_{1n} x_{f,n} + L_{f,n} b_{3n} \theta_{x,n} + h_{2n} b_{4n} M'_{f,n} + h_{3n} b_{7n} V'_{f,n} \\
\theta_{f,n+1} &= \frac{1}{3} \phi_n \cdot h_{2n} b_{5n} L_{f,n} + b_{2n} \theta_{x,n} + h_{1n} b_{6n} M'_{f,n} + h_{2n} b_{4n} V'_{f,n} \\
M_{f,n+1} &= \frac{1}{2} \phi_n L_{f,n} b_{4n} x_n + \frac{1}{6} \phi_n L_{f,n}^2 b_{5n} \theta_{f,n} + b_{2n} M'_{f,n} + L_{f,n} b_{3n} V'_{f,n} \\
V_{f,n+1} &= \phi_n b_{3n} L_{f,n} + \frac{1}{2} \phi_n L_{f,n} b_{4n} \theta_{f,n} + \frac{1}{3} \phi_n h_{2n} b_{5n} M'_{f,n} + b_{1n} V'_{f,n}
\end{aligned} \tag{11}$$

$$\begin{aligned}
\text{where } b_{1n} &= (\lambda_1^2 \cosh \lambda_1 L_{f,n} + \lambda_2^2 \cos \lambda_2 L_{f,n}) / (\lambda_1^2 + \lambda_2^2) \\
b_{2n} &= (\lambda_2^2 \cosh \lambda_1 L_{f,n} + \lambda_1^2 \cos \lambda_2 L_{f,n}) / (\lambda_1^2 + \lambda_2^2) \\
b_{3n} &= (\lambda_1 \sinh \lambda_1 L_{f,n} + \lambda_2 \sin \lambda_2 L_{f,n}) / (\lambda_1^2 + \lambda_2^2) L_{f,n} \\
b_{4n} &= 2 (\cosh \lambda_1 L_{f,n} - \cos \lambda_2 L_{f,n}) / (\lambda_1^2 + \lambda_2^2) L_{f,n}^2 \\
b_{5n} &= 6 (\lambda_2 \sinh \lambda_1 L_{f,n} - \lambda_1 \sin \lambda_2 L_{f,n}) / (\lambda_1^2 + \lambda_2^2) \lambda^2 L_{f,n}^3 \\
b_{6n} &= (\lambda_2^3 \sinh \lambda_1 L_{f,n} + \lambda_1^3 \sin \lambda_2 L_{f,n}) / (\lambda_1^2 + \lambda_2^2) \lambda^2 L_{f,n} \\
b_{7n} &= 6 (\lambda_1^3 \sinh \lambda_1 L_{f,n} - \lambda_2^3 \sin \lambda_2 L_{f,n}) / (\lambda_1^2 + \lambda_2^2) \lambda^4 L_{f,n}^3 \\
h_{1n} &= L_{f,n} / EI; \quad h_{2n} = L_{f,n}^2 / 2EI; \quad h_{3n} = L_{f,n}^3 / 6EI \\
\phi_n &= \omega^2 \rho A L_{f,n}
\end{aligned} \tag{12}$$

The solution for the foundation in the y-direction is similar to the above.

THREE-LEVEL SYSTEM

Details of the rotor-pedestal-foundation models are shown in figure 5. Using the notation shown, the equations governing the harmonic motion of this system in the x-z plane are:

$$\begin{Bmatrix} F_{xcn} \\ F_{xsn} \end{Bmatrix} = \begin{bmatrix} K_{xx} & \omega C_{xx} & K_{xy} & \omega C_{xy} \\ -\omega C_{xx} & K_{xx} & -\omega C_{xy} & K_{xy} \end{bmatrix} \begin{Bmatrix} x_{cn} - x_{cnp} \\ x_{sn} - x_{snp} \\ y_{cn} - y_{cnp} \\ y_{sn} - y_{snp} \end{Bmatrix} \quad (13)$$

$$\begin{Bmatrix} F_{xcnf} \\ F_{xsnf} \end{Bmatrix} = \begin{bmatrix} K_{xp} & \omega C_{xp} \\ -\omega C_{yp} & K_{yp} \end{bmatrix} \begin{Bmatrix} x_{cnp} - x_{cnf} \\ x_{snp} - x_{snf} \end{Bmatrix} \quad (14)$$

$$\begin{Bmatrix} F_{xcnf} - F_{xcn} \\ F_{xsnf} - F_{xsn} \end{Bmatrix} = \begin{bmatrix} M_{px} & 0 \\ -0 & M_{px} \end{bmatrix} \begin{Bmatrix} x_{cnp} \\ x_{snp} \end{Bmatrix} \quad (15)$$

where ω is the rotor exciting frequency. Similar expressions apply in the y-z direction. These expressions are used to obtain expressions for the rotor forces F_{xcn} , etc., the foundation forces F_{xcnf} , etc., and the pedestal displacements x_{cnp} , etc., in terms of the displacements of the rotor and the foundation. The transfer matrix procedure described in the previous section is then used to obtain the system transfer matrix. Assuming that the shear force and bending moment are zero at both ends of the structure, the boundary conditions may be written:

<u>Rotor</u>	<u>Foundation</u>
$\begin{aligned} V_{xc1} &= V_{xs1} = V_{yc1} = V_{ys1} = 0 \\ M_{xc1} &= M_{xs1} = M_{yc1} = M_{ys1} = 0 \\ V'_{xcr} &= V'_{xsr} = V'_{ycr} = V'_{ysr} = 0 \\ M'_{xcr} &= M'_{xsr} = M'_{ycr} = M'_{ysr} = 0 \end{aligned} \quad (16)$	$\begin{aligned} V_{xc1f} &= V_{xs1f} = V_{yc1f} = V_{ys1f} = 0 \\ M_{xc1f} &= M_{xs1f} = M_{yc1f} = M_{ys1f} = 0 \\ V'_{xcrf} &= V'_{xsrf} = V'_{ycrf} = V'_{ysrf} = 0 \\ M'_{xcrf} &= M'_{xsrf} = M'_{ycrf} = M'_{ysrf} = 0 \end{aligned} \quad (17)$

Starting from rotor station 1, the above equations are used to solve for the rotor equilibrium as described in reference [11]. Each unknown is applied separately, by setting $x_{c1} = 1$, with the other displacements zero; then apply $x_{s1} = 1$, others zero etc., through $y_{c1f} = 1$, others = zero; $y_{s1f} = 1$, others zero. This requires a total of sixteen calculations (eight rotor x,y; eight

foundations, x, y). A 16 by 16 matrix is formed from the resulting expressions. The determinant of the matrix is the system stability determinant. The lowest speed for which this matrix becomes zero is the instability threshold speed.

In general, there is no particular relationship between the number of stations of the rotor and the number of stations of the foundation, or from which locations the rotor is supported from pedestals and foundation in relation to the foundation support locations themselves. This independent rotor/foundation support situation is incorporated within the computer code by allowing a three-level support at all rotor and foundation support locations.

INSTABILITY THRESHOLD ALGORITHM

The stability determinant contains two unknowns, the rotational speed ω and the whirl frequency ratio fr_1 . In the general case, the eight dynamic fluid-film coefficients are functions of both ω and fr_1 , so that a closed form solution is not tractable. The solution is conveniently obtained by iteration as follows.

Step 1. Obtain points for Δc vs. fr_1 and Δs vs. fr_1 .

For a fixed value of ω , the real part Δc and the imaginary part Δs of the stability determinant are functions of fr_1 and so may be calculated. Several points for Δc vs. fr_1 are shown in figure 7(a), and data for Δs vs. fr_1 are shown in figure 7(b).

Step 2. Find zero points of Δc and Δs by quadratic interpolation.

As shown in figure 7(a), the program determines two frequency ratios fr_1 and fr_2 where the sign of Δc changes. Then a frequency ratio fr_3 which equals to $(fr_1 + fr_2)/2$ is applied for an additional calculation and obtain Δc of fr_3 . The three points with fr_1 , fr_2 and fr_3 form a quadratic curve which intersects the abscissa at f_{fcw} where Δc is zero. Similarly, in figure 7(b), the zero point of Δs is obtained at frequency ratio f_{rsw} .

Step 3. Obtain points for $fc(\Delta c = 0)$ vs. ω and $fs(\Delta s = 0)$ vs. ω .

Repeat Step 1 and Step 2 with different ω until the specified speed range has been calculated. Several points for $fc(\Delta c = 0)$ vs. ω may be obtained, and similarly for $fs(\Delta s = 0)$ vs. ω , as shown in figure 7(c).

Step 4. Determine threshold speed ω_{th} and corresponding frequency ratio f_{rth} .

Quadratic interpolation is again used. The program determines two speeds ω_1 and ω_2 where the sign of $(fc - fs)$ changes. Then a speed ω_3 which equals to $(\omega_1 + \omega_2)/2$ is applied for an additional calculation and obtain fc and fs of ω_3 . The three points of fc vs. ω form a quadratic curve, and similarly for fs vs. ω . The computer program then determines the intersection point of these two curves, i.e., ω_{th} and f_{rth} . ω_{th} is the threshold speed where both Δc and Δs are equal to zero, and f_{rth} is the corresponding frequency ratio of ω_{th} .

Theoretically, the real parts and imaginary parts of the determinants become higher order polynomials in ω and fr , and may have many zero points for each

value of ω . But in practical use, only the zero value encountered at the lowest speed is of interest. The computer program organizes the procedure and the lowest threshold speed is obtained.

Other features of this procedure may also be described briefly as follows. There are two ways to obtain the real and imaginary parts of the determinant of a matrix. One of them is to use a complex number for each determinant calculation. But for many digital computers, this will reduce accuracy because both real and imaginary parts of the complex number have only about a half of the significant digits that the real constant has in the double precision. Another way is to use a real constant for the determinant calculation to obtain real and imaginary parts, and both parts have the same significant digits in the double precision. The latter way was used in the computer program developed here. Greater accuracy is thereby obtained.

Because a higher exponent (either positive or negative) may occur on the real and imaginary parts of the stability determinant, measures have been taken to prevent from computer overflow or underflow in the determinant calculations. Furthermore, the eight bearing coefficients are often sensitive to the results of the threshold speed, so that they should be checked carefully beforehand. A parametric study of variation of bearing coefficients on the result of threshold speed has also been performed which confirms the above comments.

EXAMPLE 1. RIGID ROTOR ON TWO BEARINGS

The cylindrical rotor shown in figure 8 has been studied by Lund [4], and is supported in damped flexible bearings and pedestals. In this instance this system has been mounted upon a continuous foundation mounted on damped flexible columns. Details are given in table 1. The threshold speed of the rotor was calculated as (a) one-level system (rotor in damped flexible bearings, rigid pedestals, and rigid foundation), (b) a two-level system (rotor in the same damped flexible bearings, very stiff pedestals, and rigid foundation), (c) as a three-level system (rotor, bearings, very stiff pedestals, and very stiff foundation and foundation supports), (d) as a three-level system (rotor, bearings, very stiff pedestals, and soft foundation and foundation supports) and (e) as a two-level system (rotor, bearings and soft pedestals). Computed results for these five cases are shown in table 2. The one-level result was checked against the one-level result given by Lund. The two-level result (with very stiff pedestals) was also checked against the same result. The analysis and results were verified through two levels against known data. The effect of very stiff pedestals in case (b) did not differ from the case (a) result. The influence of a very stiff foundation in case (c) was also found to be small. The influence of a soft foundation in case (d) was found to be large, and the effect of soft pedestals in case (e) was also found to be large, showing that the effect of pedestals and/or foundation can be very important. These results are in agreement for a rigid rotor system with a massive foundation.

**ORIGINAL PAGE IS
OF POOR QUALITY**

TABLE 1.- DETAILS OF THREE-LEVEL, TWO-BEARING ROTOR SYSTEM EXAMPLE

TEST: INSTABILITY, 9 STATIONS, 2 BRG. (3 LEVEL)																		
INSTABILITY ANALYSIS		LEVEL	FRG-RATIO	IUNIT	IOMEGA	ICOEFF	NLIST	ALIST										
2		3	4	0	1	0	0	0.00E 00										
DATA FOR ROTOR:		STATIONS	BEARINGS															
		9	2															
DATA FOR FOUNDATION:		STATIONS	FOUNDATION SUPPORTS															
		9	2															
DATA OF EACH ROTOR STATION																		
STA	MASS	POL	MOM	TRS	MOM	LGTH	OD	STF	ID	S	OD	MASS	ID	M	YME7	DENS	SHME7	
1	13.6	0.23E	03	0.11E	03	3.70	3.45	0.00	2.50	0.00	3.000	0.283	0.862					
2	31.1	0.51E	03	0.25E	03	7.75	3.83	0.00	2.50	0.00	3.000	0.283	0.862					
3	11.5	0.00E	00	0.00E	00	8.30	3.61	0.00	2.50	0.00	3.000	0.283	0.862					
4	2.1	0.00E	00	0.00E	00	6.15	3.45	0.00	2.50	0.00	3.000	0.283	0.862					
5	27.6	0.51E	03	0.25E	03	10.40	3.83	0.00	2.50	0.00	3.000	0.283	0.862					
6	43.1	0.12E	04	0.58E	03	8.65	3.65	0.00	2.50	0.00	3.000	0.283	0.862					
7	27.8	0.00E	00	0.00E	00	5.75	3.45	0.00	2.50	0.00	3.000	0.283	0.862					
8	5.8	0.00E	00	0.00E	00	4.25	3.45	0.00	2.50	0.00	3.000	0.283	0.862					
9	18.2	0.33E	03	0.17E	03	0.00	0.00	0.00	0.00	0.00	3.000	0.283	0.862					
DATA OF EACH FOUNDATION STATION																		
STA	MASS	RSIXY(1)	RSIXY(2)	LGTH	AXY	YME7	DENS	SHMXE7	SHMYE7									
1	43.1	0.12E	11	0.58E	10	2.88	0.37E 07	0.30E 01	0.28E 00	0.86E 00	0.86E 00							
2	43.1	0.12E	11	0.58E	10	2.88	0.37E 07	0.30E 01	0.28E 00	0.86E 00	0.86E 00							
3	43.1	0.12E	11	0.58E	10	2.88	0.37E 07	0.30E 01	0.28E 00	0.86E 00	0.86E 00							
4	43.1	0.12E	11	0.58E	10	2.88	0.37E 07	0.30E 01	0.28E 00	0.86E 00	0.86E 00							
5	43.1	0.12E	11	0.58E	10	2.88	0.37E 07	0.30E 01	0.28E 00	0.86E 00	0.86E 00							
6	43.1	0.12E	11	0.58E	10	2.88	0.37E 07	0.30E 01	0.28E 00	0.86E 00	0.86E 00							
7	43.1	0.12E	11	0.58E	10	2.88	0.37E 07	0.30E 01	0.28E 00	0.86E 00	0.86E 00							
8	43.1	0.12E	11	0.58E	10	2.88	0.37E 07	0.30E 01	0.28E 00	0.86E 00	0.86E 00							
9	43.1	0.12E	11	0.58E	10	2.88	0.37E 07	0.30E 01	0.28E 00	0.86E 00	0.86E 00							
AT EACH OF FOLLOWING ROTOR STATION THERE IS A BEARING																		
2 8																		
AT EACH OF FOLLOWING FOUNDATION STATIONS THERE IS A FOUNDATION SUPPORT																		
2 8																		
BEARING DATA																		
BEARING AT STATION 2																		
KXX		BXX		KXY		BXY		KYY		BYY								
0.13E 06		0.13E 07		0.62E 06		0.12E 06		- .88E 05		0.12E 06		0.11E 06 0.18E 06						
BEARING AT STATION 8																		
KXX		BXX		KXY		BXY		KYY		BYY								
0.48E 06		0.77E 06		0.33E 06		0.16E 06		0.11E 05		0.16E 06		0.12E 06 0.92E 05						
PEDESTAL DATA																		
STATION	MASS-X			STIFF-X			DAMP-X			MASS-Y			STIFF-Y			DAMP-Y		
2	0.100E-17			0.100E 11			0.100E 03			0.100E-17			0.100E 11			0.100E 03		
8	0.100E-17			0.100E 11			0.100E 03			0.100E-17			0.100E 11			0.100E 03		
FOUNDATION SUPPORT DATA																		
STATION	STIFF-X			DAMP-X			STIFF-Y			DAMP-Y								
2	0.100E 18			0.100E 01			0.100E 18			0.100E 01								
8	0.100E 18			0.100E 01			0.100E 18			0.100E 01								
STATIONS WITH INTERCONNECTION BETWEEN ROTOR AND FOUNDATION, FOR ROTOR AS FOLLOW																		
2 8																		
STATIONS WITH INTERCONNECTION BETWEEN ROTOR AND FOUNDATION, FOR FOUNDATION AS FOLLOW																		
2 8																		

TABLE 1.- CONCLUDED.

FIRST SPEED	LAST SPEED	SPEED INCR.	
0.831000E 04	0.851000E 04	0.500000E 02	
FREQUENCY RATIOS			
0.500000E 00	0.495000E 00	0.490000E 00	0.480000E 00

TABLE 2.- RESULTS OF EXAMPLE 1

Case	System	Threshold Speed, rpm		Difference
		Program	Lund [4]	
(a)	one-level	8317	8350	-0.4%
(b)	two-level, stiff pedestals	8317*		-0.4%
(c)	three-level, very stiff foun.	8204**		-1.7%
(d)	three-level, soft foundation	7217***		-13.6%
(e)	two-level, soft pedestals	7916****		-5.2%

- * The two-level system with very stiff pedestals has negligible difference in threshold speed from the one-level system.
- ** The three-level system with very stiff foundation has a little less threshold speed than that of a one-level system.
- *** The three-level system with soft foundation has a much less threshold speed than that of one-level or two-level system. This shows where the foundation effect is important.
- **** The two-level system with soft pedestals has a somewhat lower threshold speed less than that of the one-level system. This also shows pedestals effect cannot be ignored.

EXAMPLE 2. FLEXIBLE ROTOR IN FOUR DAMPED FLEXIBLE BEARINGS ON A FLEXIBLE FOUNDATION

A four bearing rotor system given by Lund [4] as an unbalance response example is shown in figure 9. Details of the system are given in table 3. The rotor was modeled using a 27-station representation and calculated using the eight coefficient bearing data. A suitable foundation model was then developed and the threshold speed of the rotor was calculated (a) as a one-level system, (b) as a two-level system (with very stiff pedestals), (c) as a three-level system (with very stiff foundation), (d) as a three-level system (with soft foundation), and (e) as a two-level system (with soft pedestals). Computed results for these five cases are given in table 4. The foundation effect was found to be relatively small in case (c) and larger in case (d). Similar results were found for the pedestals effect in case (b) and (e). These results further show that in this case the effects of foundation exact a significant influence on the whirl threshold speed.

TABLE 3.- CONCLUDED.

AT EACH OF FOLLOWING ROTOR STATION THERE IS A BEARING

3 16 22 27

AT EACH OF FOLLOWING FOUNDATION STATIONS THERE IS A FOUNDATION SUPPORT

5 9 13 17

BEARING DATA

BEARING AT STATION 3

KXX	BXX	KXY	BXY	KYX	BYX	KYY	BYY
0.15E+07	0.34E+07	80E+06	0.13E+07	0.97E+06	0.13E+07	0.15E+06	0.10E+07

BEARING AT STATION 16

KXX	BXX	KXY	BXY	KYX	BYX	KYY	BYY
0.15E+07	0.34E+07	80E+06	0.13E+07	0.97E+06	0.13E+07	0.15E+06	0.10E+07

BEARING AT STATION 22

KXX	BXX	KXY	BXY	KYX	BYX	KYY	BYY
0.15E+07	0.33E+07	10E+07	0.18E+07	0.12E+07	0.18E+07	12E+06	0.18E+07

BEARING AT STATION 27

KXX	BXX	KXY	BXY	KYX	BYX	KYY	BYY
0.15E+07	0.33E+07	10E+07	0.18E+07	0.12E+07	0.18E+07	12E+06	0.18E+07

PEDESTAL DATA

STATION	MASS-X	STIFF-X	DAMP-X	MASS-Y	STIFF-Y	DAMP-Y
3	0.100E-04	0.100E+14	0.100E+00	0.100E-04	0.100E+14	0.100E+00
16	0.100E-04	0.100E+14	0.100E+00	0.100E-04	0.100E+14	0.100E+00
22	0.100E-04	0.100E+14	0.100E+00	0.100E-04	0.100E+14	0.100E+00
27	0.100E-04	0.100E+14	0.100E+00	0.100E-04	0.100E+14	0.100E+00

FOUNDATION SUPPORT DATA

STATION	STIFF-X	DAMP-X	STIFF-Y	DAMP-Y
5	0.100E+33	0.100E+01	0.100E+33	0.100E+01
9	0.100E+33	0.100E+01	0.100E+33	0.100E+01
13	0.100E+33	0.100E+01	0.100E+33	0.100E+01
17	0.100E+33	0.100E+01	0.100E+33	0.100E+01

STATIONS WITH INTERCONNECTION BETWEEN ROTOR AND FOUNDATION, FOR ROTOR AS FOLLOW

3 16 22 27

STATIONS WITH INTERCONNECTION BETWEEN ROTOR AND FOUNDATION, FOR FOUNDATION AS FOLLOW

4 14 17 21

TEST: INSTABILITY, 27 STATIONS, 4 BRG. (3 LEVEL)

FIRST SPEED	LAST SPEED	SPEED INCR.
0.900000E+04	0.100000E+05	0.200000E+03

FREQUENCY RATIOS

0.500000E+00	0.495000E+00	0.490000E+00	0.480000E+00	0.400000E+00
0.350000E+00	0.300000E+00			

TABLE 4 RESULTS OF EXAMPLE 2

Case	System	Threshold Speed, rpm	Frequency Ratio, fr	Whirl Speed, rpm	Percentage Difference
(a)	one-level	9910	0.4990	4945	0%
(b)	two-level	9910	0.4990	4945	0%
(c)	three-level, stiff foun.	9873	0.4996	4943	-0.24%
(d)	three-level, soft foun.	9625	0.4998	4811	-2.71%
(e)	two-level, soft pedestal	9732	0.4995	4861	-1.7%

EXAMPLE 3. 300 MW TURBINE-GENERATOR UNIT

The turbine-generator rotor shown in figure 10 operates at 3600 rpm and is mounted in six fluid-film bearings, ranging in size from 200 mm (7.87 in) to 400 mm (15.75 in) shaft diameter. Bearing oil inlet viscosity is 16 cp at 160°F. The bearings are supported on flexible pedestals, mounted upon a stiff foundation, which was effectively a two-level system. The rotor model has 15 stations. The threshold speed of the system was calculated (a) using two plain cylindrical bearings for the generator (i.e., #4 and #5 bearings), and four MFG-Type bearings for the other supports, and (b) using six MFG-Type bearings for all supports.

The results of the stability threshold speed calculations are shown in table 5. For case (a), the threshold speed is 2200 rpm. The corresponding frequency ratio is 0.3518, which corresponds to a whirl speed of $2200 \times 0.3677 = 809$ rpm. This is close to the first flexible critical speed of the generator, which occurs at 837 rpm. For case (b), no threshold speed was found below 4000 rpm. These results agree with field observations, and demonstrate the capability of MFG-Type bearings for preventing rotor whirl instability.

TABLE 5 RESULTS FOR EXAMPLE 3

Case	System	Threshold Speed, rpm	Frequency Ratio	Whirl Speed $N_w = N_{th} \times fr$ rpm
(a)	Two Plain Cylindrical Brgs. for Generator, Four MFG Type Brgs. for Others	2200	0.3677	809
(b)	Six MFG Type Brgs.	No	No	No

CONCLUSIONS

1. A general-purpose rotordynamics analysis procedure and computer code has been described for the calculation of instability threshold conditions for damped flexible rotor-bearing systems mounted in pedestals, and supported on a distributed mass-elastic flexible foundation.

2. The procedure described has been verified using several established results from the open literature, and close correlation between pedestal threshold speed and whirl frequencies has been found.
3. Application of this procedure to a six-bearing, five-rotor, turbine-generator system has been described. Results were consistent with field observations for this case.
4. The procedure is suitable for evaluating the influence of pedestals and of distributed support foundations on the stability of multi-span rotor systems. The transfer matrix procedure is efficient, and double-precision accuracy is ensured using the complex eigenvalue algorithm described.

ACKNOWLEDGEMENT

The authors are grateful to the Brown Boveri Company of Baden, Switzerland, for permission to publish the 300 MW turbine-generator results used in Example 3. Particular thanks are due to Dr. Anton Roeder, Manager and to Dr. Raimund Wohlrab, Senior Engineer, Steam Turbine Department, for their valuable comments and encouragement during this study.

REFERENCES

1. Borowicz, M. "Beitrage zur Berechnung krit. Geschwindigkeiten zwei und mehrfach gelagerter Wellen," Dr.-Ing. Thesis, Munich Technical University, 1915.
2. Prohl, M. A. "A General Method for Calculating Critical Speeds of Flexible Rotors," Trans. ASME, Jnl. Appl. Mech., Vol. 12, p. A-142, 1945.
3. Koenig, E. C. "Analysis for Calculating Lateral Vibration Characteristics of Rotating Systems with any Number of Flexible Support," Trans. ASME, Jnl. Appl. Mech., Vol. 28, p. 585, 1961.
4. Lund, J. W. "Rotor-Bearing Dynamics Design Technology. Part V: Computer Program Manual for Rotor Response and Stability." Technical Report TR-65-45 Part V, U.S. Air Force Systems Command. WPAFB, Dayton, OH, May 1965.
5. Lund, J. W., Orcutt, F. K. "Calculations and Experiments on the Unbalance Response of a Flexible Rotor," Trans. ASME, Paper 67-Vibr-27, Jnl. Eng. Ind. pp. 785-792. November 1967.
6. Lund, J. W. "Stability and Damped Critical Speeds of a Flexible Rotor in Fluid-Film Bearings," Jnl. of Eng. for Ind., Trans. ASME, p. 509, May 1976.
7. Crook, A. W., Grantham, F. "An Approach to the Prediction of Vibrations of Turbine-Generators on Under-Tuned Foundations," First ASME Vibration Conference, Boston, MA, 1967.
8. Shapiro, W., "Unbalance Response and Instability Computer Code," Franklin Institute Research Laboratories, Philadelphia, PA, July 1975.

9. Zorzi, E., Nelson, H. "Finite Element Simulation of Rotor-Bearing Systems with Internal Damping," J. Eng. Power, Trans. ASME, Vol. 99, Series A, No. 1, pp. 71-76, January 1977.
10. Gunter, E. J., "Multi-Bearing Rotordynamics Computer Code," February 1982.
11. Zhou, S., Rieger, N. F. "Development and Verification of an Unbalance Response Analysis Procedure for Three-Level Multi-Bearing Rotor-Foundation Systems," Paper for Ninth Biennial Vibrations Conference, Design Engineering Division ASME, Cincinnati, OH, September 10-13, 1985.

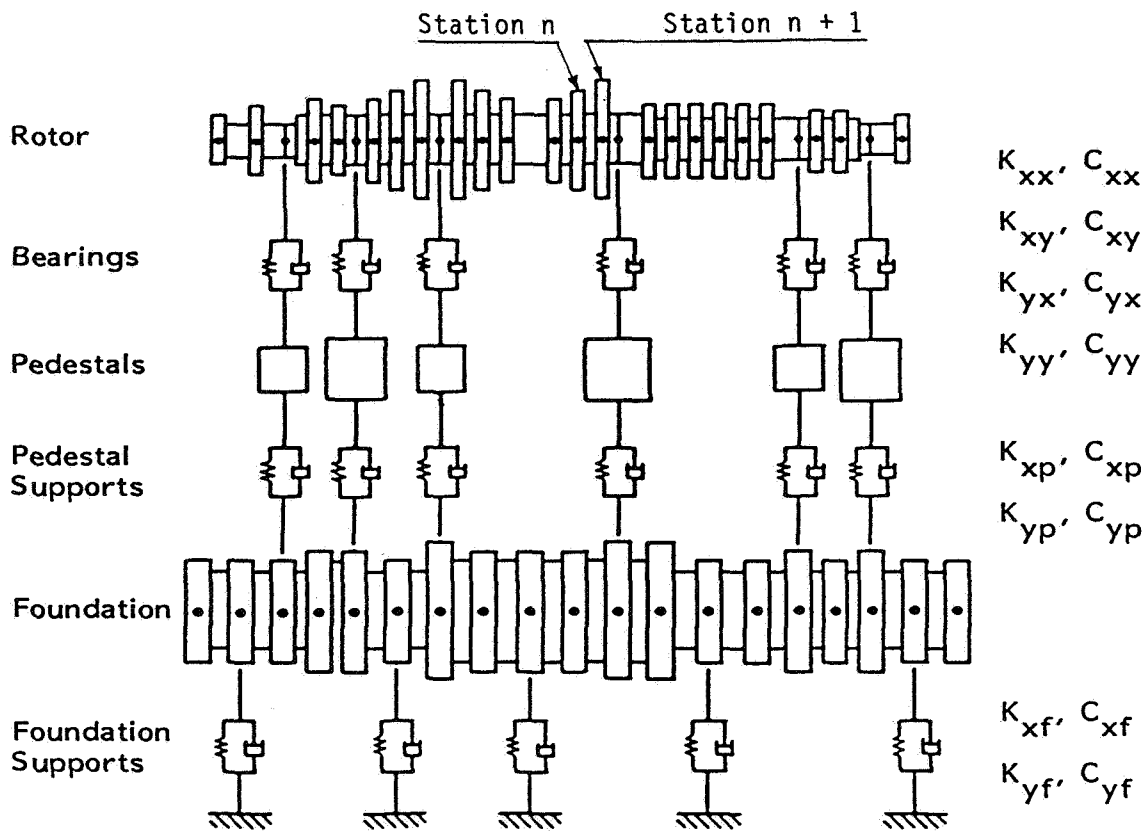
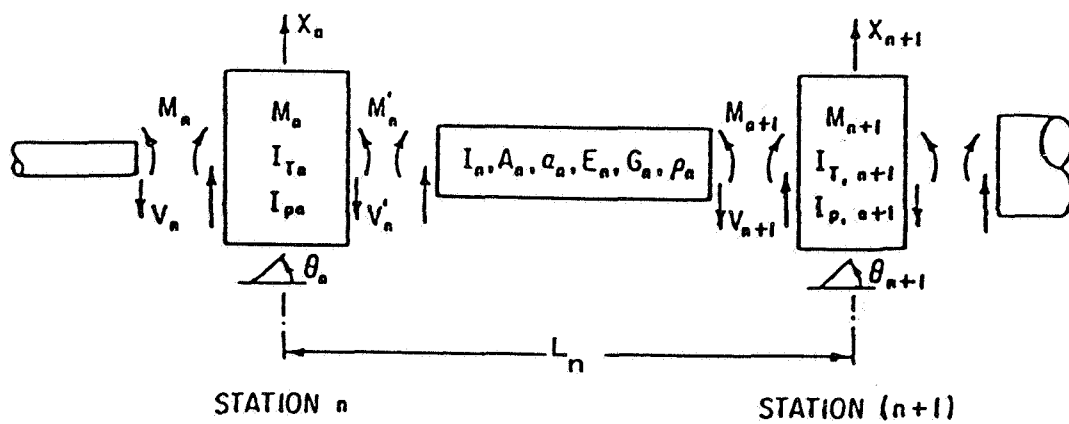
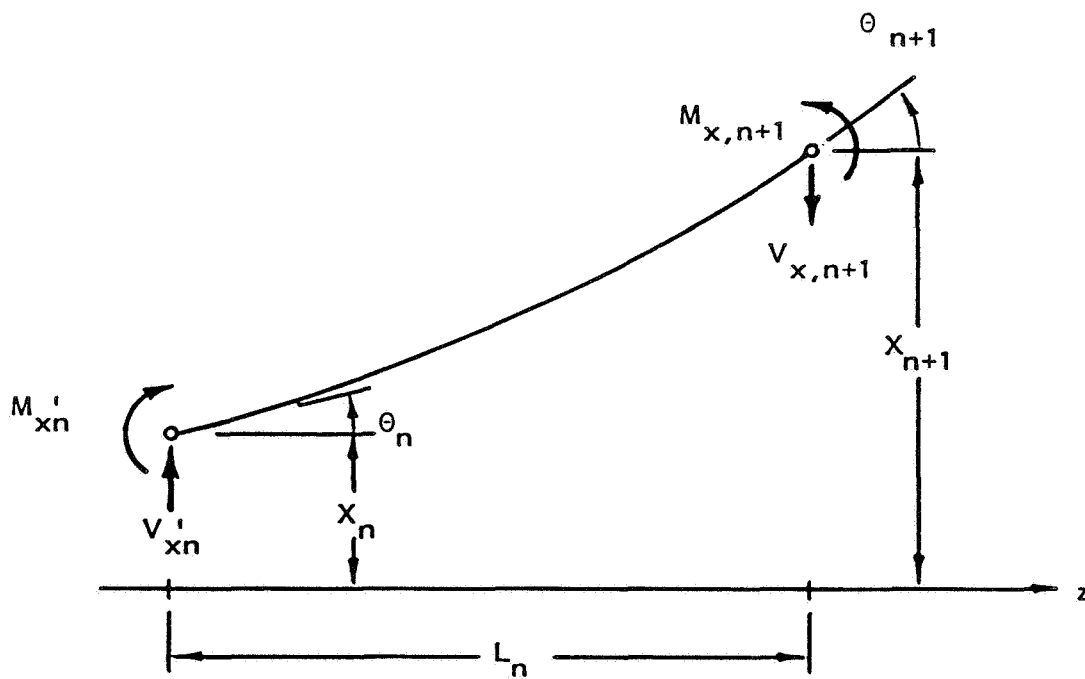


Figure 1 Rotor-Bearing-Pedestal Foundation System



a. End Station and Shaft Nomenclature



b. Shaft Section Between Rotor Stations n and n+1

Figure 2 Convention and Nomenclature for End Stations and Shaft Sections

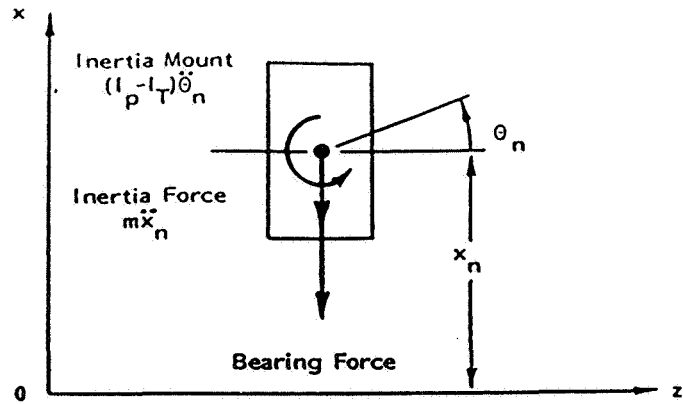
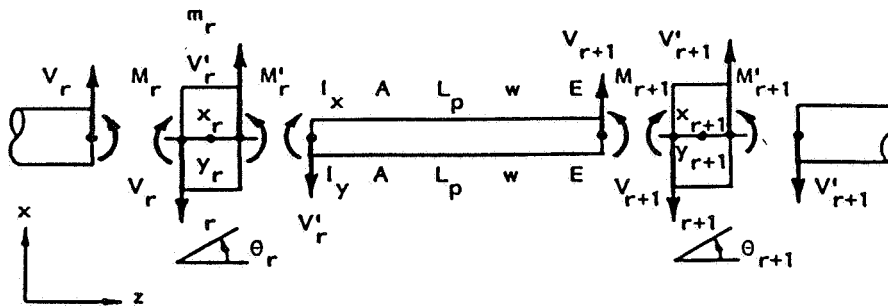
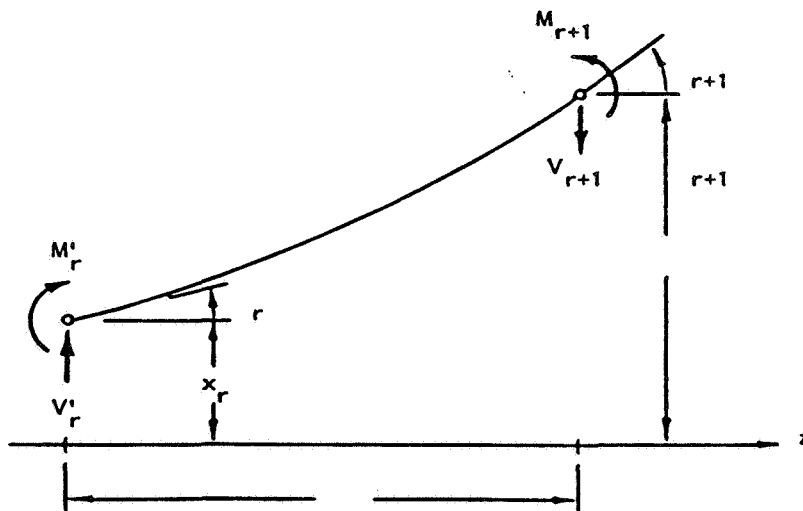


Figure 3 Forces on n-th Rotor Station



a. Notation and Convention for Foundation



b. Moments and Shears on Foundation Section

Figure 4 Notation and Convention for Foundation

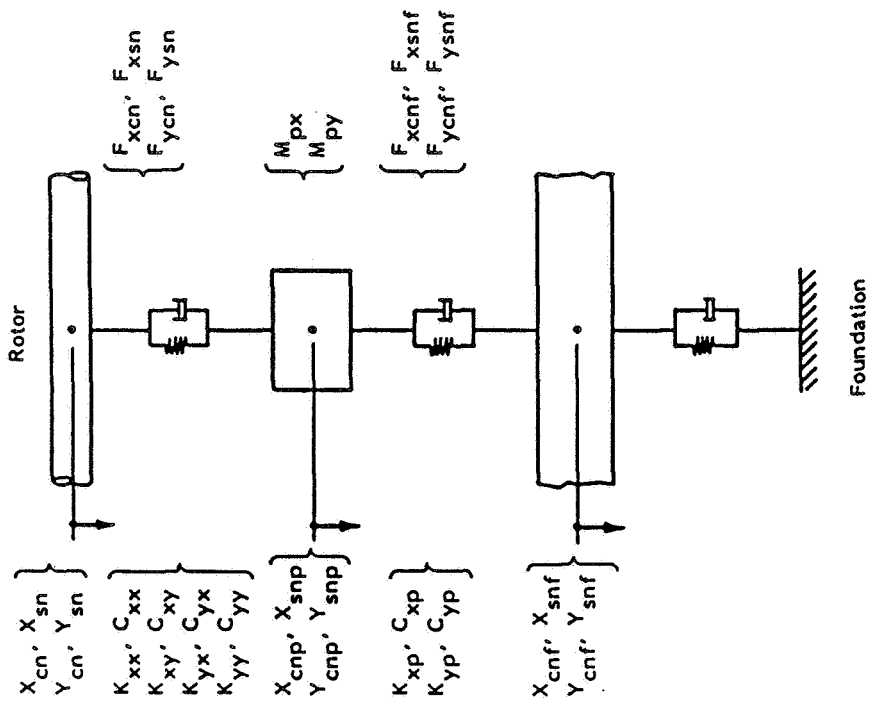


Figure 5 Three-Level Support System for Solution Algorithm

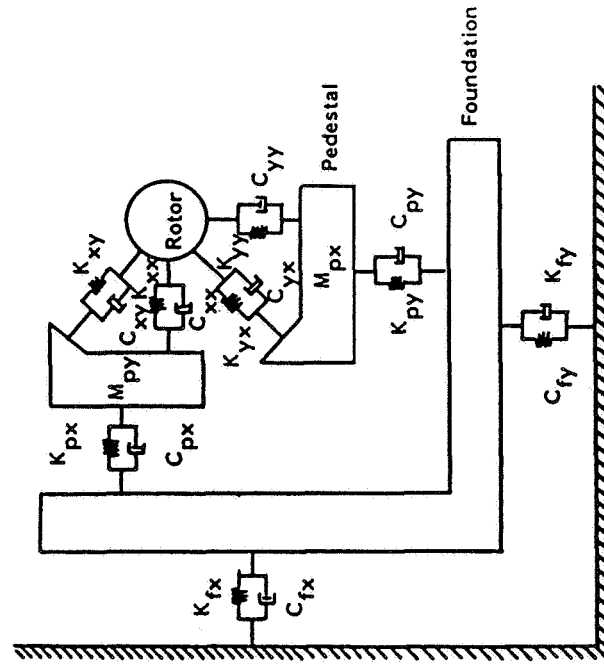


Figure 6 Bearing, Pedestal and Foundation Model for System

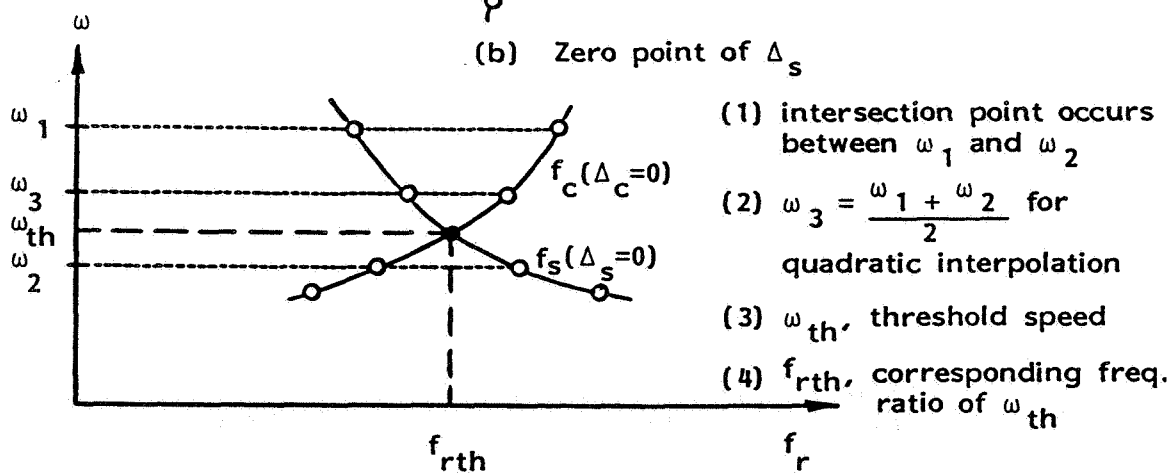
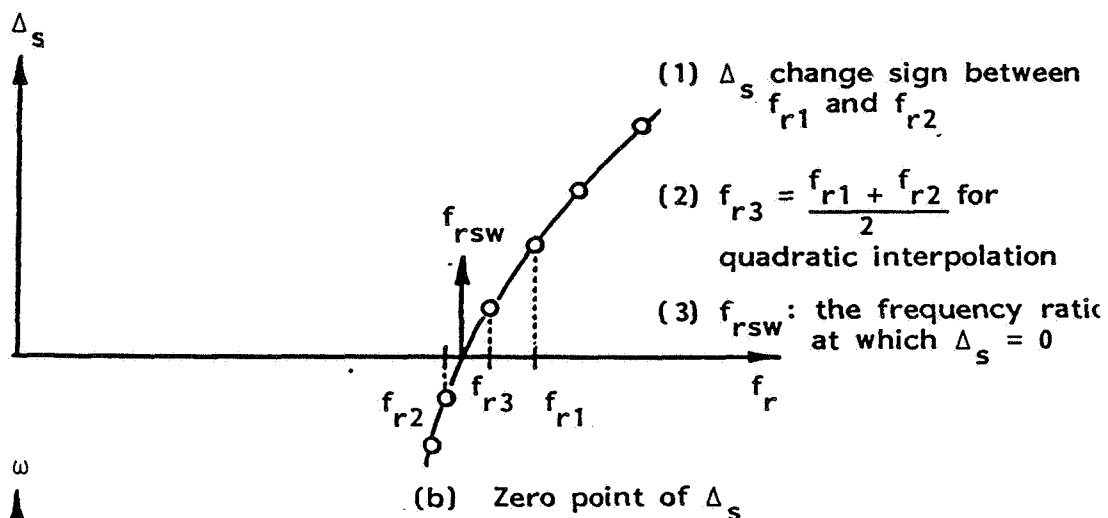
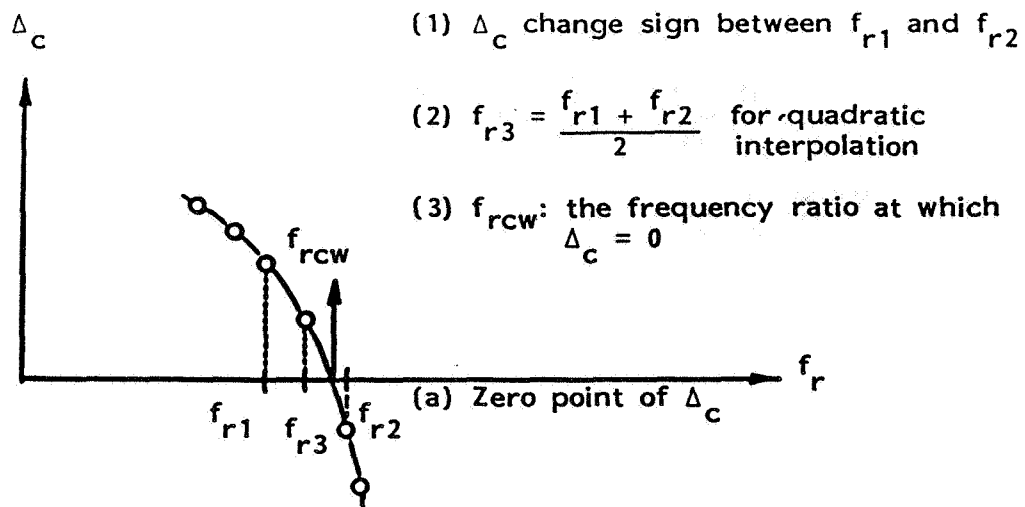


Figure 7 Threshold Speed Determination from the Computer

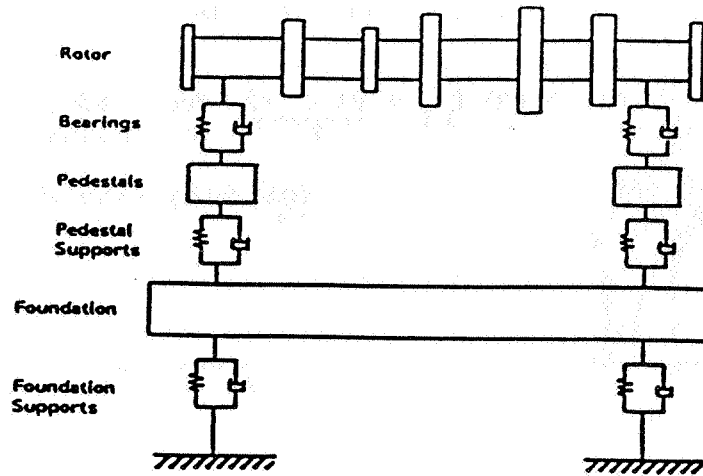


Figure 8 Rigid Rotor System. Example 1. After Lund [4]

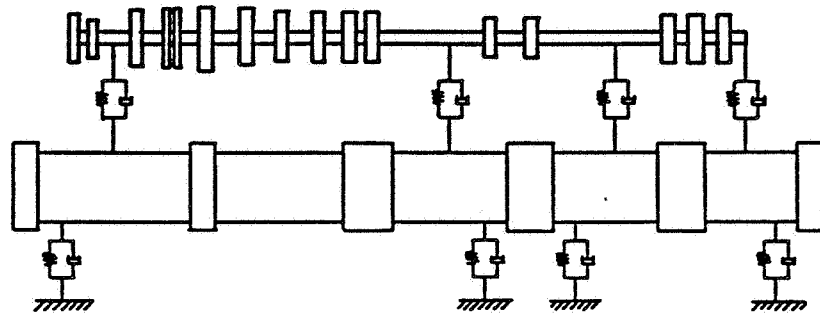


Figure 9 Flexible Rotor in Four Bearings. After Lund [4]

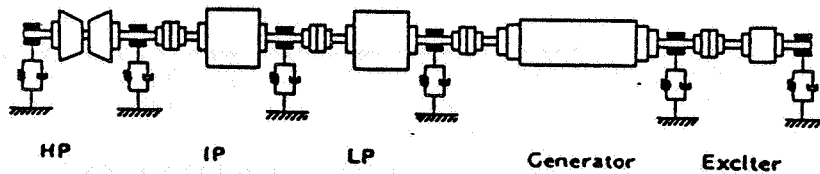


Figure 10 300 Mw Turbine-Generator Rotor System. Five Rotors; Six Bearings

SIMULATION OF NON-LINEAR BEARING FORCES
FOR POST-STABILITY INVESTIGATION

Z.A. Parszewski, J.M. Krodkiewski, K. Krynicki, and A.E. Salek
University of Melbourne
Parkville, Victoria 3056 Australia

Advanced rotor-bearing design requires increasingly non-linear analysis to give a comprehensive view of the effects caused by journal bearings. Journal bearings introduce into the system a nonlinear asymmetry and strong damping. Unstable regions predicted from a linear analysis of the bearing, (i.e. using stiffness and damping matrices) are understood as regions in which amplitude of vibrations increases with time. The non-linear mechanism limits the amplitudes of vibration of unstable rotor-bearing systems and forms limit cycles. Disbalance of the rotor existing in the system frequently causes subharmonic resonances to appear.

Different types of bearing designs have been developed to improve dynamic properties of rotor-bearing systems. Elliptical bearings, multi-sleeve bearings, tilting pad and other designs such as herringbone groove have been utilized to increase resistance to the onset of self-excited vibrations.

Experimental trials are costly, two alternative methods are possible to gain a qualitative insight. The first one creates mathematical model and applies both a digital or an analog computer simulation. The second one investigates phenomena occurring on the laboratory rig with the bearing replaced by an electronic simulating device, working in a feedback loop, which produces forces which are function of journal displacement and velocity. The simulated hydrodynamic forces are produced according to assumed characteristics matched to the bearing type.

The principal benefit of the analog simulation is that non-linear characteristics of a subsystem may be precisely identified and mathematical methods applied for a wide class of problems can be checked on the experimental instalation.

JOURNAL BEARING SIMULATION

Integration of the Reynold's equation results in values of the hydrodynamic force components. The hydrodynamic forces are functions of a journal displacement and velocity, but they are not given explicitly.

A hydrodynamic force representation can be assumed as a combination of chosen a priori functions f :

$$F_x = C_{11} f_1 + C_{22} f_2 + \dots + C_{nn} f_n \qquad F_y = D_{11} f_1 + D_{22} f_2 + \dots + D_{nn} f_n \qquad / 1 /$$

8810E-2AV

The coefficients C and D can be matched by minimizing the errors between values coming from /1/ and the integration of the Reynold's equation for given motion parameters.

In the alternative method, using the shape function characteristics of a journal bearing [1], the functions f play the role of shape functions and the nodal values play the role of coefficients C and D. This assures directly minimization of the error. Moreover the nodal values of hydrodynamic force can be evaluated from an experimental measurement. However in this concept a microprocessor should be involved for the bearing forces transfer in the simulator.

In order to modify a system characteristics e.g. a soft or hard stiffness, the electronic device has been designed to produce the components of the force according to the formula /2/:

$$F_x = k_{xx} f(x) + k_{xy} f(y) + c_{xx} \dot{x} + c_{xy} \dot{y} \quad / 2 /$$

$$F_y = k_{yx} f(x) + k_{yy} f(y) + c_{yx} \dot{x} + c_{yy} \dot{y}$$

where function f has been modeled as:

$$f(z) = z(z - z_0) \quad / 3 /$$

The system characteristic is built by a superposition of both characteristics: a mechanical one and an electronic one. A proper choice of the coefficients k results in a hard or soft stiffness. By shifting the electronic characteristics along x or y co-ordinates an unsymmetrical stiffness can be obtained which allows modeling of bearing external static load.

In some cases when linear effects introduced by a journal bearing have to be taken into consideration the function f in /3/ can be modeled as a linear one. The coefficients k and c in the formula /2/ will represent stiffness and damping coefficients corresponding to the statical position determined by the Sommerfeld number.

BEARING SIMULATOR

- The electronic device has been designed according to the following assumptions:
- input data analog conversion to satisfy the conditions of real-time active feedback control.
 - biaxial input/output,
 - input maximum of signal 8 V which corresponds to a journal displacement of 1 mm,
 - frequency range 500 Hz,
 - output maximum of signal 8-12 V which corresponds to 10 N force.

The block structure and performance of the analog support simulator are shown in Fig.1. The input amplifier IA amplifies the sum of input signals and D.C. voltages produced by the sources RPX and RPY(allowing for balancing), and protects the device against overloads. The gain of IA amplifier can be chosen by the displacement range selector DS.

The gain of the DA amplifier, which differentiates the signals, is selected depending on frequency. The frequency selector FS protects the DA amplifier and other stages of the device against saturation at the higher frequencies and differentiates with good linearity.

The function generator FG produces a linear or nonlinear function, according to Fig.2, dependent on the position of the mode selector MS. The output signals are amplified by the linear amplifiers A1-A4 (damping and stiffness matrices). The voltage comparators CPX detect overload (saturation) stages. The output amplifiers OAX and OAY provide the final gain for the output signals.

EXPERIMENTAL RIG

The experimental rig has been designed to observe and study non-linear phenomena introduced by a non-linear support e.g. a journal bearing. The main aims of experiment are to study self-excited vibrations and effects of an external harmonic force acting in an unstable region.

The journal bearing has been replaced by the analog support simulator working in a feedback loop to create wider facilities. The non-linear element can be identified with high precision, so theoretical results can be checked on an experimental rig. The scheme of the rig structure is shown in a block diagram (Fig.5).

The experiments have been designed in such a way that substructure identification, self-excited vibrations and disbalance effects (subharmonic resonances) can be studied on the same rig (Fig.4-5).

The active feedback control loop contains the following devices: displacement transducers DT, analog support simulator SS, voltage amplifier ASA, power amplifier PA, electronic vibrators V (shakers) and force transducers FT.

Biaxial displacements x,y of the journal are converted into voltage signals by transducers DT. The analog support simulator has these signals as an input. The output signals of two channels can be mixed by the analog amplifier ASA with two signals in time quadrature produced by the tuned generator G, if necessarily (simulating shaft disbalance). Then the signals are amplified by the power amplifier and supply the electrodynamic vibrators. The vibrators convert the signal to the biaxial interaction forces between the bearing and the journal.

Both displacement and force signals are observed on the two-channel oscilloscopes. The displacement signals are currently analysed by the spectrum analyser, so the frequencies of the vibrations can be found immediately.

The experimental data are collected by a PDP-computer. The analog adaptor AA memorizes periodically the analog input signals and sends them to A/D computer converter without any phase shift errors.

IDENTIFICATION OF MECHANICAL SUBSYSTEM

The receptance method has been used for parameter identification of the mechanical subsystem. Responses of the subsystem along the connecting co-ordinates have been found experimentally for harmonic excitations in the range of frequency 5-60 Hz.

The receptances were measured directly on the same experimental rig, by introducing signals to the shakers from a frequency synthesizer FS, and at the same time cutting off signals coming from the bearing simulator. The forces produced by the shakers and journal displacements are measured and stored in computer memory for various values of frequency.

A computer program is used to estimate subsystem parameters in the neighbourhood of a working point.

IDENTIFICATION OF ELECTRO-MECHANICAL SUBSYSTEM

The forces modifying the system are the result of a electro-mechanical loop which involves the bearing simulator, mixer, power amplifier and shakers. So the characteristics of the subsystem should be found entirely.

By cutting the feedback loop and introducing the signals coming from the frequency synthesizer instead of measured journal displacements, corresponding output forces are measured and stored together with the input signals. The input voltages are multiplied by the scale-factors of the displacement transducers to obtain values of the simulated journal displacements.

Introducing a harmonic signal:

$$z = Z \exp(i\omega t) \quad / 4 /$$

the damping matrix in /2/ can be found as the imaginary part of the force produced by the unit input signal. the real part is associated with the stiffness of the subsystem. The influence of frequency on the stiffness and damping matrices has been investigated. It has been proved that in the electro-mechanical loop both stiffness and damping coefficients kept constant values, it is shown in Fig.6-7.

According to the design assumptions the bearing simulator produces non-linear stiffness, independent of frequency /3/. This has been confirmed by measurements at different frequencies when damping coefficients were zero, the results are shown in Fig.8. The non-linear characteristics can be found at low frequencies as then the contribution of damping may be neglected. Introducing a harmonic signal with a low frequency, separately for each channel, the force components are measured as functions of the amplitudes (Fig.7).

An electro-mechanical identification does not depend on rotor motion except when the system resonates. To estimate the error introduced by a resonance for the same setting of the bearing simulator the measurements have been repeated and compared with a fixed journal. The deviations between system characteristics were not higher than 10 percent (Fig.6).

EXPERIMENTAL RESULTS

In the first phase of the experimental investigations the possibility of existence of more than one equilibrium position has been shown. Diagonal elements of non-linear stiffness matrices having negative values at zero have been introduced. For some values of stiffness the equilibrium position vanished. Zero was a fixed point but it could not exist physically because it was unstable (Fig.3). The system would move at one of the four existing stable positions. Any small perturbation caused a motion decaying with time around an equilibrium position.

An asymmetry caused by the cross-elements destabilized the system. Due to the existence of non-linearity limit cycles were formed. Some examples have been shown in Fig.9-11. These figures present the trajectories of the journal displacements and corresponding generated forces as well as their time representation. For some settings of the non-linear stiffness and damping multi-frequency limit cycles have been observed (Fig.10). A limit cycle with a jumping amplitude around two equilibrium positions has been also found (Fig.11).

The effects of shaft disbalance simulated by an external harmonic force have been observed. When the external frequency corresponding to the rotational speed of the rotor was remote enough from the frequency of self-excited vibrations in the system, both self-excited vibrations and subharmonic resonances existed. When the distance between frequencies was about 1-10 Hz the type of vibration was determined by the magnitude of the excitation (rotor disbalance). For small values of external excitation no steady state was achieved. A combination of self-excited vibrations and subharmonic resonances appeared in the system. Over a certain value of external excitation, the system established only one type of vibration.

REFERENCE

1. Parszewski Z.A., Krynicki K.: Shape Function Characteristics of Journal Bearing. Proceeding of Tenth CANCAM 85.

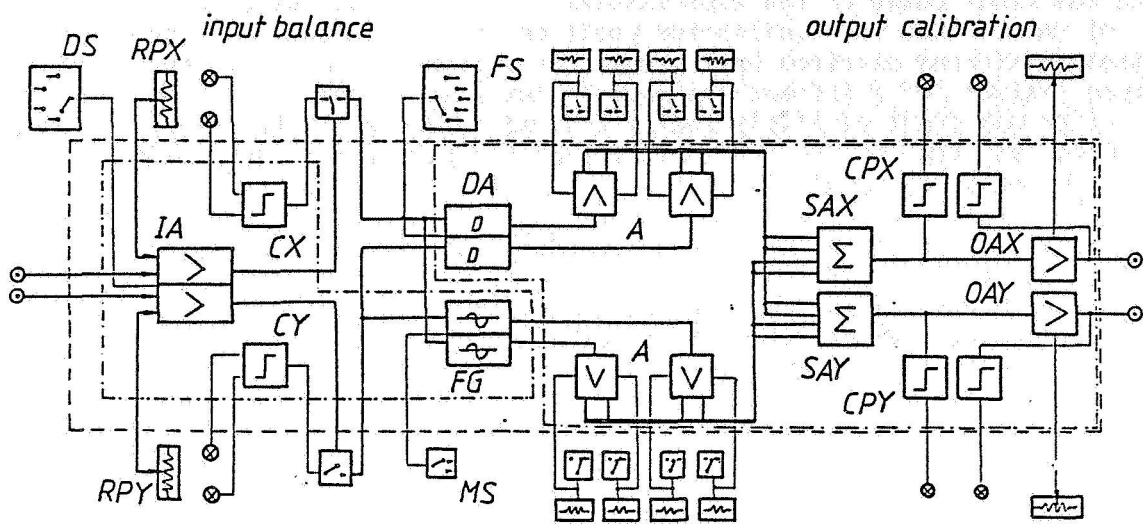


Fig.1. Analog support simulator

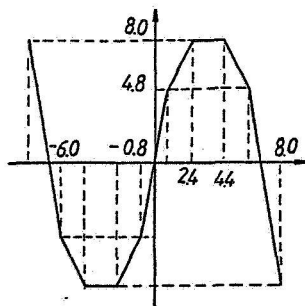


Fig.2. non-linear characteristic

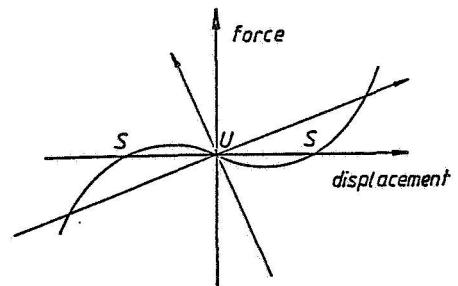


Fig.3.

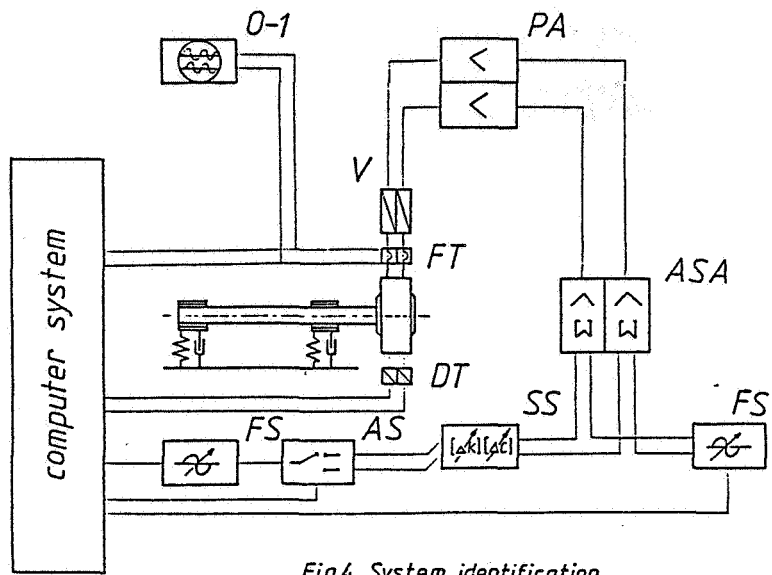


Fig.4. System identification

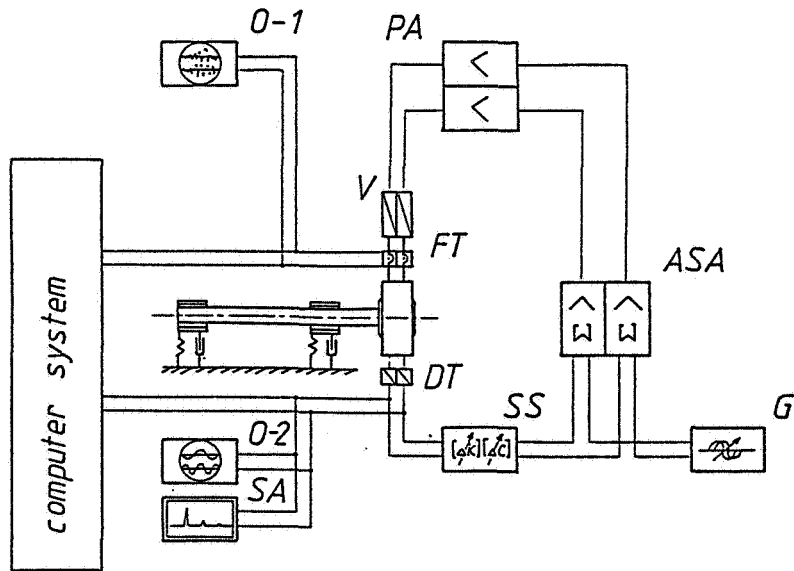


Fig.5. Experimental rig

ORIGINAL PAGE IS
OF POOR QUALITY

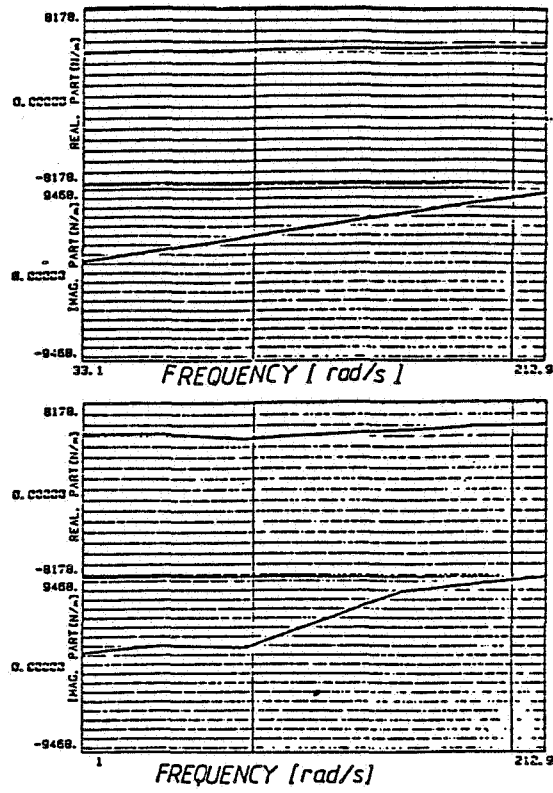


Fig.6

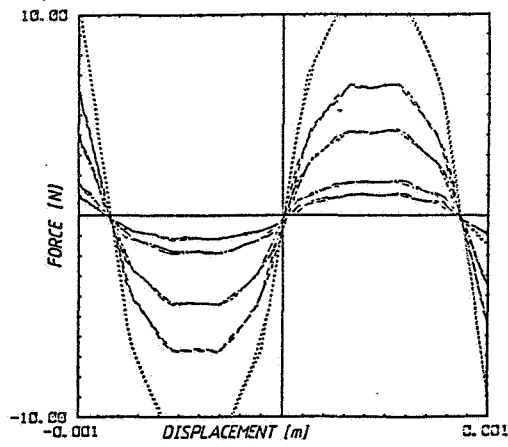


Fig.7

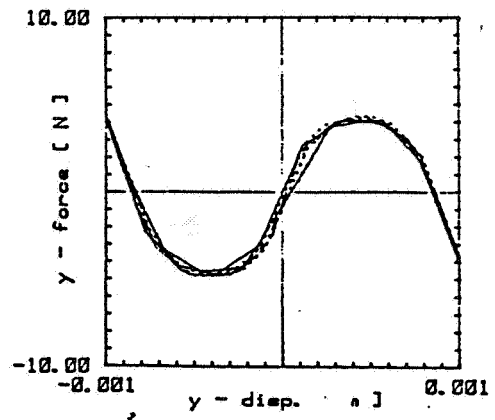
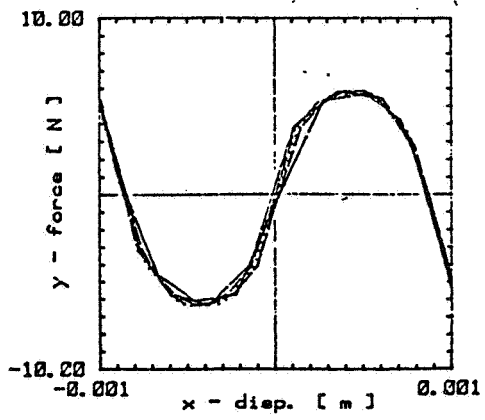


Fig. 8

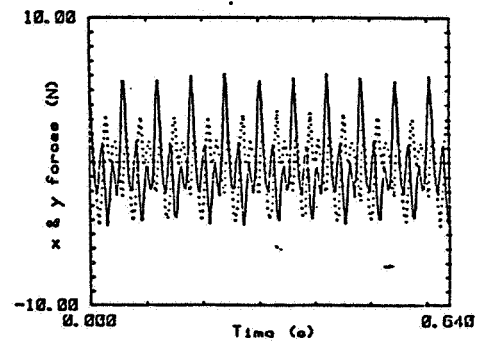
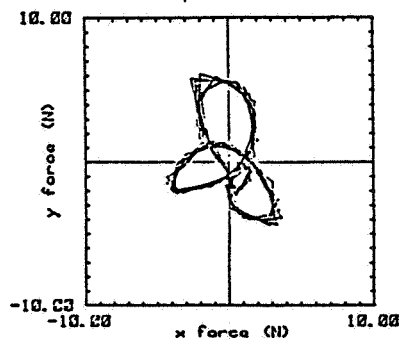
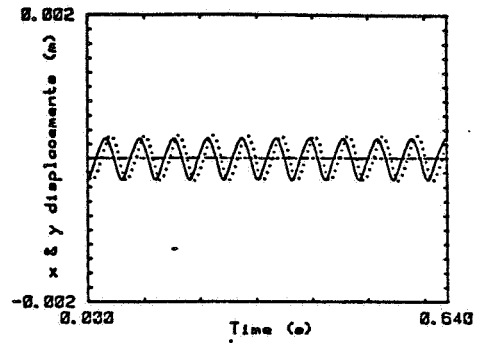
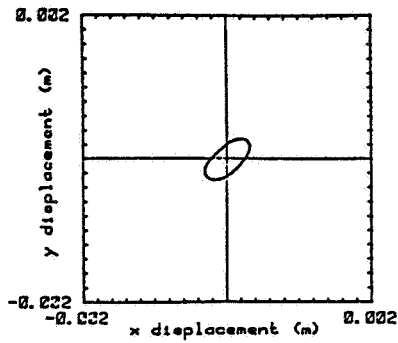


Fig. 9

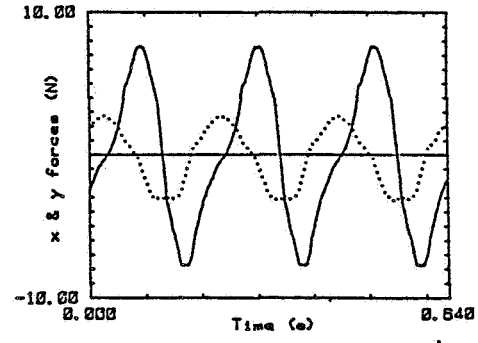
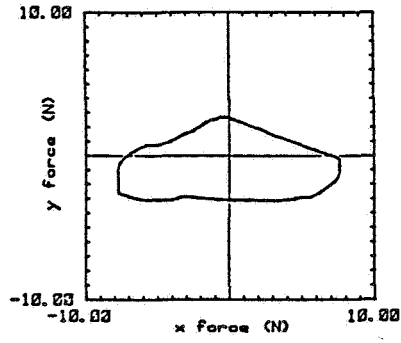
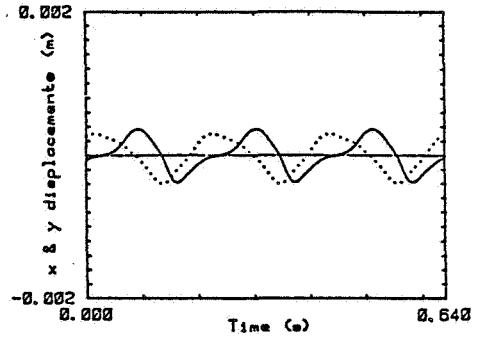
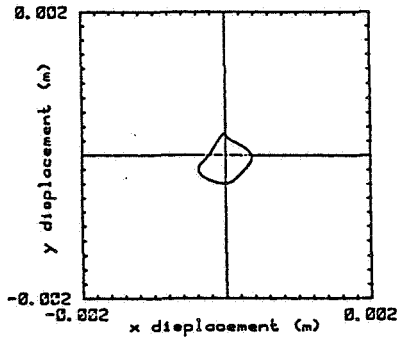


Fig.10

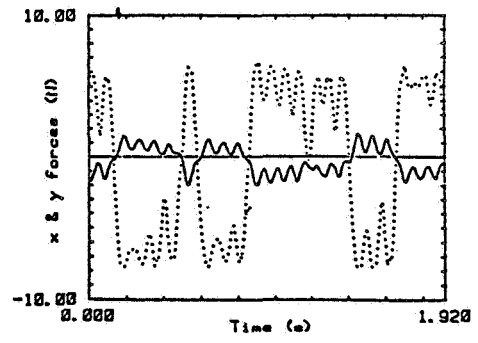
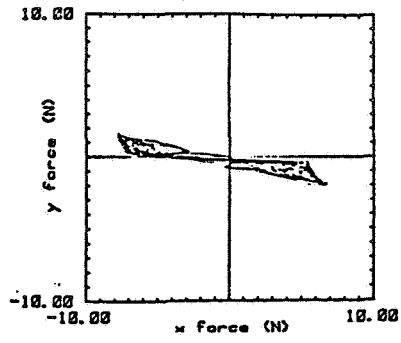
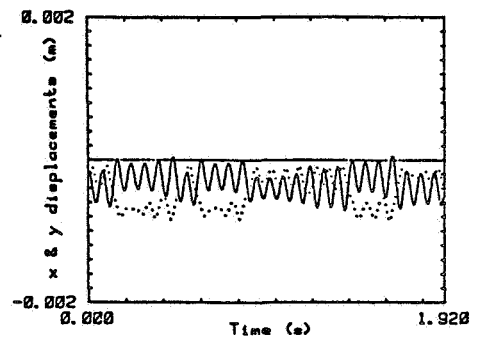
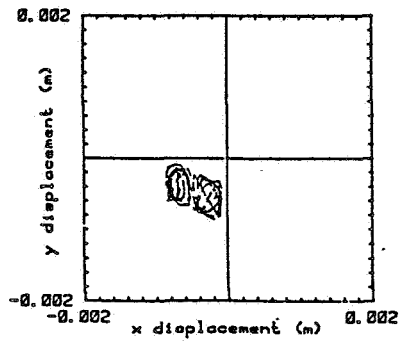


Fig.11

ORIGINAL PAGE IS
OF POOR QUALITY

MEASUREMENT OF ROTOR SYSTEM DYNAMIC STIFFNESS BY PERTURBATION TESTING

Donald E. Bently and Agnes Muszynska
Bently Rotor Dynamics Research Corporation
Minden, Nevada 89423

Specific aspects of the application of Modal Analysis to rotating machines are discussed in this paper. For lowest mode analysis, the circular-force perturbation testing gives the best results. Examples of application are presented.

1. MODAL ANALYSIS OF A ROTATING MACHINE

Experimental Modal Analysis or Modal Testing, as it is sometimes called, has become a popular method for studying practical vibration problems of mechanical structures. Application of Modal Testing for parameter identification and diagnostics of rotating machines, representing an important class of mechanical structures, has several specific aspects and requires a special approach. The results and predictions obtained by applying the classical "passive structure" Modal Testing to a rotating machine are usually incomplete and not sufficiently accurate for the most important modes, while providing information which is insignificant, for the rotating machine operating performance.

The specific aspects of rotating machines as subjects of Modal Analysis are discussed below.

1. All dynamic phenomena occurring during the performance of a rotating machine are closely related to the rotative motion of the rotor. The continuous supply of rotative energy makes the system "active." Numerous vibrational phenomena in rotating machines occur due to the transfer of energy from rotation (main performance) to vibration (undesirable side effects). Rotation of the shaft and all mechanical parts attached to it, as well as involvement in rotation of the working fluid (in fluid-flow machines), causes important modifications in modes and natural frequencies. In large turbomachines additional changes can be generated by thermal effects and foundation deformation. All these factors cause the results of Modal Testing of rotating machines "at rest" ("passive structure" approach) to differ significantly from the results of testing during machine operational conditions ("active structure" approach).

2. Rotors, which represent the main parts of rotating machines are equally constrained in two lateral directions; therefore, they perform vibrational motion which always has two inseparable lateral components (conventionally called "vertical" and "horizontal"). The result forms two-dimensional precessional motion of the rotor. Unidirectional impulse testing widely used in Modal Analysis, when applied to a rotating shaft, will undoubtedly result in a response containing both vertical and horizontal components.

3. In practical performances of rotors the precessional motion can contain multi-frequency components, each of them having a definite relation to the direction of rotation. In a most general case, each individual component can be either forward (direction of precession the same as direction of rotation) or backward (direction of precession opposite to rotation). Direction of precessional motion is vital to the rotor integrity. The net deformation frequency of the shaft is equal to the difference between rotative and precessional frequencies, taking into account their signs. During backward precession the shaft is therefore a subject of high frequency deformation (sum of both frequencies). This significantly increases a fatigue hazard. When measuring rotating machine vibrations it is very important to identify each vibrational frequency component whether it is forward or backward. Narrow band filtering and time base orbit analysis is extremely helpful for this purpose. In classical Modal Testing, "negative" frequencies have no meaning. Applied to rotating machines, "negative" frequency has a direct and very significant physical interpretation related to backward precession. Classical unidirectional impulse testing of a rotating shaft will result in a response containing elements of forward and backward precession.

4. Most important vibrational phenomena of rotating machines are related to the rotor lateral vibrations (sometimes coupled lateral/torsional/longitudinal vibrations). Each mode of rotor lateral vibration contains two components (vertical and horizontal), the characteristics of which are usually slightly different, as a result of elastic/mass nonsymmetry of the rotor and supporting structure in two lateral directions. Modal Testing of structures with closely spaced modes presents numerous difficulties. Rotating machines belong to this category. An alleviation of this problem consists, however, in close-to-symmetry modes; it is therefore reasonable to talk about "pair modes" in rotating machines (e.g., "first mode vertical" and "first mode horizontal").

5. Classical Modal Testing deals with a high number of modes of a structure in a wide spectrum of frequencies. In the performance of rotating machines, the most important are the lowest modes and low frequency precessional phenomena. This fact is related to the rigidity of the rotor system and to the relationship between the actual rotative speed and rotor precessional dynamic phenomena. Firstly, rigidity/mass characteristics of a rotor are always placed in a lower range of frequencies than those of the supporting structure. The lowest modes of the rotating machine correspond therefore to the modes of the rotor itself. Secondly, the rotating machine has its own continuously active forcing function, the unbalance, an inseparable feature of the rotating system. The frequency of this forcing is equal to the rotor actual rotative speed. The resulting motion is referred to as synchronous precession. A rotating machine operational speed, even if it represents dozens of thousands of rpm, seldom exceeds third balance resonance frequency; therefore, main interest is concentrated on investigating the rotor first two or three modes, as the rotating machine has to survive resonances of the lowest modes during each start-up and shutdown. The amplitudes of rotor deformation at low modes are the highest; therefore, they are of the greatest concern.

6. Another aspect of importance focused on rotor lowest modes is the fact that all self-excited vibrational-precessional phenomena occurring during a performance of a rotating machine are characterized by low frequencies, always located in the sub-synchronous region (frequencies lower than synchronous frequency). The self-excited vibrations occur when rotative speed is sufficiently high, and they are often referred to as rotor instabilities, significantly affecting the machine operation. The frequency of self-excited vibrations is either equal to a fraction of the actual rotative speed, and the same ratio to rotative speed is maintained if the rotative

speed varies (oil whirl, partial rub) or it is equal to the rotor first bending mode natural frequency (oil whip, full annular rub). Due to the specific role of internal friction, subsynchronous vibrations of rotating machines are always characterized by much higher amplitudes than supersynchronous vibrations [1].

7. During classical Modal Testing when dealing with high number of modes, the accuracy of the phase angle readings is usually low. In rotating machines the phase angle represents an extremely important parameter. It not only gives the information on the force/response relationship, but also can be related to the shaft rotative motion. It also yields significant information for the identification of modal parameters. Limiting Modal Analysis to the lowest modes permits one to increase accuracy in the phase angle readings.

8. Finally the most important aspect: the results of Modal Testing of rotors during operational conditions in low-frequency regions reveal the existence of special modes, unknown in "passive" structures. These modes are generated by solid/fluid interaction, e.g., in fluid-lubricated bearings and seals. During rotating machine performances, these modes show their activity through rotor self-excited vibrations (e.g., "oil whirl" is the rotor/bearing system self-excited vibration; "oil whirl resonance" and "oil whirl mode" are revealed by perturbation testing [2-7]).

Summarizing all these aspects, Modal Analysis and Modal Testing of rotating machines have to be focused on the lowest bending modes and applied to the rotor during normal operational conditions. The sophisticated Modal Testing, as used in case of "passive" structures, is not the most efficient for this purpose. Better results can be obtained by applying limited frequency sweep circular-force perturbation testing.

2. PERTURBATION TESTING OF ROTATING MACHINES

Perturbation modal testing is one of the commonly-used methods for parameter identification of mechanical modal structures. The method requires perturbing the dynamic equilibrium of the structure, represented by a "black box," by a known input force, and measuring the dynamic response of the structure. Most often the response represents motion, measured in terms of displacement, velocity, or acceleration, as functions of time (Fig. 1). The input force is applied to a selected point of the structure. Output measuring devices can be installed in several points of the structure, giving a set of structure point responses. Changing the point of force application, and measuring the structure response again, one can eventually get a matrix of responses corresponding to the 'vector' of inputs.

In the case of mechanical structures, the input is usually a force; the output is usually motion. The "black" (or "grey") box, representing the structure should then be described in terms of the structure Transfer Function with the units [Motion]/[Force]. In the linear case the Transfer Function represents a matrix, whose components could be real or complex numbers. The matrix order is equal to the number of points of force application and to the number of the assumed degrees of freedom of the structure.

Perturbation technique is widely applied for identification of "passive" structures, i.e., the structures whose dynamic equilibrium represents the static equilibrium. For "passive" structures, such as bridges, masts or buildings, the dynamic equilibrium means "no motion." A different situation occurs in the case of "active" struc-

PERTURBATION TECHNIQUE

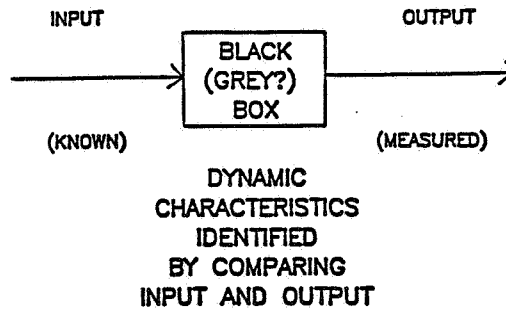


Figure 1. - Block diagram of a mechanic structure dynamic perturbation.

tures, such as rotating machines. Their dynamic equilibrium means rotation at a particular rotative speed, i.e., in the "active" structures there exists a continuous flow of kinetic energy. It is well known that due to several physical mechanisms the rotational energy of shafts can be transferred into various forms of vibrational energy of the shafts themselves (e.g., shaft lateral vibrations), supporting pedestals, cases, foundations, etc. It is then very important to know "how stable" the rotating machine dynamic equilibrium is. The perturbation method can give the answer to this question. Perturbation method applied to the "active structures" at their dynamic equilibrium give better evaluation of the structure parameters, as their value becomes affected by the shaft/rotational speed.

In "active" structures such as rotating machines, the best input force is a circular rotating force applied to the shaft in a plane perpendicular to the shaft axis. This force perturbs the shaft simultaneously in two lateral directions. Shaft motion in these two directions is closely coupled; a unilateral perturbation would result in shaft motion in both directions. An important advantage is related to the circular rotating force: the direction of its rotation can be chosen, i.e., the force can rotate "forward," in the direction of the shaft rotation, or "backward," in the opposite direction. For rotating structures the modes "forward" and "backward" are different. A unilateral shaft perturbation (or a perturbation applied to the pedestals or other nonrotating elements of the rotating machine) would result in mixed "forward" plus "backward" perturbation of the rotating shaft [8]. The shaft response will then contain both modes and the results might be ambiguous.

Another advantage of a circular rotating force is the ease of control of the force magnitude and phase by applying a controlled unbalance in the perturbation system and the ease of controlling its frequency, usually varying from about 20 rad/sec to a chosen value (sweep-frequency type of perturbation).

The perturbation system of a rotating machine can consist of an unbalanced rotating free spinner driven by compressed air blow (Fig. 2a) or can consist of an unbalanced perturbing shaft driven by a separate motor and attached to the main rotating machine shaft through a pivoting bearing (Figure 2b). These types of systems allow for "non-synchronous" shaft perturbation, i.e., the frequency (angular speed) of the perturbing force is entirely independent of the rotational speed of the main shaft. They also allow one to perturb the shaft either in a forward or a backward direction. Such perturbation systems also give very good results when the shaft does not rotate.

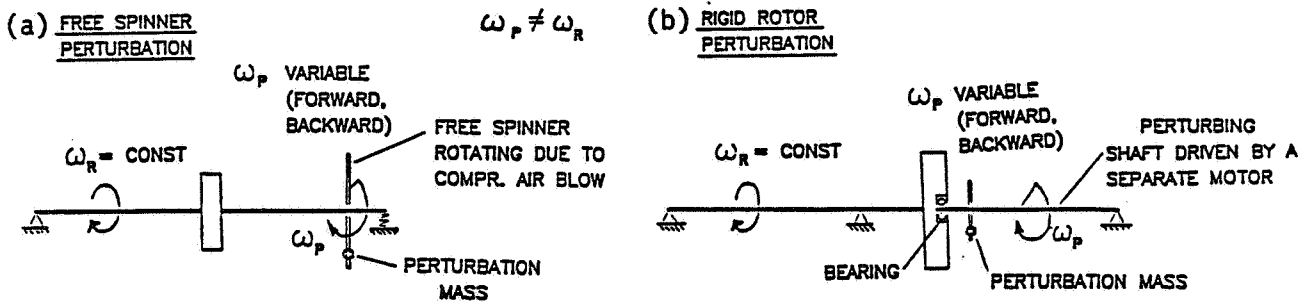


Figure 2. - Nonsynchronous perturbation of rotors.

"Nonsynchronous" perturbation, applied to a rotating machine, requires additional perturbing devices which, in case of big heavy machines, might be difficult to install. For some machines "synchronous" perturbation will give sufficient and very important information.

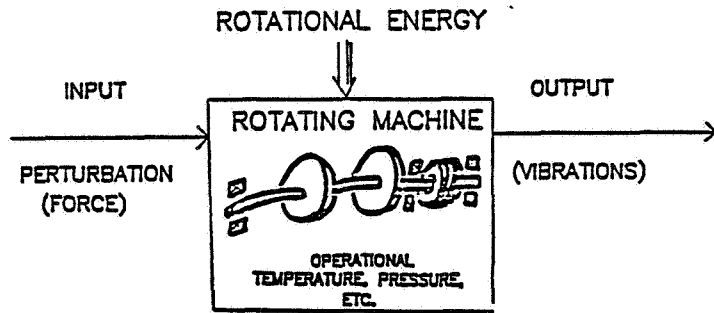
The "synchronous" perturbation force is created by a controlled unbalance introduced directly to the machine. The system response filtered to the synchronous component ($1 \times$), is measured during machine start-up or shutdown (for instance, this type of synchronous perturbation is used during balancing). By comparing the input force and the rotor output response, the rotor "synchronous" characteristics can be identified. In particular, in the case of the calibration weight balancing for one particular speed, the matrix of the rotor influence vectors representing the rotor transfer function as well as correcting weights can be calculated. Synchronous perturbation allows one to identify the rotor synchronous modal mass, stiffness and damping, by applying the Dynamic Stiffness Method [2,9]. This synchronous testing should be recommended for all rotating machines, as a routine practice.

In summary, the modal perturbation method is very efficient in the identification of dynamic characteristics of rotating machines (Fig. 3). "Nonsynchronous" perturbation should be superimposed on the rotational motion of the machine, while the machine operates at its normal conditions (including temperature, pressure, etc.). The best perturbing input for rotating machines is a rotating, circular unbalance force applied directly to the shaft. This force has slowly variable frequency (sweep method) and it can have direction "forward" or "backward" relative to the direction of the shaft rotation. The "synchronous" rotor perturbation, during start-up or shutdown, by a controlled unbalance, introduced directly to the rotor does not require any additional devices and it allows one to identify very important rotor "synchronous" modal dynamic characteristics.

3. RESULTS OF PERTURBATION TESTING OF ROTORS

3.1 Identification of Natural Frequencies as Functions of Rotative Speed for Rotors with Strong Gyroscopic Effects

Rotative energy of shafts has a significant influence on rotor dynamic characteristics. In particular, rotating shaft natural frequencies differ from nonrotating shaft natural frequencies. The perturbation testing has been used for determining the relationship between the rotor natural frequencies and rotative speed. The rig with a rotor showing strong gyroscopic effect presented in Fig. 4 yields the results of forward and backward perturbation given in Fig. 5 [2,10].



- PERTURBATION BY CONTROLLED UNBALANCE IS EASY TO GENERATE, CONTROL, AND MEASURE
- CIRCULAR PERTURBATION IN THE PLANE PERPENDICULAR TO SHAFT AXIS PROVIDES THE BEST ROTOR DYNAMIC BEHAVIOR INSIGHT
- CIRCULAR PERTURBATION CAN BE APPLIED TO THE ROTOR IN FORWARD OR REVERSE DIRECTION (RELATIVE TO SHAFT ROTATION)

Figure 3. - Perturbation technique for rotating machinery.

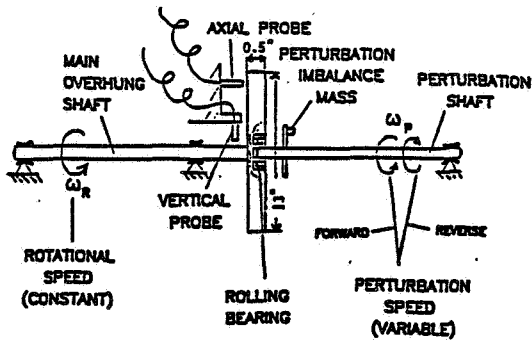


Figure 4. - Gyroscopic effect test rig (nonsynchronous perturbation method).

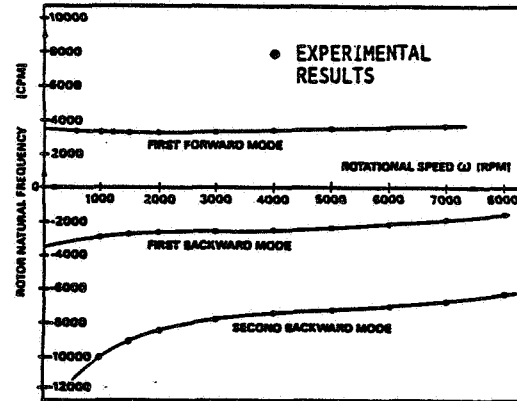


Figure 5. - Rotor natural frequencies versus rotative speed. Second forward mode in higher range of frequencies.

3.2 Identification of Rotor First Mode Parameters by Perturbation Testing (Dynamic Stiffness Method)

Synchronous perturbation combined with Dynamic Stiffness Method testing was successfully used for the identification of Rotor First Bending Mode generalized parameters (Fig. 6) [2,9]. When applied to a system with two degrees of freedom (rotor horizontal and vertical displacements), the Dynamic Stiffness Method clearly yields the system modal (generalized) parameters. Figs. 7 and 8 present the results for the vertical mode. The controlled unbalance was introduced to the rotor disk at a chosen location for the first run, then the same unbalance was placed at the same radius, 180° from the previous location for the second run. The results of these two runs are then vectorially subtracted. This eliminates all existing residual synchronous effects, and the results of the perturbation testing are very clean.

3.3 Identification of Bearing Fluid Dynamic Forces

The nonsynchronous perturbation method proved to be very efficient for the identification of bearing fluid dynamic forces [2,7]. This method was also applied by several researchers in order to identify the radial and tangential fluid forces acting on impellers in centrifugal flow pump [11,12]. Fig. 9 presents the rotor rig used for identification of bearing fluid dynamic forces. Figs. 10 and 11 illustrate some results of low frequency perturbation, covering oil whirl resonance. The perturbation testing yielded several important conclusions, concerning dynamic behavior of rotor/bearing/seal systems. These include a determination of oil whirl resonance frequency as being a rotor/bearing system natural frequency and existing only for forward directions, a specific relationship between bearing coefficients (such as "cross" stiffness proportional to radial damping, rotative speed, and average oil swirling ratio), a significant fluid inertia effect, stability margin, stabilizing effect of high oil pressure (Fig. 12), as well as allowed for full identification of the bearing fluid force coefficients.

The perturbation testing covering higher frequency range reveal both oil whirl and oil whip resonances as the rotor/bearing system characteristics as well as the specific whirl mode, governed by bearing radial damping. The Dynamic Stiffness Technique allowed for the identification of the rotor/bearing system parameters, and creation of an adequate rotor/bearing model [7] (Figs. 13-15).

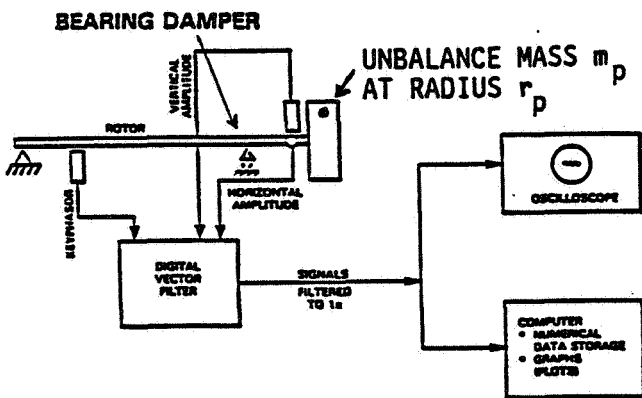


Figure 6. - Synchronous perturbation and dynamic stiffness method applied for identification of rotor first bending mode vertical and horizontal parameters.

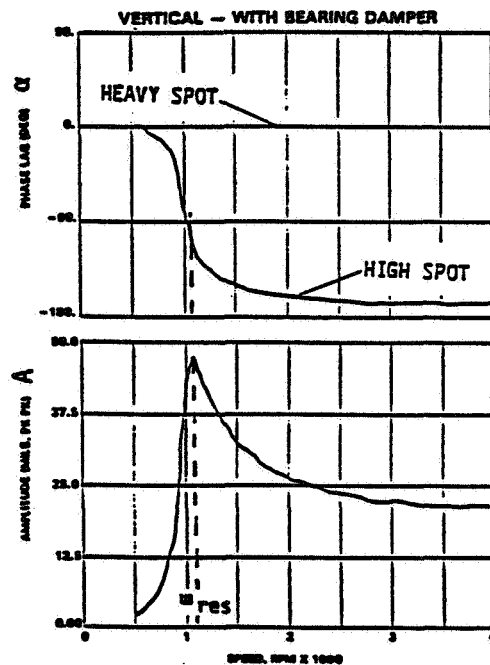


Figure 7. - Rotor vertical response: phase and amplitude versus rotative speed.

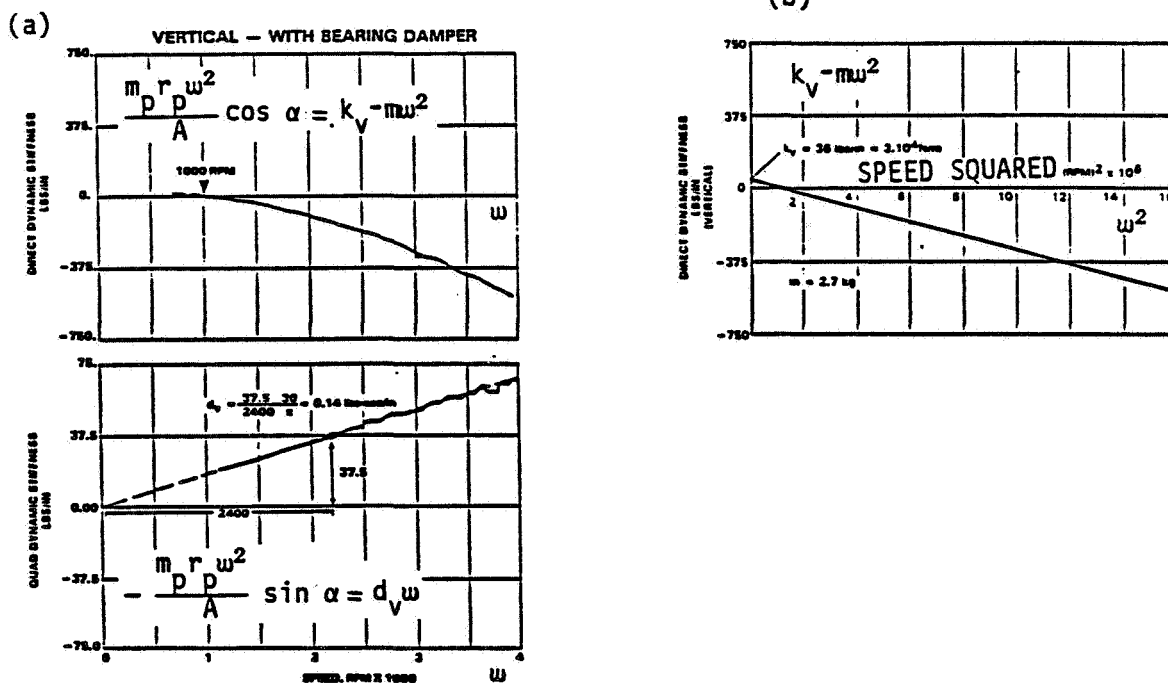


Figure 8. - Vertical dynamic stiffnesses versus rotative speed (a) and versus rotative speed squared (b). Identification of modal vertical damping coefficient d_v , stiffness k_v , and mass m .

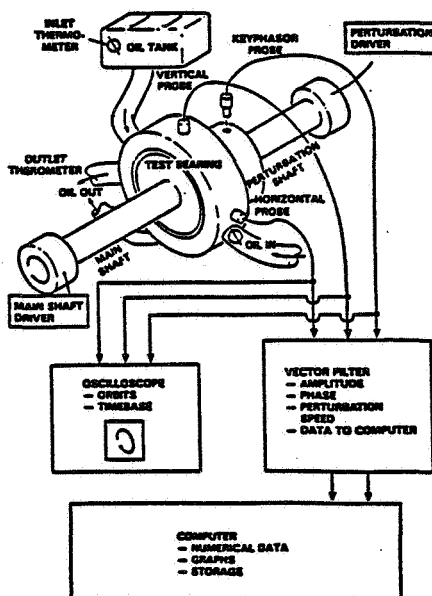


Figure 9. - Scheme of the perturbation testing for bearing fluid dynamic force identification.

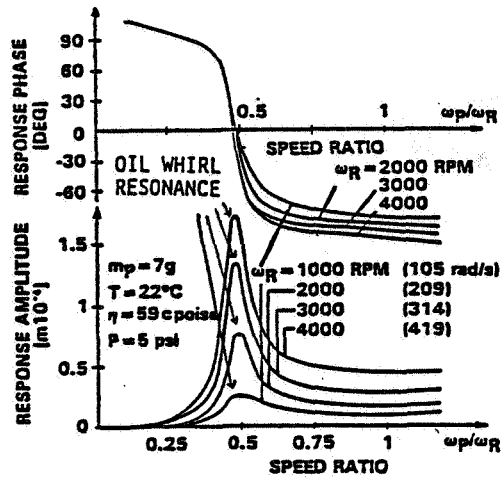


Figure 10. - Phase and amplitude of rotor response to forward perturbation versus perturbation speed ratio for several values of rotative speed ω_R . Oil whirl resonance revealed at frequency of approx $0.48 \omega_R$. At low perturbation speeds phase of response is leading (force phase angle, 0°).

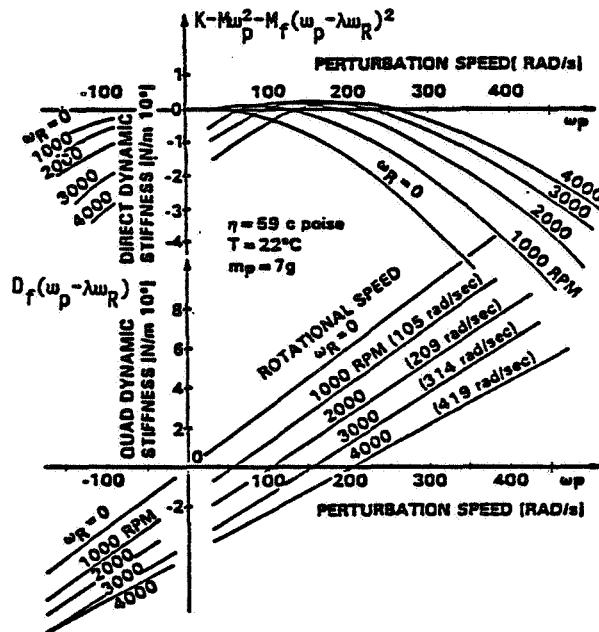


Figure 11. - Direct and quadrature dynamic stiffnesses versus perturbation speed: identification of rotor/bearing system parameters. Cross stiffness generated by radial damping; cross damping a function of fluid inertia. (M_f denotes fluid inertia; D_f , fluid radial damping coefficient; λ , fluid average swirling ratio; K and M , rotor modal parameters.)

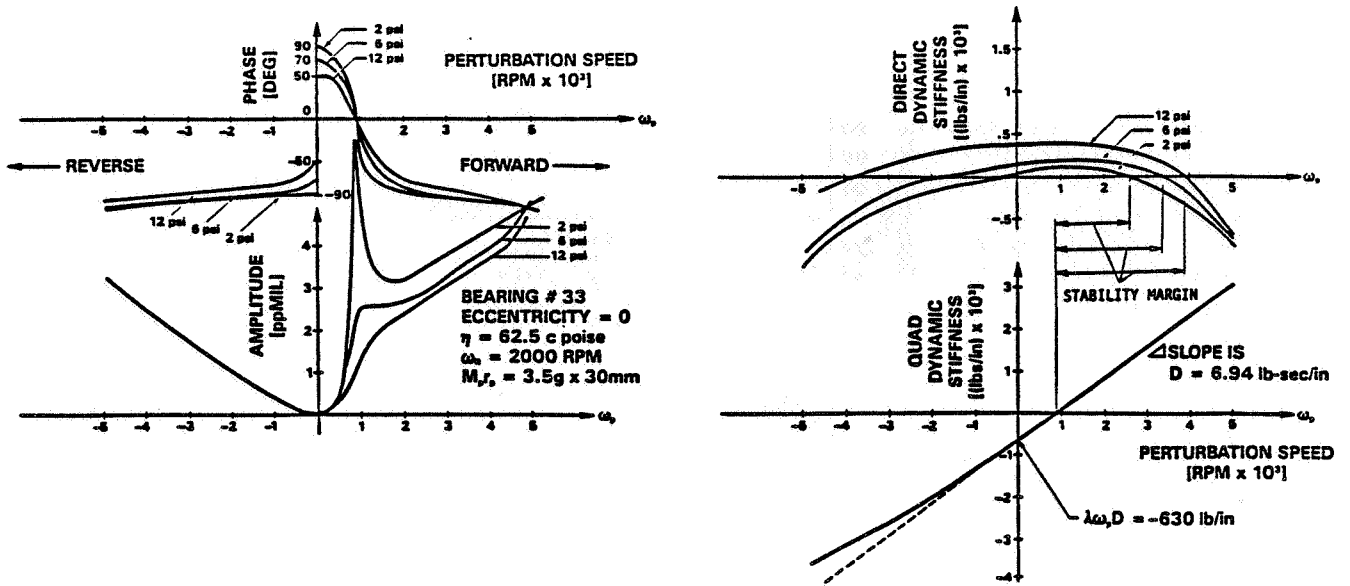


Figure 12. - Phase, amplitude, and dynamic stiffnesses versus perturbation speed for several values of oil pressure: increase of stiffness and stability margin for higher pressure.

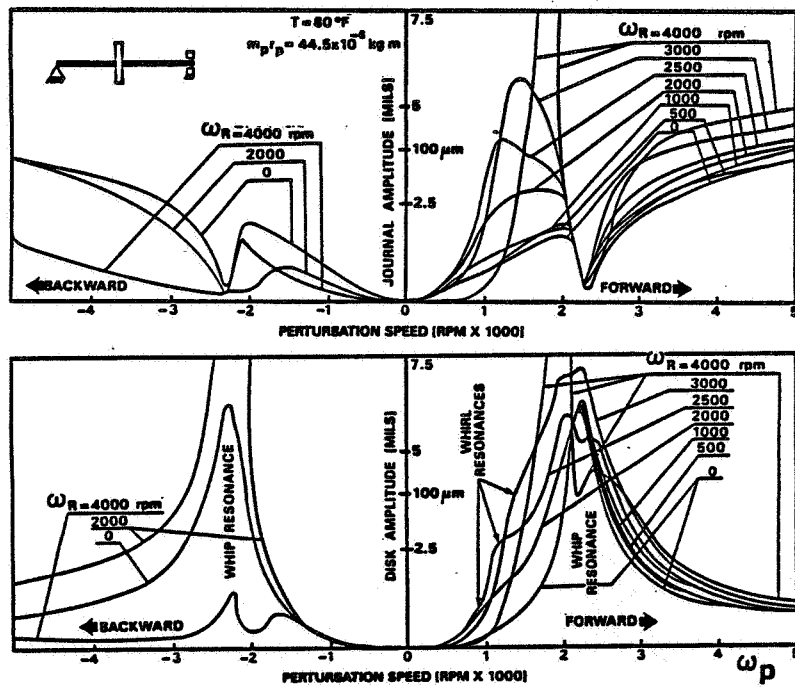


Figure 13. - Journal and disk response amplitude versus perturbation frequency ω_p for several values of rotative speed ω_R . Whirl resonance exists only for forward perturbation. Whip resonance (corresponding to rotor first bending mode) exists for both forward and backward perturbation.

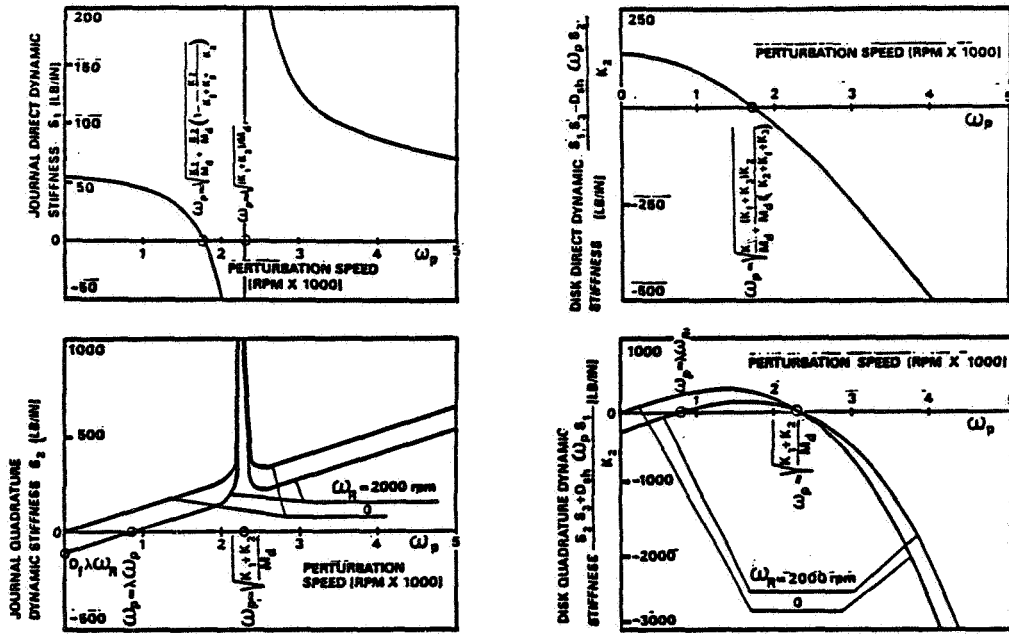
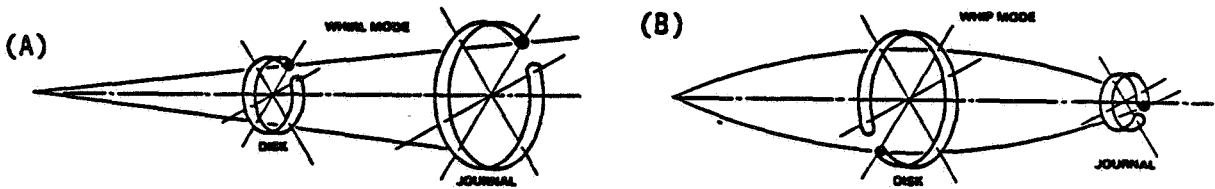


Figure 14. - Journal and disk dynamic stiffnesses versus perturbation frequency ω_p . Rotative speed ω_R affects quadrature dynamic stiffness only.

$$[S_1 = K_f + K_3 + K_2 - M_f(\omega_p - \lambda\omega_R)^2 - M_b\omega_p^2 - K_2^2 S_3 / (S_3^2 + D_{sh}^2 \omega_p^2), S_2 = D_f(\omega_p - \lambda\omega_R) + K_2^2 D_{sh} \omega_p / (S_{sh}^2 + D_{sh}^2 \omega_p^2), S_3 = K_1 + K_2 - M_d \omega_p^2].$$



(a) Whirl mode, disk and journal motion in phase.
 (b) Whip mode, journal 90° ahead of disk motion.

Figure 15. - Modes of rotor/bearing system revealed by perturbation testing.

SYMBOLS

A	Rotor amplitude of response
D_f, K_f, M_f	Bearing fluid damping, stiffness and inertia coefficients
D_{sh}	Rotor external viscous damping coefficient
K, K_1, K_2	Shaft stiffnesses
K_3	External spring stiffness
m_p, r	Perturbation mass and radius of unbalance correspondingly
M_b^p, M_d^p, M_d	Modal masses of the rotor

α	Phase of Response
η	Oil dynamic viscosity
λ	Oil average swirling ratio
w	Perturbation speed
w_R^p	Rotative speed of the main rotor

REFERENCES

1. Muszynska, A.: Rotor Internal Friction Instability, Proc. of the Symposium on Instability in Rotating Machinery, Bently Rotor Dynamics Research Corporation, Carson City, NV, June 1985.
2. Muszynska, A.: Application of the Perturbation Method to Rotating Machines. BNC Senior Mechanical Engineering Seminar, Carson City, NV, June 1984.
3. Bently, D.E., Muszynska, A.: Stability Evaluation of Rotor/Bearing System by Perturbation Tests, Rotordynamic Instability Problems in High Performance Turbomachinery, Proc. of a Workshop, Texas A&M University, College Station, TX, 1982.
4. Bently, D.E., Muszynska, A.: Oil Whirl Identification by Perturbation Test. Advances in Computer-aided Bearing Design, ASME/ASLE Lubrication Conference, Washington, DC, October 1982.
5. Bently, D.E., Muszynska, A.: Perturbation Tests of Bearing/Seal for Evaluation of Dynamic Coefficients. Symposium on Rotor Dynamical Instability, Summer Annual Conference of the ASME Applied Mechanics Division, Houston, TX, June 1983.
6. Bently, D.E., Muszynska, A.: The Dynamic Stiffness Characteristics of High Eccentricity Ratio Bearings and Seals by Perturbation Testing. Workshop on Rotordynamic Instability Problems in High Performance Turbomachinery, Texas A&M University, May 1984.
7. Bently, D.E., Muszynska, A.: Perturbation Study of Rotor/Bearing System : Identification of the Oil Whirl and Oil Whip Resonances. Tenth Biennial ASME Design Engineering Division Conference on Mechanical Vibration and Noise, Cincinnati, OH, September 1985.
8. Subbiah, R., Bhat, R.B., Sankar, T.S.: Modal Parameter Identification in Rotors Supported on Hydrodynamic Bearings, Proc. of Eight Machinery Dynamics Seminar, National Research Council Canada, Halifax, N.S., October 1984.
9. Muszynska, A.: Dynamic Stiffness Measurements for Better Mechanical System Identification. Bently Nevada Corporation, Paper presented at EPRI-Nuclear Power Division Pump Workshop, Toronto, Canada, August 1982.
10. Bently, D.E., Muszynska, A., Olas, A.: Identification of the Parameters of a Rotor with the Strong Gyroscopic Effect by Perturbation Testing, Bently Nevada Corporation, 1984.
11. Ohashi, H., Shoji, H.: Lateral Fluid Forces Acting on a Whirling Centrifugal Impeller in Vaneless and Vaned Diffuser. Proc. of the Texas A&M Workshop on the Rotor Dynamic Instability Problems in High Performance Turbomachinery, College Station, TX, May 1984.
12. Jery B., Acosta, A.J., Brennen, C.E., Caughey, T.K.: Hydrodynamic Impeller Stiffness Damping and Inertial on the Rotor Dynamics of Centrifugal Flow Pumps. *ibid.*

WHY HAVE HYDROSTATIC BEARINGS BEEN AVOIDED AS A
STABILIZING ELEMENT FOR ROTATING MACHINES?

Donald E. Bently and Agnes Muszynska
Bently Rotor Dynamics Research Corporation
Minden, Nevada 89423

The paper discusses the advantages of hydrostatic, high pressure bearings as providing higher margin of stability to the rotor/bearing systems.

INTRODUCTION

Despite the fact that the hydrostatic bearing was invented in 1862 by L. Girard, it appears to have been carefully avoided as a means of stabilizing rotor systems.

This is very interesting because it is perfectly obvious that if a cylindrical bearing could provide a higher Direct Dynamic Stiffness term (see Appendix) in the low eccentricity region, then the stability of a rotor system is, in normal situations, greatly enhanced. The hydrostatic principle not only provides this stiffness term easily, it may also supply its controllability.

It is an interesting exercise to examine the history of rotor dynamics and lubrication theory to guess what went right and what went wrong, and for what reasons. In this instance, as is typical in other such histories, there appears to be other engineering considerations which caused the path to go in the wrong direction.

Very early in lubrication theory (in 1919), Harrison correctly pointed out that a fully lubricated cylindrical bearing is inherently unstable. As a result of this natural behavior, Newkirk and Kimball introduced the pressure dam modification in order to provide a static load to the bearing to alleviate the instability when they showed the basic rules of oil whirl and oil whip in 1924. Numerous research since that time deals with stabilization by means of static loading, and this method of static load to a seal or bearing to hold it at high eccentricity position. At high eccentricity position, of course, the Direct Dynamic Stiffness term is always very high, thus providing stability to the system.

In addition to internal static loading (the pressure dam) and external static loading (by whatever means, such as gravity or deliberate misalignment), there has been a great deal of work on various modifications of the cylindrical form of bearings. It is the author's observation that all of these modifications are helpful for the simple reason that they provide a modification of the flow pattern, as a pure cylinder inside a cylinder is the worst possible situation, if stability is desired. There are lobe bearings, offset halves, tapered land, and hundreds of other helpful geometric modifications of bearings. These methods, however, cannot be applied to seals.

With all these studies and designs, surely someone must have tried hydrostatic principles on the basic bearing. Even so, the only known high pressure lubrication

systems for rotating machinery are very successful designs by a few manufacturers using a combination of tapered land bearings plus high pressure supply. Beyond these, the field appears barren.

As nearly as can be reconstructed, the blockade against hydrostatics occurred in the 1950s. Papers published in this period noted that the sleeve bearing went unstable if the bearing was 360° (fully) lubricated, but was stable with partial lubrication. (This is more or less correct; there usually is wider stability margin with partial lubrication.) The obvious and unfortunate conclusion, however, appears to have been that high pressure oil supply can cause 360° lubrication, therefore, use only low pressure oil supply!

Thus, while correct in its own context, this conclusion apparently blocked the use of Girard's great invention. It is interesting to note that Rayleigh followed upon the original hydrostatic bearing to make the first of the more widely used hydrostatic thrust bearing, but no one applied this idea to oil and gas-lubricated radial bearings [1].

HIGH PRESSURE BEARING RESULTS

The plots of the Direct Dynamic Stiffness as a function of static load-related eccentricity ratio (a) for a bearing with "normal" oil supply, i.e., with hydrodynamic pressure or about 20 psi, and (b) for the same bearing with four oil supply ports and four hydrostatic segments generating pressure about ten times high is shown in Figure 1. The increase of the Direct Dynamic Stiffness, especially for low eccentricity ratios, is very significant, as this increase powerfully increases the stability margin of the rotor system if the values are significant, especially for low eccentricity ratio.

The Quadrature Dynamic Stiffness (see Appendix) is virtually unaffected by the addition of the hydrostatic bearing, exhibits very regular relationship with the eccentricity ratio for various values of rotative speed and circular preloads, as shown in Figure 2.

For a more dramatic presentation of the extent of control over instability at the bearing, the Direct Dynamic Stiffness as a function of perturbation frequency yielded from perturbation testing is shown for the same bearing at low, medium, and high oil supply pressures in Figure 3a.

Figure 3b shows the Quadrature Dynamic Stiffness. It is, as in the steady-state tests, essentially independent of oil supply pressure.

Very similar to the high pressure bearing effect was described in the paper [2] reviewing the Lomakin effect. All that is required to match up to Lomakin effect is that the fluid pressure to the seals (or other rotor/stator periphery) goes up with the square of rotative speed, because the hydrostatic stiffness increases linearly with oil pressure. Obviously this creates a Direct Dynamic Stiffness which increases with square of speed, therefore looks like the Lomakin effect of the "negative mass."

CONCLUSIONS

The conclusions are as follows:

1. It is readily apparent that deliberate use of hydrostatic bearing high pressure lubricated (any gas or liquid) can easily be used to build higher stability margin into rotating machinery, in spite of the thirty years bias against high pressure lubrication.
2. Since this supply pressure is controllable, the Direct Dynamic Stiffness at lower eccentricity is also controllable, so that within some rotor system limits, the stability margin and dynamic response of the rotor system is more readily controllable.
3. It may be possible to take advantage of this effect in the various seals, as well as the bearings, to assist with stability margin and dynamic response of rotating machinery.
4. The stability of the bearing can be additionally improved by taking advantage of the anti-swirling concept. The high pressure fluid supply inlets should be located tangentially at the bearing circumference and directed against rotation. The incoming fluid flow creates stability by reducing the swirling rate.

REFERENCES

1. Cameron, A.: Basic Lubrication Theory. Third Edition, John Willey & Sons, 1981.
2. Gopalakrishnan, S., Fehlau, R., Loret, J.: Critical Speed in Centrifugal Pumps. ASME 82-GT-277, 1982.

APPENDIX

It is the easiest to explain Dynamic Stiffness terms on the example of a one-degree-of freedom mechanical oscillator, modelled by the equation:

$$M\ddot{x} + D\dot{x} + Kx = Fe^{j\omega t}, \quad j = \sqrt{-1} \quad (1)$$

where M is mass, D is damping coefficient, K is stiffness coefficient, x is vibrational displacement and F represents the amplitude of the periodic exciting force with frequency ω . Dots indicate derivation with respect to time, t.

The forced response of the oscillator has the following form:

$$x = Ae^{j(\omega t + \alpha)} \quad (2)$$

where

$$Ae^{j\alpha} = \frac{F}{K - M\omega^2 + Dju} \quad (3)$$

In the expression (2) A is the amplitude of the vibration response, α is the phase of response with respect to the forcing function F. The product $Ae^{j\alpha}$ has a name of the Complex Response Vector. It is proportional to the excitation amplitude F and inverse proportional to the Complex Dynamic Stiffness:

$$\text{Complex Dynamic Stiffness} = K - M\omega^2 + Dj\omega \quad (4)$$

Complex Dynamic Stiffness has the components:

$$\text{Direct Dynamic Stiffness} = K - M\omega^2 \quad (5)$$

and

$$\text{Quadrature Dynamic Stiffness} = D\omega \quad (6)$$

The equation (3) yields

$$\text{Direct Dynamic Stiffness} = \frac{F}{A} \cos \alpha \quad (7)$$

$$\text{Quadrature Dynamic Stiffness} = -\frac{F}{A} \sin \alpha \quad (8)$$

The expressions (5) through (8) are used for the identification of the system parameters.

Plotted versus excitation frequency ω the Direct Dynamic Stiffness is a symmetric parabola; the Quadrature Dynamic Stiffness is a straight line crossing the origin of the coordinates.

Similar formulation of the Dynamic Stiffness terms can be applied to the systems modelled by more sophisticated equations.

In particular, for a symmetric rotor supported in one rigid and one fluid lubricated bearing the model is as follows:

$$M\ddot{z} + M_f(\ddot{z} - 2j\lambda\omega_R\dot{z} - \lambda^2\omega_R^2z) + D(\dot{z} - j\lambda\omega_Rz) + Kz + K_bz = Fe^{j\omega t} \quad (9)$$

$$z = x + jy \quad j = \sqrt{-1}$$

where M , K are rotor mass and stiffness respectively, M_f , D , K_b are bearing fluid inertia, radial damping, and radial stiffness correspondingly, ω_R is rotative speed, λ is the average oil swirling ratio, ω is perturbation (excitation) frequency. The variable $z = z(t)$ represents the rotor radial displacement composed with the horizontal (x) and vertical (y) displacements.

For the steady-state periodic response

$$z = Ae^{j(\omega t + \alpha)} \quad (10)$$

the Direct and Quadrature Dynamic Stiffnesses for the rotor model (9) are as follows:

$$\text{Direct Dynamic Stiffness} = \frac{F}{A} \cos \alpha = K - M\omega^2 - M_f(\omega - \lambda\omega_R)^2 + K_b \quad (11)$$

$$\text{Quadrature Dynamic Stiffness} = -\frac{F}{A} \sin \alpha = D(\omega - \lambda\omega_R) \quad (12)$$

The Direct Dynamic Stiffness versus frequency ω is a parabola shifted from the symmetric origin due to fluidic inertia. The effect of higher pressure, which causes an increase of K_b is shown in Figure 3. For small values of $K + K_b$ the Direct Dynamic Stiffness at zero frequency ω can be negative (Fig. 3).

The Quadrature Dynamic Stiffness versus frequency ω is a straight line crossing the vertical axis at its negative side. This value is equal to the bearing "cross" stiffness coefficient, $-D\lambda\omega_R$, Fig. 3b.

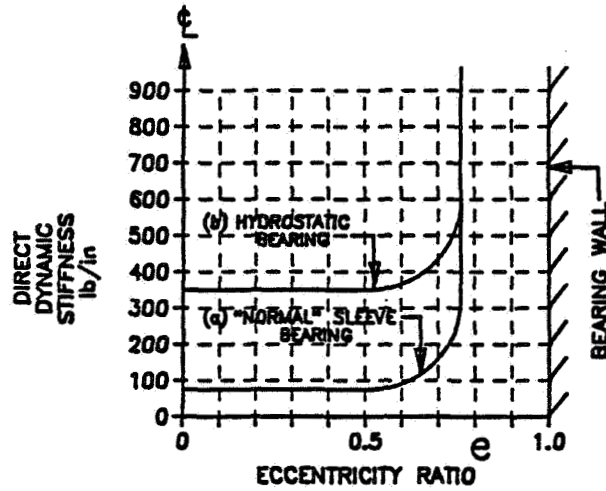


Figure 1. - Direct dynamic stiffness versus eccentricity ratio for a hydrodynamic bearing (a) and a hydrostatic bearing (b). (Eccentricity ratio = ratio of journal displacement to radial clearance).

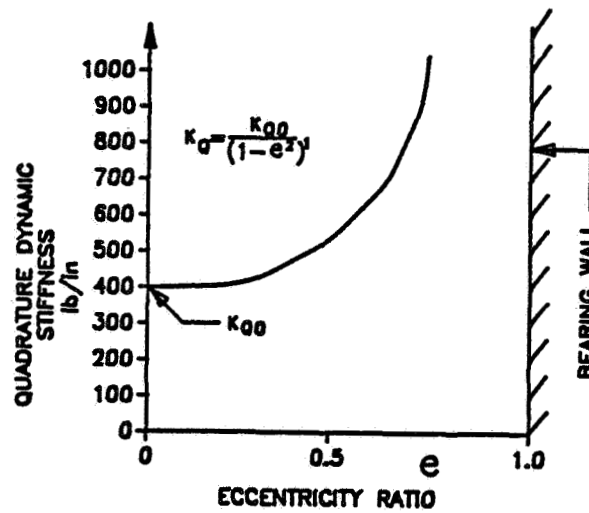


Figure 2. - Experimentally obtained quadrature dynamic stiffness versus eccentricity ratio, indicating insensitivity to oil pressure.

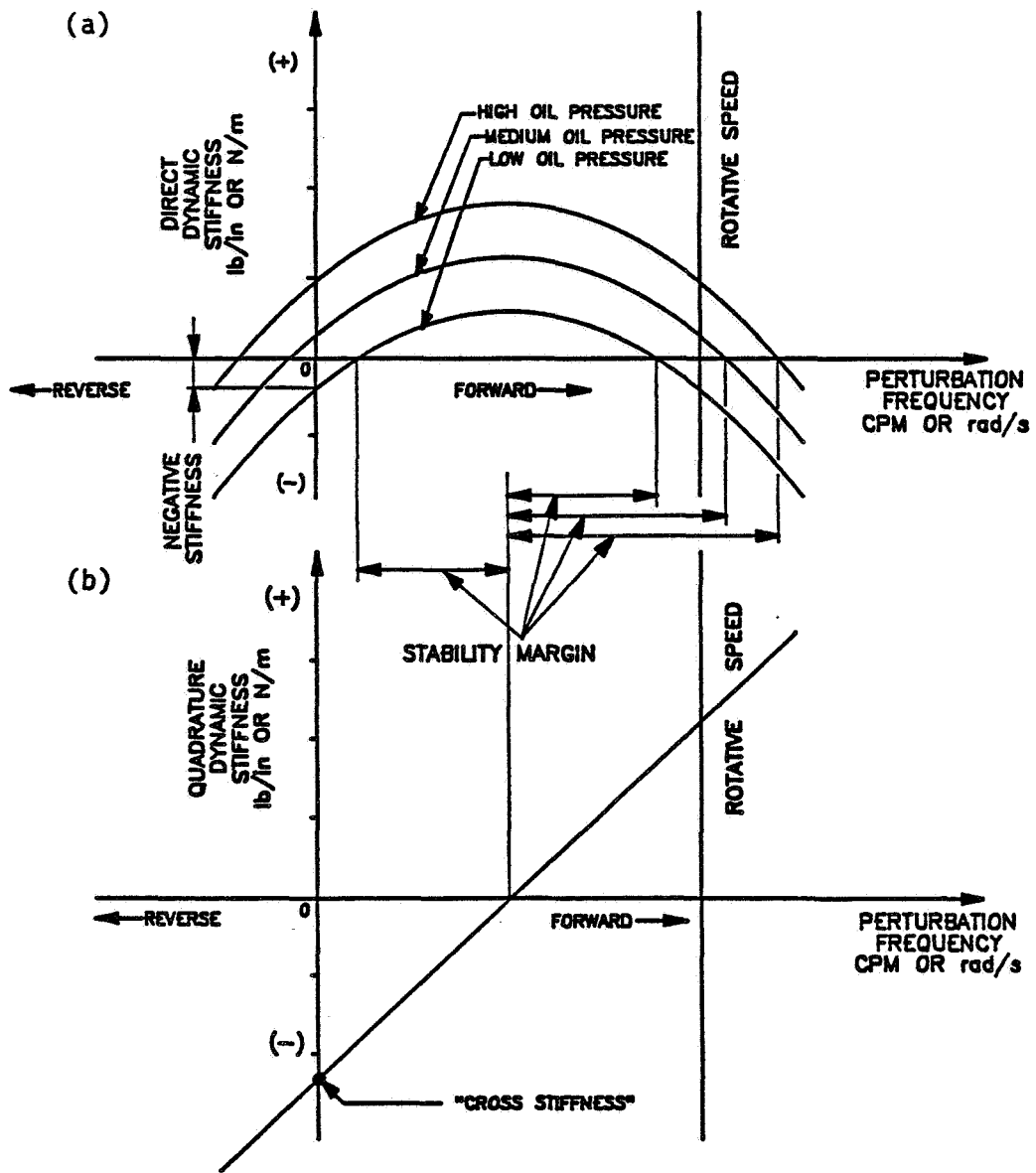


Figure 3. - Dynamic stiffnesses versus frequency for several values of oil supply pressure, indicating stability margins.

TURBINE INSTABILITIES - CASE HISTORIES

C.W. Laws
Bently Nevada (UK) Limited
Birchwood, Warrington, United Kingdom

Several possible causes of turbine rotor instability are discussed and the related design features of a wide range of turbomachinery types and sizes are considered. The instrumentation options available for detecting rotor instability and assessing its severity are discussed.

INTRODUCTION

Turbines of course are built in many forms, from very large multi-cylinder power generation units, through process/feed pump drives to the smaller specialized designs using process fluid in an integrated expander/compressor configuration. The causes of rotor instability in turbines, whether they are steam or gas driven, relate closely to the causes of instability in compressors and pumps. In recent years, instability problems with high pressure compressors have been perhaps more prominent than with turbines - light rotors, high rotational speeds and high stage pressure ratios inevitably result in a rotor system which is really fundamentally unstable in the presence of very significant fluid derived forces. Only the adoption of bearing designs with strong stabilizing characteristics and seal designs with resistance to the development of destabilizing static and dynamic forces can ensure the stable operation of many high pressure compressor designs; the position is similar with turbines.

Arguably, it was the electricity generation industry which pushed forward the design of large rotating machinery, particularly turbines and high pressure pumps. Paradoxically, in power generation, rotor speeds are effectively limited to 3000/3600 rpm by system frequencies of 50/60 Hz; gear-box transmission of 660 MW is absolutely not economically desirable. In the petrochemical process industries, attention has centered on improved efficiency and reliability (common to both industries), but in turbine design there has been freedom to exploit the use of increased rotor speeds, as well as elevated steam conditions, to achieve improved efficiency.

Rotor instability problems have occurred therefore in a somewhat cyclical manner as technological progress occurred in the thermodynamic sense; in many ways the design of steam turbines in the power generation and petrochemical process industries has converged. In two important respects however, the steam turbines employed in these industrial environments still differ - partial admission of steam is a necessity in most process-drive steam turbines, but is a rarely used technique in power generation turbines, and fortunately not usually necessary (except in feed pump drives) since the size of the machine permits the use of full admission with reasonable nozzle areas. Coupling between multi-cylinder turbines and to the driven machine is universally solid or rigid in the power generation industry, almost universally flexible in the process industries. The effect of coupling flexibility is profound

in terms of coupled rotor dynamic behavior; from the point of view of turbine stability, both of these design differences have a large influence on the potential for instability in the turbine and driven machine.

Several years ago, the most common type of rotor instability experienced on turbines was associated with bearing oil film instability resulting in "oil whirl" or "oil whip." Very often the cause was relatively simple - turbine designers tended to be more concerned about ensuring that the bearings used were unlikely to suffer from premature failure due to overloading, either due to dynamic stresses leading to fatigue of the babbit metal, or wipes when oil film thickness was minimal at low rotational speeds.

Solidly coupled power-generation type turbines (and their associated generators) were quite commonly affected by this problem some twenty or so years ago. Ensuring that a bearing load at least approximating to the natural proportion of the rotor weight associated with the bearing location was maintained was obviously a problem, since changes in alignment could easily deload a bearing during normal operation.

Nevertheless, the bearings used in large turbines are rarely more sophisticated than fixed geometry, elliptical bore designs, perhaps with central grooving and sometimes with a tri-lobal geometry. Use of variable geometry bearings, typically of four or five shoe design is very unusual, indeed is positively avoided. The disadvantages of initial cost, high losses in operation and risk of damage during slow turning (provision of jacking oil is difficult) are very significant when very large, heavy rotors are involved. Insufficient system damping at the critical speed(s) may also be a problem.

Even on relatively small process drive turbines, the amplification factor at the first flexural critical speed is often quite high when tilt-shoe bearings are employed. Although this is largely due to the characteristics of the bearing, it may also be due to a relatively poor state of balance. Process-drive turbine rotors are often balanced in low-speed balancing machines or balanced at high speed using a multiplane technique optimized for good running speed vibration levels. Very accurate correction of balance at the critical speed(s) may require the application of a true "modal" technique, widely practiced by the manufacturers of large turbines and generators, simply because the inherent balance defects present in new rotors demand balancing at each critical speed in order to run the rotor up to its normal operating speed. Even with the application of good balancing techniques, the trade between available damping at critical speeds and inherent stability at normal operating speed is a very significant one. Ironically, the achievement of a truly excellent state of balance manifested as near zero levels of synchronous (1X) vibration amplitudes at the rotor bearings can lead to instability of the rotor due to oil whirl or whip; quite understandably, in the absence of any distinct 1X forcing function, it is easier for the rotor system to cross the stability/instability threshold if the margin of stability is small.

1. MEASUREMENT OF TURBINE VIBRATION - DETECTION OF ROTOR INSTABILITY

Unstable rotor operation, generally indicated by the presence of nonsynchronous vibration behavior, is normally interpreted as a malfunction or fault condition. Often, the additive effect of synchronous or 1X vibration due to residual unbalance and nonsynchronous (typically subsynchronous) vibration leads to overall vibration levels in excess of agreed acceptance or tolerance limits whether during initial customer acceptance tests or later in commercial operation. Existing manufacturing

standards, etc. generally state a maximum level of rotor relative or casing absolute vibration at synchronous (1X) frequencies and at nonsynchronous frequencies, but little guidance is offered as to the real significance or potential for damage of vibration related to instability of the rotor system. This leads, in the author's experience, to two fundamentally different problems. On one hand, sometimes undue importance is attributed to well controlled vibration resulting from a suppressed level of instability, while on the other hand, potentially or actually serious instability may be underestimated or even ignored.

The vibration measurement technique used on a particular machine may significantly affect the user's perception of the severity of an instability condition. The inherent frequency dependent relationship between vibration displacement, velocity, and acceleration is very well known and understood; clearly, subsynchronous vibration of a rotor will be measured on a one-for-one basis, compared with other frequencies if expressed in displacement terms, but will be measured in velocity terms as an amplitude proportional to frequency.

In acceleration units, the relationship with displacement is proportional to frequency squared; consequently, low frequency vibration due to instability, typified by "oil whip" or re-excitation of the rotor's first critical speed will be measured in acceleration terms as an apparently insignificant vibration level - a potentially dangerous situation when very flexible rotors are being considered. Some vibration monitoring systems fitted to turbines may actually conceal the presence of unstable rotor vibration completely.

There is clearly a need to do two things. One, ensure that the vibration monitoring technique used is capable of measuring all relevant vibration behavior of the rotor. Two, use a sensible interpretation technique which neither overstates nor understates the importance of any measured unstable rotor vibration. In many respects, it is more important to assess how much margin of stability a turbine system possesses, so that in conditions of unusually severe operation it may be expected to remain stable, rather than simply documenting unstable operation of a gross nature. Although the solution to the latter problem may not be so easy, the vibration levels experienced on turbines suffering from severe instability are often so unsatisfactory that an immediate solution to the problem is mandatory.

Quite often, a change in the instrumentation system used for vibration measurement on a particular turbine, for instance, after a retrofit, will reveal an unstable condition, perhaps several years after the machine was commissioned. If the turbine has not been a problem, is it justifiable to be worried? In some cases the answer is quite definitely no; in others, an investigation of the turbine's operating history may reveal that certain problems have occurred which can be attributed retrospectively to the continued or occasional presence of unstable rotor vibration.

2. CASE HISTORIES

Bearing oil film instability, leading to "oil whip" on a 3,000 rpm double-end drive gas turbine-driven generator set, produced unacceptably high rotor vibration at a frequency of 800 c.p.m., corresponding to the first flexural critical speed of the generator rotor. The unit was intended for rapid start-up and loading for peaking and system support during emergencies; near 100% reliability of synchronization was an essential requirement.

Instability, when it occurred, developed during start-up at about 2,000 rpm; the standard vibration monitoring instrumentation was a single velocity seismoprobe at each end of the machine train. Even when rotor vibration amplitudes due to "oil whip" were virtually as large as the bearing clearances, high bearing vibrations were not indicated, due to the poor frequency response of the velocity transducer and the high bearing pedestal stiffness relative to the oil film stiffness. This misleading situation was discovered when eddy current proximity probes were installed for analysis purposes.

The bearing oil film instability and resultant rotor "whip" were not of particularly unique character; however, the solution of the problem through the adoption of improved bearing design was made unusually difficult by the design of the generator rotor, its bearing locations and the use of extremely heavy clutch couplings overhung at the generator rotor ends.

Due to the overhung masses, the first flexural critical mode shape resulted in nodal points very close to the bearing centerlines at both ends of the generator rotor. The bearings were therefore relatively ineffective in terms of controlling the rotor response, either at the first critical speed during start-up or shutdown, or whenever re-excitation of the first critical occurred. The adoption of tilting-shoe bearings, which would have solved the oil film instability problem at normal operating speed, would have resulted in totally unacceptable rotor vibrations when passing through the first critical speed due to the inevitable reduction in system damping which would have resulted. Very precise rotor balancing was already necessary to obtain an acceptable maximum level of vibration at the first critical speed and small, but significant, thermally induced bow of the rotor was present so that sufficiently good effective balance could not be maintained at all times.

This case history illustrates the importance of ensuring that the bearings are located as far away from nodal points as possible; coupling overhang effects are influential on virtually all turbines, indeed on rotating machinery of all types, and will often influence the position of nodal points sufficiently to make the solution of rotor instability problems particularly difficult.

The second case history refers to a typical modern process-drive turbine of single casing design using relatively high steam inlet pressure. Considering the horsepower developed and the "energy density" within the expansion, the rotor weight was small; tilting-shoe journal bearings of conventional design were employed, indeed were necessary, at the operating speed range of about 5,000-12,000 rpm.

It was found that during normal operation, when synchronous (1X) rotor vibrations were very acceptable, small changes in process conditions could initiate high vibration levels on the inlet and exhaust end bearing journals, leading to frequent trips of the unit. The standard vibration monitoring instrumentation was eddy current proximity probes at each bearing in conventional X-Y configuration.

On-site vibration analysis showed that the problem was one of re-excitation of the first flexural critical speed of the turbine rotor, leading to a "whip" type response, illustrated in Figure 1. Oil film instability was not suspected. Analysis of the rotor position within the bearing clearance showed that, particularly at the inlet end, the rotor was being lifted into the top half of the bearing (see Figure 2). Steam induced lifting/perturbing forces were considered to be responsible, but were difficult to quantify in a field situation.

The subsynchronous vibration frequency corresponded closely to the first flexural critical speed of the rotor, confirmed during start-up/shutdown tests. A temporary modification was installed by the turbine manufacturers, effected by reducing the mean bearing clearance in the inlet and exhaust end bearings by shimming behind the tilting shoes in the top half of each bearing bush. This was very successful in suppressing the subsynchronous vibration so that, even under the worst steam inlet/extraction pressure transients, the rotor re-excitation was below 0.25 mils peak-peak (see Figure 3). At a later date, modified bearings with increased shoe stiffness and preload were installed, leading to a further reduction in subsynchronous vibration amplitudes. Although steam-induced forces within the turbine continued to lift the rotor journals into an abnormally high position in the (reduced) bearing clearance, particularly at the inlet end, the modification was considered to be a completely acceptable method of overcoming the problem.

Low amplitude subsynchronous vibration response can be detected on many turbines of virtually every manufacture. Figure 4 illustrates the point; this turbine drive operated in the long term without any failure. Although complete elimination of subsynchronous vibration is of course a desirable objective, it should be remembered that the cost and inconvenience incurred may not be justifiable in every case.

Case history number three documents an unusual instability found on a relatively old Ljungstrom type radial-flow steam turbine generator which had been in service for many years without suffering the problem; machinery of this type rarely exhibits unacceptable vibration, except of course when rotor balance is poor. It was found that at loads above 4.0 MW (the unit was rated at 6.25 MW), casing vibration levels, particularly at the exciter end (see Figure 5) increased rapidly as the load increased. At about 4.8 MW the measured casing vibrations were totally unacceptable (above 30 mm/sec peak velocity). Although casing vibration measurements clearly indicated that a problem existed, even very detailed measurements could not identify the source of excitation of the machine; it was possible only to determine that, when high vibration developed, the main component of casing excitation was at 3700 cpm (61.67 Hz) at the normal operating frequency of 3000 cpm (50 Hz system). Below 4.0 MW load the super-synchronous frequency was completely absent. Eddy current displacement probes were temporarily installed on the machine at the four main bearing locations and at the exciter bearing; integrated velocity transducer measurements were also taken at the exciter bearing housing to permit, by electronic summation, exciter rotor absolute vibration levels to be determined.

It was found that, when the increasing super-synchronous vibration developed, the rotor response was greater than the bearing housing at the exciter end, although during start-up the structure responded strongly at the same frequency when 2X rotor vibration frequency corresponded to the 3700 cpm (61.67 Hz) frequency.

Clearly a structural response of the turbine generator and a strong rotor response were present at the 3700 cpm (61.67 Hz) frequency, capable of being excited by 2X rotor vibration during start-up and also, when on load, at a super-synchronous frequency on the rotor (see Figures 6 and 7).

However, study of the rotor position, particularly at the exciter bearing showed that when the unit was operating at 3000 rpm, the exciter bearing was totally deloaded, with the journal virtually at the center of the bearing clearance (see Figure 8). In this condition, the exciter rotor was clearly unsupported at the outboard end and was effectively a cantilevered overhung mass which would be expected to considerably change the response characteristics of the rotor system. At a later date the exciter bearing was raised to retain a gravity preload at normal op-

erating speed, allowing for the greater lift of the much larger diameter main generator bearing journal; full load (6.25 MW) was then achieved with acceptable overall vibration levels and negligible super-synchronous vibration components.

The fourth case history deals with two examples of rotor instability found on turbo-expander compressors of the integral double overhung design, although they were of different manufacture. One unit was found to exhibit strong subsynchronous vibration at 0.47X rotor rotational frequency; clearly "half speed" oil whirl of the rotor, which operated well below its first flexural critical speed. Rotor relative vibration was monitored with eddy current probes located at each end of the rotor in "X-Y" configuration. This machine has been in operation for over 5 years without any mechanical failure or process interference through trips. Some reduction in the whirl amplitude was achieved by selecting a less viscous oil, but no opportunity to cure the condition through bearing design change has been permitted; the rotor orbit and run-up cascade spectrum are shown in Figure 9.

Another expander compressor of similar design but smaller size and higher speed was found to suffer from occasional heavy seal rubs. Rotor vibration was measured using a single eddy current probe positioned approximately mid-way between the two bearings. Tests showed that when the oil temperature at bearing inlet was increased from 35°C to 45°C, the normally stable rotor started to go through a cyclical rise and fall in 1X vibration; a second eddy current probe was installed during testing to permit the analysis of the rotor orbit - examples are shown in Figure 10. These measurements also identified that when the vibration at 1X rotational speed increased, the phase angle increased in lag by about 50 degrees. Increasing the oil inlet temperature by 10°C had a significant affect on the viscosity and would therefore change the bearing coefficients. However, the rotor vibration was considered to be occurring in an essentially rigid conical mode; therefore, measurements made at the central region of the rotor were likely to be in the region of a node and potentially much smaller than at the bearings and seals. Changes in bearing oil film parameters due to oil inlet condition changes, especially if the effect was greater on one bearing than the other, were predicted to affect both the frequency of occurrence and node position for such a coaxial mode. Vibration measurements taken on the machine casing were extremely small and increased insignificantly when the rotor vibration levels increased; detailed analysis of the rotor behavior and adequate machine protection would clearly have required installation of shaft-relative probes next to both bearing journals.

CONCLUSIONS

Turbine rotor instability can occur for a variety of reasons associated with fundamental bearing design, interaction with the rotor dynamics and perturbation forces developed within the machine as a direct or indirect result of fluid forces.

Application of high speed lightweight flexible rotors demands bearings with strong stabilizing characteristics, typically of the tilting shoe or multi-lobe profile type. Unless the design of the turbine eliminates rotor lifting and perturbing forces derived from the expanding fluid within the machine case, it is almost inevitable that some evidence of well suppressed instability, seen typically as re-excitation of the rotor first flexural critical speed, will be detectable. Provided that the level of re-excitation is small at all times, such behavior may not be necessarily considered to be a problem or a defect in the machine; clearly good judgement must be used in assessing turbine behavior of this type.

Bearings with high intrinsic stability cannot always be specified since the available damping, particularly at the critical speed during start-up or shutdown, may be insufficient to prevent the occurrence of unacceptably high rotor vibration.

Some types of turbomachinery appear to be able to operate with the rotor vibrating relatively strongly in an unstable regime without failure; most are not of course. Establishing the level of stability available on marginally stable turbines is possibly the most important objective.

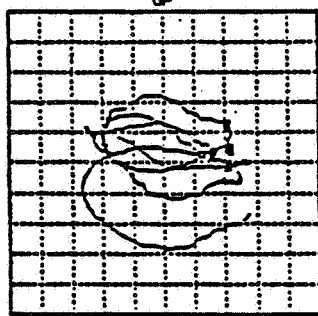
A most important requirement, both for machine protection and investigation of rotor behavior, is the selection of an appropriate vibration measurement technique. Use of the wrong technique can conceal potentially serious rotor instability and prevent effective machine protection or meaningful analysis of machine behavior.

Although good rotor dynamics/bearing analysis techniques are available for initial design and post-design assessment of turbine behavior, it is still difficult to use this type of facility in the field.

There is a considerable need for the development of portable hardware and software systems capable of being used in the field to enable more specific analysis of both machinery instability and stability margins to be made. In many situations it is more important to establish how much margin of stability a rotor system has, particularly when it is in as-designed condition. It is often of even greater importance to establish how sensitive the rotor system stability margin is to deterioration in bearing condition, effective bearing load and the development of perturbing forces within the turbine.

ORIGINAL PAGE IS
OF POOR QUALITY

UNFILTERED



AMP SCALE= 0.20 MILS/DIV

ROTATION: CCM



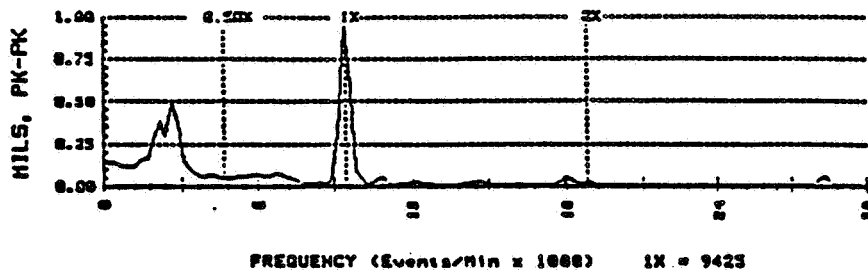
AMP SCALE= 0.20 MILS/DIV

TIME SCALE= 5.00 MSEC/DIV

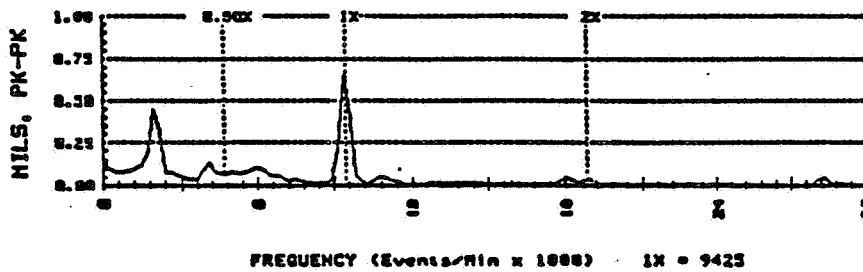
RPH(START)= 9432 RPH(END)= 9433



RUN: 2 DATE: 16MAY1983 TIME: 1605 PROBE ID: INLET END VERT



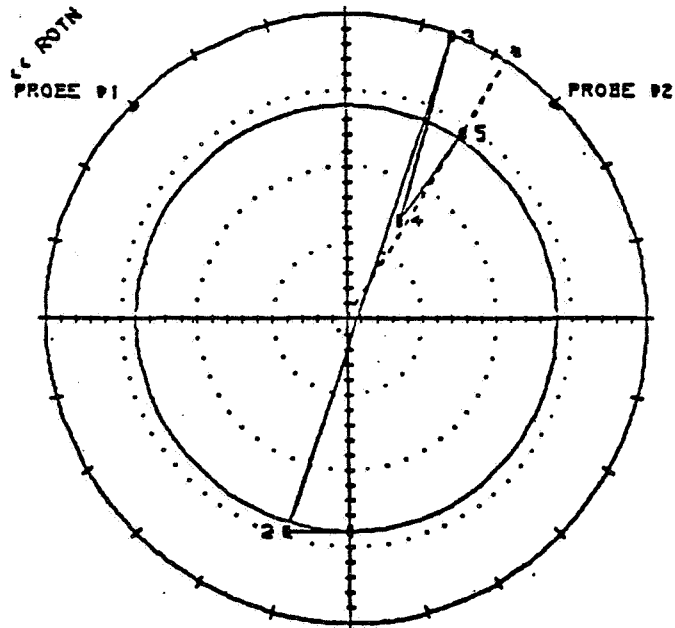
RUN: 2 DATE: 16MAY1983 TIME: 1605 PROBE ID: INLET END HORIZ



PEAK HOLD SAMPLE, 16 SAMPLES TAKEN SHIMS REMOVED BOTH BEARINGS

Figure 1. - Process drive turbine inlet end orbit, waveform, and spectrum plots.

ORIGINAL PAGE IS
OF POOR QUALITY

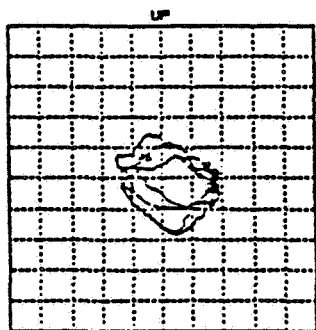


SHAFT CENTERLINE PLOT
PLOT RADIUS = 10.00 MILS/ 2.00 VOLTS
TIC SPACING = 0.50 MILS
SHAFT MOVEMENT VECTOR = 13.65 MILS @ 73°

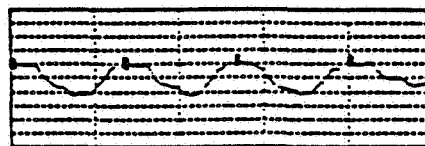
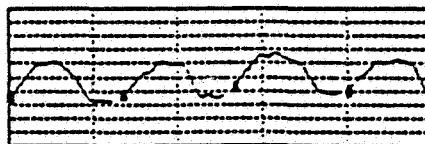
ATTITUDE ANGLE (α) = 147°
BEARING CLEARANCE = 14.0 MILS
PROBE 01 SCALE FACTOR = 200 mV/MIL
PROBE 02 SCALE FACTOR = 200 mV/MIL

Figure 2. - Process drive turbine inlet end rotor position.

ORIGINAL PAGE IS
OF POOR QUALITY

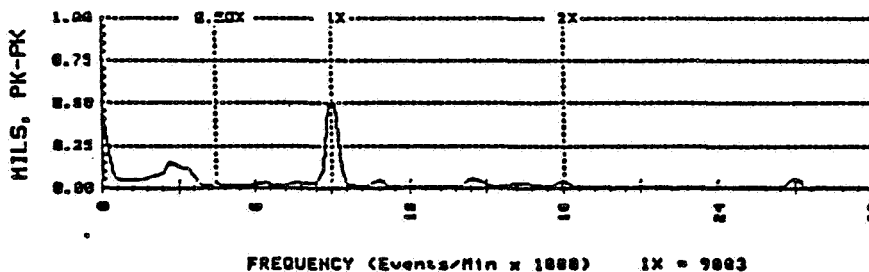


AMP SCALE= 0.20 MILS/DIV
ROTATION: CCM



AMP SCALE= 0.20 MILS/DIV
TIME SCALE= 5.00 MSEC/DIV
RPM(START)= 8996 RPM(END)= 8996

RUN: 2 DATE: 17MAY1983 TIME: 1930 PROBE ID: INLET END VERT



RUN: 2 DATE: 17MAY1983 TIME: 1930 PROBE ID: INLET END HORIZ

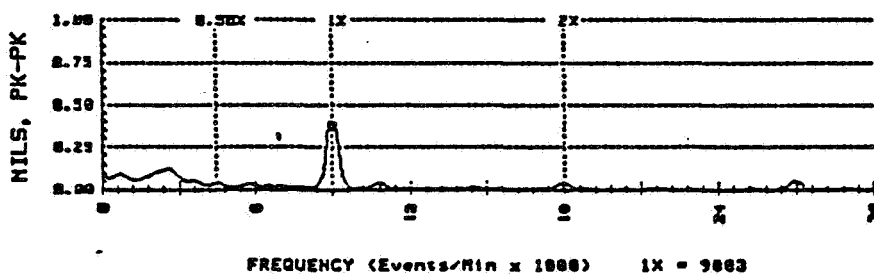


Figure 3. - Process drive turbine modified bearings.

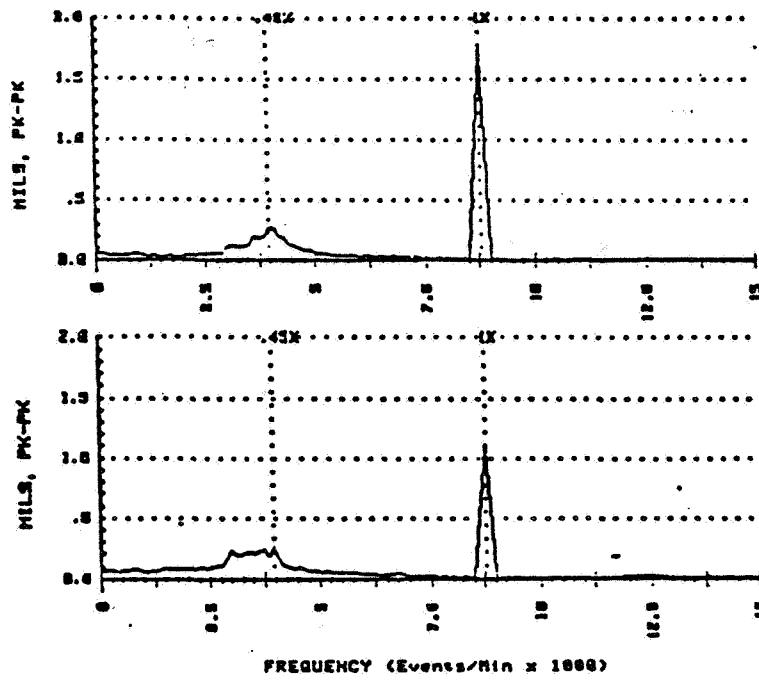


Figure 4. - Example of subsynchronous vibration - process drive turbine B.

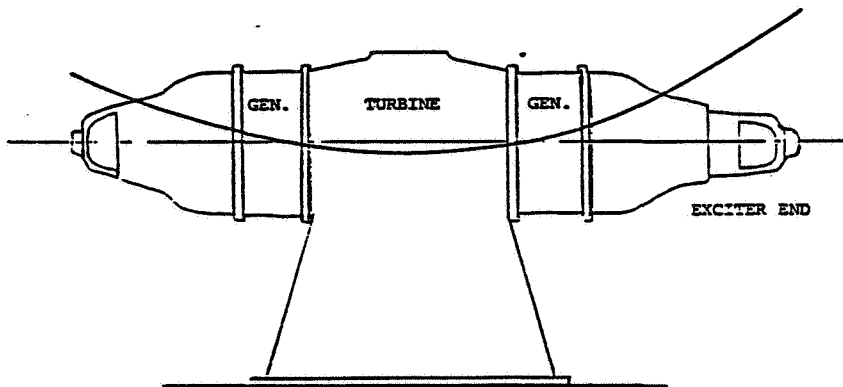
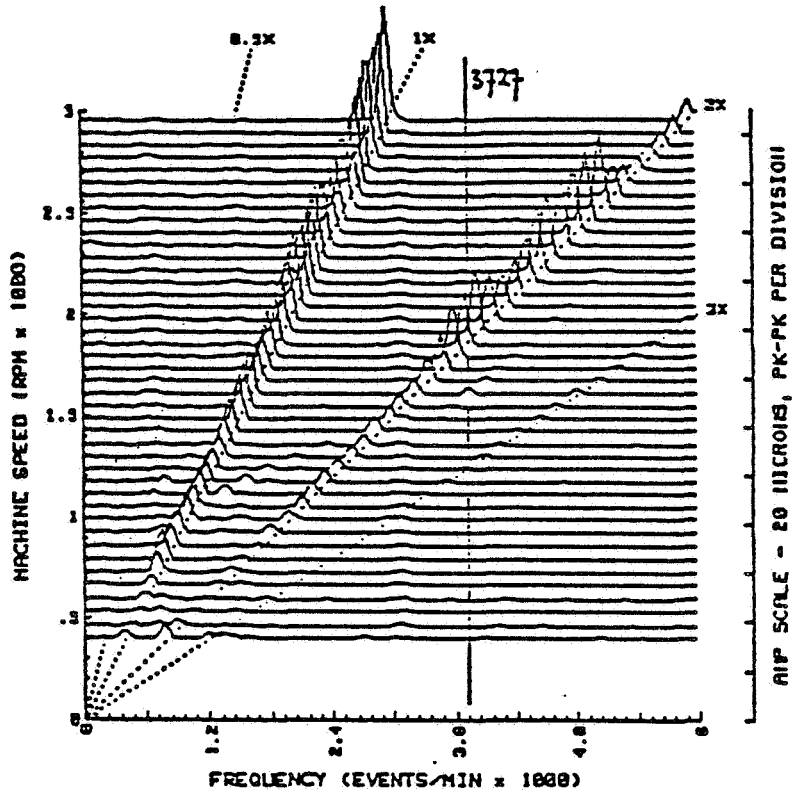


Figure 5. - Radial flow steam turbine generator casing vibration.

RUNUP MACHINE ID: EXCITER
 PROBE ID: SVD(ABS)
 RUN: 1b DATE: 8 MARCH '84 TIME: 12.21 >>12.37



START UP DATA AS SAMPLED OF THE ADDED VIBRATION TRANSDUCERS.
 SVD(ABS)=LOCATION 3, VERTICAL(LABELED), SHAFT RELATIVE DISPLACEMENT
 SIGNAL PLUS CASING DISPLACEMENT.

Figure 6. - Cascade spectrum plot for radial flow turbine generator exciter outboard bearing - rotor absolute vibration.

ORIGINAL PAGE IS
OF POOR QUALITY

RUNUP MACHINE ID: EXCITER
PROSE ID: 5VD(CAS)
RUN: 1c DATE: 8 MARCH '84 TIME: 12.21 >>12

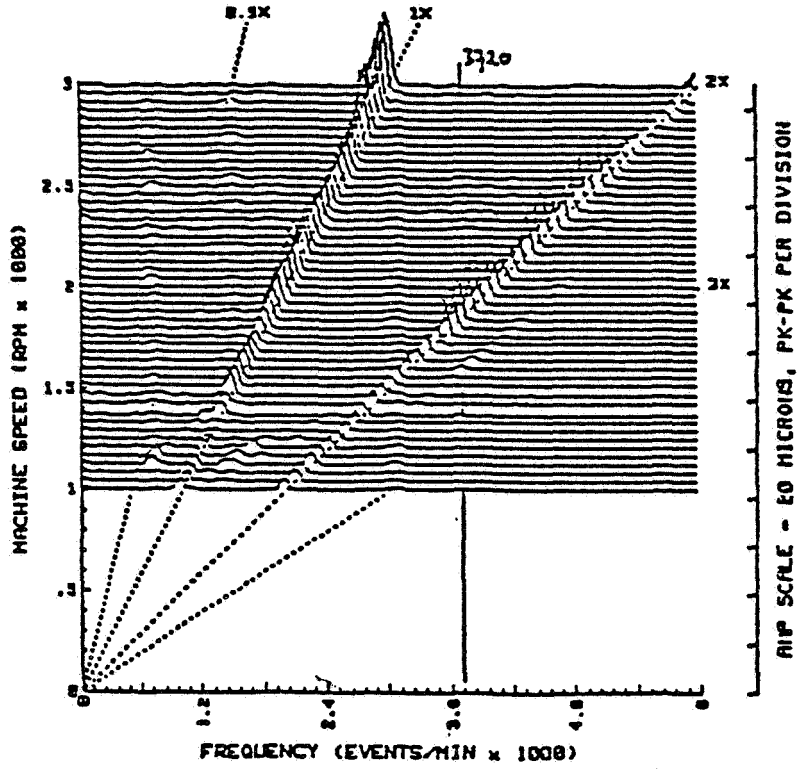
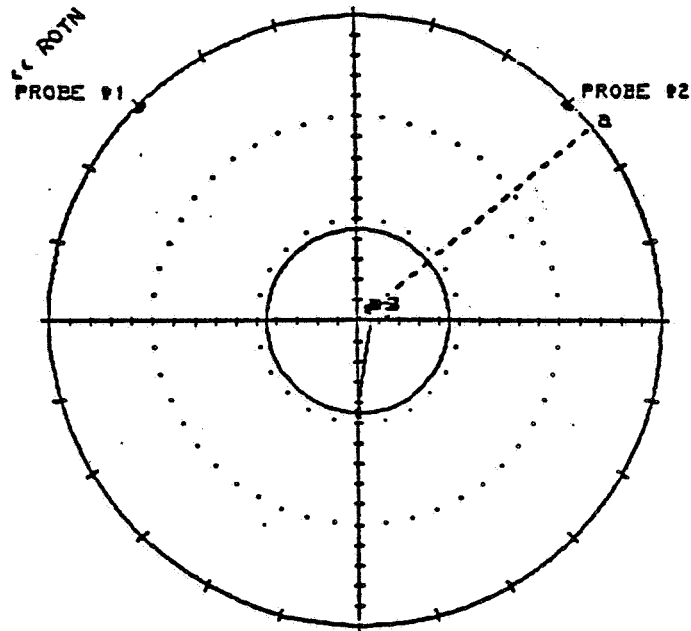


Figure 7. - Cascade spectrum plot for radial flow turbine generator exciter outboard bearing - housing absolute vibration.



SHAFT CENTERLINE PLOT

ATTITUDE ANGLE (α) = 129°

BEARING CLEARANCE = 90 MICRONS

PLOT RADIUS = 150 MICRONS / 1.10 VOLTS PROBE #1 SCALE FACTOR = 8 mV/MICRON

PROBE #2 SCALE FACTOR = 8 mV/MICRON

TIC SPACING = 10 MICRONS

SHAFT MOVEMENT VECTOR = 34 MICRONS @ 79°

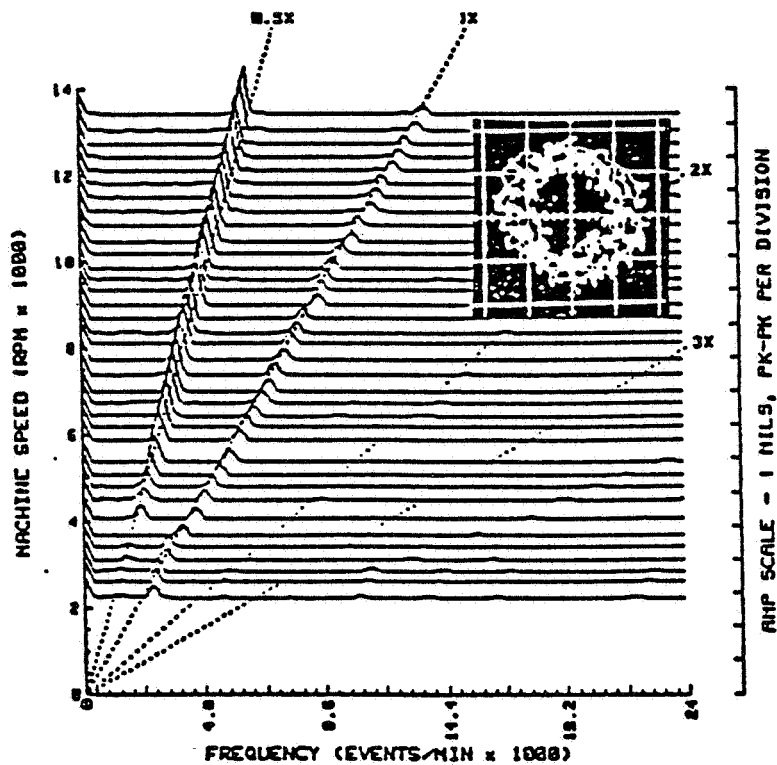
#	RPM	TIME	DC VALUES (Volts)		REMARKS
			PROBE #1	PROBE #2	
1	0	1210	-8.94	-9.83	LOAD 0 Mwatt
2	3000	1235	-8.69	-8.69	LOAD 1 Mwatt
3	3000	1325	-8.69	-8.72	LOAD 1 Mwatt
4	3000	1544	-8.70	-8.68	LOAD 4.6 Mwatt

SHAFT AVERAGE POSITION PLOTTED USING BEARING CLEARANCE OF 90 MICRONS

Figure 8. - Journal position of radial flow turbine generator exciter outboard bearing.

ORIGINAL PAGE IS
OF POOR QUALITY

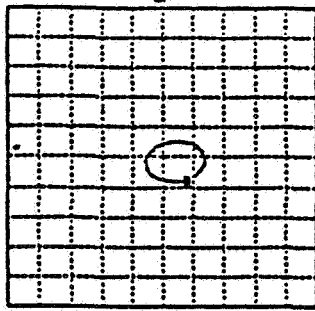
RUNDOWN PROBE ID: COMP VERT
 PROBE ID: COMP VERT
RUN: 1 DATE: 17SEPT81 TIME: 1836



NO KEYPHASOR-BVF2 MANUALLY SHEPT!

Figure 9. - Cascade spectrum plot and rotor orbit for turboexpander/compressor A rundown.

1X FILTERED



AMP SCALE= 0.10 MILS/DIV
 ROTATION: CW



AMP SCALE= 0.10 MILS/DIV
 TIME SCALE= 1.00 MSEC/DIV
 RPH(START)= 38837 RPH(END)= 38796

NOTE: BOTH ORBITS COMPENSATED FOR NON-VERT/HORIZ PROBE ORIENTATION

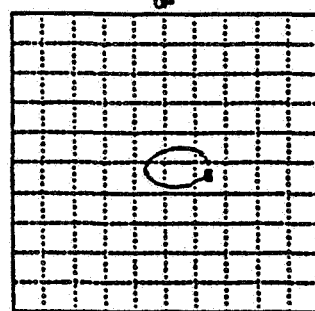
PROBE 01 ID: TURB EXP VERT

ORIENTATION= 70 DEG
 1X VECTOR= 0.15 MILS PK-PK @ -94

PROBE 02 ID: TURB EXP HORZ

ORIENTATION= 340 DEG
 1X VECTOR= 0.21 MILS PK-PK @ -160

1X FILTERED



AMP SCALE= 0.10 MILS/DIV
 ROTATION: CW



AMP SCALE= 0.10 MILS/DIV
 TIME SCALE= 1.00 MSEC/DIV
 RPH(START)= 38852 RPH(END)= 38893

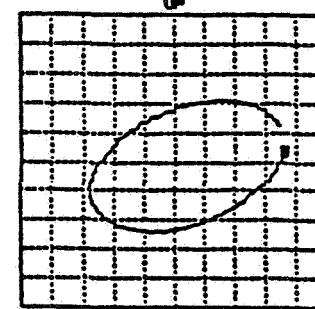
PROBE 01 ID: TURB EXP VERT

ORIENTATION= 70 DEG
 1X VECTOR= 0.35 MILS PK-PK @ -106

PROBE 02 ID: TURB EXP HORZ

ORIENTATION= 340 DEG
 1X VECTOR= 0.37 MILS PK-PK @ -166

1X FILTERED



AMP SCALE= 0.10 MILS/DIV
 ROTATION: CW



AMP SCALE= 0.10 MILS/DIV
 TIME SCALE= 1.00 MSEC/DIV
 RPH(START)= 38782 RPH(END)= 38704

NOTE: BOTH ORBITS COMPENSATED FOR NON-VERT/HORIZ PROBE ORIENTATION

Figure 10. - Rotor orbit changes at high oil temperature for turboexpander/compressor B.

ORIGINAL PAGE IS
OF POOR QUALITY

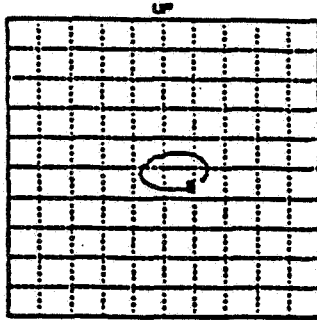
PROBE 01 ID: TURB EXP VERT

ORIENTATION= 70 DEG
IX VECTOR= 0.13 MILS PK-PK @ -38

PROBE 02 ID: TURB EXP HORZ

ORIENTATION= 348 DEG
IX VECTOR= 0.21 MILS PK-PK @ -124

IX FILTERED



AMP SCALE= 0.10 MILS/DIV

ROTATION: CW



AMP SCALE= 0.10 MILS/DIV
TIME SCALE= 1.00 NSEC/DIV
RPN(START)= 38767 RPN(END)= 38766

NOTE: BOTH ORBITS COMPENSATED FOR NON-VERT/HORIZ PROBE ORIENTATION

Figure 10. - Concluded.

TWO-PHASE FLOWS WITHIN SYSTEMS WITH AMBIENT PRESSURE
 ABOVE THE THERMODYNAMIC CRITICAL PRESSURE

R.C. Hendricks
 National Aeronautics and Space Administration
 Lewis Research Center
 Cleveland, Ohio 44135

M.J. Braun and R.L. Wheeler III
 University of Akron
 Akron, Ohio 44325

R.L. Mullen
 Case Western Reserve University
 Cleveland, Ohio 44106

In systems where the design inlet and outlet pressures P_{amb} are maintained above the thermodynamic critical pressure P_c , it is often assumed that two-phase flows within the system cannot occur. Designers rely on this simple rule of thumb to circumvent problems associated with a highly compressible two-phase flow occurring within the supercritical pressure system along with the uncertainties in rotordynamics, load capacity, heat transfer, fluid mechanics, and thermophysical property variations. The simple rule of thumb is adequate in many low-power designs but is inadequate for high-performance turbomachines and linear systems, where two-phase regions can exist even though $P_{amb} > P_c$. Rotordynamic-fluid-mechanic restoring forces depend on momentum differences, and those for a two-phase zone can differ significantly from those for a single-phase zone. Using the Reynolds equation the angular velocity, eccentricity, geometry, and ambient conditions are varied to determine the point of two-phase flow incipience. Subsequent dynamic effects and experimental verification remain as topics for future research.

SYMBOLS

- a dimensionless eccentricity, e/C
- C clearance, cm
- D diameter, cm
- e eccentricity
- f,h functions scaling working fluid to reference fluid
- G_r reduced mass flux, G/G^*
- G mass flux, $g/s\text{-cm}^2$

G^* thermodynamic parameter, $(P_c \rho_c / Z_c)^{1/2}$, 6010 g/s cm² for nitrogen
 H fluid film thickness, cm
 L spacer or bearing length, cm
 l aperture (orifice, Borda) length, cm
 M molecular weight
 N rotational speed, rad/sec (rpm)
 P pressure, MPa
 P_r reduced pressure, P/P_c
 R radius, mm
 R_g gas constant
 S entropy, J/g K
 T temperature, K
 T_r reduced temperature, T/T_c
 w mass flow rate, g/s
 Z axial coordinate, cm
 Z_0 compressibility factor, $P/\rho R_g T$
 η viscosity, Pa-s
 θ circumferential coordinate, rad
 Λ bearing parameter
 ρ density, g/cm³
 Φ, Θ shape functions
 Ω angular velocity, rad/s

Subscripts:

amb ambient
 c thermodynamic critical point (also superscript)
 ex exit
 in inlet

- s saturation
- 0 reference fluid
- α working fluid

INTRODUCTION

As a rule of thumb the extent and nature of the cavity formed downstream of the minimum clearance in a bearing or seal can be controlled, even eliminated, by increasing the ambient pressure. Even for systems operating above the thermodynamic critical pressure the rule of thumb - maintain the design inlet and outlet pressures well above the thermodynamic critical pressure - is used to circumvent two-phase flow and cavity formation (fig. 1). Uncertainties in stability, load capacity, heat transfer, fluid mechanics, and thermophysical property variations are thereby avoided. This simple rule of thumb usually works for low-power designs, but it is inadequate for high-performance turbomachines and linear systems.

In many cases the two-phase flow cavity enhances bearing stability (refs. 1 and 2) and seal load capacity (ref. 3). The inception of cavity flow is important to both turbomachine stability and load capacity.

Cavity flows are engendered by local "violations" of thermodynamics, termed "metastabilities." Classic among these are the fine capillary work of Skripov (ref. 4) and applied work such as fracture, boiling, and condensing (refs. 5 and 6).

Thus a two-phase flow cavity within a supercritical pressure system would be considered unstable, perhaps even unrealistic. Such conditions do not violate thermodynamics but are a source of incompatibility for the practicing engineer. Yet it has been demonstrated that two-phase cavity flows can be "nested" within a supercritical pressure system and that conditions for the existence of such nested cavities are prevalent for sharp-edge inlets and for eccentrically loaded high-performance turbomachines (ref. 7).

In this paper we will fix a turbomachine configuration, and for a series of parametric variations, establish a point of incipient two-phase flows by using the Reynolds equation and methods of corresponding states.

TURBOMACHINE CONFIGURATIONS

Normally seals and bearings for high-performance turbomachines operate at small eccentricities. However, during abnormal events or at high loads, the dimensionless eccentricity a can approach 1 (rubbing). The load W supported by a stable constant-property 360° fluid film H becomes (refs. 1 and 8)

C-2

$$\left(\frac{W}{A \Delta P}\right)_{\text{theory}} = \Lambda \frac{a}{(2 + a^2)\sqrt{1 - a^2}} \quad (1)$$

where Λ is the modified bearing parameter

$$\Lambda = \frac{6RL\eta\Omega}{c^2 \Delta P} \quad (2)$$

and A the surface area, $A = 2\pi RL$. For a short bearing Holmes (ref. 1) gives

$$\left(\frac{W}{A \Delta P}\right)_{\text{theory}} = \frac{\Lambda}{48\pi} \left(\frac{L}{R}\right) \frac{a}{(1 - a^2)^2} \left[\pi^2 (1 - a^2) + 16a^2\right]^{1/2} \quad (3)$$

Departures from theory are represented by the normalized load capacity, which is obtained from integrating the numerically calculated pressure profiles

$$\text{Load capacity ratio} = (W/A \Delta P)_{\text{calc}} / (W/A \Delta P)_{\text{theory}} \quad (4)$$

Later we will make use of these relations in comparing full-film to incipient-film capacities.

Seals

Figure 2(a) illustrates the geometry of a high-performance turbomachine seal such as those used in the space shuttle main engine (SSME) (ref. 3). The working fluid is parahydrogen ($P_c = 1.2928$ MPa, $T_c = 32.976$ K, $\rho_c = 0.0314$ g/cm³). The pressure profiles (fig. 2(b)) are for a fully eccentric, nonrotating shaft. The inlet pressure is greater than P_c , as is the pressure at the inlet to the third step. However, immediately downstream of the step the pressure on one "side" of the seal ($\theta = 0$) remains above P_c while the pressure on the opposite "side" ($\theta = \pi$) is nearly P_s . Thus the circumferential pressure profile possesses all states from $P_{in} > P_c$ at $\theta = 0$ to approximately $P_s < P_c$ at $\theta = \pi$, which represents two-phase cavity flow nested within a supercritical pressure regime.

With eccentric seals pressure gradients of sufficient magnitude can exist to engender two-phase cavity flows both axially and circumferentially while embedded or nested within a supercritical pressure system.

Bearings

Unlike those for a seal the axial pressure gradients for a bearing are usually small, but the circumferential gradients are usually much larger. Embedded two-phase cavity flow zones in seal flows have been established and should occur naturally in bearings. High-speed motion pictures (to 5000 pps) of the incipience, development, and collapse of the two-phase flow cavity and pressure-temperature profiles on the stator have been mapped for a low-performance machine (refs. 10 and 11). It is also noted in reference 10 that the two-phase zone begins to collapse as system ambient pressure is increased.

However, for calculations using Reynolds equations (ref. 11), a high-performance bearing configuration in fluid hydrogen at high eccentricity (table I) reveals a two-phase flow cavity embedded within the system where $P_{in} > P_{ex} > P_c$ (fig. 3). The cavity flow may be similar to that found for sharp-edge inlets (ref. 12). The pressure P drops abruptly from P_{in} to below P_s ; in the recovery zone P increases to P_s ; in the diffusion zone the pressure can recover or remain monotone; either case terminates in a two-phase choke (fig. 4).

The onset of the embedded two-phase flow cavity zone depends on the parameters of equation (1) and is prevalent at lower ambient pressure (e.g., one-tenth those of table I), high eccentricity, and high rotating speed and for large geometries. To illustrate the effects of two-phase flow cavity control, the pressure difference $(P_0 - P_{min})/P_c$ is tabulated (table II) as a function of running speed N for three eccentricities at two temperatures. A similar table (table III) was constructed for the load capacity ratio for numerically finite, infinitely short, and infinitely long bearings. The fluid is hydrogen. This effect remains to be verified experimentally. If it is correct, this demonstrates yet another method of achieving and controlling embedded two-phase flow cavities, which do not require a sharp geometrical configuration to "trigger" the event. Spontaneous nucleation within the metastable field is necessary and sufficient.

Using the principles of corresponding states, extensions to other single-component fluids (perhaps multicomponent fluids) appear reasonable (refs. 13 and 14) where viscosity becomes

$$\eta_\alpha (P, T) = \eta_0 \left(P \frac{h}{f}, \frac{T}{f} \right) F_n \quad (5)$$

and from equation (2)

$$\Lambda_\alpha (P, T) = \Lambda_0 \left(P \frac{h}{f}, \frac{T}{f} \right) F_n \quad (6)$$

where for single-component fluids

$$F_n = \frac{\left(\frac{M_\alpha}{M_0} f \right)^{1/2}}{h^{2/3}} \quad (7)$$

$$f = \left(\frac{T_\alpha^c}{T_0^c} \right) \Theta \quad (8)$$

$$h = \left(\frac{V_\alpha^c}{V_0^c} \right) \Phi = \frac{M_\alpha}{M_0} \frac{\rho_0^c}{\rho_\alpha^c} \Phi \quad (9)$$

for extensions to multicomponent fluids, which are complex (refs. 13 and 14). Example: Let the reference fluid (0) be oxygen and the working fluid (α) be nitrogen. The bearing temperature and pressure are 100 K and 1.5 MPa. Assuming constant properties and $\Theta = \Phi = 1$, solve equation (2) for nitrogen by using the thermophysical properties of oxygen. First we need the thermodynamic properties at the critical point.

Fluid	T_c , K	P_c , MPa	ρ_c , g/cm ³	M , g/g-mole	Θ	Φ	f	h	F_n
N ₂	126.3	3.417	0.3105	28.016	1	1	0.816	1.22	0.74
O ₂	154.78	5.082	.4325	31.9988					

$$f = 126.3/154.78 \times 1 = 0.816 ; h = (28.016/31.9988)(0.4325/0.3105) \times 1 = 1.22$$

$$F_n = [(31.9988/28.016) 0.816]^{0.5}/1.22(2/3) = 0.74$$

$$P_0 = P(f/h) = 1.5 (1.22/0.816) = 2.242 \text{ MPa}$$

$$T_0 = T/f = 100/0.816 = 122.5 \text{ K.}$$

From the thermophysical properties of oxygen (e.g., ref. 15) the viscosity at (P_0, T_0) is 0.936×10^{-3} g/cm s. The predicted nitrogen viscosity then becomes

$$\eta_0 F_n = 0.936 \times 10^{-3} \times 0.74 = 0.693 \times 10^{-3} \text{ g/cm s}$$

From the thermophysical properties of nitrogen (ref. 15) the viscosity at (P, T) is 0.777×10^{-3} g/cm s, which represents a 12-percent error. Once the bearing geometry and speed are defined, the solution to equation (2) follows from equation (5)

$$\frac{\Lambda(P, T)}{\Lambda(P_0, T_0)} = 0.74$$

to within 12 percent.* Reynolds equation (ref. 11) is now solved once using the bearing parameter for nitrogen at $P = 1.5$ MPa and $T = 100$ K and again using the bearing parameter predicted for nitrogen from oxygen properties at $P_0 = 2.242$ MPa and $T = 122.5$ K. The reduced circumferential pressure profiles at the center of the bearing, with speed as a parameter, are illustrated in figure 5.

Boilers and Rotors

A corollary class of nested two-phase flows occurs in turbomachine systems as rotating boilers and cooled rotor windings and in a multiplicity of superconducting machinery applications.

*In reference 11 the solution of the Reynolds equation is in dimensional form and $\Delta P \equiv 1$ (pressure units). For solutions that are in dimensionless form, with fixed P_{amb} and both P_0 and P much larger than P_{amb} , then $\Lambda/\Lambda_0 = fF_n/h$.

A pressure containment vessel, axial flow of a cooling (heating) fluid, and rotation of the fluid about an axis parallel to the flow path result in centrifugal and Coriolis body forces, which in turn produce pressure and shear forces within the fluid. Further, the radial position of the critical pressure surface can be adjusted to occur very close to the fluid-vapor interface.

For a cylindrical boiler rotating at N -rpm the fluid to be evaporated is forced against the outer wall at a pressure $P_{wall} = P_C$; for all $M > N$ P_{wall} is greater than P_C and vapor moves from the wall to the region where $P < P_C$; the two-phase region is nested. Here the Coriolis forces are small, but cannot be neglected when, for example, cooling a superconducting motor (generator) to prevent the winding from going normal. Again the pressure in the winding coolant tube becomes greater than P_C for all $M > N$ while the pressure at the centerline of rotation is less than P_C ; the system is weakly nested. In this case two-phase flow can occur within the coolant tube and become distributed in an unusual axial pattern because of the Coriolis forces. In some instances it may be possible to find a spiral weakly nested region.

To the dynamicist the location and extent of the nested regions may become important only after the system instabilities are encountered.

SUMMARY OF RESULTS

Two-phase cavity flow zones have been shown to be embedded within a supercritical pressure envelope. For a fixed geometrical configuration these zones are established by controlling inlet stagnation conditions, exit backpressure, or combinations. The zones can be "triggered" by discontinuous changes in geometry or by significant pressure gradients.

For high-performance turbomachine seals and possibly bearings, nested two-phase zones can be found in the circumferential and axial coordinates. By using the Reynolds equation a surface of incipient two-phase flows was established. The load capacity of the bearing degrades significantly but not before an overshoot occurs. It is speculated that this overshoot "saves" the design. With the corresponding-states relations these results can be extended to other fluids. These phenomena remain to be demonstrated experimentally.

REFERENCES

1. Holmes, R.: On the Role of Oil-Film Bearings in Promoting Shaft Instability: Some Experimental Observations. NASA CP-2133, 1980, pp. 345-357.
2. Bently, D.E.; and Muszynska, A. : Stability Evaluation of Rotor/Bearing System by Perturbation Tests. NASA CP-2250, 1982, pp. 307-322.
3. Hendricks, R.C.: A Comparative Evaluation of Three Shaft Seals Proposed for High Performance Turbomachinery. Presented at the ASLE/ASME Joint Lubrication Conference, Washington, DC, Oct. 5-7, 1982. NASA TM-83021, 1982.
4. Skripov, V.P.: Metastable Liquids. John Wiley, New York, 1974.

5. Frenkel, J.: Kinetic Theory of Liquids. Dover Publications, New York, 1955.
6. Hendricks, R.C.; Mullen, R.L.; and Braun, M.J.: Analogy Between Cavitation and Fracture Mechanics. ASME/JSME Thermal Engineering Conference, March 21-26, 1983, Honolulu, Hawaii.
7. Hendricks, R.C.; Braun, M.J.; Wheeler, R.L.; and Mullen, R.L.: Nested Supercritical Flows Within Supercritical Systems. 20th Annual Cavitation and Multiphase Flow Forum, Albuquerque NM, June 24-26, 1985.
8. Crandall, S.H.: Heuristic Explanation of Journal Bearing Instability. NASA CP-2250, 1982, pp. 274-283.
9. Childs, D.W.; Hendricks, R.C.; and Vance, J.M., eds.: Rotordynamic Instability Problems in High-Performance Turbomachinery. Proceedings of a Workshop held at Texas A&M University, May 12-14, 1980. NASA CP-2133. (See also NASA CP-2250 (1982) and NASA CP-2338 (1984)).
10. Braun, M.J.; and Hendricks, R.C.: An Experimental Investigation of Vaporous/Gaseous Cavity Characteristics of an Eccentric Shaft Seal (or Bearing). Presented at the ASLE/ASME Joint Lubrication Conf. Washington, DC, Oct 5-7, 1982. ASLE Trans. vol. 27, no. 1, pp. 1-14, 1982.
11. Braun, M.J.; and Hendricks, R.C.: An Experimental Investigation of the Effect of Pressure and Temperature Levels on the Development and Nature of the Cavitation Region in a Submerged Journal Bearing. Bioengineering and Fluids Engineering Conference, Univ. of Houston, Houston, TX, June 20-22, 1983, ASME Bound Volume G00223.
12. Hendricks, R.C.; and Stetz, T.T.: Flow Through Aligned Sequential Orifice-Type Inlets. NASA TP-1967, 1982.
13. Mollerup, Jorgen: Correlated and Predicted Thermodynamic Properties of LNG and Related Mixtures in the Normal and Critical Regimes. Advances in Cryogenic Engineering, K.D. Timmerhaus (ed.), vol. 20, Plenum Press, New York, pp. 172-194.
14. Hendricks, R.C.; and Sengers, J.V.: Application of the Principle of Similarity to Fluid Mechanics. Water and Steam: Their Properties and Current Industrial Applications. 9th International Conference on Properties of Steam, J. Straub and K. Scheffler, eds., Pergamon Press, Oxford, 1980. Unabridged version as NASA TM X-79258, 1979.
15. Hendricks, R.C.; Baron, A.K.; and Peller, I.C.: GASP - A Computer Code for Calculating the Thermodynamic and Transport Properties for Ten Fluids: Parahydrogen, Helium, Neon, Methane, Nitrogen, Carbon Monoxide, Oxygen, Fluorine, Argon, and Carbon Dioxide. NASA TN D-7808, 1975.

TABLE I. - BEARING PARAMETERS FOR ANALYTICAL SOLUTION

Geometry:	
Diameter, mm (in)	25.4 (1)
Length, mm (in)	25.4 (1)
Clearance, mm (in)	0.0254 (0.001)
Eccentricity	0.97
Hydrodynamic:	
Inlet pressure, MPa (psia)	13.8 (2000)
Outlet pressure, MPa (psia)	13.45 (1950)
Maximum pressure, MPa (psia)	27.16 (3938)
Minimum pressure, MPa (psia)	0.079 (11.5)
Inlet temperature, K (°R)	20 (36)
Rotational speed, rad/s (rpm)	7850 (75 000)

TABLE II. - CAVITY PRESSURE DIFFERENCE

$$(P_{in} - P_{min})/P_c \text{ ALONG CENTERLINE}$$

[Clearance, 0.076 mm (0.003 in); radius, 38 mm (1.5 in); spacer or bearing length, 76 cm (3 in); inlet pressure, 1.628 MPa (236 psia); exit pressure, 1.524 MPa (221 psia); viscosity, 0.127×10^{-4} Pa-s (0.187×10^{-8} lbf-s).]

Inlet temperature, T_{in}		Dimensionless eccentricity, a	Rotational speed, N , rpm		
K	°R		10×10^3	50×10^3	100×10^3
22.1	39.8	0.1	0.041	0.043	0.046
		.5	.045	.064	.087
		.95	.24	.646	-----
28.1	50.5	0.1	0.041	0.042	0.044
		.5	.043	.056	.071
		.95	.18	-----	-----

TABLE III. - LOAD CAPACITIES FOR NUMERICALLY FINITE, INFINITELY SHORT, AND INFINITELY LONG BEARINGS

[Clearance, 0.076 cm (0.003 in); radius, 38 mm (1.5 in); length, 76 cm (3 in); inlet pressure, 1.628 MPa (236 psia); exit pressure, 1.524 MPa (221 psia); viscosity, 0.127×10^{-4} Pa-s (0.187×10^{-8} lbf-s).]

Inlet temperature, T_{in}		Dimensionless eccentricity, a	Rotational speed, N , rpm	Bearing parameter, Λ	Numerically finite bearing	Infinitely short bearing	Infinitely long bearing	Pinkus/Sternlicht
K	°R							
22.1	39.8	0.1	10×10^3	5.87	0.99	0.71	4.1	1.4
			50	29.3	4.9	3.5	20.6	7.2
			100	58.7	9.9	7.1	41.3	14.3
		.5	10	5.87	6.3	6.6	21.2	2.6
			50	29.3	31.3	33.1	106	13.2
			100	58.7	62.7	66.1	212	26.4
		.95	10	5.87	53	863	87	20
			50	29.3	265	4318	433	100
			100	58.7	-----	-----	-----	200
28.1	50.5	0.1	10×10^3	3.9	0.66	0.47	2.7	-----
			50	19.5	3.3	2.3	13.7	-----
			100	39.1	6.6	4.7	27.5	-----
		.5	10	3.9	4.2	4.4	14.1	-----
			50	19.5	20.9	22	70.6	-----
			100	39.1	41.7	44	141	-----
		.95	10	3.9	35.4	574	57.7	-----

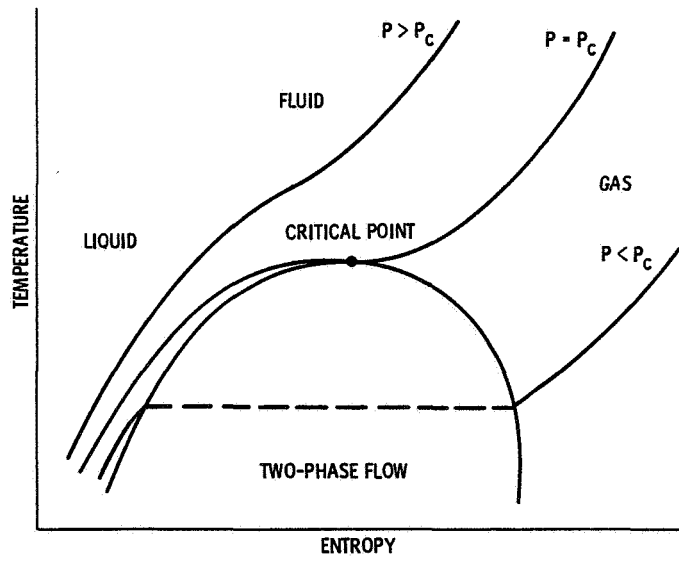
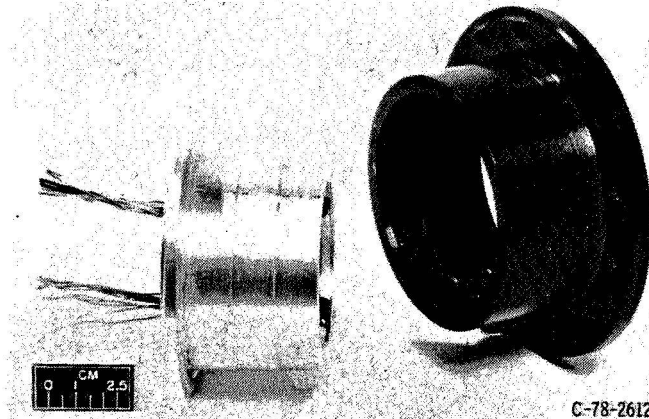
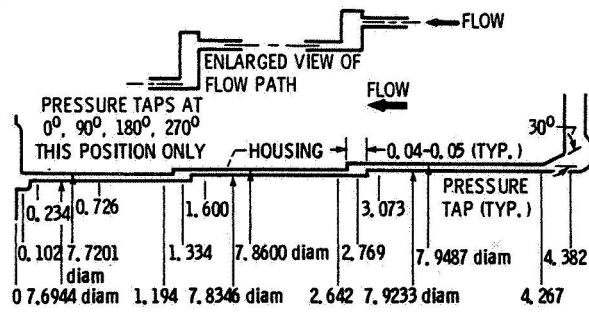
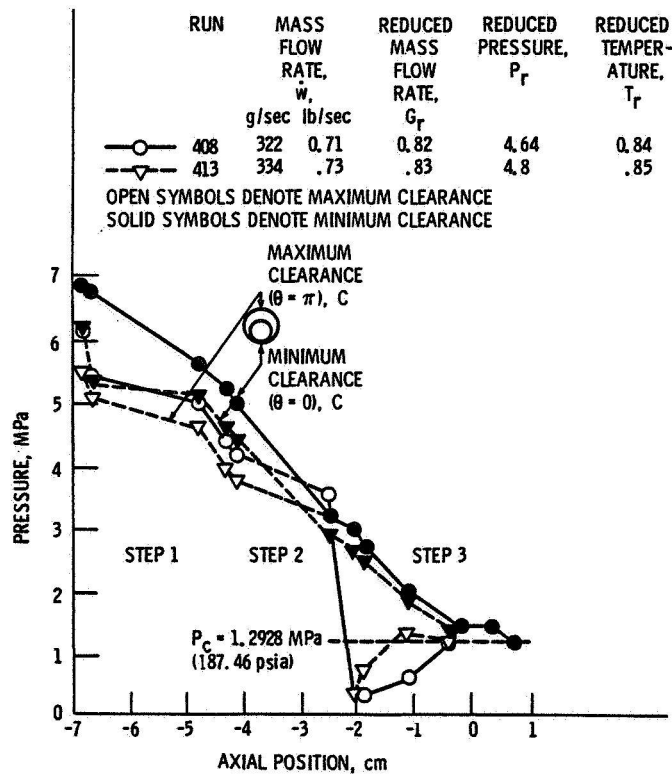


Figure 1 - Temperature-entropy schematic.

ORIGINAL PAGE IS
OF POOR QUALITY



(a) Three-step shaft seal.



(b) Applied backpressure.

Figure 2. - Pressure profile for fully eccentric, nonrotating, three-step SSME seal configuration.

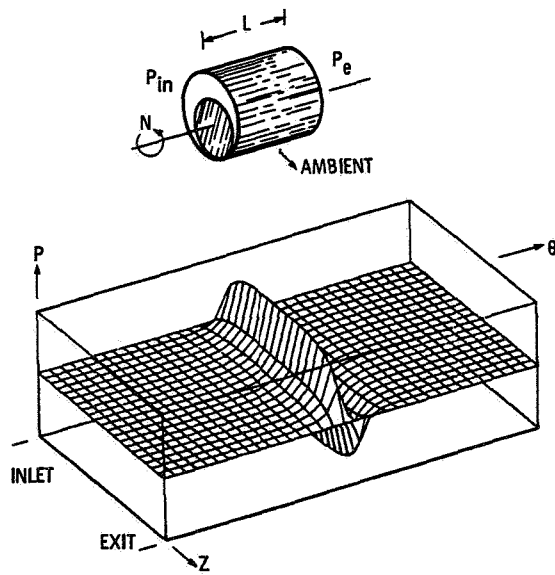
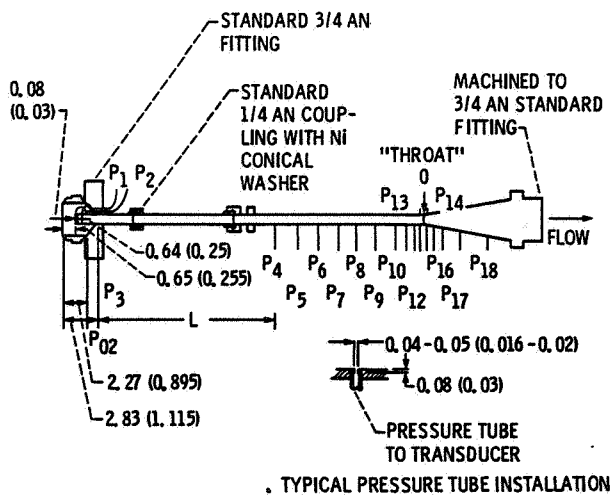


Figure 3. - Analytical pressure map for high-speed journal bearing with $P_{in} > P_e > P_c$; $P_{in} = 13.8 \text{ MPa}$ (2000 psi); $P_e = 13.45 \text{ MPa}$ (1950 psi); $N = 75\,000 \text{ rpm}$; $e_x = e_y = 0.68$; $T_{in} = 20 \text{ K}$ (36°R); $P_{amb} = 0.1 \text{ MPa}$ (14.7 psi); $T_{amb} = 56 \text{ K}$ (100°R).



(a) Configuration geometry.

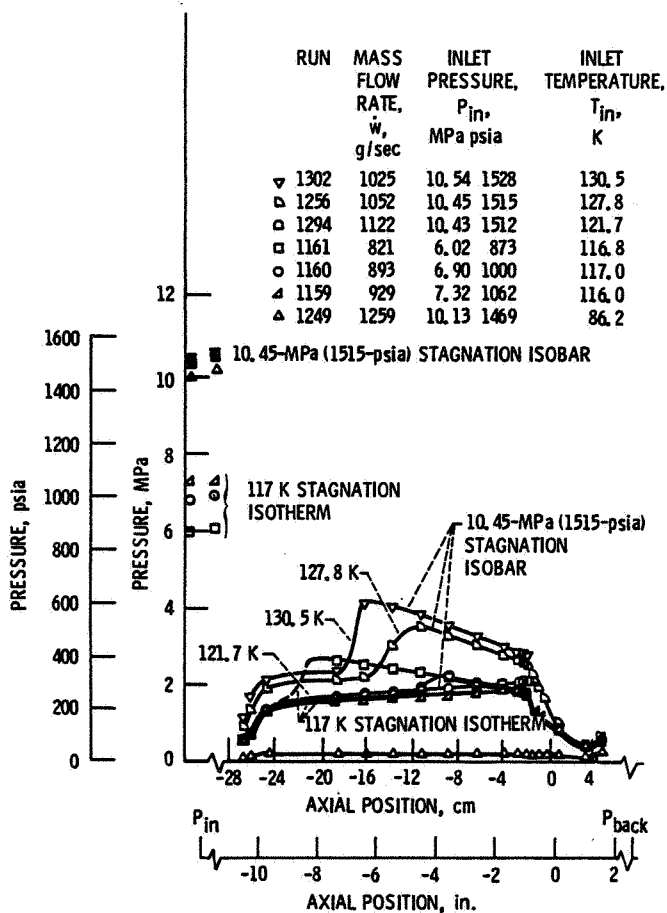


Figure 4. - Pressure profile for nitrogen flow through high-L/D tube with Borda inlet. (Dimensions are in centimeters (inches).)

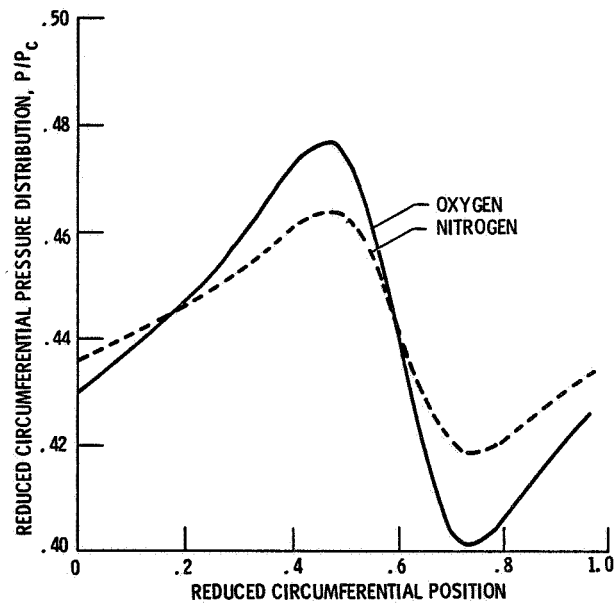


Figure 5. - Reduced midbearing circumferential pressure profiles based on corresponding states for fluids nitrogen and oxygen.

MODELING OF ELASTICALLY MOUNTED VERTICAL ROTOR

Seyyed Said Dana
Federal University of Paraiba
Paraiba, Brazil

Hans Ingo Weber
State University of Campinas
Sao Paulo, Brazil

The evaluation of the dynamic behavior of a rotating system is possible by means of modal parameters (Eigenvalues and Eigenvectors). A mixed analytical and experimental approach is used to identify the modal parameters of a specially-designed test rig. The modal identification is done both for nonrotating as well as rotating systems. These modal parameters are used to validate a developed Finite Element Model.

INTRODUCTION

In the design of a rotating turbomachine, there is a great deal of concern about the stability and the level of vibration. Unstable vibration may occur caused by different effects, like internal damping, oil film forces, etc. There is also a big discussion about the number of bearings used to guarantee a safe level of vibration during operation.

There are several difficulties to identify the dynamic characteristic of large turbomachinery. The problem is very complex. Normally there are few points at the rotor where it is possible to excite the system; also the positions of the point to measure the response of the system are not arbitrary. In operating conditions, it is not always easy to identify the system. Turn on and off procedures may be very fast, and in steady state, it is frequently difficult to estimate the disturbing forces.

As an attempt to understand and to analyze specific problems related to vertical shaft Francis Hydrogenerators, a special test rig was designed and constructed, which is described by Eiber (Ref. 1). The test rig is designed in a way that facilitates changing the parameters of the rotor (stiffness, damping, mass distribution). The study of the dynamic behavior of the rig gives important information on how to proceed measuring the real machine.

The stability of a linear rotor-system is given by the real part of the complex eigenvalues which correspond to the damping constants. Natural frequencies are obtained from the imaginary part. Together with the natural modes (Eigenvectors), they allow the evaluation of the dynamic behavior in free as well, as in forced, vibration. Eigenvalues and natural modes are called the "modal parameters" of a system.

The classical "modal analysis," a combined experimental and analytical method which was developed some years ago, is used to identify modal parameters of nonrotating systems. The method makes assumption of symmetric matrices for the analytical model. Although the method is not admissible in the case of rotating systems (nonsymmetrical matrices), it is a very useful tool to identify the modal parameters while the system is on rest.

It is the aim of this paper to identify the modal parameters of the rig in several stages of its mounting on the test stand. In this case, the modal parameters provide us the necessary information to adjust gradually the mathematical model.

It has been shown in Reference 2 that a generalized modal analysis, in connection with an expansion in series of the right eigenvectors and the left eigenvectors, allows the identification of modal parameters of a system. This method will be applied to the rotor test rig. Some experimental data are presented.

ROTOR TEST RIG

The rotor system is shown schematically in Figure 1. The vertical shaft represents a body with a rigid upper and an elastic lower part. On the rigid section, there is axially clamped the rotor of an asynchronous motor with 4 kw power. The stator itself is hinged with leaf springs on swinging platforms. These leaf springs are adjustable and, therefore, allow us to vary the stiffness in a very wide range. The total suspension of the stator is carried out by eight platforms.

Because of noncontact transducers, an inductive displacement measuring system allows the recording of vibration of the rotating shaft. This system is used in one horizontal plane to measure the state variables of the lower disc.

MODAL ANALYSIS OF THE UNDAMPED NONROTATING SYSTEM

There are different possibilities in the description of the mentioned rotor with continuous mass and stiffness distribution. The exact formulation is described by partial differential equations together with appropriate boundary conditions, as described by Wauer (Ref. 3).

For practical calculations, however, a Finite Element Model is employed with finite number of coordinates. Basically, the bending vibration of the rotor shaft is the focus of interest. Making use of scalar energy quantities in a variational form, the Hamilton's Principle leads us directly to the equations of motion. The unknown deflection functions are substituted by deflection shapes formed by third-order polynomials with free parameters. In this model, the free parameters are the deflection and the angle at the boundary of the beam elements.

The Finite Element model for the rig is shown in Figure 2. The model has 6 nodes. It consists of 5 beam elements, 4 spring elements, and 6 inertia elements. All the elements which are related to the stator and its spring leafs, and also the upper discs, are condensed at the node number 1. For making the model more flexible for parameter variation, the rotating part of the stator (rotor) and the rotating parts of the intermediate bearing are considered as separate inertia elements. The system is allowed to vibrate in the XY plane and also in the XZ plane. The rotation of the system about X axis, and also its translation in the same direction, is

suppressed. As a result, the system has 24 degrees number of freedom. Having the system matrices $[M]$, $[K]$, the solution of the ordinary eigenvalue problem gives the natural frequencies and the corresponding modes.

The modal analysis of the rig is done in three steps. In the first step, the "vertical shaft," a body with rigid upper and an elastic lower part, is considered as a free-free body in space.

In the second step, the rotor is modeled as a free-free body in space. The rotor consists of the vertical shaft, the upper disc, the lower disc, and the intermediate bearing.

Finally, the model considers the rotor mounted on the rigid test stand by leaf springs.

IDENTIFICATION OF MODAL PARAMETERS OF THE NONROTATING SYSTEM

Usually a combined experimental and analytical method identifying modal parameters of nonrotating elastic systems has been applied in various fields. The aim of the method is to analyze a structure in its elementary modes and to determine its characteristics.

In this case, the first nine measurement points along the X axis of the rotor in the XY plane are chosen. The rotor is excited by applying an impulse on the measurement points, and the response is measured in a specific point. After transformation (FFT) of the input and the output signals into frequency domain, different frequency response functions are determined. Analytical functions are fitted to the measured functions by variation of the modal parameters. The results of this iterative fitting procedure are the modal parameters.

The same as theoretical analysis, identification of modal parameters is done in the three steps as already was explained. The same method was also applied for identifying the modal parameters of the rotor in the XZ plane.

COMPARISON OF THE RESULTS

The results obtained by the F.E.M. and the identification of modal parameters are presented as corresponds to different stages. Table 1 shows the natural frequencies of the free-free "vertical shaft." The natural modes for the first three frequencies are shown in Figure 3.

Table 2 shows the natural frequencies of the free-free rotor. The corresponding modes are shown in Figure 4.

Figure 5 shows the natural modes of the mounted rotor on XY plane. The corresponding natural frequencies are shown in Table 3. Also the natural frequencies of the mounted rotor on XZ plane are shown in Figure 5. As the natural modes in XZ plane are almost the same as in XY plane, the modes are not presented.

The results obtained for natural frequencies of different stages by Finite Element Model are very close to experimental ones. This gives us a model to be used in predicting the frequencies while the rotor is running.

MODAL ANALYSIS OF ROTATING SYSTEM

Due to gyroscopic effect and asymmetry in damping and stiffness matrices, the classical method for modal analysis fails to decouple the equations of motion of the rotor while running. The modal parameters are also speed dependent in this case.

However, working with eigenvectors and natural modes of the nonconservative system leads to the desired decoupling as shown by Nordmann in Reference 2.

MODAL PARAMETERS OF ROTORS

The first step in modal analysis is always the determination of eigenvalues and eigenvectors. These parameters can be calculated by the homogenous equation:

$$[M]\{\ddot{x}\} + [D]\{\dot{x}\} + [K]\{x\} = 0 \quad (1)$$

where $[M]$, $[D]$, $[K]$ are respectively mass, damping, stiffness matrices with order $N \times N$. The solution of equation (1) is of the form:

$$\{x\} = \{\phi\}e^{\lambda t} \quad (2)$$

Substitution yields the quadratic eigenvalue problem

$$(\lambda^2[M] + \lambda[D] + [K])\{\phi\} = 0 \quad (3)$$

with $2N$ eigenvalues λ_j and corresponding modes $\{\phi\}_j$. The eigenvalue, as well as the eigenvectors, mainly occur in conjugate complex pairs (real eigenvalues and eigenvectors are not considered).

$$\text{Eigenvalues} \quad \lambda_j = \alpha_j + i\omega_j \quad ; \quad \bar{\lambda}_j = \alpha_j - i\omega_j \quad (4)$$

$$\text{Eigenvectors} \quad \phi_j = s_j + it_j \quad ; \quad \bar{\phi}_j = s_j - it_j \quad (5)$$

The part of the solution which belongs to such a conjugate complex pair can be written as:

$$x_j(t) = B_j e^{\alpha_j t} \{s_j \sin(\omega_j t + \theta_j) + t_j \cos(\omega_j t + \theta_j)\} \quad (6)$$

where ω_j is the circular frequency and α_j the damping constant. The damping constant α_j (real part of λ_j) determines whether the solution $x_j(t)$ is stable ($\alpha_j < 0$) or unstable ($\alpha_j > 0$).

The constants B_j and the phase angle θ_j depend on the initial conditions. Normally all of the conjugate complex pairs contribute to the solution of the natural vibrations. To explain the natural modes is not so easy as in the case of conservative systems.

The expression in parentheses in Equation (6) can be defined as natural modes representing a time dependent curve in space.

IDENTIFICATION OF MODAL PARAMETERS OF THE RUNNING ROTOR

The natural frequencies of the rotor are identified by the same method as Reference 2. Some experimental data are shown in Fig. 6. The figure shows the variation

of the first three eigenvalues (only the imaginary part), due to rotational speed of the rotor. It is clearly shown that the natural frequencies are speed dependent. It is worth mentioning that the identification process becomes more difficult as the running speed increases. It is necessary to develop special hammers which could excite the rotor at higher speeds.

REFERENCES

1. Eiber, A. Weber, H.I. "Experiments in Rotordynamic," VII Cobem, December 1983, Uberlandia -- MG, Brasil.
2. Nordmann, R., "Modal Parameters Identification and Sensitivity Analysis in Rotating Machinery." Proceedings of International Conference on "Rotordynamic Problems in Power Plants," Page 95, September 1982, Rome, Italy.
3. Wauer, J., "Modal Analysis of Non-Conservative Distributed Parameter Rotor Systems. Proceedings of the XIVth Conference on Dynamics of Machines," page 199, September 1983. Prague, Liblice, Czechoslovakia.

The Natural Frequencies of The Free-Free
Vertical Shaft

Table 1

	F1 Hz	F2 Hz	F3 Hz
Finite Element Model	36.42	153.2	412.5
Identification Of Modal Parameters	36.18	153.1	410.5

The Natural Frequencies of The Free-Free
Rotor

Table 2

	F1 Hz	F2 Hz	F3 Hz
Finite Element Model	14.74	51.27	92.29
Identification Of Modal Parameters	14.65	49.81	97.66

The Natural Frequencies of The Mounted Rotor
on XY Plane

Table 3

	F1 Hz	F2 Hz	F3 Hz
Finite Element Model	8.224	14.11	27.43
Identification Of Modal Parameters	8.380	13.01	22.11

The Natural Frequencies of The Mounted Rotor
on XZ Plane

Table 4

	F1 Hz	F2 Hz	F3 Hz
Finite Element Model	8.199	13.34	24.71
Identification Of Modal Parameters	8.508	12.27	21.87

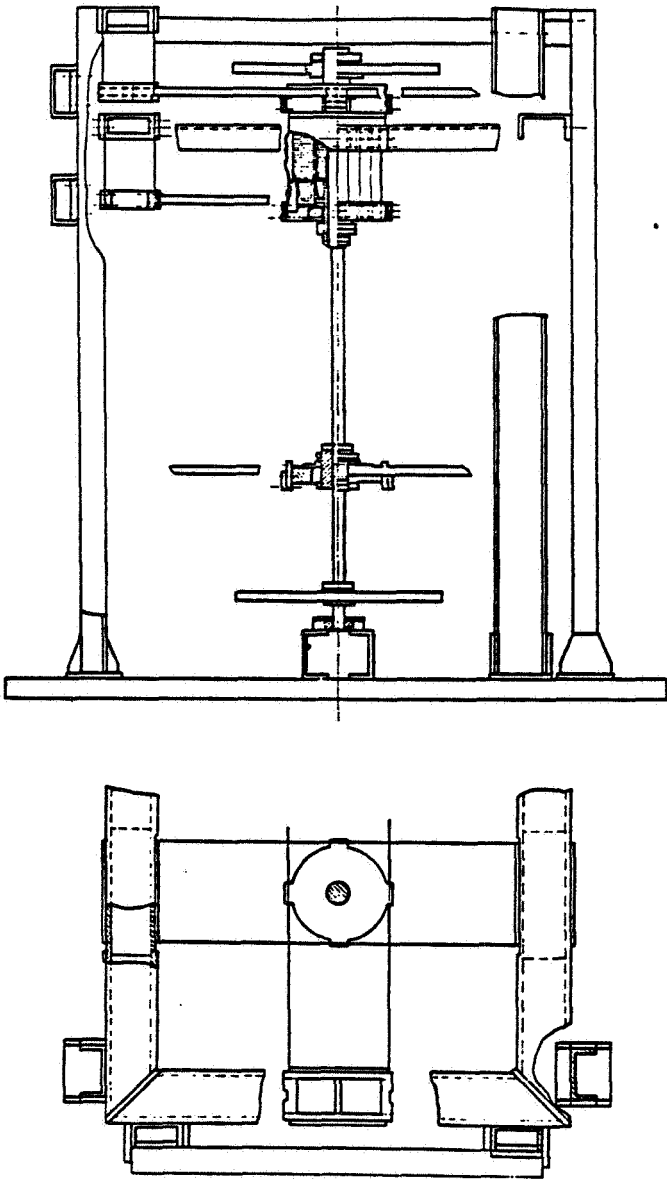


Figure 1. - Test rig (scale 1:20).

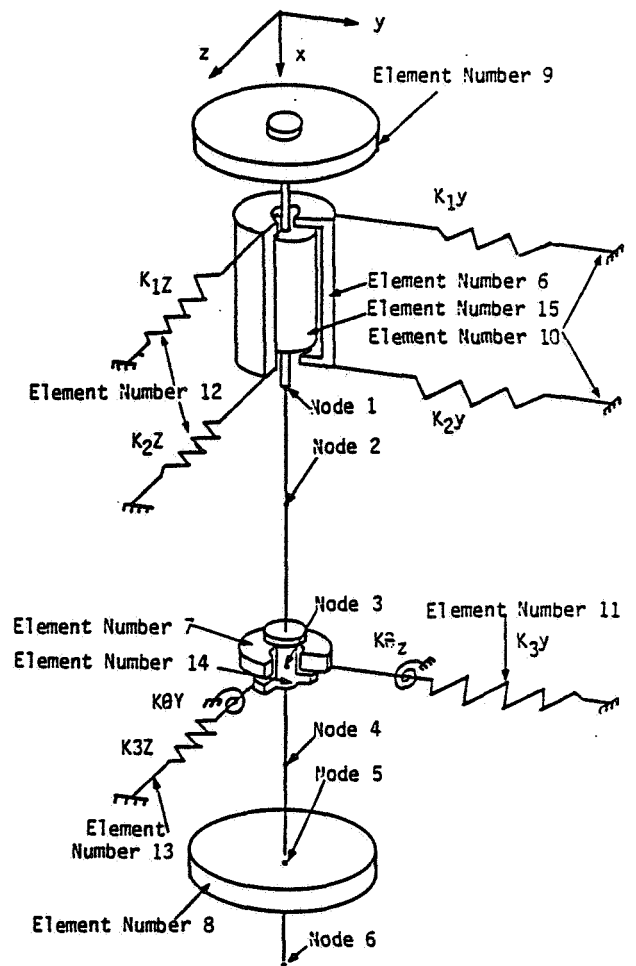


Figure 2. - Finite element model for rig.

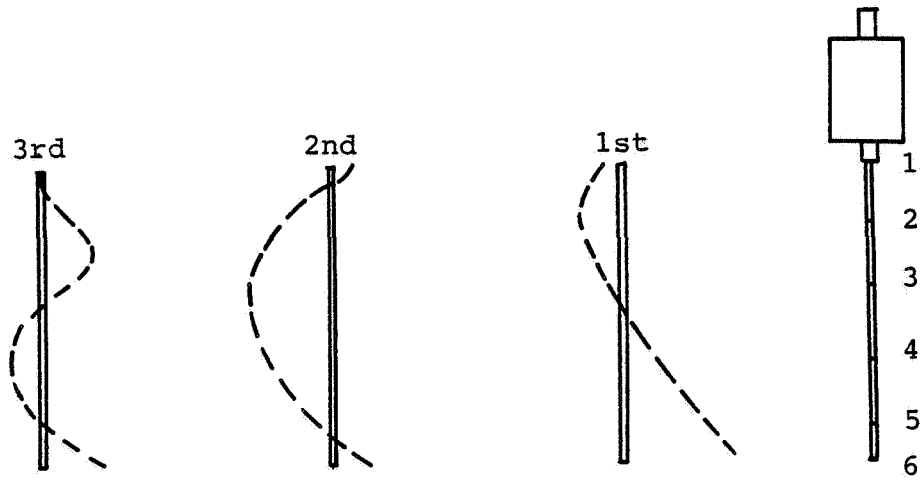


Figure 3. - Natural modes for free-free vertical shaft.

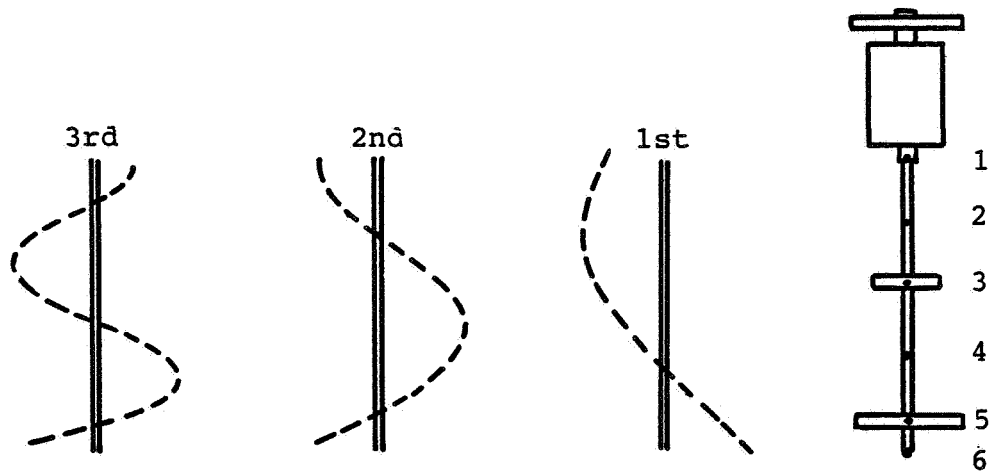


Figure 4. - Natural modes for free-free rotor.

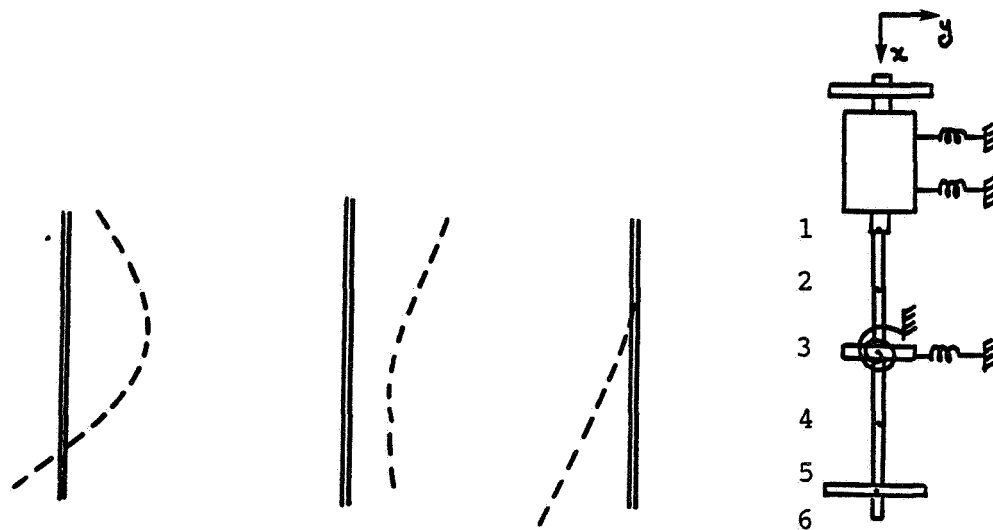


Figure 5. - Natural modes for mounted rotor in XY plane.

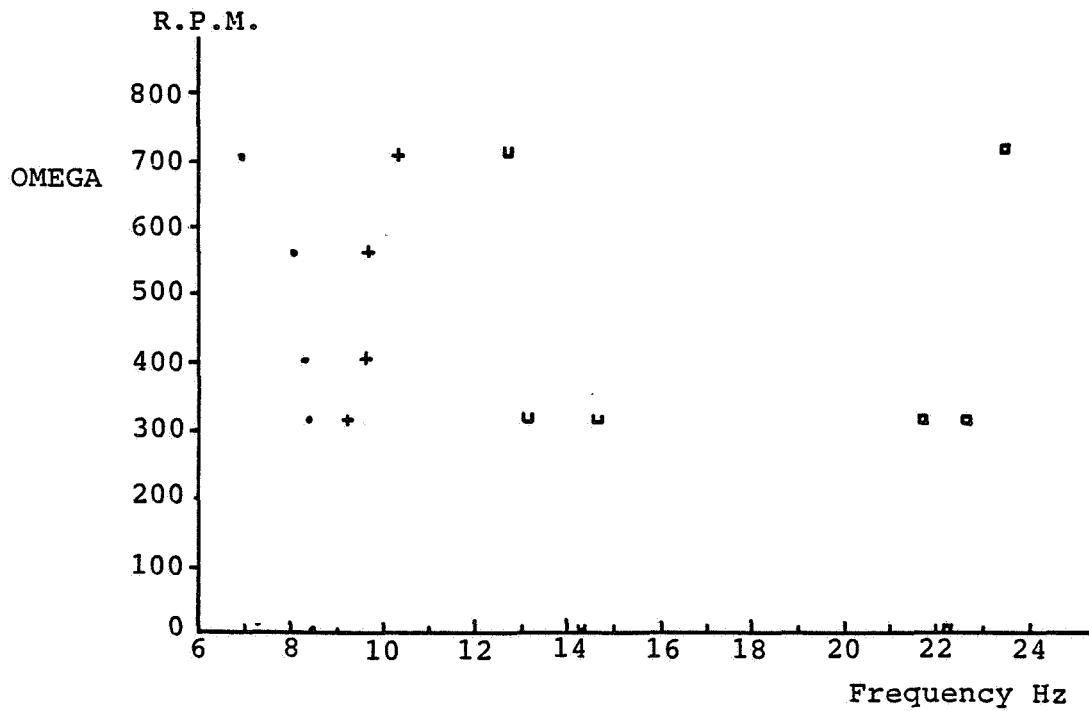


Figure 6. - Variation of eigenvalues of mounted rotor with rotor running speed.

EXPERIMENTAL VERIFICATION AND PRACTICAL APPLICATION
OF TORQUEWHIRL THEORY OF ROTORDYNAMIC INSTABILITY

J.M. Vance and S.T. Noah
Texas A&M University
College Station, Texas 77843

K.B. Yim
Sunstrand Aviation
Rockford, Illinois

A theory developed by the first author in 1978 to explain the destabilizing effect of torque on a whirling rotor has been experimentally verified. The measurements made on a specially designed test apparatus are described.

New computer models have also been developed to investigate the effect of torque on rotordynamic stability of multi-disk flexible rotor-bearing systems. The effect of torque has been found to be most pronounced when the system is already marginally stable from other influences. The modifications required to include torque in a typical shaft transfer matrix are described, and results are shown which identify the type of rotor design most sensitive to load torque.

INTRODUCTION

Since at least the early 1950's, it has been known that large values of load torque can depress the natural frequencies of a uniform shaft on short or long bearings [1,2,3], and that any value of torque on a cantilevered shaft, without damping, produces dynamic instability [4,5,6,7]. These results have limited application to most rotating machinery, however, since the values of torque required to depress critical speeds are seldom approached and all real machines have at least some amount of damping. Although the effect of torque on critical speeds is mostly of academic interest, recent experimental and analytical investigations by the authors have shown that the effect on whirl stability, with damping included, for some rotor-bearing configurations which are representative of contemporary machines, can be significant. In 1978 the first author published a nonlinear analysis with damping included [8] which showed that tangential load torque on a rotor disk (e.g., the stage torque on a fluid impeller) can produce nonsynchronous whirling with amplitude dependent on the ratio of torque to damping.

Figure 1 shows the model analyzed in reference [8] where all of the rotor flexibility was concentrated in the joint at 0' (the shaft was assumed rigid). This is the simplest possible model which can demonstrate the torquewhirl phenomenon, as considerations of the effect of the torque on the shaft deflection mode shape are avoided.

Subsequently, Tison [9] linearized the equations of motion for the same model and applied the Routh-Hurwitz criteria to obtain the required condition for whirl stability, which is

$$\frac{T}{C_t \omega_d l^2} < 2 \quad (1)$$

where C_t is the translational viscous coefficient of damping acting at the disk and ω_d is the whirling frequency.

More recently, Yim [10] has extended the torquewhirl analysis to more realistic rotor models, including the disk cantilevered on an elastic shaft (Figure 2), and even to generalized multi-disk rotors using the transfer matrix method.

An experimental program has also been conducted [10] to verify the existence of nonsynchronous whirl produced exclusively by tangential load torque.

The purpose of this paper is to present the main results of the experimental program and to condense the useful results of the recent analyses (since reference 9) which are relevant to practical applications in rotor-dynamics. The work reported here was supported by the National Science Foundation, Grant #MEA-8115330.

EXPERIMENTAL VERIFICATION

Apparatus and Instrumentation

To facilitate isolation of the torquewhirl effect, a special test rig was designed to represent the model of Figure 1. The test rig design concept was by Professor George N. Sandor at the University of Florida. This is the simplest possible rotor configuration capable of demonstrating the torquewhirl phenomenon. In particular, there is only one mode of whirling (conical), and the torque has no effect on the mode shape. Also, an exact solution to the nonlinear equations of motion was available for this model [8], which extended the opportunities for comparison with theory.

Figures 3 and 4 are a photograph and schematic, respectively, of the test rig hardware. From left to right there is a 15 KW variable speed electric motor, driving through a toothed belt speed reducer, and the rotor which is mounted on ball bearings (vertical axis) inside a finned housing. The purpose of the housing is to apply a load torque to the rotor which always remains aligned with the rotor axis, even while whirling occurs. Thus the housing precesses with the rotor in its conical whirl mode, but is restrained from spinning by the four springs. The springs are radially oriented while the system is at rest. In operation, torque rotates the housing through an angle until an equilibrium of moments is reached.

Figure 5 shows a cross section of the rotor and housing. Torque is applied to the rotor by viscous shear in the conical clearance space when it is filled with a silicone fluid. The clearance is adjustable by a threaded collar which moves the housing up or down relative to the rotor.

The flexible joint (O' in Figure 1) is provided in the test rig by a laminated disk coupling on the shaft just above the housing. The forward natural frequency of the test rig at 1000 rpm was calculated to be 10.78 Hz, and turned out to be about 10.5 Hz.

During the testing, the drag cylinder attached to the bottom of the housing was immersed to a controlled depth in oil, so that the damping of the whirl motion

was adjustable. Three different values of damping, as determined by measurements of the logarithmic decrement of free vibration, were used in the test program: 2.2%, 3.8%, and 5.2% of the critical value.

Two proximity probes are installed near the upper part of the drag cylinder for measurement of the whirl orbit (x-y vibration displacement signals). Rotor speed (0-1200 rpm) is measured with a digital tachometer excited once per revolution from the shaft by a fiberoptic transducer with reflective tape. A strain gage mounted on one of the spring restraining brackets was calibrated to measure the rotor torque.

All signals were electronically converted from analog to digital form for plotting by a desktop computer. The x-y vibration signals were filtered with a bandpass range of 18%, for measurement of the 10.5 Hz whirl frequency. Both the filtered and unfiltered signals were recorded and plotted. Calibration procedures are described in reference [10].

The variable parameters in the test program were speed, external damping, and to a lesser extent, torque. A factor which limited the time duration of each test was heating of the rotor and housing from viscous shear, in spite of the cooling fins on the housing and forced air cooling with a Hilsch tube.

Experimental Results

Figure 6 shows measured data for speed, torque, and whirl amplitude, plotted in the time domain with no load torque (air in the clearance space). Figure 7 shows the frequency spectrum of the unfiltered vibration signal (whirl amplitude). The two components are synchronous whirl (from rotor unbalance and misalignment) and subsynchronous whirl excited by the drive belt. The latter vibration was found to track at a frequency of exactly .56 times rotor speed, which is the ratio of teeth on the large pulley to teeth on the belt.

Figures 6 and 7 were obtained with the drag cylinder immersed to a depth which gives 2.2% of critical damping. This was found to be the minimum damping required to suppress subsynchronous whirl produced by internal friction in the laminated disk coupling. The internal friction effect was explored experimentally [10] and found to be independent of torque.

Figures 8 and 9 show the same measurements made with load torque applied (silicone fluid in the clearance space). Note the large increase in whirl amplitude (Figure 8), which is seen to be largely subsynchronous at the predicted torque-whirl frequency (Figure 9). Figures 10 and 11 show similar results with increased external damping (5.2%).

A nonlinear relationship between applied torque and whirl amplitude was observed. Figure 12 shows the whirl amplitude decreasing as the torque (and speed) are increasing above the initial destabilizing value. This phenomenon is explained by a nonlinear analysis presented in reference [10]. It cannot be predicted or simulated by a linearized stability analysis.

PRACTICAL APPLICATIONS

Effect of Rotor Configuration and Geometry

Rotordynamic stability analyses have been conducted to evaluate the effect of tangential load torque on a wide variety of rotor configurations. Several different methods were used to determine the eigenvalues, including flexibility influence coefficients, the transfer matrix, and the Galerkin method [10,11], with excellent agreement of results.

The destabilizing effect of torque on rotor whirl has been found to be most pronounced on overhung (cantilevered) rotors, and in rotors with a high ratio of torque to bending stiffness (TL/EI). There is, however, a strength of materials limitation on this latter ratio. To illustrate, Figure 13 shows that $TL/EI < 0.5$ for uniform shafts of typical L/D and for typical steels of shear strength τ .

Besides the value of TL/EI , the mode shape is the most important factor in determining the sensitivity of a rotor to torquewhirl. The mode shape determines the misalignment of the tangential torque vectors applied at different axial locations along the rotor, and also has a large influence on another important factor, the ratio of torque to damping. The mode shape determines the effectiveness of bearing damping, since bearings located near nodal points can make little contribution to the system damping.

The sense of the torques (positive or negative) relative to the direction of shaft speed determines the direction of whirl. For a cantilevered rotor with load torque applied along the axis of the overhung disk, positive torque (e.g., a turbine) produces backward whirl, and negative torque (e.g., a compressor) produces forward whirl (provided the ratio of torque to damping is high enough).

For a multi-disk rotor, the situation is similar, but more complex. Figure 14 shows the mode shapes for two different configurations, each with two disks. Configuration A has both disks inboard of the bearings, while configuration B has one of the disks overhung.

Figure 15 shows the effect of torque on the stability of the four natural whirl frequencies. Damping is omitted and $TL/EI > 1$ to maximize the torque-whirl effect. In each case, one disk is a driver (e.g., turbine) and the other is a load (e.g., compressor). Case B has the load torque on the overhung wheel.

Without torque, both cases (A1, B1) have zero logarithmic decrements as expected. With torque, the logarithmic decrement of case A2 is little changed, but case B2 is destabilized in forward whirl (F) and stabilized in backward whirl (B). The opposite torques have a cancelling effect on the symmetric rotor A, but destabilize case B due to the unsymmetric mode shape.

A torquewhirl analysis of several existing turbomachines has been conducted. In most cases torque was found to be a second order effect when compared to the destabilizing influences from fluid-film bearings, seals, and Alford-type forces [12]. Two examples of the machines analyzed are an eight-stage centrifugal compressor [13], and the High Pressure Oxygen Turbopump used in the NASA Space Shuttle engine [10,14].

There are, however, potential exceptions such as the single-stage overhung

centrifugal compressor illustrated in Figure 16. This machine is representative of the general type described in reference [15]. Although the numerical values used in the rotordynamic model were approximated by scaling a drawing, they are believed to be realistic. In this case it was found that at least 12% of critical damping is required to suppress rotordynamic instability from load torque alone.

Whirl instabilities in turbomachines are often caused by several destabilizing influences acting in concert [12], so the torquewhirl effect should be added in any case to improve the accuracy of predicted threshold speeds and loads. The studies referenced here have shown the torquewhirl effect to be much more pronounced on a system which is already unstable than on an otherwise stable system. This helps to explain why marginally stable turbomachines have been observed to be very sensitive to the load.

Computer Modeling of Torque Effects

Most computer programs for rotordynamic stability analysis are based on the transfer matrix method [13,16], while others use a characteristic matrix [17] based on either stiffness or flexibility elements to model the elastic shaft forces and moments.

The flexibility matrix approach with torque effects included is illustrated in a companion by the authors [11] and in reference [10].

The transfer matrix for a shaft section, or elastic element of the n^{th} "station", with torque included is given by

$$\begin{Bmatrix} x \\ y \\ \alpha \\ \beta \\ v_x \\ v_y \\ M_x \\ M_y \end{Bmatrix}_{n+1} = \begin{bmatrix} 1 & 0 & l & 0 & C_{11} & C_{12} & C_{13} & C_{14} \\ 0 & 1 & 0 & l & C_{21} & C_{22} & C_{23} & C_{24} \\ 0 & 0 & 1 & 0 & C_{31} & C_{32} & C_{33} & C_{34} \\ 0 & 0 & 0 & 1 & C_{41} & C_{42} & C_{43} & C_{44} \\ 0 & 0 & 0 & 0 & 1 & 0 & 0 & 0 \\ 0 & 0 & 0 & 0 & 0 & 1 & 0 & 0 \\ 0 & 0 & 0 & 0 & C_{51} & C_{52} & C_{53} & C_{54} \\ 0 & 0 & 0 & 0 & C_{61} & C_{62} & C_{63} & C_{64} \end{bmatrix} \begin{Bmatrix} x \\ y \\ \alpha \\ \beta \\ v_x \\ v_y \\ M_x \\ M_y \end{Bmatrix}_n \quad (2)$$

where the state variables are defined by Figure 17 and the C_{ij} are as follows:

$$\begin{aligned}
C_{11} &= C_{22} = \xi(l - \xi T \sin \gamma) \\
C_{12} &= -C_{21} = \xi^2 T(1 - \cos \gamma) - \frac{l^2}{2T} \\
C_{13} &= C_{24} = C_{31} = C_{42} = \xi(1 - \cos \gamma) \\
C_{14} &= -C_{23} = C_{32} = -C_{41} = \xi \sin \gamma - \frac{l}{T} \\
C_{33} &= C_{44} = \left(\frac{1}{T}\right) \sin \gamma \\
C_{34} &= -C_{43} = \left(\frac{1}{T}\right)(\cos \gamma - 1) \\
C_{51} &= C_{62} = \xi T \sin \gamma \\
C_{52} &= -C_{61} = \xi T(\cos \gamma - 1) \\
C_{53} &= C_{64} = \cos \gamma \\
C_{54} &= -C_{63} = -\sin \gamma
\end{aligned} \tag{3}$$

where $\xi = EI/T^2$ and $\gamma = Tl/EI$.

In more compact form, Eq. (2) becomes

$$\{X\}_{n+1}^L = [T_s]_n \{X\}_n^R \tag{4}$$

where

$\{X\}_{n+1}^L$ = state vector on the left side of station $n + 1$

$\{X\}_n^R$ = state vector on the right side of station n

$[T_s]$ = transfer matrix for the shaft section between

Conclusions

The destabilizing effect of load torque on a rotating machine, to produce non-synchronous whirl, has been demonstrated experimentally.

Analytical studies have shown that whirl instability due to torque alone requires a high ratio of torque to damping and a whirling mode shape which misaligns the driving and driven torque vectors with respect to each other. This combination of conditions are usually not obtained in most contemporary turbo-machines, but load torque can have a significant effect when combined with other destabilizing mechanisms. The type of machine most sensitive to torque-whirl was found to be the single-overhung wheel on a flexible shaft with negative work load (i.e., compressor).

The destabilizing effect of torque can be incorporated into the shaft transfer matrices used in most contemporary computer programs for rotordynamic stability analysis, but a nonlinear analysis is required to explain the effect of torque which exceeds the threshold value.

REFERENCES

1. Golomb, M., and Rosenberg, R. M., "Critical Speeds of Uniform Shafts Under Axial Torque," Proceedings of The U.S. National Congress on Applied Mechanics, New York, 1951, pp. 103-110.
2. Eshleman, R. L., and Eubanks, R. A., "On the Critical Speed of a Continuous Rotor," ASME Journal of Engineering for Industry, Nov. 1969, pp. 1180-1188.
3. Biezeno, C. B., and Grammel, R., Engineering Dynamics, Volume III, London, 1954.
4. Ziegler, H., Principles of Structural Stability, Blaisdell Publishing Company, London, 1968.
5. Nikolai, E. L., "On the Stability of the Rectilinear Form of a Compressed and Twisted Bar (in Russian)," Izvest. Leningr. Politekhn. in-ta 31, 1928.
6. Morris, J., "Torque and the Flexural Stability of a Cantilever," Aircraft Engineering, Vol. 23, 1951, pp. 375-377.
7. Shieh, R. C., "Some Principles of Elastic Shaft Stability Including Variational Principles," ASME Journal of Applied Mechanics, March 1982, pp. 191-196.
8. Vance, J. M., "Torquewhirl - A Theory to Explain NonSynchronous Whirling Failure of Rotors with High Load Torque," ASME Journal of Engineering for Power, Apr. 1978, pp. 235-240.
9. Tison, J. D., Dynamic Stability Analysis of Overhung Rotors with High Load Torque, Master of Engineering Thesis in Mechanical Engineering, University of Florida, 1977.
10. Yim, K. B., Load-Induced Rotordynamic Instabilities in Turbomachinery, Ph.D. Dissertation in Mechanical Engineering, Texas A&M University, December 1984.
11. Yim, K. B., Noah, S. T., and Vance, J. M., "Effect of Tangential Torque on the Dynamics of Flexible Rotors," to be published, 1985.
12. Vance, J. M., "Instabilities on Turbomachinery," Proceedings of the 5th Annual Seminar on Machinery Vibration Analysis, The Vibration Institute, New Orleans, La., April 7-9, 1981.
13. Lund, J. W., "Stability and Damped Critical Speeds of a Flexible Rotor in Fluid-Film Bearings," ASME Journal of Engineering for Industry, May 1974, pp. 509-517.
14. Childs, D., and Moyer, D., "Vibration Characteristics of the HPOTP of the SSME," ASME Journal of Engineering for Gas Turbine and Power, pp. 152-159, Vol. 107, ASME Transactions, January 1985.

15. Pennink, H., "The State of the Art of High Speed Overhung Centrifugal Compressors for the Process Industry," proceedings of the Seventh Turbomachinery Symposium, Texas A&M University, Dec. 1978, pp. 35-46.
16. Murphy, B. T., and Vance, J. M., "An Improved Method for Calculating Critical Speeds and Rotordynamic Stability of Turbomachinery," ASME Journal of Engineering for Power, Vol. 103, July 1983, pp. 591-595.
17. Thomson, W. T., Theory of Vibration With Applications, 2nd Edition, Prentice-Hall, Inc., Englewood Cliffs, New Jersey, 1981, pp. 174-184.

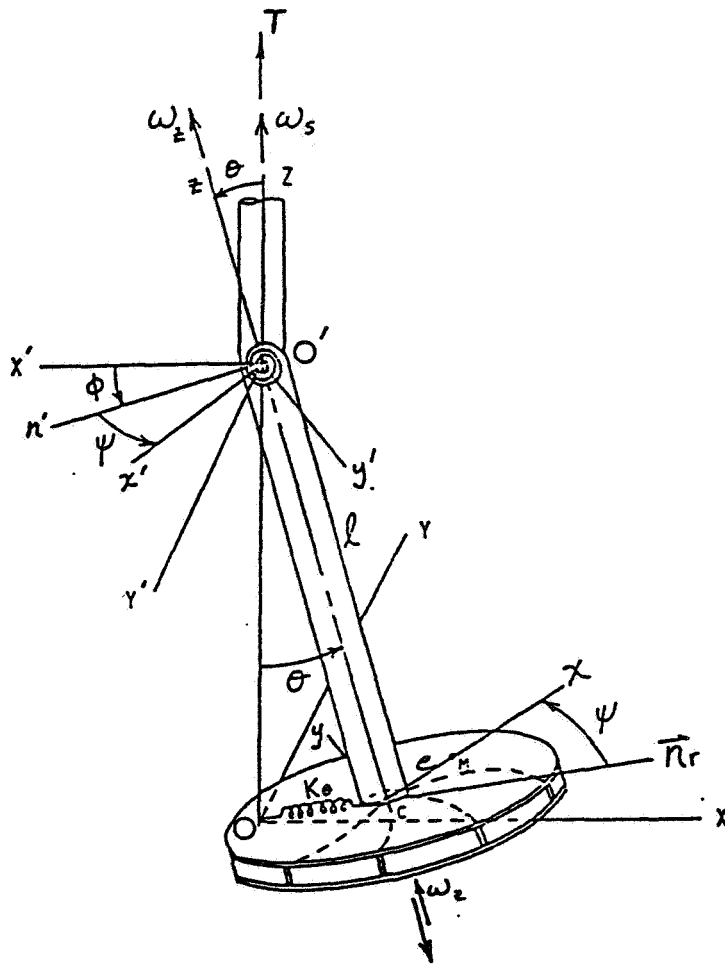


Figure 1. - Rigid-shaft model from Reference [8].

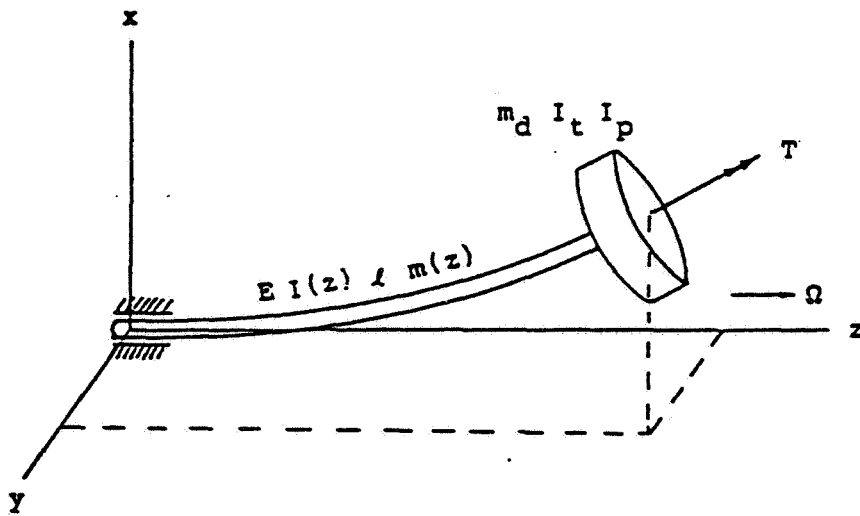


Figure 2. - Cantilevered rotor with flexible shaft.

ORIGINAL PAGE IS
OF POOR QUALITY

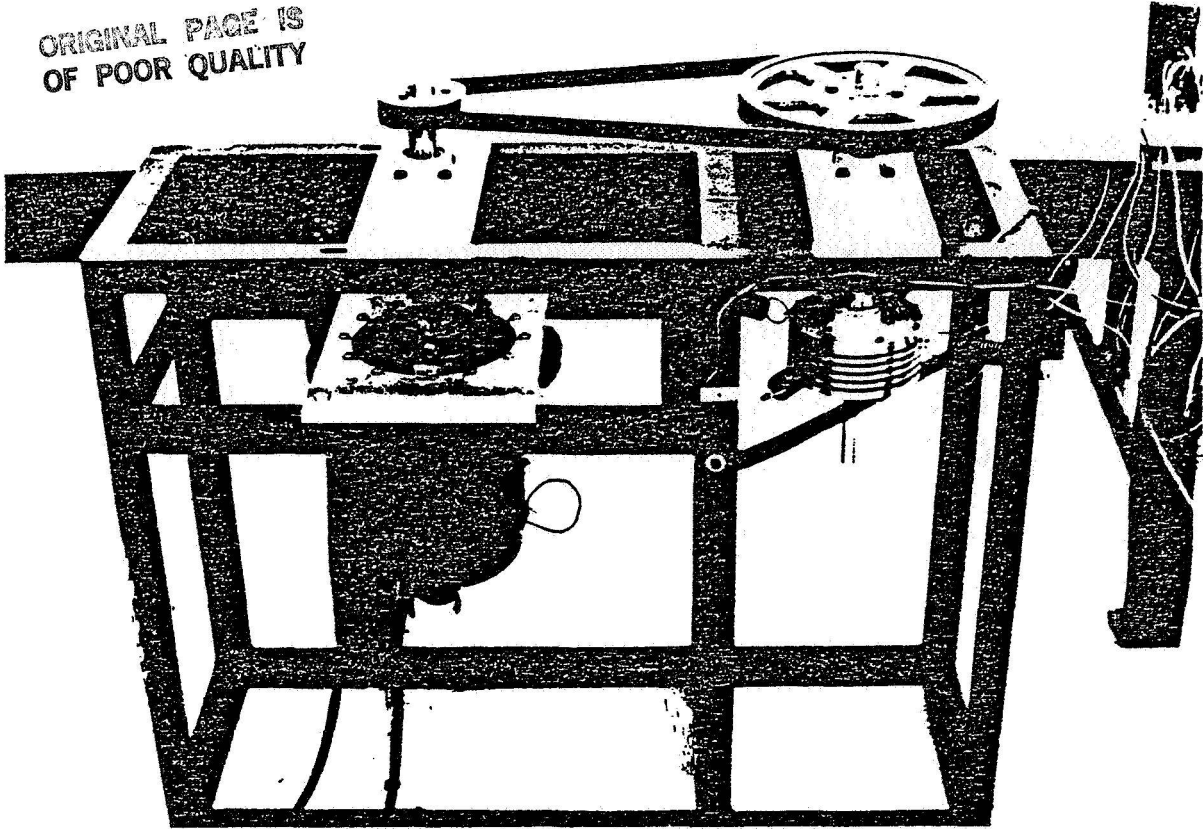


Figure 3. - Test rig.

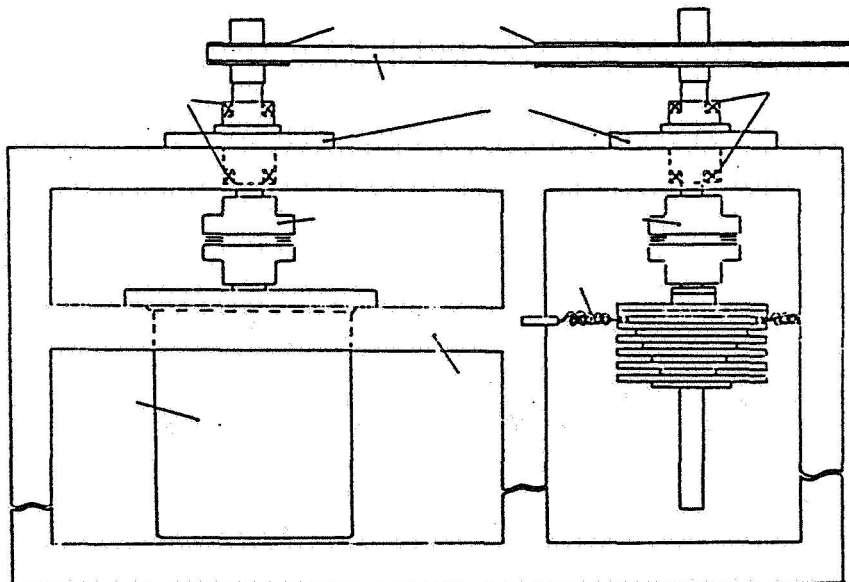


Figure 4. - Sketch of test rig.

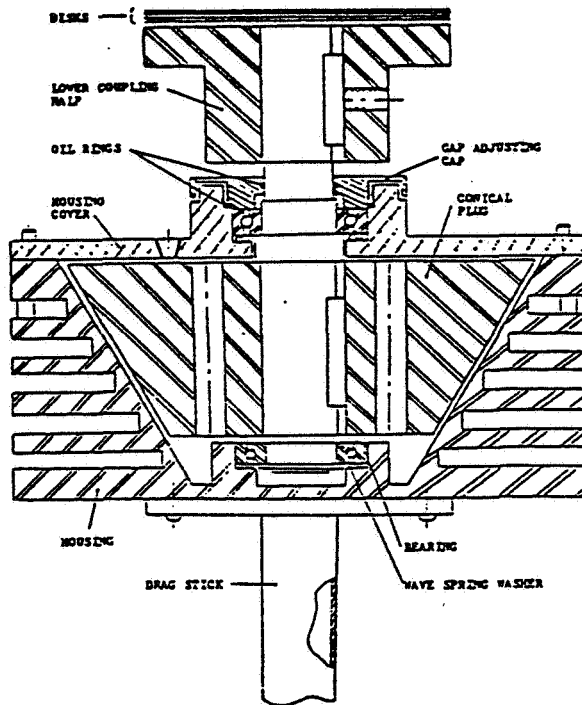


Figure 5. - Cross section of housing.

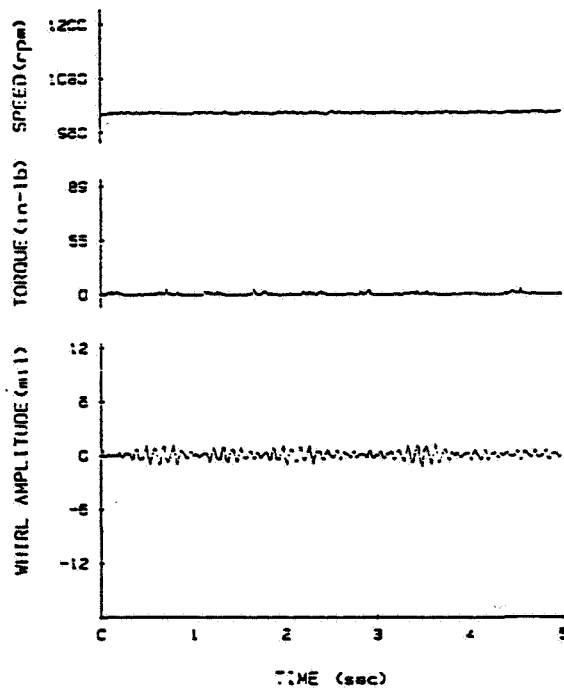


Figure 6. - Time domain data without load torque (2.2 percent damping; 1000 rpm).

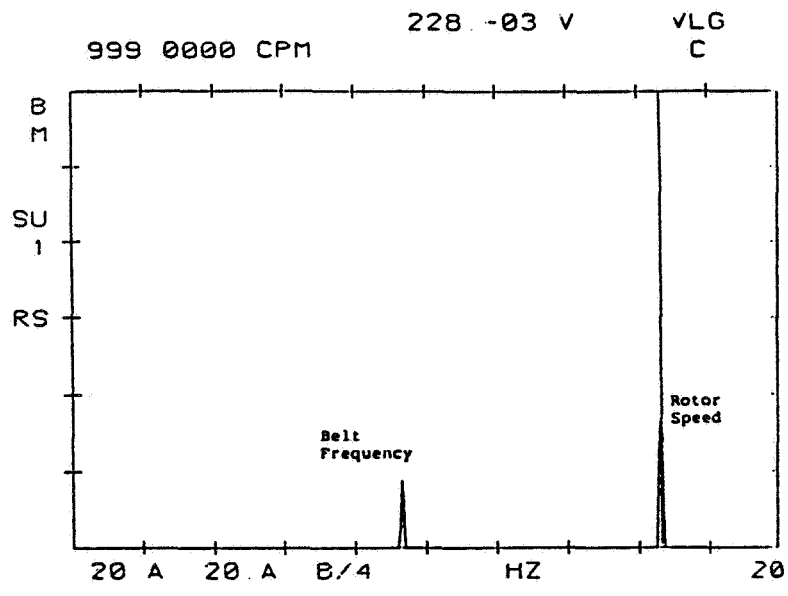


Figure 7. - Frequency domain data without load torque (2.2 percent damping; 1000 rpm).

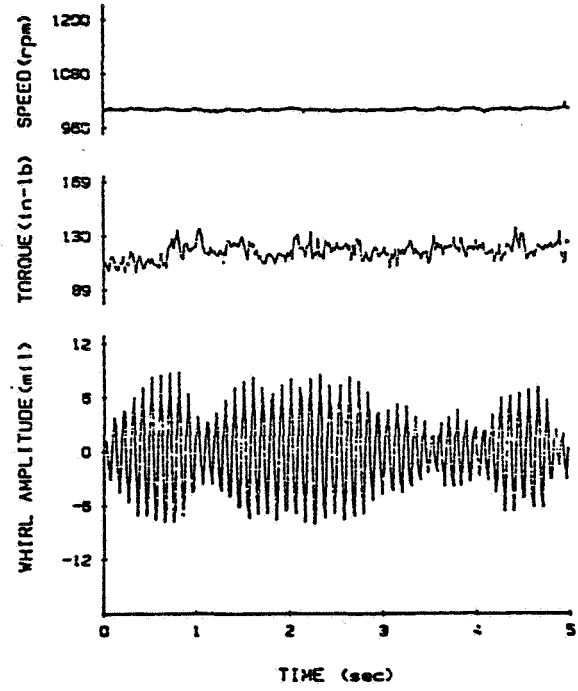


Figure 8. - Time domain data with load torque (2.2 percent damping; 1000 rpm).

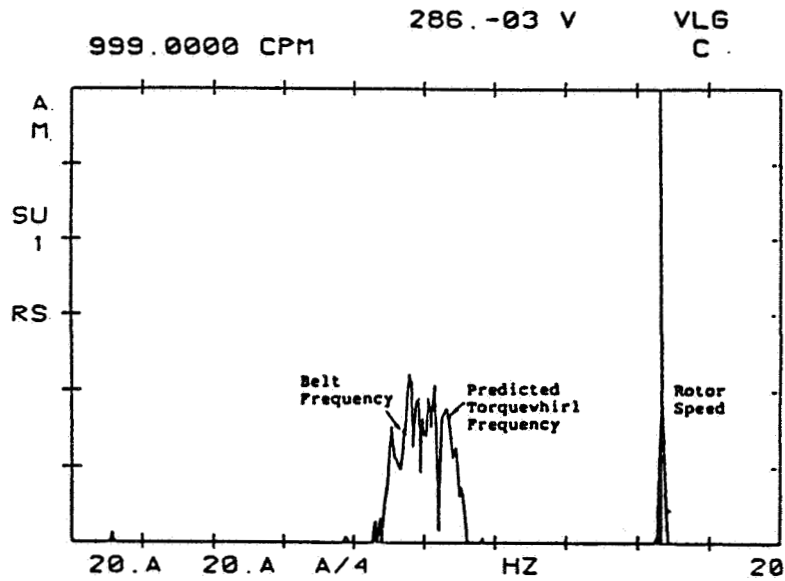


Figure 9. - Frequency domain data with load torque (2.2 percent damping; 1000 rpm).

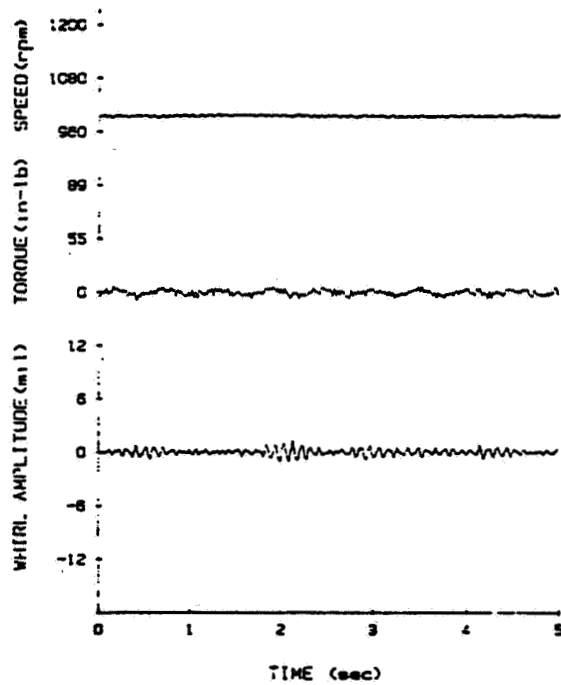


Figure 10. - Time domain data without load torque (5.2 percent damping; 1000 rpm).

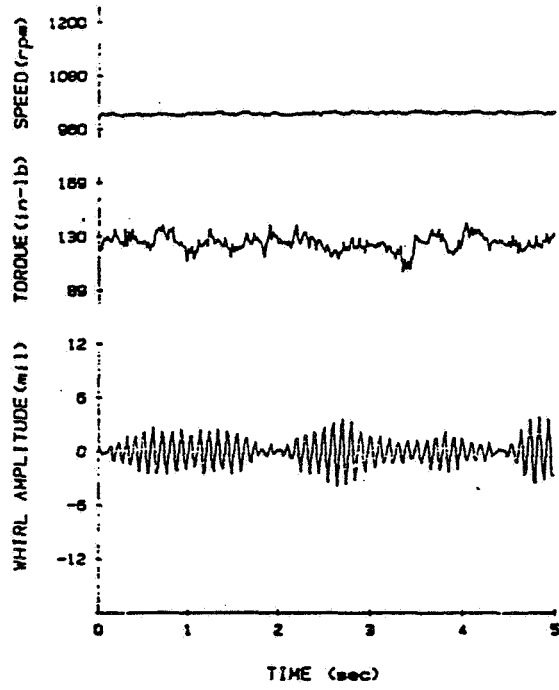


Figure 11. - Time domain data with load torque (5.2 percent damping; 1000 rpm).

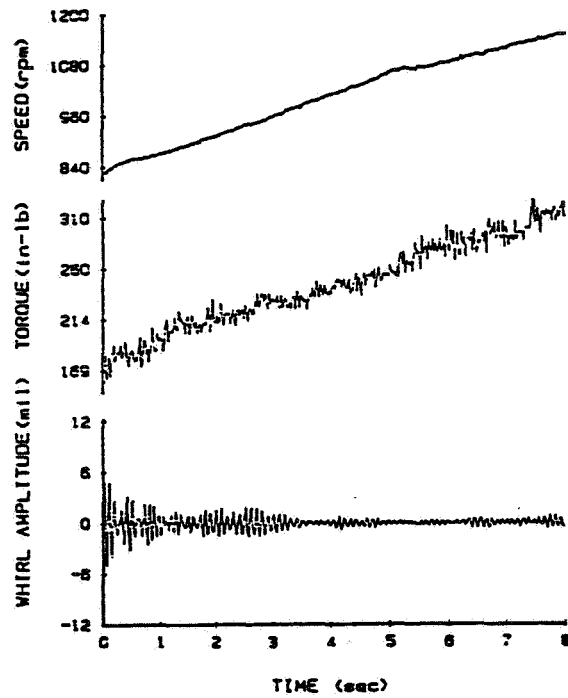


Figure 12. - Time domain data as rotor speed and torque increased continuously.

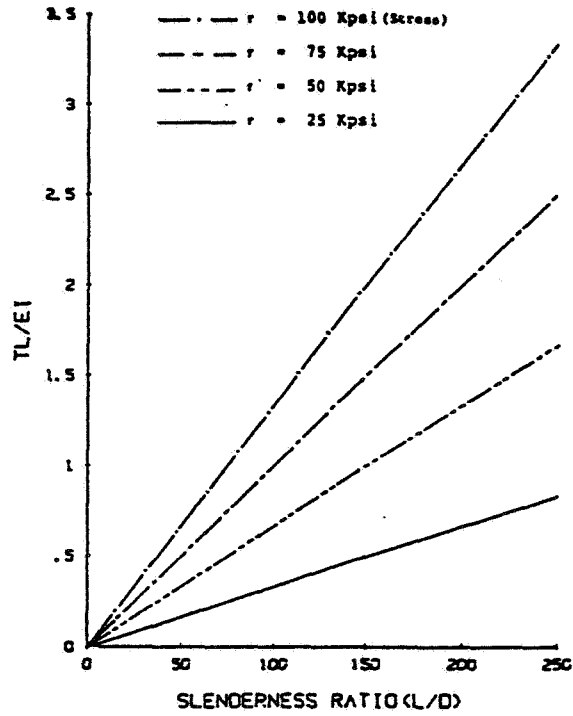
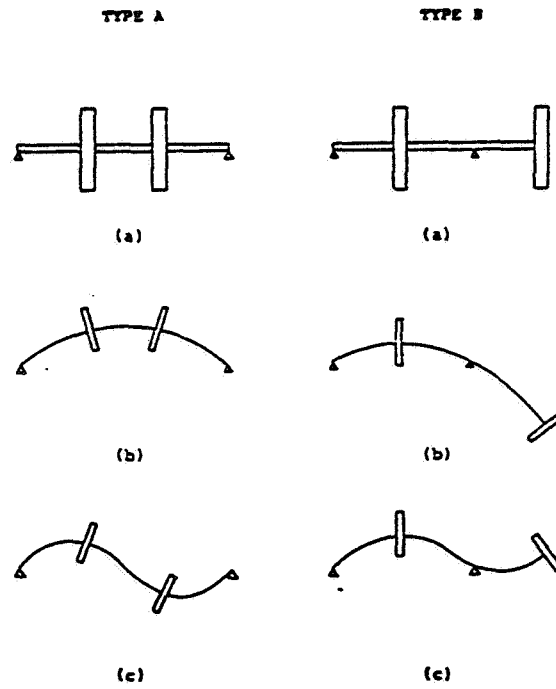


Figure 13. - Dimensionless torque term versus slenderness ratio.



(a) Models. (b) First mode. (c) Second mode.

Figure 14. - Two disk models and their first and second modes.

$l = 60 \text{ in}$ $d = 1 \text{ in}$
 $m_d g = 60 \text{ lb}$ $m g = 13.3 \text{ lb}$
 $I_c = 0.8 \text{ lb-in-s}^2$ $I_p = 1.6 \text{ lb-in-s}^2$
 $E = 3 \times 10^7 \text{ psi}$ $T = 40000 \text{ in-lb}$
 $K_{xx} = K_{yy} = 5 \times 10^6 \text{ lb/in}$ $N = 7500 \text{ rpm}$

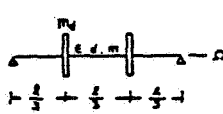
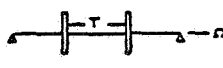
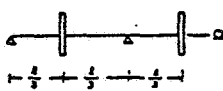
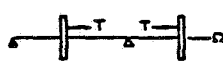
CASES	Logarithmic Decrement	Frequency (rpm)
A1 	0.0	312.1B
	0.0	376.6F
	0.0	1221.4B
	0.0	1419.4F
A2 	-2.8×10^{-13}	309.9B
	4.6×10^{-13}	375.1F
	3.9×10^{-12}	1217.0B
	-1.0×10^{-11}	1414.5F
B1 	0.0	205.9B
	0.0	416.8F
	0.0	945.4B
	0.0	1062.2F
B2 	1.997	202.2B
	-0.496	410.7F
	0.071	944.0B
	-0.023	1058.6F

Figure 15. - Effect of tangential torque on stability of two-disk rotors.

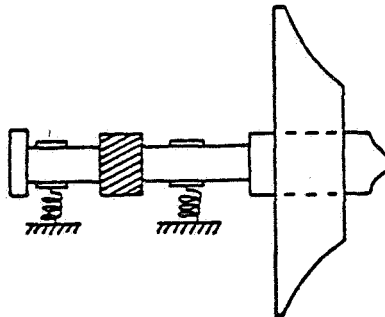
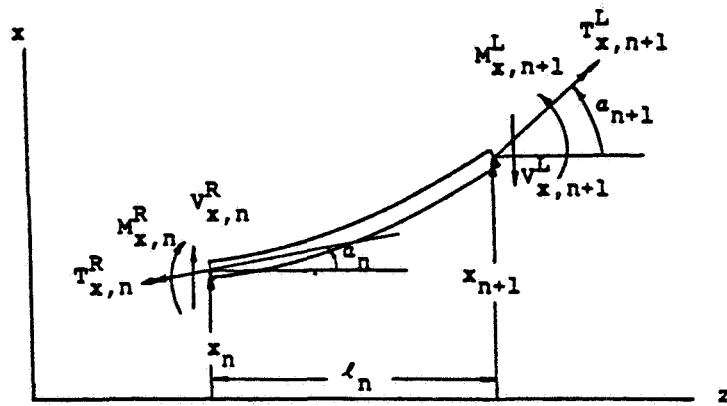
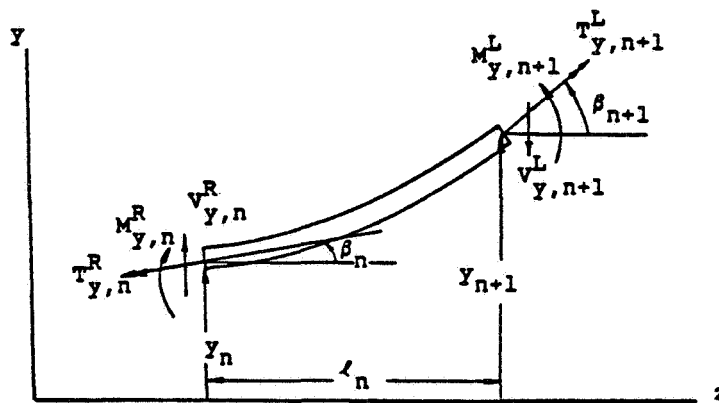


Figure 16. - Single-stage overhung compressor.



(a)



(b)

(a) xz-plane. (b) yz-plane.

Figure 17. - Sign convention for n^{th} shaft section.

CO₂ COMPRESSOR VIBRATION AND CAUSE ANALYSIS

Ying Yin Lin
 Liaohe Chemical Fertilizer Plant
 Panjin, Liaoning Province
 The People's Republic of China

This paper covers the operational experience of a large turbine-driven CO₂ compressor train in a urea plant with capacity of 1620 tons/day.

After the initial start-up in 1976, the vibration in the HP cylinder was comparatively serious. The radial vibration reached 4.2 to 4.5 mils and fluctuated around this value. It was attributed to the rotating stall based on our spectrum analysis. Additional return line from the 4th to 4th and higher temperature of the 4th inlet has cured the vibration.

This paper also describes problems encountered in the operation, their solutions, and/or improvements.

1. INTRODUCTION

The CO₂ compressor described here is a key installation of whole sets of the equipment in a 1620 ton/day urea plant. The steam turbine-driven compressor consists of two cylinders and four stages as shown in the flow diagram, Figure 1.

CO₂ gas from the CO₂-removing section of the ammonia plant is pressurized in this compressor to 144-150 kg/cm², sent to an HP condenser via a stripper and finally reacts with liquid ammonia forming urea. Main parameters and characteristics of the unit train are listed in Table 1.

2. CO₂ COMPRESSOR VIBRATION

From the commissioning in September, 1976, to the overhaul in 1980, vibration of the CO₂ compressor remained the bottleneck in urea production. During commissioning, radial vibration was found at comparatively high value, on the HP cylinder in particular.

The CO₂ compressor train has nine radial probes for vibration sensing on its turbine and gearbox and three axial displacement probes on the rotor's shaft of the LP cylinder, HP cylinder and turbine: twelve points in total.

1st point	turbine	front	bearing	radial	probe
2nd point	turbine	rear	bearing	radial	probe
3rd point	LP cylinder	front	bearing	radial	probe
4th point	LP cylinder	rear	bearing	radial	probe
5th point	gearbox	front	bearing	radial	probe
6th point	gearbox	rear	bearing	radial	probe
7th point	HP cylinder	front	bearing	radial	probe

8th and 9th points: HP cylinder rear bearing radial probe
(symmetrical about vertical axis and 90° included angle)

10th, 11th, 12th points: LP and HP cylinders, turbine rotor axial displacement probes.

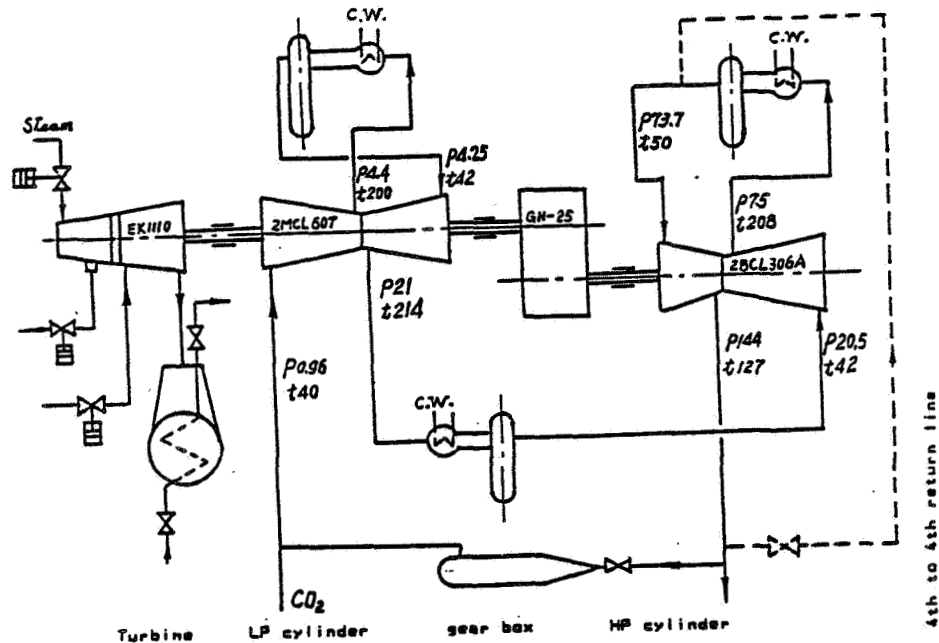


Figure 1. FLOW DIAGRAM OF CO₂ COMPRESSOR

description	LP cylinder		HP cylinder	
	1st stage	2nd stage	3rd stage	4th stage
inlet P kg/cm ²	10.96-1.021	4-4.5	20-24	74-80
outlet P kg/cm ²	4-4.5	20-24	74-80	144-150
inlet T °C	40	42	42	140-45(55-60)
outlet T °C	220	220	200	120-130
impeller No.	3	4	4	2
rated speed RPM	7200		13900	
max. continuous speed RPM	7540		14400	
1st order critical speed RPM	4100		8000	
2nd order critical speed RPM	9200		17500	
designed cylinder P kg/cm ²	26		195	
designed cylinder T °C	250		250	
working medium	CO ₂			
rated power KW	7210			
molecular weight of CO ₂	43.17			
inlet flow NM ³ /h	27636			

Table 1. Main Parameters and Characteristics of the CO₂ Compressor

The unit train has proved satisfactory in producing 1620 tons of urea per day since commissioning; however, some problems were also found during these years. In September, 1976, the O-ring between the 3rd and 4th stages was blown off by the CO₂ stream; it thus caused increased axial displacement of the HP rotor and thrust bearing shoes burnt. During the overhaul in 1978, the brace ring of the last stage and the next to last were found broken. In April 1979, scalings on the LP cylinder impeller and subsequent ill balance of the rotor brought the radial vibration up to 5 mils, resulting in a forced shutdown and replacement of the rotor.

Drains and instrument tubes of the HP cylinder were broken by vibration several times. Vibration on the HP cylinder was one of the most difficult problems. Shortly after commissioning, vibration on the 7th point was as high as 2.7 mils which was already beyond the limit specified in API 617. However, the HP cylinder was still kept running at this high vibration value since the CO₂ stream of greater molecular weight had significant influence on rotor running, and the specified vibration range of API 617 is applicable during manufacturer's shop test rather than end user's production. The vibration value in the HP cylinder went higher in February 1979 and fluctuated sometimes. Table 2 gives the record made on 26 February.

Table 2. Vibration Record on February 26, 1979

		1st stage	2nd stage	3rd stage	4th stage					
P	kg/cm ² inlet/outlet	1.1/3.8	3.8/24.5	24.5/82	82/140					
T	°C inlet/outlet	32/210	30/250	29/160	47/112					
point	mils	1/1.2	2/0.4	3/0.8	4/0.6	5/0.7	6/0.7	7/2.5	8/2.9	9/4.5

Rotor vibration of the HP cylinder was indicated by the 7th point's high value, sometimes by the 8th and 9th point's values or high values of these three points. During the replacement of the LP cylinder rotor in April 1979, the bearing of the HP cylinder was readjusted. The bearings of 8th and 9th points were replaced. The clearances between shoes and shaft were smaller (≈ 0.124), whereas the shoe clearance of 7th point became a little bigger (≈ 0.175), as no replacement was made on it. The normal clearance would be 0.12-0.155. After start-up, the vibration value on the 7th point was 4.0-4.2 mils and 0.7-0.8 mils on the 8th and 9th points. But the vibration of these three points went towards the same level half a month later, i.e., 3.4-4.0 mils. Since then, each time the train was temporarily shut down and started up without replacement or adjustment, vibration values of the three points did have small changes but fluctuated synchronously ranging between 0.5-1.5 mils. Intervals between adjacent fluctuations were not equal; the shortest was several times per minute, the longest fifteen times per minute. The most severe case occurred after the overhaul in 1979. Drain tubes and process lines vibrated as the HP cylinder vibrated. One of the drain tubes in the HP cylinder was vibrated to breakage four times around the weld's heat-affected zone and resulted a forced shutdown.

3. VIBRATION CAUSE ANALYSIS AND SOLUTION

3.1 Imperfect Balance of Rotors

The changes of vibration during running were found to have a certain relationship to rotor speed and could be attributed to its imperfect balance. Since it was not possible to perform dynamic balancing at working speed and the urea product was in urgent demand then, the test on the HP cylinder was delayed until the overhaul in

1980. The vibration of the HP rotor decreased a little, but was far from elimination.

3.2 Misalignment of the Unit Train

Poor hot alignment of the unit train shafts connected could provide a cause for vibration. Therefore, realignment of the coupling between the HP cylinder and gearbox was performed during several overhauls but it made little improvement. During overhaul, inspection of the rotor before disassembly indicated that the points of high vibration lost their original alignment values, as did the other points. Based on our experience during these years, the alignment of the train gives little effect to the vibration with the self-centering gear coupling. So alignment between rotor connection does have some tolerance but shouldn't be neglected. Misalignment was not the main cause of HP cylinder vibration. Stresses of pipelines and large deviation when resting longitudinal slide key between casings were first suspected as the source of the unit's misalignment and the vibration of the HP cylinder. The stainless steel pipe at the CO₂ inlet of the 4th stage had to be replaced due to serious corrosion. During the replacement, fabrication errors resulted 10 mm offset between centerlines of the pipe flange and the equipment flange. In order to produce urea earlier than expected, the flanges were forced to alignment and then bolted. During the overhaul in 1979, the piece of pipe was removed, cut, and rewelded according to the requirement of initial routing until full alignment was reached without residual stress of piping system to the unit train. Besides this, regularity was found when realigning, i.e., HP cylinder changed its position toward gearbox. As the position of resting longitudinal slide key was doubtful, a pow jack was used to force alignment. Once the train was put into operation, the original position as restrained by the slide key was restored and hot alignment changed. During the overhaul in 1978, two longitudinal slide keys were chiselled off to free the unit from restriction and rewelded after alignment.

Two measures taken, as mentioned above, didn't eliminate the vibration of the HP cylinder.

3.3 Possibility of Oscillation of Oil Film

The radial shoes of the HP cylinder are of the tilt type and are capable of protecting the unit from vibration and oscillation of oil film. The oscillation couldn't be terminated unless the viscosity of the lub oil and the load on bearing shoes were changed. Although the temperature of the lub oil, i.e., its viscosity, was changed, the vibration value remained the same as before. In addition, 0.4-0.5 multiple frequency did not appear during frequency measurement. Therefore, the vibration of HP cylinder was not caused by oscillation of oil film.

3.4 Influence of Pulsating Gas Flow

In order to reduce CO₂ inlet temperature and raise gas transferring capability of the unit, a directly countflowing water cooler had been added on the inlet pipeline. Its side effect was introducing C₁ into the CO₂ system via cooling water, hence, the corrosion and leakage of stainless steel tubes in CO₂ intercoolers. Among them the 3rd cooler came first and received the worst damage. Did this leakage and pulsation of gas flow in CO₂ system cause the vibration? Furthermore, leakage of the relief valve on the 4th stage outlet was found several times. Sometimes the valve popped under its rated pressure. The pressure pulsation raised our doubt that subsequent popping of the outlet relief valve in the 4th stage might have resulted in the unit's vibration. That's why the relief valve was reset or blinded off for a period

during overhauls. Unfortunately, replacement of the interstage cooler and reset of the relief valve or even blind-off didn't terminate or cure vibration of the HP cylinder.

3.5 Influence of Rotating Stall and Solution

We have explored some possible sources causing serious vibration through the practice of several years. Among them, rotating stall has been the doubtable factor since fluctuation and high vibration value with 3.8-5.6 mils changes existed. Flow pulsation was revealed by local indication of outlet flow. The pulsation was about 3000 NM₃/H and was accompanied by low and deep humming from the compressor like surging but not so strong. Indication of temperature and pressure changed little at that time. When fluctuation went out, vibration became stable; the strange sound disappeared, and the indication of the 4th outlet flow came to rest.

The sound we heard usually came from the unit or pipe vibration rather than from turbulent steam inside the unit or pipes. In the morning of September 19, 1980, gas inside rushed out from a suddenly-cracked thermowell on the 4th stage outlet and a strange sound was generated which was never heard before. Vibration values fluctuated during the sound; gas gushed from the cracked area in intermittent puffs strong or weak. When the vibration became stable without change, escaping gas snorted continuously. The sound of the gas stream strongly suggested rotating stall.

In order to find out the real source of vibration on the HP cylinder, we invited some research institutes and colleges, specialists in joint analysis. Table 3 is the record measured with frequency detector.

Rotative speed of the turbine and LP cylinder was 7200 rpm, whereas that of the HP cylinder was 13,900 rpm. During selection, 240 Hz was taken as the same frequency of HP cylinder, so 120 Hz was the half frequency, 60 Hz the quarter, and 480 Hz the double.

It is evident from Table 3 that base frequency was always present, which suggested the HP cylinder rotor was probably not in balance. Since the rotor was still running then, it was difficult to trace the source causing unbalance. Fitting parts coming off, impurities blocked in the channel of impellers, scaling on rotors or unbalance as manufactured were possibly the causes.

Table 3. Records of Frequency Spectrum

No.	location	vibess frequency mils	frequency selection component				
			60Hz	120Hz	240Hz	360Hz	480Hz
1	turbine inlet	11.23	10.1	11.15	10.275	10.085	10.10
2	turbine outlet						
3	ILP cylinder in	10.8	10.336	10.142	10.48	10.48	10.06
4	ILP cylinder out	10.8	10.38	10.48	10.2	10.225	
5	lgear box in	11.0	10.145	10.83	10.145	10.064	
6	lgear box out	11.0	10.22	10.10	10.708		10.310
7	IHP 4th stage in	13.4	12.0	11.1	12.8		10.11
8	IHP 3rd in(south)	13.6	11.15	10.9	13.2		10.4
9	IHP 3rd in(north)	13.4	10.6	10.8	13.0		10.4
10	ILP displacement	116	13.2	110	12.6	13.7	
11	IHP displacement	112	13.7		19		13.3

Besides the base frequency, 120 H₂ and 60 H₂ come next and the third, the double, and other multiple frequencies also stood in a certain proportion. The lower frequencies of 120 H₂ and 60 H₂ were considered caused by rotating stall since a strange sound, changed flow and pressure were observed as vibration fluctuated. Big clearances between shoes and shaft or outer ring would result in half-frequency vibration; however, not all vibration values changed after replacement of radial shoes. Eddy turbulence of bearings at half speed might bring lower frequencies, but after raising oil temperature, vibration did not change. Eddy turbulence was also discounted.

Double and multiple frequencies, in minor proportion as they were, shouldn't be neglected. Misalignment of rotors being the source of double frequency was not the main cause of the vibration of the HP cylinder. The decisive factor was the base frequency resulting in rotor's unbalance and half and quarter frequencies resulting in rotating stall. Of course, this should be proved through practice including dynamic balancing of the rotor and increased inlet flow.

As mentioned above, dynamic balance at high speed done during the overhaul in 1980 brought down vibration a little. In order to solve the problem completely, two measures were taken as follows.

- A. Erection of a return pipe from and to the 4th stage. A length of pipe being 32.5*3.25 size, 1Cr18Ni9Ti material was routed from the outlet and to the inlet of the 4th stage.
- B. Raising the inlet temperature of the 4th stage. It was increased from 55°C to 65°C to get more volumetric flow at the 4th stage inlet and thus cleared up stalling.

On September 19, 1980, two experiments were made as follows: Opened the block valve on the 4th to 4th return line and the vibration of the 7th point decreased gradually. It was performed in 3 steps. Ten minutes after two turns opening of the valve, the vibration of the 7th point went down from 2.5-2.6 mils to 2.2-2.3 mils but came back just two seconds later. Two more turns made the vibration down again 2.2-2.3 mils with obvious increased indication of flow percent on the control panel. At the same time the outlet pressure from the 3rd stage increased from 82 kg/cm² to 87 kg/cm². Full opening of the valve on the 4th to 4th return line brought vibration of the 7th point down from 2.2-2.3 mils to 1.7 mils; fluctuation and the strange noise disappeared; vibration of the 4th stage outlet pipe decreased. The 8th and 9th points had corresponding changes to the 7th point.

Raising the inlet temperature of the 4th stage had the purpose of increasing volumetric flow at the 4th stage inlet. Temperature increase from 50-55°C to 65°C brought the vibration of the HP cylinder down and produced stable running of the train. On the contrary, decreasing the 4th stage inlet temperature from 65° to 55°C made the vibration of the 7th point increase from 1.7 mils to about 2.5 mils; a strange noise appeared and vibration of pipes increased.

Two measures were taken for increasing volumetric flow at the 4th stage and curing the rotating stall of the stage. Our practice proved them effective but adverse to energy saving.

On April 14, 1982, for the purpose of lowering steam consumption, the valve on the 4th to 4th return line was closed gradually; vibration of the HP cylinder went up slowly. The vibration of the 9th point was up to 4.5 mils when the valve was fully closed and the strange noise was heard again. Finally, the valve on the 4th to 4th return line had to be opened to ease the train.

4. IMPROVEMENTS ON THE CO₂ COMPRESSOR TRAIN

4.1 Retrofit on Power Supply System

After put into operation, the motor-driven oil pump tripped several times due to instant fluctuation in the power supply system. If the spare oil pump couldn't be started promptly, the oil pressure became too low, the interlocking system would work immediately and finally the CO₂ compressor train got tripped. Therefore, the power supply of the interlocking system was rearranged from the ordinary civil power source to the uninterrupted power system from the ammonia plant. This cured the problem.

The interlocking solenoid valve worked normally energized. Fluctuated voltage would make the solenoid valve release its action due to lower tension and trip the train because of oil system cutoff. The interlocking solenoid valve after improvement worked normally; deenergized and got energized when abnormal. This cured trips from false action of solenoid valve due to fluctuation in the power system and eliminated shutdowns when quick on-off in power source occurred possibly in thunder and storm on a summer's day. Two years' practice had proved the measures effective.

4.2 Retrofit on Oil Supply System

There is a cubic "U-tube" oil heater in the lub oil sump to heat cool oil with LP steam after protracted shutdown of the train. Every year sludge layers about 50 mm thick accumulated on the inside surface of the oil sump and should be cleaned up during overhaul because of corrosion and scaling resulting from comparatively high temperature and small amount CO₂ and water in the oil. The cleaning was difficult and the oil might be damaged. A stainless steel partition plate was added in the lower portion of the oil sump. The oil heater was changed to a coil-type heater and put under the partition plate like a flat drawer which could be pulled out or pushed in as needed. Two-millimeter stainless steel lining was provided on the surface of the sump. No dirt or scalings from the heater and the inside surface have been found in the oil sump since then.

4.3 Backing Ring to the Rubber Seal in the HP Cylinder

The 3rd and 4th stage are in the HP cylinder which is of a barrel type. The outer casing and end covers are forgings, whereas the inner casing is a cast piece. The inner casing is half split horizontally. The two halves are bolted together and put into the outer casing. Rubber O-rings were provided to prevent leakage through and between inner and outer casings. During the trial running in 1976, the "O" rubber ring was blown off and displacement of the rotor in the HP cylinder occurred due to overload of axial force. This resulted in a serious incident in which thrust bearings, rotor, diaphragms and labyrinth at different stages were damaged. Another ring of PTFE was added to back up the rubber one which was already blown off. The backing ring was added as illustrated in Figure 2.

Blow-off of the rubber ring hasn't happened again since the addition of PTFE backing ring, thus it gave trouble-free and safe production.

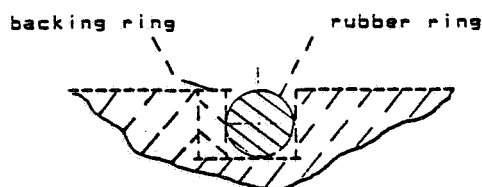


Figure 2

4.4 Rearrangement of Vent Pipes

Besides the vent pipe upstream from the stripper, at the side wall of compression building, there were other vent pipes with horseshoe-like nozzles toward manways between the process steel structure and control room and compression building. During starting, the HP cylinder was operated at low pressure and flow which was not in balance with the inlet flow of the LP cylinder. The vent pipe of the second stage in particular had to be opened in time to avoid over-pressure in the stage. Therefore, a large amount of dense CO₂ gas vented moved down to the ground and diffused around. At this point, operators in the urea plant were busy up and down the steel structure. Suffocating made operators uncomfortable. During the overhaul in 1980, the original vent pipes were extended by 1.5 m which was long enough to make them higher than the building. The horseshoe-like nozzles were turned to the opposite direction. This eliminated pollution and harm to operators when starting.

4.5 Shortening the Drains of HP Cylinder

The CO₂ compressor rested on the second floor with drain tubing from the compressor's bottom to the first ground floor, which was designed rationally and serviced. Long drains and instrument tubing always vibrated when the HP cylinder vibrated seriously. The over-stress on the drains and instrument copper tubing made them break several times, hence forced shutdowns, e.g., in 1979. Changing the instrument tube material to plastics, shortening the drain tube from 6 m to 0.5 m, and moving the drain valve from downstairs to upstairs cured the trouble because the shortened drain tube would vibrate together with the HP cylinder; no shutdown and overstress occurred after that.

4.6 Improvements of the 3rd-Stage Cooler

The temperature of the CO₂ incoming stream from the ammonia plant increased after each compression stage; therefore, interstage coolers were provided. After several years' usage, the 3rd-stage cooler was found badly corroded due to two reasons. A direct cooler for incoming CO₂ was designed and put into operation; therefore, the radical C₁- in circulating water was introduced into the CO₂ system causing stress corrosion in the "U-type" cooling tubes. The inlet temperature of the 4th stage had been increased in order to cure the rotating stall. Under the same cooling area, reducing the quantity of cooling water would increase its outlet temperature. The outlet temperature of cooling water changed from 42-47°C to 70-80°C, which was beyond the limit 45°C specified to prevent stainless steel of TP304 and TP316 from stress corrosion. The 3rd-stage cooler was improved in two ways. The average

length of welded "U" tubes was reduced from 13.3 m to 7.55 m and heat transfer area from about 100 M² to 51.6 M², whereas the quantity of cooling water increased from 30 T/H to 150 T/H. After that, the outlet temperature was down to about 45°C. Besides this, a bypass of Dg200 was provided on the inlet pipe of cooling water for the purpose of outlet temperature control. The 3rd-stage cooler was found to have almost no damage or trouble after the improvements in 1980.

REFERENCES

1. Vibration Analysis on the CO₂ Compressor Train in Liaohe Chemical Fertilizer Plant. Vibration Research Group, Mechanical Dept., Zheng Chou Engineering College, China, October 1980.
2. Vibration Problems of Rotors in Turbine Machines. Turbine & Compressor Teaching & Research Section, Sian Communication University, China, March 1980.
3. Tang Guo Fu: Analysis and Solution for Big Fluctuation of Vibrations on CO₂ Compressor HP Cylinder. Liaohe Chemical Fertilizer Plant, Liaoning Province, China, July 1980.
4. Procedure for Maintenance and Overhaul of CO₂ Compressor Train. Chemical Fertilizer Dept., The Ministry of Chemical Industry, China, 1983.

INFLUENCE OF DESIGN PARAMETERS ON OCCURRENCE OF OIL WHIRL
IN ROTOR-BEARING SYSTEMS

Peter J. Ogrodnik and Michael J. Goodwin.
North Staffordshire Polytechnic
Stafford, England

John E.T. Penny
Department of Mechanical and Production Engineering
University of Aston in Birmingham
England

Oil whirl instability is a serious problem in oil lubricated journal bearings. The phenomenon is characterised by a sub-synchronous vibration of the journal within the bush and is particularly apparent in turbogenerators, aeroengines and electric motors. This paper presents a review of previous papers on the subject of oil whirl, and describes a simple theory which has been used to aid the design of an oil whirl test rig.

Predictions of the onset of oil whirl made by the theory presented in this paper were found to agree with those of previous researchers. They showed that increasing the shaft flexibility, or the lubricant viscosity, and decreasing the bearing radial clearance tended to reduce the oil whirl onset speed thus making the system more unstable.

NOTATION

A_{ab}	Net stiffness coefficient: Force in a direction per unit displacement in b direction	{F}	Force Vector.
B_{ab}	Net damping coefficient: Force in a direction per unit velocity in b direction	$[K_j]$	Bearing stiffness matrix
c	Bearing radial clearance.	$[K_s]$	Shaft stiffness matrix
C_{1-5}	Coefficients of system characteristics equation.	L	Length of bearing.
D	Diameter of bearing.	M	Mass of rotor.
F_s	Static force acting on bearing	S_{1-4}	Roots of system characteristic equation.
		{U}	Displacement vector for journals relative to bearing bushes
		{V}	Displacement vector for mass relative to journals

[K _e]	Equivalent stiffness matrix.	$\alpha_{1,2}$	Real parts of roots of system characteristic equation
x	Displacement in horizontal direction	$\beta_{1,2}$	Imaginary part of roots of system characteristic equation
X	Function of displacement amplitude in horizontal direction.	ω	Vibration frequency
y	Displacement in vertical direction.	<u>Suffices</u>	
Y	Function of displacement amplitude in vertical direction.	x	Refers to horizontal direction
{Z}	Displacement vector of rotor mass relative to bushes	y	Refers to vertical direction

INTRODUCTION

The phenomenon of oil whirl was first discussed and investigated in the 1920's, the most important paper of that time being by Newkirk and Taylor (1). It was found that whipping of the shaft ceased when the oil supply was halted which led to the conclusion that it was due to vibrations within the oil film. A simplified explanation was proposed that relied upon the fact that there is a pressure difference around the journal surface.

Work by Robertson (2) and Hagg (3) led to an improved theory to predict the presence of oil whirl. Robertson solved Reynolds equation to determine the oil film forces and then equated these with body forces to predict the motion of a rotor mounted on both a stiff and an elastic shaft. In contrast, Hagg determined oil film force by examining the continuity of the oil flow and then determined the system stability by assuming the bearing oil film to behave as a spring and a damper. Both methods were found to agree with the results of Newkirk and Taylor. Hagg also determined, experimentally, that tilting pad bearings were unable to sustain oil whirl vibrations and hence were more stable.

In 1956 Hagg and Sankey (4) suggested that by assuming the oil film to behave as pairs of springs and dampers, hence having two displacement coefficients and two velocity coefficients, the coefficients may be added to the rotor system properties and a more reliable estimate of oil whirl may be calculated. To improve stability estimates further, Morrison (5) proposed that four further coefficients are required which link forces in the horizontal directions to velocity and displacement in the vertical direction, and vice-versa (the "cross-coupling coefficients"). In 1959, Hori (6) noted that in certain cases the displacements could well be comparatively large compared to the oil film and so the analysis should be essentially non-linear. Hence, Holmes (7) and Bannister (8) were able to argue the case for utilising non-linear coefficients when modelling the oil film and therefore improving the estimate of oil whirl onset.

Bannister (8), Newkirk and Lewis (9), and Downham (10) have all examined the effect of misalignment of the journal within the bush. Bannister and Newkirk and Lewis have determined experimentally that misalignment was a stabilising factor, and Downham

suggested that misalignment effectively stiffens the oil film and that this was the stabilising factor. Later, Mukherjee and Rao (11) carried out a numerical analysis to determine the values of damping and stiffness coefficients for an inclined journal bearing but no comparison was made between these coefficients and those for an aligned bearing. Dhagat et al (12) investigated the stability of journal bearings with lateral and skew motions by determining a total of sixteen coefficients. However, neither stated the effect misalignment had upon stability. More recently Gupta (13) found that misalignment of the bearing caps, which he termed preset, had an advantageous effect upon stability.

Simmons and Marsh (14) showed experimentally and theoretically that increased pedestal flexibility has a detrimental effect upon whirl onset. They also postulated the possibility of a cessation of oil whirl as rotor speed increases and a subsequent secondary whirl onset; this however, has not been validated in practice. Lund (15,16) both calculated, and illustrated experimentally, the effect of shaft flexibility on whirl onset. As with pedestal flexibility it was found that a more flexible shaft has a detrimental effect upon stability. More recently Ruddy (17) has modelled a rotor-mounted on a flexible shaft with various bearing designs to investigate system stability. Ruddy, however, does not investigate the effect of varying shaft flexibility.

The effect of imbalance has been examined by Barret et al (18) who used a time transient non-linear analysis to examine the motion of the journal. They found that if a rotor operated above whirl onset an increase of imbalance can reduce the magnitude of the whirl orbit to below that of a fully balanced rotor. Akers et al (19) have also utilised a non-linear analysis to solve the equation of motion for the shaft in both the vertical and horizontal directions. Although they examined the effect of an out of balance load there is much confusion over the interpretation of results the conclusions being that imbalance may or may not increase stability, and it was unclear what the deciding factor was. More recently Bannister (20) used a finite difference technique to solve Reynolds equation and hence produce the oil film force, and then proceeded to solve the equations of motion, which was a similar method to that of Akers. Bannister states that the bearing operation goes through a transition stage, before entering a region of instability, where he states that an examination of the magnitude of the non-synchronous component of vibration can indicate when the system is about to go unstable. Bannister also agrees with Barrett that imbalance does produce a degree of stability.

It was earlier stated that the oil film may be represented by a series of springs and dampers. Much work has been carried out to determine these coefficients empirically, especially by Lund (21), Morton (22), Bannister (9) and more recently Parkins (23). Unlike previous researchers Bannister and Parkins allowed for oil film non-linearity and so their coefficients may be used to produce a more accurate estimate of oil whirl. More recently, Bentley and Muszynska (24,25) have used the application of a sinusoidal perturbing force to examine the oil film dynamic stiffness and stability of journal bearings. It was found that an increase in oil supply pressure or a decrease in oil temperature causes a subsequent increase in dynamic stiffness. A method for determining whirl onset experimentally was also described, although the effect of oil temperature and feed pressure on whirl onset was not examined.

In general, the conclusions reached by most of the previous investigators are that reducing the flexibility of the shaft and pedestal does tend to promote instability, whereas the inclusion of misalignment tends to stabilise the system. There is also a general consensus that when determining whirl onset and whirl orbits the use of

non-linear theory leads to greater accuracy. However, there is confusion over the effect of imbalance and further research is needed in this area.

This paper presents a theoretical method of predicting stability based on linear oil film coefficients derived by Lund (21) and is similar to the method suggested by Cameron (26). The analysis is developed further to allow for the presence of shaft flexibilities using matrix notation to express the equations which model the bearing and shaft properties. The effects of varying shaft flexibility, radial clearance and oil viscosity on whirl onset have been examined and the results were found to agree in general with those of previous researchers.

THEORY

This analysis applies to the case of a single mass M mounted at the centre of a light flexible shaft of stiffness K which runs in two identical oil film journal bearings as illustrated in Figure 1. The oil film in the journal bearings is assumed to be described by the eight linearised oil film force coefficients. The force-displacement relationships for the journal bearings are, in matrix form:

$$\{ F \} = [K_j] \{ U \} \quad (1)$$

where the matrix K_j contains the oil film force coefficients for the two oil films acting in parallel. Similarly, a force displacement relationship may be written for the shaft itself

$$\{ F \} = [K_s] \{ V \} \quad (2)$$

Inverting the stiffness matrices of equations (1) and (2) and adding together the resulting displacements gives

$$\{ U \} + \{ V \} = [[K_j]^{-1} + [K_s]^{-1}] \{ F \} \quad (3)$$

where $[K_s]$ is of the form

$$\begin{bmatrix} K_{xx} & 0 & 0 & 0 \\ 0 & K_{xx} & 0 & 0 \\ 0 & 0 & K_{yy} & 0 \\ 0 & 0 & 0 & K_{yy} \end{bmatrix} = [K_s]$$

since both damping and cross-couple terms have been considered as negligible for the shaft itself or simply

$$\{ Z \} = [K_e]^{-1} \{ F \} \quad (4)$$

which on re-inverting gives

$$\{ F \} = [K_e] \{ Z \} \quad (5)$$

where K_e contains equivalent stiffness and damping coefficients, A_{xx} , B_{xx} , etc., which allow for both oil film and shaft flexibility. The matrix $[K_e]$ is, however, more complicated since it is itself an inversion of the summation of two inverted matrices. However, it is still of the form of the matrices $[K_s]$ and $[K_j]$ and may be written as

$$\begin{bmatrix} K_{xx} & -\omega C_{xx} & K_{xy} & -\omega C_{xy} \\ \omega C_{xx} & K_{xx} & \omega C_{xy} & K_{xy} \\ K_{yx} & -\omega C_{yx} & K_{yy} & -\omega C_{yy} \\ \omega C_{yx} & K_{yx} & \omega C_{yy} & K_{yy} \end{bmatrix} = [K_e]$$

The equations of motion of the rotor mass in the horizontal and vertical directions may now be written as

$$A_{xx} \cdot \ddot{x} + A_{xy} \cdot \ddot{y} + B_{xx} \cdot \dot{x} + B_{xy} \cdot \dot{y} = -M\ddot{x} \quad (6)$$

and

$$A_{yx} \cdot \ddot{x} + A_{yy} \cdot \ddot{y} + B_{yx} \cdot \dot{x} + B_{yy} \cdot \dot{y} = -M\ddot{y} \quad (7)$$

Assuming sinusoidal displacements of the form

$$x = X_e e^{st} \quad (8)$$

and

$$y = Y_e (st + \phi) \quad (9)$$

in the horizontal and vertical directions respectively, these may be differentiated to obtain expressions for velocity and acceleration. Substituting back into equations (6) and (7), dividing throughout by e^{st} and eliminating the ratio X/Ye^ϕ leads to the system characteristic equation

$$M^2 S^4 + (B_{xx} + B_{yy})M S^3 + [(A_{xx} + A_{yy})M + B_{xx} B_{yy} - B_{xy} B_{yx}] S^2 + (A_{yy} B_{xx} + B_{yy} A_{xx} - A_{xy} B_{yx} - B_{xy} A_{yx}) S + (A_{xx} A_{yy} - A_{xy} A_{yx}) = 0 \quad (10)$$

The roots of equation (10) usually occur in conjugate pairs of the form

$$S_{1,2} = \alpha_1 \pm j\beta_1 \text{ and } S_{3,4} = \alpha_2 \pm j\beta_2 \quad (11)$$

For motion of the mass to be unstable at least one value of α must be greater than zero, the value of β indicates the frequency of the resulting vibrations.

RESULTS

A computer program based on the theory presented was written to investigate the stability of journal bearing-rotor systems. The bearing stiffness and damping coefficients used in the analysis were calculated from dimensionless groups determined by Lund (21) for plain journal bearings.

The analysis was used to investigate the effects of shaft stiffness, journal diameter, bearing clearance, and lubricant viscosity, as indicated by the enclosed graphs. Unless otherwise stated as a variable, the system parameters used were shaft stiffness 85 kN/m, journal diameter 58.4 mm, bearing L/D ratio 1, bearing radial clearance 0.1 mm and lubricant viscosity 0.046 Ns/m².

DISCUSSION

Figures 2 and 3 show stability maps for the cases when shaft stiffnesses are 85 kN/m and 85 MN/m respectively. It can be seen from Figures 2 and 3 that the occurrence of whirl onset corresponds to a much lower value of system operating parameter for the stiffer shaft; this means that a much larger value of journal rotational speed is necessary for whirl onset and so the system is more stable. To further illustrate the effect of shaft stiffness, Figure 4 shows whirl onset boundaries for a series of shafts having different stiffnesses. It is clear that as shaft stiffness increases stability increases; these conclusions are in agreement with those reached by Simmons and Marsh (14) and Lund (15, 16) as discussed previously.

Generally, the whirl onset boundary associated with a particular system, as illustrated in Figures 2 and 3 may be approximated to a horizontal line, for example, in Figure 3, below an operating parameter of 0.8×10^{-3} the roots α are either positive or only marginally negative. Hence the area between the horizontal line and the whirl onset boundary may be discussed as a transition stage; this tends to agree with Bannister's findings (20) that a system reaches a transitional stage of instability before finally becoming unstable.

The effect of varying viscosity on the system is illustrated in Figure 5. It can be seen that by decreasing the viscosity of the lubricant the whirl onset boundary attains a lower operating parameter, thus a decrease in viscosity tends to cause an increase in stability. This has been demonstrated in the past on several large machines, where it has been found that when initially running a rotor up to operating speed oil whirl may exist, but after a period of running, that is after the oil increases in temperature and hence its viscosity is reduced, the oil whirl may often disappear (27).

Figure 6 illustrates the effect of bearing radial clearance upon system stability. It may be seen that as clearance is reduced the whirl onset boundary coincides with a larger operating parameter. However, it is unclear how much a particular change in clearance affects the system stability, this is because bearing clearance forms a part of the operating parameter to which the vertical axis refers. In this case it is more meaningful to plot whirl onset speed against radial clearance as shown in Figure 7. From this graph, it may be seen that for relatively large clearances an increase in clearance gives greater stability. However, for relatively small clearances this may not be the case and in fact the converse may occur. In this light it is interesting to note the conflicting opinions of Newkirk and Taylor (1) who determined experimentally that a decrease in clearance will increase stability and that of Barwell (28).

CONCLUSIONS

The authors agree with past researchers that design parameters do have an effect on rotor bearing stability. These may be summarised as follows:-

- (i) Journal/bush-misalignment tends to promote stability.
- (ii) Reducing shaft/pedestal stiffness reduces system stability.
- (iii) Reducing lubricant viscosity increases system stability.
- (iv) Reducing radial clearance decreases stability.

- (v) The effect of imbalance upon stability is not clear and needs further investigation

REFERENCES

1. B L Newkirk and H D Taylor. *"Shaft Whipping due to Oil Action in Journal Bearings"*, General Electric Review, Vol. 28, 1925.
2. D Robertson. *"Whirling of a Journal in a Sleeve Bearing"*. Phil. Mag. Series 7 Vol. 17, Pages 113-130, 1933.
3. A C Hagg. *"The Influence of Oil Film Bearings on the Stability of Rotating Machines"*. Jrnl. App. Mech. Trans ASME Vol. 14 Pages A211-220, 1946.
4. A C Hagg and G O Sankey. *"Some Dynamic Properties of Oil Film Journal Bearings with Reference to unbalance vibration of rotors"*. Jrnl. Appl. Mech. Trans ASME Vol. 23 Pages 302-306, 1956.
5. D Morrison. *"Influence of a Plain Journal Bearing on the Whirling Action of an Electric Rotor"*. Proc. Inst. Mech. E. Vo. 176 No. 2 Pages 542-553, 1962.
6. Y Hori. *"A Theory of Oil Whip"*. Trans. ASME. Vol. 81 Page 189, 1959.
7. R Holmes. *"Oil Whirl Characteristics of a Rigid Rotor in 360 Degree Journal Bearings"*. Proc. Inst. Mech. E. Vol. 177 No. 11, 1963.
8. R H Bannister. *"Theoretical and Experimental Investigation Illustrating the Influence of Non-Linearity and Misalignment on the Eight Oil Film Force Coefficients"*. I.Mech. Conference on Rotating Machinery, 1976.
9. B L Newkirk and J F Lewis. *"Oil Film Whirl - An Investigation of Disturbances due to Oil Films in Journal Bearings"*. Trans. ASME. Vol. 78 Page 21, 1956.
10. E Downham. *"The Influence of Plain Bearings on Shaft Whirling"*. Aeronautical Research Reports and Memoranda. No. 3046. October 1955. Printed HM Stationery Office, 1958.
11. A Mukherjee and J S Rao. *"Stiffness and Damping Coefficients of an Inclined Journal Bearing"*. Mech. Mach. Theory. Vol. 12 Part 14, Pages 339-355, 1975.
12. S Dhagat, R Sinhasan, D V Singh. *"Stability of Hydrodynamic Journal Bearings Under Combined Lateral and Skew Motions"*. Microtecnic 1. Pages 43-47, 1982.
13. B K Gupta. *"Effect of Preset on the Performance of Finite Journal Bearings Supporting Rigid and Flexible Rotors"*. Jrnl. Lub. Tech. Trans ASME Vol. 104 Pages 203-209, April 1982.
14. J E L Simmons and H Marsh. *"An Experimental Method for the Determination of Journal Bearing Parameters. Parts 1 and 2"*. J Mech. Eng. Sci. Vol. 21. No.3. Page 179, 1979.
15. J W Lund. *"Stability and Damped Critical Speeds of a Flexible Rotor in Fluid Film Bearings"*. Jrnl. Eng. for Ind. Trans. ASME. Pages 509-517, May 1974.

16. J W Lund and F K Orcutt. *"Calculations and Experiments on the Unbalance Response of a Flexible Rotor"*. Jrnl. Eng for Ind. Trans ASME Pages 785-795, November 1967.
17. A W Ruddy. *"The Dynamics of Rotor Bearing Systems with Particular Reference to the Influence of Fluid Film Journal Bearings and the Modelling of Flexible Rotors"*. PhD Thesis, University of Leeds, 1979.
18. L E Barrett, A Akers and E J Gunter. *"Effect of Unbalance on a Journal Bearing Undergoing Whirl"*. Proc. Inst. Mech. E. Vol. 190, 31/76 Pages 535-544, 1976.
19. A Akers, S Michaelson, A Cameron. *"Stability Contours for a Whirling Finite Journal Bearing"*. Jrnl. Lub. Tech. Trans. ASME. Vol. 93 No.1, Page 177, 1971.
20. R H Bannister and J Makdissy. *"The Effects of Unbalance on Stability and its Influence on Non-Synchronous Whirling"*. Third I.Mech.E Conference on Vibration in Rotating Machinery. Paper C310/80 Pages 395-400, 1980.
21. J W Lund. *"Rotor Bearing Dynamic and Design Technology - Part II - Design Handbook for Fluid Film Type Bearings"*. Wright Patterson Air Force Base, Ohio, Report AFAPL-TR-65-45, 1965.
22. P G Morton. *"Measurement of Dynamic Characteristics of a Large Sleeve Bearing"*. Jrnl. Lub. Tech. Trans ASME. Vol. 93, No. 1, Page 43, 1971.
23. D W Parkins. *"Measured Characteristics of a Journal Bearing Oil Film"*. Jrnl. Lub. Tech. Trans ASME. Vol. 103 No. 1, Pages 120-125, 1981.
24. D E Bently and A Muszynska. *"The Dynamic Stiffness Characteristics of High Eccentricity Ratio Bearings and Seals by Perturbation Testing"*. Conference Publication Rotordynamic Instability Problems in High Performance Turbomachinery. Texas A and M University, 1984.
25. D E Bently and A Muszynska. *"Stability Evaluation of Rotor/Bearing System by Perturbation Tests"*. Nasa Conference Publication Rotor Dynamic Instability Problem in High Performance Turbomachinery. Texas A and M University 1982.
26. A Cameron. *"Principles of Lubrication"*. Published by Longmans Green and Co Ltd. First Edition, 1966.
27. Private Communication. GEC Power Division, Stafford.
28. F T Barwell. *"Bearing Systems - Principle and Practice"*. 1st Edition, Oxford University Press, 1979. ISBN 0 19 856319 1.

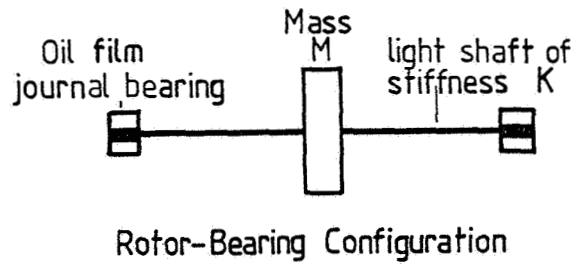


Figure 1

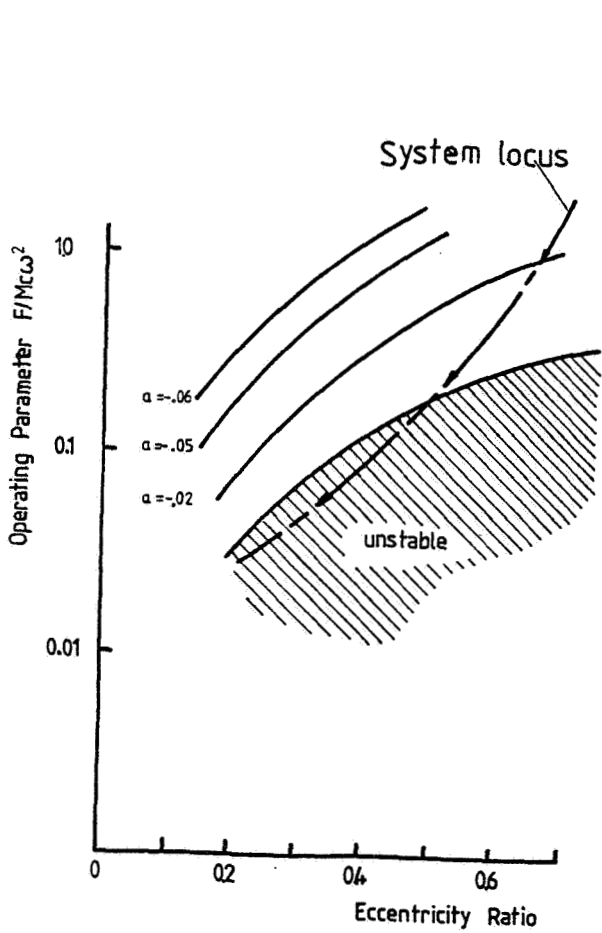


Figure 2

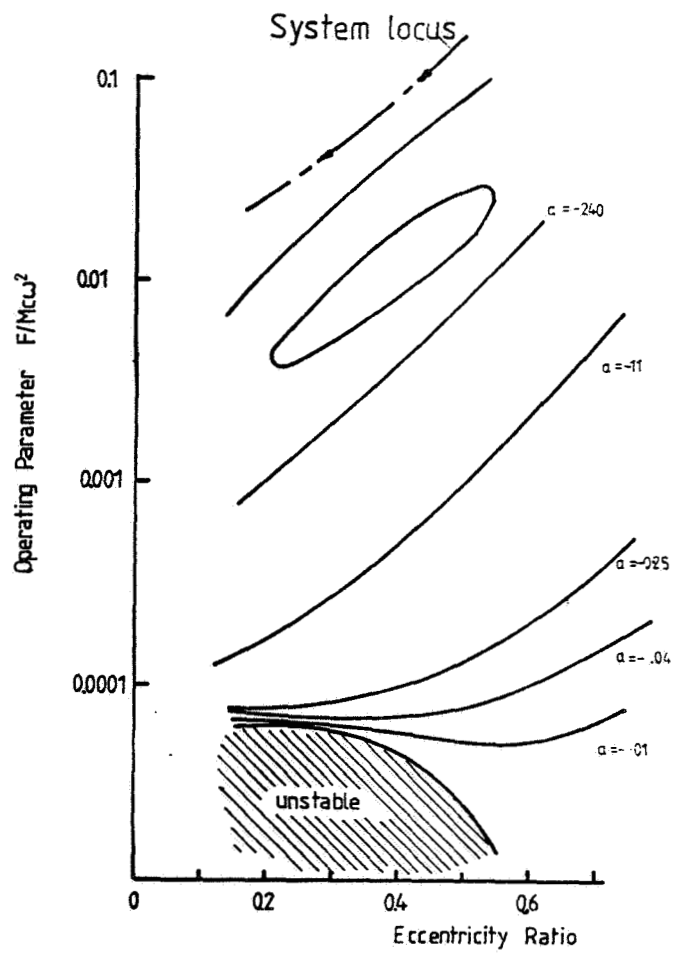
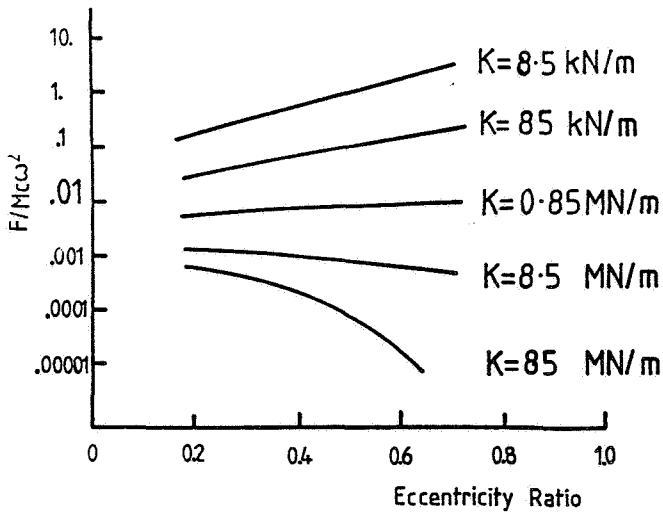
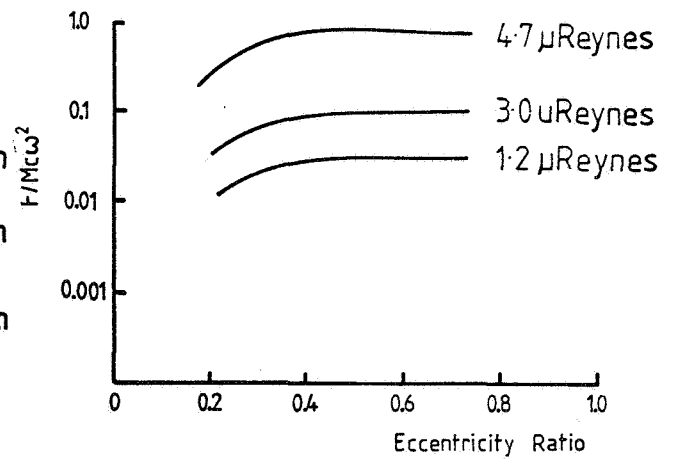


Figure 3



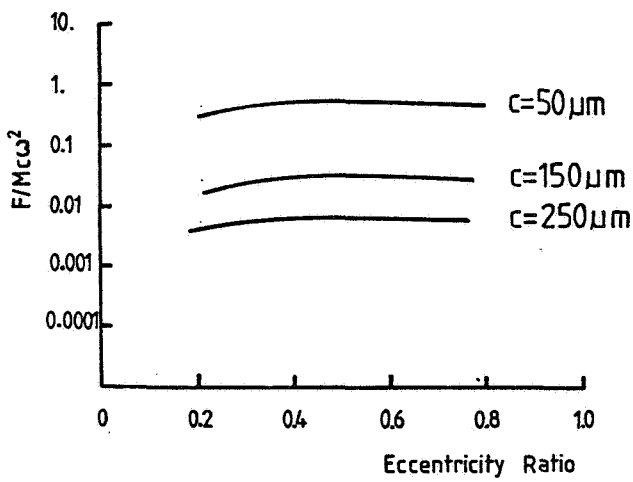
Variation of whirl onset boundary with shaft stiffness

Figure 4



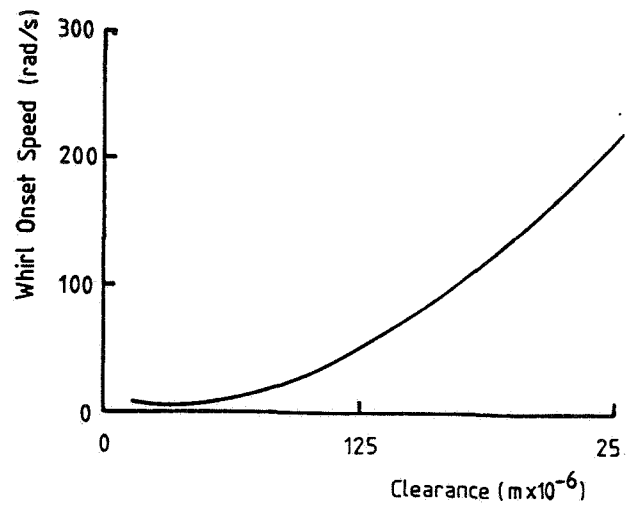
Variation of whirl onset boundary with lubricant viscosity

Figure 5



Variation of whirl onset boundary with radial clearance

Figure 6



Variation of whirl onset speed with clearance

Figure 7

BACKWARD WHIRL IN A SIMPLE ROTOR SUPPORTED ON HYDRODYNAMIC BEARINGS

R. Subbiah, R.B. Bhat, and T.S. Sankar
Concordia University
Montreal, Canada

J.S. Rao
Indian Embassy
Washington, D.C.

The asymmetric nature of the fluid film stiffness and damping properties in rotors supported on fluid film bearings causes a forward or a backward whirl depending on the bearing parameters and the speed of the rotor. A rotor was designed to exhibit backward synchronous whirl. The rotor-bearing system exhibited split criticals, and a backward whirl was observed between the split criticals. The orbital diagrams show the whirl pattern.

INTRODUCTION

The design of a rotor system must consider several aspects such as critical speeds, peak unbalance response, regions of change of whirl directions, and instability. In general, large rotor systems in continuous operation are supported on hydrodynamic bearings. These hydrodynamic bearings exhibit asymmetric cross-coupled stiffness and damping properties that vary with the speed of operation. Such a property influences the dynamic behavior of the rotors significantly.

The dynamic behavior of such rotors can be predicted by using transfer matrix methods, finite elements, modal analysis, etc. [1-6]. Rao [7] and Rao et al. [8] used a simple analytical technique to predict the dynamic behavior of such rotors. They studied a single-disk rotor on fluid film bearings and observed that for specific rotor-bearing parameter combinations the system may exhibit two distinct peaks in the response but sometimes it may show only one peak in the response. Kollmann and Glienicke [9] have shown experimentally the existence of the split criticals in a simple rotor supported on fluid film bearings. Kellenberger [10] derived equations for double frequency accelerations in turbogenerator rotors resulting from anisotropy in the plain cylindrical bearings and showed the occurrence of backward whirl between the criticals. These studies predict a forward whirl before the first critical and after the second critical, whereas the rotor executes a backward whirl between the two criticals. Also, the simple rotor with only a single peak in its response is known to whirl in the forward direction at all speeds.

Several experimental investigations are reported in the literature regarding the dynamic behavior of different types of rotor systems supported on hydrodynamic bearings. A few notable works are by Yamamoto [11], Hull [12], and Lund and Orcutt [13].

Most of the referred work on practical rotors supported on hydrodynamic bearings does not satisfy conditions for a clear backward whirl and hence the phenomenon of backward whirl has so far not been observed experimentally. The occurrence of backward whirl is also not desirable in practice. In the present work conditions are derived for backward whirl considering bearing damping. Further results of the

experiments carried out on a laboratory rotor model designed so as to exhibit backward whirl are reported.

NOMENCLATURE

a	disk eccentricity
c	shaft damping
$c_{zz}, c_{yy}, c_{yz}, c_{zy}$	fluid film damping coefficients
E_1, \bar{E}_1	forward and backward component, respectively, of i^{th} modal force vector
F	overall exciting force vector
K	overall stiffness matrix
k	shaft stiffness
$k_{zz}, k_{yy}, k_{yz}, k_{zy}$	fluid film stiffness coefficients
M	overall mass matrix
N_1, \bar{N}_1	forward and backward component of i^{th} modal displacement vector
q	displacement vector at disk location
q_1	displacement vector at bearing location
r	maximum unbalance response of rotor
z, y	displacement of rotor at disk location in Z and Y directions
z_0, y_0	displacement of rotor at bearing location in Z and Y directions
η_1	i^{th} modal displacement vector
λ_1	i^{th} complex eigenvalue
ϕ	right eigenvector of system
ϕ^*	left eigenvector of system

ANALYSIS

A schematic of the rotor is shown in Fig. 1. Equations of motion of the rotor are

$$m \frac{d^2}{dt^2} (z + a \cos \omega t) + k(z - z_0) + c(\dot{z} - \dot{z}_0) = 0 \quad (1a)$$

$$m\dot{z} - m\dot{z}_0 = 0 \quad (1b)$$

$$m\ddot{y} - m\dot{y} = 0 \quad (1c)$$

$$m \frac{d^2}{dt^2} (y + a \sin \omega t) + k(y - y_0) + c(\dot{y} - \dot{y}_0) = 0 \quad (2)$$

and the constraint equations are

$$k(z - z_0) + c(\dot{z} - \dot{z}_0) = 2k_{zz} \cdot z_0 + 2c_{zz} \cdot \dot{z}_0 + 2k_{zy} \cdot y_0 + 2c_{zy} \cdot \dot{y}_0 \quad (3)$$

$$k(y - y_0) + c(\dot{y} - \dot{y}_0) = 2k_{yy} \cdot y_0 + 2c_{yy} \cdot \dot{y}_0 + 2k_{yz} \cdot z_0 + 2c_{yz} \cdot \dot{z}_0 \quad (4)$$

Equations (1) to (4) can be written in the form

$$[M] \{\dot{Q}\} + [K] \{Q\} = \{F\} \quad (5)$$

where

$$[M] = \begin{bmatrix} \ddot{z} & \ddot{y} & \dot{z} & \dot{y} & \dot{z}_0 & \dot{y}_0 \\ 0 & 0 & m & 0 & 0 & 0 \\ 0 & 0 & 0 & m & 0 & 0 \\ m & 0 & c & 0 & -c & 0 \\ 0 & m & 0 & c & 0 & -c \\ 0 & 0 & c & 0 & -(c+2c_{zz}) & -2c_{zy} \\ 0 & 0 & 0 & c & -2c_{yz} & -(c+2c_{yy}) \end{bmatrix}$$

$$[K] = \begin{bmatrix} \dot{z} & \dot{y} & z & y & z_0 & y_0 \\ -m & 0 & 0 & 0 & 0 & 0 \\ 0 & -m & 0 & 0 & 0 & 0 \\ 0 & 0 & k & 0 & -k & 0 \\ 0 & 0 & 0 & k & 0 & -k \\ 0 & 0 & k & 0 & -(k+2k_{zz}) & -2k_{zy} \\ 0 & 0 & 0 & k & -2k_{yz} & -(k+2k_{yy}) \end{bmatrix}$$

$$\{Q\} = [\dot{z}, \dot{y}, z, y, z_0, y_0]^T$$

$$\{F\} = [0, 0, m\omega^2 \cos \omega t, m\omega^2 \sin \omega t, 0, 0]$$

The eigenvalues and eigenvectors of the system are obtained by solving the homogeneous form of equations (6) as shown below:

$$[M] \{\dot{Q}(t)\} + [K] \{Q(t)\} = 0 \quad (6)$$

Assuming a solution of the form

$$\{Q(t)\} = \{\varphi\} \exp(\lambda t) \quad (7)$$

where $\{\varphi\}$ represent the system eigenvectors, and substituting equation (7) in equation (8) the eigenvalue problem becomes

$$\lambda[M]\{\varphi\} + [K]\{\varphi\} = 0 \quad (8)$$

Because of the presence of asymmetric cross-coupled stiffness and damping coefficients in the bearings, the matrices $[M]$ and $[K]$ are nonsymmetric, resulting in a non-self-adjoint system. Hence a conventional normal-mode method is not possible, and it is essential to consider that the biorthogonality property of the modes of the original system are those of the transposed system to the uncoupled equations of motion. The left eigenvectors are obtained by transposing matrices $[M]$ and $[K]$ in equation (6). The eigenvalues of the original and transposed systems are identical, but the eigenvectors are different.

The solution of equation (5) is assumed in the form

$$\{Q(t)\} = [\varphi]\{\eta(t)\} \quad (9)$$

where $[\varphi]$ contains the eigenvectors of the original system (which are called right eigenvectors). Introducing equation (9) in equation (5) and premultiplying the result by $[\varphi^*]^T$, which is the left eigenvector of the system, lead to the following uncoupled equations:

$$[\mu]\{\dot{\eta}(t)\} + [\kappa]\{\eta(t)\} = \{\sigma\} \quad (10)$$

where

$$[\mu] = [\varphi^*]^T [M] [\varphi]$$

$$[\kappa] = [\varphi^*]^T [K] [\varphi]$$

and

$$\{\sigma\} = [\varphi^*]^T \{F\}$$

Equation (10) results in uncoupled equation of the form

$$\mu_1 \dot{\eta}_1(t) + \kappa_1 \eta_1(t) = \sigma_1(t) \quad (11)$$

This is solved by assuming steady-state solution of the form

$$\eta_1(t) = N_1 \exp(j\omega t) + \bar{N}_1 \exp(-j\omega t) \quad (12)$$

and

$$\sigma_1(t) = E_1 \exp(j\omega t) + \bar{E}_1 \exp(-j\omega t)$$

Substituting equation (12) in equation (11) results in

$$(\kappa_1 + j\omega\mu_1) N_1 \exp(j\omega t) + (\kappa_1 - j\omega\mu_1) \bar{N}_1 \exp(-j\omega t) = E_1 \exp(j\omega t) + \bar{E}_1 \exp(-j\omega t) \quad (13)$$

Equating the coefficients of the forward and backward rotation terms, we obtain

$$N_1 = \frac{E_1}{\kappa_1 + j\omega\mu_1} \quad (14)$$

$$\bar{N}_1 = \frac{\bar{E}_1}{\kappa_1 - j\omega\mu_1}$$

Hence the displacements are determined from equations (10) to (14) and then the unbalance response of the rotor is obtained nondimensionally as

$$r = \frac{z + jy}{a} \quad (15)$$

where a is the disk eccentricity. The complex eigenvalues are obtained from equation (6).

Depending on the bearing parameters the rotor will have either split criticals or just a single peak in the fundamental critical speed region, corresponding to synchronous whirl. In the case of the split criticals in the synchronous whirl, the backward component \bar{N}_1 is larger than the forward component N_1 between the split criticals.

EXPERIMENTAL RESULTS

The details of the test rotor are given in table 1. It consists of a circular shaft with a circular disc at the center and supported on two identical hydrodynamic bearings at the ends. These bearings are mounted on cast iron pedestals at the two ends, and in turn these pedestals are rigidly fastened to the support, which is made of steel angles. The pedestals were impact excited both in the horizontal and vertical directions, and the resulting acoustical response was measured close to the pedestals. A frequency analysis of the measured sound showed that the first peak occurred at a much higher frequency than the critical speeds of the rotor, indicating that the pedestals were rigid. The bearings are supplied with oil through a gravity feed. The unbalance response of the shaft is measured in both the x and y directions by two proximity pickups. The signals from the pickups are fed to a twin-channel FFT analyzer, and the orbit diagrams are obtained with a x - y plotter. The direction of plotter pen motion indicated the direction of rotor whirl.

In designing the rotor such that it exhibits a backward whirl, the bearing coefficients to be used in equations (3) and (4) were taken from the results of Lund [14]. These results can also be found in [15]. Lund's results agree well with the experimentally determined bearing coefficients by Glienicke [9].

The whirl orbits obtained experimentally are shown normalized with respect to the disc eccentricity in Figs. 2 to 4 for different rotor speeds. Orbital diagrams are shown for a bearing clearance of 1.8796×10^{-4} m, since a backward whirl could be identified only for this case. The two critical speeds are 2200 and 2600 rpm. The rotation of the rotor is in the counterclockwise direction and hence Figs. 2 and 4 show forward whirls and Fig. 3 shows backward whirl. The speed corresponding to the backward whirl in Fig. 3 is 2500 rpm, which falls between the two criticals at 2200 and 2600 rpm. Since the backward whirl between the criticals is of interest, a photograph of backward whirl motion of the rotor at 2500 rpm was taken from the FFT analyzer screen. Theory also predicts these whirl directions, and hence there is a qualitative agreement between theory and experiments.

REFERENCES

1. Lund, J.W., 1965, Mechanical Technology Inc., Latham, N.Y., U.S.A., AFAPL-Tr-65-45, "Rotor Bearing Dynamics Design Technology, Part V: Computer Program Manual for Rotor Response and Stability".
2. Kramer, E., 1977, ASME Publication 77-DET-13, "Computation of Unbalance Vibrations of Turborotors".
3. Nelson, H.D. and McVaugh, J.N., 1976, Journal of Engineering for Industry, ASME, Vol. 98, p. 593, "The Dynamics of Rotor Bearing Systems Using Finite Elements".
4. Lalanne, M. and Queau, J.P., 1979, Societe Nationale des Industries Aeronautiques, "Calcul par Elements Finis du Comportement Dynamique des Chaines Cinematiques de Reducteur".
5. Morton, P.G., 1967-68, Proc. Inst. Mech. Engrs., Vol. 182, Part 1, No. 13, "Influence of Coupled Asymmetric Bearings on the Motion of a Massive Flexible Rotor".
6. Gunter, E., Choy, K.C. and Allaire, P.E., "Modal Analysis of Turborotors using Planar Modes - Theory", Journal of the Franklin Institute, Vol. 305, No. 4, April 1978.
7. Rao, J.S., 1982, Mechanism and Machine Theory Journal, Vol. 17, No. 2, "Conditions for Backward Synchronous Whirl of a Flexible Rotor in Hydrodynamic Bearings".
8. Rao, J.S., Bhat, R.B. and Sankar, T.S., 1980-81, Transactions of the Canadian Society of Mechanical Engineers, Vol. 6, No. 3, pp. 155-161, "A Theoretical Study of the Effect of Damping on the Synchronous Whirl of a Rotor in Hydro-Dynamic Bearings".
9. Kollmann, K. and Glienicke, J., JSME, 1967, Semi-International Symposium 4th-8th Sept. 1967, Tokyo, "The behaviour of turbine bearings with respect to instability prediction".
10. Kellenberger, W., Proceedings of the Institution of Mechanical Engineers (London), 1980, Paper No. C312/80, P.415-520, "Double frequency

accelerations in turbogenerator rotors resulting from anisotropy in the bearings".

11. Yamamoto, 1954, Memoirs of the Faculty of Engineering, Nagoya University Vol. 6, No. 2, p. 755, "On the Critical Speeds of a Shaft".
12. Hull, E.H., 1961, Journal of Engineering for Industry, Vol. 83, p. 219, "Shaft Whirling as Influenced by Stiffness Asymmetry".
13. Lund J.W. and Orcutt, F.K., 1967, Transactions of ASME, Journal of Engineering for Industry, Vol. 89, No. 4, "Calculations and Experiments on the Unbalance Response of a Flexible Rotor".
14. Lund, J.W., 1965, Mechanical Technology, Inc., AFAPL-Tr-65-45, "Rotor Bearings Dynamic Design Technology, Part III: Design Handbook for Fluid Bearings".
15. Rao, J.S., 1983, Wiley Eastern Limited, New Delhi, Rotor Dynamics.

TABLE 1: DETAILS OF TEST ROTOR

Shaft Diameter	0.0222 m
Shaft Length	0.5080 m
Weight of Disk	89 N
Shaft Stiffness	8.9×10^5 N/m
Bearing Diameter	0.0254 m
Bearing L/D Ratio	1
Oil Viscosity at 25.5°C	0.96×10^{-5} Pascal sec.
Unbalance of Rotor	1.084×10^{-4} kg.m
Bearing Clearance	1.8796×10^{-4} m (0.0074 in)

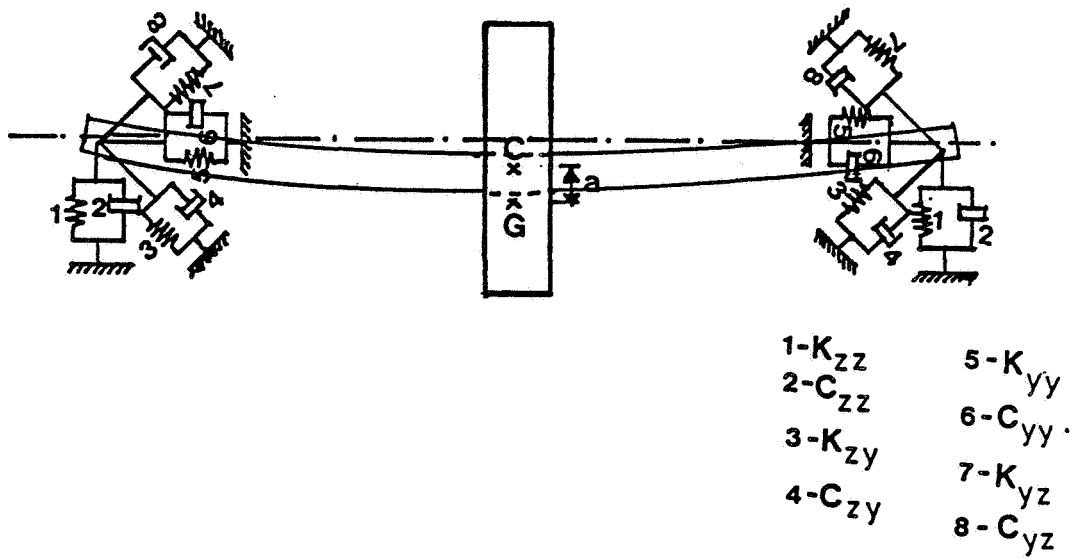


Figure 1. - Schematic diagram of single mass rotor.

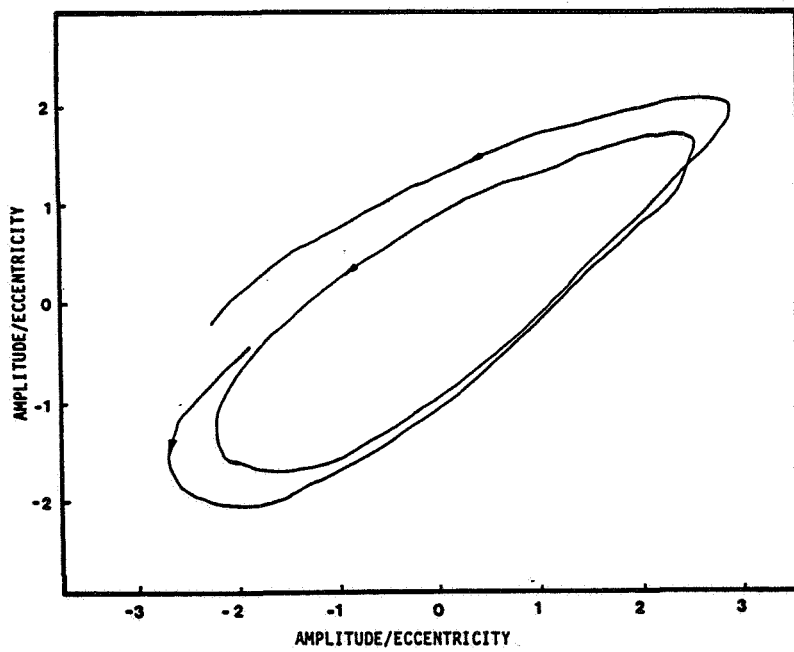


Figure 2. - Rotor whirl orbit at 2150 rpm (counterclockwise direction corresponds to forward whirl).

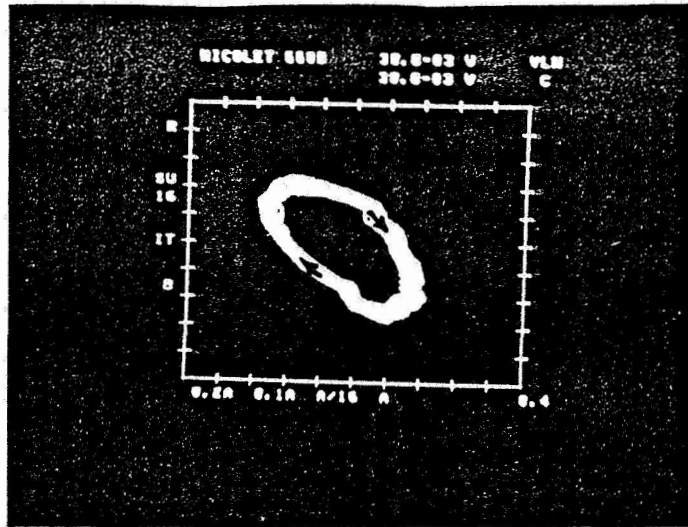


Figure 3. - Rotor whirl orbit at 2500 rpm (clockwise direction corresponds to backward whirl).

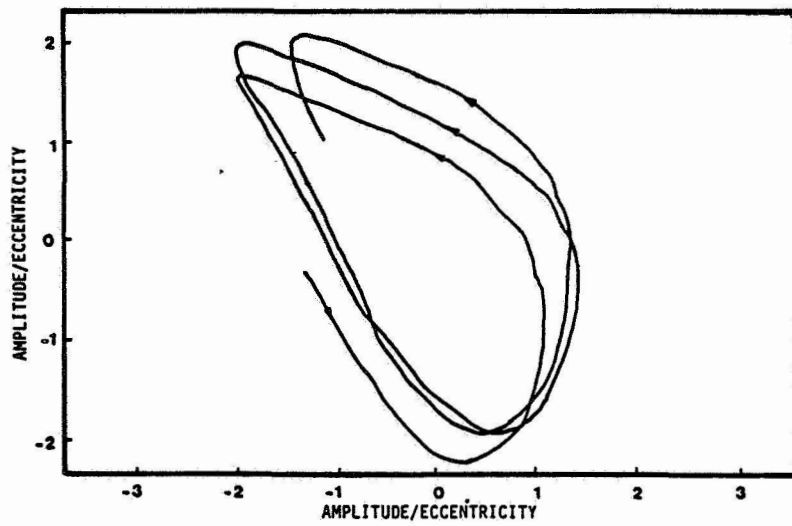


Figure 4. - Rotor whirl orbit at 3000 rpm (counterclockwise direction corresponds to forward whirl).

WHIRL AND WHIP - ROTOR/BEARING STABILITY PROBLEMS

Agnes Muszynska
Bently Rotor Dynamics Research Corporation
Minden, Nevada 89423

A mathematical model of a symmetric rotor supported by one rigid and one fluid lubricated bearing is proposed in this paper. The rotor model is represented by generalized (modal) parameters of its first bending mode. The rotational character of the bearing fluid force is taken into account. The model yields synchronous vibrations due to rotor unbalance as a particular solution of the equations of motion, rotor/bearing system natural frequencies and corresponding self-excited vibrations known as "oil whirl" and "oil whip." The stability analysis yields rotative speed threshold of stability. The model also gives the evaluation of stability of the rotor synchronous vibrations. In the first balance resonance speed region two more thresholds of stability are yielded. The width of this stability region is directly related to the amount of rotor unbalance.

The results of the analysis based on this model stand with very good agreement with field observations of rotor dynamic behavior and the experimental results.

1. INTRODUCTION

Dynamic phenomena induced by interaction between the rotor and bearing or seal fluid motion and creating severe rotor vibrations have been recognized for over 50 years. High amplitude shaft vibrations which can sustain over a wide range of rotational speeds not only perturb the normal operation of a rotating machine, but may also cause serious damage to the machine and the entire plant.

Literature related to rotor/bearing and rotor/seal phenomena is very rich [1-7]. Availability of computers and fast development of numerical methods are bringing more and more results based on analytical models of the solid/fluid interaction phenomena.

There is still, however, a big gap between theory and practice.

Practical rotating machinery instability problems in the field are being corrected ad hoc by applying trial and error approach with a number of measures such as increasing rotor radial load, modifying lubricant temperature and/or pressure, shortening and stiffening the shaft, or replacing bearings or seals with "more stable" ones. However, the only measure which corrects the causative agent is the recently introduced anti-swirling technique.

Researchers and engineers do not always agree upon the physical description of the shaft/bearing or shaft/seal solid/fluid interaction dynamic phenomena. The complex-

ity of these phenomena and the long list of factors affecting them make the picture tremendously obscure.

Most often bearing and/or seal fluid forces generated during rotating machine operation are considered separately from the shaft motion, assuming only that the shaft rotates with constant angular velocity and has a perfect geometry.

Practically observed phenomena indicate that this approach can be justified only for specific conditions, in particular, for low values of shaft rotative speed. In most other cases, rotor and bearings (or rotor/bearings/seals) should be considered as a system. The dynamic behavior of this system will then reflect the rotor/bearing coupled system features.

In this paper, an attempt to build a simple rotor/bearing system model is made. The simplicity allows for obtaining analytical solutions and yields clear conclusions on how various parameters of the rotor/bearing system affect its dynamic behavior. The model is based on modal behavior of the rotor. The model of bearing fluid dynamic forces is developed through a classical approach applied to nonconservative mechanical systems [8].

The model yields results which are in perfect agreement with the observed dynamic phenomena of the rotor/bearing system.

2. OBSERVED VIBRATIONAL PHENOMENA

Lightly loaded and slightly unbalanced symmetrical rotors rotating in fluid 360° lubricated cylindrical bearings, exhibit the following dynamic phenomena:

(i) When the shaft starts rotating with a slowly increasing rotative speed, SYNCHRONOUS (1x) lateral vibrations with minor amplitudes are observed all along the rotor axis. These vibrations are caused by the inertia forces of unbalance of the rotor. At low rotative speeds, these vibrations are stable, an impulse perturbation of the rotor causes a short time transient vibration process, and the same vibration pattern is reestablished (Fig. 1).

(ii) At higher rotational speeds (usually below the first balance resonance), the forced synchronous vibration is not the only regime of vibration. Along with 1x vibrations, OIL WHIRL appears. Oil whirl is the rotor lateral forward precessional subharmonic vibration around the bearing center at a frequency close to half the rotative speed. In this range of the rotative speed, the rotor behaves as a rigid body. The amplitudes of oil whirl are usually much higher than those of synchronous vibrations; they are, however, limited by the bearing clearance and the fluid non-linear forces. With increasing rotative speed, the pattern of vibration remains stable. The oil whirl "half" frequency follows the increasing rotative speed, maintaining the $\approx 1/2$ ratio with it. The vibration amplitudes remain nearly constant and usually high. At the bearing, the vibration amplitude may cover nearly all bearing clearance. In the considered range of rotative speed, the bearing fluid dynamic effects clearly dominate. The forced synchronous vibration represents a small fraction of vibration response, as the spectrum indicates (Fig. 1).

(iii) When the increasing rotative speed approaches the first balance resonance, i.e., the first natural frequency of the rotor, oil whirl suddenly becomes unstable and disappears, being suppressed and replaced by increasing SYNCHRONOUS vibrations. The forced vibrations dominate, reaching the highest amplitudes at resonant frequency corresponding to the mass/stiffness/damping properties of the rotor. The bearing fluid dynamic effects now yield priority to the elastic rotor mechanical effects.

(iv) Above the first balance resonance speed, the synchronous forced vibrations decay. Again, the bearing-fluid forces come back into action. With increasing rotative speed, shortly after the first balance resonance, OIL WHIRL occurs again. The previously described pattern repeats. The width of the rotative speed region in which the synchronous vibration dominate depends directly on the amount of rotor unbalance: higher unbalance, wider is this region.

(v) When the rotative speed approaches double the value of the rotor first balance resonance, the half-speed oil whirl frequency reaches the value of the first balance resonance -- the first natural frequency of the rotor. The oil whirl pattern is replaced by OIL WHIP -- a lateral forward precessional subharmonic vibration of the rotor. Oil whip has a constant frequency: independently of the rotative speed increase, the oil whip frequency remains close to the first natural frequency of the rotor. In this range of high rotative speed, the shaft cannot be considered rigid. Its flexibility, i.e., additional degrees of freedom, causes that rotor/bearing system is closely coupled. The rotor parameters (its mass and stiffness, in particular) become the dominant dynamic factors. The amplitude of oil-whip journal vibration is limited by the bearing clearance, but the shaft vibration may become very high, as the shaft vibrates at its natural frequency, i.e., in the resonant conditions.

In various machines furnished with fluid lubricated bearings and/or seals, the above-described phenomena may take various forms, as other external factors may affect the system dynamic behavior. Generally, however, similar patterns can be expected [9].

Among the described dynamic phenomena, there is a clear distinction related to their nature: (a) rotor synchronous lateral vibration (1x) due to unbalance and (b) rotor fluid-related vibration. The first type is typically forced vibration. The rotating periodic inertia force considered "external" to rotor lateral motion causes the rotor response with the same frequency. The resulting motion has the form of the classical synchronous (1x) excited vibration.

As there is no other external force to excite the vibrations, it is quite reasonable to refer to the second type of vibration, as SELF-EXCITED vibrations, occurring due to an internal feedback mechanism transferring the rotative energy into vibrations. Self-excited vibrations cannot occur in a conservative or "passive" structure, with no energy supply (in nonrotating systems in particular). In passive structures, the free vibrations following an external perturbing impulse usually have a decaying character, due to the stabilizing effect of damping, naturally existing in the system. Another situation takes place if the system is subject to a constant supply of energy (an "active", nonconservative structure). Well recognized are wind induced vibrations known as flutter. The rotating machine belongs also to this category. The internal energy transfer mechanism, in this case a bearing fluid involvement in motion, uses a part of the rotative energy to create forces, having the direction opposite to the damping force. The result consists of reduction, then with their

increasing value, a nullification of effective damping, the stabilizing factor. In such conditions, free vibrations do not have the decaying character anymore (effect of negative damping). While vibration amplitude increases, nonlinear factors become significant and eventually amplitudes are limited. Vibrations become periodic with a constant amplitude. The stable limit cycle is reached. This represents the practically observed case of the oil whirl and oil whip. As the oil whirl and oil whip occur in the system having a constant energy supply, the resulting vibration is referred to as self-excited. The last term is also closely related to the nonlinear character of the phenomena. In particular, the size of the oil whirl/whip orbits (limit cycle vibration amplitudes) are determined exclusively by the nonlinear factors in the oil bearing.

Simple linear modelization of the rotor/bearing system can be applied as a first approximation in mathematical description of the observed phenomena. The linear model provides the spectrum of natural frequencies of the system, as these frequencies are very insensitive to nonlinear factors. The linear model also gives the evaluation of stability threshold, closely related to the delicate balance between the system's natural damping and the bearing fluid forces acting in antiphase and opposing damping.

Very often oil whirl and oil whip are described as "unstable" rotor motion in a sense which is rather close to the terms "undesirable" or "unacceptable" rotor vibrations. Obviously, oil whirl/whip vibrations are highly undesirable; they disturb the machine's normal operation. The "normal operation" is related to the pure rotational motion of the rotor, around the proper axis and following a suitable angular speed. This is the only regime of motion which is required. The occurrence of the oil whirl/whip vibrations signifies that this pure rotational regime becomes UNSTABLE*, and the oil whirl/whip vibrations represent a STABLE regime. The term "stability" is used here in the most popular sense (following Lyapunov's definition). The pure rotational motion (meaning zero lateral vibration) is unstable, oil whirl/whip lateral vibrations are stable. They exist, and any impulse perturbation cannot significantly modify their pattern. After a short-time transient process, the oil whirl/whip pattern is reestablished.

A practical stability definition for a rotating machine is discussed in [10].

3. FLUID FORCES

Derivation of fluid forces in a bearing (or a seal) is based on the consideration that the fluid rotation (dragged into motion by shaft rotation) plays an appreciable role in resulting dynamic phenomena and may, therefore, have a significant effect on rotor vibrations [8, 11, 12].

In the following presentation, an assessment of this effect is attempted in simplified terms. It is assumed that when the shaft is rotating centered, fully developed fluid flow is established in the circumferential direction, that is, on the average, the fluid is rotating at the rate $\lambda\omega_R$ where ω_R is the shaft rotative speed and λ is the fluid average swirling ratio which value is close to a half (Fig. 2). It is

* Actually, with existing residual imbalance, the rotor pure rotational motion of a rotor does not exist. The only regime is forced synchronous lateral vibration along with the rotation. "Stability" refers then to the stability of this regime.

supposed that shaft lateral vibrations are small enough to make modifications of this pattern negligible. The flow axial component is supposed to affect values of the fluid forces in the x,y plane in a parametric way only, i.e., the fluid circumferential force may proportionally increase with increasing axial flow. However, it is assumed that there is no feedback, i.e., the fluid axial motion is uncoupled from the circumferential motion (and not investigated in this paper). It is also assumed that the axial flow does not modify the average swirling ratio λ .

The vital assumption is that the fluid force which results from averaging the circumferential flow is rotating with angular velocity $\lambda\omega_R$. In rotating reference coordinates x_r, y_r (Fig. 2), the average fluid flow is purely rectilinear and the fluid force is as follows:

$$F = [K_0 + \psi_1(|z_r|)] z_r + [D + \psi_2(|z_r|)] \dot{z}_r + M_f \ddot{z}_r \quad (1)$$

where $z_r = x_r + jy_r$ $j = \sqrt{-1}$ $|z_r| = \sqrt{x_r^2 + y_r^2}$

In the equation (1) $K_0, D,$ and M_f are fluid stiffness, damping and inertia coefficients respectively. ψ_1 and ψ_2 are nonlinear functions of the radial displacement $|z_r|$. It is assumed that these functions have analytical character (or at least are continuous, with continuous first two derivatives). Later on, as an example, the following nonlinear functions will be analyzed (the first symmetric term of the Taylor series for any nonlinear analytical function):

$$\psi_{1,2} = B_{1,2} |z_r|^2, \quad (2)$$

where B_1 and B_2 are positive constants.

The average fluid force (1) has, therefore, nonlinear character. Stiffness and damping components of the fluid force increase with increasing journal eccentricity.

In fixed reference coordinates x,y (Fig. 2), the fluid force will have the following form:

$$F = [K_0 + \psi_1(|z|)] z + [D + \psi_2(|z|)] (\dot{z} - j\lambda\omega_R z) + M_f (\ddot{z} - 2j\lambda\omega_R \dot{z} - \lambda^2\omega_R^2 z) \quad (3)$$

where $z = x + jy$, $|z| = \sqrt{x^2 + y^2}$. The equation $z = z_r e^{j\lambda\omega_R t}$ represents transformation of coordinates.

The fluid force (3) can be presented in a classical "bearing coefficient" format:

$$\begin{bmatrix} F_x \\ F_y \end{bmatrix} = \begin{bmatrix} M_f & 0 \\ 0 & M_f \end{bmatrix} \begin{bmatrix} \ddot{x} \\ \ddot{y} \end{bmatrix} + \begin{bmatrix} D & 2\lambda\omega_R M_f \\ -2\lambda\omega_R M_f & D \end{bmatrix} \begin{bmatrix} \dot{x} \\ \dot{y} \end{bmatrix} + \begin{bmatrix} K_0 - \lambda^2\omega_R^2 M_f & \lambda\omega_R D \\ -\lambda\omega_R D & K_0 - \lambda^2\omega_R^2 M_f \end{bmatrix} \begin{bmatrix} x \\ y \end{bmatrix} + \begin{bmatrix} \psi_2(|z|) & 0 \\ 0 & \psi_2(|z|) \end{bmatrix} \begin{bmatrix} \dot{x} \\ \dot{y} \end{bmatrix} + \begin{bmatrix} \psi_1(|z|) & \lambda\omega_R \psi_2(|z|) \\ -\lambda\omega_R \psi_2(|z|) & \psi_1(|z|) \end{bmatrix} \begin{bmatrix} x \\ y \end{bmatrix}$$

The last two matrices contain nonlinear components of the fluid force. As it is easily noticed, the fluid force is supposed to have a symmetric character: the diagonal terms are identical, the off-diagonal terms are skew symmetric. More important, however, is the fact that the off-diagonal terms are generated as the result

of rotational character of the fluid force: the tangential (or "cross") damping is the result of Coriolis inertia force, the tangential (or "cross") stiffness is generated by the relative velocity and radial damping. In addition, the radial stiffness K_0 appearing at the main diagonal of the stiffness matrix is now modified by the centripetal fluid inertia force which appears with the negative sign.

During experimental testing by applying perturbation method [13], the character of the fluid force expressed by the equation (3) was fully confirmed. For relatively large clearance-to-radius ratio, the fluid inertia force become significant, and modifies "damping" and "stiffness" matrices considerably. The resultive radial stiffness can very easily reach negative values.

Another important conclusion relates to the "cross stiffness" coefficient, the most important component affecting rotor stability. This term is directly generated by the linear radial damping D , as the result of rotating character of the damping force. This term is proportional to the rotative speed ω_R , i.e., its significance increases with rotative speed. An immediate conclusion is that an increase of the bearing damping D will not help to prevent rotor instability as the "cross stiffness" increases proportionally to D . The only help in decreasing the "cross stiffness" term is a modification of the average swirling ratio λ . This feature is now being widely used in "anti-swirling" devices [14, 15].

4. MATHEMATICAL MODEL OF A SYMMETRIC FLEXIBLE SHAFT ROTATING IN ONE RIGID ANTI-FRICTION BEARING AND ONE OIL 360° LUBRICATED CYLINDRICAL BEARING

Oil whirl and oil whip phenomena are characterized by low frequency, that is why it seems reasonable to limit the rotor model to its lowest bending mode. It is obvious that the considerations presented below can be applied to more complex rotor model (including more modes, gyroscopic effect, internal damping, etc.) as well.

The mathematical model representing balance of forces in the symmetric rotor shown in Fig. 3 is as follows:

$$M_1 \ddot{z}_1 + D_s \dot{z}_1 + (K_1 + K_2)z_1 - K_2 z_2 = mr\omega_R^2 e^{j\omega_R t} \quad (4)$$

$$M_2 \ddot{z}_2 + M_f(\ddot{z}_2 - 2j\lambda\omega_R \dot{z}_2 - \lambda^2\omega_R^2 z_2) + [D + \psi_2(|z_2|)](\dot{z}_2 - j\lambda\omega_R z_2) + [K_0 + \psi_1(|z_2|)]z_2 + \quad (5)$$

$$+ K_3 z_2 + K_2(z_2 - z_1) = 0 \quad , \quad z_1 = x_1 + jy_1 \quad , \quad z_2 = x_2 + jy_2$$

where M_1 , M_2 are rotor generalized (modal) masses, D is external generalized (viscous) damping coefficient, K_1 , K_2 , and K_3 are shaft generalized (modal) stiffness coefficients (K_3 may also include an external spring stiffness), m and r are mass and radius of modal unbalance respectively. The bearing fluid dynamic force is introduced to the equation (5) in the form (3).

The equation (4) presents the classical relationship for an unbalanced symmetric rotor at its first bending mode. Any classical method of modal reduction can be applied to obtain the rotor generalized (modal) coefficients. The equation (5) describes balance of forces, including nonlinear fluid force, acting at the journal. Radial forces (such as gravity) are balanced by external spring forces and are not included in the model (4), (5).

5. SYNCHRONOUS SOLUTION: 1× ROTOR FORCED VIBRATIONS DUE TO UNBALANCE

In this section, the particular solution of equations (4) and (5) will be discussed. This solution describes rotor synchronous vibrations due to unbalance force and has the following form:

$$z_1 = A_1 e^{j(\omega_R t + \alpha_1)} \quad , \quad z_2 = A_2 e^{j(\omega_R t + \alpha_2)} \quad (6)$$

where the amplitudes A_1 , A_2 and phase angles α_1 , α_2 can be found from the following algebraic equations resulting from (4), (5) and (6):

$$(K_1 + K_2 + D_s j \omega_R - M \omega_R^2) A_1 e^{j\alpha_1} - K_2 A_2 e^{j\alpha_2} = m r \omega_R^2 \quad (7)$$

$$\{K_0 + K_2 + K_3 + \psi_1(A_2) + j[D + \psi_2(A_2)] \omega_R (1 - \lambda) - M_2 \omega_R^2 - M_f \omega_R^2 (1 - \lambda)^2\} A_2 e^{j\alpha_2} - K_2 A_1 e^{j\alpha_1} = 0$$

Note that the fluid inertia and radial damping carry coefficients $1 - \lambda$, which value is usually slightly higher than 1/2. This signifies that the effective damping is two times and the fluid inertia effect on synchronous vibrations four times, smaller than their actual values.

The equations (7) can be solved for any given nonlinear functions ψ_1 , and ψ_2 , as their arguments now become equal to A_2 , the journal amplitude of synchronous vibrations. When the nonlinear forces are neglected ($\psi_1 = \psi_2 = 0$) the equations (7) yield simple expressions for the amplitudes and phase angles:

$$A_1 = \frac{m r \omega_R^2}{\sqrt{h_4^2 + D_s^2 \omega_R^2}} \sqrt{1 + \left(\frac{K_2 A_2}{m r \omega_R^2}\right)^2 + 2 \frac{K_2 A_2 \cos \alpha_2}{m r \omega_R^2}} \quad , \quad A_2 = \frac{K_2 m r \omega_R^2}{\sqrt{h_2^2 + h_3^2}} \quad (8)$$

$$\alpha_1 = \arctan(-D_s \omega_R / h_4) + \arctan \frac{\tan \alpha_2}{1 + m r \omega_R^2 / (K_2 A_2 \cos \alpha_2)} \quad , \quad \alpha_2 = \arctan(-h_3 / h_2) \quad (9)$$

or, further

$$A_1 = \frac{m r \omega_R^2}{\sqrt{h_4^2 + D_s^2 \omega_R^2}} \sqrt{(h_2 + K_2^2)^2 + h_3^2} \quad , \quad \alpha_1 = \arctan(-D_s \omega_R / h_4) + \arctan [K_2^2 h_3 / (h_2^2 + h_3^2 + K_2 h_2)] \quad (10)$$

$$\text{where} \quad h_2 = h_4 h_5 - D D_s \omega_R^2 (1 - \lambda) - K_2^2 \quad , \quad h_3 = [h_5 D_s + D h_4 (1 - \lambda)] \omega_R \quad (11)$$

$$h_4 = K_1 + K_2 - M \omega_R^2 \quad , \quad h_5 = K_0 + K_2 + K_3 - \omega_R^2 [M_2 + M_f (1 - \lambda)^2] \quad (12)$$

When the nonlinear forces are given in the form (2), then the amplitude A_2 can be found as the solution of the following polynomial equation:

$$A_2^6 (h_6^2 + h_7^2) + 2 A_2^4 (h_2 h_6 + h_3 h_7) + A_2^2 (h_2^2 + h_3^2) - (K_2 m r \omega_R^2)^2 = 0 \quad (13)$$

$$\text{where} \quad h_6 = B_1 h_4 - \omega_R^2 B_2 (1 - \lambda) \quad , \quad h_7 = \omega_R [B_2 (1 - \lambda) h_4 + B_1 D_s] \quad (14)$$

The phase α_2 in this case is slightly modified by the nonlinear force:

$$\alpha_2 = \arctan \frac{A_2^2 \omega_R [D_s B_1 + (1 - \lambda) h_4 B_2] + h_3}{A_2^2 [\omega_R^2 (1 - \lambda) D_s B_2 - h_4 B_1] - h_2} \quad (15)$$

The amplitude A_1 , and phase α_1 are given by equations (8) and (9).

The equation (13) can be solved graphically (Fig. 4). The simple graphical method reveals important qualitative features of the nonlinear system. It is possible that three solutions for A_2 are yielded (Fig. 4a). This corresponds to the well known nonlinear case [16]. More probable, however, is that only one solution exists. The nonlinear force causes a reduction of the vibration amplitude A_2 . Figure 5 gives some numerical examples of Bodé plots for the rotor synchronous response. An insensitivity of the response to fluid inertia and journal generalized (modal) mass is noted.

6. STABILITY OF THE PURE ROTATIONAL MOTION OF THE SHAFT

To investigate the stability of the pure rotational motion of the shaft, assume that the unbalance force is equal to zero. For the stability analysis, the nonlinear terms in the equation (5) are neglected, as they are small of the second order. Stability of the pure rotational motion of the shaft means stability of the zero solution of the equations (4) and (5) for $m_r=0$, perturbed by small lateral deflections. The eigenvalue problem with the solution for linearized equations (4), (5) of the form

$$z_1 = E_1 e^{st}, \quad z_2 = E_2 e^{st} \quad (16)$$

leads to the corresponding characteristic equation:

$$[M_2 s^2 + M_f (s - j\lambda\omega_R)^2 + D(s - j\lambda\omega_R) + K_0 + K_3](K_1 + K_2 + D_s s + M_1 s^2) + K_2(K_1 + D_s s + M_1 s^2) = 0 \quad (17)$$

where s is the system eigenvalue, and E_1, E_2 are constants of integration. The equation (17) can easily be solved numerically. An example is presented in Figure 6. The eigenvalues are given as functions of rotative speed ω_R .

After computing several examples, it has been noticed that the modal mass M_2 and the fluid inertia M_f , when not exceeding certain "critical" values, have very little effect on the eigenvalues. It has also been noticed that one of the eigenvalues has always the imaginary part proportional to the rotative speed ω_R , when the latter is low, and that it tends to the constant value corresponding to the rotor natural frequency $\sqrt{(K_1 + K_2)/M_1}$ when ω_R increases. The corresponding imaginary part of this eigenvalue crosses zero at a specific rotative speed. That is, after this specific speed, the pure rotational motion of the rotor becomes unstable.

These observations led to an important conclusion about the character of the system eigenvalues, and to approximate eigenvalue formulas.

The approximate values of three eigenvalues, i.e., three solutions of equation (17) are as follows (obtained from extensive parametric analysis of numerical solutions to eq. (17)):

$$s_1 \approx -\frac{K_0 + K_3}{D} - \frac{K_2(K_1 - M_1 \lambda^2 \omega_R^2)}{D(K_1 + K_2 - M_1 \lambda^2 \omega_R^2)} + j\lambda\omega_R \quad (18)$$

$$s_{2,3} \approx \pm j\sqrt{R_1 - jR_2} = (-\sqrt{-R_1 + \sqrt{R_1^2 + R_2^2}} \pm j\sqrt{R_1 + \sqrt{R_1^2 + R_2^2}}) / \sqrt{2} \quad (19)$$

$$\text{where } R_1 \approx \frac{K_1 + K_2}{M_1} - K_2^2(K_0 + K_3)/R_3, \quad R_2 \approx -K_2^2 D (\sqrt{\frac{K_1 + K_2}{M_1}} - \lambda \omega_R) / R_3$$

$$R_3 = \{ [K_0 + K_3 - M_2(K_1 + K_2)/M_1 - M_f(\sqrt{(K_1 + K_2)/M_1} - \lambda \omega_R)^2]^2 + D^2(\sqrt{\frac{K_1 + K_2}{M_1}} - \lambda \omega_R)^2 \} M_1$$

The formulas (18), (19) give approximate eigenvalues of the rotor/bearing model (4), (5). The imaginary parts of the eigenvalues (18) and (19) represent natural frequencies. The first natural frequency, $\text{Im}(s_1)$ is close to $\lambda \omega_R$. The second natural frequency, $\text{Im}(s_{2,3})$ is close to the shaft natural frequency $\pm \sqrt{(K_1 + K_2)/M_1}$. Stronger coupling (high K_2) causes more significant divergence from these "uncoupled" natural frequencies of the system.

The real part of the eigenvalue (18) predicts the threshold of stability: For

$$\omega_R \leq \frac{1}{\lambda} \sqrt{\frac{K_1}{M_1} + \frac{K_2(K_0 + K_3 - M_2 K_1/M_1)}{M_1 [K_2 + (K_0 + K_3 - M_2 K_1/M_1)]}} \equiv \omega_R^{(ST)} \quad (20)$$

the rotor pure rotative motion is stable. For $\omega_R > \omega_R^{(ST)}$ the pure rotational motion becomes unstable. The first term under the radical (20), mainly K_1/M_1 , is definitely dominant. The second term contains two stiffnesses in sequence, K_2 and $(K_0 + K_3 - M_2 K_1/M_1)$. Usually the stiffnesses K_0 and K_3 are small, mass M_2 is also small. Connection in sequence with K_2 (independently of value K_2) makes the total smaller than $K_0 + K_3 - M_2 K_1/M_1$. It is reasonable, therefore, to reduce the expression for the rotor/bearing system stability threshold to

$$\omega_R^{(ST)} \approx \frac{1}{\lambda} \sqrt{\frac{K_1}{M_1}} \quad (21)$$

For the unstable conditions the vibration amplitude increases exponentially in time and eventually bearing nonlinear forces become significant causing final limitation and stabilization of the vibration amplitude.

The experimental results entirely confirm this result. An increase of the stiffness K_1 (disk mounted on the shaft moved toward the rigid antifriction bearing) causes a significant increase of the system threshold of stability [17].

7. STABILITY OF THE SYNCHRONOUS SOLUTION

The stability of the synchronous vibrations (6) will be analyzed by applying the classical perturbation method [16]. Introducing the variational real variables $w_1(t)$, $w_2(t)$ (amplitude perturbation) according to the relation

$$z_1 = [A_1 + w_1(t)] e^{j(\omega_R t + \alpha_1)}, \quad z_2 = [A_2 + w_2(t)] e^{j(\omega_R t + \alpha_2)} \quad (22)$$

the linearized variational equations are obtained by substituting into equations (4) and (5).

$$\begin{aligned}
M_1(\ddot{w}_1 + 2\dot{w}_1\omega_R j - \omega_R^2 w_1) + (K_1 + K_2)w_1 - K_2 w_2 e^{j(\alpha_2 - \alpha_1)} &= 0 \\
M_2(\ddot{w}_2 + 2\dot{w}_2\omega_R j - \omega_R^2 w_2) + M_f[\ddot{w}_2 + 2j\omega_R \dot{w}_2(1-\lambda) - \omega_R^2 w_2(1-\lambda)^2] + & \\
+ [D + \psi_2(A_2)] [\dot{w}_2 + j\omega_R w_2(1-\lambda)] + \frac{d\psi_2(A_2)}{dA_2} w_2 A_2 j\omega_R(1-\lambda) + & \\
+ [K_0 + \psi_1(A_2)] w_2 + \frac{d\psi_1(A_2)}{dA_2} w_2 A_2 + (K_2 + K_3) w_2 - K_2 w_1 e^{j(\alpha_1 - \alpha_2)} &= 0
\end{aligned} \tag{23}$$

The solution of the variational equations (23) has the following form

$$w_1 = E_1 e^{(st - j\omega_R t - j\alpha_1)}, \quad w_2 = E_2 e^{(st - j\omega_R t - j\alpha_2)} \tag{24}$$

where s is the eigenvalue and E_1, E_2 are constants of integration. By introducing (24) into (23), the characteristic equation is obtained:

$$\begin{aligned}
[M_2 s^2 + M_f (s - j\lambda\omega_R)^2 + (D + \psi_2)(s - j\lambda\omega_R) + \psi_2' A_2 j\omega_R(1-\lambda) + & \\
+ K_0 + \psi_1 + \psi_1' A_2 + K_3](K_1 + K_2 + D_s s + M_1 s^2) + K_2(K_1 + D_s s + M_1 s^2) &= 0
\end{aligned} \tag{25}$$

where ψ_1 and ψ_2 are functions of A_2 and $\psi_{1,2}' = \frac{d\psi_{1,2}(A_2)}{dA_2}$.

Stability of the synchronous solution (6) is assured if all eigenvalues of the equations (23) have non-positive real parts.

The characteristic equation (25) differs from the characteristic equation (17) by the nonlinear terms which cause an apparent increase of the bearing radial damping, "cross stiffness" effect, and radial stiffness. The threshold of stability calculated the same way as previously, has now the following form (M_2 is neglected):

$$\omega_R^{(ST)} \equiv \frac{1}{\lambda\sqrt{M_1}[1 + \chi(A_2)]} \sqrt{K_1 + \frac{K_2(K_0 + K_3 + \psi_1 + \psi_1' A_2)}{K_2 + K_0 + K_3 + \psi_1 + \psi_1' A_2}} \tag{26}$$

$$\text{where } \chi(A_2) = -\psi_2' A_2(1/\lambda - 1)/(D + \psi_2). \tag{27}$$

With increasing eccentricity A_2 an apparent decrease of the average swirling ratio λ is noticed, as $\chi(A_2)$ has a negative sign.

More interesting is, however, the modification of the instability threshold due to increase of stiffness from $(K_0 + K_3)$ in (20) to $(K_0 + K_3 + \psi_1 + \psi_1' A_2)$ in (26). The last expression includes the amplitude of synchronous vibration A_2 which is a function of rotative speed ω_R . Following (20) and (26), the criterion of stability can be written in the form:

$$\lambda\sqrt{M_1}[1 + \chi(A_2)]\omega_R < \sqrt{K_1 + \frac{K_2(K_0 + K_3 + \psi_1 + \psi_1' A_2)}{K_2 + K_0 + K_3 + \psi_1 + \psi_1' A_2}} = \sqrt{K_1 + \frac{K_2 \psi}{K_2 + \psi}} \tag{28}$$

and solved graphically (Fig. 7). The graphical solution is very effective in showing qualitative features of the rotor dynamic behavior. Having the amplitude/rotative speed relationship from equation (8) or (13) (lower graph of Fig. 7) and having the plot of the radical (28) versus amplitude A_2 which includes the nonlinear function ψ_1 of A_2 (left-hand side graph), the graph of the radical from the right-hand side of the inequality (28) versus rotative speed ω_R can be built up as the small arrows indicate (right side plot). The left-hand side of the inequality (28) versus ω_R is a straight line $\lambda\omega_R\sqrt{M_1}$ slightly modified by the factor $\chi(A_2)$. The regions of stability are found at intersections of the corresponding plots on the

upper right-hand side graph. It clearly shows that the synchronous solution is stable for rotative speeds below the first threshold of stability, which differs very little from the stability threshold (21), and that they are stable in the resonant speed region.

It is easily noticed that higher unbalance will increase stability region for the synchronous vibrations around the resonant speed $\sqrt{(K_1+K_2)/M_1}$ (Fig. 8).

The series of experiments with a balanced and unbalanced rotor confirm this analytical prediction; higher unbalance causes wider interval of rotative speeds where synchronous vibrations are stable (Figs. 9 through 11).

8. ROTOR SELF-EXCITED VIBRATIONS: OIL WHIRL AND OIL WHIP

For the case of the absence of imbalance, the equations (4), (5) have a particular solution describing self-excited vibrations (oil whirl and oil whip).

$$z_1 = G_1 e^{j(\omega t + \beta)} \quad , \quad z_2 = G_2 e^{j\omega t} \quad (29)$$

where G_1, G_2 are corresponding constant amplitudes, β is the relative phase angle, and ω is the self-excited vibration frequency.

By introducing (29) into (4) and (5), the algebraic equations for calculating G_1, G_2, β , and ω are obtained:

$$\begin{aligned} & \{-M_2\omega^2 - M_f(\omega - \lambda\omega_R)^2 + j[D + \psi_2(G_2)](\omega - \lambda\omega_R) + K_0 + \psi_1(G_2) + K_3\}(K_1 + K_2 - M_1\omega^2 + D_s j\omega) + \\ & + K_2(K_1 + D_s j\omega - M_1\omega^2) = 0 \end{aligned} \quad (30)$$

$$G_1 = \frac{K_2 G_2}{\sqrt{(K_1 + K_2 - M_1\omega^2) + D_s^2 \omega^2}} \quad , \quad \beta = \arctan \frac{D_s \omega}{M_1\omega^2 - K_1 - K_2} \quad (31)$$

The real and imaginary parts of the equation (30) provide relationships for obtaining G_2 and ω , for each case of the nonlinear functions $\psi_1(G_2)$ and $\psi_2(G_2)$:

$$\psi_1(G_2) = M_2\omega^2 + M_f(\omega - \lambda\omega_R)^2 - K_0 - K_3 - K_2 \frac{(K_1 + K_2 - M_1\omega^2)(K_1 - M_1\omega^2) + D_s^2 \omega^2}{(K_1 + K_2 - M_1\omega^2)^2 + D_s^2 \omega^2} \equiv \phi_1(\omega) \quad (32)$$

$$\psi_2(G_2) = -D - \frac{K_2^2 D_s \omega}{(\omega - \lambda\omega_R)[(K_1 + K_2 - M_1\omega^2)^2 + D_s^2 \omega^2]} \equiv \phi_2(\omega) \quad (33)$$

The frequency ω is yielded from the equation

$$\psi_2\{\psi_1^{-1}[\phi_1(\omega)]\} = \phi_2(\omega) \quad (34)$$

where ψ_1^{-1} is the inverse function (32); $G_2 = \psi_1^{-1}[\phi_1(\omega)]$.

For example, in case of the "parabolic" nonlinear functions (2) and small damping D_s

the frequency equation (34) has the following form:

$$(K_1+K_2-M_1\omega^2)(\omega-\lambda\omega_R)\{(K_1+K_2-M_1\omega^2)\left[\frac{B_2}{B_1}(K_0+K_3-M_2\omega^2-M_f(\omega-\lambda\omega_R)^2)-D\right] + \frac{B_2}{B_1}K_2(K_1-M_1\omega^2)\} \approx D_S\omega K_2^2 \approx 0 \quad (35)$$

It yields immediately three important real solutions for the frequency:

$$\omega_1 \approx \lambda\omega_R \quad (36)$$

$$\omega_{2,3} \approx \pm \sqrt{(K_1+K_2)/M_1 + D_S B_1/[M_1 B_2(1-\lambda\omega_R/\sqrt{(K_1+K_2)/M_1})]} \approx \pm \sqrt{(K_1+K_2)/M_1} \quad (37)$$

which are close to the linear rotor/bearing system "whirl" and "whip" natural frequencies at the threshold of stability (21). The remaining solutions can be also easily obtained from equation (35). For the small shaft damping D_S the similar consideration can be extended to any case of nonlinear functions ψ_1, ψ_2 : in (35) the ratio B_2/B_1 should be replaced by the ratio $\psi_2(G_2)/\psi_1(G_2)$. Three frequency solutions (36), (37) exist, therefore, independently of nonlinearities and independently of journal mass and fluid inertia.

The corresponding amplitude G_2 of the self-excited vibrations can be calculated from (32). For example, the "parabolic" nonlinearity (2) yields:

$$\text{Whirl amplitude: } G_2|_{\omega=\lambda\omega_R} \approx \frac{1}{B_1} \sqrt{M_2\lambda^2\omega_R^2 - K_0 - K_3 - K_2 \frac{K_1 - M_1\lambda^2\omega_R^2}{K_1 + K_2 - M_1\lambda^2\omega_R^2}} \quad (38)$$

$$\text{Whip amplitude: } G_2|_{\omega=\sqrt{(K_1+K_2)/M}} \approx \frac{1}{B_1} \sqrt{M_2(K_1+K_2)/M_1 + M_f(\sqrt{(K_1+K_2)/M_1} - \lambda\omega_R)^2 - K_0 - K_2 - K_3} \quad (39)$$

The expression under the radical (38) should be positive, therefore, the self-excited vibrations with the whirl amplitude (38) exist only for the limited range of the rotative speed (M_2 neglected):

$$\frac{1}{\lambda} \sqrt{\frac{K_1}{M_1} + \frac{K_2(K_0+K_3)}{M_1(K_0+K_2+K_3)}} \lesssim \omega_R \lesssim \sqrt{(K_1+K_2)/M_1}/\lambda \quad (40)$$

The left-hand side of the inequality (40) represents the threshold of stability (20), the right-hand side term separates the whirl from the whip.

The similar reason causes that the self-excited vibrations with the whip amplitude (39) exist for the following rotative speed range:

$$\omega_R \gtrsim \frac{1}{\lambda} \sqrt{\frac{K_1+K_2}{M_1}} + \frac{1}{\lambda} \sqrt{[K_0+K_2+K_3 - (K_1+K_2)M_2/M_1]/M_f} \quad (41)$$

From equations (31) and (32) the corresponding whirl and whip amplitudes and phases of the rotor can be obtained. For example for whip frequency (37), in case of "parabolic" nonlinearities (2) they are as follows:

$$G_1 = G_2 \left| \frac{K_2}{D_s \sqrt{(K_1+K_2)/M_1} \sqrt{B_1^2 / [B_2(\sqrt{(K_1+K_2)/M_1} - \lambda \omega_R)]^2 + 1}} \right| \quad (42)$$

$$\beta = \arctan [B_2(\sqrt{(K_1+K_2)/M_1} - \lambda \omega_R) / B_1] \quad (43)$$

During whip, the shaft vibrates at its resonant conditions, the whip amplitude is controlled mainly by the shaft damping D_s and the nonlinear fluid forces.

The phase between the rotor and journal at whip vibrations is controlled by nonlinear forces in the bearing. It was experimentally verified that during both oil whirl and oil whip, the rotor and journal vibrate nearly in phase (Fig. 12). This may serve as an indication concerning the values of nonlinear forces ψ_1 and ψ_2 .

9. DISCUSSION OF RESULTS

In this paper, a simple mathematical model of a symmetric shaft rotating in one rigid and one 360° lubricated bearing is proposed. The model yields results which stand in very good agreement with the experimentally observed rotor dynamic phenomena concerning stability, thresholds, and the self-excited vibrations known as oil whirl and oil whip.

The rotor in the model is represented by the generalized (modal) parameters of its first bending mode. These parameters can be analytically obtained by applying any classical method of modal reduction. The fluid force acting at the journal is represented in the model by the nonlinear expression based on rotating character of this force. The latter approach yields the bearing coefficients in an "inter-related" form: the tangential ("cross") stiffness is a product of the relative velocity and radial damping, the tangential damping results from Coriolis acceleration, the radial stiffness is reduced due to centripetal acceleration and fluid inertia.

The fluid nonlinear force is introduced in a very general form, where the nonlinearity is related to the journal radial displacement (eccentricity in the journal bearing). The nonlinear character of the fluid stiffness force and especially fluid damping force is well known. This nonlinearity has a "hard" character: the forces increase with eccentricity. Actually they grow to infinity when the journal touches the bearing wall. Since, in this paper, low eccentricity ratios were considered only (to justify the symmetric character of the rotor model), an example of the fluid nonlinear forces was discussed: the first terms of the Fourier expansion of any nonlinear function representing the fluid force.*

The results obtained from the analysis of the rotor model and concerning the rotor, synchronous vibrations due to imbalance, and self-excited vibrations known as "oil whirl" and "oil whip" very well reflect the observed rotor dynamical behavior.

The classical eigenvalue problem yields three important eigenvalues of the rotor/bearing system. The first eigenvalue has the imaginary part (natural frequency) close to $\lambda \omega_R$ and corresponds to oil whirl frequency. The real part of this eigen-

value predicts the threshold of stability (the rotative speed at which the pure rotational motion or 1x synchronous vibrations of an unbalanced rotor become unstable). This threshold of stability is determined by the rotor mass and its partial stiffness, as well as the oil average swirling ratio ($\omega_R^{(ST)} \approx \sqrt{K_1/M_1}/\lambda$ expression (21)). The latter result was noticed in the fifties by Poritsky [18] and discussed by Boeker and Sternlicht [19]. Since then, this seems to have been forgotten for 30 years.

The second and third eigenvalue of the rotor/bearing system have the imaginary part close to the rotor natural frequency ($\pm\sqrt{(K_1+K_2)/M_1}$) of the first bending mode. The latter is referred to as "whip frequency".

The model yields the self-excited vibrations (known as oil whirl and oil whip) as a particular solution. The frequencies of oil whirl and oil whip are very close to the natural frequencies of the linear system. The model permits evaluation of the amplitudes and relative, journal/disk phase angles of these self-excited vibrations.

The most important and new (to the author's knowledge) result presented in this paper concerns the analytical evaluation of the stability of the synchronous vibrations of the rotor and relationship between the width of the stability region and the amount of the rotor imbalance. This result is yielded from the classical investigation of stability through equations in variations. The bearing nonlinear force, increasing with rotor radial deflection causes an increase of the journal supporting radial stiffness force which is directly related to the actual synchronous vibration amplitude. The increased radial stiffness affects the threshold of stability. The synchronous vibration amplitude varies with the rotative speed, and in the first balance resonance region of speeds the effect of stable synchronous vibrations is observed. Two additional thresholds of stability are noted. The width of this region depends directly on the amount of imbalance in the rotating system. A simple graphical method (Figs. 7 and 8) explains qualitatively this feature. The expressions (26) and (28) give the analytical relationships for these additional thresholds of stability.

In the rotor/bearing system analysis, as well as in experimental testing, rather small effect of the bearing fluid inertia has been noted. The fluid inertia has a negligible influence on the synchronous vibrations, thresholds of stability, natural frequencies, and frequencies of the self-excited vibrations. The journal generalized (modal) mass is also usually relatively small. These aspects led to the conclusion regarding further simplifications of the rotor/bearing model to the one and a half degree of freedom system. The fluid radial damping force which is proportional to the relative journal velocity is definitely dominant fluid force in the bearing, and it determines the order of the equation (5), as the forces of inertia M_f and M_2 are negligible.

There is still no clear picture of what affects the fluid average swirling ratio λ . It has been assumed in this paper that λ is constant. However, during experimental testing some variations of value of λ have been noticed. This aspect is being studied and requires further investigation.

* Fluid force is often modeled proportional to $(1-e^2)^{-n}$, where e is the eccentricity ratio (journal radial displacement $|z_2|$ to radial clearance), n is a number (usually 1/2, 1, 3/2, 2, 5/2, or 3). In the first approximation $(1-e^2)^{-n} \approx 1 + 2ne^2$, which in turn, is proportional to the example forces (2) considered in this paper.

SYMBOLS

A_1, A_2	Amplitudes of synchronous vibrations of the rotor and journal respectively
B_1, B_2	Coefficients of bearing nonlinear "parabolic" force (2)
D, K_0, M_f	Bearing fluid radial damping, stiffness, and inertia coefficients
D^S	Shaft external damping coefficient
E_1, E_2	Constants of integration
F	Bearing fluid force
G_1, G_2	Amplitudes of the rotor and journal self-excited vibrations
$j = \sqrt{-1}$	
K_1, K_2, K_3	Rotor modal stiffness coefficients
m, r	Mass and radius of imbalance respectively
M_1, M_2	Rotor and journal modal masses respectively
s, s_1, s_2, s_3	Eigenvalues
$w_1(t), w_2(t)$	Variational variables for the synchronous vibration/stability investigation
$z=x+jy, z_2=x_2+jy_2$	Journal radial displacement x-horizontal, y-vertical (fixed coordinates)
$z_1 = x_1+jy_1$	Rotor radial displacement (x_1 -horizontal, y_1 -vertical)
$z_r = x_r+jy_r$	Journal radial displacement (rotating coordinates)
α_1, α_2	Rotor and journal phase of the synchronous vibrations
β	Phase of rotor/journal self-excited vibrations
λ	Fluid average swirling ratio
ψ_1, ψ_2	Bearing fluid nonlinear functions of journal radial displacement
ψ'_1, ψ'_2	Derivatives of ψ_1, ψ_2 in respect to radial displacement correspondingly
ω	Circular frequency of the rotor self-excited vibrations
ω_R	Rotative speed
$\omega_R^{(ST)}$	Threshold of stability (rotative speed).

REFERENCES

1. Symposium of Dynamics of Rotors IUTAM. Lyngby, Denmark, 1974. Proceedings, Springer Verlag, 1975.
2. Vibrations in Rotating Machinery. Proceedings of the Conference, University of Cambridge, UK, 1976.
3. Rotordynamic Instability Problems in High Performance Turbomachinery. NASA CP-2133, Texas A&M University Workshop, 1980.
4. Vibrations in Rotating Machinery. Proceedings of the Conference, University of Cambridge, UK, 1980.
5. Rotordynamic Instability Problems in High Performance Turbomachinery. NASA CP-2250, Texas A&M University Workshop, 1982.
6. Rotordynamic Instability Problems in High Performance Turbomachinery. Texas A&M University Workshop, 1984.
7. Vibrations in Rotating Machinery. Proceedings of the Third International Conference, York, UK, 1984.
8. Bolotin, V.V.: The Dynamic Stability of Elastic Systems (translated from Russian), Holden-Day Inc., San Francisco, 1964.

9. Humphris, R.R., Gunter, E.J.: The Influence of Rotor Characteristics in Oil Whirl. Rotor Dynamics Laboratory, University of Virginia, Charlottesville, VA, June 1983.
10. Muszynska, A.: Rotor Instability. Senior Mechanical Engineering Seminar, Bently Nevada Corporation, Carson City, Nevada, June 1984.
11. Black, H.F.: Effects of Hydraulic Forces in Annular Pressure Seals on the Vibrations of Centrifugal Pump Rotors. Journal of Mechanical Engineering Science, Vol. II, No. 2, 1969.
12. Black, H.F., Jensen, D.N.: Dynamic Hybrid Bearing Characteristics of Annular Controlled Leakage Seals. Proceedings Journal of Mechanical Engineering, Vol. 184, 1970.
13. Bently, D.E., Muszynska, A.: Perturbation Tests of Bearing/Seal for Evaluation of Dynamic Coefficients. Symposium on Rotor Dynamical Instability, Summer Annual Conference of the ASME Applied Mechanics Division, Houston, TX, June 1983.
14. Ambrosch, F., Schwaebel, R.: Method of and Device for Avoiding Rotor Instability to Enhance Dynamic Power Limit of Turbines and Compressors. United States Patent, #4,273,510, June 1981.
15. Miller, E.H.: Rotor Stabilizing Labyrinth Seal for Steam Turbines. United States Patent #4,420,161, Dec. 1983.
16. Minorsky, N.: Introduction to Nonlinear Mechanics. J. W. Edwards, Ann Arbor, 1947.
17. Bently, D.E., Muszynska, A.: Perturbation Study of a Rotor/Bearing System: Identification of the Oil Whirl and Oil Whip Resonances. Tenth Biennial ASME Conference on Mechanical Vibration and Noise, Cincinnati, Ohio, September 1985.
18. Poritsky, H.: Contribution to the Theory of Oil Whip. Trans. ASME v. 75, 1953.
19. Boeker, G. F., Sternlicht, B.: Investigation of Translatory Fluid Whirl in Vertical Machines. Trans. ASME, January 1956.

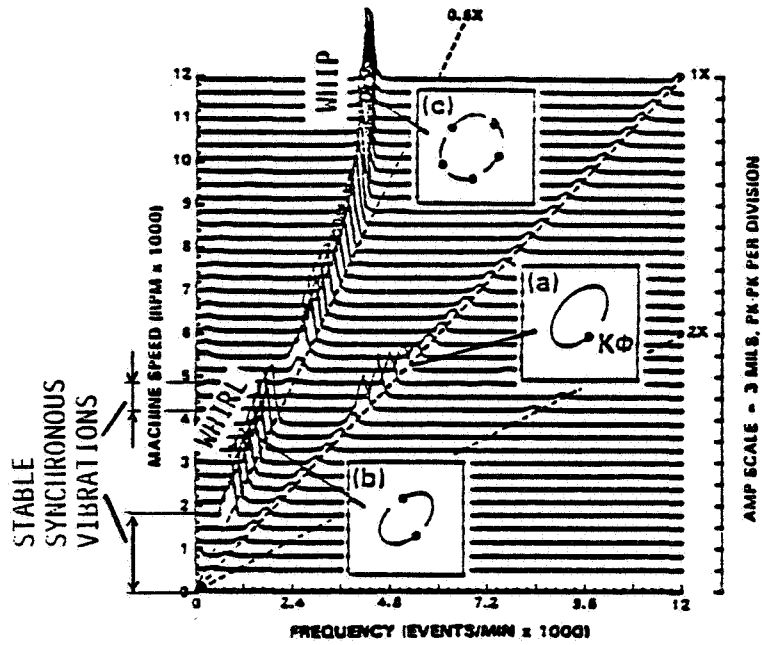


Figure 1. - Cascade spectrum of rotor vibrational response measured at oil bearing. Spectrum indicates regions of synchronous (1X) vibrations due to unbalance, oil whirl ($\approx 1/2X$), and oil whip with constant frequency close to first balance resonance (slightly lower). (a) Orbit display of synchronous vibrations, (b) oil whirl orbit, (c) oil whip orbit ($K\phi$ - keyphasor pulse indicating relationship with rotative speed frequency).

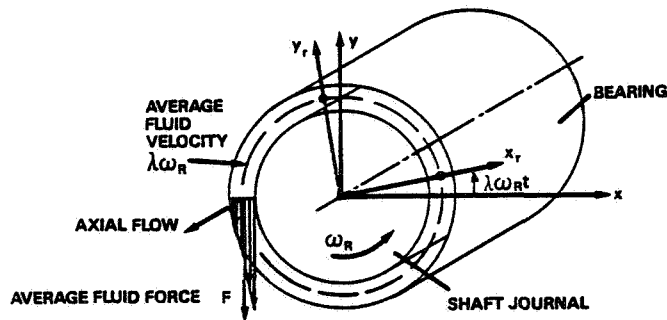


Figure 2. - Bearing mode: Fluid force rotating with angular velocity $\lambda\omega_R$.

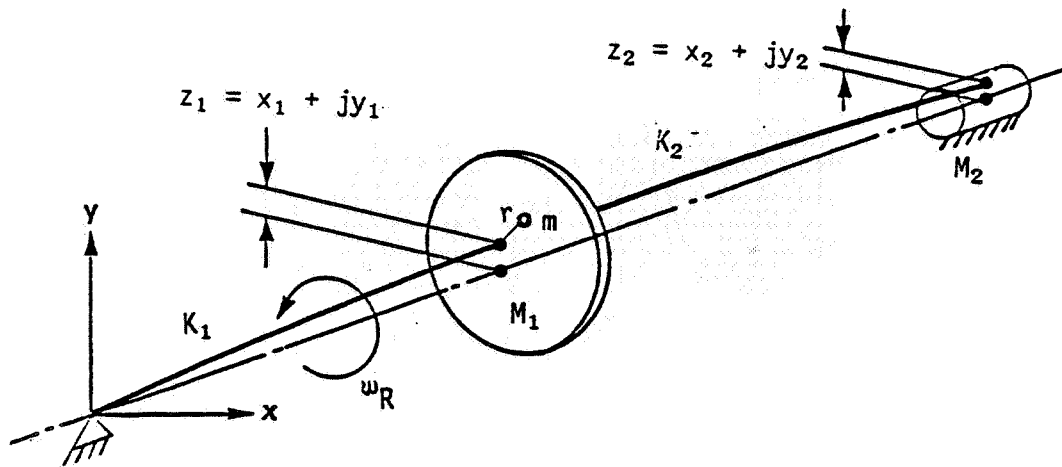
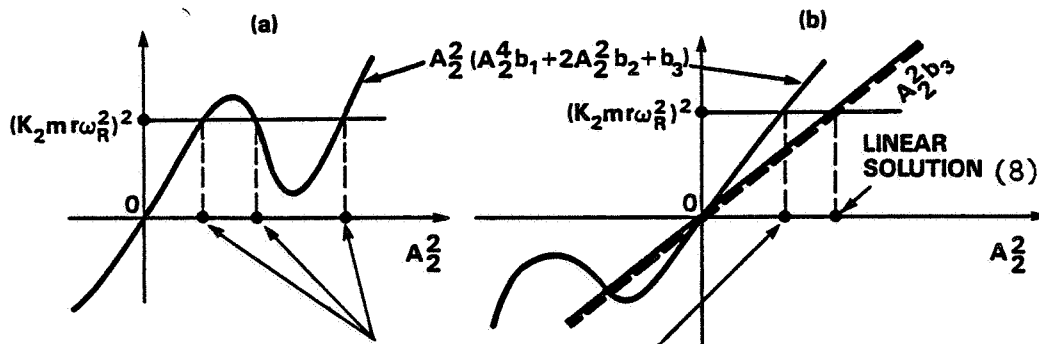


Figure 3. - Model of symmetric rotor in one antifriction and one oil bearing.



(a) Case $2b_2 < -\sqrt{\frac{3b_1 b_3}{13}}$: three amplitudes A_2 yielded.

(b) Case $2b_2 \geq -\sqrt{\frac{3b_1 b_3}{13}}$: one amplitude A_2 exists.

Figure 4. - Graphical solution of equation (13) (notation: $b_1 = h_6^2 + h_7^2$, $b_2 = h_2 h_6 + h_3 h_7$, $b_3 = h_2^2 + h_3^2$).

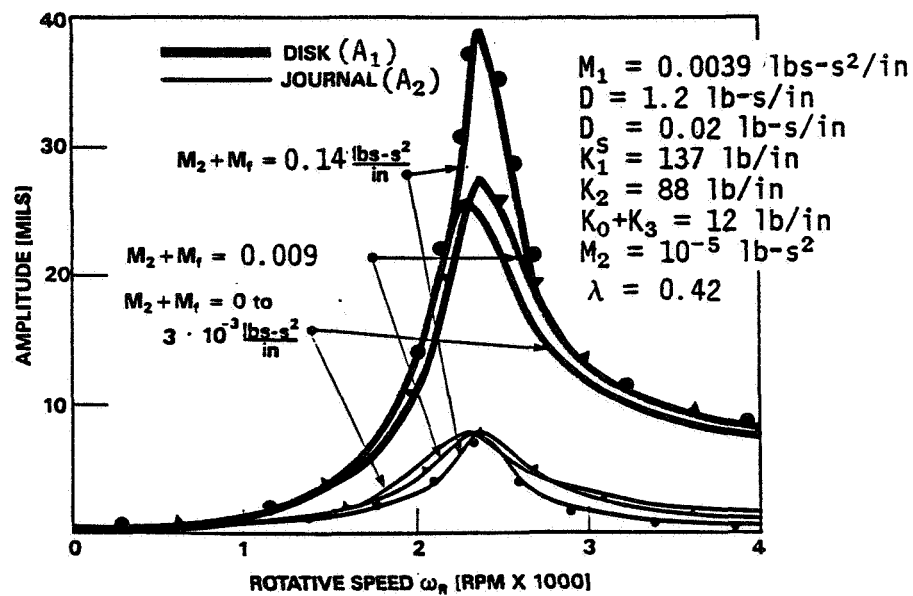
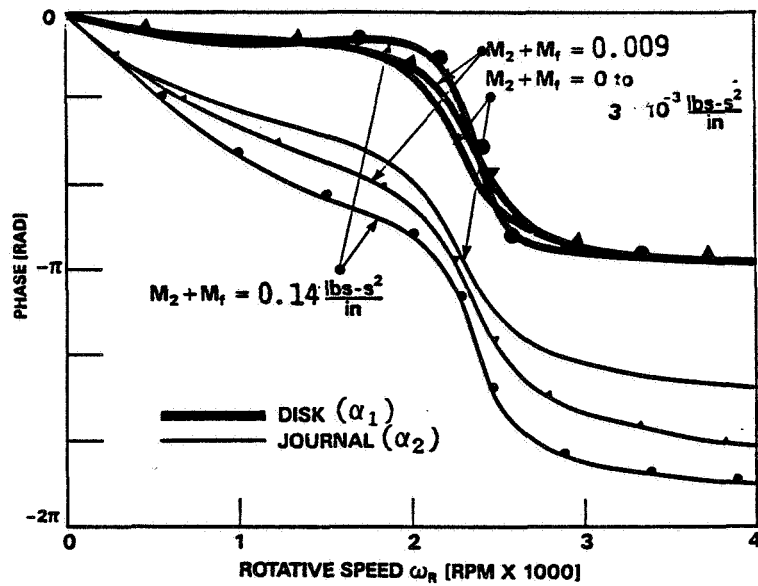


Figure 5. - Phase and amplitude of rotor and journal synchronous vibrations (6) versus rotative speed. Note a significant insensitivity to fluid inertia and journal generalized mass M_2 .

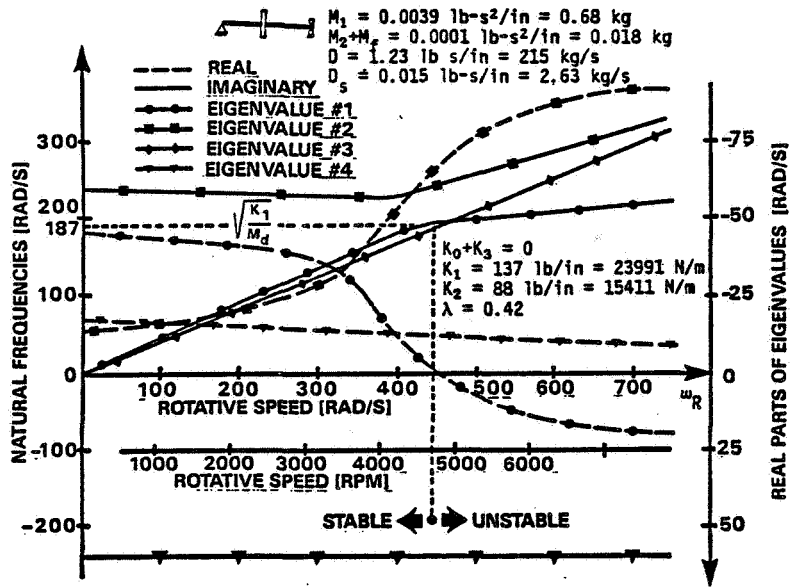


Figure 6. - Eigenvalues of rotor/bearing system (eigenvalue "3" has a high-value negative real part, not shown in graph).

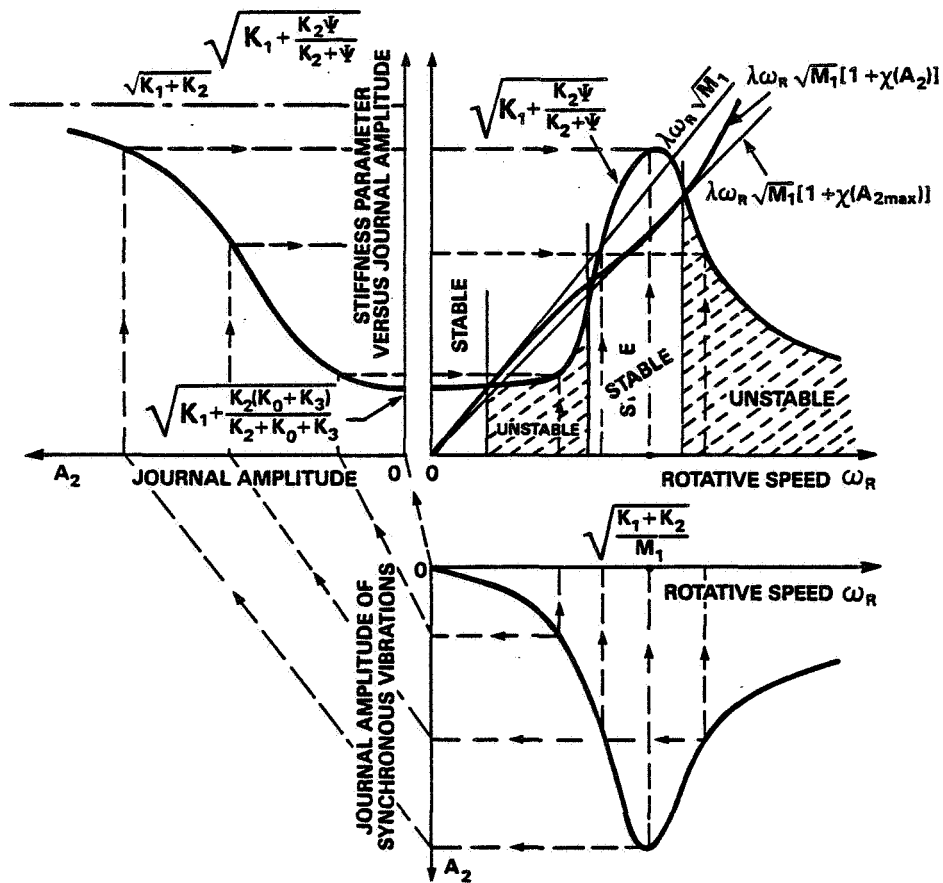


Figure 7. - Stability chart for rotor synchronous vibrations due to unbalance. Graphical solution of inequality (48). [Notation: $\psi = K_0 + K_3 + \psi_1(A_2) + A_2\psi_1'(A_2)$.]

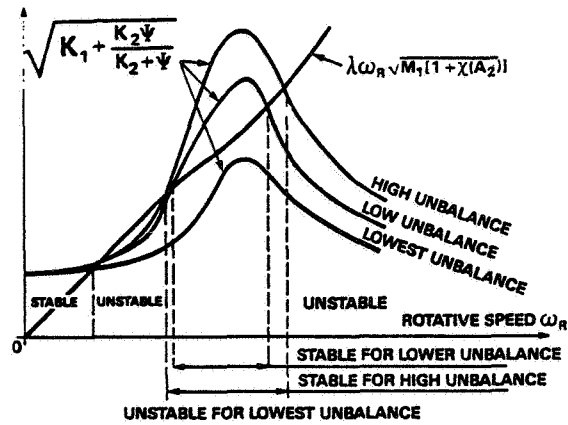


Figure 8. - Modification of synchronous vibration stability regions by unbalance (ψ same as in fig. 7).

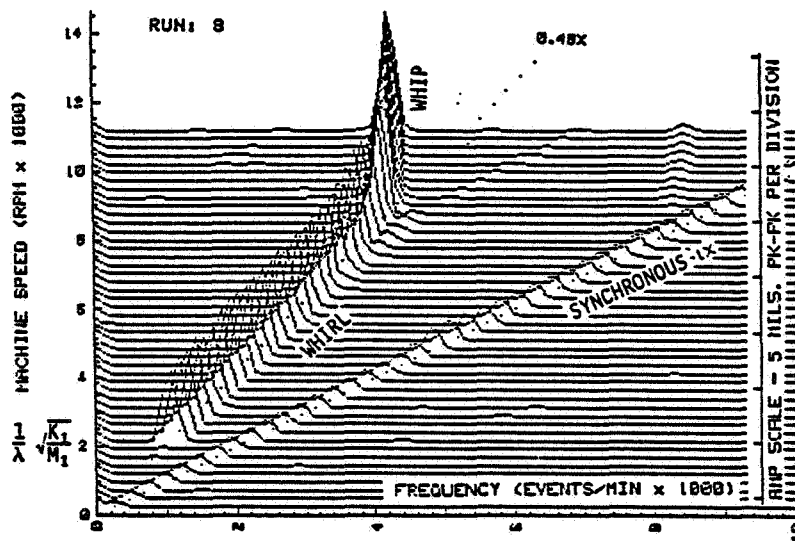


Figure 9. - Cascade spectrum of rotor with residual unbalance. Vertical response measured at journal. Synchronous vibrations unstable for rotative speed higher then ~ 2100 rpm.

ORIGINAL PAGE IS
OF POOR QUALITY

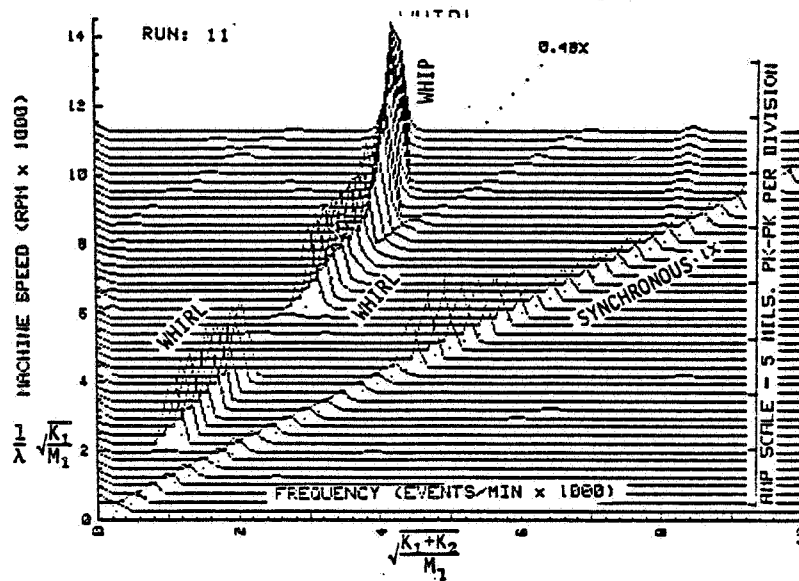


Figure 10. - Cascade spectrum of rotor with 1 g x 1.2 in. of imbalance. Vertical response of journal. Synchronous vibrations stable for rotative speed lower than ~2100 rpm and in resonance region: from ~4200 to ~4900 rpm.

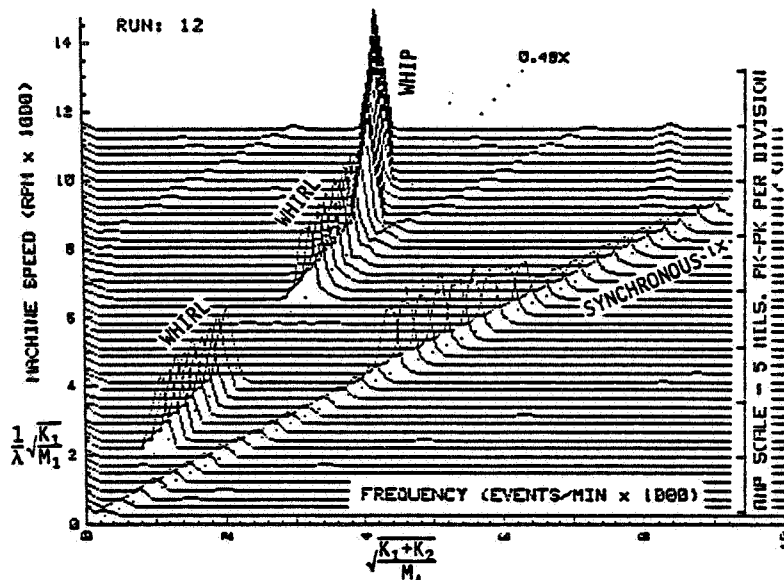


Figure 11. - Cascade spectrum of rotor with 1.2 g x 1.2 in. of imbalance. Vertical response of journal. Synchronous vibrations stable for rotative speed lower than ~2100 rpm and in wider resonance region: from ~4100 to ~5200 rpm.

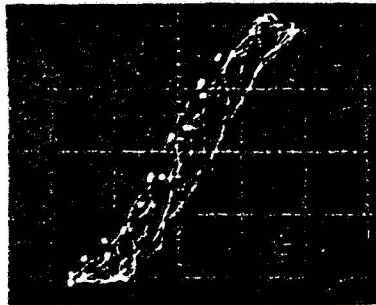


Figure 12. - Vertical transducer signals of journal and rotor vibrations during oil whip. Oscilloscope display in XY mode indicates nearly in-phase vibrations.

SOME NEW RESULTS CONCERNING THE DYNAMIC BEHAVIOR OF ANNULAR TURBULENT SEALS*

H. Massmann and R. Nordmann
University of Kaiserslautern
Federal Republic of Germany

The dynamic characteristics of annular turbulent seals applied in high-pressure turbopumps can be described by stiffness, damping, and inertia coefficients. This paper presents an improved procedure for determining these parameters by using measurements made with newly developed test equipment. The dynamic system seal, consisting of the fluid between the cylindrical surfaces of the rotating shaft and the housing, is excited by test forces (input), and the relative motion between the surfaces (output) is measured. Transformation of the input and output time signals into the frequency domain leads to frequency response functions. An analytical model, depending on the seal parameters, is fitted to the measured data in order to identify the dynamic coefficients. Some new results are reported that show the dependencies of these coefficients with respect to the axial and radial Reynolds numbers and the geometrical data of the seal.

INTRODUCTION

In high-pressure turbopumps different types of annular seals are used, as illustrated in figure 1. The neck or wear ring seals are provided to reduce the leakage flow back along the front surface of the impeller face, and the interstage seals reduce the leakage from an impeller inlet back along the shaft to the back side of the preceding impeller. The geometry of pump seals may be similar to that of plain journal bearings, but they have a higher clearance-to-radius ratio and normally a fully developed turbulent flow (axial and circumferential).

Besides their designed function of reducing the leakage flow, turbulent seals have the potential to produce significant forces and have a large influence on the bending vibrations of turbopump rotors. To determine more about the pump's dynamic behavior, calculation should be carried out in the design stage. For this task the machine designer needs to know the dynamic characteristics of seals as expressed by inertia, damping, and stiffness coefficients.

Different theoretical models exist to determine the dynamic seal coefficients (refs. 1 to 4), but more experimental data are needed to compare with theoretical results and to modify existing seal models. Until now only a few measured data have been available (refs. 5 to 10). The authors have developed a test procedure to find the inertia, damping, and stiffness coefficients of annular turbulent seals. First measurement results reported in earlier publications (refs. 9, 10) pointed out the usefulness of the employed method. Meanwhile a new test rig was built that has some improved measurement possibilities and interchangeable seals. However, the measurement principle did not change essentially from the first test facility.

*This research work was supported by "Deutsche Forschungsgemeinschaft", German Federal Republic.

This paper briefly reviews the theoretical seal models and describes the employed experimental procedure for the determination of the seal coefficients. Some new results are reported, pointing out the dependence of the coefficients on the rotational frequency (circumferential Reynolds number), the axial velocity of the fluid (axial Reynolds number), and the geometrical data of the seals. They are compared with predictions from theoretical models.

DYNAMIC SEAL COEFFICIENTS - THEORETICAL MODELS

Most of the existing theoretical seal models have been developed for the simplest geometry with a fluid surrounded by a cylindrical rotating part (impeller or shaft) and a cylindrical housing (fig. 1). Such annular contactless seals separate the two spaces with pressure p_E and p_A , respectively. Caused by the pressure difference $\Delta p = p_E - p_A$, the leakage flow in the axial direction is almost always turbulent with average velocity V . Because of the rotation of the shaft a velocity is superimposed in the circumferential direction.

From a rotordynamic point of view the various theoretical models usually express a relation between the radial forces acting on the rotor and the corresponding displacements, velocities, and accelerations of the shaft. If the motions about a centered position are small, the dynamic system "seal" can be modeled by a linear system with stiffness, damping, and inertia coefficients

$$-\begin{bmatrix} F \\ y \\ F \\ z \end{bmatrix} = \underbrace{\begin{bmatrix} m_{yy} & m_{yz} \\ m_{zy} & m_{zz} \end{bmatrix}}_{\underline{M}} \begin{bmatrix} y \\ z \end{bmatrix} + \underbrace{\begin{bmatrix} c_{yy} & c_{yz} \\ c_{zy} & c_{zz} \end{bmatrix}}_{\underline{C}} \begin{bmatrix} \dot{y} \\ \dot{z} \end{bmatrix} + \underbrace{\begin{bmatrix} k_{yy} & k_{yz} \\ k_{zy} & k_{zz} \end{bmatrix}}_{\underline{K}} \begin{bmatrix} y \\ z \end{bmatrix} \quad (1)$$

where \underline{M} is the mass matrix, \underline{C} the damping matrix, and \underline{K} the stiffness matrix of the seal.

Black was the first to derive a dynamic model for short annular seals, taking into account a leakage relation for flow between concentric rotating cylinders and a fully developed shear flow $U = R\Omega/2$ (where R is seal radius and Ω shaft angular velocity) in the circumferential direction but neglecting the pressure-induced circumferential flow. His analysis and results are discussed in references 1 and 2.

Childs (ref. 3) recently applied Hirs' lubrication equation to the dynamic analysis of seals. He used a perturbation method of Hirs' equation to obtain a closed-form analytical definition for a short seal. The zeroth-order equations for the centered position lead to a leakage pressure drop relation

$$\Delta p = (p_E - p_A) = (1 + \xi + 2\sigma) \rho V^2 / 2 \quad (2)$$

with

$$\begin{aligned} u & \text{ inlet pressure loss coefficient} \\ \sigma & \text{ dimensionless friction loss coefficient (L = seal length,} \\ & \text{S = radial seal clearance), } \lambda L / S \end{aligned} \quad (3)$$

C-3

$$\lambda = n_o R_a^{m_o} [1 + 1/4b^2]^{(1+m_o)/2}; \quad b = R_a/2R_c \quad (4)$$

The friction loss coefficient λ depends on the axial Reynolds number R_a and the circumferential Reynolds number R_c , respectively

$$R_a = 2VS/\nu; \quad R_c = R\Omega S/\nu \quad (5)$$

defined with the radial clearance S and the fluid viscosity ν . The empirical coefficients n_o and m_o have to be determined by a test for the special case.

The first-order perturbation equations lead to a pressure distribution and after integration directly to the short seal dynamic coefficients

$$E = \frac{1 + \xi}{2(1 + \xi + B\sigma)}$$

$$B = 1 + 4b^2 B(1 + m_o)$$

$$T = \frac{L}{V}$$

$$a = \sigma[1 + B(1 + m_o)]$$

$$B = \frac{1}{1 + 4b^2}$$

$$v_0 = \text{initial swirl}$$

and

$$k_{yy} = k_{zz} = \frac{\pi R \Delta p}{\lambda} \frac{2\sigma^2}{1 + \xi + 2\sigma} \left\{ E(1 - m_o) - \frac{(\Omega T)^2}{4\sigma} \right. \\ \left. \times \left[\frac{1}{2} \left(\frac{1}{6} + E \right) + \frac{2v_0}{a} \left[\left(E + \frac{1}{2} \right) (1 - e^{-a}) - \left(\frac{1}{2} + \frac{1}{a} \right) e^{-a} \right] \right] \right\}$$

$$k_{yz} = -k_{zy} = \frac{\pi R \Delta p}{\lambda} \frac{\sigma^2 \Omega T}{1 + \xi + 2\sigma} \\ \times \left\{ \frac{E}{\sigma} + \frac{B}{2} \left(\frac{1}{6} + E \right) + \frac{2v_0}{a} \left[EB + \left(\frac{1}{\sigma} - \frac{B}{a} \right) \left[(1 - e^{-a}) \left(E + \frac{1}{2} + \frac{1}{a} \right) - 1 \right] \right] \right\}$$

$$c_{yy} = c_{zz} = \frac{\pi R \Delta p}{\lambda} T \frac{2\sigma^2}{1 + \xi + 2\sigma} \left[\frac{E}{\sigma} + \frac{B}{2} \left(\frac{1}{6} + E \right) \right]$$

$$c_{yz} = -c_{zy} = \frac{\pi R \Delta p}{\lambda} \frac{2\sigma \Omega T}{1 + \xi + 2\sigma} \left[\frac{1}{2} \left(\frac{1}{6} + E \right) + \frac{v_0}{a} \left[(1 - e^{-a}) \left(E + \frac{1}{2} + \frac{1}{a} \right) - \left(\frac{1}{2} + \frac{e^{-a}}{a} \right) \right] \right]$$

$$m_{yy} = m_{zz} = \frac{\pi R \Delta p}{\lambda} T^2 \frac{\sigma \left(\frac{1}{6} + E \right)}{1 + \xi + 2\sigma}; \quad m_{yz} = m_{zy} = 0$$

They are in reasonable agreement with prior results of Black (ref. 1) when $v_0 = 0$. The expressions point out the dependence of the seal coefficients on several parameters, like operating conditions V , Ω , the fluid temperature, the friction and entry loss coefficients σ , λ , ξ with the empirical constants m_0 and n_0 and the seal geometrical data R , L , and S . It can be shown that a few dimensionless parameters are sufficient to determine the stiffness, damping, and inertia quantities. In the later discussion the two Reynolds numbers R_a and R_c are used as test parameters as well as the geometrical data for seal clearance and seal length.

In addition to equations (6), the effect of an inlet swirl is also included in Child's original paper (ref. 3), pointing out this influence especially to the cross-coupled terms. Childs (ref. 4) as well as Black (ref. 2) have also extended their analysis to finite-length seals, and Childs has continued his work by deriving expressions for seals with different housings and rotor roughnesses.

IDENTIFICATION OF THE SEAL COEFFICIENTS

The experimental determination of the inertia, damping, and stiffness coefficients of turbulent seals is possible by means of parameter identification. Working with this method, first of all the dynamic seal model with corresponding mathematical equations, particularly frequency response functions, is required.

In the measurement step test forces (input signals) are applied to the system surface in the radial direction, and the relative motions between the two surfaces are measured (output signals). From input and output signals mobility frequency response functions can be calculated.

Finally a parameter estimation procedure is applied, requiring a good correlation between analytical and measured frequency response functions.

Dynamic Seal Model

The test rig seal model consists of the fluid, surrounded by the two cylindrical surfaces of the rotating shaft and the housing, respectively (fig. 2). The shaft of the test rig is designed to be very stiff and is supposed to have only one degree of freedom concerning the rotation about the axis. On the other hand the surface of the housing is movable only in the radial direction, having the two degrees of freedom y and z .

In these circumstances the dynamic system seal can be modeled by means of the above presented inertia, damping, and stiffness coefficients. With external time dependent forces F_y and F_z applied to the seal center in the y and z directions, the equations of motion are (see eqs. (1) and (6))

$$\begin{bmatrix} m_{yy} & | \\ \hline & m_{zz} \end{bmatrix} \begin{bmatrix} \ddot{y} \\ \ddot{z} \end{bmatrix} + \begin{bmatrix} c_{yy} & | & c_{yz} \\ \hline c_{zy} & | & c_{zz} \end{bmatrix} \begin{bmatrix} \dot{y} \\ \dot{z} \end{bmatrix} + \begin{bmatrix} k_{yy} & | & k_{yz} \\ \hline k_{zy} & | & k_{zz} \end{bmatrix} \begin{bmatrix} y \\ z \end{bmatrix} = \begin{bmatrix} F_y(t) \\ F_z(t) \end{bmatrix} \quad (7)$$

Corresponding to this two-degree-of-freedom system, a total of four stiffness frequency functions exist, assembled in the complex matrix \underline{K}_{kin}

$$\underline{K}_{kin} = \begin{bmatrix} k_{yy} - \omega^2 m_{yy} + i\omega c_{yy} & | & k_{yz} + i\omega c_{yz} \\ \hline k_{zy} + i\omega c_{zy} & | & k_{zz} - \omega^2 m_{zz} + i\omega c_{zz} \end{bmatrix} = \underline{K} - \omega^2 \underline{M} + i\omega \underline{C} \quad (8)$$

where ω is the exciter frequency. The inverse functions of equation (8) are the mobility frequency response functions

$$\underline{H}_{kin} = \begin{bmatrix} k_{zz} - \omega^2 m_{zz} + i\omega c_{zz} & | & -(k_{yz} + i\omega c_{yz}) \\ \hline -(k_{zy} + i\omega c_{zy}) & | & k_{yy} - \omega^2 m_{yy} + i\omega c_{yy} \end{bmatrix} \cdot \frac{1}{\Delta} = (\underline{K} - \omega^2 \underline{M} + i\omega \underline{C}) \quad (9)$$

$$\Delta = [k_{yy} - \omega^2 m_{yy} + i\omega c_{yy}] [k_{zz} - \omega^2 m_{zz} + i\omega c_{zz}] - [k_{yz} + i\omega c_{yz}] [k_{zy} + i\omega c_{zy}]$$

represented by the matrix \underline{H}_{kin} .

Measurements of Frequency Response Functions

From the frequency response functions (8) and (9), it is easier to measure the mobilities (9). They can be obtained by picking up input and output signals in the time domain and transforming them into the frequency domain by fast Fourier transformation. The ratio of the Fourier-transformed signals leads to the frequency response. Figure 3 shows in principle the measurement equipment. The housing is excited by a hammer impact, which is equal to an impulse force as broadband excitation. The relative displacements between the two seal surfaces (housing and shaft) are measured with eddy current pickups. After amplification and an analog-to-digital conversion the Fourier analyzer calculates the frequency response characteristics. A bus system transfers the measured data to a digital computer, where the unknown seal coefficients are calculated by means of the following identification procedure.

Estimation of Dynamic Seal Coefficients by Means of Least-Squares and Instrumental Variable Method

For the estimation of the dynamic seal coefficients a least-squares procedure, improved by an instrumental variable method, has been applied. From a theoretical point of view the product of the mobility matrix \underline{H}_{kin} and the stiffness matrix \underline{K}_{kin} should be the identity matrix \underline{E} . An additional error matrix \underline{S} , caused by measurement noise, has to be considered if measured mobilities \underline{H}_{kin}^M are combined with analytical stiffnesses $\underline{K}_{kin} = \underline{K} - \omega^2 \underline{M} + i\omega \underline{C}$.

$$\left. \begin{aligned} \underline{H}_{kin} \underline{K}_{kin} &= \underline{E} + \underline{S} \\ \underline{H}_{kin} (\underline{K} - \omega^2 \underline{M} + i\omega \underline{C}) &= \underline{E} + \underline{S} \end{aligned} \right\} \quad (10)$$

The complex equation (10) can be rearranged into two real equations

$$\begin{aligned} \underline{H}_k^r \text{in} \underline{K} - \omega^2 \underline{H}_k^r \text{in} \underline{M} - \omega \underline{H}_k^i \text{in} \underline{C} &= \underline{E} + \underline{S}^r \\ \underline{H}_k^i \text{in} \underline{K} - \omega^2 \underline{H}_k^i \text{in} \underline{M} + \omega \underline{H}_k^r \text{in} \underline{C} &= \underline{0} + \underline{S}^i \end{aligned} \quad (11)$$

corresponding to one exciter frequency. In the case of a broadband excitation we have as many equations as frequency lines. This results in an overdetermined equation system

$$\underline{A} \underline{X} = \underline{E}' + \underline{S}' \quad (12)$$

where \underline{A} consists of the measured frequency response functions related to the exciter frequencies ω , \underline{X} represents the unknown coefficients \underline{M} , \underline{C} , and \underline{K} , \underline{E}' is a modified identity matrix, and \underline{S}' is the error matrix.

Solution of equation (12) in the sense of least squares means to minimize a loss function, defined as the Euclidean norm of \underline{S}' . By deriving the loss function with respect to the seal coefficients, the so-called normal equations

$$\underline{A}^T \underline{A} \underline{X} = \underline{A}^T \underline{E}' \quad (13)$$

are obtained. They can be used to calculate a first set of unknown coefficients \underline{X}^1 , by the matrices \underline{M}^1 , \underline{C}^1 , \underline{K}^1 , respectively. Figure 4 shows this branch on the left side. However, the use of the described procedure may fail if the noise-to-signal ratio in the measurement is too high.

Fritzen (ref. 11) has suggested an instrumental variable method that is less sensitive to noise in the measurement data and reduces the error of the identified coefficients. With matrices \underline{M}^1 , \underline{C}^1 , and \underline{K}^1 from the first step, analytical mobility functions can be calculated. Instead of the matrix \underline{A}^T a new matrix \underline{W}^T with instrumental variables is built up using the above-mentioned matrices \underline{M}^1 , \underline{C}^1 , and \underline{K}^1 . Matrix \underline{A}^T is substituted by \underline{W}^T , and a new set of seal dynamic coefficients can be determined with

$$\underline{W}^T \underline{A} \underline{X} = \underline{W}^T \underline{E}' \quad (14)$$

This procedure is repeated and after each step the actual estimation is compared with that of the last step. Measurement and model frequency response functions are also compared. The procedure stops if the correlation is satisfactory. Our experience is that the combination of the classical least-squares method with the instrumental variable method shows much better results than the least-squares procedure alone.

TEST SETUP

Figure 5 shows a cross section of the actual test rig, which was very similar to the one described in references 9 and 10. Two annular seals were integrated symmetrically in a very rigid housing. A stiff shaft, driven by an ac motor, rotated inside the housing and acted as the second part of the seals. By using metal inserts as seal construction parts, we were able to vary the seal length, the

radial clearance, and the surface structure. The shaft was fixed to the foundation via roller bearings; the housing was connected to this system by two bolt springs and eight flexible bars. Other connections between the housing and the shaft were two mechanical seals (lip rings) in the end flanges of the casing and the most important part, the water film inside the annular seals.

The hydraulic part of the test setup consisted of a centrifugal pump that fed water into the seals. Filter and slide valves regulated the flow and the temperature of the water circulation. Flexible hose pipes connected this circuit and the movable housing. With this configuration (throughput of the pump, $4.5 \text{ m}^3/\text{h}$; shaft speed 6000 rpm), Reynolds numbers of about 12 000 were reached in the axial direction and up to 6500 in the circumferential direction. The water temperature was kept constant at $30 \text{ }^\circ\text{C}$.

Besides this mechanical part of the test setup there was the important electronic side for the data acquisition and manipulation. Three different groups of measured values can be distinguished:

- (1) Data of the fluid
- (2) Data of the exciter
- (3) Response data of the system

Pressure, temperature, density, and viscosity characterized the fluid state. Several pressure and temperature pickups were distributed over the test plant. The fluid velocity determined from the mass flow rate was measured in the supply line, and the shaft speed was displayed by the motor control. With these all measured data needed to calculate the seal coefficients were available. The excitation force, a blow of a hammer, was registered with a piezoelectric accelerometer mounted in the hammer head. The third group of data belonged to the motion of the housing relative to the shaft. Eddy current pickups surveyed the distance between both parts of the seal without contact. Two working planes with two orthogonal measurement directions permitted the control of housing displacement (translational and rotational).

The actual data of force and displacement as functions of time were transformed to the frequency domain by a digital spectrum analyzer that calculated the transfer functions. The parameter identification itself was carried out by desktop computer (fig. 3).

ADAPTATION OF THEORETICAL CONSIDERATIONS TO TEST SYSTEM

General Remarks

As shown in equation (7) it is possible to describe the dynamic behavior of the seal with differential equations. We can do the same for the test rig, ignoring the seal fluid mechanics. With the mass of the housing ($m_H = 32.5 \text{ kg}$), the stiffnesses of its attachment ($k_{sy} = 10 \text{ kN/m}$; $k_{sz} = 14 \text{ kN/m}$) and an assumed damping and stiffness matrix for the mechanical seals (k^l, c^l), the equation of motion was written in the following form:

$$\begin{bmatrix} m_H & 0 \\ 0 & m_H \end{bmatrix} \begin{bmatrix} \ddot{y} \\ \ddot{z} \end{bmatrix} + \begin{bmatrix} c_{yy}^l & c_{yz}^l \\ c_{zy}^l & c_{zz}^l \end{bmatrix} \begin{bmatrix} \dot{y} \\ \dot{z} \end{bmatrix} + \begin{bmatrix} k_{sy} + k_{yy}^l & k_{yz}^l \\ k_{zy}^l & k_{sz} + k_{zz}^l \end{bmatrix} \begin{bmatrix} y \\ z \end{bmatrix} = \begin{bmatrix} F_y \\ F_z \end{bmatrix} \quad (15)$$

Looking at the complete test apparatus, equation (7) could be replaced with equation (15). So we are only able to measure both influences and identify only "total" parameters (fig. 6). Later on we can correct the coefficients (i.e., reduce them to the seal coefficients) by using additional information about the system. At the moment we deal with the correction terms of the mass and the attachment stiffnesses and assume the lip ring coefficients are negligible (some more comments about this appear in the last passage of the paper).

Realization of Measurements

Every measurement set consists of four frequency response functions H_{ik} because we have a two-degree-of-freedom system. As mentioned our input data resulted from multiple-impact signals in order to reach a high energy level and a good noise-to-signal ratio during the sampling. This force and the system's response were measured simultaneously and later processed in a digital Fourier analyzer. The data set obtained in this way represented a single working condition of the test system (i.e., fluid velocity, fluid temperature, and shaft speed were constant). For all measurements the shaft speed was varied between 2000 and 6000 rpm, the water volume per time was varied between 2.5 and 4.5 m³/h, and the temperature was constant at 30 °C.

Identification Procedure

A desktop computer was used for the subsequent treatment of the measured and stored data. A program containing both the identification procedure and an in-core solver for the determinant equations with respect to the unknown coefficients was used to calculate the parameters and the fitted frequency response functions. Both functions (measurement and curve fit) could be displayed to estimate the quality of the identification algorithm (a typical readout is shown in fig. 7). The next step in data processing was to approximate the parameters for a fixed fluid velocity with dependence of the shaft speed by using polynomial equations. Only this last representation was used in finding the measurement results.

DISCUSSION OF RESULTS

The statements written down in this passage refer to figures 8 and 9. In both cases the identified values are presented as functions of the Reynolds numbers and in relation to the theory in order to compare the different seal geometries. Figure 8 demonstrates the influence of growing axial fluid velocity R_a and two seal clearances ($S_1 = 0.2$ mm, $S_2 = 0.4$ mm); figure 9 demonstrates the parameter changes for two seal lengths ($L_1 = 35$ mm, $L_2 = 23.5$ mm) and constant R_a . The following remarks are more general than those figures imply because they are influenced by further measurements not given in this paper.

Variation of Fluid Velocity and Shaft Speed

Higher shaft speed led to higher coefficients regardless of geometry. Mass and direct damping values were nearly independent of shaft speed, cross-coupled stiffness (x stiffness) and cross-coupled damping (x damping) were linearly related to shaft speed, and main stiffness was parabolically related. In the case of x -stiffness and x -damping the substantial aspect, higher gradients for higher velocities, is not as clear as the parallel shifts of the main damping and stiffness terms. The general behavior of the values is in good agreement with one of the theories (refs. 1 to 4), for both damping values (the x -damping is approximately a linear function of the shaft speed, but there is hardly an influence of the axial velocity) and the main stiffness coefficient. The inertia term and the x -stiffness differ distinctly from the expectations. According to theory the inertia term should be only slightly influenced by the velocity, and x -stiffness should show a remarkable increase with the flow.

Comparing the absolute values with the predicted parameters (calculated for our test rig with two seals, additional stiffnesses, and the mass of the housing) showed that the measurements overestimated the main stiffness (up to 15 percent) and the mass (up to 50 percent) and underestimated the x -stiffness clearly (up to 60 percent). These errors decreased with larger seal clearances and sometimes turned around. We may suppose that there could exist an optimal seal geometry with "zero error" to the theory. The measured damping values were always in good agreement with theory. The difference was within a 5 percent range. At this point we do not want to evaluate these results, but one remark should be permitted. In the case of the mass term there was a disadvantage we had to deal with: its theoretical value of about 2 kg for both seals was less than 7 percent of the additional mass of the housing. Probably the identification algorithm or the measurement system was not sensitive enough to reflect the proper values.

Influence of Seal Clearance

The good agreements between measurement and theory are evident for the examples in figure 8 for two clearances ($S_1 = 0.2$ mm, $S_2 = 0.4$ mm). In all cases the parameters followed the predictions although the results for the x -stiffness and the x -damping were better for larger clearances than for smaller one's. Increasing the clearance reduced all coefficients. The main aspects of fluid velocity and shaft speed are reproduced for all clearances.

Influence of Seal Length

The statements for seal length are the same as in the last paragraph. The behavior of all coefficients due to the shaft speed, the fluid velocity, and the seal length were comparable to the theory. Sometimes the deviations from the pre-calculations were slightly higher, but in general, short seals and larger clearance were in better agreement with theory than long seals and small clearances. Probably this can be explained by the pressure drop across the seal. Short seals and wide clearances produced small pressure drops and so less energy for the system's dynamic. The result was small stiffnesses and dampings, and so we were able to excite the system with the hammer easier as if there was a high pressure drop. Therefore the best measurable seal would be a short, wide annular seal.

CONCLUSIONS

From the results we can extract some tendencies, but some results do not fit into the theory for many reasons. First, the test system is complex. We only want to determine some special characteristics, and the influences of all others should be neglected or assumed to be well known in order to find out the right values. The lip rings are one great uncertainty. Some additional measurements without seal inserts and the exact application of the described method for this special case led to stiffness, damping, and inertia terms for the test setup. For example, the mass of the housing had been found out with this method with an error less than 5 percent to the weighted mass. We found setup damping and stiffness values that showed a distinct dependence on the fluid state in the lip rings (i.e., pressure and shaft speed clearly influence these parameters). But without searching for the roots of these coefficients we corrected the measured seal coefficients with them and found some interesting results:

1. The difference between theory and measurement was smaller than without the seal inserts.
2. The skew symmetry of the matrices improved.
3. The error in the mass term was constant.

The lip rings can presently be described as a conservative element with damping and stiffness attributes. But this should be verified in the near future.

The second critical remark touches the inlet swirl. We were not able to measure the circumferential velocity of the fluid at the entrance of the seal. For short seals we assumed a fully developed Couette flow with an inlet swirl of zero because of the geometric configuration of the test rig. This was not the case for longer seals, so that could explain once more some differences between theory and measurements.

REFERENCES

1. Black, H.F., "Effects of Hydraulic Forces in Annular Pressure Seals on the Vibrations of Centrifugal Pump Rotors", I.M.Eng. Sci., Vol. 11, No. 2, pp. 206-213, 1969
2. Black, H.F. and Jensen, D.N., "Dynamic Hybrid Properties of Annular Pressure Seals", Proc. J. Mech. Engin., Vol. 184, pp. 92-100, 1970.
3. Childs, D.W., "Dynamic Analysis of Turbulent Annular Seals Based on Hirs' Lubrication Equation", Journal of Lubrication Technology, ASME-Paper No. 82-Jub 41, 1982.
4. Childs, D.W., "Finite Length Solutions for Rotordynamic Coefficients of Turbulent Annular Seals", Journal of Lubrication Technology, ASME-Paper No. 82-Lub 42, 1982.
5. Childs, D.W. and Dressman J.B., "Testing of Turbulent seals for Rotordynamic Coefficients", NASA Conference Publication 2250, Rotordynamic Instability Problems of High Performance Turbomachinery, Proceedings of a workshop held at Texas A&M University, 10-12 May 1982, pp. 157-171, 1982.

6. Childs, D.W. et al, "A High Reynolds Number seal Test Facility: Facility Description and Preliminary Test Data", NASA Conference Publication 2250, Rotordynamic Instability Problems of High Performance Turbomachinery, Proceedings of a workshop held at Texas A&M University, 10-12 May 1982, pp. 172-186.
7. Iino, T. and Kaneko, H., "Hydraulic Forces by Annular Pressure Seals in Centrifugal Pumps", NASA Conference Publication 2133, Rotordynamic Instability Problems of High Performance Turbomachinery, Proceedings of a workshop held at Texas A&M University; 12-14 May 1980, pp. 213-225, 1980.
8. Kanki, H. and Kawakami, T., "Experimental Study on the Dynamic Characteristics of pump annular seals, Conference "Vibrations in Rotating Machinery", York 1984, C 297/84, IMechE 1984.
9. Nordmann, R. and Maßmann, H., "Identification of Stiffness, Damping and Mass Coefficients for Annular Seals, Conference "Vibrations in Rotating Machinery", York 1984, C280/84, IMechE 1984.
10. Nordmann, R. and Maßmann, H., "Identification of Dynamic Coefficients of Annular Turbulent Seals, "NASA Conference Publication 2338, Rotordynamic Instability Problems in High-Performance Turbomachinery 1984, Proceedings of a workshop, May 28-30, 1984, pp. 295-311.
11. Fritzen, C.-P., "Identification of Mass, Damping and Stiffness Matrices of Mechanical Systems", submitted to 10th ASME Conference on Mechanical Vibration and Noise, Sept. 85, Cincinnati

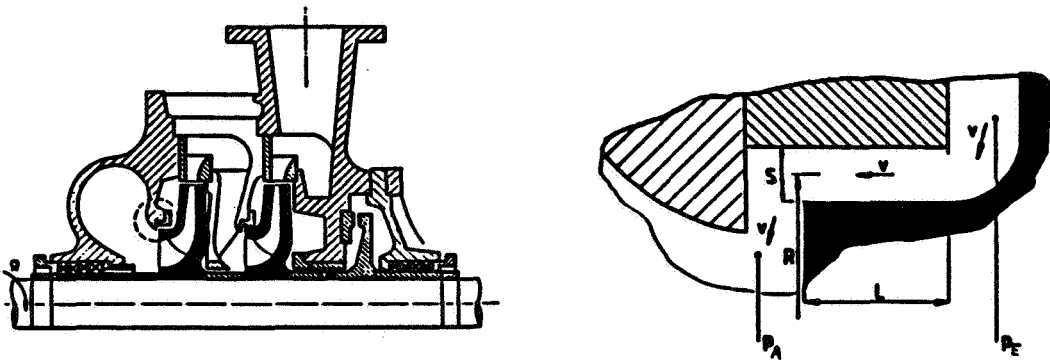


Figure 1. - Annular seal types in turbopumps.

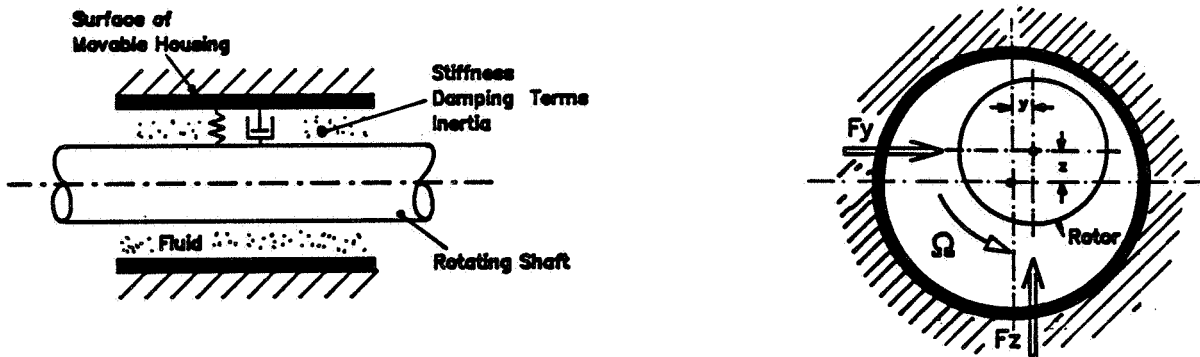


Figure 2. - Hydraulic forces in seal.

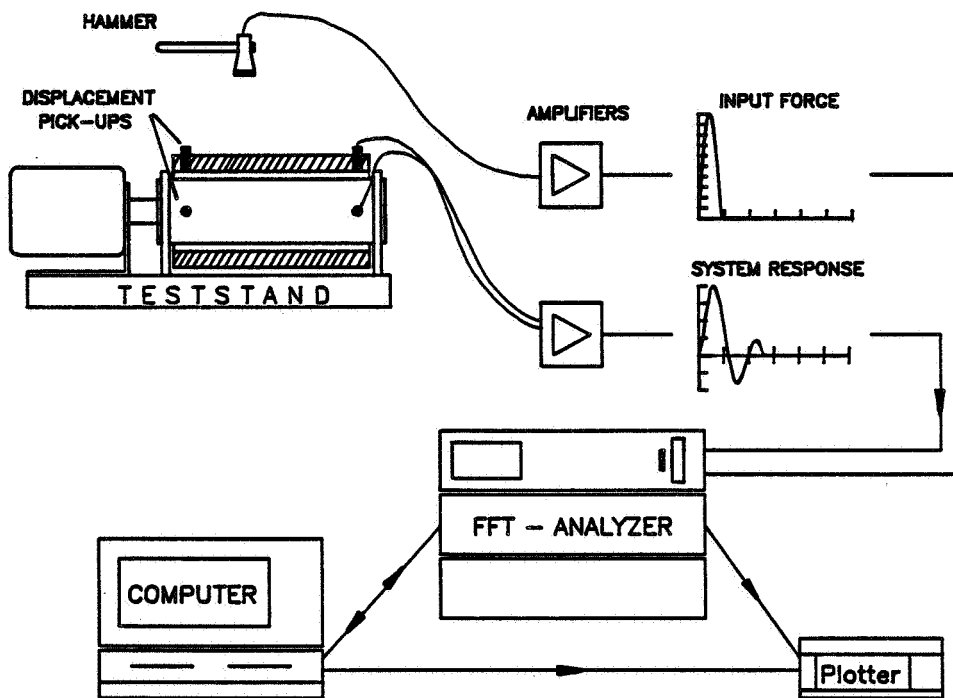


Figure 3. - Data acquisition and processing.

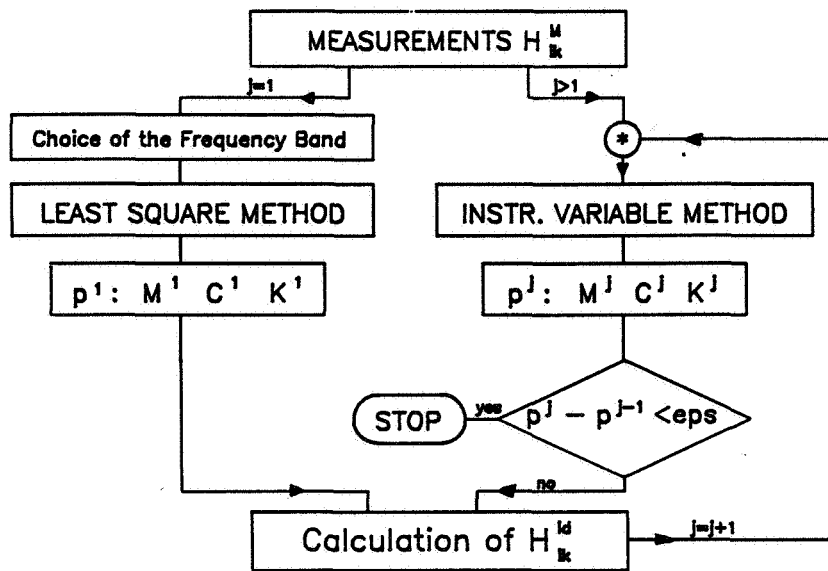


Figure 4. - Principle of instrumental variable method.

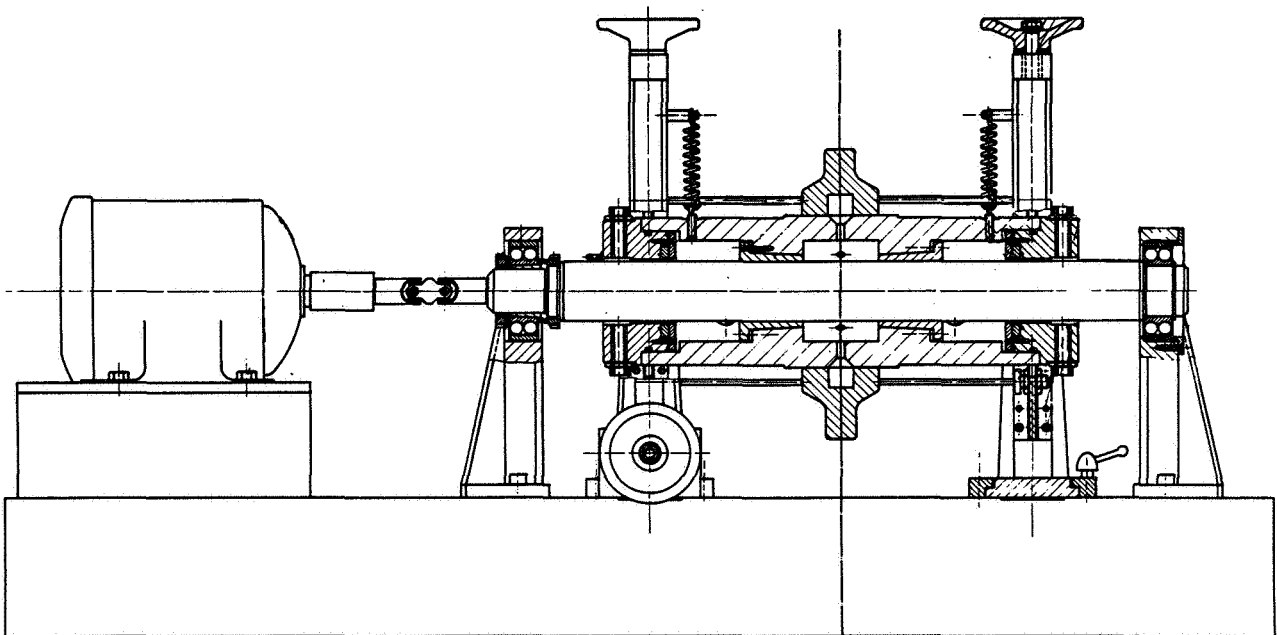


Figure 5. - Cross section of test rig.

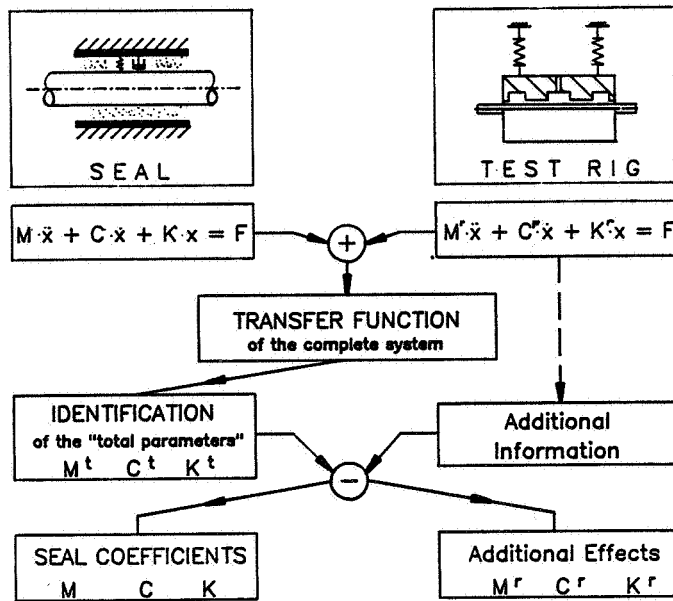


Figure 6. - Adaptation of theoretical considerations to real system.

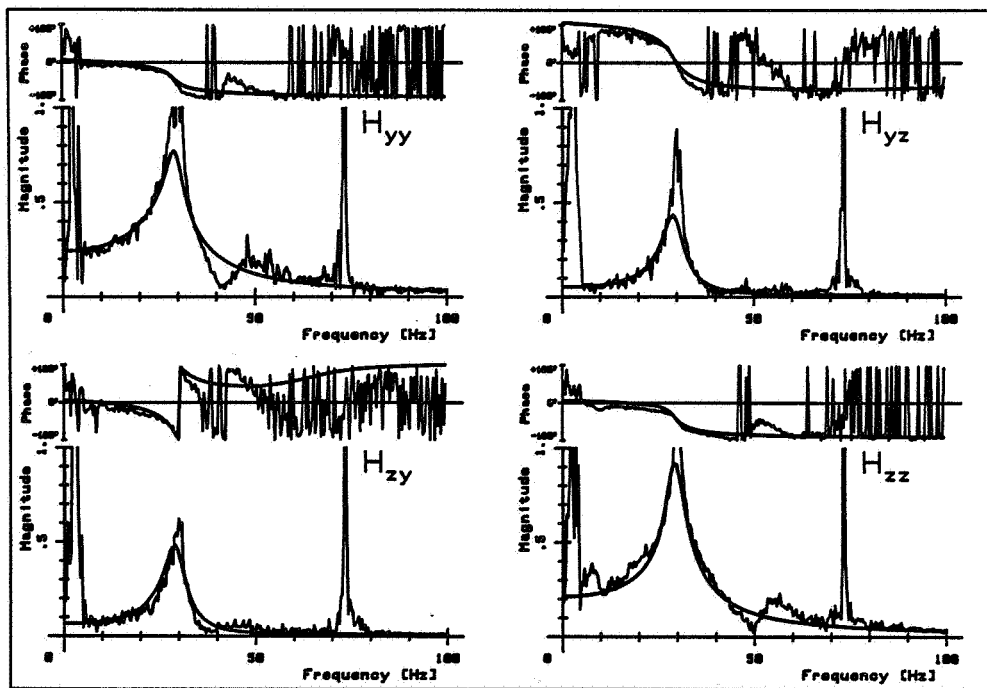


Figure 7. - Example of measurements and curve-fit data.

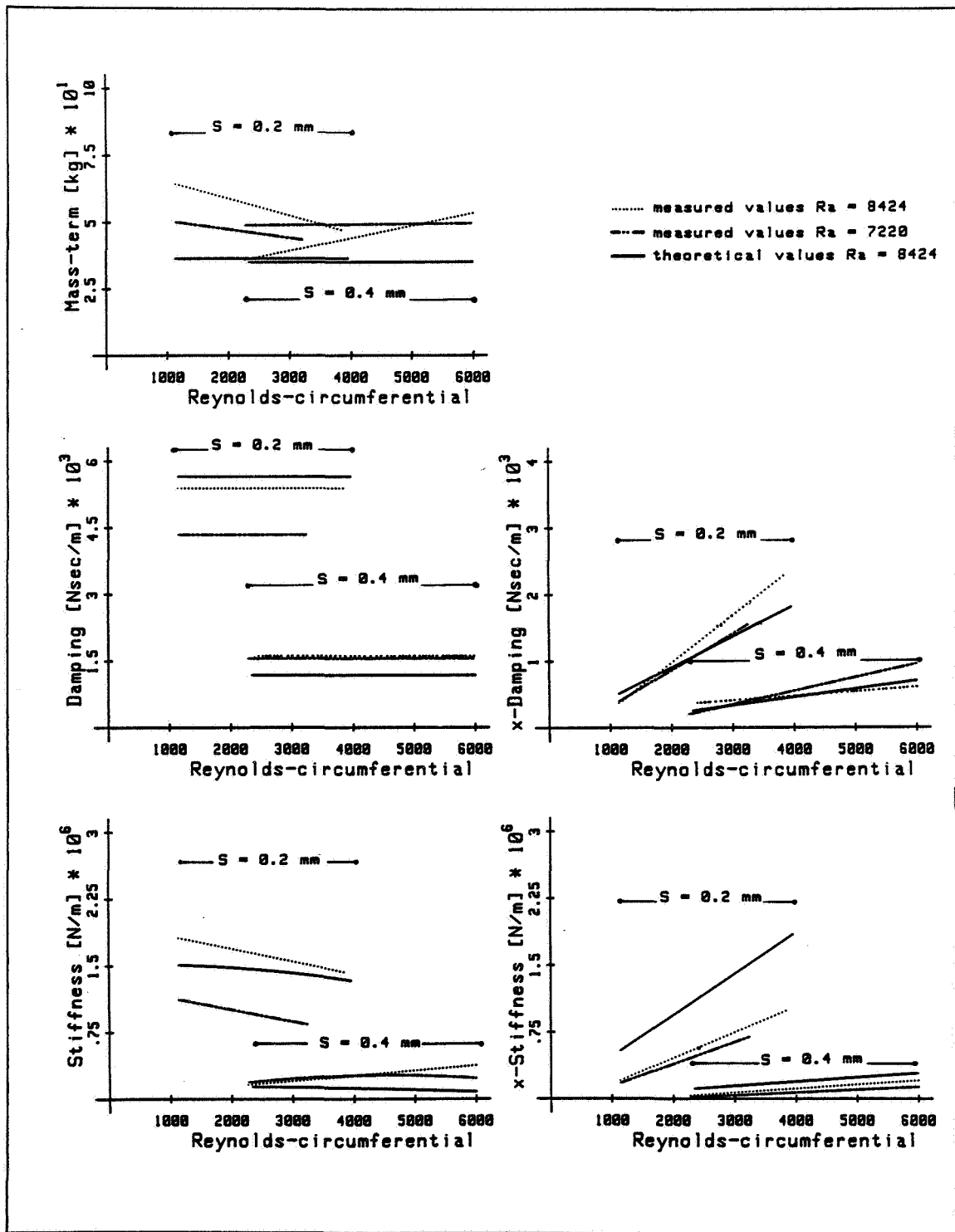


Figure 8. - Influence of seal clearance S for $L = 35$ mm and $T = 30$ °C.

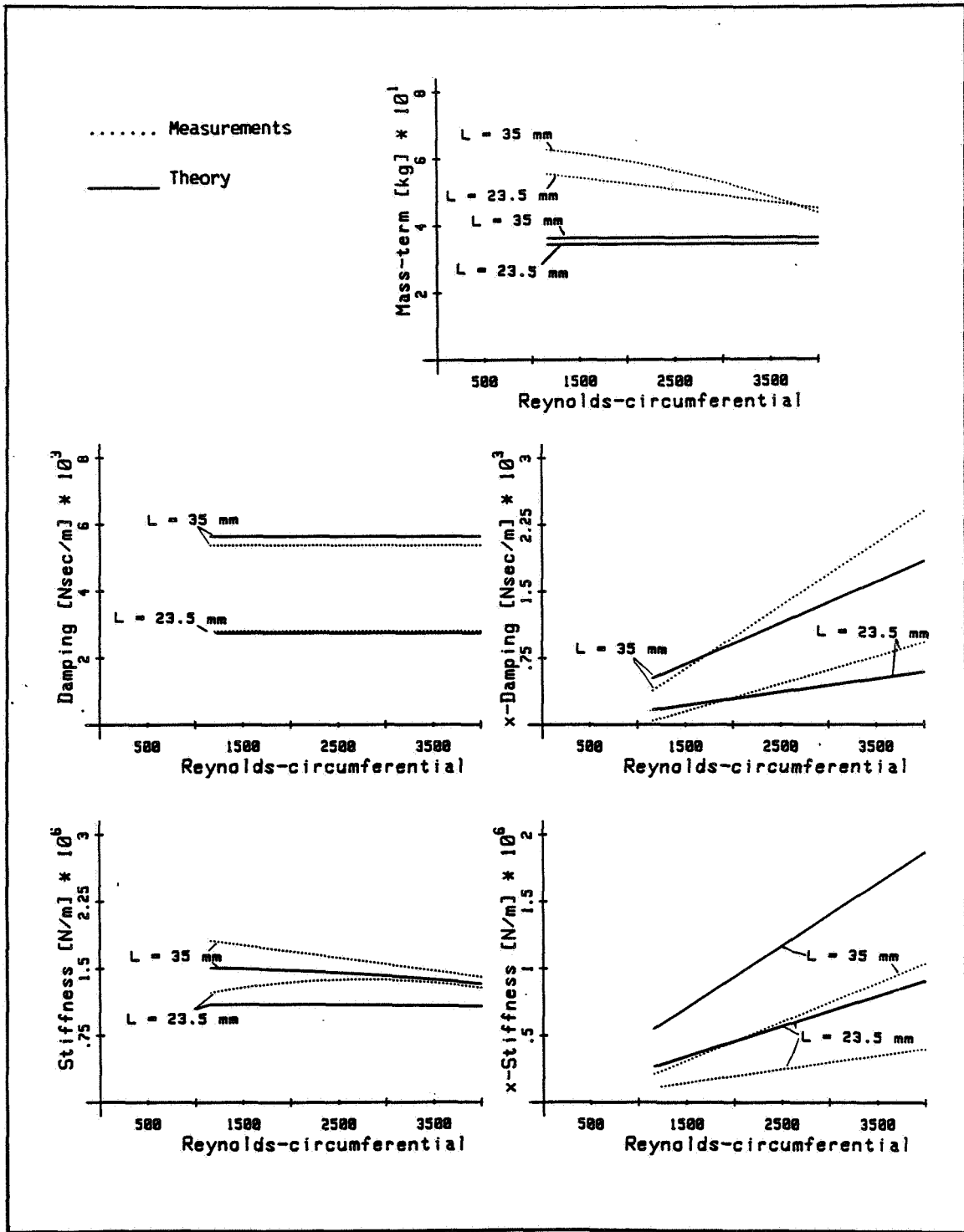


Figure 9. - Influence of seal length L for $S = 0.2 \text{ mm}$, $R_a = 8424$, and $T = 30 \text{ }^\circ\text{C}$.

ANALYTICAL PREDICTION OF LABYRINTH-SEAL-FLOW-INDUCED ROTOR EXCITATION FORCES

C. Rajakumar and E. Sisto
 Stevens Institute of Technology
 Hoboken, New Jersey 07030

An analytical method to calculate the rotor excitation forces arising from labyrinth seals is presented. The objective is to model the gas flow through the seal clearance passages and cavities when the rotor is positioned eccentric relative to the stator center. The seal flow model used in the analysis yields solutions which validate the experimentally observed influence of seal parameters on seal forces reported in the literature. The analytically predicted seal pressure distributions and forces have been compared with published experimental results.

INTRODUCTION

While performing the function of sealing, labyrinth seals have been identified as a potential source of destabilizing forces which cause self excited rotor whirl of turborotors. Typically these seals are employed to effect sealing of the working fluid between two stages of a compressor or turbine and in adjacent cooling air compartments which are maintained at different pressures. Labyrinth seals which have a configuration as shown in figure 1 are designed to minimize the leakage flow by successively expanding the gas past the orifice-like clearance passages at the seal fin locations.

An analytical model describing the excitation of turborotors by labyrinth seals was first published by Alford (ref. 1). In the recent literature (ref. 2 to 7) experimental and analytical methods of predicting labyrinth seal forces have been reported. Experimental results presented by Benckert and Wachter (ref. 2) show that a restoring force along the line of centers and a lateral force normal to the line act on the rotor when the rotor center is displaced to an eccentric position with respect to the seal center as shown in figure 2. The present work is aimed at analytically predicting these seal forces which result from the circumferentially varying pressure distributions within the seal cavities.

SYMBOLS

C	seal radial clearance
Cc	orifice flow coefficient
Ce	energy recovery factor
Co	nominal radial clearance
e	rotor eccentricity
e _r	eccentricity ratio (e/Co)
f	circumferential flow area
Fr, Ft	radial and tangential seal forces
h	seal fin height

l	cavity width
m	number of circumferential nodes
N	rotor rpm
n	number of seal fins
P	pressure (Po- seal inlet, Pe- seal exit)
q	axial mass flow rate per unit circumferential length
R	gas constant
Re	reynolds number
Rs	rotor radius
t	axial pitch
T	gas temperature
u	circumferential flow velocity
u _o	inlet swirl velocity
U	length of wetted surface
α	flow coefficient
λ	friction coefficient at the walls
μ	coefficient of viscosity
φ	reference angle shown in figure 2
ρ	gas density
τ	shear stress
θ	circumferential coordinate
ω	angular velocity of rotor rotation
Subscripts	
i	fin and cavity number designations
j	circumferential node number
r	rotor
s	stator

GOVERNING EQUATIONS

The intricate flow path of labyrinth seals, combined with the asymmetry caused by rotor eccentricity complicate the analysis employing fundamental fluid mechanics governing equations. A relatively simpler set of labyrinth seal governing equations derived by Kostyuk (ref. 8) are employed in the analysis here. For the fluid macro-element shown in figure 1, the following conservation of mass and circumferential momentum equations are derived, neglecting the curvature effect for small clearance-to-radius ratios.

$$\frac{\partial}{\partial t} (\rho_i f_i) + \frac{1}{R_s} \frac{\partial}{\partial \theta} (\rho_i u_i f_i) + (q_{i+1} - q_i) = 0 \quad (1)$$

$$\begin{aligned} & \frac{\partial}{\partial t} (\rho_i u_i f_i) + \frac{1}{R_s} \frac{\partial}{\partial \theta} (\rho_i u_i^2 f_i) + (q_{i+1} u_i - q_i u_{i-1}) \\ & = - \frac{f_i}{R_s} \frac{\partial P_i}{\partial \theta} + (\tau_{r_i} U_{r_i} - \tau_{s_i} U_{s_i}) \end{aligned} \quad (2)$$

Frictional resistance at the seal walls are calculated using the following relationships.

$$\tau_{si} = \lambda_{si} \frac{\rho_i u_i^2}{2}, \quad \tau_{ri} = \lambda_{ri} \frac{\rho_i (\omega R_s - u_i)^2}{2} \quad (3)$$

where:

$$\lambda = \frac{8}{Re} \quad 0 < Re \leq 1000, \quad \lambda = \frac{0.045}{Re^{.25}} \quad 1000 < Re$$

The Reynolds numbers are given by:

$$Re_{si} = \frac{|u_i| h_i \rho_i}{2\mu}, \quad Re_{ri} = \frac{|\omega R_s - u_i| h_i \rho_i}{2\mu} \quad (4)$$

Proper signs are attached to the friction coefficient λ based on the relative velocity of the fluid with respect to the rotor and stator walls. Assuming isothermal flow process, Martin's (ref. 9) leakage flow equation for small pressure drop across each fin is given by:

$$q_i = \alpha_i (p_{i-1}^2 - p_i^2)^{.5} \quad (5)$$

where:

$$\alpha_i = \frac{1}{\sqrt{RT}} \frac{Cc_i}{(1-Ce_i)^{.5}} \quad (6)$$

Orifice flow coefficients Cc for annular orifices presented by Vermes (ref. 10) have been used in the calculations. The residual energy factor Ce accounts for the part of the kinetic energy in the leakage flow from the $(i-1)$ th orifice that is present at the inlet to the i -th orifice. Representing the orifice flow by one half of a flat symmetrical jet, Vermes (ref. 10) derived the following expression for the residual energy factor:

$$Ce_i = \frac{8.52}{(l_i/C_i) + 7.23} \quad (7)$$

Equations (1), (2), (5) and the ideal gas relationship

$$P_i = \rho_i RT \quad (8)$$

form the system of equations to be solved for the circumferential pressure distribution resulting due to the rotor eccentricity. Although figure 1 shows fins on the rotor, the equations derived are also valid for a labyrinth with fins on the stator.

NUMERICAL PROCEDURE

For the rotor undergoing steady rotational motion about a given eccentric position (fig. 2), we can drop off the time derivative terms in equations (1) and (2). After substituting for q_i and p_i from equations (5) and (8), equations (1) and (2) become:

$$\frac{1}{RTRs} \frac{d}{d\theta} (P_i u_i f_i) + \alpha_{i+1} C_{i+1} (P_i^2 - P_{i+1}^2) \cdot 5$$

$$- \alpha_i C_i (P_{i-1}^2 - P_i^2) \cdot 5 = 0 \quad (9)$$

$$\frac{1}{RTRs} \frac{d}{d\theta} (P_i u_i^2 f_i) + \alpha_{i+1} C_{i+1} (P_i^2 - P_{i+1}^2) \cdot 5 u_i$$

$$- \alpha_i C_i (P_{i-1}^2 - P_i^2) \cdot 5 u_{i-1} + \frac{f_i}{R_s} \frac{dP_i}{d\theta} + (\tau_{si} U_{si} - \tau_{ri} U_{ri}) = 0 \quad (10)$$

The seal clearance and circumferential flow area for the eccentric rotor configuration are given by:

$$C_i = C_{o_i} - e \cos\theta \quad (11)$$

$$f_i = l_i (h_i + C_{o_i} - e \cos\theta) \quad (12)$$

Equations (9) and (10) are nonlinear ordinary differential equations to be solved to get the pressure and velocity distributions, $p_i(\theta)$ and $u_i(\theta)$ in each seal cavity.

After introducing the central finite difference approximations given below we divide the circumferential coordinate length, $R_s\theta$ into m equal parts.

$$\frac{dP_i}{d\theta} = \frac{P_{ij+1} - P_{ij-1}}{2\Delta\theta} \quad (13)$$

$$\frac{du_i}{d\theta} = \frac{u_{ij+1} - u_{ij-1}}{2\Delta\theta} \quad (14)$$

The resulting system of nonlinear algebraic equations are represented symbolically as:

$$F(P_{ij}, u_{ij}) = 0 \quad (15)$$

$$G(P_{ij}, u_{ij}) = 0 \quad i=1,2..(n-1) \quad j=1,2..m \quad (16)$$

Equations (15) and (16) are solved employing the Newton Raphson iteration procedure in the multidimensional space formed by the variables P_{ij} and u_{ij} . After dropping the second and higher order terms from the Taylor series expansions of equations (15) and (16), we arrive at the iteration scheme given by:

$$\begin{Bmatrix} P_{ij} \\ u_{ij} \end{Bmatrix}_{k+1} = \begin{Bmatrix} P_{ij} \\ u_{ij} \end{Bmatrix}_k - \begin{bmatrix} \frac{\partial F}{\partial P_{ij}} & \frac{\partial F}{\partial u_{ij}} \\ \frac{\partial G}{\partial P_{ij}} & \frac{\partial G}{\partial u_{ij}} \end{bmatrix}_k^{-1} \begin{Bmatrix} F(P_{ij}, u_{ij}) \\ G(P_{ij}, u_{ij}) \end{Bmatrix}_k \quad (17)$$

By assuming an initial guess for the vector $[P_{ij} u_{ij}]_k$, the Jacobian matrix and the function values are evaluated to calculate the new vector of variables $[P_{ij} u_{ij}]_{k+1}$. The iterations are continued until the change in each component of the solution vector is less than a predetermined error value. The seal forces are obtained by integration of the pressure distribution over the rotor surface using the summation equations given by:

$$F_r = R_s \Delta \theta \sum_{i=1}^{n-1} l_i \sum_{j=1}^m P_{ij} \cos \theta_j \quad (18)$$

$$F_t = R_s \Delta \theta \sum_{i=1}^{n-1} l_i \sum_{j=1}^m P_{ij} \sin \theta_j \quad (19)$$

RESULTS

Seal cavity pressure distributions obtained were compared with the experimental results of Leong and Brown (ref. 4) shown in figure 3. The 11-cavity seal having fins on the stator with inlet and exit pressure of $P_o=2.914$ bar, $P_e=1$ bar was investigated at a rotor speed of 7504 rpm and eccentricity ratio of 0.6. The analytically predicted pressure distribution patterns in the first two seal cavities are in agreement with the experimentally measured patterns, with a peak pressure occurring near the 180 degrees location in the first cavity while the pressure is minimum near this location in the second cavity. Pressure levels predicted by the theory beyond the first three cavities are in fair agreement with the experimental results. The difference in cavity pressure levels between the theory and experiment is attributable to possible difference between the orifice flow coefficients used in the calculations and the actual flow coefficients in the experiment. Also, possible random variations of the seal clearance at successive fin locations in the test seal could contribute to the difference between the experimental and analytical results.

The experimental results of Benckert and Wachter (ref. 2) were used to verify the seal forces calculated analytically. Figures 5 and 6 show the variation of seal forces with eccentricity ratio for a 17-cavity seal with fins on the stator. Tangential forces generated when the rotor rotates at 9482 rpm and 4773 rpm, for the seal inlet and exit pressures of $P_o=1$ bar, $P_e=1$ bar are shown in figure 4(a). The negative eccentricity ratios indicate that the rotor center has been displaced along the negative x-axis in figure 2. The analytically predicted tangential seal forces are in good agreement with the experimental results showing an average deviation of about 16 percent, excluding the zero eccentricity ratio case where the experimental results show a nonzero force. Radial forces predicted by the analysis are shown in figure 4(b); experimental results on radial forces were not reported in the reference for the case investigated. These results show that the seal force magnitudes increase with rotor rotational speed for any given eccentricity ratio. The tangential forces act in a direction that would initiate or promote forward whirl motion of the rotor center. The radial forces are decentering where they tend to push the rotor away from the seal center.

The seal forces variation with eccentricity ratio for zero rotor speed, but nonzero swirl velocity at the seal inlet are presented in figures 5(a) and 5(b). The seal pressures in this case are $P_o=2.041$ bar, $P_e=1$ bar. The tangential seal forces have been predicted quite close to the experimental results, the maximum difference being 17 percent. The radial forces from the experiment, again were not

reported in the reference. The two different inlet swirl velocities investigated show that the seal forces increase with the inlet swirl velocity and appreciable magnitudes of tangential forces are generated which would promote forward whirl instability in rotor systems. The radial forces in this case are of relatively small magnitude and they act in a centering direction tending to restore the rotor center back to the seal center.

CONCLUSIONS

Employing the seal flow governing equations derived by Kostyuk (ref. 8), methods of predicting seal forces for an infinitesimal eccentricity have been reported in the literature where seal stiffness coefficients are presented. In this analysis the radial and tangential components of seal forces for large eccentricity ratios have been predicted, for the first time, employing Kostyuk's equations. The analysis yields results which validate the experimentally observed variation of seal forces with rotor eccentricity, inlet swirl velocity and rotor rotational speed. The tangential force components predicted by the theory, especially the swirl flow-induced forces are in good quantitative agreement with the experimental results. The analysis also shows the nonlinear dependence of the forces with eccentricity beyond $e \approx .4$. This behavior needs to be given appropriate consideration in large amplitude rotor dynamic investigations where nonlinear stability problems may be encountered.

REFERENCES

1. Alford, J.S.: Protecting Turbomachinery From Self Excited Rotor Whirl. ASME Journal of Engineering for Power, Vol. 87, No. 4, Oct. 1965, pp. 333-344.
2. Benckert, H.; and Wachter, J.: Flow Induced Spring Coefficients of Labyrinth Seals for Application in Rotor Dynamics. NASA CP 2133, 1980, pp. 189-212.
3. Hauck, L: Exciting Forces Due to Swirl Type Flow in Labyrinth Seals. Proceedings of the IFTOMM Conference on Rotordynamics, Rome, Sept. 1982.
4. Leong, Y.M.M.S.; and Brown, R.D.: Circumferential Pressure Distributions in a Model Labyrinth Seal. NASA CP 2250, 1982, pp. 223-241.
5. Leong, Y.M.M.S.; and Brown, R.D.: Experimental Investigations of Lateral Forces Induced by Flow Through Model Labyrinth Glands. NASA CP 2338, 1984, pp. 187-210.
6. Murphy, B.T.; and Vance, J.M.: Labyrinth Seal Effects on Rotor Whirl Instability. Institution of Mechanical Engineers CP C306/80, 1980, pp. 369-373.
7. Wright, D.V.: Labyrinth Seal Forces on a Whirling Rotor. ASME Publication on Rotor Dynamical Instability AMD, Vol. 55, 1983, pp. 19-31.
8. Kostyuk, A.G.: A Theoretical Analysis of the Aerodynamic Forces in the Labyrinth Glands of Turbomachines. Teploenergetica, 19(11) 29-33, 1972, pp. 39-44.

9. Martin, H.M.: Labyrinth Packings. Engineering, Vol. 85, Jan. 10, 1908, pp. 35-38.
10. Vermes, G: A Fluid Mechanics Approach to the Labyrinth Seal Leakage Problem. ASME Journal of Engineering for Power, Vol. 83, April 1961, pp. 161-169.

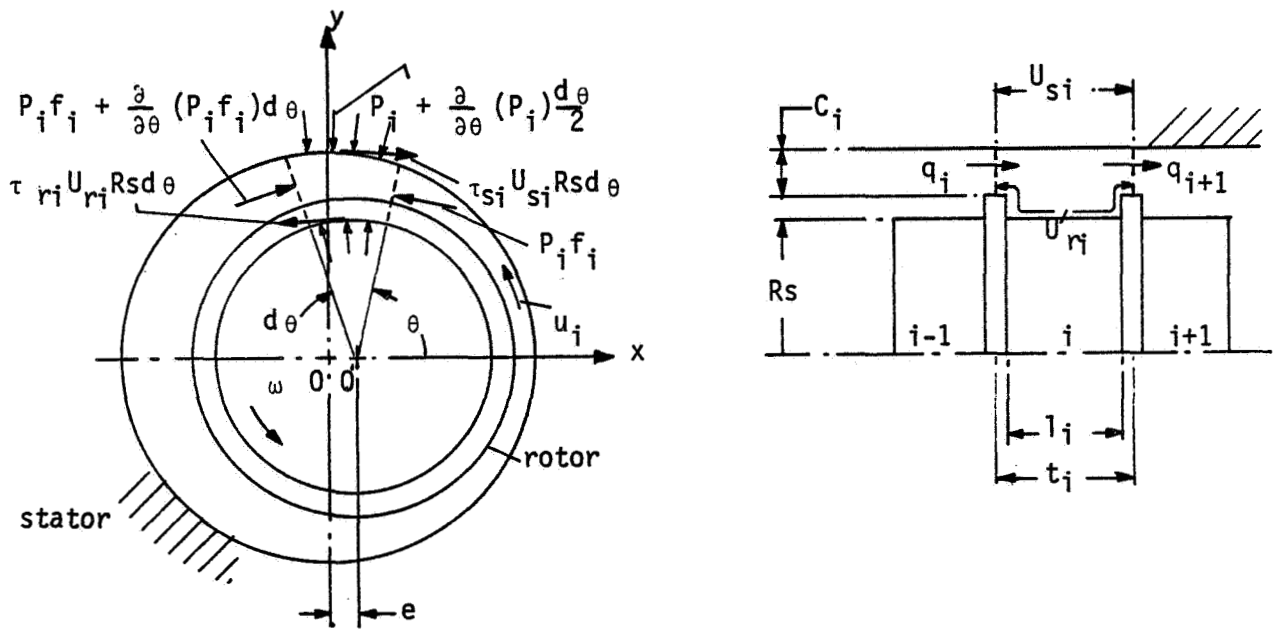


Figure 1. - Labyrinth seal fluid element.

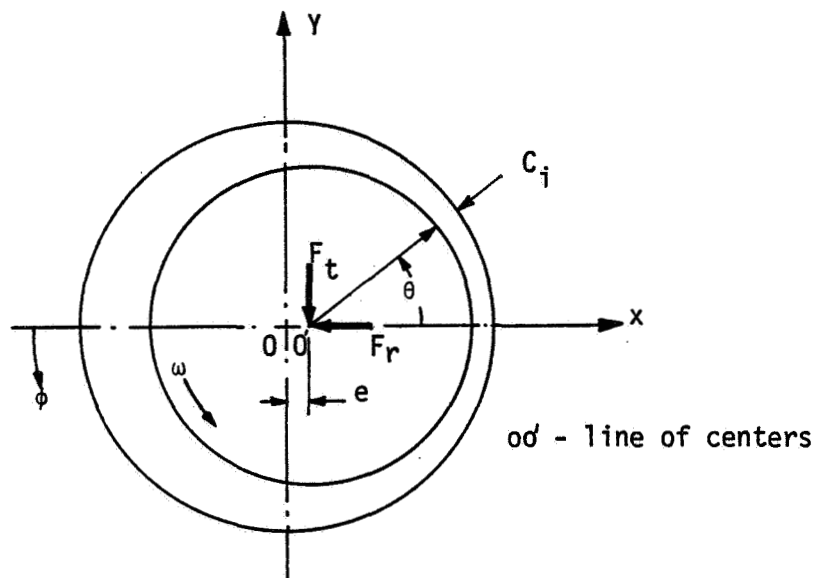


Figure 2. - Seal forces.

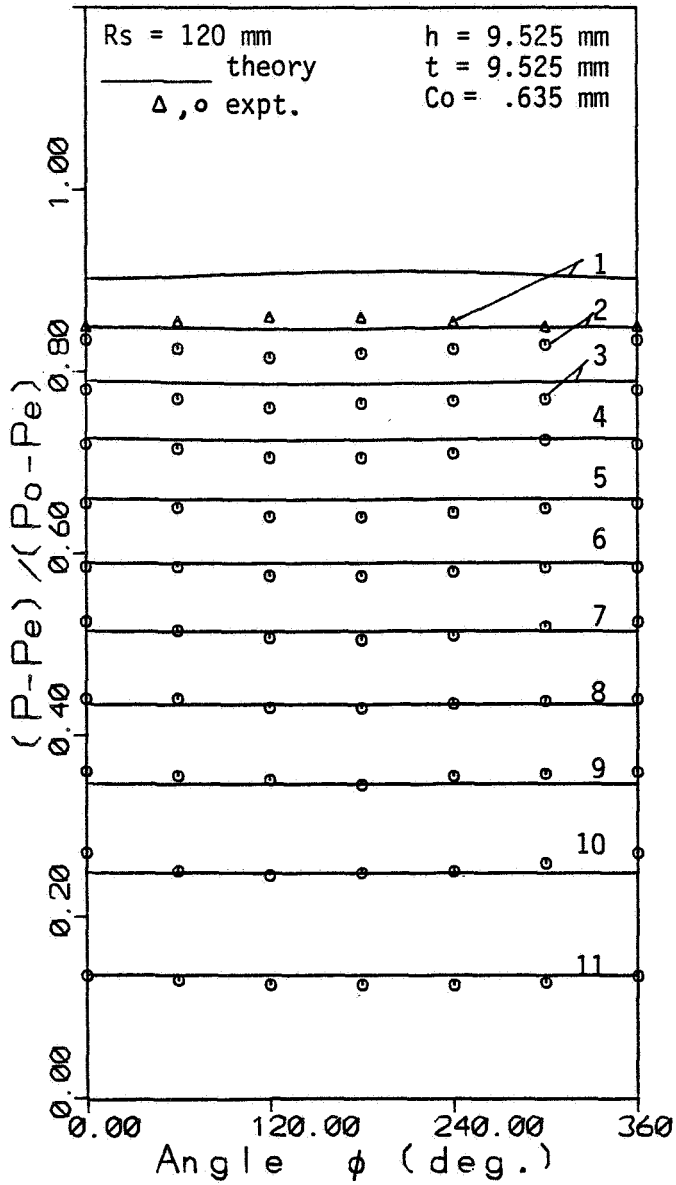


Figure 3. - Seal pressure distribution.

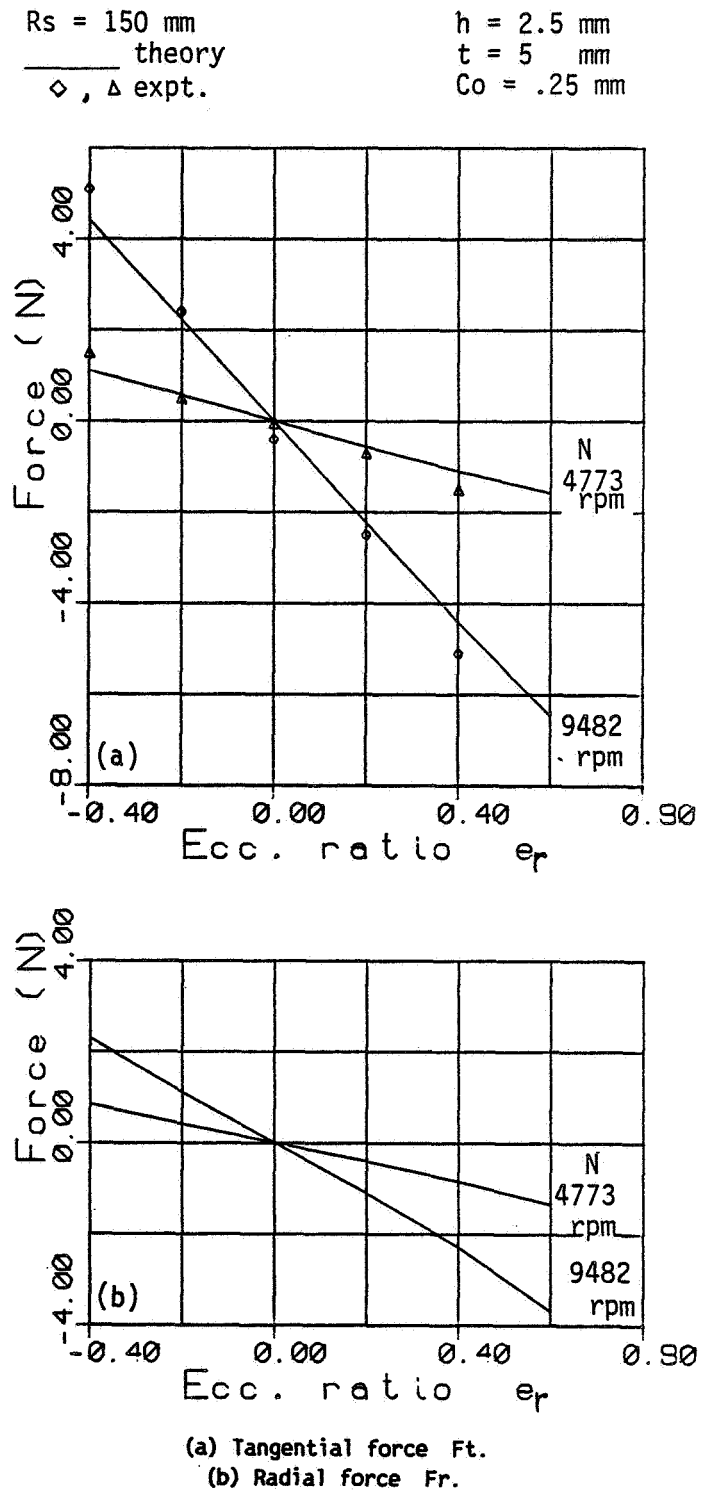
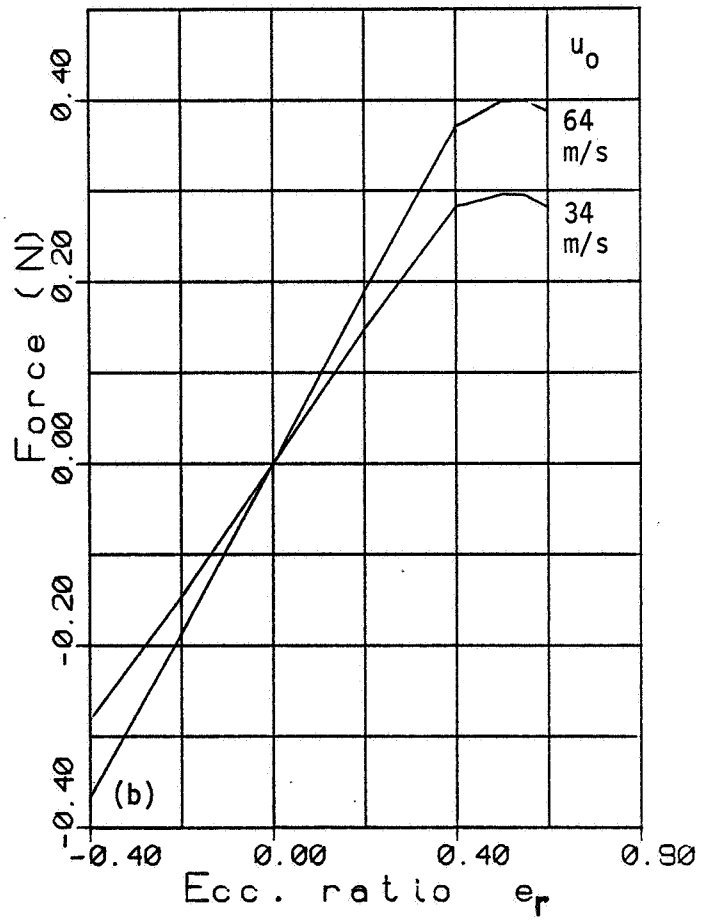
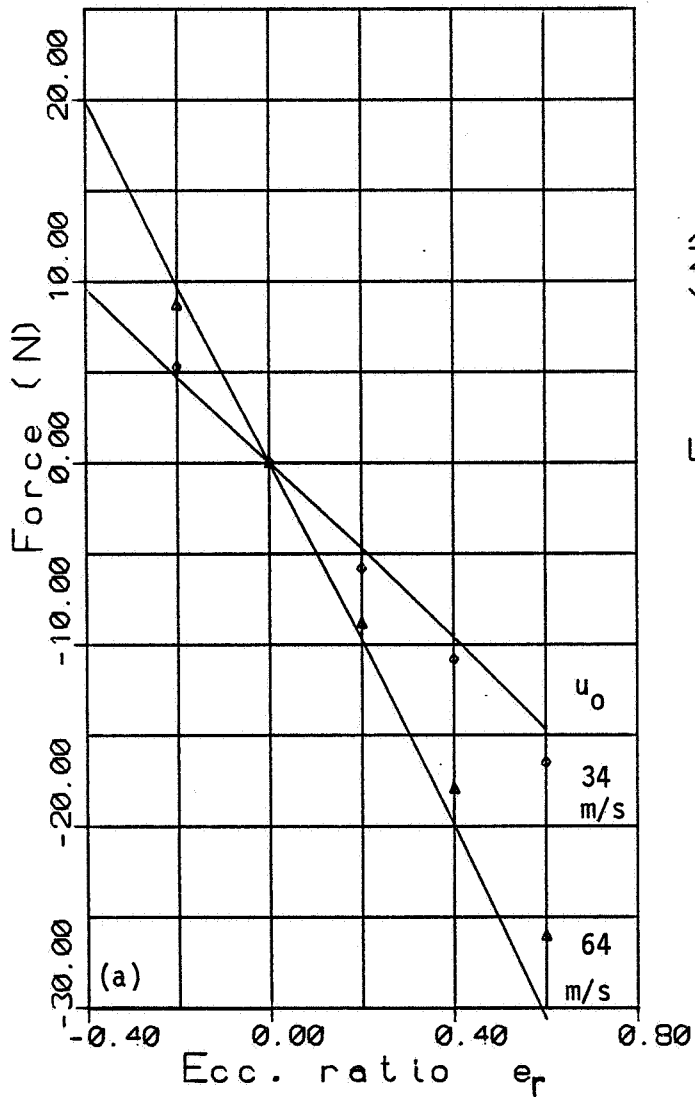


Figure 4. - Seal forces with variable rotor speed.

Rs = 150 mm
 — theory
 ◇, △ expt.

h = 2.5 mm
 t = 5 mm
 Co = .25 mm



(a) Tangential force F_t .
 (b) Radial force F_r .

Figure 5. - Seal forces with variable inlet swirl velocity.

OIL SEAL EFFECTS AND SUBSYNCHRONOUS VIBRATIONS IN HIGH-SPEED COMPRESSORS

Paul E. Allaire and John A. Kocur, Jr.
 University of Virginia
 Charlottesville, Virginia 22901

Oil seals are commonly used in high speed multistage compressors. If the oil seal ring becomes locked up against the fixed portion of the seal, high oil film crosscoupled stiffnesses can result. This paper discusses a method of analysis for determining if the oil seals are locked up or not. The method is then applied to an oil seal in a compressor with subsynchronous vibration problems.

NOMENCLATURE

<u>Symbol</u>	<u>Definition</u>
A_r	Unbalanced Seal Ring Area
c_j	Tilting Pad Bearing Clearance
c_r	Oil Seal Ring Clearance
D	Shaft Diameter
e_j	Shaft Eccentricity in Bearing
e_r	Shaft Eccentricity in Oil Seal Ring
F_{rmax}	Maximum Available Radial Friction Force Acting on Oil Seal Ring
L	Seal Length
n	Pressure Law Power
N	Shaft Speed (RPM)
N_d	Shaft Speed at Design Conditions
O_s	Shaft Centerline
O_r	Oil Seal Ring Centerline
P	Pressure Drop Across Oil Seal
P_d	Pressure Drop Across Oil Seal at Design Conditions
Re	Reynolds Number Based on Clearance
W_r	Oil Seal Ring Weight
x_j, y_j	Horizontal and Vertical Positions of the Shaft Centerline (Relative to the Bearing Centerline)
x_r, y_r	Horizontal and Vertical Positions of the Oil Seal Ring Centerline (Relative to the Bearing Centerline)
ϵ_j	Shaft Eccentricity Ratio ($\epsilon_j = e_j/c_j$)
ϵ_r	Oil Seal Ring Eccentricity ($\epsilon_r = e_r/c_r$)
ϕ_j	Shaft Attitude Angle (Relative to the Load Vector)
ϕ_r	Oil Seal Ring Attitude Angle (Relative to the Load Vector)
μ_s	Coefficient of Static Friction On Oil Seal Ring Face
ω	Shaft Angular Velocity (rad/sec)
μ	Viscosity

INTRODUCTION

Oil seals are frequently used in compressors to minimize the leakage of the process gas into the atmosphere. The type of design discussed in this work has a seal ring which permits a limited axial flow under the ring to produce a pressure drop.

If the desired pressure drop across the seal ring is adequate, only one seal ring is employed. The seal ring is part of the non-rotating component of the compressor seal assembly. The clearances involved are small - on the order of bearing clearances - so the flow can be analysed by Reynolds equation in one form or another. It differs from conventional bearing analysis because there is an axial pressure gradient which can have a significant effect on the oil film properties.

It is observed in the field that some compressors with oil seal rings are subject to subsynchronous vibration while others are not. The key feature of the oil seal ring is the stiffness and damping coefficients developed by the fluid film between the rotating shaft and non-rotating seal ring. Often the seal ring is designed to orbit with the shaft as it vibrates (rotation is prevented by some pin or other device which still allows radial ring motion). If the seal ring orbits with the shaft, the oil film force, and thus the dynamic coefficients, between the shaft and ring are necessarily very small. However, the compressor may still be unstable due to effects other than the oil seals such as labyrinth seals between the compressor wheels in a multistage compressor or aerodynamic crosscoupling associated with the flow near the wheels themselves. Alternatively, the seal rings may be prevented from moving (called seal ring lockup) due to one effect or another. This in turn causes large oil film forces to act between the shaft and ring which may produce large stiffness and damping coefficients. If the crosscoupled stiffness coefficient is high enough, the oil seals can cause subsynchronous vibration by themselves or contribute to it with other effects.

Kirk and Miller [1] reported on the effect of oil seals on instability in compressors. They presented a method of analysis for low Reynolds number axial flow seals where the axial flow is neglected. Stiffness and damping coefficients were developed for short cavitated and noncavitated lubricant films. Also a time transient analysis method was shown for evaluating the operating eccentricity of such seals. Kirk and Nicholas [2] extended the analysis to include a heat and flow balance.

Emerick [3] discussed a compressor case history where shaft vibrations were a problem. Over time the rotor vibrations increased until the machine had to be shut down. After extensive measurements and calculations, it was found that large subsynchronous vibrations were caused by wear to one of the seal components which eventually lead to seal ring lockup. Modifications were made to reduce the wear and to pressure balance the seal to permit shaft tracking. Other references on compressor subsynchronous vibration [4,5] discuss possible effects of oil seals. Usually such seals orbit (float) with the shaft so that lockup problems do not occur. In some cases, seals which appeared to cause the problems were changed with no reduction in vibration.

This paper discusses the action of oil seal rings in a compressor subject to subsynchronous vibration problems. While the vibration problems were not severe, it was desired to remove the subsynchronous component of vibration if possible to prevent future problems. The main purpose of the paper is to discuss the operation of the oil seal and its dynamic coefficients. The effects of seal ring lockup, determination of stiffness and damping coefficients, interaction of seals with bearings (tilting pad), and the final influence on the compressor are discussed. Some of the differences between this and previous works include the quasi-steady state method of determining the lockup conditions, the effect of axial pressure gradient, and the seal ring/bearing interactions.

DESCRIPTION OF COMPRESSOR AND OIL SEAL GEOMETRY

The example centrifugal compressor considered in this paper is driven by a steam turbine through a flexible gear type coupling. The compressor has six closed face impellers as shown in Figure 1. The shaft is mounted between bearings in a straight through design with the bearings located at the ends. It also has oil seals inside the bearings and a balance piston at the stepped region of the shaft. Rotor weight is 1620 lbs and the bearing span is 68 inches. The bearing configuration is a 5 pad, tilt pad design with load on pad. The journal diameter is 4.5 inches and the bearing L/D ratio is 0.44. Bearing preload ranges from 0.45 to 0.55 and installed diametral clearance ranges from 0.005 inches to 0.007 inches. The rotor is designed to run at 9800 RPM and has a rigid bearing first critical speed at 3900 RPM.

At speeds above 9000 RPM, subsynchronous whirl was observed at a frequency of 4200 RPM. Figure 2 shows the subsynchronous and synchronous vibration components at a running speed of 9210 RPM. The amplitude of the subsynchronous vibration was erratic and occasionally, without warning, would spike at two to three times its usual level. A waterfall diagram could not be obtained for this compressor because of the startup and shutdown procedures.

The oil seals are located just inboard of the bearings and are each composed of two rings mounted axially on the shaft with close running clearance. The outboard side of each ring forms a face seal with the stationary seal housing and is kept from rotating by an anti-rotation pin, figure 3.a. Oil is introduced between the rings at a pressure slightly above compressor suction pressure. Part of the oil flows through the shaft-to-ring clearance on the process gas side and is carried off by the process gas. The remainder of the oil flows through the shaft-to-ring clearance on the ambient side and is returned to the oil reservoir. The inner ring seals against process gas leakage while the outer ring limits seal oil leakage to the outside.

QUASI-STATIC SEAL RING LOCKUP ANALYSIS

The purpose of this section is to describe the method of calculating seal lockup conditions. As the oil film crosscoupled stiffness coefficients vary strongly with shaft position relative to the oil seal ring, it is important to have a method of estimating the positions during actual lockup and then during running conditions. A quasi-static method, now presented, is used.

Because the Reynolds number is quite small for these lubricant flows, it is assumed here that the inertia forces are small compared to the viscous forces. The transient motions of the seal ring and shaft (up to the threshold of instability at least) are relatively quickly damped without inertia forces. Thus the shaft has a small orbit around the steady state operating eccentricity of either the seal ring or tilting pad bearing. Relative sizes may be found in Emerick [3] where the shaft vibration (after removal of the subsynchronous instability) was about 0.00254 mm (0.1 mils) as compared to the seal ring clearance of 0.0508-0.0762 mm (2-3 mils). A typical lockup eccentricity ratio of 0.5 gives a ratio of shaft vibration to steady state eccentricity of approximately 0.08. Thus the analysis can be reasonably approximated as a quasi-static analysis rather than a transient analysis such as described in [1]. This provides a first evaluation to determine the dynamic coefficients. If desired, the transient analysis can still be carried out to verify the quasi-static approach. The steps involved in the quasi-static analysis are:

1. Before shaft rotation begins, the oil ring is resting on the top of the shaft. The eccentricity ratio is 1.0. As the rotational speed increases, the oil seal fluid

film supports the weight of the oil seal ring W . The force in the oil film acting on the seal ring exactly matches the weight.

2. The pressure drop across the seal ring increases with machine speed. This in turn increases the axial force due to unbalanced pressures, and correspondingly, the radial friction force acting on the seal ring (given by the coefficient of friction times the axial force). When the radial friction force acting on the seal exceeds the oil film radial force, the seal will lock up.

3. As the shaft speed continues to increase, the tilting pad bearing oil film forces tend to force the shaft upward in the bearing. The seal ring oil film forces tend to oppose this because the the shaft is now taking an eccentric position within the fixed seal ring.

4. Unbalances are always present in rotors. These produce forces which make the shaft undergo dynamic orbits. These dynamic orbits in turn produce dynamic oil film forces in the lubricant between the shaft and fixed seal ring. If the combination of static and dynamic forces is larger than the radial friction force, the oil seal ring will move. If the dynamic forces are not large enough to overcome the available radial friction force at a given speed, the seal ring is likely to lockup.

There are several possibilities to be explored for any particular seal geometry and operating conditions.

INITIAL LOCKUP POSITION

Figure 4 shows the shaft, seal ring inner radius, and bearing pad circle at the initial position for zero speed. The clearances are exaggerated for clarity in the illustrations. Note that the seal ring clearance c_r at 0.097485 mm (3.838 mils) is larger than the bearing pivot clearance c_j at 0.07620 mm (3.0 mils). Relative to the bearing center (which is assumed to be the only fixed point as both the shaft and oil seal ring move), the shaft position is $x_j = 0.0$ and $y_j = -0.07620$ mils (-3.0mils) while the seal ring position is $x_r = 0.0$ and $y_r = -0.173685$ mm (-6.838 mils).

As the speed increased, the pressure drop across the seal was assumed to follow a power law curve of the form

$$\frac{P}{P_d} = \left(\frac{N}{N_d}\right)^n \quad (1)$$

Usually the power n is in the range of 1.5 to 2.0. For illustration purposes here the value $n=2.0$ is used. The maximum available friction force is given by the expression

$$F_{rmax} = \mu_s P A \quad (2)$$

With Equation (1) this becomes

$$F_{rmax} = \mu_s P_d A \left(\frac{N}{N_d}\right)^n \quad (3)$$

The oil film radial force is equal to the maximum available radial friction force at lockup. It has also been noted that during start up the oil film radial force must equal the seal ring weight W . Finally the ring weight equals

$$W_r = \mu_s P_d A \left(\frac{N_{lock}}{N_d}\right)^n \quad (4)$$

This is easily solved for the desired ring lockup speed with the result

$$N_{\text{lock}} = N_d \left(\frac{W_r}{\mu_s P_d A} \right)^{\frac{1}{n}} \quad (5)$$

Note that the dynamic forces due to shaft orbiting are assumed small at the low speeds where lockup takes place.

Table 1 gives the parameters used for calculating the lockup speed of 611 rpm. with the 0.2 coefficient of friction, the required radial friction force is only 147 N (33.2 lbf) which is easily attained when the seal ring is not pressure balanced. The large face area of 8540 mm² (13.24 in²) requires only a small fraction of the design pressure drop across the seal to produce this friction force.

Perhaps the least well known value is the friction coefficient. Standard tables give a value of about 0.1 for carbon to steel surfaces while a measured value for lubricated face seals of 0.3 has been published by Metcalf [6]. Thus an average value of 0.2 was chosen for use here. Actually a range of highest to lowest possible initial lockup speeds was considered but space considerations prevent presentation of all of the calculations made. Overall, the range of possible lockup speeds for this seal design did not produce major differences in the calculated oil seal ring stiffness and damping coefficients evaluated at running speed.

As the shaft speed increases, it lifts off of the bottom pad of the tilting pad bearings. The calculated shaft eccentricity ratio e_j [7,8,9] relative to the bearing is 0.731 at 611 rpm. Note that the rotor weight carried by one bearing of 3600 N (809 lbf) is very large compared to the oil seal ring weight of 29.5 N (6.64 lbf) so the seal ring oil film force has little effect on the bearing load at this low speed. The shaft position relative to the bearing center line is $x_j = 0.0$ mm (0.0 mils) and $y_j = -0.0556$ mm (-2.19 mils).

The oil seal ring eccentricity and attitude angle were calculated for the load capacity of 29.5 N (6.64 lbf). A finite element method due to Schmaus [7], described in Appendix A, was used to evaluate the pressures around the shaft including the axial pressure gradient. The calculated ring eccentricity ratio relative to the shaft was 0.463 while the attitude angle for a fully cavitated oil film (as the lubricant film in the seal was taken to be due to the high seal pressure) is 90.0 degrees relative to the load vector. Thus the oil seal ring moves horizontally relative to the shaft and the final oil ring position expressed in terms relative to the bearing center line is $x_r = -0.0452$ mm (-1.78 mils) and $y_r = -0.0556$ mm (-2.19 mils). Figure 5 illustrates the final shaft and seal ring positions at lockup.

OIL SEAL RING PROPERTIES AT STABILITY THRESHOLD SPEED

The compressor was observed to have the onset of subsynchronous vibrations at approximately 9000 rpm. The purpose of this section is to determine the seal ring stiffness and damping coefficients at that speed. It is assumed (and verified) that the seal ring remains fixed at the location just calculated as the initial lockup position. As the speed increases from the 611 rpm lockup speed to 9000 rpm, the tilting pad bearing oil film forces make the shaft rise relative to the bearing centerline. This creates an eccentric position of the shaft in the oil seal ring which in turn generates fairly large oil film forces in the seal ring. Both steady state load capacity and dynamic coefficients are developed in the seal ring.

If the shaft had only the shaft weight of 3600 N (809 lbf) acting on it, the calculated bearing eccentricity ratio would be 0.235. The shaft center would then be located at $x_j = 0.0$ mm (0.0 mils) and $y_j = -0.0179$ mm (-0.705 mils). The shaft is about 45 degrees to the right and above the ring center. However, the oil film forces acting on the seal ring are important if the seal ring is locked up in the eccentric position described here. These contribute to the total load seen by the bearing.

Table 2 gives the calculated load value and attitude angle for a range of eccentricity ratios using the method of Schmaus [7]. Here the shaft position vector was taken temporarily along the negative y axis and the resulting fluid film forces had the attitude angle shown (relative to the positive x axis). It is easily seen that the load capacity varies from values small compared to the weight carried by each bearing 3600 N (809 lbf) to values above that. However in the mid range of interest here (forces around 890 N (200 lbf)), the attitude angle is nearly constant at about 45 degrees. This means that the relative angle between the oil ring position vector and the oil film force is about 45 degrees. The force acting on the shaft will be about 45 degrees on the counter-clockwise side of the shaft position vector, assuming counter-clockwise shaft rotation. In the range of forces generated in the ring oil film, the force is nearly vertical and can be added directly on to the static bearing load.

The shaft eccentricity in the bearing vs. load is given in Table 3. Matching the vertical position of the shaft y_j from Table 3 to the corresponding eccentricity in the oil seal ring from Table 2 gives the shaft position $y_j = -0.216$ mm (-0.85 mils). This corresponds to a shaft/bearing eccentricity ratio of 0.283 and a shaft/ring eccentricity of 0.583. The downward load imposed by the oil seal ring on the shaft is 756 N (170 lbf) for a total bearing load of 4356 N (979 lbf). Figure 6 indicates the final shaft and oil seal ring positions at 9,000 rpm.

The stiffness and damping coefficients were calculated for the seal ring assuming lockup at the 611 rpm speed. Initially they were obtained from Schmaus [7] using an attitude angle of -90 degrees. The coordinates were then rotated to an attitude angle of -135 degrees to represent the approximate relative position of the shaft relative to the center of the oil seal ring (illustrated in Figure 3). Table 4 gives the calculated values vs. shaft/ring eccentricity. Field engineers noted that the measured axial flow rates varied over approximately the same range as the calculated values, 10-20 gal/min, over a period of time including a number of startups. This gives some confirmation of the analysis.

At the subsynchronous vibration threshold speed, the above results indicate that the lowest possible stiffness and damping values which can occur are the zero eccentricity values if the oil seal ring is locked up. Table 5 shows these values. Note that even if the shaft is centered in the locked up seal ring, the crosscoupled stiffness values are 52,000 lbf/in. This may be enough to drive the compressor into subsynchronous whirl. A more typical value of eccentricity is likely to be about 0.62 which was used in this study for the actual values. Then the crosscoupled stiffness value is 163,000 lbf/in or about three times the centered value. The value of 0.62 was taken to be somewhat on the conservative side in the final design calculations.

The principal stiffness and damping coefficients are not as important as the crosscoupled coefficients because the seals are close to the bearings. Bearing principal stiffness and damping coefficients are much larger and tend to dominate the seal coefficients. Tilting pad bearings have no crosscoupled coefficients when

symmetric loading occurs, as it does in this case, so the oil seal cross coupled coefficients are very significant. The bearing coefficients are presented later.

Here the calculated seal ring dynamic coefficients can be compared to a formula presented in Emerick [3]. The oil seal crosscoupled stiffness and principal damping coefficients are

$$\begin{aligned}
 K_{yx} &= -\frac{\pi}{4} \omega D \mu \left(\frac{L}{c_r}\right)^3 \\
 K_{xy} &= \frac{\pi}{4} \omega D \mu \left(\frac{L}{c_r}\right)^3 \\
 C_{xx} &= \frac{2}{\omega} K_{xy} \\
 C_{yy} &= \frac{2}{\omega} K_{xy}
 \end{aligned}
 \tag{6}$$

These formulas assume that there is no axial pressure gradient, the seal ring is locked up with the shaft centered and all cavitation is suppressed. Numerical values for the example seal here give

$$\begin{aligned}
 -K_{yx} &= K_{xy} = 39,000 \text{ lbf/in} \\
 C_{xx} &= C_{yy} = 82 \text{ lbf-sec/in}
 \end{aligned}$$

These are compared to the theory used in this paper in Table 5. For the eccentric case, Equation (6) would estimate only one fourth of the crosscoupled stiffness as compared to the full quasi-steady method described here.

SEAL RING BREAKAWAY LOADS

It must be verified that the seal ring is indeed locked up. This can be done by comparing the available radial friction force to the static plus dynamic force exerted on the seal ring by the oil film. The axial pressure drop across the seal is about 600 psi at 9,000 rpm. With an unbalance seal face area of 13.24 in², the axial force on the seal ring is 7944 lbf. Assuming a friction factor of 0.2, the available radial friction force is 1589 lbf. Even with a friction factor of 0.1, the friction force is 794 lbf.

The static force on the ring is about 250 lbf even at the largest expected eccentricity of 0.62. An estimate of the dynamic force can be obtained by multiplying the stiffness times the displacement. Field measurements of the orbit size indicate a vibration level of approximately 0.8 mils. For a crosscoupled stiffness of 163,000 lbf/in, the dynamic force would be about 130 lbf. The total of static plus dynamic forces is well below the smallest expected available friction force tending to lockup the seal. A comparable analysis can be done for any speed from the lockup speed on up to operating speed and the conclusion is that the seal ring will be locked up.

STABILITY ANALYSIS

A full rotor dynamic analysis was carried out. This included an undamped critical speed analysis, stability and unbalance response. Due to length restrictions only the results of the stability analysis, which are relevant to the oil seal, are presented. The overall rotor dynamics analysis will be reported in a later paper.

The rotor was examined to determine the sensitivity to different destabilizing mechanisms. These included oil seals, balance piston and aerodynamic crosscoupling at the compressor wheels. Again the volume of analysis done on these effects requires that only partial results be given here. Table 6 gives the logarithmic decrement and damped natural frequencies for the various cases. First, the shaft was taken alone. The logarithmic decrement was zero as expected due to no system damping. When the bearings were added, the system has a good log decrement of 0.19. Next, a value of 19,800 lbf/in was added for the balance piston at one end of the machine near the bearings [10]. Now the log decrement is reduced to 0.14 or a change of about 0.5. The locked up seal with stiffness of 163,000 lbf/in was added (without the balance piston) and the value of log decrement dropped to 0.09. The two effects combined dropped the log decrement to 0.006. The major effect is seen to be the oil seals at both ends of the shaft which produce a change in log decrement of 0.10.

Overall, the balance piston crosscoupling and the seal crosscoupling are not enough to make the rotor unstable. Compressor wheel aerodynamic crosscoupling is often added to complete the list of instability mechanisms [5]. A typical value of 10,000 lbf/in (1667 lbf/in per wheel) placed at the center of the rotor gives the final log decrement discussed in this paper of -0.06. The rotor is finally unstable (at least the calculations indicate instability). The calculated whirl speed is 3780 rpm while the observed whirl speed is 4200 rpm. The calculated value is lower than the measured value by about 10% which is typical of compressor instability calculations with many machines.

DESIGN CHANGE RECOMMENDATIONS

Several possible design changes were proposed to the existing seal which have been known to improve seal performance from a stability viewpoint. The objectives used in assessing the proposed changes were

1. Reduce cross coupled stiffness of the seal while maintaining the flow rate.
2. Reduce the radial friction force (by pressure balancing).

The analysis of the proposed seal design modifications assumes a shaft eccentricity of 0.5 and an attitude angle of -135° for the seal. A smaller eccentricity was selected to represent the largest expected lock up condition for a balanced seal. Also the speed at which the analysis was performed was increased to the actual operating speed of 9800 rpm.

Several possible design modifications were considered.

Type 1: Clearance Region Modifications

- Two Groove Seal with $c = 3.838$ mils (40 mil groove width)
- Three Groove Seal with $c = 3.838$ mils (30 mil groove width)
- Two Groove Seal with $c = 5.0$ mils (40 mil groove width)

Type 2: Ring Balance Modifications

- Balanced Ring Face

Figure 7 illustrates the geometries of the grooved and balanced oil seals.

Cutting circumferential grooves, as in type 1, in the seal land region has the effect of reducing the crosscoupled stiffness while keeping the flow rate low. A case with an increased seal clearance is also considered. While this should reduce the cross coupled stiffness, it will also increase the flow rate across the seal.

The existing oil seal's properties were recalculated at 9800 rpm and serve as a comparison for the proposed seal design modifications. Table 7 contains the operating properties of the existing and grooved seals. As expected the grooves greatly reduce the crosscoupled stiffness, by an order of magnitude in the three groove seal over the existing design. The load capacity of the seal is also reduced. It should be noted that the two groove seal with the expanded clearance has crosscoupling terms ten times less than the existing seal but with a flow rate twice as great.

The objective of balancing the oil seal, as mentioned earlier, is to decrease the maximum available friction force tending to lock up the seal ring. This will prevent the seal ring from locking up at a very large eccentricity which could produce large crosscoupling stiffnesses in the seal.

Figure 7.c shows the proposed modified seal face to decrease the axial loading on the seal. The unbalanced axial force is determined from the area of the face shown as 1.047 in². This is much less than the face area of the original seal (over 13 in²). The maximum frictional force at the operating speed is then 202 lbf. This is much more reasonable as a friction force than the 1700-2500 lbf range for the original seal.

Finally, the three grooved seal was selected as the best design. It had the lowest crosscoupled stiffness while maintaining the same flow rate as the existing seal. Balancing of the three groove seal was recommended to assure that highly eccentric seal operation would not occur.

REDUCTION OF SUBSYNCHRONOUS VIBRATIONS

To reduce the subsynchronous vibrations two possible machine changes have been studied: seals and bearings. Only the changes in stability due to seal modifications are presented. The bearing effects will be presented in another paper.

As previously mentioned, stability at the operating speed of 9800 rpm is desired. To predict the stability at this speed, the aerodynamic crosscoupling has been assumed to vary linearly with speed. Namely, at 9800 rpm the aerodynamic crosscoupling is 8490 lb/in. The balance piston stiffness was assumed to be constant with speed.

With the existing seals the system has a log-decrement of -0.075 at 9800 rpm (unstable). By replacing the original seals with 3-groove seals the log decrement increases to 0.12 (stable).

CONCLUSIONS

An unbalanced seal design such as the one considered here is likely to produce large available friction forces acting on the seal ring. These will tend to lock the seal ring against the fixed components at some speed well below running speed. As the shaft increases in speed, the oil film forces in the bearings will lift the shaft in the bearing. This will create an eccentric position of the shaft relative to the locked up oil seal ring. This in turn will produce large crosscoupling stiffness terms acting on the shaft due to the oil film in the seal ring. In the case considered here, the crosscoupled stiffness could be as large as 163,000 lbf/in for each oil seal.

A quasi-steady method of determining the seal ring lockup conditions has been presented. It involves matching the radial friction force to the seal ring weight. While no direct evidence of its accuracy, such as ring measured orbits are available for comparison, indirect verification by matching calculated instability thresholds with measured ones is shown here. The method appears to be much easier to use than the time transient method described by other authors [1,2].

If a seal ring does lockup, the possible range of dynamic coefficients goes from the centered position to the largest likely eccentricity. The centered position can produce fairly large crosscoupled stiffness values for the seal ring oil film. In this case the value was about 52,000 lbf/in. The eccentric values are typically several times this value, in this case about three times as large.

Use of the centered-no axial flow formula presented in Emerick [3] would result in an oil seal crosscoupled stiffness of 39,000 lbf/in. Compared to the value of 163,000 when the eccentric case with axial flow is considered, Equation (6) does not appear to be a good approximation. Also the principal stiffness terms are neglected by Equation (6). The centered-no axial flow formula probably should not be employed particularly as it seems to strongly underestimate the oil seal effects.

The oil seal ring fluid film will generate additional loads acting on the bearing. In this case, the additional load was about 25% of the steady bearing load due to shaft weight. It appears likely that the seal ring added load will normally be in the vertically downward direction although no general studies were carried out to verify this. The change in the bearing dynamic coefficients was found to be only about 10% or less with the additional load. Thus the effect of the bearing on moving the shaft eccentrically in the locked up seal ring was the major effect. Put another way, the change in eccentricity in the seal ring produced a large effect in the oil seal ring dynamic coefficients while the change in eccentricity in the bearing did not modify the bearing dynamic coefficients very much.

The oil seal lockup was found to be the major effect in driving the compressor into subsynchronous vibration. It produced a lowering of logarithmic decrement of 0.10 or more as compared to balance piston (0.05) or aerodynamic crosscoupling (0.066). Calculation of a negative log decrement to drive the rotor unstable required all three mechanisms of instability. The calculated value of whirl speed at 3780 rpm compares fairly well with the measured value of 4200 rpm.

To reduce the subsynchronous vibrations, modifications were recommended to the oil seals. The existing seal was modified to have three grooves cut in the land region. A groove width of 0.7616 mm (30 mils) and a groove depth of about 2.54 mm (0.1 in) was recommended. The three groove design reduced the crosscoupled stiffness from 109,000 lbf/in to an average value of 6,000 lbf/in. Further, grooving did not increase the seal leakage significantly. Balancing of the seal was recommended to prevent the seal ring from locking up at large eccentricities. Thus very large crosscoupled stiffness terms were prevented. Cutting a relief on the face of the seal reduced the friction force (tending to lock the seal up) from about 1700-2500 lbf in the existing seal to about 200 lbf in the proposed seal design.

The stability of the existing compressor was then examined at the operating speed of 9800 rpm. Replacing the original oil seals with the three groove design increased the log decrement to 0.12 (stable). Due to plant shutdown, the proposed seal redesign has not yet been implemented.

REFERENCES

1. Kirk, R. G., and Miller, W. H., "The Influence of High Pressure Oil Seals of Turbo-Rotor Stability," A. S. L. E. Transactions, Vol. 22, No. 1, January 1979, pp. 14-24.
2. Kirk, R. G., and Nicholas, J. C. "Analysis of High Pressure Oil Seals For Optimum Turbocompressor Dynamic Performance," Vibrations in Rotating Machinery Second International Conference, Institution of Mechanical Engineers, Cambridge, September, 1980, pp. 125-134.
3. Emerick, M. F., "Vibration and Destabilizing Effects of Floating Ring Seals in Compressors," Rotordynamic Instability Problems in High-Performance Turbomachinery Conference, Texas A. & M. University, May 1980, pp. 187-204.
4. Doyle, H. E., "Field Experiences With Rotordynamic Instability in High-Performance Turbomachinery," Rotordynamic Instability Problems in High-Performance Turbomachinery Conference, Texas A. & M. University, May 1980, pp. 3-14.
5. Wachel, J. C., "Rotordynamic Instability Field Problems," Rotordynamic Instability Problems in High-Performance Turbomachinery Conference, Texas A. & M. University, May 1982, pp. 1-19.
6. Metcalfe, R., Kittmer, and Brown, "Effects of Pressure and Temperature Changes on End-Face Seal Performance," A.S.L.E. Transactions, Vol. 25, No. 3., pp. 361-371.
7. Schmaus, R. H., "Static and Dynamic Properties of Finite Length Turbulent Annular Flow Seals," M.S. Thesis, University of Virginia, January 1981.
8. Elrod, H. G. and Ng, C. W., "A Theory for Turbulent Fluid Films and Its Application to Bearings," Journal of Lubrication Technology, Transactions A. S. M. E., Series F, Vol. 89, No. 3, July 1967, p. 346.
9. Hirs, G. G., "A Bulk-Flow Theory for Turbulence in Lubricant Films," Journal of Lubrication Technology, Transactions A. S. M. E., Series F, Vol. 95, No. 2, April 1973, p. 137.
10. Iwatsubo, T., Motooka, N., and Kawai, R., "Flow Induced Force of Labyrinth Seal," Rotordynamic Instability Problems in High Performance Turbomachinery, Texas A&M University, May 1982, pp. 205-222.

Table 1. Oil Seal Ring Parameters For Initial Lockup Condition

$$\begin{aligned}
 W_r &= 29.5 \text{ N (6.64 lbf)} \\
 \mu_s &= 0.2 \\
 P_d &= 1.85 \times 10^6 \text{ N/mm}^2 \text{ (644 lbf/in}^2\text{)} \\
 A_r &= 8,540 \text{ mm}^2 \text{ (13.24 in}^2\text{)} \\
 N_d &= 9800 \text{ rpm}
 \end{aligned}$$

Table 2. Load Capacity For Original Seal With Shaft Along Negative y Axis at 9,000 RPM

ECC	W_x (LB)	W_y (LB)	LOAD (LB)	ANGLE
0.00	.00	.00	.00	-89.93
.10	20.21	22.04	29.90	-42.52
.20	41.79	44.06	60.72	-43.48
.30	66.43	65.91	93.58	-45.22
.40	96.85	87.96	130.83	-47.76
.50	138.07	109.93	176.49	-51.47
.60	200.35	131.78	239.81	-56.66
.70	309.57	153.40	345.49	-63.64
.80	516.45	261.65	578.95	-63.13
.90	1019.89	1393.99	1727.24	-36.19

Table 3. Tilting Pad Bearing Load vs Eccentricity and Shaft Position

Load (lbf)	Bearing Eccentricity ϵ_j	Shaft Position In Bearing y_j (mils)
784	0.229	-0.69
827	0.240	-0.72
834	0.242	-0.73
945	0.270	-0.81
1071	0.300	-0.90
1205	0.330	-0.99
1350	0.360	-1.08
1508	0.390	-1.17

Table 4. Subsynchronous Threshold Stiffness and Damping for Existing Seal

ECC	LOAD (lbf)	KXX	KXY (lbf/in)	KYX	KYY
0.00	1.	57401.	52065.	-52063.	57400.
0.10	30.	57968.	53201.	-53209.	56820.
0.20	61.	59842.	56880.	-56917.	54889.
0.30	94.	63843.	64289.	-63806.	51183.
0.40	131.	71161.	76957.	-76772.	43574.
0.50	176.	85577.	100239.	-100344.	28850.
0.60	240.	116701.	146478.	-146928.	-2744.
0.70	345.	195577.	263713.	-254970.	-82789.
0.80	579.	698264.	781308.	-112971.	140389.
0.90	1727.	5334498.	5226771.	2383265.	3082203.

a) Stiffness at -135° Attitude Angle and 9,000 RPM

ECC	LOAD (lbf)	CXX	CXY (lbf-sec/in)	CYX	CYY
0.00	1.	110.	0.	0.	110.
0.10	30.	110.	-1.	-1.	110.
0.20	61.	119.	3.	3.	119.
0.30	94.	134.	12.	12.	134.
0.40	131.	162.	28.	28.	163.
0.50	176.	212.	60.	60.	214.
0.60	240.	313.	130.	129.	315.
0.70	345.	548.	306.	306.	553.
0.80	579.	1176.	704.	692.	841.
0.90	1727.	4170.	2681.	2567.	2124.

b) Damping at -135° Attitude Angle and 9,000 RPM

Table 5. Stiffness and Damping For Existing Seal At Subsynchronous Vibration Analysis (At 9,000 RPM and -135° Angle)

Case	K_{xx}	K_{xy} (lbf/in)	K_{yx}	K_{yy}	C_{xx}	C_{xy} (lbf-sec/in)	C_{yx}	C_{yy}
Centered with Axial Flow	0	57,400	52,060	- 52,060	57,400	110	0	0 110
Eccentric with Axial Flow	0.62	128,000	163,000	-163,000	147,000	360	165	164 363
Centered -No Axial Flow-Eq.(6)	0	0	39,000	- 39,000	0	82	0	0 82

Table 6. Sensitivity of Current Design to Different Destabilizing Mechanisms at 9,000 RPM

	<u>Logarithmic Decrement</u>	
	δ	Whirl Speed (cpm)
Shaft Only (0.5×10^6 lb/in Supports)	0.00	3070
Shaft, Bearings	0.19	3555
Shaft, Bearings, Balance Piston (19.8 Klbf/in)	0.14	3550
Shaft, Bearings, Seals	0.09	3770
Shaft, Bearings, Seals, Balance Piston	0.006	3770
Shaft, Bearings, Seals, Balance Piston, Aerodynamic Cross Coupling at Wheels (10 Klbf/in)	-0.06	3780

Seal Design	Load (lbf)	Flow Rate (gal/min)	Stiffness (lbf/in)			Damping (lbf-sec/in)				
			K _{xx}	K _{xy}	K _{yx}	K _{yy}	C _{xx}	C _{xy}	C _{yy}	
Existing	186	13.5	88,200	109,300	-109,600	26,000	213	61	61	215
Two Groove (1A)	92	12.8	46,300	6,680	-13,910	41,400	20	5	5	20
Three Groove (1B)	84	12.1	40,500	1,750	-9,930	37,900	11	3	3	11
Two Groove Large Clearance (1C)	46	21.6	50,300	-360	-11,800	48,100	11	2	2	11

Table 7 Summary of Seal Properties At 9,800 RPM with Attitude Angle -135° and Eccentricity 0.5

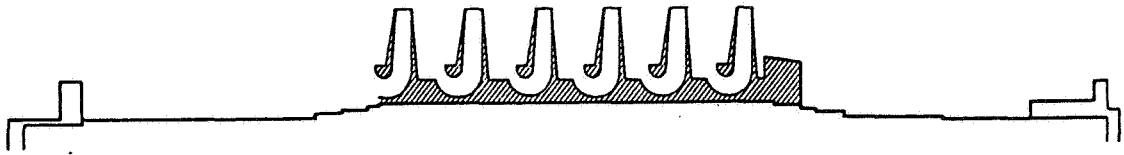


Figure 1. Compressor Geometry

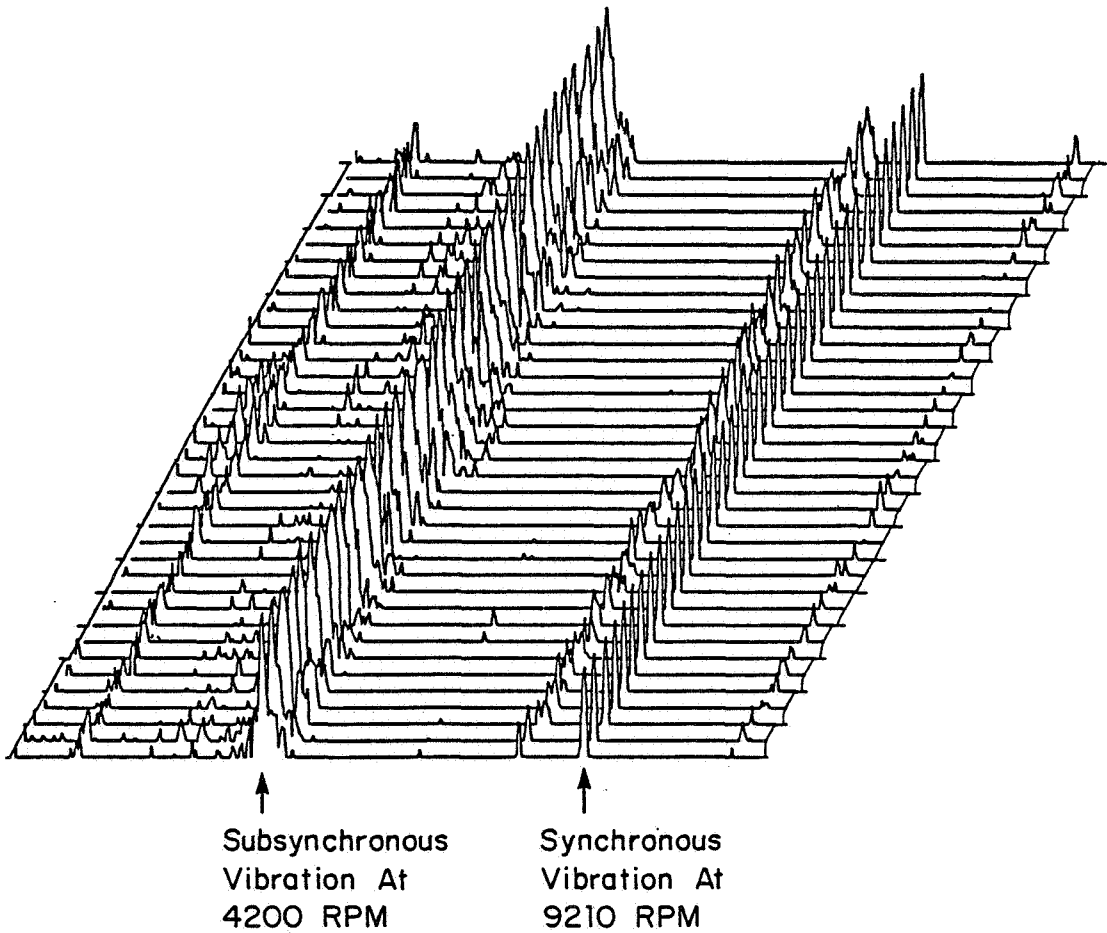
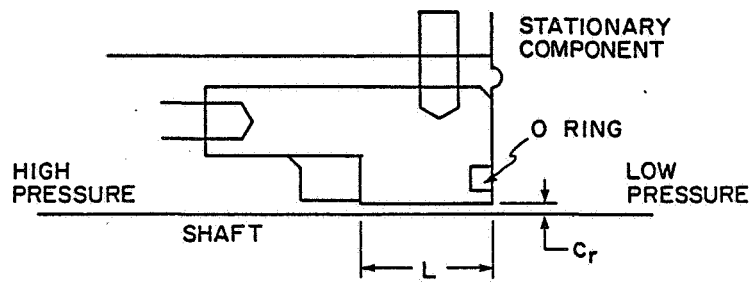
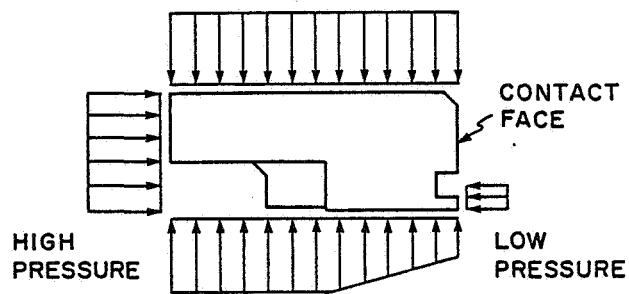


Figure 2. Vibration Pattern At 9210 RPM



(a) Seal Ring Geometry



(b) Pressure Forces Acting On Seal Ring

Figure 3. Seal Ring Geometry and Pressure Forces

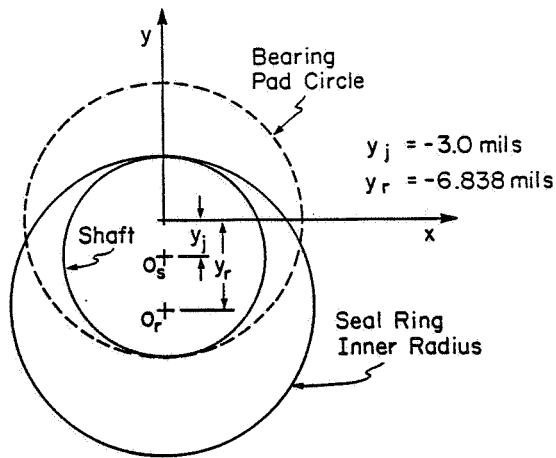


Figure 4. Bearing and Seal Ring Clearance Circle Plots At Zero Speed

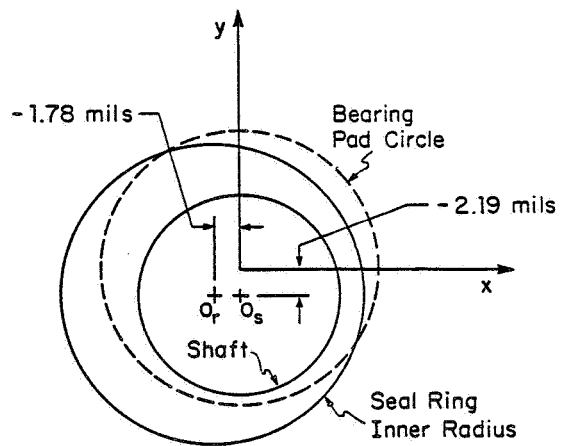


Figure 5. Bearing and Seal Ring Clearance Circle Plots At Lockup Speed (611 RPM)

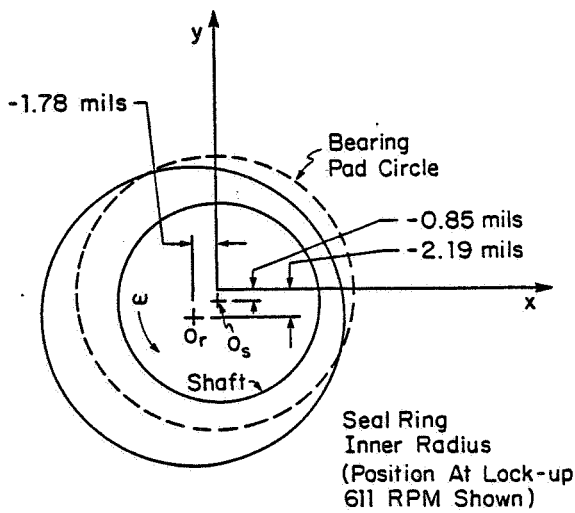
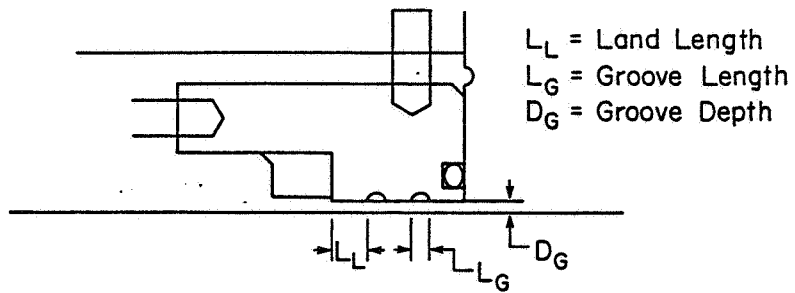
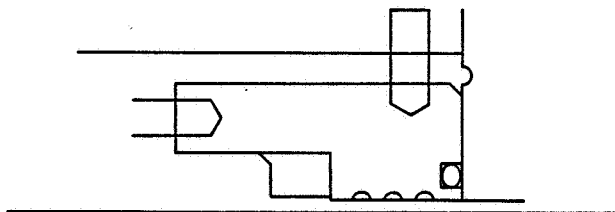


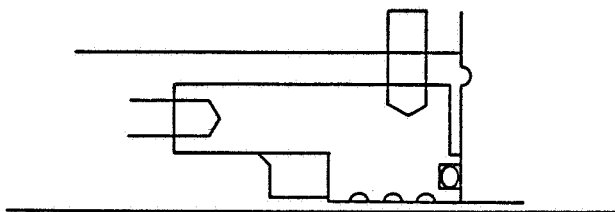
Figure 6. Bearing and Seal Ring Clearance Circle Plots At Instability Threshold Speed (9,000 RPM)



(a) Two Groove Design



(b) Three Groove Design



(c) Balance Ring Face Design

Figure 7. Geometry For Circumferential Groove And Balancing Seal Modifications

EFFECT OF COULOMB SPLINE ON ROTOR DYNAMIC RESPONSE

C. Nataraj, H.D. Nelson, and N. Arakere
 Arizona State University
 Tempe, Arizona 85287

A rigid rotor system coupled by a coulomb spline is modelled and analyzed by approximate analytical and numerical-analytical methods. Expressions are derived for the variables of the resulting limit cycle and are shown to be quite accurate for a small departure from isotropy.

SYMBOLS

a, b	semi-major, minor axis of the elliptical response
a_m	$(a+b)/2$
a_d	$(a-b)/2$
c	external viscous damping coefficient
e	amplitude of the circular limit cycle
\bar{F}	coulomb spline force vector
I_p	equivalent polar moment of inertia
$k_{y,z}$	equivalent stiffness in y, z direction
$l_{1,2}$	length of shaft 1,2
m	equivalent mass of the system
t	time, nondimensionalized using ω_y
T	torque transmitted by the coupling
v, w	response in the y, z direction (nondimensionalized relative to l_1)
α	gyroscopic parameter = I_p/ml_1^2
α_0	attitude angle of the elliptical response
γ	orthotropy parameter = ω_z/ω_y
ξ	viscous damping ratio
λ	nondimensional nonlinearity parameter (16 splines) $= 0.64\mu T (1+l_1/l_2)/m\omega_y^2 l_1^2$
μ	coefficient of friction
$\bar{\Omega}$	nondimensional spin speed of the rotor = Ω/ω_y
$\bar{\omega}$	nondimensional whirl speed of the rotor = ω/ω_y
ω_y	$\sqrt{k_y/m}$
ω_z	$\sqrt{k_z/m}$

INTRODUCTION

A spline coupling connecting two rotors is often used in the turbine engine industry. When it is not sufficiently lubricated, the resulting coulomb friction can produce a driving force that sustains an asynchronous whirling motion.

A simple rigid rotor system coupled by such a spline was analyzed by Williams and Trent (ref. 1) using simulations on an analog computer. Morton (ref. 2) considered the effect of coulomb friction in drive couplings on the response of a flexible shaft and concluded that misalignments had the effect of stabilizing such a system. Marmol, Smalley and Tecza (ref. 3) modelled a coulomb spline by equivalent viscous friction and comparisons of their analytical results to those from a test rig were satisfactory.

The model to be analyzed in this paper is very similar to the one in reference 1, and contains only two degrees of freedom. The supports have, in general, orthotropic stiffness and the model includes the gyroscopic effect.

The emphasis here is on obtaining an improved understanding of the underlying phenomena rather than a detailed quantitative analysis of a large order system. It is for this reason that analytical and numerical-analytical methods have been applied to this problem (in addition to numerical simulation) so that a better insight could be gained.

MATHEMATICAL MODEL

A system consisting of two rigid rotors coupled by a coulomb spline is considered (fig. 1). They are supported on a mount with linear isotropic viscous damping and (in general) anisotropic stiffness. This is essentially a two degree-of-freedom model and the equations of motion are found to be:

$$\begin{bmatrix} 1 & 0 \\ 0 & 1 \end{bmatrix} \begin{Bmatrix} \ddot{v} \\ \ddot{w} \end{Bmatrix} + \left(\begin{bmatrix} 2\zeta & 0 \\ 0 & 2\zeta \end{bmatrix} - \bar{\Omega} \begin{bmatrix} 0 & -\alpha \\ \alpha & 0 \end{bmatrix} \right) \begin{Bmatrix} \dot{v} \\ \dot{w} \end{Bmatrix} + \begin{bmatrix} 1 & 0 \\ 0 & \gamma^2 \end{bmatrix} \begin{Bmatrix} v \\ w \end{Bmatrix} = \bar{F} \quad (1)$$

The above equations are in nondimensional form and the derivatives are with respect to a nondimensional time. The spin speed of the rotor is denoted by Ω , α denotes a gyroscopic parameter, ζ the damping ratio and γ represents an orthotropy parameter ($\gamma = 1$: isotropic support). An equivalent force vector, \bar{F} arises due to the friction excitation in the coulomb spline and is given by:

$$\bar{F} = - \frac{\lambda}{[(\dot{w} - \bar{\Omega}v)^2 + (\dot{v} + \bar{\Omega}w)^2]^{1/2}} \begin{Bmatrix} \dot{v} + \bar{\Omega}w \\ \dot{w} - \bar{\Omega}v \end{Bmatrix} \quad (2)$$

where, λ is a nondimensional parameter denoting the strength of the nonlinearity.

The system is thus modelled by a set of coupled, second order, nonlinear, autonomous equations (eqn. 1) and a closed form analytical solution is difficult, if not impossible.

SOLUTION: ISOTROPIC CASE

When the support is isotropic ($\nu=1$), an exact solution can be obtained by assuming a circular response of amplitude e and a frequency $\bar{\omega}$.

$$\begin{aligned} \text{i. e.,} \quad v &= e \cos \bar{\omega}t \\ w &= e \sin \bar{\omega}t \end{aligned} \quad (3)$$

Substitution of this assumed solution form into equations (1) and (2) yields the following results:

$$\begin{aligned} \bar{\Omega} < \bar{\omega} & \quad \text{No Limit Cycle Possible} \\ \bar{\Omega} > \bar{\omega} & \quad \text{Limit Cycle Exists} \end{aligned}$$

$$\text{with } \bar{\omega} = \bar{\Omega}\alpha/2 + \sqrt{1 + (\bar{\Omega}\alpha/2)^2} \quad (4)$$

$$e = \lambda/2\zeta\bar{\omega} \quad (5)$$

It is interesting to note that the frequency of the limit cycle is the same as the undamped natural frequency of the linearized system and is independent of the strength of the nonlinearity (λ) and the linear viscous damping ratio (ζ). The amplitude of the resulting circular limit cycle is directly proportional to λ and reduces with increasing spin speed Ω . Figure 2 shows the frequency spectrum of the numerically simulated response at a nondimensional spin speed of 3. Clearly, a single peak occurs at a frequency of 1.56 that agrees with the analytical prediction (eqn. 4).

The onset of instability speed, at which a bifurcation into a limit cycle takes place, can be found to be

$$\bar{\Omega}_{01} = \frac{1}{\sqrt{1-\alpha}} \quad (6)$$

Similar results were obtained in reference 1, but without the inclusion of the gyroscopic effect.

Figure 3 shows the force balance diagram for the isotropic system at a spin speed above the onset of instability. From energy considerations, it can also be shown that when the spin speed Ω is less than the whirl speed ω , the coulomb spline dissipates energy and hence cannot sustain a limit cycle. When $\Omega > \omega$ however, the spline gives rise to equivalent negative damping. Then, the amplitude of the limit cycle can be determined by equating the energy dissipated by the linear

viscous damping to the energy added (to the system) by the coulomb spline forces.

The stability of the limit cycle can be investigated by perturbing the limit cycle and writing linear variational equations for the perturbed motion. A detailed stability analysis indicates that the circular limit cycle is stable for all possible values of the parameters.

SOLUTION: ORTHOTROPIC CASE

When the support is not isotropic ($\gamma \neq 1$), the solutions are no longer amenable to an exact analysis. Hence, two approximate methods have been used and they are outlined below.

Trigonometric Collocation Method (TCM)

This is a numerical-analytic method that has been used quite widely for the solution of nonlinear boundary value problems. Ronto (ref. 4) has recently developed and formalized the method for application to periodic solutions and the basic philosophy is outlined below, omitting all the details and proofs. Given a set of nonlinear ODE's

$$\ddot{\bar{x}} = \bar{f}(\bar{x}), \quad (7)$$

a periodic solution $\bar{x}_0(t)$ is sought in the form:

$$\bar{x}_0(t) = \bar{a}_0 + \sum_{n=1}^N (\bar{a}_n \cos n\bar{\omega}t + \bar{b}_n \sin n\bar{\omega}t) \quad (8)$$

where the i th typical coefficients \bar{a}_i and \bar{b}_i and the frequency $\bar{\omega}$ are unknown. This assumed solution is substituted into the differential equations and the resultant errors are forced to be zero at a prescribed number of time points (at least $2N+1$). This leads to a sufficient number of nonlinear algebraic equations in the unknown coefficients and the frequency and can be solved using various numerical methods.

Though this method was developed mainly for the solution of nonautonomous equations in reference 4, it has been successfully developed and applied for autonomous systems as well.

Application of the TCM to the orthotropic system reveals some interesting results. The response is nearly elliptical (as can be expected) but also has several higher frequency components. These higher harmonics have very low amplitudes and hence are not easily observed by numerical simulation.

The effect of the higher harmonics is best seen in a semi-log plot of the frequency spectrum (fig. 4) that has been generated by numerical simulation. The nondimensional spin speed $\bar{\Omega}$ is equal to 3 and peaks are seen to occur at $\bar{\omega}$, $3\bar{\omega}$, $5\bar{\omega}$, etc., where the fundamental frequency $\bar{\omega}$ is ~ 2.92 . This may be contrasted with the frequency spectrum for the

isotropic case (fig. 2). The fundamental frequency of the limit cycle is seen to be independent of the strength of the nonlinearity (λ) and the damping (ζ). The higher harmonic amplitudes are seen to increase with an increase in orthotropy.

Numerical simulation has been carried out for a range of parameters and the results compare very well with those obtained by the TCM.

Analytical Approximation (AM)

In order to obtain some idea about how the response variables vary with the system parameters, analytical expressions that approximate the response are quite useful. To derive these, since the higher frequency components have low amplitudes, the solution is assumed in the form of a single frequency elliptical component. As the system is autonomous, the time origin of the response is arbitrary. Hence,

$$v = a_m \cos(\bar{\omega}t + \alpha_0) + a_d \cos(\bar{\omega}t - \alpha_0) \quad (9)$$

$$w = a_m \sin(\bar{\omega}t + \alpha_0) - a_d \sin(\bar{\omega}t - \alpha_0)$$

Substituting this assumed form of the solution into the equations of motion, equation 1, and after substantial algebraic manipulations and retention of only first order approximations, an approximate expression for the fundamental frequency of the limit cycle is seen to be:

$$\bar{\omega}^2 \approx A \{1 + \sqrt{1 - (\gamma/A)^2}\} \quad (10)$$

where: $A = (1 + \gamma^2 + \alpha^2 \bar{\Omega}^2)/2 \quad (11)$

and, $b/a \approx (\bar{\omega}^2 - 1)/\alpha \bar{\Omega} \bar{\omega} \quad (12)$

$$b \approx \lambda/2\zeta\bar{\omega} \quad (13)$$

The approximate expression for the fundamental frequency is the same as the undamped natural frequency of the linearized orthotropic system. The general variation of the frequency and amplitude is very similar to the isotropic case. However, in contrast to the isotropic case, the limit cycle appears to exist at all spin speeds. This is consistent with the simulation results of Williams and Trent (ref. 1).

Table 1 shows a comparison between the analytical predictions and the values obtained by the TCM for several values of γ (orthotropy). The frequency prediction is correct to within 10% for γ up to 3.0 and the amplitude prediction has less than 10% error for γ up to 1.6.

The stability of the limit cycle in the orthotropic case has not yet been analyzed and further investigations will be reported elsewhere.

CONCLUSION

A two degree-of-freedom model of rigid rotors coupled by a coulomb spline is analyzed. Two different cases are considered.

When the support is isotropic, a bifurcation into a stable, circular limit cycle takes place at a spin speed equal to the forward undamped critical speed. The frequency of the limit cycle is the same as the undamped natural frequency of the system and is independent of the strength of the nonlinearity.

When the support is orthotropic, the limit cycle has many frequency components but is still nearly elliptical. The undamped natural frequency of the system, however, approximates the fundamental whirl frequency of the response to a very good accuracy. The higher harmonic amplitudes increase with an increase in orthotropy. The stability of the response in the orthotropic case is of considerable interest and remains to be investigated.

Similar qualitative phenomena can be expected to occur in large flexible rotor-bearing systems with a spline coupling. Work is continuing along these lines.

REFERENCES

1. Williams, R., Jr.; and Trent, R.: The Effects of Nonlinear Asymmetric Supports on Turbine Engine Rotor Stability. SAE Transactions, Vol. 79, pp. 1010-1020, 1970.
2. Morton, P.G.: Aspects of Coulomb Damping in Rotors Supported on Hydrodynamic Bearings. Rotordynamic Instability Problems in High-Performance Turbomachinery, NASA Conference Publication 2250, 1982.
3. Marmol, R.A.; Smalley, A.J.; and Tecza, J.A.: Spline Coupling Induced Nonsynchronous Rotor Vibrations. ASME Journal of Mechanical Design, Vol. 102 (1), pp. 168-176, 1980.
4. Samoilenko, A.M.; and Ronto, N.I.: *Numerical-Analytic Methods of Investigating Periodic Solutions*. Mir Publishers, Moscow, 1979.

TABLE 1. - COMPARISON BETWEEN ANALYTICAL AND TCM RESULTS

($\Omega = 3.0$, $\lambda = 0.01867$, $\zeta = 0.1$, $\alpha = 0.3$)

γ	ω_{AM}	ω_{TCM}	$(b/a)_{AM}$	$(b/a)_{TCM}$	$b_{AM} \times 10^2$	$b_{TCM} \times 10^2$
1.0	1.5466	1.5466	1.0000	1.0000	6.0348	6.0348
1.1	1.5470	1.570	1.0007	1.0007	5.8511	6.0169
1.2	1.6495	1.6490	1.1591	1.1513	5.6584	5.8875
1.3	1.7093	1.7081	1.2491	1.2348	5.4605	5.6251
1.5	1.8433	1.8386	1.4453	1.3929	5.0633	4.6291
3.0	3.1466	2.8387	3.1431	1.1148	2.9662	0.4871

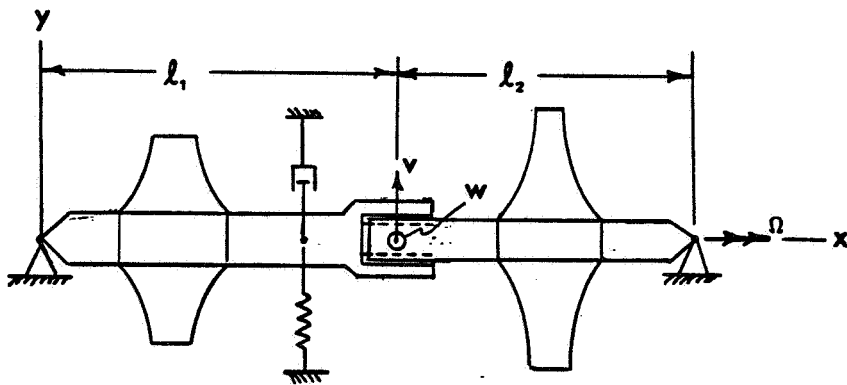


Figure 1. - Schematic of typical rotor.

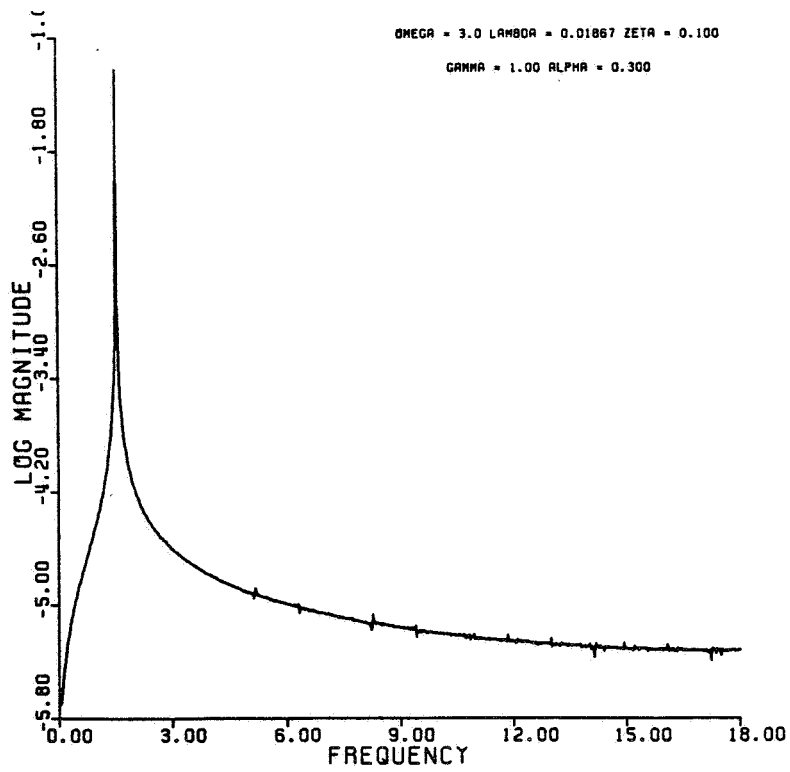


Figure 2. - Response frequency spectrum: isotropic case.

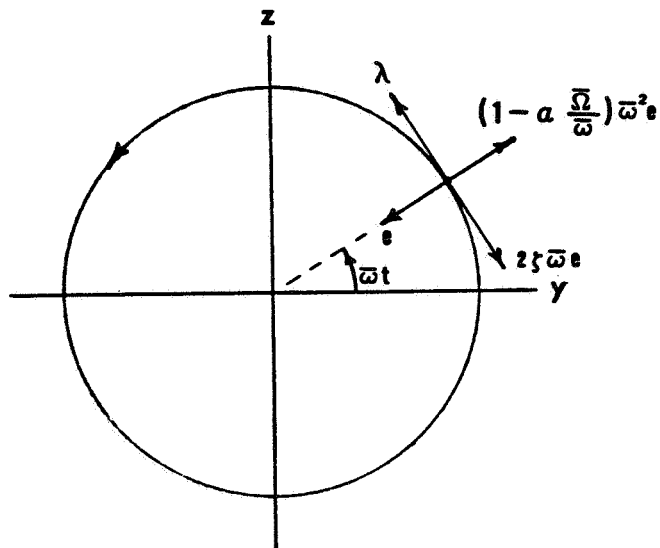


Figure 3. - Force balance diagram: isotropic case.

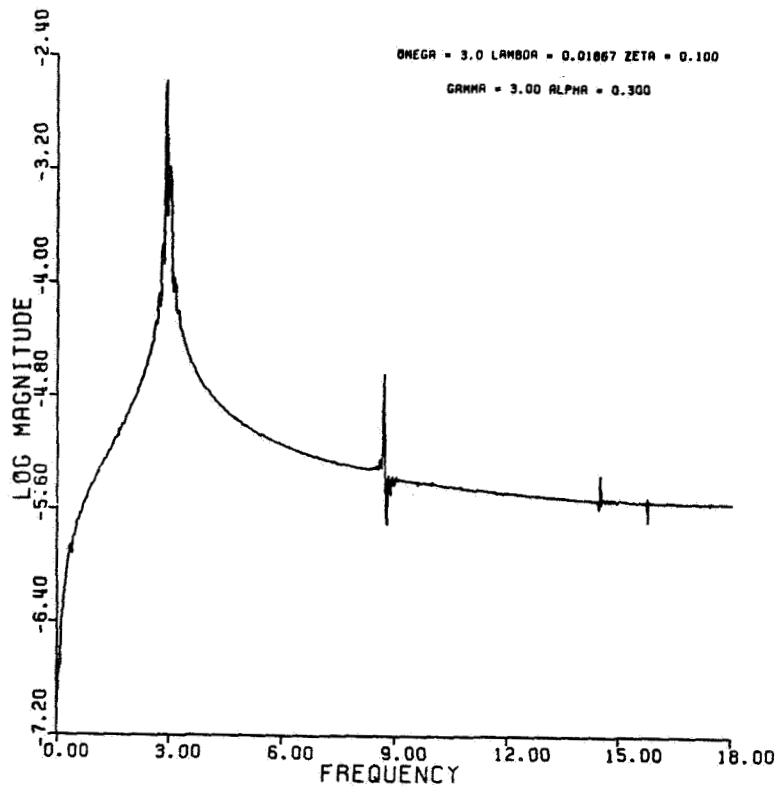


Figure 4. - Response frequency spectrum: orthotropic case.

ROTOR-TO-STATOR RUB VIBRATION IN CENTRIFUGAL COMPRESSOR

Gao Jin Ji and Qi Qi Min
Liaoyang Petrochemical Fiber Company
Liaoning, The People's Republic of China

This paper discusses one example of excessive vibration encountered during loading of a centrifugal compressor train (H type compressor with HP casing).

An investigation was made of the effects of the dynamic load on the bearing stiffness and the rotor-bearing system critical speed. The high vibration occurred at a "threshold load," but the machine didn't run smoothly due to rubs even when it had passed through the threshold load.

This paper shall present the acquisition and discussion of the data taken in the field, as well as a description of the case history which utilizes background information to identify the malfunction condition. The analysis shows that the failures, including full reverse precession rub and exact one half subharmonic vibration, were caused by the oversize bearings and displacement of the rotor center due to foundation deformation and misalignment between gear shafts, etc.

The corrective actions taken to alleviate excessive vibration and the problems which remain to be solved are also presented in this paper.

INTRODUCTION

Modern rotating machines, if taken off-line, can cost hundreds of thousands of dollars in revenue due to production loss caused by the machine downtime. Therefore, machinery condition monitoring can prevent mechanical failures by warning operators of problems in the early stage, so that corrective action can be taken to prevent catastrophic failures. Detection and early diagnosis of potential failures of rotating machinery is a developing technology (Ref. 1).

Spectrum analysis, which is very effective in diagnosing rotating machinery problems and in quality control of new machinery, is widely used and can do an excellent job. However, in many cases it is difficult to pinpoint the cause of a failure in rotating machinery by spectrum analysis only. When combined with more information, for example, dynamic phase angle, shaft centerline position, orbits of dynamic motion and so on, which offer the most insight into the behavior of the machine, it will become more effective. In some cases of detecting the cause of a failure, it is necessary to acquire and analyze those dynamic motion parameters in a variety of operating conditions. This is an effective method often used in "clinical diagnosis" in the field.

According to the results of spectrum analysis, $1\times$ and $1/2\times$ vibrations are usually caused by unbalance and oil whirl. Often this is true, but this paper describes one case history wherein excessive vibration in the centrifugal compressor, detected by "clinical diagnosis," was caused by rotor to stator rubs.

FAILURES

The subject machine is the H type compressor with one HP casing, one LP body including two shaft-lines mounted on a gear box with 3 compression stages, and one HP casing with 3 aligned impellers, mounted at shaft-line end of third LP stage (see Fig. 1).

This machine was commissioned on August 1, 1980, and put into operation smoothly. On October 28, 1981, the machine incurred an excessive vibration condition on #3 bearing. Usually high rotor vibration occurs near the #3 bearing. Maximum amplitude of the rotor vibration was 45 μm and continued 45 seconds with increase in opening the guide vane after start-up, then soon dropped. But in the malfunction condition, maximum rotor vibration amplitude was more than 125 μm and didn't drop with continuous increase in opening the vane. As a result, the machine couldn't be put into operation (Fig. 2).

The same failures had occurred in August 1982, and August 1984, after overhaul. It took ten days to dismount and remount the machine many times to alleviate the malfunction.

THRESHOLD LOAD

To detect the exact moment and cause of this high rotor vibration, the spectrum cascade during start-up and the curve of amplitude vs. degrees of the opened van had been recorded (see Figs. 3 and 4). Obviously, there is no amplitude peak in machine speed from 0 rpm to 13987 rpm. This means that the machine did not pass through a critical speed during start-up. But, with an increase in opening the vane, an amplitude peak occurred.

The results of calculation and analysis show that the high speed rotor and the #3, #4 bearings in the LP casing belong in the variable stiffness bearing system. It is different from most compressors. With an increase in dynamic load during opening the guide vane, both machine power and load of the #3, #4 bearings are increased. Fig. 5 shows radial load of the #3 bearing and direction angle vs. power of the machine. Because the bearing stiffness directly affects the critical speed of the rotor-bearing system (Fig. 6), at the moment when the dynamic load reaches a certain value, the critical speed can coincide with the operation speed, and the resonance will occur. This value of dynamic load is called "threshold load." In normal cases the machine runs smoothly as soon as it passes through the threshold load (Ref. 2).

DATA ACQUISITION AND REDUCTION

In the malfunction condition, excessive vibration did not drop even when A passed through the threshold load. To determine the exact cause of the failure, the dynamic data of the rotor vibration on the #3 bearing had been acquired and processed by Bently Nevada instrumentation in the field while assessing the troubles.

(1) rotor orbit plots

The change course of the orbit plots during loading the machine is shown in Fig. 7.

(2) vibration waves

In the excessive vibration condition, there are two types of waves and orbit plots (A), (B) (see Fig. 7).

(3) comparative spectrum plots

Corresponding to waves and orbit plots (A), (B), different spectrum plots are shown in Fig. 7.

(4) polar plots

At the moment when excessive $1\times$ rpm vibration was dropping, the phase angle changed 720° (see Fig. 8).

DIAGNOSIS

The above-mentioned measurement provides us with information to recognize the causes of the malfunction condition.

(1) $1\times$ rpm vibrations

At the moment of passing through the critical speed on the threshold load, $1\times$ rpm high vibration occurred and soon dropped, but in the malfunction condition, excessive vibration did not drop even if passed through the threshold load. As shown in the Fig. 7 (A), the rotor motion orbit plot was elliptical with one fixed bright spot. During dismantling the machine, some wearing plots were discovered in the exact same direction on the #3 bearing. And at the moment when the excessive $1\times$ rpm vibration was dropping, the change of 720° in phase angle had been recorded by chance (see Fig. 8). It shows the excessive vibration was reverse precession due to full rub, because high friction forces may cause a dramatic change of the precession direction from forward to continuous backward whirl (Ref. 3). This is self-excited vibration. If harmful energy accumulates long enough, the orbit plots will diffuse (see Fig. 7 (A)). At this moment the machine must be shut down immediately.

(2) exact $1/2\times$ rpm vibration

Oil whirl (hydrodynamic instability of bearings) is the most popular forced sub-rotative speed mechanism, but in this case according to the instability threshold curves of offset halves bearing (Ref. 4) and the results of the calculation of speed term and clearance term, the operation condition point on the #3 bearing was far from the region of instability. And it was exact $1/2\times$ rpm but not less than $1/2$ rpm vibration, which often occurs during oil whirl. In addition, the vibration wave was different from oil whirl and coinciding with subharmonic vibration (Ref. 5), so that the failure was not caused by oil whirl.

Exact $1/2$ subrotative vibration may be caused by partial rub or by a loose non-rotating part (Ref. 3 and 6). During dismantling the machine, no loose part was found on the bearing shell, bearing housing, or pedestal support. As observed in the performance of many machines, the partial rotor to stator rub, or rub in oversized or poorly lubricated bearings, often causes steady subharmonic vibration of the frequency equal to exactly half of the rotating speed (Ref. 3). In the subject machine, the top clearances of the #3 and #4 offset halves bearings was 0.48 mm.

The diameter of the bearings was 120 mm, the ratio of the diameter to the clearance was 0.4%; obviously it is too excessive. For this reason, the failure can be attributed mainly to the oversized bearings.

Rotor rub against the bearing generates very complex rotor vibration. Rubs are created in machines by introducing a contact between the rotor and the bearing. The contact may be initiated by displacement of rotor center to stator center, which is caused by misalignment, foundation deformation, unparallel between gear shafts and eccentricity of the bearings. Displacement is prerequisite to introduction of rubs. That is why the machine may be put into operation by chance after remounting the bearings and exact alignment even in the oversize bearing condition. But in most cases, full rubs or partial rubs in the oversize bearing frequently occur due to rotor center displacement.

CORRECTIVE ACTION

It was impossible to take enough time to correct all the defects and keep machine downtime short, so the following temporary corrective actions were taken:

(1) The top clearances of both #3, #4 bearings were reduced from 0.48 mm to 0.31 mm on November 2, 1984.

(2) To increase oil viscosity the PRESLIA 20 type lub oil was replaced by PRESLIA 30 and oil temperature was reduced from 42°C to 28-30°C on November 3, 1984.

(3) The gear coupling was replaced by a new one and exact alignment was taken in December 1984.

Instant improvement results from modifying the bearings. After reducing the top clearances of the bearings, it was easy to pass through the threshold load and put the machine into operation. But the machine couldn't run smoothly with the same oil viscosity as before, even the #4 bearing had been cracked due to poor alignment condition. The vibration record shows the amplitude of rotor vibration was higher when the figure-8-shaped orbit appeared and was lower when it disappeared. This means the rubs were not eliminated completely. Since corrective action (2), (3) was taken with sufficiently high damping, the subharmonic vibration hasn't recurred at all and the machine has run smoothly up to now.

The problem which remains to solve is that it is necessary to reduce the inlet lub oil temperature below 30°C, otherwise rotor to stator rub vibration will occur again. Therefore, other defects should be eliminated in the future.

SUMMARY AND CONCLUSIONS

This case history shows that it is not enough to diagnose complex rotor vibration by the spectrum analysis method only, because there are several possible causes of failures in the machine corresponding to certain characteristic spectrums. Therefore, for detecting the potential failures of rotating machinery, it is necessary to acquire as much information as possible, for example, orbit plots, polar plots, vibration waves, and other parameters of dynamic motion in a variety of operation conditions. The more information obtained, the more possibilities to eliminate the false and retain the true, and finally pinpoint the real cause.

In the H type centrifugal compressor with HP casing, the high vibration during loading the machine is an unavoidable transient due to passing through the critical speed on the threshold load. But, excessive full rub reverse precession or exact 1/2 subharmonic vibration may be caused by oversize bearings and displacement of the rotor center.

In this case history, the corrective actions, i.e., reduce the top clearances of the bearings, increase the lub oil viscosity and exact alignment, provided instant results to alleviate excessive vibration caused by rotor to stator rubs in the centrifugal compressor.

REFERENCES

1. Bosmans, R. F.: Detection and Early Diagnosis of Potential Failures of Rotating Machinery. Joint ASME/IEEE Power Generation Conference, St. Louis, Missouri, October 4-8, 1981.
2. 高金吉: H型离心压缩机转子启动负荷对临界转速影响的探讨. 1982, 12
3. Muszynska, A.: Partial Lateral Rotor to Stator Rubs. C 281/84 © IMECHE 1984.
4. Martin, F. A.: The Effect of Manufacturing Tolerances on the Stability of Profile Bore Bearing, C273/84, © IMECHE 1984.
5. [日] 白木万博 「振動測定による故障診断」
日本機械学会第489回講演会記録 (79-8-23, 24. 東京. フォトリソグラフィにおける光阻液の流動特性と予知制御)
6. Bently, D. E.: Forced Subrotative Speed Dynamic Action of Rotating Machinery. ASME Publication, 74-pet-16.

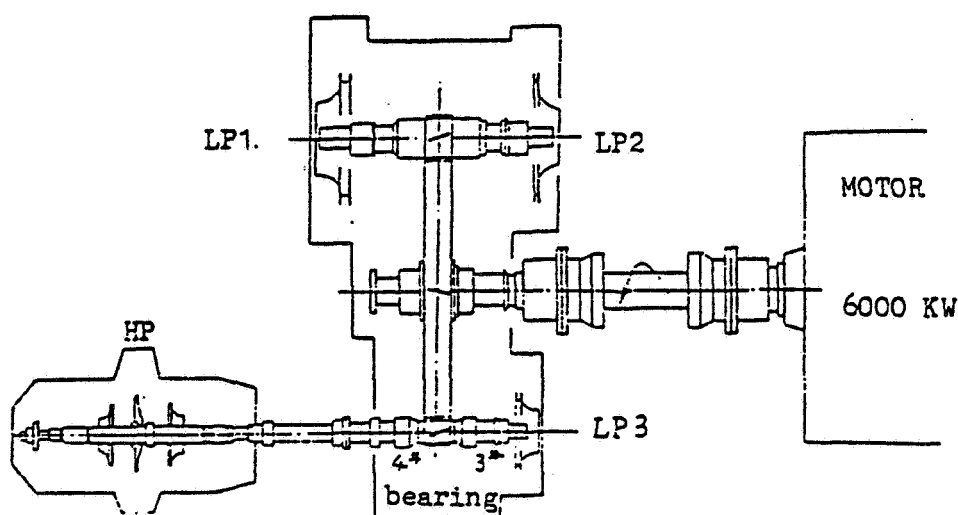


Figure 1.- H type of centrifugal compressor with HP casing.

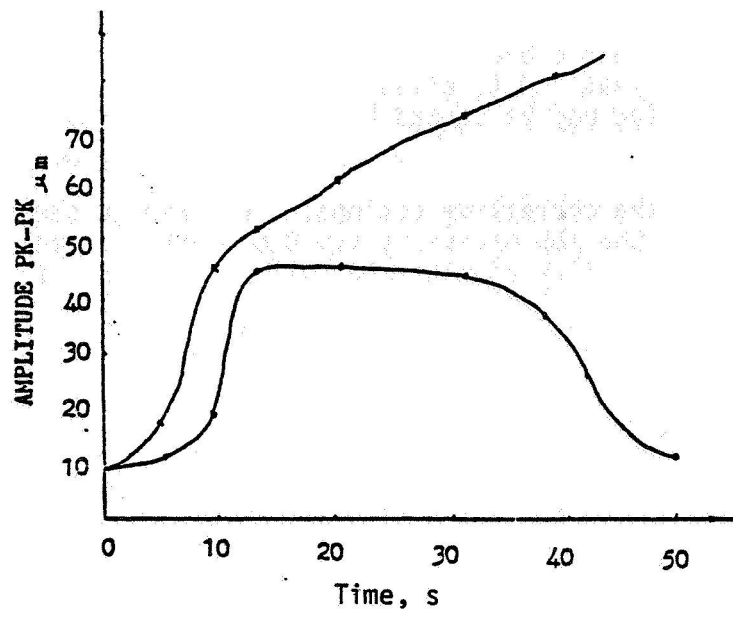


Figure 2.- Vibration versus time during startup. November 30, 1981.

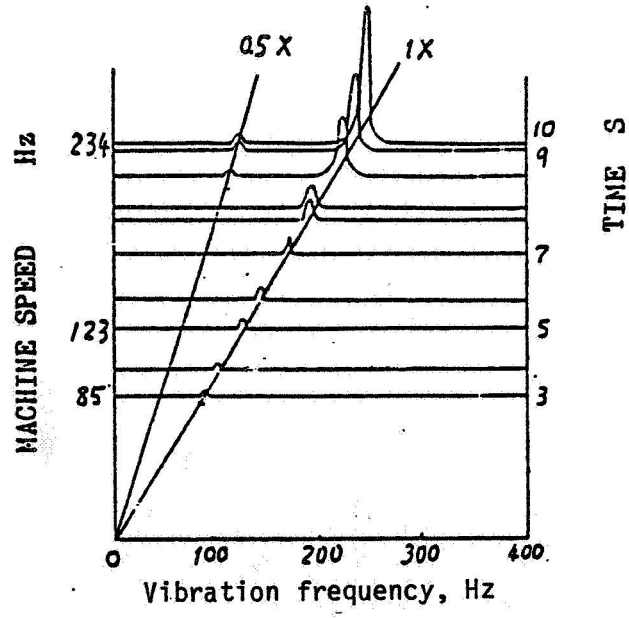


Figure 3.- Spectrum cascade during startup. February 10, 1983.

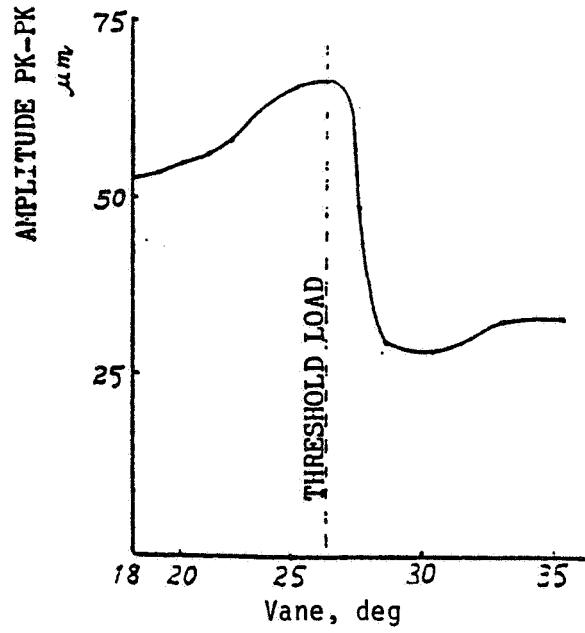


Figure 4.- Effect of dynamic load on vibration. February 10, 1982.

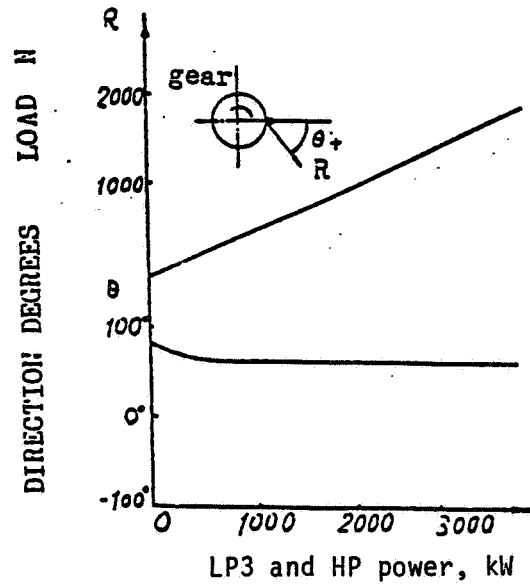


Figure 5.- Radial load versus machine power.

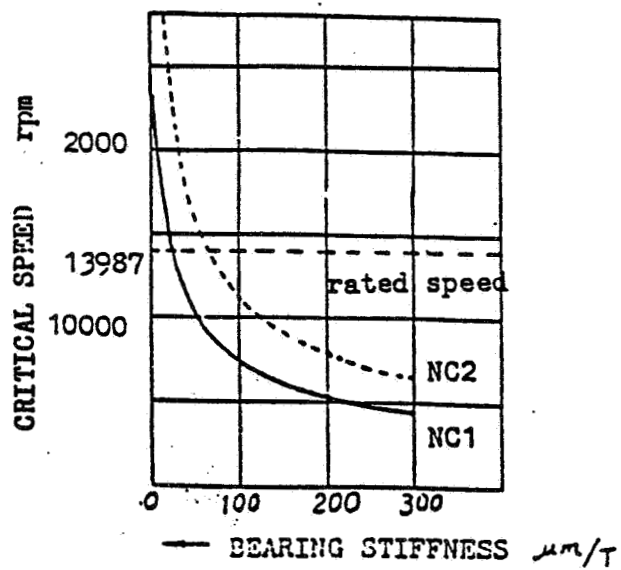
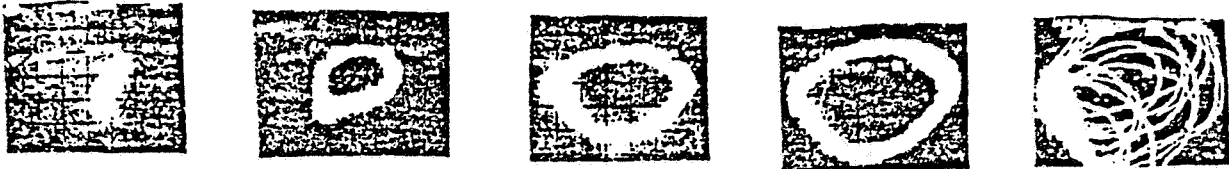
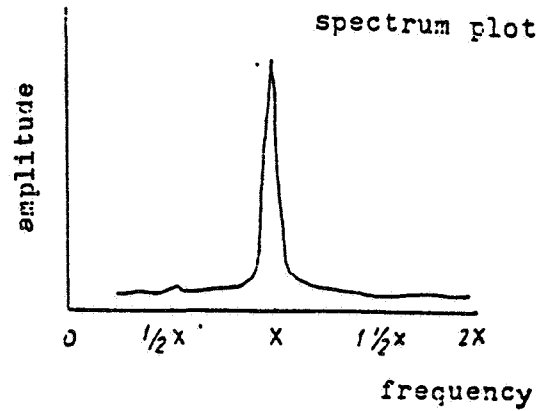
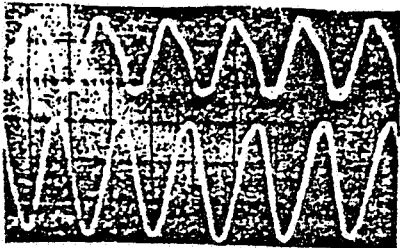


Figure 6.- Critical speed versus bearing stiffness.



orbit plots

time base

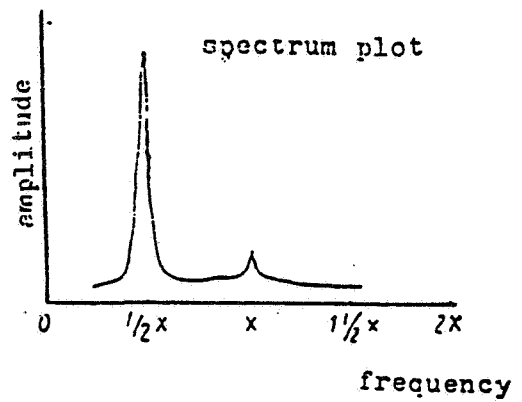


(a) Full-rub, reverse-precession vibration.



orbit plots

time base



(b) Exact 1/2 subharmonic vibration.

Figure 7.- Orbit, spectrum, and frequency plots.

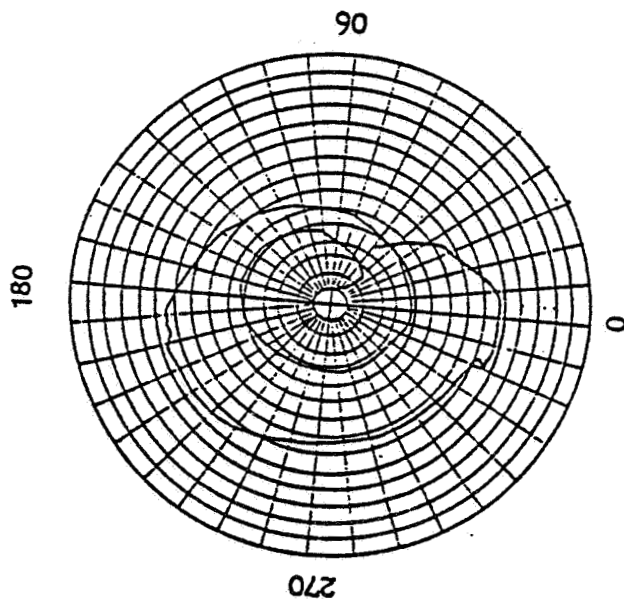


Figure 8.- Polar plot. February 13, 1982.

MEASURING DYNAMIC OIL FILM COEFFICIENTS OF SLIDING BEARING

Guan-ping Feng and Xi-kuan Tang
Qinghua University
The People's Republic of China

This paper presents a method for determining the dynamic coefficients of bearing oil film. By varying the support stiffness and damping, eight dynamic coefficients of the bearing have been determined. Simple and easy to apply, the method can be used in solving practical machine problems.

INTRODUCTION

An understanding of the properties of sliding bearings is important for solving the vibration problems of rotating machines, such as steam turbine generators. The dynamic oil film coefficients of a sliding bearing, as well as pedestal dynamic coefficients, are necessary for calculating rotor critical speed, unbalance response, system stability, etc. Many experts have set up test rigs for performing experiments on sliding bearings to obtain the eight dynamic oil film coefficients and calculate the experiment results, but the test rigs are often very complex.

This paper presents a method for determining the dynamic coefficients of the bearing oil film, using a new continually-changing stiffness pedestal. By varying twice the support stiffness, eight dynamic coefficients of the bearing have been determined. The continuously-changing stiffness pedestal is described.

1. A MEASURING PROCEDURE

Figure 1 illustrates the measuring procedure for determining the dynamic coefficient of bearing oil film. The procedure requires two steps:

1.1 Determining the pedestal dynamic coefficients:

The electric or hydraulic actuator is first used for actuating the pedestal vibration. According to the actuating force amplitude and phase and the pedestal vibration amplitude and phase, the pedestal dynamic coefficients can be determined. Next, the pedestal stiffness is changed, and the experiment is repeated to obtain the second pedestal dynamic coefficients.

The two pedestal dynamic coefficients are important for determining the dynamic coefficients of the bearing oil film.

1.2 Determining the dynamic coefficients of bearing oil film:

The rotor is run at the different speeds to obtain the pedestal vibration and the relative rotor vibration measurements. Next the pedestal stiffness is changed, and the experiment is repeated. According to the amplitude and phase

measurements for the rotor and pedestal, the eight dynamic coefficients of sliding bearing will be determined.

2. DETERMINING THE BEARING DYNAMIC OIL FILM COEFFICIENTS

Figure 2 illustrates the model of sliding bearing and pedestal.

The following notation has been used:

K_{xx}, K_{yy} = horizontal and vertical bearing oil film stiffness coefficients

K_{xy}, K_{yx} = bearing oil film cross-stiffness coefficients

C_{xx}, C_{yy} = horizontal and vertical bearing oil film damping coefficients

C_{xy}, C_{yx} = bearing oil film cross-damping coefficients

K'_{xx}, K'_{yy} = horizontal and vertical pedestal stiffness coefficients

K'_{xy}, K'_{yx} = pedestal cross-damping coefficients

C'_{xx}, C'_{yy} = horizontal and vertical pedestal damping coefficients

C'_{xy}, C'_{yx} = pedestal cross-damping coefficients

The force between the rotor and the bearing oil film is

$$\begin{bmatrix} P_{rx} \\ P_{ry} \end{bmatrix} = \begin{bmatrix} K_{xx} & K_{xy} & C_{xx} & C_{xy} \\ K_{yx} & K_{yy} & C_{yx} & C_{yy} \end{bmatrix} \begin{bmatrix} x_r \\ y_r \\ \dot{x}_r \\ \dot{y}_r \end{bmatrix} \quad (1)$$

where: P_{rx}, P_{ry} = the rotor unbalance force being transmitted to the oil film in the horizontal and vertical direction, x_r, y_r = the rotor center displacement in the horizontal and vertical direction relative to the pedestal.

The force being transmitted through the oil film to the pedestal can be represented by the following equation:

$$\begin{bmatrix} P_x \\ P_y \end{bmatrix} = \begin{bmatrix} K'_{xx} - \omega^2 m_{px} & K'_{xy} & C'_{xx} & C'_{xy} \\ K'_{yx} & K'_{yy} - \omega^2 m_{py} & C'_{yx} & C'_{yy} \end{bmatrix} \begin{bmatrix} x_a \\ y_a \\ \dot{x}_a \\ \dot{y}_a \end{bmatrix} \quad (2)$$

where: x_a, y_a = pedestal center displacement in the horizontal and vertical direction, m_{px}, m_{py} = the mass of the pedestal in the horizontal and vertical direction.

Omitting consideration of the oil inertia, the equations of motion can be represented by

$$P_x = P_{rx} \quad P_y = P_{ry} \quad (3)$$

When the rotor rotates at ω , synchronous vibrations of the rotor occur. Assuming that the bearing and pedestal are in contact, the vibrations are given by

$$\begin{aligned} x_{a_1} &= X_{a_1} \sin \omega t \\ y_{a_1} &= Y_{a_1} \sin(\omega t - \alpha_1) \\ x_{r_1} &= X_{r_1} \sin(\omega t - \theta_1) \\ y_{r_1} &= Y_{r_1} \sin(\omega t - \beta_1) \end{aligned} \quad (4)$$

In the same condition when the pedestal stiffness is changed, the new vibration of the rotor and the pedestal are given by

$$\begin{aligned} x_{a_2} &= X_{a_2} \sin \omega t \\ y_{a_2} &= Y_{a_2} \sin(\omega t - \alpha_2) \\ x_{r_2} &= X_{r_2} \sin(\omega t - \theta_2) \\ y_{r_2} &= Y_{r_2} \sin(\omega t - \beta_2) \end{aligned} \quad (5)$$

Substituting for equation (2) using equations (4) and (5), according to equations (1) and (3) the necessary equation is yielded:

$$\begin{bmatrix} K_{xx} \\ K_{xy} \\ C_{xx} \\ C_{xy} \end{bmatrix} = [A]^{-1}[G] \quad (6)$$

where:

$$[A] = \begin{bmatrix} X_{r_1} \cos \theta_1 & Y_{r_1} \cos \beta_1 & \omega X_{r_1} \sin \theta_1 & Y_{r_1} \omega \sin \beta_1 \\ -X_{r_1} \sin \theta_1 & -Y_{r_1} \sin \beta_1 & \omega X_{r_1} \cos \theta_1 & Y_{r_1} \omega \cos \beta_1 \\ X_{r_2} \cos \theta_2 & Y_{r_2} \cos \beta_2 & \omega X_{r_2} \sin \theta_2 & Y_{r_2} \omega \sin \beta_2 \\ -X_{r_2} \sin \theta_2 & -Y_{r_2} \sin \beta_2 & \omega X_{r_2} \cos \theta_2 & Y_{r_2} \omega \cos \beta_2 \end{bmatrix}$$

$$[G] = \begin{bmatrix} (K'_{xx_1} - m_{px}\omega^2)X_{a_1} \\ C'_{xx_1}\omega X_{a_1} \\ (K'_{xx_2} - m_{px}\omega^2)X_{a_2} \\ C'_{xx_2}\omega X_{a_2} \end{bmatrix}$$

Similarly, in the direction Y, the equation is given by

$$\begin{bmatrix} K_{yy} \\ K_{yx} \\ C_{yy} \\ C_{yx} \end{bmatrix} = [B]^{-1}[W] \quad (7)$$

where:

$$[B] = \begin{bmatrix} Y_{r_1} \cos\beta_1 & X_{r_1} \cos\theta_1 & Y_{r_1} \omega \sin\beta_1 & X_{r_1} \omega \sin\theta_1 \\ -Y_{r_1} \sin\beta_1 & -X_{r_1} \sin\theta_1 & Y_{r_1} \omega \cos\beta_1 & X_{r_1} \omega \cos\theta_1 \\ Y_{r_2} \cos\beta_2 & X_{r_2} \cos\theta_2 & Y_{r_2} \omega \sin\beta_2 & X_{r_2} \omega \sin\theta_2 \\ -Y_{r_2} \sin\beta_2 & -X_{r_2} \sin\theta_2 & Y_{r_2} \omega \cos\beta_2 & X_{r_2} \omega \cos\theta_2 \end{bmatrix}$$

$$[W] = \begin{bmatrix} (K'_{yy_1} - \omega^2 m_{py})Y_{a_1} \cos\alpha_1 + C'_{yy_1} Y_{a_1} \omega \sin\alpha_1 \\ -(K'_{yy_1} - \omega^2 m_{py})Y_{a_1} \sin\alpha_1 + C'_{yy_1} Y_{a_1} \omega \cos\alpha_1 \\ (K'_{yy_2} - \omega^2 m_{py})Y_{a_2} \cos\alpha_2 + C'_{yy_2} Y_{a_2} \omega \sin\alpha_2 \\ -(K'_{yy_2} - \omega^2 m_{py})Y_{a_2} \sin\alpha_2 + C'_{yy_2} Y_{a_2} \omega \cos\alpha_2 \end{bmatrix}$$

According to the experimental set-up, assuming that cross-stiffness and damping coefficients are equal to zero, the bearing oil film coefficients are calculated by using equations (6) and (7). If the cross-stiffness and damping are not equal to zero, the calculation is similar.

3. EXPERIMENTAL SET-UP AND MEASURING INSTRUMENTS

3.1 Experimental equipment

Figure 3 illustrates the construction of the pedestal, in which the stiffness can be changed by varying the oil pressure. When the oil pressure is changed, it affects the stiffness of the butterfly spring.

3.2 Measuring instruments

Figure 4 illustrates the measuring instruments. Two eddy current probes are

used to measure rotor vibration. Two velocity probes are used to measure pedestal vibration. The Digital Vector Filter (DVF 2) is used to measure the speed (rpm), phase, and amplitude.

CONCLUSIONS AND RECOMMENDATIONS

Table 1 shows the experimental results of $\varnothing 20$ sliding bearing oil film stiffness and damping coefficients. Most of the data are reasonable. The individual data are scattered, such as individual cross-stiffness coefficients being larger than horizontal and vertical stiffness coefficients at a specific speed, due to measuring errors. For example, the measuring phase error of 2° causes a coefficient error of 5%. When applying this method to the measurement of oil film coefficients, it is important to use the same pedestal and foundation. Changing the pedestal and foundation causes measurement errors of the oil film coefficients.

By varying the support stiffness, eight dynamic coefficients of the bearing have been determined. The method is simple and easy to apply.

REFERENCES

1. Barrett, L. E.: Experimental -- Theoretical Comparison of Instability Onset Speeds for a Three Mass Rotor Supported by Step Journal Bearings. ASME, April, 1980.
2. Guan-ping Feng: A Study on the Test of the Tilting Pad Journal Bearing. Journal of Qinghua University, No. 2, 1977.
3. Rubl, R. L., Conry, T.F., and Steger, R.L.: Unbalanced Response of a Large Rotor -- Pedestal -- Foundation System Using an Elastic Half -- Space Soil Model. ASME, Vol. 102, April, 1980.
4. Nikolazeson, J. L., Holmes, R.: Investigation of Squeeze -- Film Isotators for the Vibration Control of a Flexible Rotor. JMES, Vol. 21, No. 4, March, 1979.
5. Guan-ping Feng: Balance Technique and Balance Instruments. Journal, Instruments and Future, No. 1, 1982.
6. Guan-ping Feng: The Influence and Control of Flexible Rotor System Vibration with Changing Support Stiffness. Journal, Graduate Student Thesis of Qing Hua University, July, 1982.

Speed (rpm)	k_{xx} (kg/ μ)	k_{yy} (kg/ μ)	k_{xy} (kg/ μ)	k_{yx} (kg/ μ)	C_{xx} (kg·s/cm)	C_{yy} (kg·s/cm)	C_{xy} (kg·s/cm)	C_{yx} (kg·s/cm)
2000	0.19	0.120	-0.061	0.057	0.67	0.038	0.45	0.89
3000	0.245	0.163	-0.11	0.043	0.84	0.61	-0.002	-0.23
4000	0.55	0.287	-0.23	0.102	0.031	-0.075	-0.03	-0.67
5000	0.04	0.064	0.081	-0.042	-0.078	0.37	0.043	0.045
6000	0.134	0.07	0.096	0.037	0.66	0.45	-0.018	-0.051
7000	0.075	0.139	0.020	0.16	0.42	0.024	0.34	-0.046
8000	0.105	0.212	-0.016	-0.11	0.67	0.41	1.28	-0.062
9000	0.203	0.197	0.001	0.018	-0.013	0.07	-0.31	0.76
10000	0.348	0.296	0.078	0.062	0.076	0.105	0.69	0.46
11000	0.375	0.352	0.021	-0.030	0.26	-0.24	-0.78	0.087

Table 1 THE EXPERIMENTAL RESULT FOR $\varnothing 20$ SLIDING BEARING OIL FILM DYNAMIC COEFFICIENTS

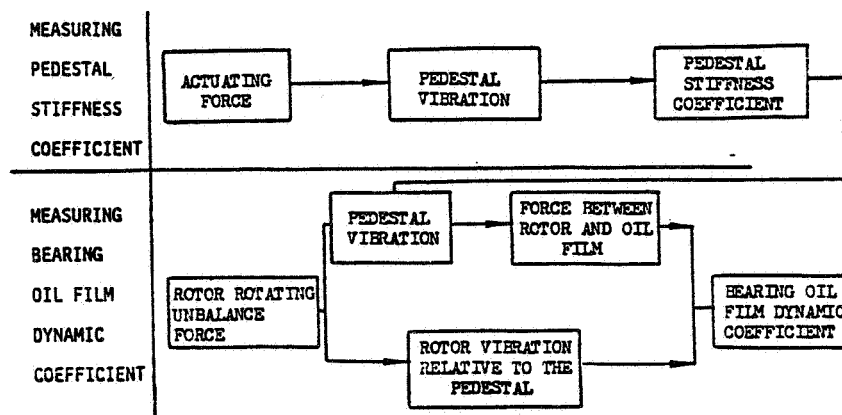


Figure 1. - Measuring procedure.

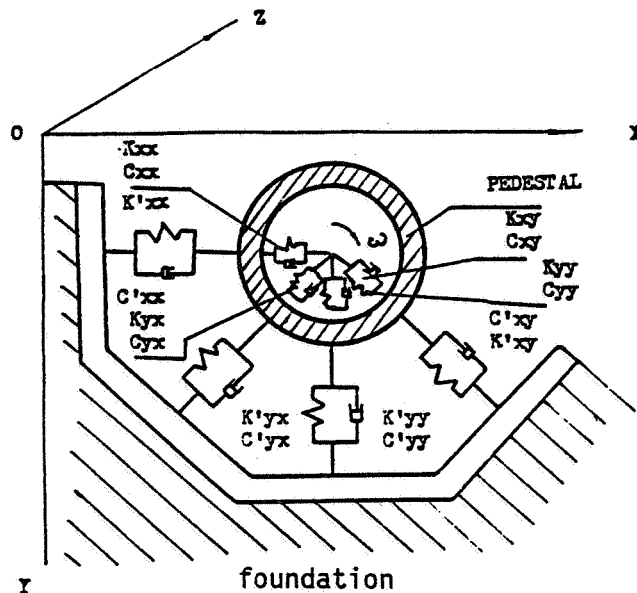


Figure 2. - Model of sliding bearing and pedestal.

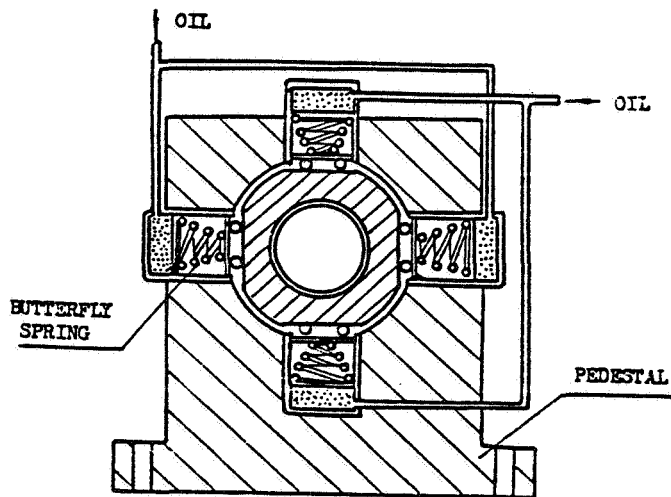


Figure 3. - Construction of pedestal with variable stiffness.

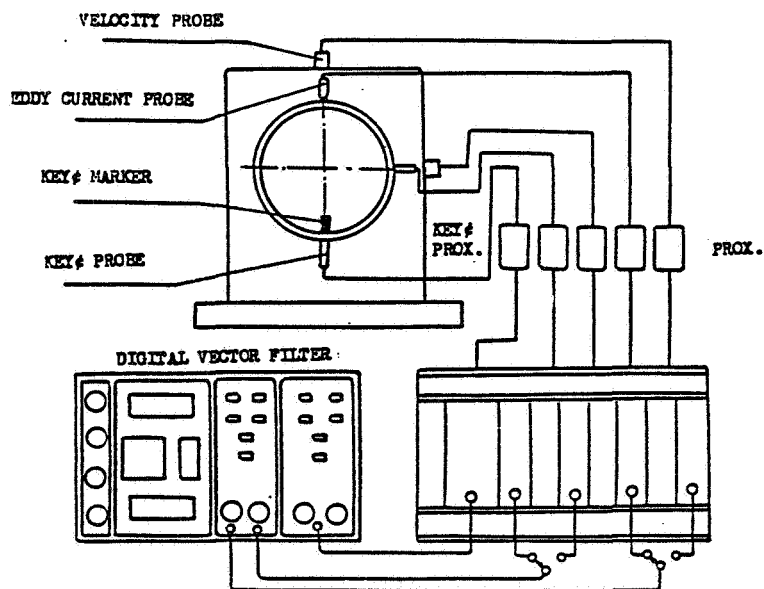


Figure 4. - Measuring instruments and their connection.

CRACKED SHAFT DETECTION ON LARGE VERTICAL NUCLEAR REACTOR COOLANT PUMP

L. Stanley Jenkins
Westinghouse Electric Corporation
Cheswick, Pennsylvania 15024

Due to the difficulty and radiation exposure associated with examination of the internals of large commercial nuclear reactor coolant pumps (RCP's), it is necessary to be able to diagnose the cause of an excessive vibration problem quickly without resorting to extensive trial and error efforts. Consequently, it is necessary to make maximum use of all available data to develop a consistent theory which locates the problem area in the machine.

This type of approach was taken at Three Mile Island (TMI), Unit #1, in February 1984 by the author to identify and locate the cause of a continuously climbing vibration level of the pump shaft. The data gathered necessitated some in-depth knowledge of the pump internals to provide proper interpretation and avoid misleading conclusions. Therefore, the raw data included more than just the vibration characteristics.

Pertinent details of the data gathered is shown herein and is necessary and sufficient to show that the cause of the observed vibration problem could logically only be a cracked pump shaft in the shaft overhang below the pump bearing.

MACHINE DESCRIPTION

TMI #1 is a Babcock and Wilcox Nuclear Steam Supply System (NSSS) with four 93A spool piece design reactor coolant pumps designed and manufactured by Westinghouse, Electro-Mechanical Division. Pump head and flow are about 107 m/7.20 m³/sec. at 288°C in the loop. The pumps are vertical and driven by Allis Chalmers 6700 kw (rated) motors (totally enclosed, water/air cooled). The spool piece design is a common feature to this type of pump whereby an 457 mm long section of shaft can be removed to permit maintenance of the seals without removal of the motor and breaking of the pump/motor alignment. The 93A pumps in this plant are a special adaption of the very common series of 93A pumps found in the majority of Westinghouse NSSS's. A cutaway view of the typical 93A RCP is shown in Figure 1. Detail differences between the TMI #1 pumps and the typical 93A pump design are insignificant relative to the discussion details in this paper.

The TMI #1 Reactor Coolant System (main primary piping only) is shown diagrammatically in Figure 2. The range of flows possible with this system design (as a percentage of total four pump operation "best estimate" flow) is depicted in Table 1 for typical combinations of pump operation. The negative values indicates reverse flow in the loop. Increasing flow rates generate radial loads (on the impeller, fixed relative to the casing) which increase approximately as the square of the flow rate. This load is estimated to be in excess of 2300 kgf for single pump operation at TMI #1.

Vibration probe locations are shown in Figure 1. This is the standard probe location for all RCP's of this design. The shaft probes "see" the 347 stainless steel shaft surface. Nominal pump shaft diameter is 200 to 230 mm.

INITIAL DETECTION OF THE PROBLEM AND VIBRATION CHARACTERISTICS OBSERVED

In late January 1984, EMD Engineering was alerted by plant personnel of a worsening vibration problem on "1B" RCP (referred to as B). The shaft vibration had been in the 225 - 280 micron (9 - 11 mil) range for several months prior to this, during which time the pump was run primarily alone. Approximately 1400 hours had been logged on the pump in this mode. A tape of the vibration signals was made prior to shutdown of the pump as the levels neared 750 microns (30 mils) and the rate of increase climbed to 25 microns/hr (1 mil/hr) (instruction book limits, single pump operation).

The investigation into the cause of the problem took the following direction:

1. Compare frequency content, vibration levels, etc., on all RCP's in the plant.
2. Determine the effect of balance weight changes on B RCP.
3. Run the motor on B RCP "no-load" and compare data to the loaded operation.

The following was noted during these tests:

1. Comparison of vibration levels between pumps indicated nothing unusual. However, B RCP contained a large amount of 2X vibration component not present to any significant degree in the other RCP's. Table 2 shows the vibration level and frequency content comparison.
2. A reduction in 1X (running speed = 20 Hz) motion due to the addition of weight to a pump coupling bolt had no impact on the 2X component. Table 3 shows the results of this test. Response to the weight was normal (approximately 3.5 grams/micron, 40° lag).
3. During no-load motor operation, all 2X components disappeared from frame and shaft (motor) data (a probe had been mounted to read motor shaft motion specifically for this one test).

Figures 2 through 6 are samples of the waveform and spectral data taken during the above tests on B RCP.

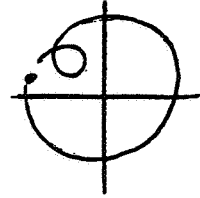
ASSESSMENT OF THE FACTS

In addition to the facts noted above, the following was known:

1. The 2X vibration level would "ratchet" up on each start of the coupled pump assembly (see Figure 7).
2. The pump and motor were found to be 812 microns (32 mils) out of alignment, laterally (centerline to centerline shift). The effect of this is depicted in Figure 8.

3. A shaft orbit with an inner loop was observed during coupled pump operation, like that shown here:

Per standard references on machinery malfunction diagnostics, it was apparent that two possibilities for the cause of the problem were pump/motor misalignment or a cracking shaft. Other possibilities such as a loose impeller, bearing deterioration, or full or partial rubs were eliminated since they were inconsistent with some or all of the data taken. The primary problem was then determining which of these two possibilities was actually correct.



RESOLUTION OF THE ALIGNMENT/CRACK CONTROVERSY

Assuming that a cracked shaft was the most logical choice of malfunctions, to rationally explain the observations and data it was necessary to: 1) choose a location for a crack in the shaft and predict the shaft motion to determine if it yields the observed shaft motion, and 2) show that the misalignment observed could not produce sufficient shaft bending to cause the observed 2X motion. The obvious method of realignment and rerunning the pump was discarded due to the time consumption for this effort, unnecessary radiation exposure, and the desire to minimize damage to the stationary parts due to additional operation.

The rationale for elimination of misalignment induced 2X is based on bearing clearances in the pump and motor plus the beneficial effect of long distances between bearings. Again, referring to Figure 8 it is easy to see that a minimum of 457 microns (18 mils) centerline shift, without any tilting of the rotor on the Kingsbury thrust bearing, is possible without incurring any bending of the rotor. Furthermore, the long distance between bearings will permit additional tilting of the motor rotor (the Kingsbury thrust bearing can accommodate this easily as will the spherically seated pump bearing) to accommodate the measured 812 micron shaft lateral misalignment with introduction of some edge loading of the motor radial tilted pad bearings. Hence, it is highly unlikely that 2X would be generated by bearing misalignment. Note that labyrinth rubbing (which was predicted on the basis of a separate evaluation of the direction of misalignment coupled with anticipated radial motion of the impeller under a fixed load in the casing) does not produce shaft bending since rubs in water wear out in a relatively short time.

The rationale for showing that the observed motion is predictable is more difficult. First of all, it is logical to place the crack below the pump bearing. (The presence of a fixed radial load in the casing, and the observation that balance weight response was normal suggest a crack below the pump bearing.) Then, by utilizing a simplified model of the pump shaft and taking the motor shaft between bearings as a "built-in beam," it is possible to relate a dynamic motion observed at the pump coupling to a stationary -- fixed in the casing -- hydraulic load at the impeller. The end result of this analytical exercise (using the principal of superposition of loadings and deflections to establish the proper phasing of the motions at the impeller and coupling) is shown in Figures 9 and 10. This effect was successful in not only predicting the observed 2X motion qualitatively but also, when the 1X motion is added in (generated by the "hinging" action of the impeller mass below the crack) the observed composite waveform was predicted. Compare Figure 10 with Figure 4 where 1X and 2X amplitudes are nearly equal.

ADDITIONAL (NON-ESSENTIAL) VERIFICATION OF CRACK EXISTENCE

For obvious reasons, there was an extreme reluctance to accept that the difficult to access pump shaft was cracked. Hence, another independent method of crack verification was desired. An Ultrasonic Test (UT) of the 3.3 m long pump shaft was attempted from the accessible coupling end. Data obtained was compared to another survey on a new pump shaft on site. The best available comparison of data (actually obtained after removal of the pump shaft) is in Figure 11. During the investigative effort and afterwards as well, it was found to be nearly impossible to predict by UT, from the coupling end of the shaft, if a crack existed in the overhang and where in the overhang it was located.

It was noted, however, that once the impeller end of the shaft was exposed that a UT of this end of the shaft produced very strong evidence of a sizeable discontinuity. The axial location predicted and its orientation relative to the coupling keyway was very close to the predictions made on the basis of vibration analysis described in this paper. From the UT check of the impeller end, approximately 60% of the cross-section was estimated to be cracked through.

CONCLUSIONS

It is evident from by this effort that it is possible to positively identify the presence of a crack in a radially loaded vertical machine by means of vibration analysis techniques and use of very simple analytical methods. A determination of response to balance weight and separation of the machine train into separate operable components to the greatest extent possible is very important to positively identifying the location of the suspected crack.

Non-destructive examination by UT of the shaft of a 93A RCP from the coupling end has not yet proven to be a reliable indicator of the presence of a crack. However, a prediction of anticipated shaft motion based on the expected location of the crack (in a bearing span or overhang) produced the observed motion with simple rotor assembly models. Knowledge of some of the characteristics of the machine is a prerequisite for this approach.

SYMBOLS AND UNITS

1 mil = 25.4 microns = .001 inch.

m	meter	kgf	kilogram (force)
°C	degrees Celsius	MPa	megapascal
kw	kilowatt	1X	running speed component of vibration
sec	second	2X	twice running speed component of vibration
mm	millimeter		

TABLE 1

TYPICAL RCP FLOWS AS A FUNCTION OF PUMP COMBINATIONS

(REFERENCE: TMI #1 OPERATING INSTRUCTIONS, VOL 1)

PUMPS RUNNING	% FLOW PER PUMP			
	A	B	C	D
A B C D	25	25	25	25
A B C	26	26	32	-10
A B	27	27	-4	-4
A C	33	-9	33	-9
A	33	-8	-2	-2

Since all RCP's have nominally identical impellers, any permutations of the above (e.g., CD instead of AB) are omitted as they are equivalent to that shown.

TABLE 2

SHAFT AND FRAME VIBRATION

RCP
A, B, C, D

RCP	TIME/ DATE, ETC	SHAFT VIBRATION				FRAME VIBRATION
A	1719	CPLG. WEIGHTS: Unchanged since March 1979				H V / .9
	2/3/84 54°C	COMPOSITE (ALL PASS): H 30 V 24				
	2.17MP _a	1/2 H .4 V .4 X 1X 25.2 21.6 2X .9	H 30 V 24		V 1.3	
B	1228	CPLG. WEIGHTS: Unchanged since March 1979				H V /
	2/1/84 54°C	COMPOSITE (ALL PASS): H 25 V 28				
	2.17MP _a	1/2 H .3 V .5 X 1X 16.8 20.8 2X 8.0	H 25 V 28		H 7.2 V 8.0	
C	1103	CPLG. WEIGHTS: Unchanged since March 1979				H V /
	2/1/84 54°C	COMPOSITE (ALL PASS): H 15 V 14				
	2.17MP _a	1/2 H .3 V .3 X 1X 11.2 11.2 2X .4	H 15 V 14		H .4 V .3	
D	1550	CPLG. WEIGHTS: Unchanged since March 1979				H V / .9
	2/3/84 54°C	COMPOSITE (ALL PASS): H 21 V 23				
	2.17MP _a	1/2 H .3 V .3 X 1X 18.8 20.4 2X .3	H 21 V 23		H .3 V .5	

All vibration levels in mills, peak-to-peak

ORIGINAL PAGE IS
OF POOR QUALITY

TABLE 3

SHAFT AND FRAME VIBRATION

CHANGES DUE TO BALANCING

RCP-8

TIME/ DATE, ETC	SHAFT VIBRATION				FRAME VIBRATION
1228	CPLG. WEIGHTS: Unchanged since 1979				H V /
2/1/85 54°C	COMPOSITE (ALL PASS): H 25 V 28				
2.17MP _a	1/2 H .3 V .5 X 1X 16.8 20.8 2X 8.0	H 25 V 28		H 8.0 V 7.2	
1938	CPLG. WEIGHTS: Add 881g to Bolt #5				H V / 1.5
2/3/84 54°C	COMPOSITE (ALL PASS): H 7.8 V 11.2 2X 8.8				
2.17MP _a	1/2 H .2 V .4 X 1X 7.8 11.2 2X 8.8	H 7.8 V 11.2 2X 8.8		H 8.8 V 8.2	

All vibration levels in mills, peak-to-peak

ORIGINAL PAGE IS
OF POOR QUALITY

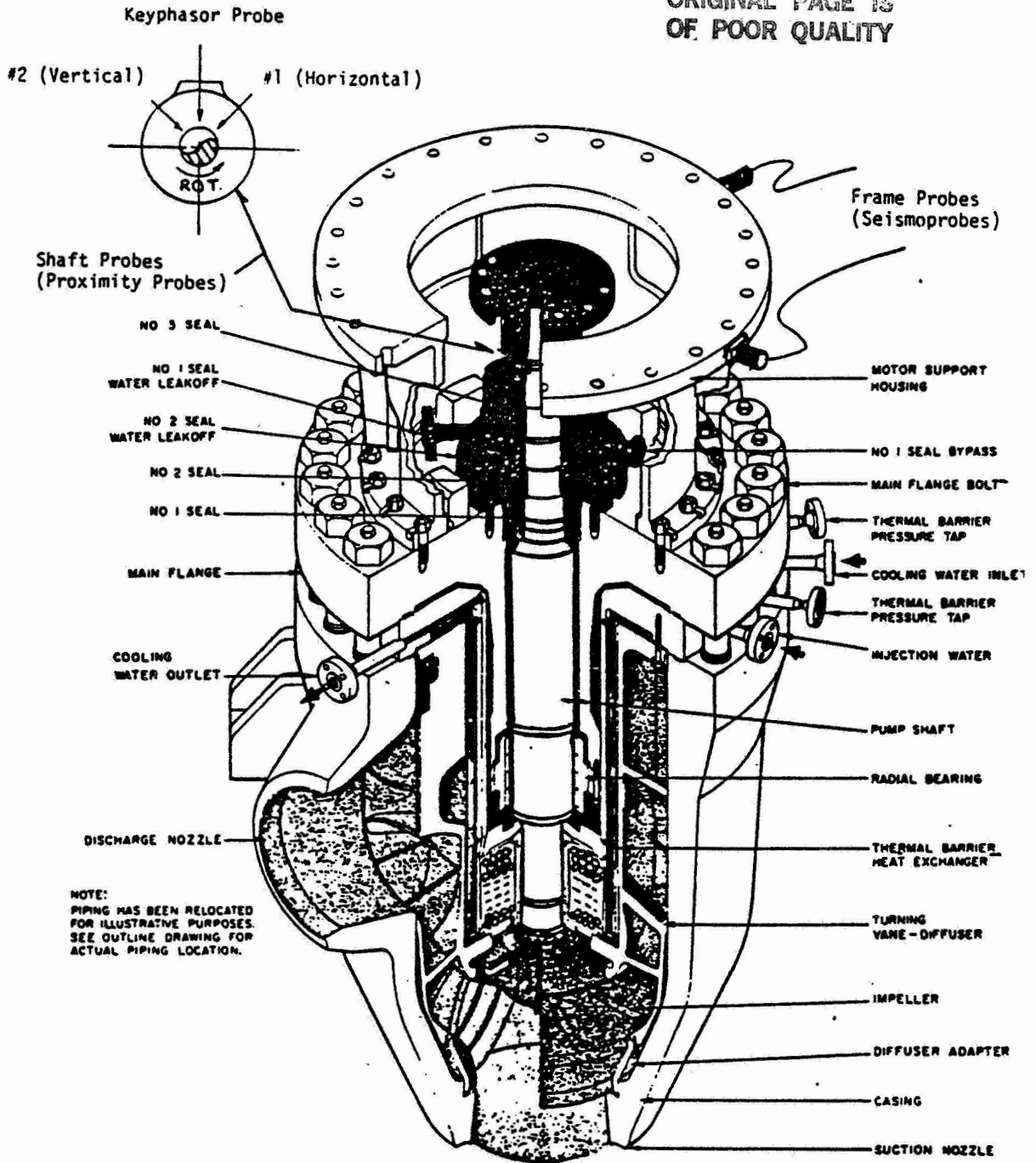
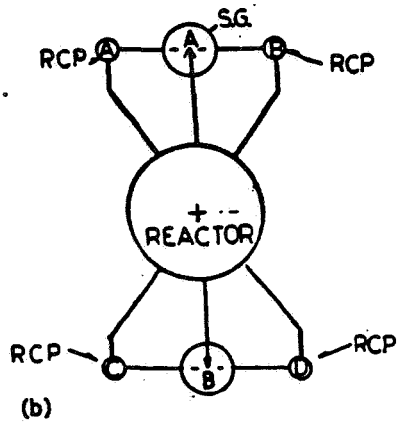
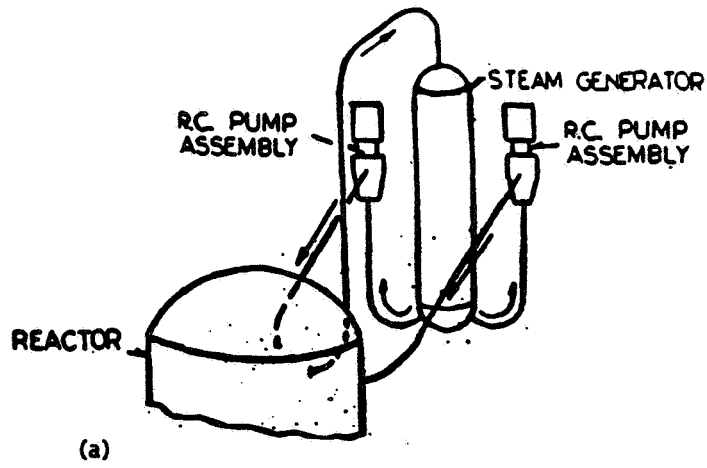


Figure 1. - Cutaway view of typical reactor coolant pump.

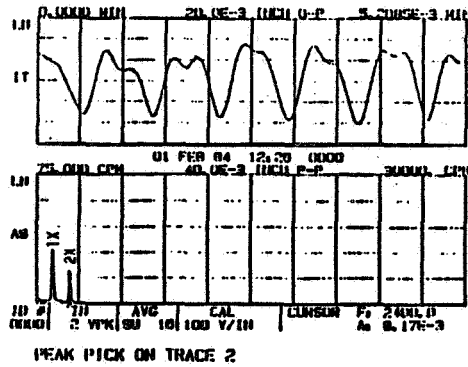


(a) Isometric view of typical primary piping at TMI #1 (one S.G. loop shown).
 (b) Plan view of primary piping at TMI #1.

Figure 2. - Piping schematic.

ORIGINAL PAGE IS
OF POOR QUALITY

RC PIB HORIZONTAL



INCH P-P CPM
16.8E-3 1200.0
8.00E-3 2400.0

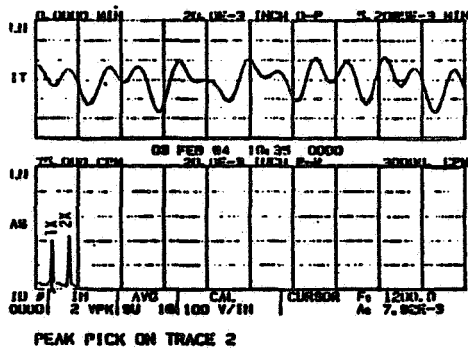
01-FEB-84
12:28:40

TIME/DATE, ETC	SHAFT VIBRATION	FRAME VIBRATION
1228 2/1/84 54°C 2.17MP	CPLG. WEIGHTS: Unchanged since March 1979 COMPOSITE (ALL PASS): 1/2 H V .3 1X H V 16.8 20.8 2X H V 7.2	H V

All vibration levels in mils, peak-to-peak

Figure 3. - Sample of waveform and spectral data taken on B RCP: February 1, 1984 (original data).

RC PIB HORIZONTAL



INCH P-P CPM
7.80E-3 1200.0
8.80E-3 2400.0

03-FEB-84
19:38:05

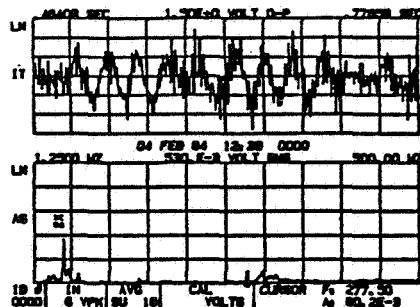
TIME/DATE, ETC	SHAFT VIBRATION	FRAME VIBRATION
1938 2/3/84 54°C 2.17MP	CPLG. WEIGHTS: Add 880g to Bolt #5 COMPOSITE (ALL PASS): 1/2 H V .2 4 1X H V 7.8 11.0 2X H V 8.8 9.5	H V .6 1.5

All vibration levels in mils, peak-to-peak

Figure 4. - Sample of waveform and spectral data taken on B RCP: February 3, 1984 (after balance).

R C PIB

FRAME HORIZ



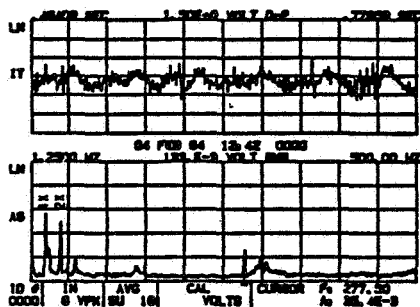
VOLT RMS	HERTZ
196. E-3	40.000
63. 6E-3	46.252
58. 3E-3	277.52
58. 3E-3	297.52

04-FEB-84.

12: 39: 35

RC PIB

FRAME VERT



VOLT RMS	HERTZ
75. 8E-3	20.001
37. 2E-3	23.751
66. 5E-3	40.000
34. 6E-3	277.52

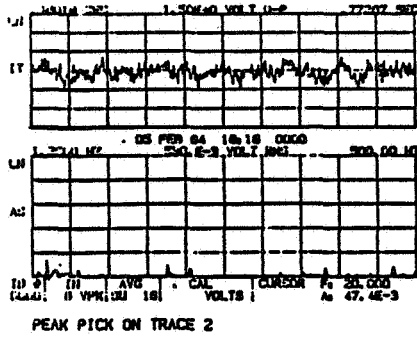
04-FEB-84

12: 43: 46

AFTER BALANCE

Figure 5. - Frame vibration spectral data: February 4, 1984 (after "balancing").

RC PIB



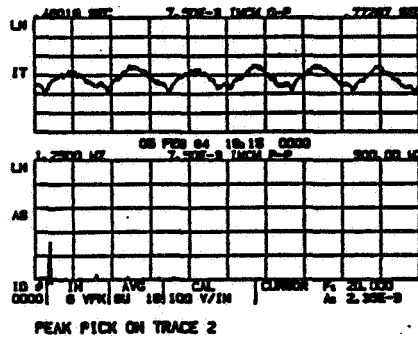
VOLT RMS	HERTZ
42.4E-3	20.001
47.7E-3	176.26
42.4E-3	470.02

Uncoupled Frame Motion

05-FEB-84

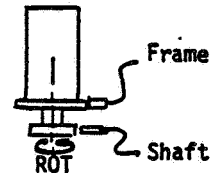
18:18:06

RC PIB



INCH P-P	HERTZ
2.33E-3	20.001

Motor Stand Not Shown



Uncoupled Motor Shaft Extension Motion

05-FEB-84

18:16:07

Figure 6. - Spectral and waveform plots from uncoupled motor run of B RCP, showing frame and shaft motion.

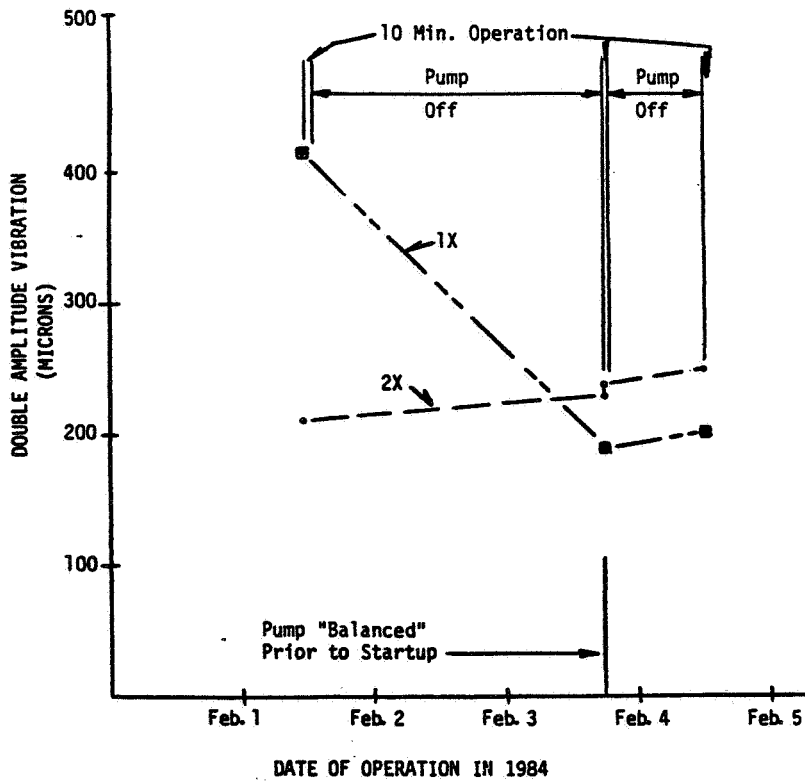


Figure 7. - Trend plot for 1X and 2X vibration levels for B RCP shaft.

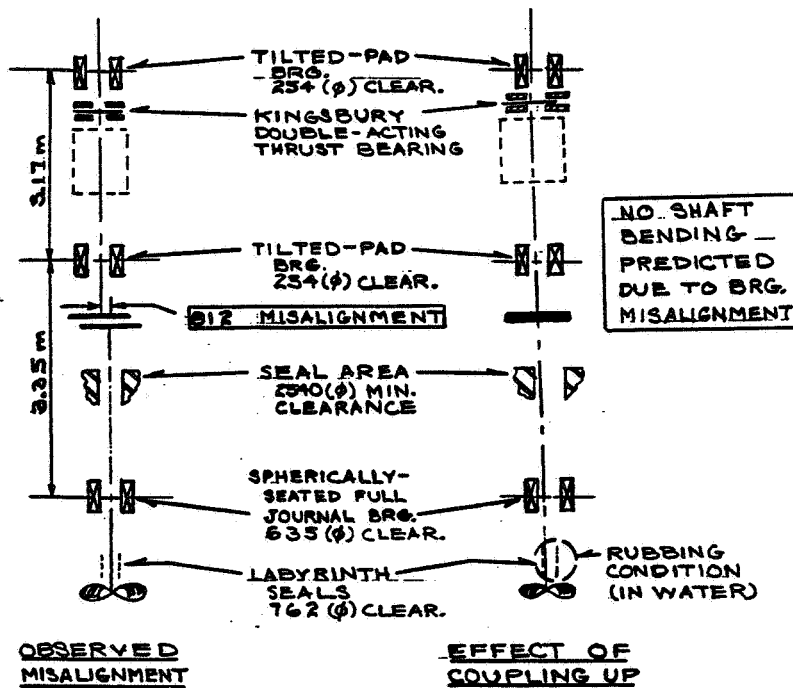


Figure 8. - Effect of 0.032-inch-bearing centerline offsets on shaft bending.

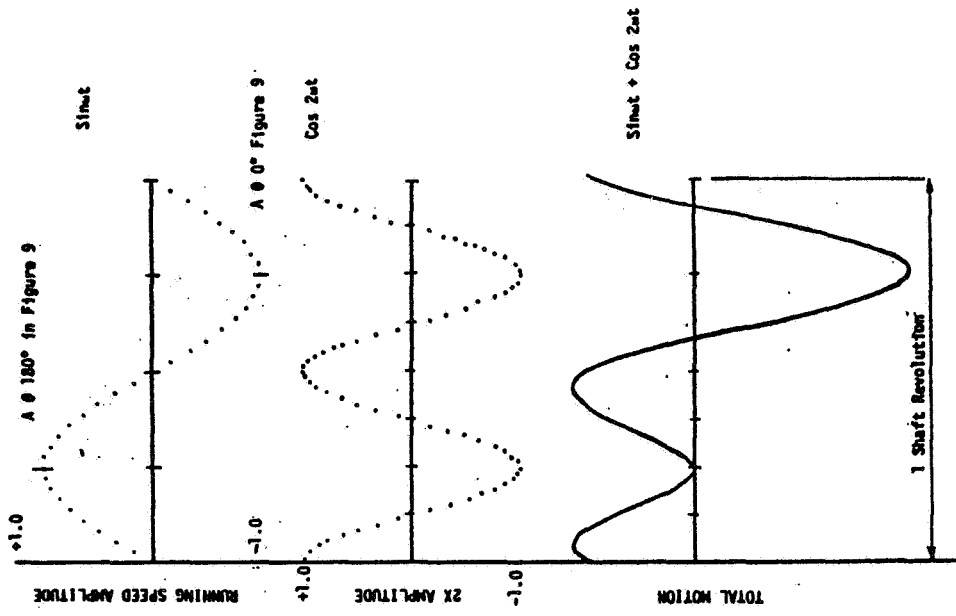


Figure 10. - Graphical summation of predicted 1X and 2X motions at pump coupling.

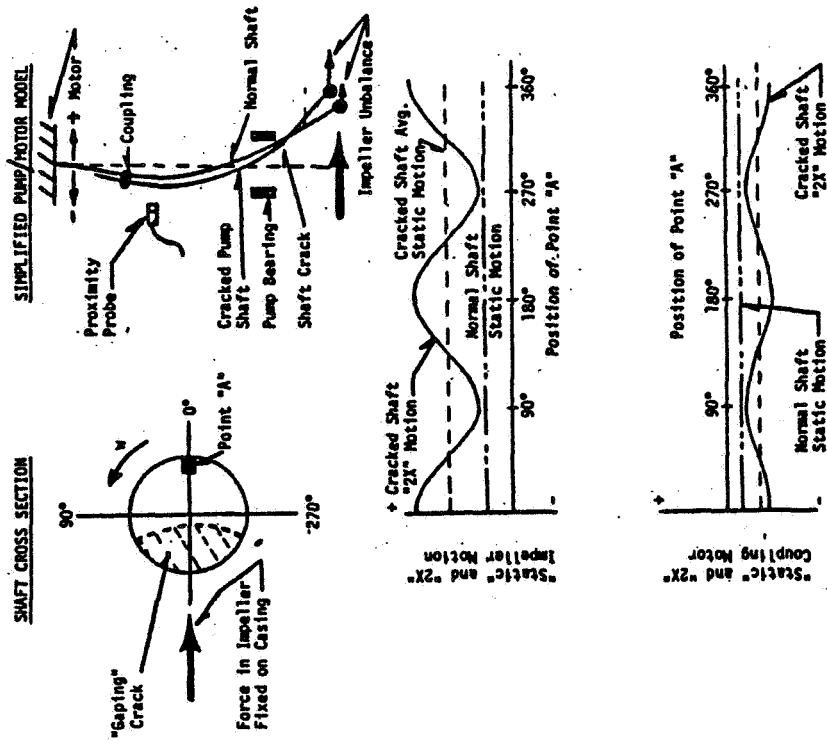
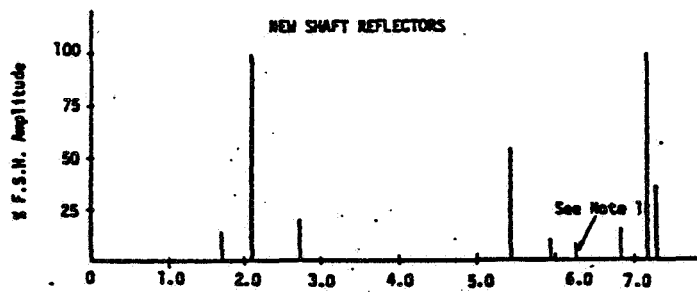
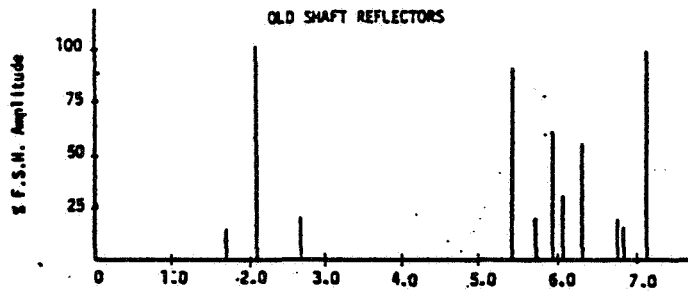
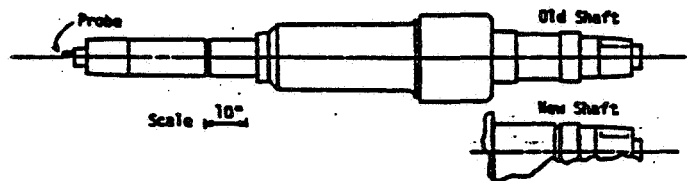


Figure 9. - Dynamic (2X) and static impeller and coupling motion.



Note 1: Probably reflection from anti-rotation pins

COUPLING
END



IMPELLER
END

Figure 11. - Comparison of old shaft and new shaft UT reflectors.

PUMP INSTABILITY PHENOMENA GENERATED BY FLUID FORCES

S. Gopalakrishnan
 Borg Warner Industrial Products, Inc.
 Long Beach, California 90802

Rotor dynamic behavior of high energy centrifugal pumps is significantly affected by two types of fluid forces: one due to the hydraulic interaction of the impeller with the surrounding volute or diffuser and the other due to the effect of the wear rings. In this paper, the available data on these forces is first reviewed. A simple one degree of freedom system containing these forces is analytically solved to exhibit the rotor dynamic effects. To illustrate the relative magnitude of these phenomena, an example of a multistage boiler feed pump is worked out. It is shown that the wear ring effects tend to suppress critical speed and postpone instability onset. But the volute-impeller forces tend to lower the critical speed and the instability onset speed. However, for typical boiler feed pumps under normal running clearances, the wear ring effects are much more significant than the destabilizing hydraulic interaction effects.

SYMBOLS

b_2	impeller exit width
c	damping coefficient associated with wear rings
\bar{c}	$= c/\omega$
c^*	critical damping
c	general damping coefficient
F^g	applied force
H	radial clearance
H^*	nominal radial clearance
j	$\sqrt{-1}$
k	stiffness coefficient
k_s	shaft stiffness
K^*	non dimensional stiffness coefficient
\bar{m}	mass
m_h, m_h'	volute-impeller interaction mass coefficient
m_L	Lomakin mass
R^L	unbalance response amplitude
r_2	impeller tip radius
t	time
U_2	impeller exit tip speed
X, Y	independent geometric coordinates
Δ	mass eccentricity
ρ	density

ω angular velocity
 Ω whirl angular velocity
 ω^n critical speed in air
 ξ^n c_g/c^*

Subscripts:

o nominal or design condition

BACKGROUND

The speed and energy requirements of centrifugal pumps in critical service have steadily increased in the last one or two decades. This increasing power density has been contributing to reliability problems as well documented for example with the space shuttle engine pumps. Less well known, however, are the problems of pumps in services involving boiler feed, water injection, reactor charge, etc. In a number of cases, pump rotor dynamic phenomena appear to be at the root of field troubles. As a consequence, considerable research is being carried out at present to identify the rotor dynamic exciting forces and the corresponding response of the pump system.

It is now clear that in high energy centrifugal pumps, rotor dynamic behavior is significantly affected by the fluid dynamic phenomena arising in the gaps between rotating and stationary members. One class of such a rotor-stator interaction arises in the gap between the impeller and the surrounding stationary member. The stationary member may be a single or a double volute or a diffuser. The typical radial gap between the tongue of the volute or diffuser and the impeller periphery is between 2 and 10 percent of the impeller radius. The other class of interaction occurs in the close-clearance gaps whose function is to minimize the leakage of pumped fluid from high pressure to low pressure areas. These gaps, which are variously called as wear-rings or seal rings, have typical clearance to radius ratios of the order of 0.2%. The forces in these gaps are much stronger than those due to volute/diffuser-impeller interactions.

In this paper, the physical mechanism for the volute-impeller interaction is first described. Available data for estimating its magnitude are then reviewed. The response of a simplified rotating system subject to the volute-impeller forces as well as wear ring forces is then calculated using an analytical model. The amplitude of response and the onset of instability are predicted by this approach. The purpose of developing this model is more to derive a physical appreciation of the effects than to obtain accurate results for practical geometries. In this spirit, the method is applied to a multistage boiler feed pump, and the results reveal certain very interesting effects of the geometries typically utilized in such pumps.

VOLUTE IMPELLER INTERACTION EFFECTS

At the design point, the flow field in the volute is characterized by a free vortex velocity distribution in the radial direction. In the circumferential direction, the velocity and static pressure are uniform. As a consequence, the relative flow in the impeller is steady. If the impeller is

now displaced with respect to the geometric center of the volute, the flow area in the direction of motion is squeezed, and the tangential velocity is increased. At the diametrically opposite position, the area is increased and the velocity is decreased. Assuming no change in total head or losses, the differences in velocity on either end results in a difference of static pressure. In particular, the static pressure in the area in the direction of the displacement is reduced. Thus a force now is exerted in the same direction as the displacement, i.e., the force does not tend to restore the deflection. Hence the resulting stiffness is negative. Further, since the tangential velocities are now different, integration of the momenta around the circumference will lead to a different value than when the impeller is centered. In particular, if we only look along the direction in which deflection has taken place, the difference in tangential momenta will lead to a force at right angles to the deflection, thus generating the cross-coupling stiffness.

At off-design conditions, the flow field is no longer uniform, and the impeller relative flow is unsteady. The computation of the flow field for such situations is quite complex. Reference 1 contains a one dimensional finite element calculation method. It is evident that even a physical understanding of the flow mechanism when the impeller is moved off center is difficult. This phenomenon is being extensively studied at CalTech and test results for stiffness coefficients are reported in reference 2. The coefficients are non-dimensionalized as below:

$$K^* = k \frac{r_2}{\left(\frac{1}{2} \rho U_2^2\right) 2\pi r_2 b_2}$$

K^* is considered to be a constant for a given geometry. Thus the dimensional stiffness k varies only with speed for a given geometry and fluid density. It is convenient to define the stiffness coefficients in the following way:

$$\begin{aligned} k_{xx} &= -m_h \omega^2 = k_{yy} \\ k_{xy} &= m_h' \omega^2 = -k_{yx} \end{aligned}$$

Here the coefficients m_h and m_h' have units of mass. Based on data of reference 2, as the direct stiffness is negative, m_h will be positive. The cross coupled terms are assumed to be equal and opposite. From the above:

$$\begin{aligned} m_h &= K_{xx}^* \pi \rho r_2^2 b_2 \\ \text{and} \\ m_h' &= K_{xy}^* \pi \rho r_2^2 b_2 \end{aligned}$$

WEAR RING PHENOMENA

The dynamic effects induced by the leakage flow in close clearance annular fits have been extensively studied. A recent review of pertinent publications

can be found in reference 3. Based on these studies, the dynamic coefficients of wear rings can be represented as below:

$$\begin{aligned} k_{xx} &= k_{yy} = m_L \omega^2 \\ c_{xx} &= c_{yy} = 2 \bar{c} \omega \\ k_{xy} &= -k_{yx} = \bar{c} \omega^2 \\ c_{xy} &= c_{yx} = m_{xx} = m_{yx} = m_{yy} = m_{xy} = 0 \end{aligned}$$

Here m_L and \bar{c} have units of mass. The equations for computing these may be found in reference 4.

SIMPLIFIED ANALYSIS

To appreciate the significance of the fluid dynamic phenomena, a simplified rotor dynamic analysis of a single degree of freedom system can be carried out. The derivation below closely follows the analysis of H. Black (ref. 5) except that the volute-impeller interaction effect is now included. Assuming that the fluid forces can be represented as described earlier, we can obtain:

$$\begin{aligned} \begin{bmatrix} m & 0 \\ 0 & m \end{bmatrix} \begin{bmatrix} \ddot{x} \\ \ddot{y} \end{bmatrix} + \begin{bmatrix} k_s + m_L \omega^2 - m_h \omega^2 & \bar{c} \omega^2 + m'_h \omega^2 \\ -(\bar{c} \omega^2 + m'_h \omega^2) & k_s + m_L \omega^2 - m_h \omega^2 \end{bmatrix} \begin{bmatrix} x \\ y \end{bmatrix} \\ + \begin{bmatrix} 2\bar{c}\omega & 0 \\ 0 & 2\bar{c}\omega \end{bmatrix} \begin{bmatrix} \dot{x} \\ \dot{y} \end{bmatrix} = \begin{bmatrix} F_x \\ F_y \end{bmatrix} \end{aligned}$$

The response of the rotor system to unbalance can be obtained by assuming circular whirling.

$$\begin{aligned} r &= x + jy = R e^{j\omega t} \\ m \dot{r} + 2 \bar{c} \omega \dot{r} + \left\{ k_s + m_L \omega^2 - m_h \omega^2 - j (\bar{c} \omega^2 + m'_h \omega^2) \right\} r \\ &= m \Delta \omega^2 e^{j\omega t} \end{aligned} \quad (1)$$

The absolute value of the amplitude of response is:

$$|R| = \frac{m\Delta}{\sqrt{\left\{ \frac{k_s}{\omega^2} - (m - m_L + m_h) \right\}^2 + (\bar{c} - m'_h)^2}} \quad (2)$$

Critical speed is obtained when $|R|$ reaches a maximum value i.e., when:

$$\omega = \sqrt{\frac{k_s}{m + m_h - m_L}}$$

It is clear from the above that the negative direct stiffness of the volute-impeller interaction leads to a reduction in critical speed. Further, if the Lomakin mass is greater than the sum of the geometric mass and the volute-impeller interaction effect, there is no critical speed.

A second interesting point that may be observed is that the critical speed is independent of damping! The peak response under damped conditions occurs at the undamped natural frequency. Of course, this is true only for the case that the damping coefficient is proportional to the speed.

The stability of the rotating system can be analyzed by assuming circular whirling

$$r = R e^{j\Omega t}$$

The solutions will be more realistic if we assume a generalized damping coefficient c_g

$$c_g = \xi c^* = 2m\xi\omega_n$$

when ω_n is the critical speed in air

$$\omega_n = \sqrt{\frac{k_s}{m}}$$

For stability analysis, the right hand side of the force equilibrium equation (1) can be assumed to be zero. Then we can get:

$$m \ddot{r} + (2m\xi\omega_n + 2\bar{c}\omega) \dot{r} + \left\{ k_s + (m_L - m_h) \omega^2 - j (\bar{c}\omega^2 + m'_h \omega^2) \right\} r = 0$$

$$-\Omega^2 + (2\xi\omega_n + \frac{2\bar{c}}{m}\omega) j \Omega + \left(\omega_n^2 + \frac{m_L - m_h}{m}\omega^2 - j \frac{\bar{c} + m_h'}{m}\omega^2\right) = 0$$

By separately equating the real and imaginary parts to be zero, we get:

$$\Omega^2 = \omega_n^2 + \frac{m_L - m_h}{m}\omega^2 \quad (3)$$

$$\Omega = \frac{\frac{\bar{c} + m_h'}{m}\omega^2}{2\xi\omega_n + \frac{2\bar{c}}{m}\omega} \quad (4)$$

The onset of instability as defined by equation (3) and (4) can be analytically expressed for two simplified cases:

Case (i): $\xi = 0$ Equation (4) yields

$$\Omega = \frac{\omega}{2} \left[1 + \frac{m_h'}{\bar{c}} \right]$$

Substitution in equation (3) yields:

$$\omega_{\text{onset}} = \frac{2\omega_n}{\sqrt{\left(1 + \frac{m_h'}{\bar{c}}\right)^2 - 4 \frac{m_L - m_h}{m}}}$$

In the absence of the volute-impeller interaction (i.e., $m_h' = m_h = 0$), the onset of instability occurs at greater than twice the air critical speed. When m_h' and m_h are not zero, the instability onset threshold is reduced.

Case (ii): In the absence of wear ring effects ($\bar{c} = m_L = 0$), and when the predominant diagonal stiffness is that due to the shaft elasticity (m_h is much less than k_s/ω^2), the damping needed to avert instability can be derived from equation (3) and (4) as below:

$$2\xi = \frac{m_h' \omega^2}{k_s}$$

i.e. since $m_h' \omega^2$ is the cross coupling stiffness due to volute-impeller interaction, instability can arise when the critical damping ratio is less than one half the ratio of cross-coupling to direct stiffness. This particular result was stated by Prof. T. Caughey of California Institute of Technology.

In the general case, when the simplifying assumptions of case (i) and (ii) are not made, equations (3) and (4) describe a quartic which can only be solved numerically.

NUMERICAL EXAMPLE

To illustrate the significance of the various fluid dynamic effects, the response of a boiler feed pump rotor has been worked out. It should be understood that the purpose is more illustrative than precise. Accurate response calculations should, of course, be done only by using a computer program which represents the geometry faithfully. Complete details of the calculation may be found in reference 4. The major results alone are reported here.

The pump contains six impellers in series. There are ten wear rings, a center stage piece and a balance sleeve. In these calculations, the balance sleeve effect is ignored because of its proximity to the end bearing. The response of the pump to unbalance as given by equation (2) is shown in Figure 1. With nominal clearance, the response is very flat with a theoretical critical speed at about 14000 RPM. If the balance sleeve effect had been included, the critical speed would have been completely suppressed. With increasing wear in the clearances, peak response is observed and the critical speed moves closer to the air critical speed.

The centerstage piece plays a dominant role in the response picture. Figure 2 shows the results when the effect of the centerstage is ignored. (In some pump designs when the impellers are aligned in the same direction, there is no need for a centerstage piece). It can be seen that the response pattern is strongly indicative of lightly damped critical conditions.

To obtain the instability onset, equations (3) and (4) were numerically solved for this case by M. L. Smith of Byron Jackson. His results are shown in figure 3 as a plot of the instability onset speed as a function of wear ratio for different values of ξ . It can be seen that even with no damping, the system is inherently stable as long as the clearance does not open up to more than twice its nominal value. At the operating speed of 5700 RPM, the system does not become unstable until the clearance opens up to about 3.8 times its nominal value. Of course, the pump hydraulic performance would have greatly degraded by then. Normally pump clearances are restored well before this condition is reached. With expected ξ values between 0.1 and 0.3, the system exhibits excellent stability.

The effect of the centerstage piece is illustrated in figure 4. At 5700 RPM, the system becomes unstable with a clearance ratio of 2.6. The volute impeller interaction has a strong effect on instability. Figure 4 shows that when this effect is neglected, the instability threshold is pushed up to very high speeds or extremely large clearances.

A very recent publication (ref. 6) has indicated that volute-impeller interaction produces strong damping and hydrodynamic mass coefficients. A strong point is also made in that publication that all of these effects should be properly included for accurate prediction of rotor dynamic behavior.

CONCLUSIONS

Several interesting conclusions can be made as a result of the analysis presented in this paper.

1. The direct hydraulic stiffness in the volute-impeller area can be thought of as a mass, which adds to the geometric mass.
2. The direct stiffness in wear rings acts as a negative mass, subtracting from the geometric mass. Critical speed can be completely eliminated if the negative mass is sufficiently large.
3. If the only damping in the system is due to the wear rings (i.e., proportional to speed), the peak-response frequency is independent of damping!
4. In the absence of damping and volute impeller forces, the instability onset speed is at least twice the air critical speed. The cross coupling stiffness of the interaction matrix can bring the onset speed closer to air critical speed.
5. The magnitude of the interaction forces appear to be small for the boiler feed pump studied. Only when the wear ring clearances are significantly opened up, does the instability onset appear to be a threat to rotor dynamic reliability.

REFERENCES

1. Loret, J. S.; and Gopalakrishnan, S.: Interaction between Impeller and Volute of Pumps at Off-Design Conditions. Presented at ASME Symposium "Performance Characteristics of Hydraulic Turbines and Pumps", November 13-18, 1983 Boston.
2. Chamieh, D. S. et al: Experimental Measurements of Hydrodynamic Stiffness Matrices for a Centrifugal Pump Impeller. 2nd Workshop on Rotordynamic Instability Problems in High Performance Turbomachinery, Texas A&M University, NASA Conf. Publ. May 10-12, 1982.
3. Gopalakrishnan, S.; and Usui, Y.: Critical Speed of Centrifugal Pumps. The Shock and Vibration Digest, Vol. 16, No. 4, April 1984.
4. Gopalakrishnan, S.: Pump Instability Phenomena Generated by Fluid Forces. Presented at the Bently Research Corporation Symposium, Minden, Nevada, June 1985.
5. Black, H. F.: Effects of Fluid Filled Clearance Spaces on Centrifugal Pump and Submerged Motor Vibrations. Proc. 8th Turbomachinery Symposium, Texas A&M University, College Station, Texas 1979.
6. Jery, B.; Brennen, C. E.; Caughey, T. K.; and Acosta, A. J.: Forces on Centrifugal Pump Impellers. 2nd International Pump Symposium, Texas A&M University, April 1985.

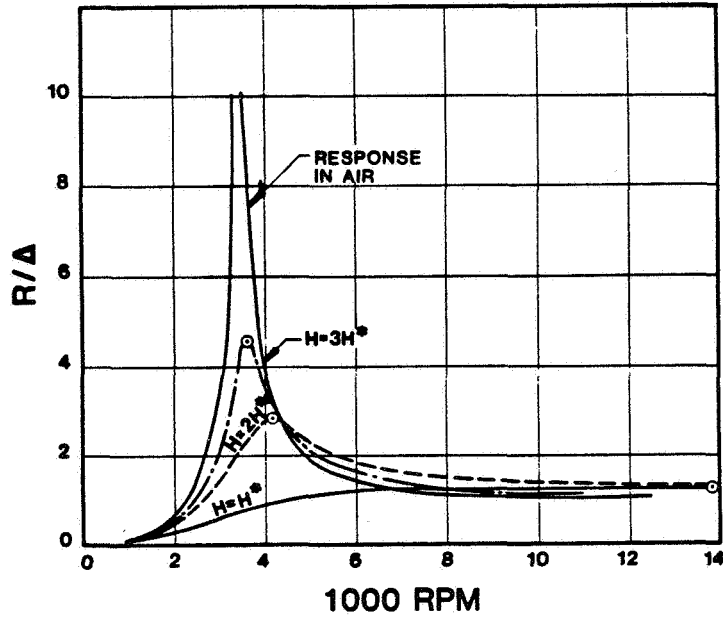


Fig. 1: Response of volute pump to unbalance for various clearances.

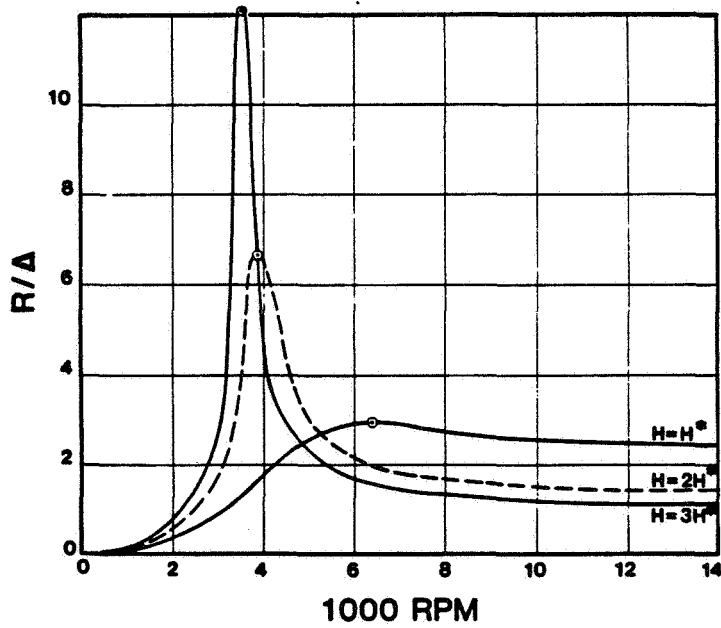


Fig. 2: Response as in Figure 1, except that the center stage piece effect is ignored.

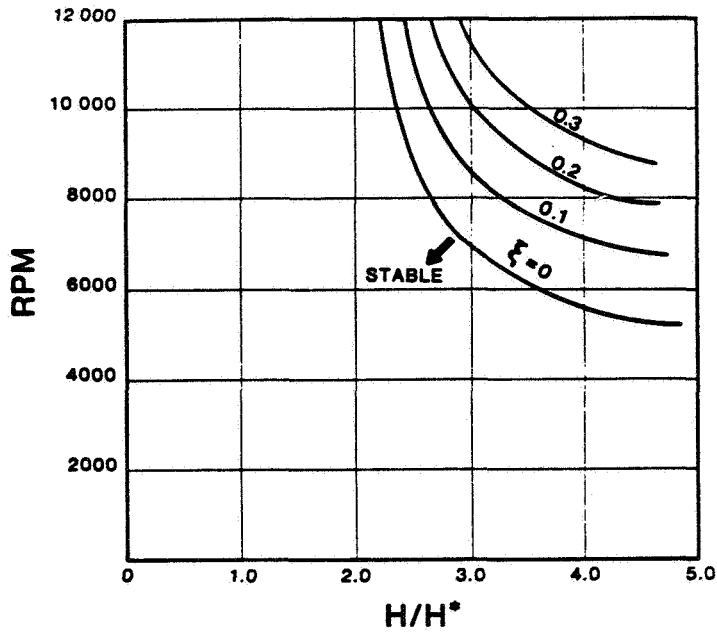


Fig. 3: Stability boundary of volute pump as a function of clearance and damping.

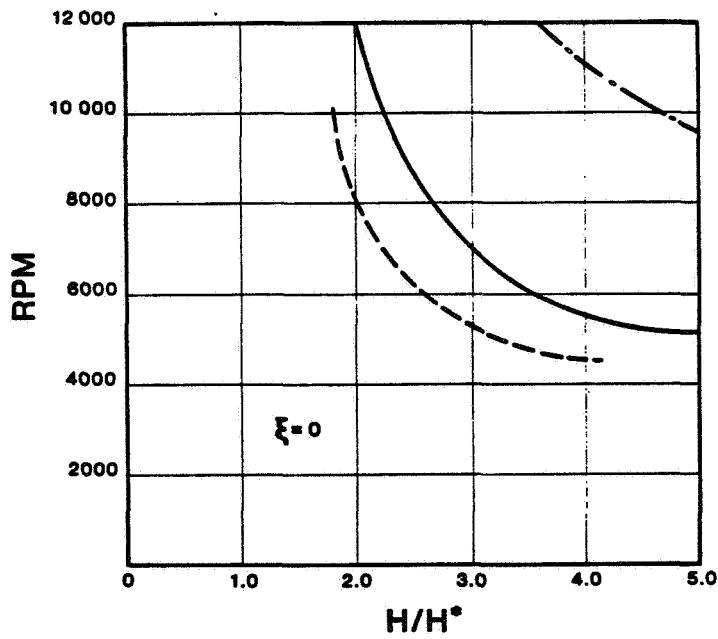


Fig. 4: Stability boundary; ———: Volute pump, - - - - -: Volute pump with the center stage effect ignored, - · - · - · -: Volute pump with hydraulic interaction effects ignored.

VERTICAL REACTOR COOLANT PUMP INSTABILITIES

Robert M. Jones
Tennessee Valley Authority
Soddy-Daisy, Tennessee 37379

This paper describes the investigation conducted at the Tennessee Valley Authority's Sequoyah Nuclear Power Plant to determine and correct increasing vibrations in the vertical reactor coolant pumps. Diagnostic procedures to determine the vibration causes and evaluate the corrective measures taken are described.

INTRODUCTION

Of the myriad pumps, motors, fans and other rotating equipment in a nuclear power plant, by far the largest and most powerful are the vertical reactor coolant pumps (RCP's). Sequoyah Nuclear Plant comprises two pressurized water reactor units (Westinghouse, 4 loop) generating 1180 megawatts each at full power. The two independent units are in operation at the site in Soddy, Tennessee. Unit 1 began commercial operation in 1981 and Unit 2 started up 1 year later. By the end of fuel cycle 2 of Unit 1, vibration trends on the RCP's were showing an unexplained increase. The investigation of this increase and the solution to the problem are the basis for this paper.

The opinions and interpretations described in this paper are based on the author's personal experience and do not necessarily represent official Tennessee Valley Authority policy.

SYMPTOMS

At a vibration seminar, Dr. Elemer Makay said in reference to vibration analysis of vertical pumps, "All bets are off". The meaning of this statement becomes clear when you attempt to directly apply the knowledge and experience gained from solutions to horizontal pump problems to a set of vertical pump problems. Even the common factor, gravity, doesn't seem to act properly. The familiar horizontal and vertical force components, are now "x" and "y" while the influences of temperature, pressure, flow, and bearing seal clearances on these components assume different and sometimes unexpected magnitudes.

Our investigation began in the fall of 1983 when trend data began to show a gradual increase in vibrations from the desired level of 3-4 mils P-P displacement. At that time, vibration levels were indicating between 6 and 10 mils for no apparent reason. (Fig 1) Fig 2 illustrates a typical RCP with bearing locations and Fig 3 shows the Bently-Nevada proximity probe location on the pump shaft.

INVESTIGATIONS

Bearing Clearances--Since the rate of vibration increase had increased after the implementation of new maintenance procedures for the setting of bearing clearances, we began our investigation by analyzing the procedure changes. Previously, bearing clearances for the 7-segment lower motor bearing were set during the "swingcheck" when the motor shaft was forced to one quadrant with sufficient force that no more shaft movement was detected. The new procedure limited the swing force to 25 ft-lbs. We immediately suspected that the bearing clearances were being set larger than the .004" to .006" listed in the pump specifications, leading to increased sensitivity of the rotating elements.

The installation location of the proximity probes and the geometry of the pump support structure (Fig 4) allowed us to make some judgements on bearing clearance without disassembly of the unit. The following procedure was used:

- 1) Gap voltage measurements were taken for the probe opposite the discharge or intake of the pump while the system was at normal operating temperature and pressure.
- 2) Immediately after pump shutdown, the voltage gap was recorded again.
- 3) The stainless pump shaft response is 283 mv/mil.
- 4) Subtracting (1) from (2) and dividing by (3) gave us the lateral shaft movement from running position to the at rest position.
- 5) Assuming that the shaft had been running in the center of the bearing, the movement in excess of the specified bearing clearance could be interpreted as excessive bearing clearance.

For example:

- 1) Running gap 8.1V
- 2) At rest gap 12.9V
- 3) Difference 4.8V
- 4) $4.8/283 = .017"$
- 5) Max movement if bearings properly set, .012", therefore, clearance is .005"

The geometric configuration of the pump results in shaft movement at the probe being 2X the movement at the bearing (Fig 3). Therefore the bearing clearance is .0085" and the excessive clearance at the bearing is .0025". (Assuming the shaft was rotating in the center of the bearing.) The accuracy of this analysis was confirmed later when a teardown revealed a bearing clearance of .008".

Balance--The second area of investigation was to determine the cause of the increased sensitivity to balance weights. During initial start-up, the observed sensitivity was in the range of 90-100 gm/mil. At the time of the investigation this sensitivity had changed to a range of 30-40 gm/mil (Fig 5,6). The first thought that this data suggests is an increased sensitivity due to reduced bearing support, i.e., excessive clearance in the motor bearings. In the arrangement of the bearings, the lower motor bearing "carries the load" and is the most susceptible to problems. One area that needs additional study under controlled conditions is the relationship between this increased sensitivity and

the critical speed of the pump. During normal operations the pump exhibits 3 critical speeds, 300, 800, and 1500 rpm. It appears that as the bearings provide less support, the third critical is moving down from 1500 rpm toward the operational speed of 1200 rpm.

Spectral Analysis--The third area we examined was the spectrum analysis in the 0-200 Hz range. Two points of interest were observed. Although the lower motor bearing is a 7-shoe segmented bearing designed to reduce oil whip, a 1/2 harmonic of over 3 mils was observed on some pumps (Fig 7). In conversations with other utilities, an incident was discussed where the entire shoe support harness had become detached allowing excessive bearing clearance and a resulting 15 mil vibration at 1/2X. The other point noted was the variation in the 2X component, the usual interpretation being possible misalignment. During the maintenance teardown of this pump, the pump/motor misalignment was found to be .014".

CORRECTIVE ACTION

Correlation of the interaction of these four items, voltage gap measurements, increased sensitivity to balance weights, possible oil whip and misalignment pointed to the need for an evaluation and revision of our local procedures for RCP maintenance to incorporate these latest observations.

A review of the maintenance procedures was conducted with the Westinghouse representative. Although this study is still in progress, general recommendations were implemented during the last Unit 2 cycle 2 outage.

These dealt with three main areas:

- 1) The motor shaft must be centered in the bearing. Swing check methods were refined to insure this point.
- 2) Seal clearances must be equal at all points on the shaft.
- 3) Only after the shaft is centered in the seal and centered in the bearing will the bearing shoes be gauged. Clearances are set at .005" and if there is any give, it is toward .004".

CONCLUSION

When maintenance is performed on large vertical pumps, extreme care must be exercised to observe all conditions during disassembly and return the unit to the manufacturers specifications. Any deviations appear to have a much greater effect than with a comparable sized horizontal pump/motor set and under certain conditions, failure to follow these specifications could have catastrophic results.

GENERAL DATA FOR REACTOR COOLING PUMPS

Model ----- W11007-A1
Type ----- Single-Stage, Centrifugal
Head ----- 277 feet
Flow ----- 88,500 gpm
Impeller ----- Seven-vane single suction
Rotating Inertia ----- 82,000 lb-ft.2
Rated Horsepower ----- 6,000 hp
Voltage ----- 6,600 volts
Starting Current ----- 3,000 amps
Flywheel ----- 13,200 lbs
Nominal Temperature -- 545 F.
Nominal Pressure ----- 2,250 psia

Frequency Analysis of Pump Vibrations

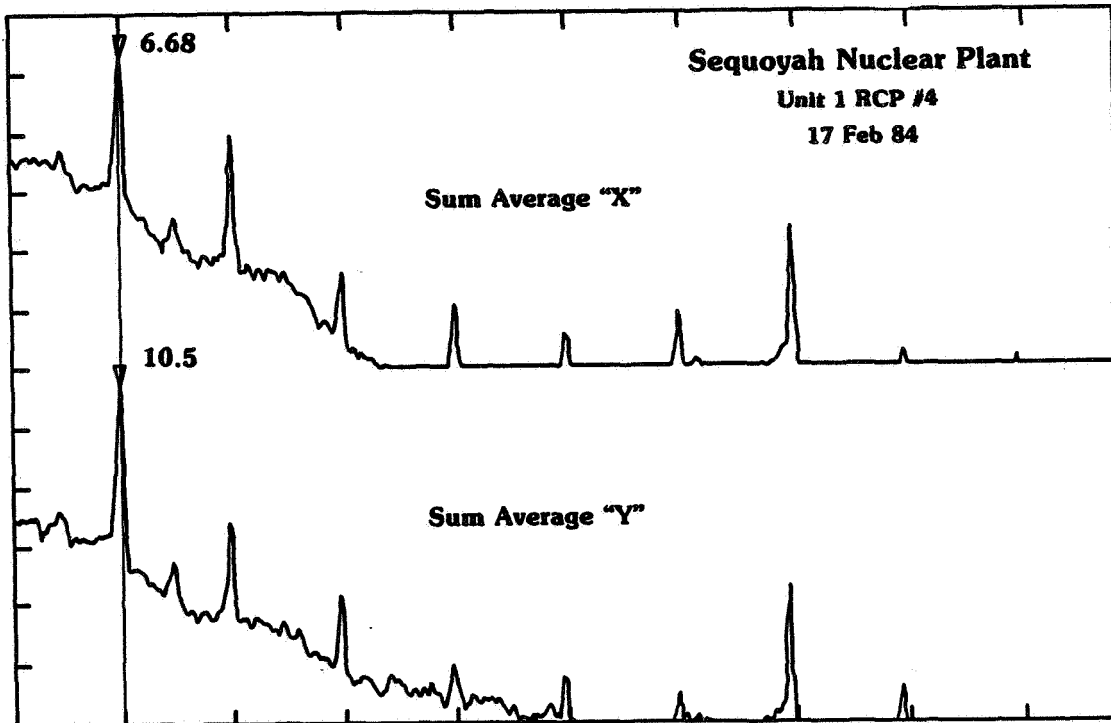


Figure 1

ORIGINAL PAGE IS
OF POOR QUALITY

Reactor Coolant Pump

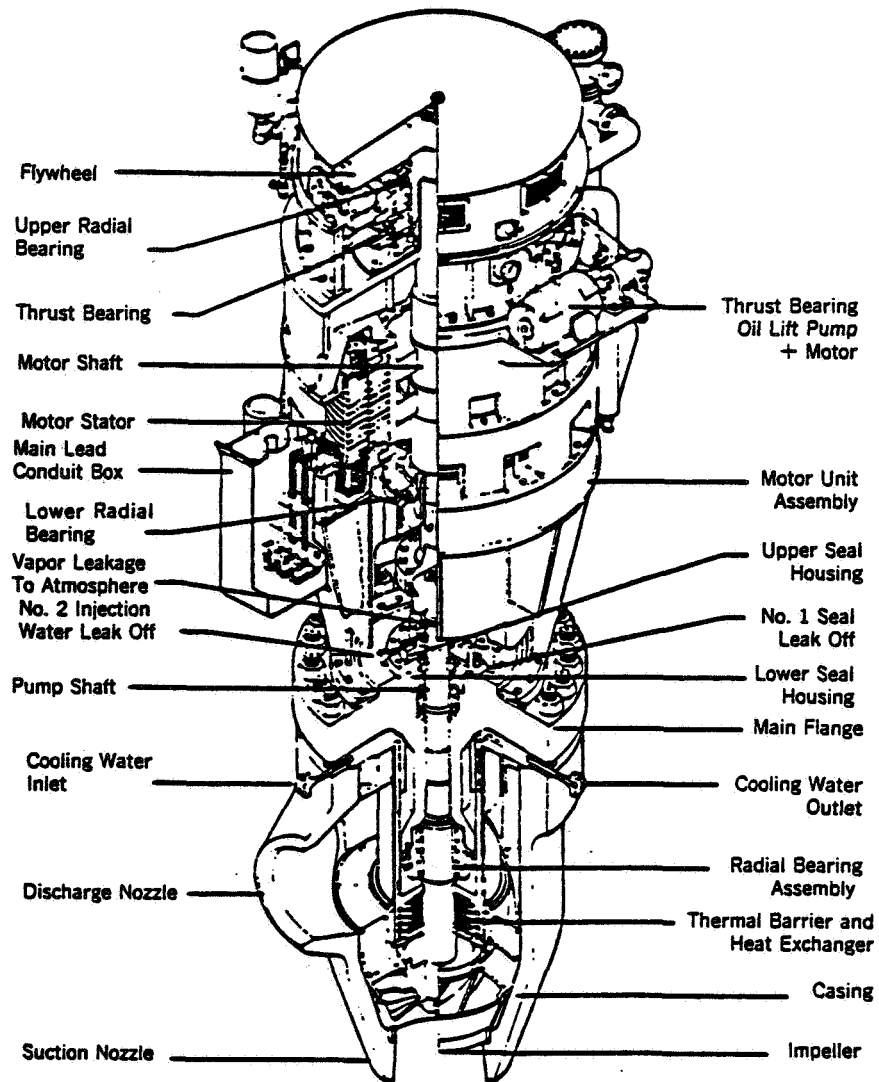
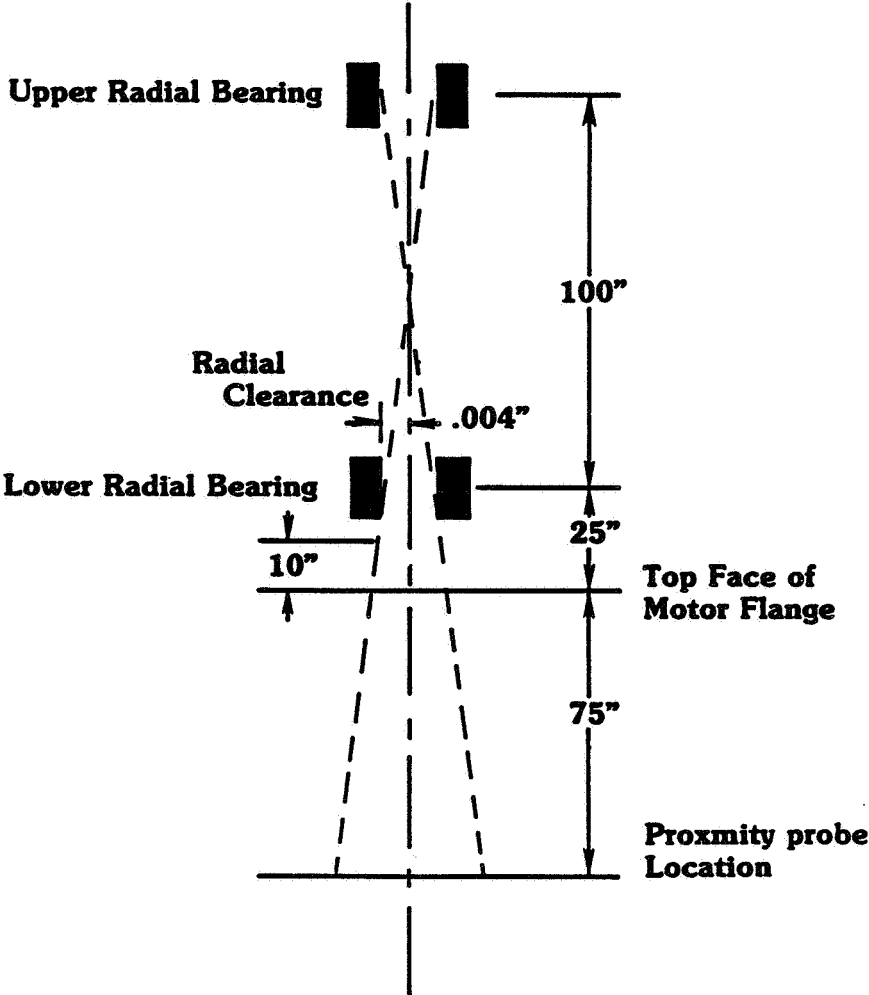


Figure 2

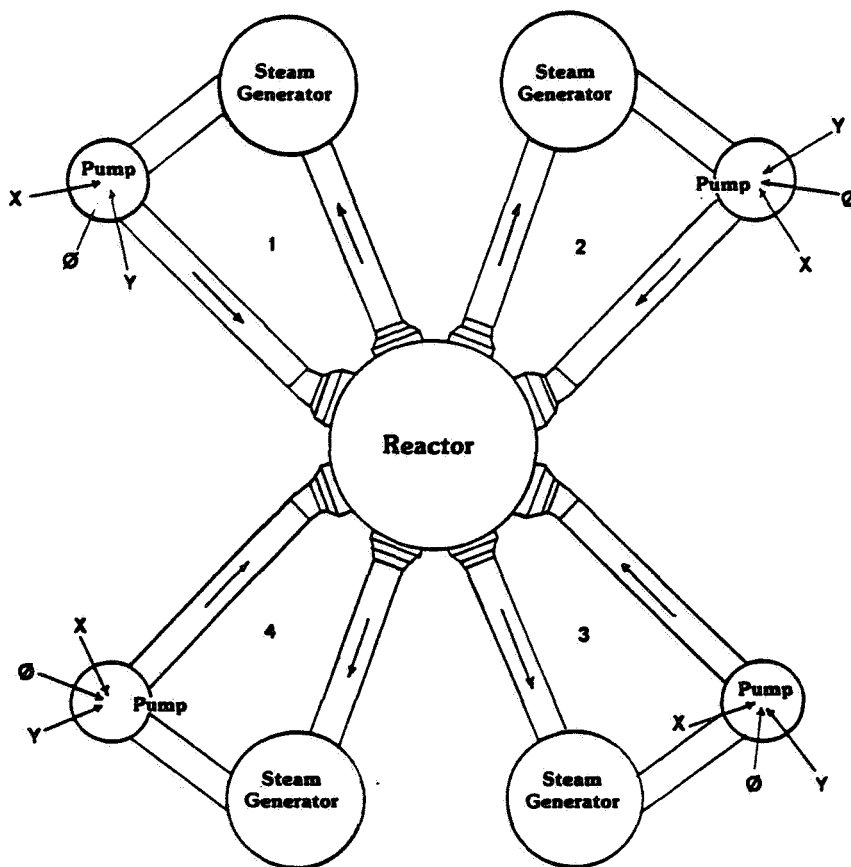
Sequoyah RCP's Physical Arrangement of Bearings and Displacement Probes



From Westinghouse instruction letter, June 1976

Figure 3

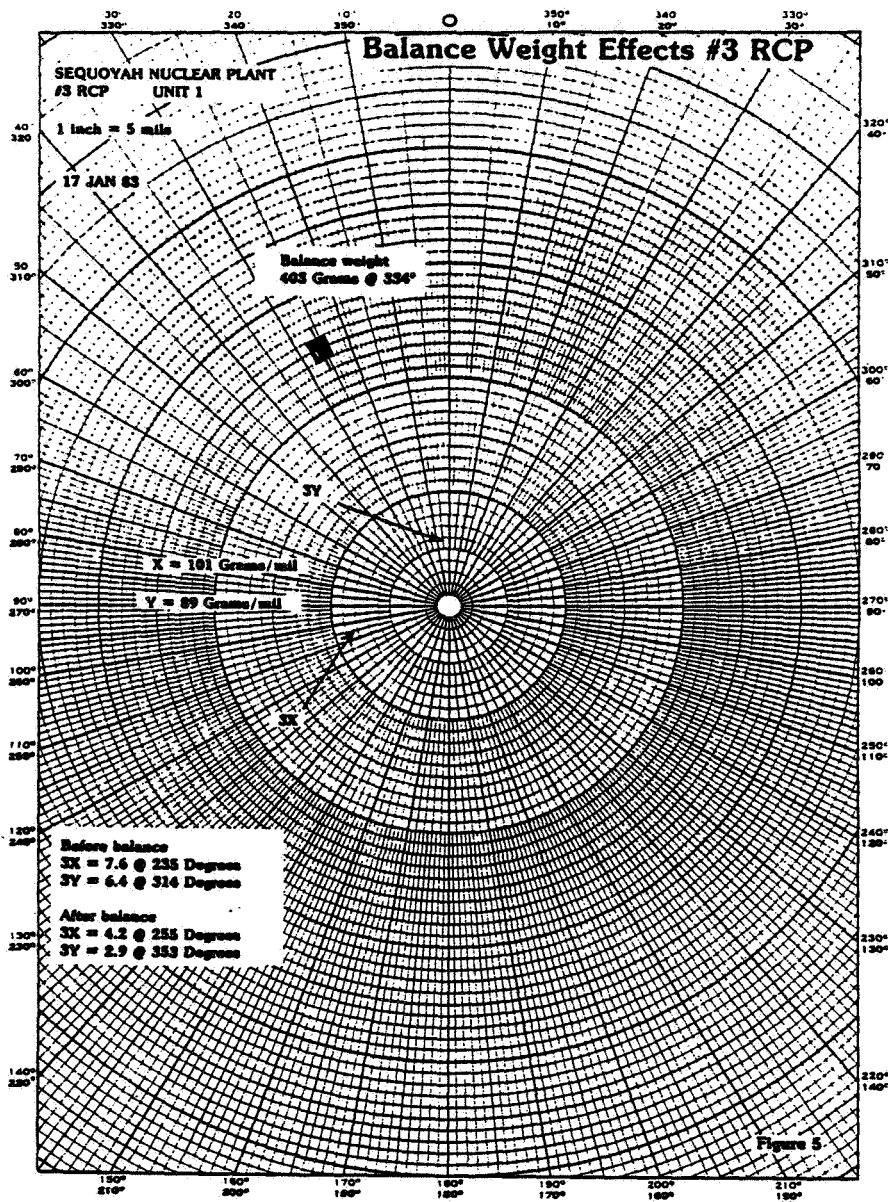
**Physical Arrangement of
Reactor, Pumps, Steam Generators**

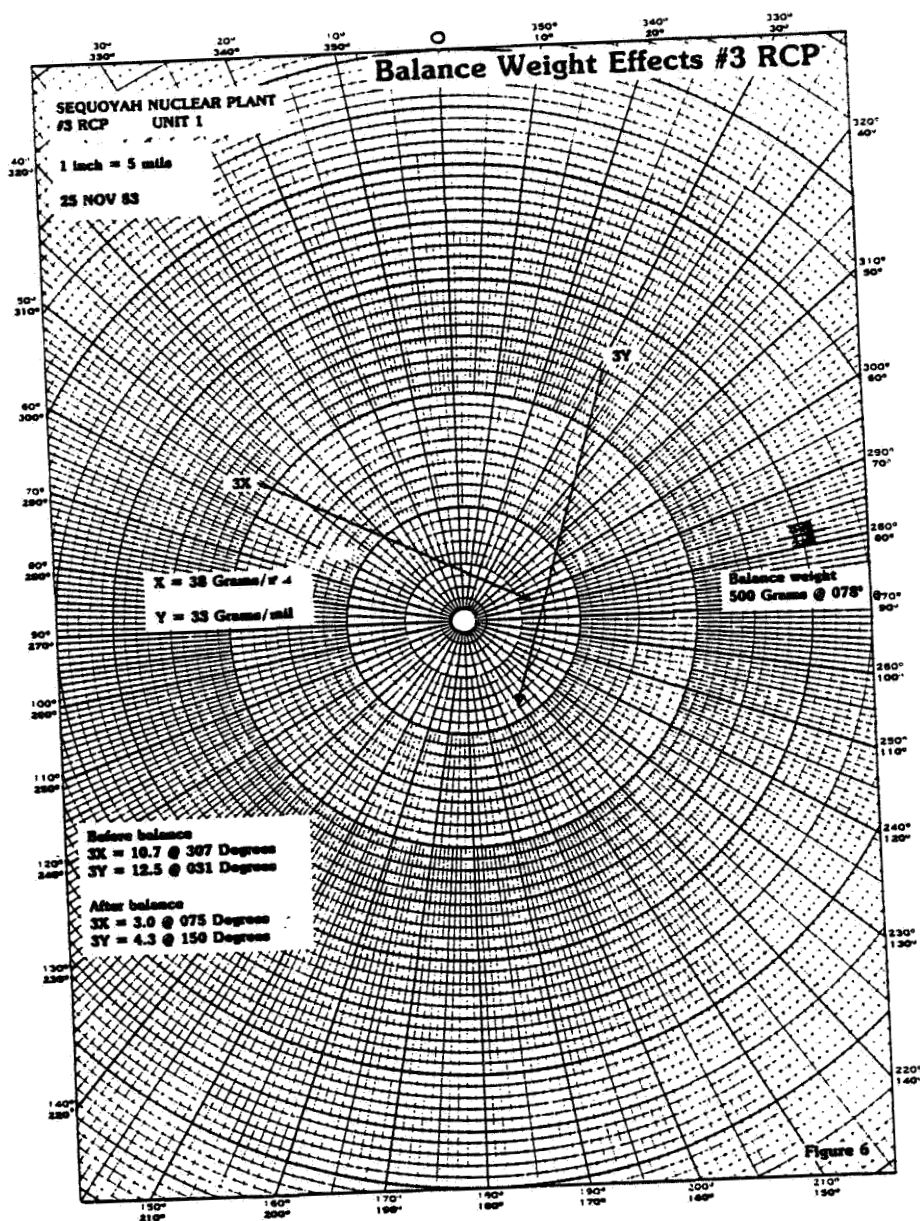


Sequoyah Nuclear Plant

Figure 4

ORIGINAL PAGE IS
OF POOR QUALITY





Frequency Analysis During Operation

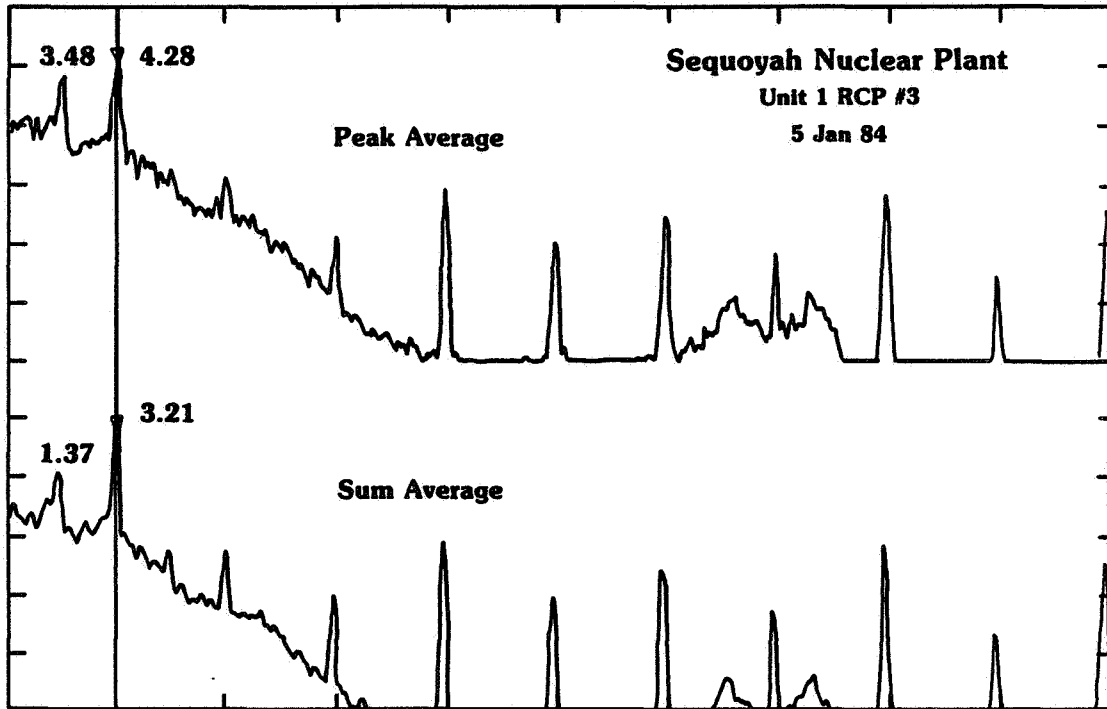


Figure 7

PREDICTION OF DESTABILIZING BLADE TIP FORCES

FOR SHROUDED AND UNSHROUDED TURBINES*

Yuan J. Qiu and M. Martinez-Sanchez
 Massachusetts Institute of Technology
 Cambridge, Massachusetts 02139

Highly loaded turbomachinery tends to exhibit noticeable subsynchronous whirl at a frequency close to one of the rotor critical frequencies when the rotating speed is well in excess of that critical. The subsynchronous whirl is not a "forced" vibration phenomenon where the vibration frequency is the same as the forcing frequency; e.g., rotor unbalancing. It is better classified as a positive feedback phenomenon tending to amplify small disturbances at the system natural frequencies. The cause of whirl can be traced back to a number of forcing mechanisms. One of these is the variation of the blade tip forces due to nonuniform blade tip clearance. Alford (1) was the first to model this aerodynamic force on the blade. By assuming uniform upstream and downstream flow fields, he was able to argue that the variation of the blade tip force would be proportional to the efficiency variation. Therefore, if a turbine rotor has some small eccentricity (Fig. 1), then due to the efficiency variation, the blade force on the narrow-gap side must be greater than the blade force on the opposite side. The resultant force F_y on the rotor, acting perpendicular to the eccentricity is then no zero. This force can cause the rotor to whirl forward, i.e., in the same direction as the rotation. Qualitatively:

if

$$\frac{\delta \eta}{\eta_m} = \beta \frac{\delta t}{H}, \quad \delta t = e_o \cos \theta$$

then

$$F_y = \frac{T_m \beta}{D_m} \frac{e_o}{H}$$

where δt is the local tip clearance at azimuth θ , e_o is the eccentricity and H is the blade height, D_m is the mean diameter of the rotor and T_m is torque on the rotor, β is a numerical factor of order unity depending on the blading.

Contrary to Alford's assumptions, the presence of the blade tip clearance variation is bound to influence the whole flow field. The purpose of this paper is to investigate the effect of this non-uniform flow field on the Alford force calculation. The ideas used here are based on those developed by Horlock and

* This work was supported by NASA contract NAS8-35018.

Greitzer (2). It will be shown that the non-uniformity of the flow field does contribute to the Alford force calculation. An attempt is also made to include the effect of whirl speed. The values predicted by the model are compared with those obtained experimentally by Urlicks(3) and Wohlrab (4). The possibility of using existing turbine tip loss correlations to predict β is also exploited.

The Model

The method of approach is to first find the flow field due to the tip clearance variation, and then, using the velocity triangles, to calculate the resultant Alford force. The detail of the analysis is given in Ref. 5. It is to be stressed that a complete three-dimensional investigation of the flow field with the non-uniform tip clearance is not attempted here.

Consider a single-stage turbine with its rotor whirling at a constant eccentricity e_0 (Fig. 2). If the hub/tip ratio is high, the flow field can be approximated to be two dimensional. Fig.3 shows an actuator disc representing a two dimensional unwrapped blade row of circumference $2\pi R$, where w is the relative flow velocity and c is the absolute flow velocity. If the Mach numbers upstream and downstream are small, the flow can be considered incompressible, as well as inviscid, outside of the blade row.

The variation of the tip clearance around the annulus can be represented by

$$\delta \frac{t}{H} = \sum E_n \left[i \frac{y}{R} n - \Omega t \right] \quad (1)$$

where Ω is the whirling speed, y is the distance in the tangential direction, R is the mean blade radius, H the blade height, and the E_n are constants.

Since only the first harmonic is of interest, as will be explained later, higher harmonics are not included in the analysis and $E_1 = e_0/H$.

The perturbation velocities c'_x and c'_y are related to the stream function ψ by

$$c'_x = \frac{\partial \psi}{\partial y} \quad (2a)$$

$$c'_y = - \frac{\partial \psi}{\partial x} \quad (2b)$$

Upstream of the stage, the flow is irrotational, $\nabla^2 \psi_1 = 0$ and downstream the flow is rotational $\nabla^2 \psi_2 = \zeta$. The flow is steady in a reference frame rotating at the whirl speed Ω , therefore the stream functions can be written as

$$\psi_1 = A \exp \left[\frac{1}{R} (x + i y) - \Omega t \right] \quad \text{upstream of the stage} \quad (3)$$

$$\psi_3 = B \exp \left[\frac{1}{R} (-x + iy) - \Omega t \right] + C \exp \left[\frac{1}{R} (-x \tan \bar{\alpha}_3 i + y i - \Omega t) \right] \text{ downstream of the stage} \quad (4)$$

where $\bar{\alpha}_3$ is the mean flow angle downstream of the rotor. Notice the irrotational term dies out far upstream and downstream. The vorticity downstream is convected by the mean flow at an angle $\bar{\alpha}_3$. Again only first harmonics are considered.

There are three matching conditions across the actuator disc surface:

- 1) The axial mass flux is constant

$$c'_{x1} = c'_{x3} \quad (5)$$

or

$$\frac{\partial \psi_1}{\partial y} (0, y) = \frac{\partial \psi_3}{\partial y} (0, y)$$

- 2) The relative flow leaving angle is constant

$$\tan \beta_3 c'_{3x} = w'_{3x} = c'_{3y} + u' \quad (6)$$

at $x = 0$

- 3) The third boundary condition involves matching perturbation quantities by using the known experimental information.

The total-to-static turbine efficiency can be written as

$$\eta = \frac{(c_{y3} - c_{y2}) u}{c_p T_{01} \left(1 - \left(\frac{p_3}{p_{01}} \right)^{\frac{\gamma-1}{\gamma}} \right)} = \frac{\text{turbine work}}{\text{ideal work}} \quad (7)$$

where c_{y2} and c_{y3} are the y-components of the absolute flow velocity before and after the rotor (defined positive in the y direction), u is the blade speed, p_3 is the static pressure downstream of the disc, and p_{01} is the total pressure upstream.

Due to the local blade tip clearance variation, the efficiency can be written as the sum of the mean efficiency and its perturbation:

$$\eta = \bar{\eta} + \eta' \quad (8)$$

where to a first approximation

$$\eta' = \frac{\partial \bar{\eta}}{\partial (t/H)} \delta (t/H) + \frac{\partial \bar{\eta}}{\partial \beta_1} \delta \beta_1 \quad (9)$$

It is known that the second term in the above expression is small compared with the first term, if β is not too far from the designed value. Hence the second term in Eq.(9) will be ignored in the analysis.

We now perturb eq.(7) and use the additional condition that the stator leaving angle is also constant to eliminate c_{y2} , the third boundary condition is obtained. We also use the downstream y -momentum equation to eliminate the downstream pressure perturbation. In terms of the perturbation streamfunctions, the three matching conditions can then be written as

$$\frac{\partial \psi_1}{\partial y} = \frac{\partial \psi_3}{\partial y}$$

$$\frac{\partial \psi_3}{\partial y} \tan \beta_3 = - \frac{\partial \psi_3}{\partial x} + u'$$

$$\begin{aligned} \frac{\partial \eta'}{\partial y} \bar{Q}_1 + \bar{Q}_2 \rho_3 \left[\bar{c}_{x3} \frac{\partial^2 \psi_3}{\partial x \partial y} + \bar{c}_{y3} \frac{\partial^2 \psi_3}{\partial y \partial x} + \frac{\partial^2 \psi_3}{\partial t \partial x} \right] \\ = - u' \left[\frac{\partial^2 \psi_3}{\partial x \partial y} + \tan \alpha_2 \frac{\partial^2 \psi_1}{\partial y^2} \right] + (c_{y3} - c_{y2}) \frac{\partial u'}{\partial y} \end{aligned} \quad (10)$$

where

$$\bar{Q}_1 = \left[\begin{array}{c} (\gamma-1)/\gamma \\ c_{pT01} \left(1 - \frac{p_3}{p_{01}} \right) \end{array} \right]; \quad \bar{Q}_2 = \left[\begin{array}{c} (\gamma-1)/\gamma \\ - \eta \frac{c_{pT01}}{p_3} \frac{\gamma-1}{\gamma} \left(\frac{p_3}{p_{01}} \right) \end{array} \right]$$

Substituting the forms given by Eqs. (3) and (4) for ψ_1 and ψ_3 , these conditions become three linear algebraic equations for the coefficients A, B and C. To obtain the blade force variation, the momentum equation is applied across the rotor blades. The tangential component of the force is given by

$$f_Y = \rho c_{x3} (c_{y3} - c_{y2}) H \quad (11)$$

Since only the perturbation of force contributes to the resultant destabilizing force

$$f_Y' = \rho c_{x1} (\bar{c}_{y3} - \bar{c}_{y2}) H + \rho_1 \bar{c}_x (c_{y3}' - c_{y2}') H \quad (12)$$

If we consider a reference frame rotating at the whirl speed Ω , and add together the forces perpendicular to the instantaneous eccentricity, we find the net cross-force

$$F_Y = \int_0^{2\pi R} \text{Real}(f_Y' e^{\Omega t}) \cos(\gamma/R) d\gamma \quad (13)$$

This expression justifies the inclusion of only the first harmonic in the stream function expansion, since the higher harmonics contribute nothing to the Alford force. A non-dimensional excitation coefficient k_{xy} is defined as

$$k_{xy} = \frac{F_y}{U_s} / \frac{e_0}{H} \quad (14)$$

where U_s is the ideal total force in the circumferential direction on the blade, and e_0/H is the dimensionless eccentricity.

Results

Cases with stationary eccentricity are considered first. A typical plot of the axial velocity perturbation and the blade force variation vs. angular position are shown in Fig. 4. As was to be expected, these quantities are almost in counterphase with the tip clearance variation, which indicates that the nonuniform flow field will tend to increase the Alford forces.

Although Alford published his paper in 1965, very few experiments have been done to verify the proposed formula. Hence it is difficult to make any good comparison between the Alford model, the present analysis, and experimental results. Two tests were done by Urlich (3) and Wolhrab (4), and more recently Vance and Laudadio (6) did verify the linearity between the Alford forces and eccentricity for a fan. Accurate experimental data seems very difficult to obtain due to the small magnitude of the forces to be measured.

For the present analysis the data of Urlich seems to be the more suitable, since he also determined the efficiency vs. average clearance for an unshrouded turbine stage. From this information the values of $\lambda = \partial\eta/\partial(t/H)$ are found by a second order polynomial curve fit to the efficiency vs. clearance data (Table 1). Values of k_{xy} are found by using λ , together with appropriate flow angles (Ref. 3) in the analytical model. The predicted values and experimentally obtained values of k_{xy} are plotted in Figs. 5 and 6, together with the values of k_{xy} obtained from the Alford formula. It can be seen that the analysis gives a value of k_{xy} higher than the Alford formula, indicating that the non-uniformity does increase the destabilizing forces.

In addition, it is also clear from Figs. 5 and 6 that the new theory overpredicts the side forces, when compared to the experimental data. However, we should at this point also consider the effect of the nonuniform pattern of pressure acting on the turbine wheel rim. Fig. 7 shows that, although the pressure field just upstream of the rotor is in phase with the clearance variation, it is shifted by 90° just downstream, and that those nonuniform pressures act in such a way as to reduce the forward cross-force.

A precise accounting of the effect of these pressure forces is not possible in the context of our actuator-disc theory. However, we can see that the 90° rotation of the pressure pattern must occur in the rotor passages, and so it is logical to calculate the induced side force by letting the rotated pressure wave act on an axial rim width equal to half a blade chord. New excitation coefficients, including this pressure force, are also shown in Fig. 6. Although the precise axial length over which the pressure forces act is difficult to determine, it can be seen that they do contribute significantly to the net force, and that their effect is to essentially remove the overprediction.

The Use of Tip Clearance Correlations

In many situations, curves of efficiency vs. clearance are not available. The possibility of using some of the existing tip clearance loss correlations is investigated here. The formula used is given by Dunham and Came (7), in the form of a tip loss coefficient which depends on flow angles and other stage variables, as well as on the clearance to chord ratio. This allows determination of η , and hence λ for use in our model. Fig. 8 shows the predicted Alford forces based on the tip loss clearance correlation(Ref.(7)), together with the experimental results. It can be seen that the prediction is very reasonable, as it compares well with the data for small axial (stator-rotor) gap, although not as well for large axial gap. The fact that k_{xy} varies with the gap between the rotor and stator is not well understood, and it may be highly dependent on the detailed geometrical arrangement of stator and rotor.

Wohlrab (Ref. 4) tested a shrouded turbine. Since he did not supply data on efficiency vs. tip clearance, λ has to be estimated, in order to compare the present analysis with the experimental values obtained. Encouraged by the results for the unshrouded turbine, an estimated tip loss coefficient is used again, but this time the effective tip clearance is given by (Ref.(7)).

$$t = (\text{geometric tip clearance}) \times (\text{number of seals})^{-0.42}$$

Since there is also a shroud, we would expect some seal forces acting on the rotor shroud band. These are found by applying a model developed by Lee, et al. (8). The results (Fig. 9) again show reasonable agreement, falling between the data obtained by Wohlrab for the two axial gaps tested.

Effect of Whirl

All the cases examined so far have been for an assumed static offset. The effect of whirl for a typical case is shown in Fig. 10. For a whirl speed equal to 50% of the rotating speed, the effect on k is small ($\pm 10\%$). This is consistent with Wohlrab's experiment, in which he found that within experimental accuracy there is no difference between the values of k_{xy} obtained from kinetic and static tests. It is noted, however, that the predicted effect of whirl (which could be expressed as an Alford damping coefficient), could not have been obtained from the original Alford model, since it depends crucially on the delays between wheel motion and disc passage of the induced flow non-uniformities, and these were ignored in the Alford model.

Conclusion

The non-uniform flow field induced by the tip clearance variation tends to increase the resultant destabilizing force over and above what would be predicted on the basis of the local variation of efficiency. On the one hand, the pressure force due to the non-uniform inlet and exit pressure also plays a part even for unshrouded blades, and this counteracts the flow field effects, so that the simple Alford prediction remains a reasonable approximation. Once the efficiency variation with clearance is known, the present model gives a slightly overpredicted, but reasonably accurate destabilizing force. In the absence of efficiency vs. clearance data, an empirical tip loss coefficient can be used to give a reasonable prediction of destabilizing force. To a first approximation, the whirl does have a damping effect, but only of small magnitude, and thus it can be ignored for some purposes. To gain more insight and understanding, more accurate

experimental determinations of the tip force must be made. It must be pointed out that the destabilizing force is also highly dependent on the geometry of the rotor and stator, as shown by the experimental dependence of the magnitude of destabilizing force on the axial gap between the stator and rotor. This effect of axial gap on the Alford force points to the need for more detailed study of the flow field around tip regions.

References

1. Alford, E.F., "Protecting Turbomachinery from Self-Excited Rotor Whirl." Journal of Engineering for Power, Oct. 1965, pp338-344.
2. Horlock, J.H. and Greitzer, E.M., "Non-uniform Flows in Axial Compressors Due to Tip Clearance Variation," Proc. Instn. Mechanical Engrs., Vol. 197c, pp173
3. Urlichs, K., Clearance Flow Generated Transverse Force at the Rotors of Thermo Turbomachines," Dissertation, Technical University of Munich, (1975). English translation in NASA TM-77 292, Oct. 1983.
4. Wohlrab, R., "Experimental Determination of Gap Flow-Conditioned Force at Turbine Stages and Their Effect on the Running Stability of Simple Rotors," Dissertation, Munich Institute of Technology (1975). English translation in NASA TM-77 293, Oct. 1983.
5. Martinez-Sanchez, M, Greitzer, E. and Qiu, Y., "Turbine Blade-Tip Clearance Excitation Forces," Report on NASA Contract Number NAS8-35018, June, 1985.
6. Vance and Laudadio, "Experimental Measurement of Alford's Force in Axial Flow Turbomachinery," Journal of Engineering for Gas Turbines and Power, 1984, pp585.
7. Dunham and Came, "Improvements to the Ainley-Mathieson Method of Turbine Performance Prediction," ASME Transactions, July 1970.
8. Lee, D.W.K., Martinez-Sanchez, M. and Czajkowski, E., "The Prediction of Force Coefficients for Labyrinth Seals," 3rd Rotordynamic Instability Workshop, Texas A&M University, May 1984.

List of Symbols

c	absolute velocity
c_p	specific heat
D_m	mean rotor diameter
e_0	eccentricity
f_y	blade force per unit circumferential length
F_y	tangential force
H	blade span
K_{xy}	excitation coefficient
p	pressure

R blade radius
 t time; tip clearance
 T temperature
 T_m mean torque on rotor
 w relative velocity
 u blade speed
 U_s ideal blade force=(ideal turbine work)/(blade speed)
 α absolute flow angle
 $\beta_{1,2,3}$ relative flow angle
 β Alford factor
 ζ perturbation vorticity
 θ circumferential angle
 Ψ stream function
 Ω whirl speed
 ρ density
 η efficiency

Superscript

' perturbation
 - mean value

subscript

y tangential direction
 x axial direction
 1 upstream of stator
 2 downstream of stator
 3 downstream of rotor
 0 stagnation

	radial clearance / blade height		
	2.6 %	5.3 %	7.8 %
axial gap 7.1 %	.705	.594	.521
21 %	.716	.570	.440

Table.1 Efficiency for tip clearances

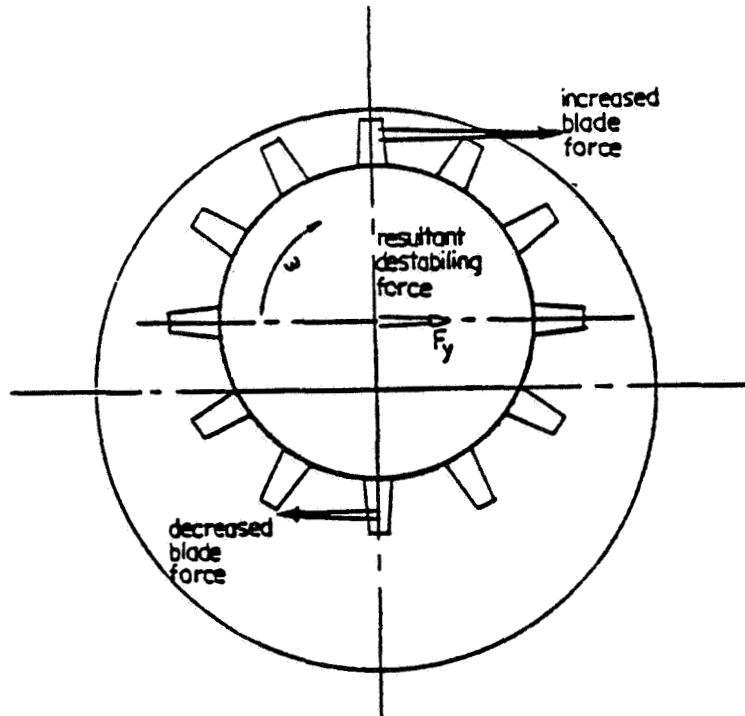


Figure 1. - Tip clearance effect for turbine rotor.

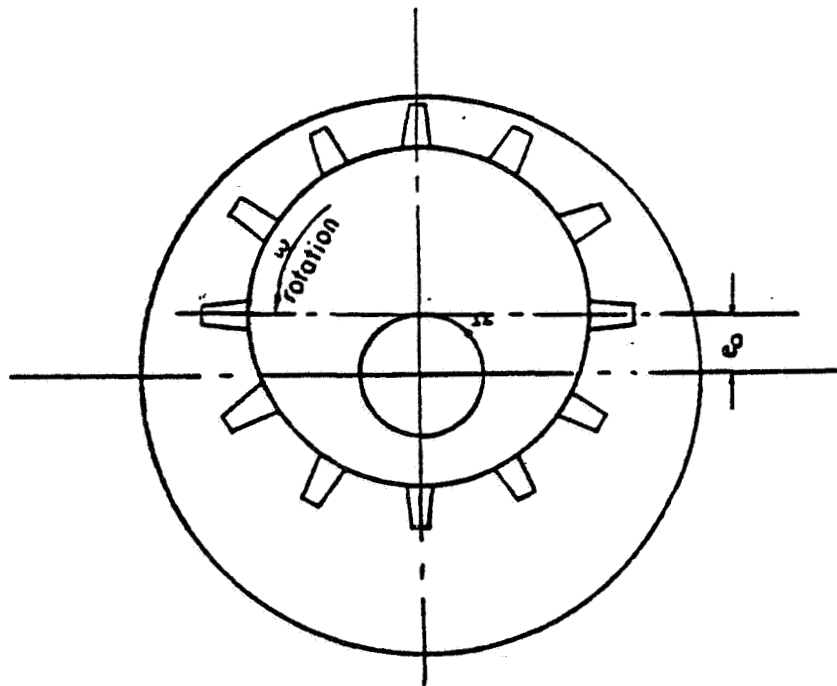


Figure 2. - Rotor under whirl.

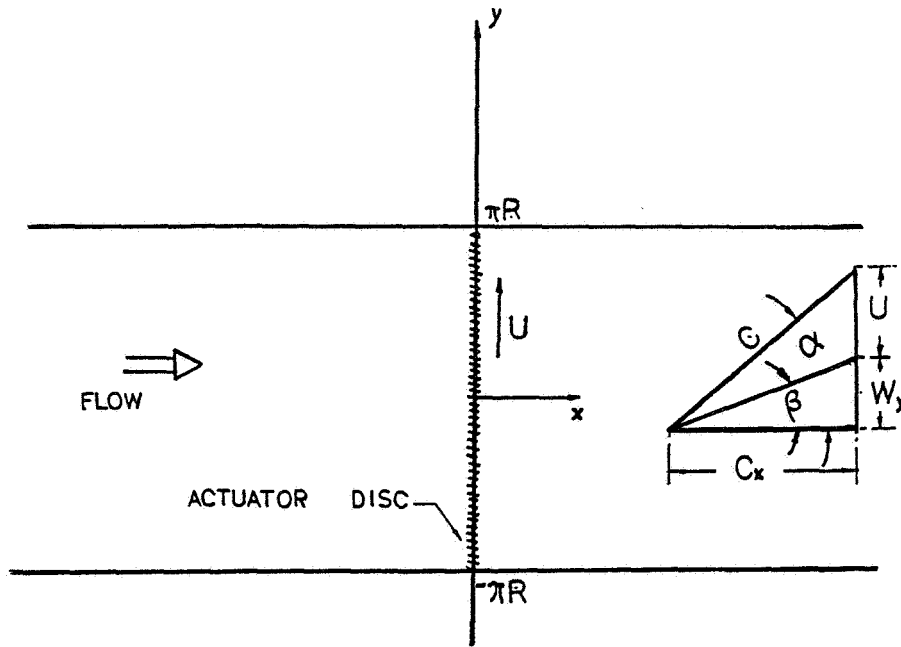


Figure 3. - Two-dimensional flow model.

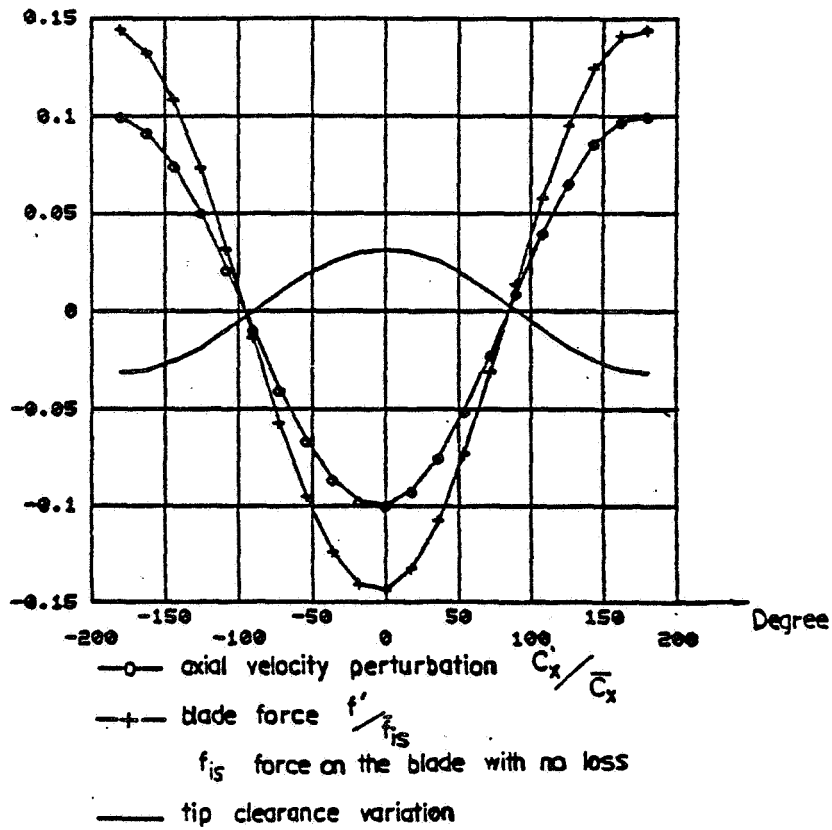


Figure 4. - Axial velocity and local blade force distribution.

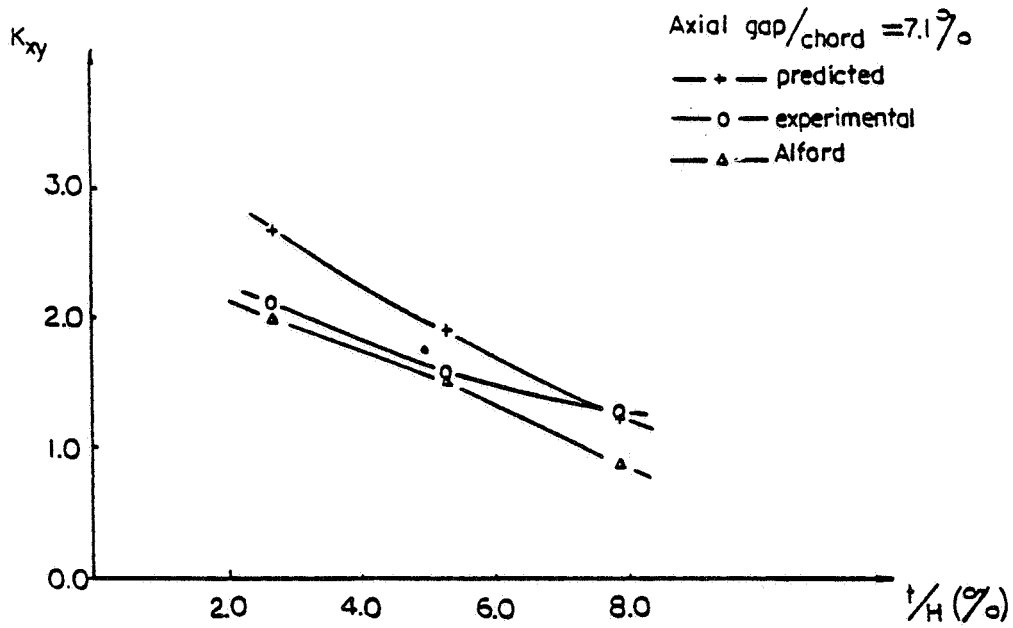


Figure 5. - Variation of excitation coefficient with tip clearance.

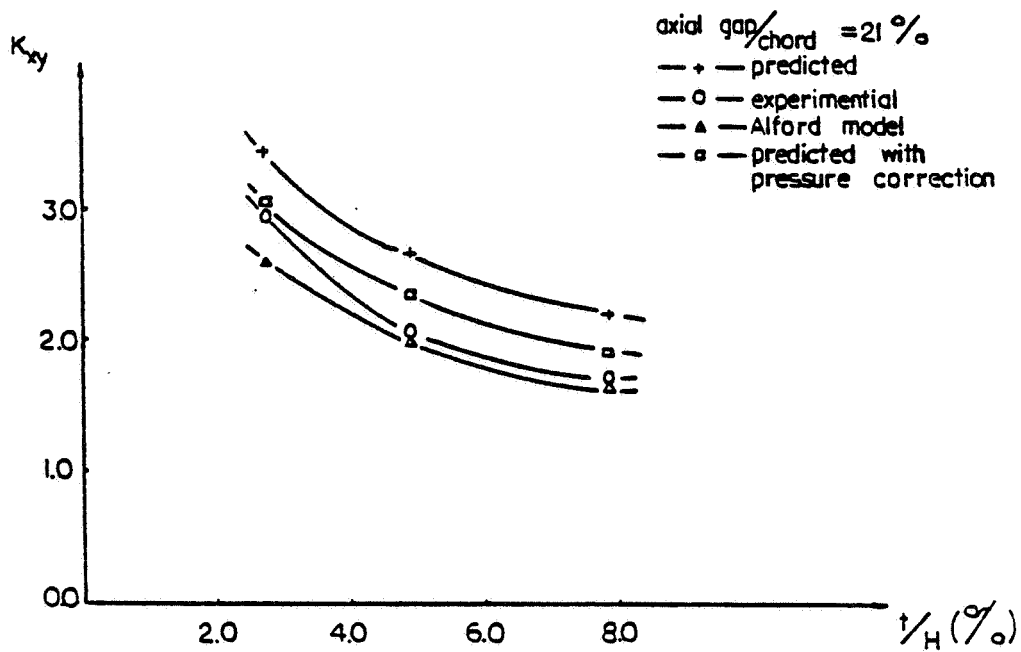


Figure 6. - Variation of excitation coefficient with tip clearance.

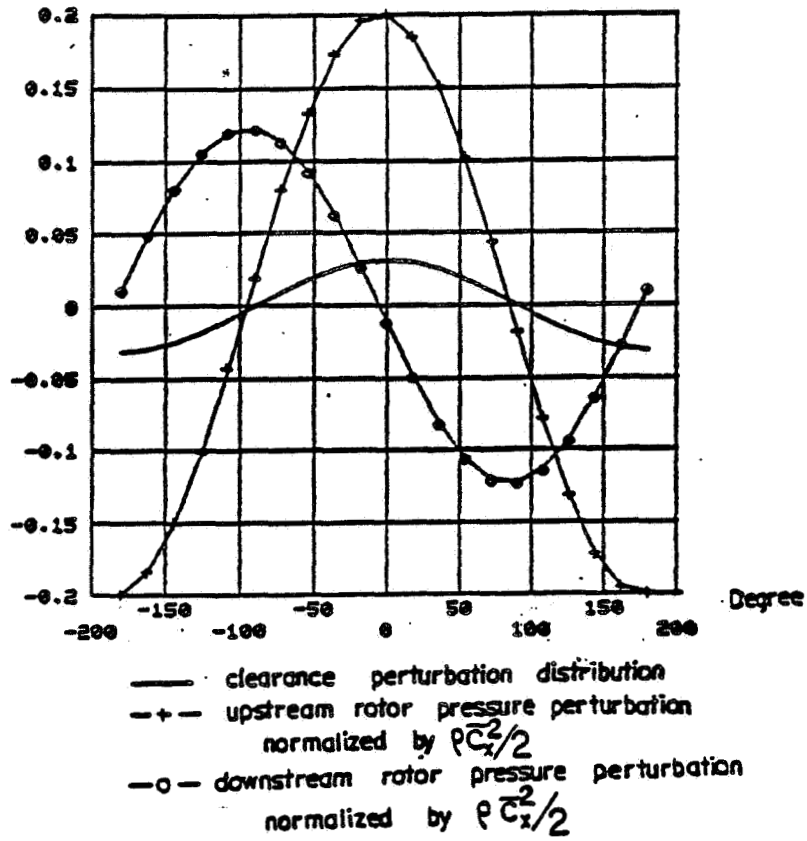


Figure 7. - Pressure perturbation distribution.

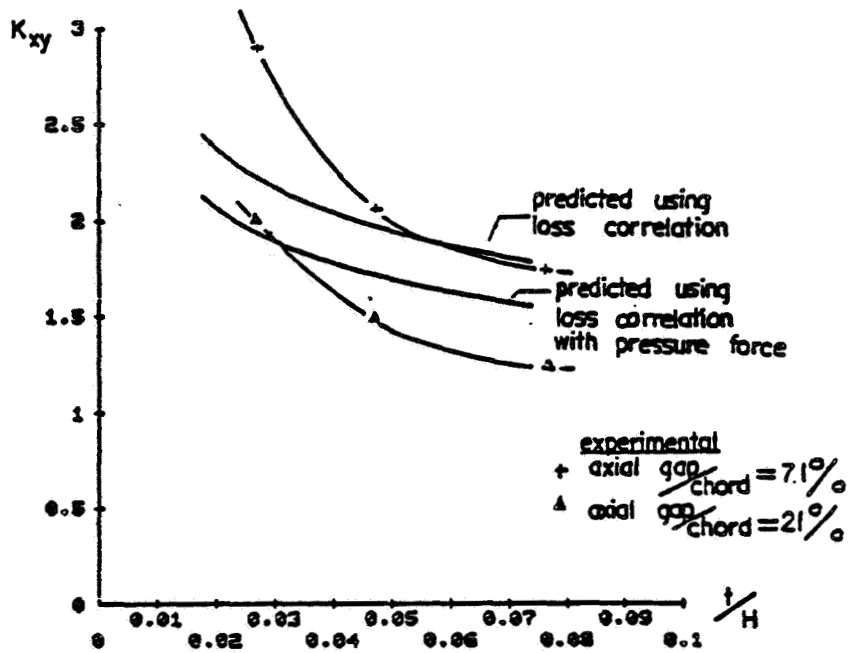


Figure 8. - Variation of excitation coefficient with tip clearance.

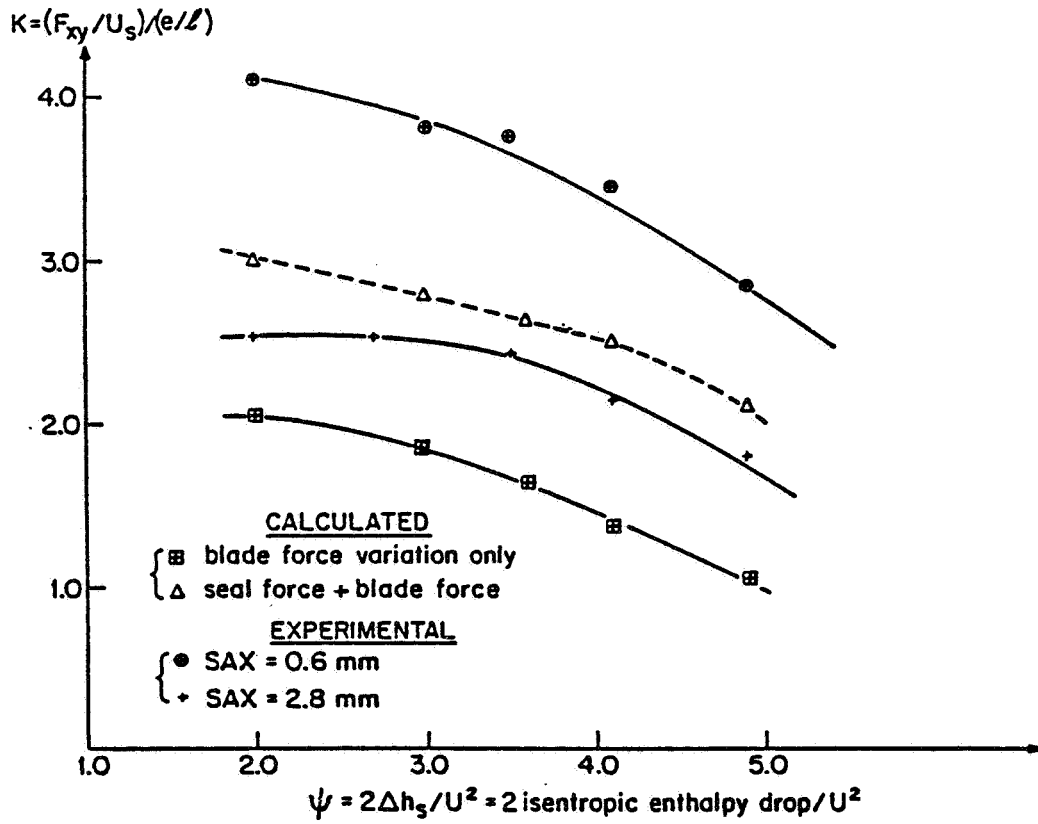


Figure 9. - Variation of clearance excitation coefficient with ψ .

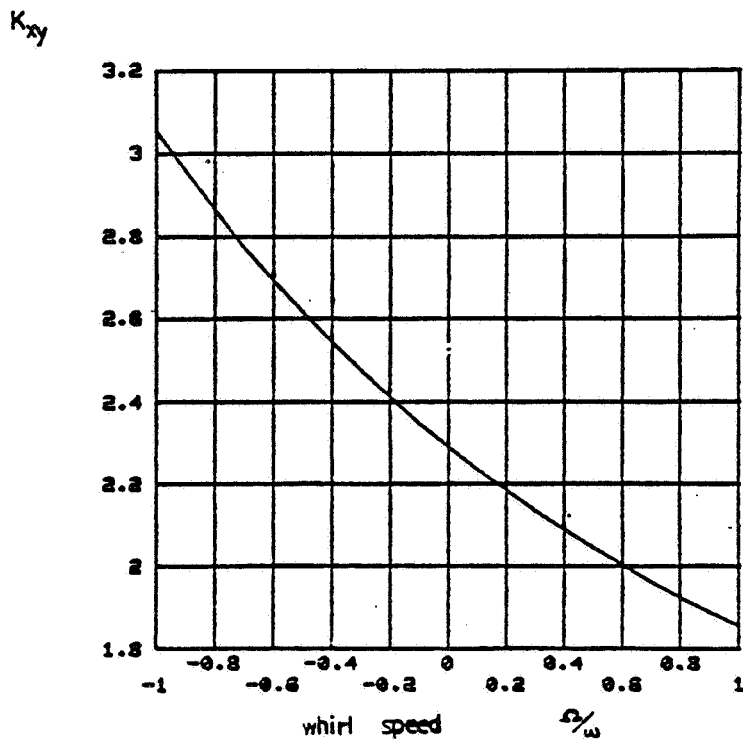


Figure 10. - Effect of whirl.

IDENTIFICATION OF BEARING AND SEAL DYNAMIC STIFFNESS PARAMETERS

BY STEADY STATE LOAD AND SQUEEZE FILM TESTS

Donald E. Bently and Agnes Muszynska
Bently Rotor Dynamics Research Corporation
Minden, Nevada 89423

This paper presents the results of two simple tests, mainly steady state load test and squeeze film test, for establishing the coefficients of bearings and seals. It also discusses methodology of the tests and some observed conclusions from the obtained data. In the last chapter, perturbation testing results are given as an example of verification and proof of validity of the two previous tests.

INTRODUCTION

In several previous papers [1-5], the utilization of perturbation methodology to identify the dynamic stiffness characteristics of cylindrical seals and bearings has been shown. These studies were deliberately limited to low eccentricity, with the rotor statically centered and with maximum motion limited to 0.6 eccentricity ratio, and produced very satisfactory results.

However, in our first attempts to observe the rotor/bearing stiffness characteristics by perturbation testing at high static eccentricities, as reported in [4], great difficulties were encountered because of the effects of the cross coupled nonlinearities of the various dynamic stiffness terms that we were attempting to evaluate. It was, therefore, necessary to retrench and develop more suitable techniques for evaluating dynamic stiffness terms at eccentricity ratios above 1/2. The first attempt was to run Squeeze Film Test (with rotative speed ω_r at zero), applying both a steady state load (to yield families of measurements from 0 to 0.8 eccentricity ratio) and then apply the circular perturbation force at various levels and speeds. Once more, a lot of effort was expended, but the results were once again not clear, as the nonlinearities of the dynamic stiffness terms were so intermeshed that they became very difficult to evaluate. The only good to come of this effort, besides showing how difficult these terms can be, was to show a different form of fluid inertia effect at very high eccentricities in squeeze film tests, which could be the results of what Dr. Hendricks of NASA Lewis calls "fluid film fracture fraction," which is an effect occurring when two flat surfaces in close proximity are separated. Since the latter did not appear to be vital to the stability situation of bearings and seals, this interesting phenomenon was not pursued.

Having learned a lot about what not to do, two elementary studies were then initiated. These tests are (i) the Steady State Loading Test (that has been successfully used in many studies across more than 80 years), and (ii) an equally simple Squeeze Film Test at Zero Eccentricity. These very limited, very simple studies yielded the desired results and proved quite successful in evaluation of the various dynamic stiffness terms. These two tests are shown herein, with several results and conclusions. Finally perturbation tests using from very low to very high input forces are shown to confirm the validity of the two basic tests.

THE STEADY STATE LOAD TESTS

The steady state load test is accomplished by applying a steady force in one direction to a seal or bearing with 1.01" diameter and 0.75" length, and observing the resultant rotor displacement in both the direct axis (in direction of the applied load) and the quadrature axis (at right angles to the applied load). The steady load was incremented in 1/2-lb. steps at low eccentricity, and one pound steps at high eccentricity. Rotative speed was held constant for each run, using 100, 200, 300, and 400 rad/sec. Temperature of oil, incoming, at bearing, and outlet were controlled as carefully as possible, so that the lubricant in the bearing was at 70°F and 80°F, yielding dynamic viscosities for the T-10 oil used of 62.5 and 50 centipoise, respectively. Since the bearing studied in this test was a hydrostatic bearing, the oil pressure was also controlled, using 4 psi, 8 psi, 12 psi, and 15 psi. A family of dynamic stiffnesses was done for bearing diametrical clearances of 10 mils, 8 mils, and 5.5 mils.

A typical plot of the steady state direct and quadrature eccentricity for oil supply pressures of 4 and 15 psi as a function of load at 400 rad/sec of a 5.5 mil diametral clearance bearing at 80°F is shown in Fig. 1.

Figure 2 shows the same parameters plotted for the bearing with 8 mils diametral clearance.

Figure 3 shows the journal eccentricity as a function of load for the bearing with 5.5 mil diametral clearance at 15 psi oil supply pressure, temperature 80°F, and at rotative speeds 100, 200, 300, and 400 radians/sec.

Figure 4 shows the journal Eccentricity plot for the bearing with 8 mils diametral clearance.

Since the stiffness characteristics as functions of the eccentricity ratio are desired, the stiffness plots are developed by dividing the input steady force vector by the resultant steady state displacement vector. The resultant dynamic stiffness vector is then converted to rectilinear form, as in the perturbation tests reported in the papers [1-5]. The stiffness in the direction of the input force is called the S.S. (Steady State) Direct Dynamic Stiffness, and the observed stiffness at 90 degrees to the input force is called the S.S. Quadrature Dynamic Stiffness. Since perturbation speed is zero, all dynamically generated stiffness terms are zero in this test, thus the prefix "S.S." (Steady State) on the Dynamic Stiffness terms.

Some typical graphs of the S.S. Quadrature Dynamic Stiffness divided by rotative speed, and the S.S. Direct Dynamic Stiffness as functions of various families of parameter-changes are shown in Figures 5 through 9.

There is one more feature to the Steady State Quadrature Dynamic Stiffness that was observed and is worthy of noting; however, it was not more detailedly studied. Figure 10 (a) shows a sharp drop in this stiffness at high eccentricity. This regularly occurs at the "corner" of the Steady State Direct Stiffness term, shown in Figure 10 (b) (as above), and at the "corner" of the plot of position vs. load shown in Figure 10 (c).

This sharp drop is repeated for both increasing and decreasing load with very little hysteresis. In the basic equation:

$$\text{Input Force} = (\text{Direct Stiffness})(\text{Direct Motion}) - (\text{Quad Stiffness})(\text{Quad Motion})$$

the principal load is carried by the Quadrature at eccentricities from 0 out to some higher eccentricity value. There often occurs a limit of the load carrying value of

this term, dependent on operating parameters. When the input force goes above this level, the attitude angle drops sharply from the 90° region toward zero. When this occurs, of course, the Direct term balances against the input force. This interesting behavior of the Steady State Quadrature Stiffness term has not been further re-searched, as it will not affect the instability onset from low eccentricity positions. It is, of course, active in determining orbital limit cycle size of an instability, and it may affect onset of instability from high eccentricity ratios.

THE SQUEEZE FILM TESTS

For each bearing configuration, a set of Squeeze Film Tests were run following the Steady State Load tests. The Squeeze Film test is accomplished at zero rotative speed, with the journal at steady state centered in the bearing, and perturbing the rotor system with steps of increasing perturbation force. The input force is circular in nature, and for zero rotative speed, there is no concept of forward or reverse. With rotative speed at zero, all dynamic stiffness terms carrying ω_R (rotative speed) drop out.

The Squeeze Film dynamic stiffness coefficients are again obtained by dividing the input perturbation force vector by the resultant dynamic motion vector at each perturbation speed. Since the input is a circular force, and the bearing is circular, the resultant dynamic motion is symmetric, the horizontal and vertical stiffnesses are identical, so that either axis can be used to derive the Squeeze Film Dynamic Stiffness terms.

As before, the dynamic stiffness vector is converted to rectangular form. The dynamic stiffness in the direction of the force is called the S.F. (Squeeze Film) Direct Dynamic Stiffness term and the dynamic stiffness at 90° to the input force is called the S.F. (Squeeze Film) Quadrature Dynamic Stiffness. Since the S.F. Quadrature Stiffness is comprised solely of the term $+j\omega_p D$, the ω_p term is divided out for final presentation to show D as a function of eccentricity for the particular set of conditions being run. (ω_p is the perturbation speed, D is bearing radial damping.)

It may be noted that in the steady state tests, the quadrature stiffness term was plotted as K_{QUAD}/ω_R with the units lb sec/in, while in the squeeze film test the quadrature term was plotted as $K_{QUAD}/\omega_p = D$ lb sec/in.

It should be noted that these terms are directly related by the oil swirling ratio λ (lambda) as $K_{QUAD}/\omega_R = \lambda D$, where ω_R is rotative speed. The graphs in Figures 6 and 7 differ from those in Figures 11 and 12 by the factor λ . By dividing the corresponding plots, the value λ is obtained. It is consistently constant for all speeds, bearing clearances, temperatures, pressures, and eccentricity ratios and is equal to 0.48.

The total Quadrature Dynamic Stiffness term for stability and other rotor studies is the sum of the steady state quadrature term and the squeeze film quadrature term:

$$K_{QUAD} = \begin{matrix} j\omega_p D & - & j\lambda\omega_R D \\ \text{(from SQZ Film)} & & \text{(from Steady State)} \end{matrix}$$

Figures 11 and 12 show the typical and summary results of the Squeeze Film test for damping as a function of eccentricity ratio. It may be observed that the damping term is quite independent of supply oil pressure and of perturbation speed.

The bearing radial damping coefficient D has been described for nearly 80 years as having the relationship to eccentricity of $D = \frac{D_0}{(1-e^2)^{3/2}}$, where D_0 is damping coefficient at low eccentricity (sometimes an additional term of $(2+e^2)$ appears in the denominator, also).

The laboratory tests consistently show a much simpler relationship, mainly $D = \frac{D_0}{(1-e^2)^1}$. The latter may be very simply derived by assuming motion in one axis in a squeeze film bearing, as Figure 13 shows.

$$D = \frac{D_0 C}{2h_1} + \frac{D_0 C}{2h_2} \quad e = \frac{Z}{C}, \quad h_1 = C-Z, \quad h_2 = C+Z$$

h_1 is thin film clearance due to motion.
 h_2 is thick film clearance due to motion.
 Z is radial displacement.
 C is radial clearance.

$$D = \frac{D_0 C}{2} \left(\frac{1}{C-Z} + \frac{1}{C+Z} \right) = \frac{D_0 C^2}{(C^2-Z^2)} = \frac{D_0}{C^2(1-e^2)^1}$$

The D_0 term is a function of dynamic viscosity η where η has units of $\left[\frac{\text{mass}}{(\text{length})(\text{time})} \right]$ or $\left[\frac{\text{lb sec}}{\text{in}^2} \right]$ so that D is expressed in $\frac{\text{lb sec}}{\text{in}}$ (English), or $\frac{\text{kg}}{\text{sec}}$ (metric). D_0 is also a function of cube of the bearing length.

Even though this derivation arises from a squeeze film (zero rotation speed) and one degree of freedom, it appears to work perfectly well for the general case. The value of D_0 has not been evaluated, and the variation of damping D with cube of bearing length was accepted without further checking.

Figure 14 shows the damping as a function of inverse cube of diametral bearing clearance for 5.5, 8, and 10 mils diametral clearance. It was pleasing to note that this term fairly closely follows the generally accepted rule.

Another interesting feature of the old standard derivation of the bearing coefficients is that it shows an interlocking relationship between the direct and quadrature terms. This series of studies, as well as prior perturbation studies, show that the direct and quadrature stiffness terms are virtually independent, except that direct damping and quadrature ("cross") spring are intimately related, with both containing D .

The Squeeze Film Direct Dynamic Stiffness term is by far the most complex of all the terms revealed by these two simple tests.

It contains at least the following individual terms:

- (1) Any spring in parallel with the tested bearing.
- (2) The rotor mass.
- (3) The fluidic inertia effect.
- (4) The hydrostatic spring.
- (5) The highly nonlinear spring as a function of eccentricity and other parameters.

(Of course, when the rotor is also turning, there are even more terms in Direct Dynamic Stiffness.)

For this reason, the S.F. Direct Dynamic Stiffness for a given set of parameters is plotted versus the square of the perturbation speed. Typical graphs are shown in Figures 15 and 16.

The first feature is the extrapolation of this curve to zero speed, which yields the Direct (Static) Spring of the system. As may be observed, the obtained spring coefficient is the same as the coefficient yielded by a corresponding test at steady state loading. This spring is a linear function of oil supply pressure of the hydrostatic bearing.

The second feature is the negative slope of the plot. As in prior studies on perturbation, using minimum rotor system mass, this slope consists principally of the fluidic inertia effect. Since the effective rotor mass is identified to be $0.002 \frac{\text{lb sec}^2}{\text{in}}$, anything more than this is the fluidic inertia.

It may be observed that the fluidic inertia term exhibits dependence on viscosity, as its value is observably lower at 80°F than at 70°F. In prior studies [2-4], we showed the fluidic inertia term to have viscosity η to zero power. This set of experiments shows viscosity η dependence to first power. Further studies will be required to adjust this function, but meanwhile, a power of one change is not too bad.

Shown in Figure 17 is a typical group of plots of direct, static stiffness, which is yielded as a remainder of the S.F. Direct Stiffness with the rotor mass and fluid inertia term subtracted and plotted against eccentricity ratio. The graphs indicate nonlinearity of the direct stiffness variable with perturbation unbalance mass. The extreme complexity of the Direct Stiffness is easily observed from Figure 17 plots which cover a wide band of perturbation speed and input perturbation force levels.

TESTS FOR THE VALIDITY OF THE MEASURED STIFFNESS TERMS

In order to check the validity of the dynamic stiffness terms obtained from the steady state load tests and the squeeze film tests, the same rotor/bearing system was then run under the similar conditions at the rotative speeds 2000 and 2500 rpm. At these speeds, forward and reverse perturbation loading was applied. This loading was supplied by perturbation imbalance weights at 1.25 inch radius of 1.75, 3.5, 7, 14, 28, and 56 grams. Total centrifugal force was limited to 16 pounds by limiting perturbation speed for the higher imbalance weights.

Figure 18 shows a summary of the results at 2000 rpm rotative speed, with oil supply at 70°F and 4 psi. It presents a plot of Direct Dynamic Stiffness vs. Perturbation Speed for the various perturbation loads. This figure also shows the displacement amplitude in pp mils vs. forward perturbation speed.

Of major interest here is the hump in the Direct Dynamic Stiffness term that occurs at the oil whirl resonance speed of about 1000 rpm. This hump occurs as the displacement motion moves from the nearly linear region of the S.S. Direct Stiffness region at low eccentricity, onto and above the "knee" of that curve (see Fig. 10b). The hump begins with the 14 gram perturbation imbalance and gets progressively higher as a function of the increasing perturbing force.

The Quadrature Dynamic Stiffness plots are not shown. They remain a straight sloping line, as is usual, except for an "S" shaped curve around 1000 rpm for high eccentricities. This is an indication that the swirling ratio does not remain constant in this region, which is a fairly necessary phenomenon for the proper description of whip instability and is being studied further.

It may be noted that the regular parabola caused by the rotor mass and fluidic inertia is distorted as the perturbation load increases. This interesting effect will modify the algorithm of fluidic inertia previously proposed [2-5], and is also being further studied.

CONCLUSIONS

- (1) It is believed that the steady state load test combined with the squeeze film tests can be used to evaluate the dynamic stiffness characteristics of seals and bearings.
- (2) Whereas many researchers appear to have very capable computer programs for the determination of stability of rotating machinery, it is considered highly important to have the dynamic stiffness characteristics correlated as closely as possible to the actual rotor/bearing situation in order to get the best stability prediction results.

With improved knowledge of the dynamic stiffness nonlinearities as functions of eccentricity, it becomes possible to not only obtain the inception of instability, and its frequency, it is also possible to predict the size of the stable orbiting when an instability occurs.

REFERENCES

1. Bently, D.E., Muszynska, A.: Stability Evaluation of Rotor/Bearing System by Perturbation Tests, Rotordynamic Instability Problems in High Performance Turbomachinery, Proc. of a Workshop, Texas A&M University, College Station, TX, 1982.
2. Bently, D.E., Muszynska, A.: Oil Whirl Identification by Perturbation Test. Advances in Computer-aided Bearing Design, ASME/ASLE Lubrication Conference, Washington, DC, October 1982.
3. Bently, D.E., Muszynska, A.: Perturbation Tests of Bearing/Seal for Evaluation of Dynamic Coefficients. Symposium on Rotor Dynamical Instability, Summer Annual Conference of the ASME Applied Mechanics Division, Houston, TX, June 1983.
4. Bently, D.E., Muszynska, A.: The Dynamic Stiffness Characteristics of High Eccentricity Ratio Bearings and Seals by Perturbation Testing. Workshop on Rotordynamic Instability Problems in High Performance Turbomachinery, Texas A&M University, May 1984.
5. Bently, D.E., Muszynska, A.: Perturbation Study of Rotor/Bearing System: Identification of the Oil Whirl and Oil Whip Resonances. Tenth Biennial ASME Design Engineering Division Conference on Mechanical Vibration and Noise, Cincinnati, OH, September 1985.

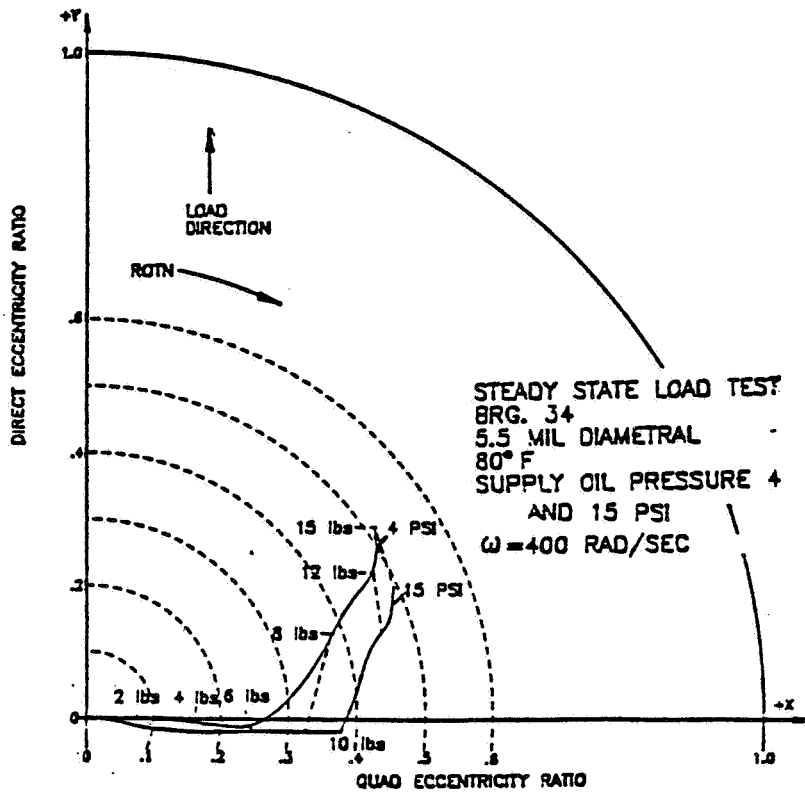


Figure 1.

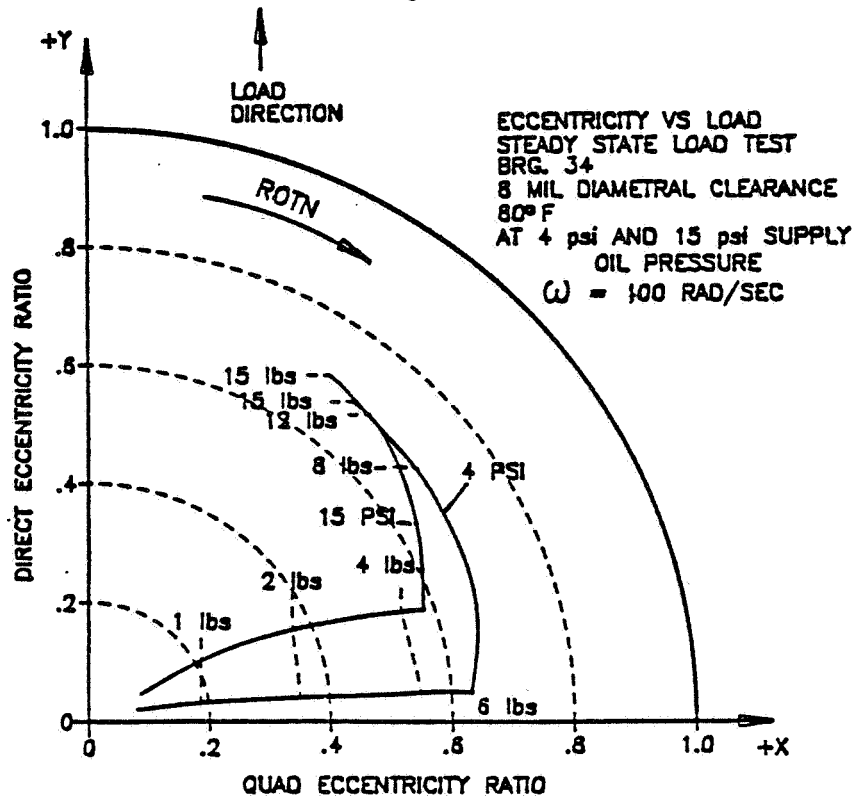


Figure 2.

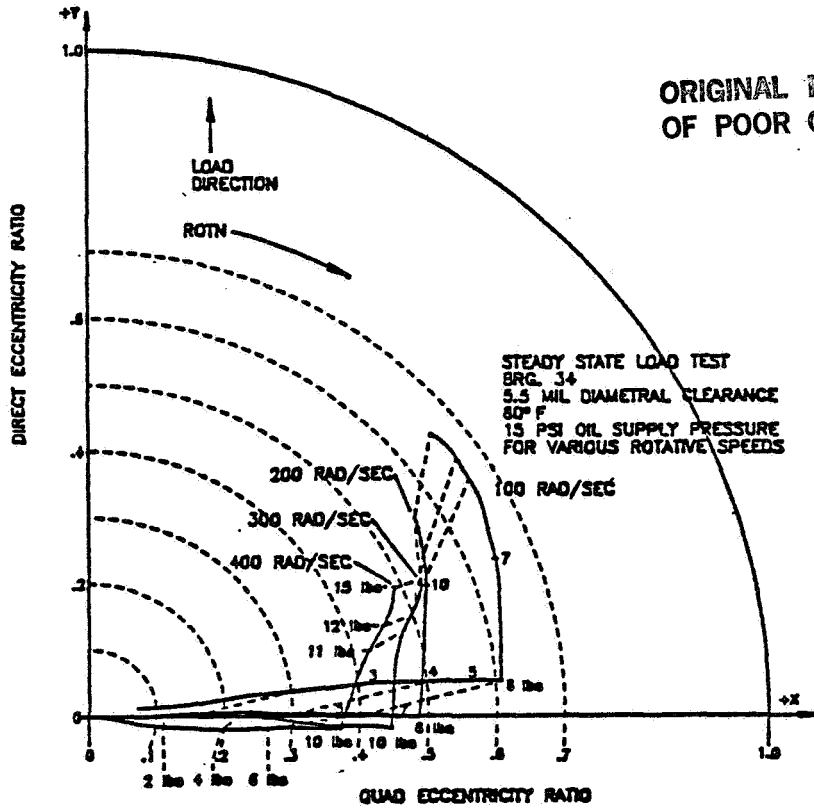


Figure 3.

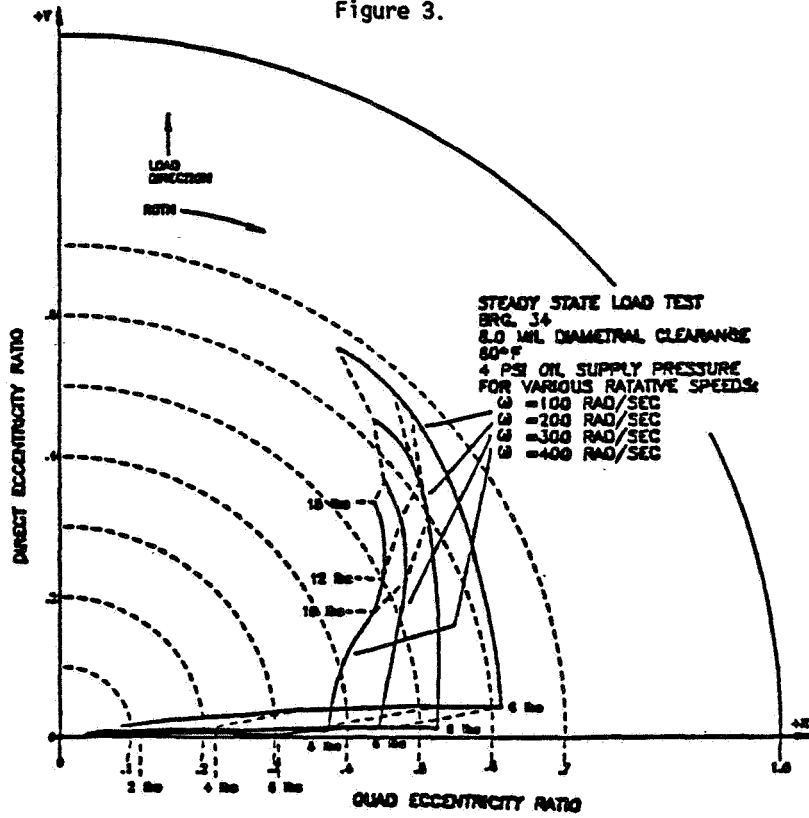


Figure 4.

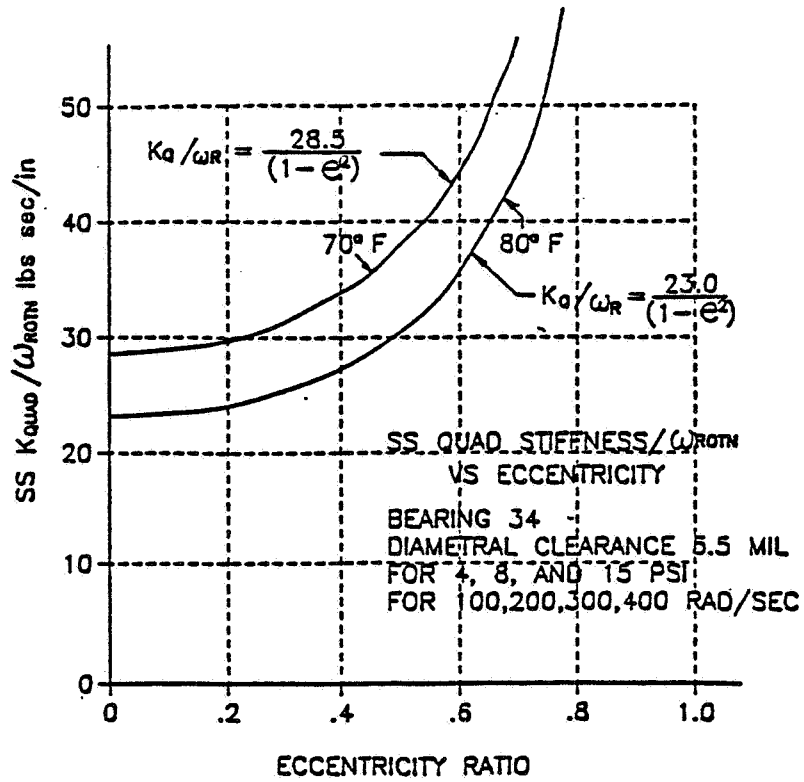


Figure 5.

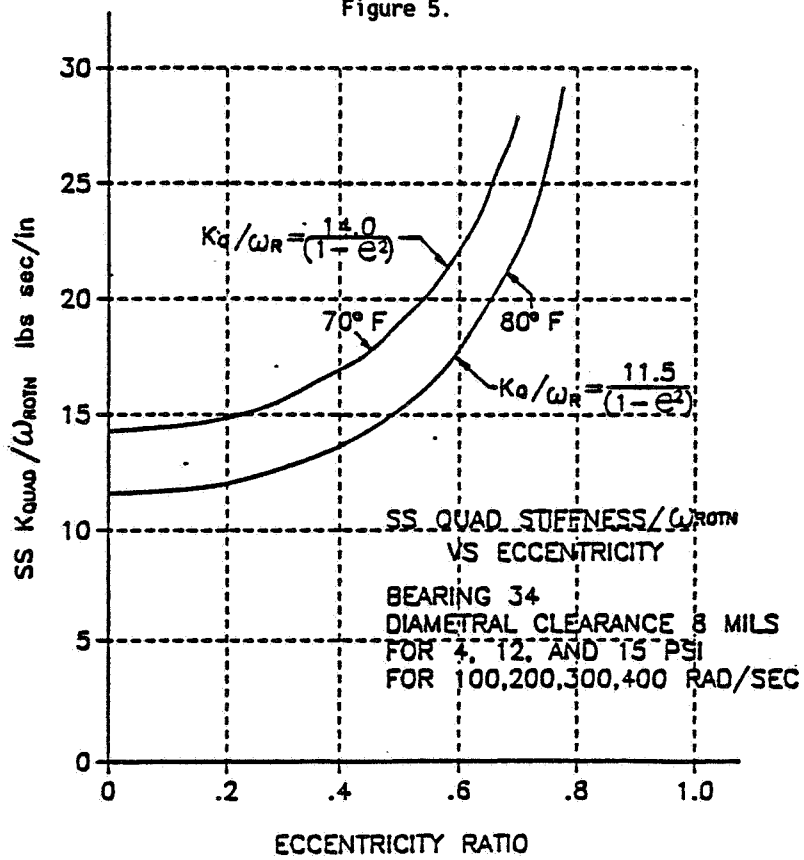


Figure 6.

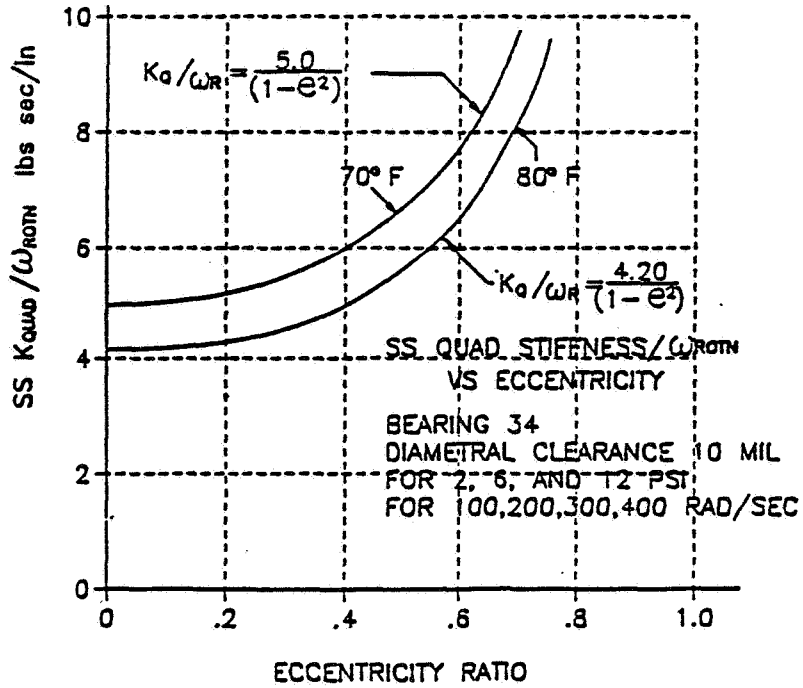


Figure 7.

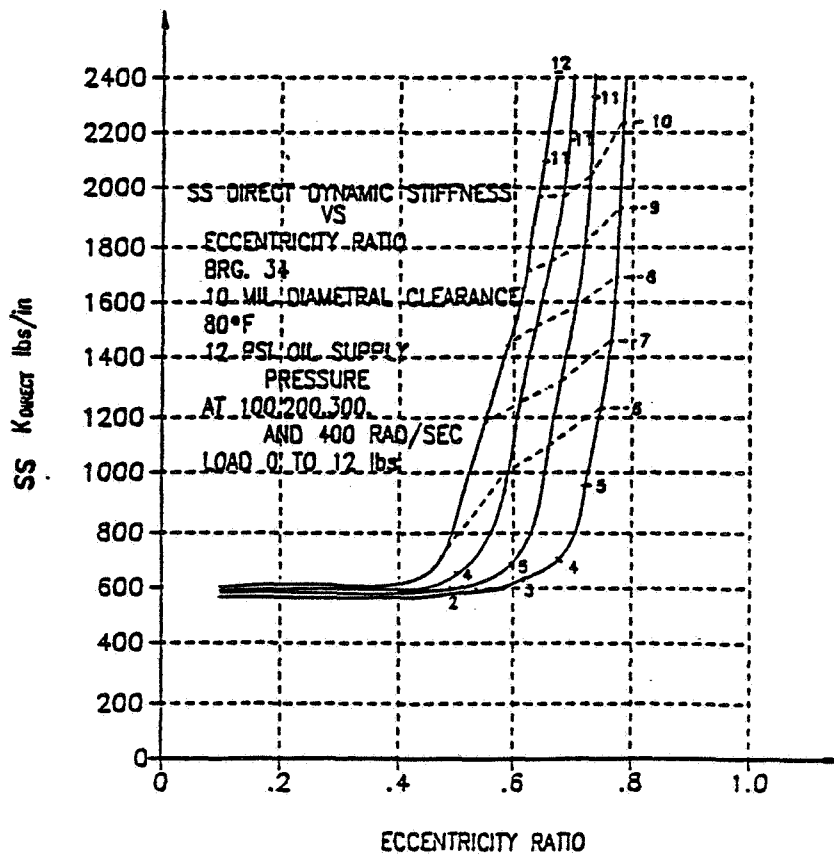


Figure 8.

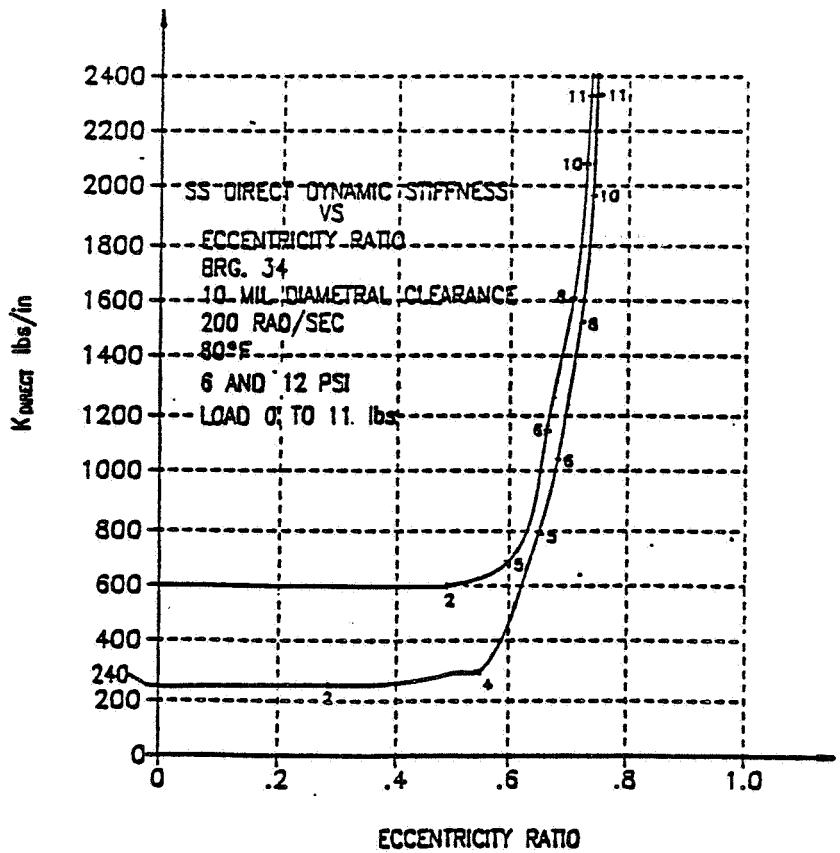


Figure 9.

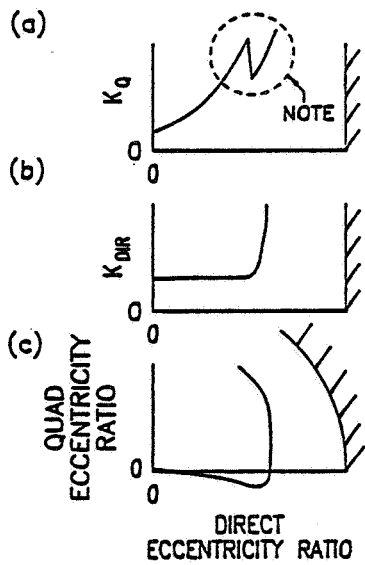
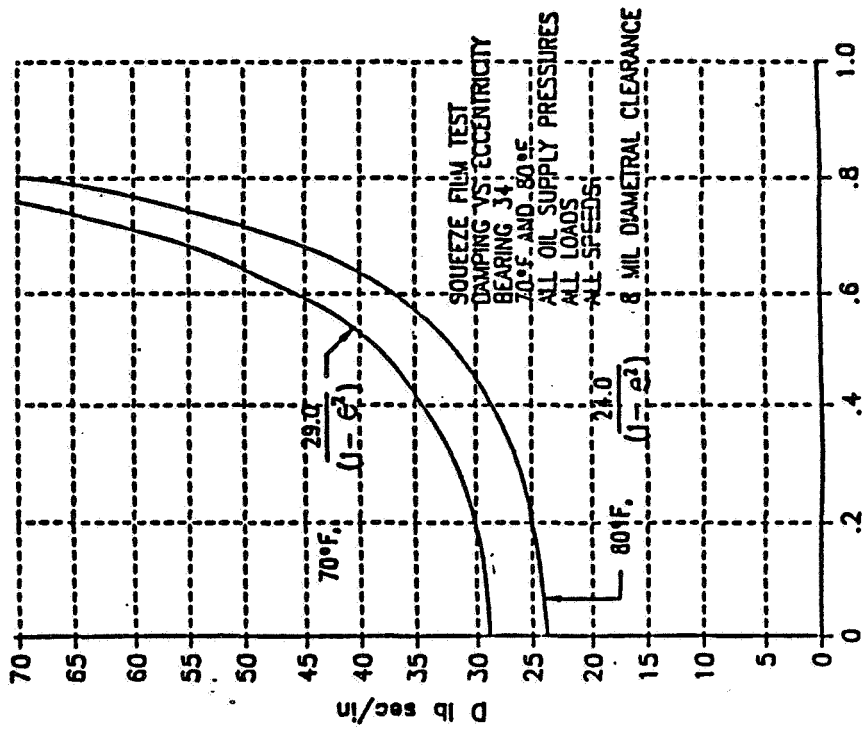
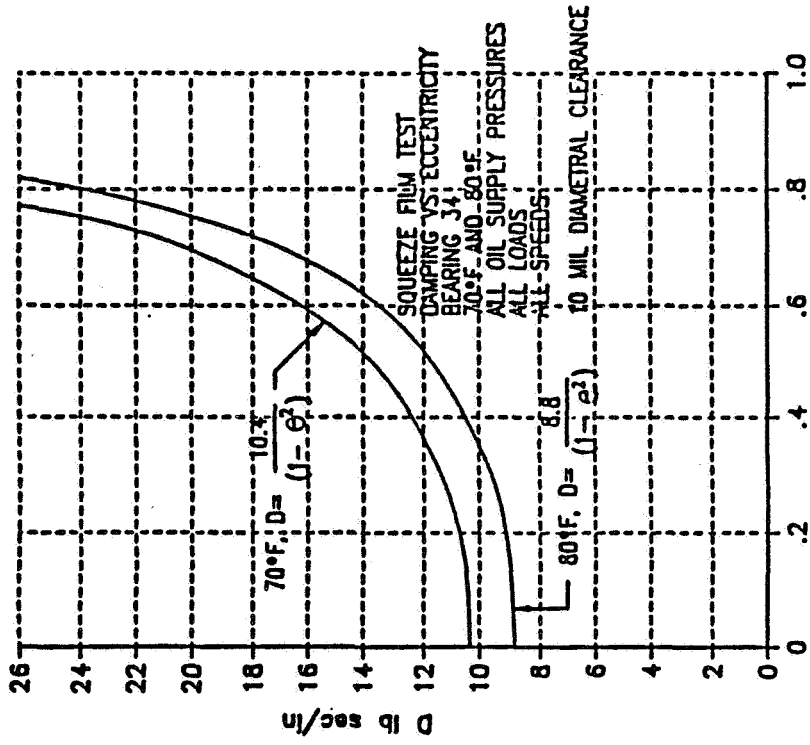


Figure 10.



ECCENTRICITY RATIO

Figure 11.



ECCENTRICITY RATIO

Figure 12.

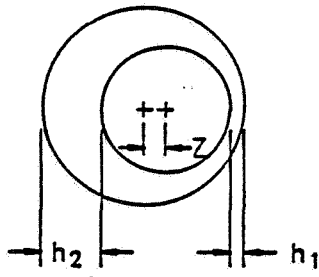


Figure 13.

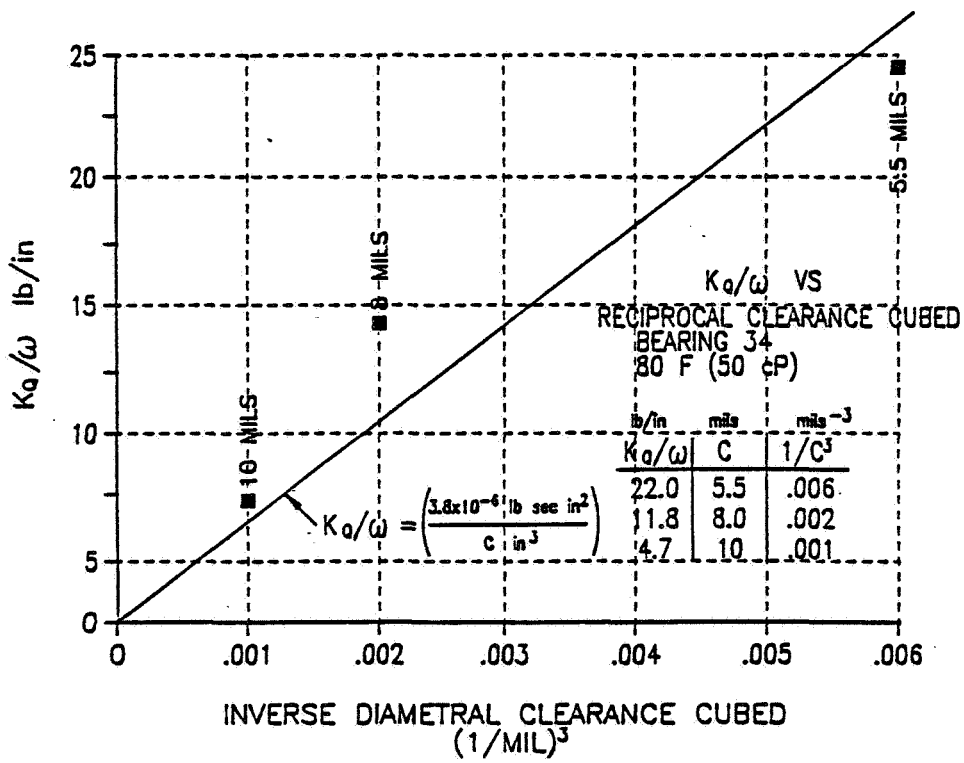


Figure 14.

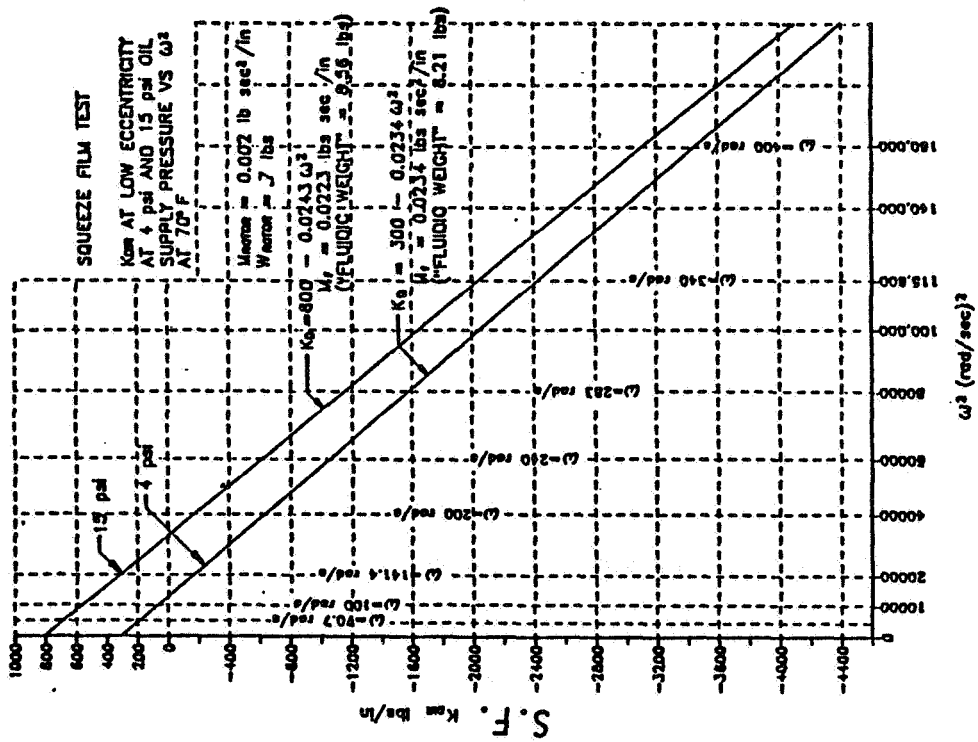


Figure 15.

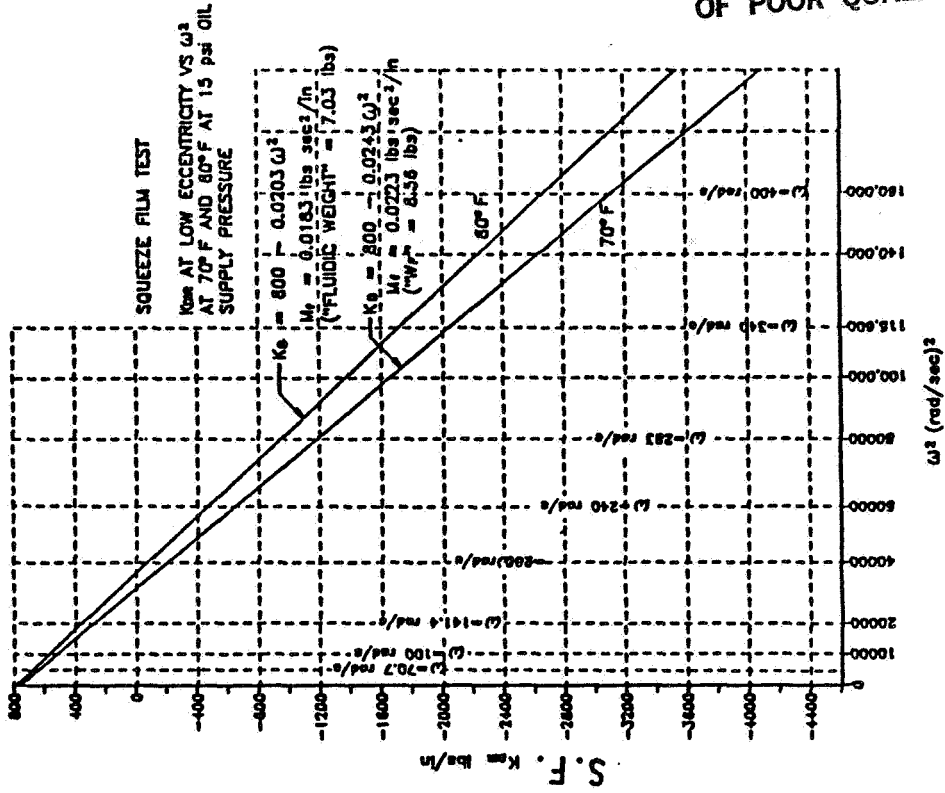


Figure 16.

MOTION AND DIRECT STIFFNESS VS SPEED FOR
 VARIOUS PERTURBATION LOADS
 (J) ROTOR = 2000 RPM, FWD
 OIL SUPPLY 70°F @ 4 PSI
 BEARING NO. 34
 DIAMETRAL CLEARANCE 5.5 MILS

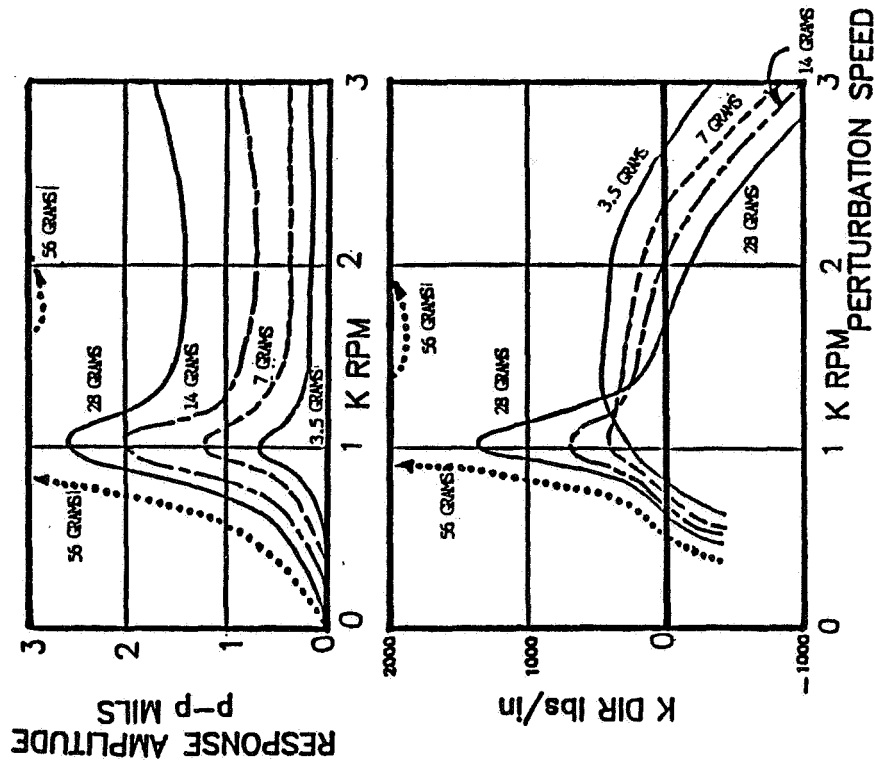


Figure 18.

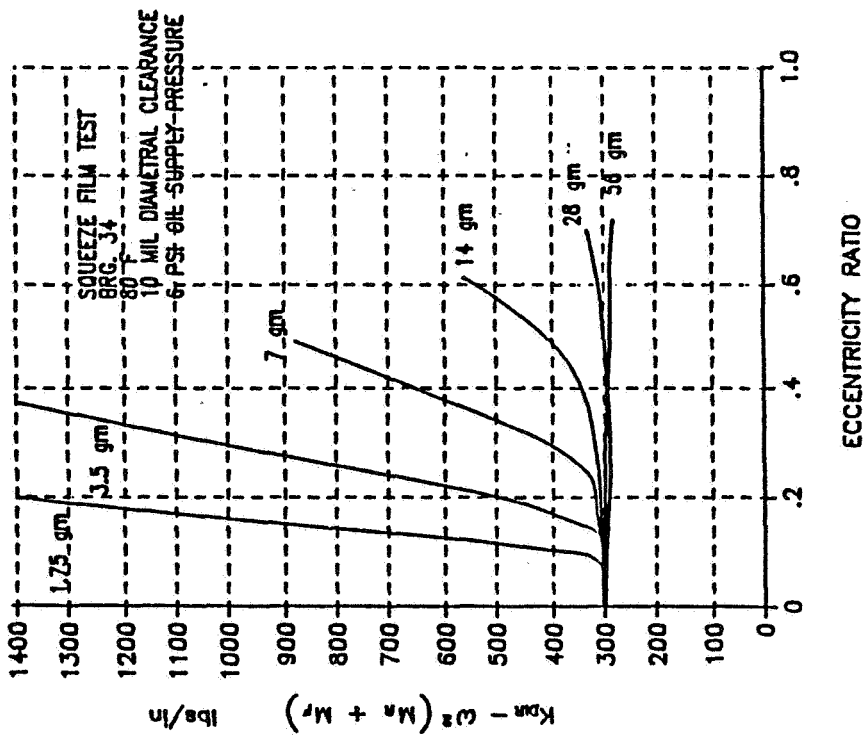


Figure 17.

MAGNETIC BEARINGS FOR VIBRATION CONTROL

G. Schweitzer
Swiss Federal Institute of Technology (ETH)
Zurich, Switzerland

The paper presents a survey on the research of the Institute of Mechanics of the ETH in the field of vibration control with magnetic bearings. It shows a method for modelling an elastic rotor so that it can be represented by a low order model amenable to control techniques, it deals with the control law and spill-over effects, and it discusses experimental results for an active resonance damper.

INTRODUCTION

Magnetic bearings can exert forces on a body without any physical contact. This makes it a very useful device to influence the position and the motion especially of a spinning rotor. Magnetic bearings are quite capable of supporting even a heavy rotor. Its application to turbomachinery, machine tools, and in the vacuum techniques is described for example by Habermann (ref. 1). Such a bearing, or more precisely such a bearing system, can be designed in a systematic way (ref. 2). By suitably designing the control loop the magnetic actuator can be adjusted to a variety of applications and dynamic requirements. Primary design goals have been to support a rigid rotor, because the rigidity of the rotor facilitates the control design essentially. The magnetic forces can be made to be a function of the rotor motion in such a way that the actuator usually has spring and damper characteristics which suitably depend on the excitation frequency.

The freedom in assigning dynamic characteristics to the actuator can be used not only for supporting a rigid rotor but for vibration control as well. Some efforts have already been undertaken to control various kinds of vibrations. Pietruszka and Wagner (ref. 3) show how an unbalanced rigid rotor can be made to rotate about its principal axis of inertia, thus avoiding vibrational unbalance forces on the magnetic bearings. In reference 4 magnetic bearings are used to shield a measuring platform from residual vibrations of its base. Gondhalekar et al. (ref. 5,6) investigate vibration control problems of an elastic rotor. Even the active damping of self-excited vibrations by internal friction and of parametric vibrations due to rotor asymmetry have been looked into. It shows that pragmatic solutions for individual problems can be found, general methods and the answers to some basic questions, however, are not yet available.

This paper will give a survey on our research in the field of vibration control. At first it presents the modelling of an elastic rotor so that the resulting low order model is amenable to control techniques. Another aspect concerns the control law and the effects of spill-over, and finally design requirements and experimental

results for an active resonance damper are discussed. The survey is based on the work of the research group of the Institute of Mechanics at the ETH, especially on the contributions of Bucher, Salm and Traxler.

FUNCTIONAL PRINCIPLE

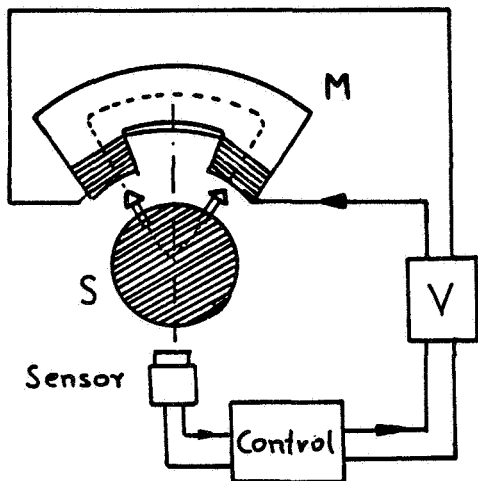


Fig. 1: Magnetic Suspension

At first the functional principle of the magnetic suspension will be explained shortly and demonstrated by examples.

Figure 1 shows a hovering shaft S. Its position is measured by a sensor, the measured signal is processed in a controller, the controller output controls via an amplifier the current through the coils of the magnet M in such a way that the magnetic force stabilizes and firmly keeps the shaft in its hovering state. This simple example shows that obviously the size of the magnetic force depends on the size of the air gap, and that the dynamics of the suspension, its stiffness and damping, to a large extent is determined by the design of the controller.

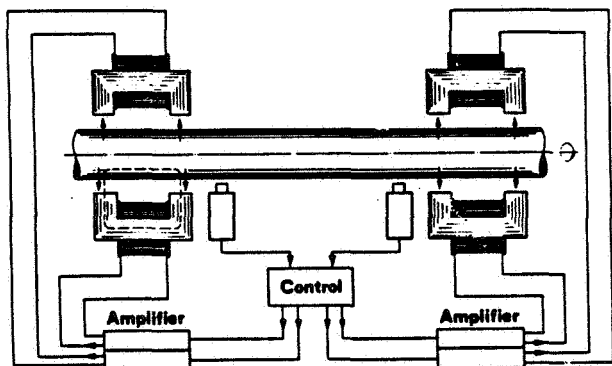


Fig. 2: Block-diagram for the radial suspension of a rotor in one plane

For suspending a full rotor the simple loop will not be sufficient. Figure 2 shows the radial suspension of a rigid rotor. For each degree of freedom a magnetic actuator has to be controlled independently. In general each bearing force will depend on each sensor signal, leading to a typical multivariable control.

ORIGINAL PAGE IS
OF POOR QUALITY

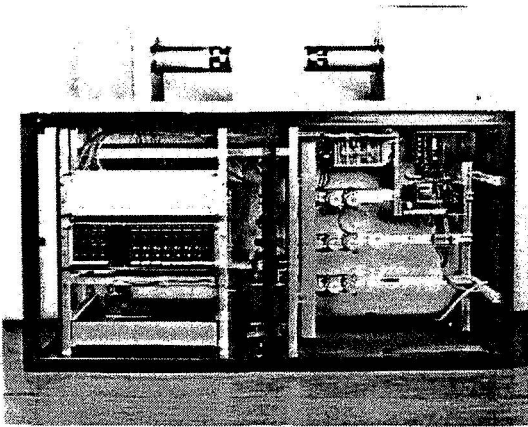


Fig. 3: Magnetic bearing system, front view with control unit, power supply and drive

Figure 3 shows the hardware setup for such a bearing system. The rotor has a length of about 1 m, a diameter of 12 cm and a mass of 12 kg. The air gap of 1 cm is extremely large for technical purposes. The device was used for an exposition. The signals of the optical CCD-sensors are processed by a microprocessor and fed to switched power amplifiers.

MODELLING OF AN ELASTIC ROTOR

For most of the current applications the rotor is considered to be rigid. The derivation of its equations of motion under the action of magnetic control forces shouldn't cause any difficulties. For an elastic structure the modelling procedure is somewhat more complex, as will be outlined in the following.

The model of the elastic rotor has to be such that it can be incorporated into the model of the closed control loop, and it has to be of low order so that the complexity of designing the control law will be reduced and a simulation of the closed loop becomes reasonable.

For the derivation of such a model, following Bucher (ref. 7), let us start with a finite element model of the elastic rotor

$$(1) \quad \underline{A}_2 \ddot{\underline{q}} + \underline{A}_1 \dot{\underline{q}} + \underline{A}_0 \underline{q} = \underline{p}$$

where \underline{q} is a $n \times 1$ vector of generalized displacements, \underline{p} is the vector of generalized forces, and the \underline{A}_i are structural coefficient matrices, characterizing inertia and elasticity as well as gyroscopic and nonconservative properties. Equation 1 may be transformed into the complex frequency domain and expressed by

$$(2) \quad \left[s^2 \underline{A}_2 + s \underline{A}_1 + \underline{A}_0 \right] \underline{Q}(s) = \underline{P}(s)$$

The matrix in brackets is termed dynamical stiffness matrix and its inverse is the dynamical flexibility matrix

$$(3) \quad \underline{H}(s) = [s^2 \underline{A}_2 + s \underline{A}_1 + \underline{A}_0]^{-1}$$

The elements of $\underline{H}(s)$, the dynamical flexibility transfer functions, are well-known in measurement and modal analysis techniques. A general way of reducing the large set of finite element equations is to truncate the modal representation of equation 1. In order to find that representation we have to solve the eigenvalue problem of equation 1. For the sake of simplicity - all the subsequent derivations can be extended to the general system (equ. 1) as well (ref. 7) - let us assume a simple elastic structure

$$(4) \quad \underline{M}_0 \ddot{\underline{q}} + \underline{K}_0 \underline{q} = \underline{p}$$

From the solution of the eigenvalue problem we obtain a set of eigenvalues $\omega_1, \dots, \omega_n$ and the corresponding real normalized eigenvectors \underline{u}_k with the modal matrix $\underline{U} = (\underline{u}_1, \dots, \underline{u}_k, \dots, \underline{u}_n)$.

Then the modal expansion of \underline{q}

$$(5) \quad \underline{q} = \sum_k \underline{u}_k z_k = \underline{U} \underline{z}, \quad k = 1, \dots, n$$

leads to the modal representation of equation 4

$$(6) \quad \underline{M} \ddot{\underline{z}} + \underline{K} \underline{z} = \underline{U}^T \underline{p}$$

with $\underline{M} = \underline{U}^T \underline{M}_0 \underline{U} = \text{diag}(m_k)$, $\underline{K} = \underline{U}^T \underline{K}_0 \underline{U} = \text{diag}(k_k)$, $\omega_k^2 = k_k/m_k$

This modal representation is a time domain representation of the partial fraction expansion of the corresponding flexibility matrix $\underline{H}(s)$. Translating equations 5 and 6 into the s-domain, yields

$$(7) \quad \underline{H}(s) = \underline{U} (\underline{M} s^2 + \underline{K})^{-1} \underline{U}^T = \sum_{k=1}^n \frac{\underline{u}_k \underline{u}_k^T}{m_k (s^2 + \omega_k^2)}$$

For the design of the controller, a model of the flexible structure, that relates the displacements and velocities at the location of the sensors to the excitation forces of the actuators, is required. By analyzing the closed loop system with respect to the actuator and sensor coupling points, it can be checked whether the design objectives have been reached, i.e., whether the system is stable and shows up with good damping performance. Also, test measurements for the closed loop system are easily carried out by exciting the structure with the available actuators. Hence, for both control design and closed loop analysis, we may confine the selection of coordinates to the coupling points of the actuators and sensors with the structure. A modal representation of the dynamical flexibility matrix of the elastic structure, with respect to the cited coordinates, provides the desired description, as will be shown subsequently.

The n_A actuator forces form the vector \underline{w} , the n_D measured displacements are given by \underline{y}_D , and the n_V measured velocities by \underline{y}_V . These vectors are related by appropriate incidence matrices to the nodal forces and displacements by

$$(8) \quad \underline{w} = \underline{T}_A^T \underline{p} \quad \underline{y}_D = \underline{T}_D \underline{q} \quad \underline{y}_V = \underline{T}_V \underline{\dot{q}} \quad \underline{y}^T = (\underline{y}_D^T, \underline{y}_V^T)$$

The elements of the incidence matrices are zero or one, when discrete actuators and sensors are located at nodal points. We assume that we can truncate the number of modes retaining only m essential modes, so that instead of equation 5 we now have

$$(9) \quad \underline{q} \approx \sum_i \underline{u}_i z_i = \underline{U}_m \underline{z}_m, \quad i = 1, \dots, m, \quad m < n$$

with the truncated $n \times m$ modal matrix \underline{U}_m and the truncated modal vector \underline{z}_m . This leads to the truncated set of modal equations

$$(10) \quad \underline{M}_m \ddot{\underline{z}}_m + \underline{K}_m \underline{z}_m = \underline{U}_m^T \underline{p}$$

With the subset of retained coordinates (equ. 8) we have in the s -domain a transfer matrix representation

$$(11) \quad \underline{Y}(s) = \underline{H}_G \underline{W}(s) \quad \underline{H}_G = \begin{bmatrix} \underline{T}_D \underline{U}_m (s^2 \underline{M}_m + \underline{K}_m)^{-1} \underline{U}_m^T \underline{T}_A \\ s \underline{T}_V \underline{U}_m (s^2 \underline{M}_m + \underline{K}_m)^{-1} \underline{U}_m^T \underline{T}_A \end{bmatrix}$$

Here the transfer matrix \underline{H}_G is a generalized dynamical flexibility matrix, since it relates a force excitation (actuator forces) to nodal displacements and velocities (sensor signals).

By introducing the state vector

$$\underline{x}^T = (\underline{z}_m^T, \underline{\dot{z}}_m^T)$$

an equivalent state space representation is obtained

$$(12) \quad \begin{aligned} \dot{\underline{x}} &= \underline{A} \underline{x} + \underline{B} \underline{w} \\ \underline{y} &= \underline{C} \underline{x} \end{aligned}$$

$$\underline{A} = \begin{bmatrix} \underline{0} & \underline{E} \\ -\underline{M}_m^{-1} \underline{K}_m & \underline{0} \end{bmatrix} \quad \underline{B} = \begin{bmatrix} \underline{0} \\ \underline{U}_m^T \underline{T}_A \end{bmatrix} \quad \underline{C} = \begin{bmatrix} \underline{T}_D \underline{U}_m & \underline{0} \\ \underline{0} & \underline{T}_V \underline{U}_m \end{bmatrix}$$

All of the representations (equ. 10,11,12) will be suitable for the control design. The method can be extended to include other structural elements as well, i.e. foundation dynamics, by applying the building block approach. Problems left over and to be discussed in the next section are that of truncation and the control design.

CONTROL OF AN ELASTIC ROTOR

When the control design is based on a reduced-order model of the rotor (equ. 10) the question arises whether the real rotor will indeed be controlled correctly by such a simplified controller. Actually there may be detrimental effects, and we can explain and classify them in the following way (ref. 6).

A direct output feedback is known to have these properties and to show robustness qualities with respect to parameter errors and truncation effects (ref. 8). Then the control forces depend linearly on the displacement and velocity measurements

$$(15) \quad \underline{w} = -\underline{G}_D \underline{y}_D - \underline{G}_V \underline{y}_V$$

with the yet unknown gain matrices \underline{G}_i . Introducing this control law and the measurement equations 8 into the full-order system equations 6 leads to the full-order closed-loop system (FOCL)

$$(16) \quad \underline{M} \ddot{\underline{z}} + \underline{U}^T \underline{T}_A \underline{G}_V \underline{T}_V \underline{U} \dot{\underline{z}} + (\underline{K} + \underline{U}^T \underline{T}_A \underline{G}_D \underline{T}_D \underline{U}) \underline{z} = \underline{0}$$

In order to avoid the spillover effects the solutions of equation 16 should be stable. Then the FOCL is stable despite the fact that its gain matrices will be based on the reduced-order model. The stability conditions, derived from definiteness properties of the coefficient matrices (ref. 6), are certainly fulfilled,

- if the sensors and actuators are arranged in collocated pairs, i.e. if $\underline{T}_A^T = \underline{T}_D = \underline{T}_V$. And when the actuators have to support the rotor additionally to controlling its vibrations the number of reasonably placed sensors and actuators has to be at least equal to the number of not stable rigid body modes.
- if the gain matrices \underline{G}_i are symmetric and positive definite.

The procedure how to construct such gain matrices will be explained shortly. The reduced-order model, including the rigid-body modes, and all other vibration modes that should be controlled, is given by equation 14. Introducing the control equation

$$\underline{w} = -\underline{G}_D \underline{y}_{Dm} - \underline{G}_V \underline{y}_{Vm}$$

into equation 14 leads to the closed-loop equation of the reduced-order model

$$(17) \quad \underline{M}_m \ddot{\underline{z}} + \underline{D}_m \dot{\underline{z}} + (\underline{K}_m + \underline{S}_m) \underline{z} = \underline{0}$$

$$(18) \quad \underline{D}_m = \underline{U}_m^T \underline{T}_A \underline{G}_V \underline{T}_V \underline{U}_m, \quad \underline{S}_m = \underline{U}_m^T \underline{T}_A \underline{G}_D \underline{T}_D \underline{U}_m$$

The terms \underline{D}_m , \underline{S}_m are the additional modal damping and stiffness introduced by the control feedback. The required symmetry and definiteness properties of the yet unknown gains \underline{G}_i will be guaranteed by a design approach of Salm (ref. 6). First we assign desired additional modal damping and stiffness values and thereby choose the diagonal matrices \underline{D}_m and \underline{S}_m , and then we solve equations 18 for the unknown gains. However, as most often the number of n_A , n_D of actuators and sensors will be smaller than the number m of modelled modes, it is not possible to solve equation 18 uniquely. An approximation for the gains \underline{G}_i , in the sense of minimized quadratic differences using Pseudo-Inverses, is feasible and leads to the following design rules:

The reduced-order control of large, and even infinite dimensional vibration systems will result in a robust and certainly stable FOCL, if

- the vibration system is not unstable (rigid body modes are allowed),
- the reduced-order model contains at least all rigid-body modes,
- the sensors and actuators are collocated and their number is at least equal to the number of rigid-body modes.

This control approach includes the technically most interesting case where a real flexible rotor is suspended by actuators which at the same time have to control its elastic vibrations. An example and experimental results will be shown in the next section.

EXAMPLES AND EXPERIMENTAL RESULTS

Active suspension and vibration control of a flexible beam (ref. 6). The transverse vibrations of a flexible beam, supported and controlled by actuators on both ends, are described by the modal equation 6. The mode shapes (equ. 5) used in this case are the free-free modes, the rigid body modes are included in the modal transformation matrix \underline{U} .

As a design goal the two actuators will have to control the two rigid-body modes, and additionally two elastic modes should be strongly damped, too. Therefore the reduced-order model is chosen to consist of the two rigid-body modes and the first two elastic modes. Displacement and velocity signals are coming from sensors at the actuator locations. The gain matrices \underline{G}_i for the direct-output control are derived from equation 18, where in our case the assigned modal stiffness and damping, that we want to obtain, is characterized by

$$\underline{S}_m = \underline{\text{Diag}} \omega_{mi}^2 \quad \underline{D}_m = \underline{\text{Diag}} (2D \omega_{mi})$$

The stiffness of the suspension was assigned by prescribing ω_1, ω_2 . The damping value D was varied between 0 and 1. Several general and anticipated results could be corroborated numerically:

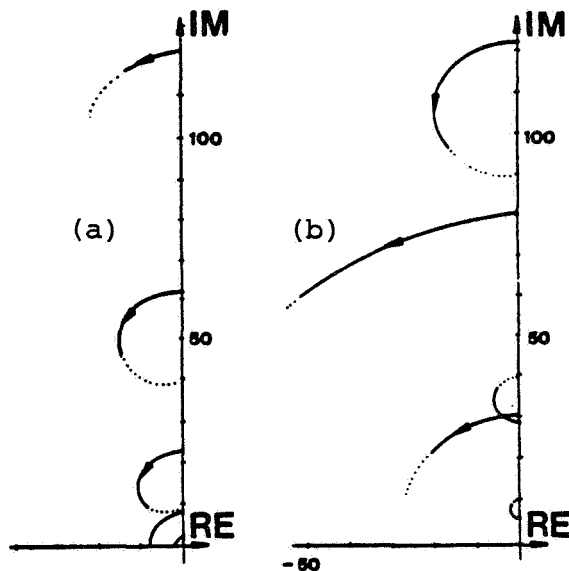


Fig. 5: Typical eigenvalue-curves of the controlled full-order system with increasing damping values D assigned to the modes

- For "low" bearing stiffness (Fig. 5a) the eigenvalues of the controlled system have a typical behaviour when we increase the assigned damping value D . For very high damping the modal frequencies of a fixed-fixed beam are approximated.
- For a "stiff" bearing design (Fig. 5b), where we want the bearing stiffness to be near the first elastic frequency of the beam, the behaviour is similar, but some eigenvalues now go upwards to higher eigenfrequencies of the fixed-fixed beam. The

ORIGINAL PAGE IS
OF POOR QUALITY

poor controllability of these modes comes from the fact that high control forces tend to "clamp" the beam, and to shift modal nodes into the actuator location itself.

- Limiting values for the attainable stiffness are given by the lowest frequencies of an equivalent beam with fixed ends.
- The control design always produces a stable system. It provides stability and damping for the modelled and the unmodelled modes.

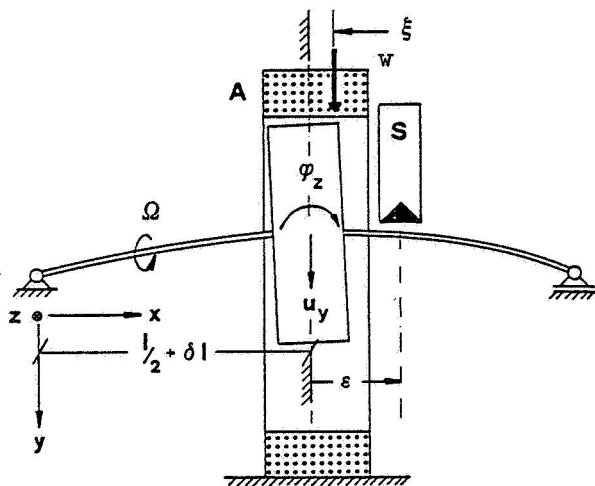


Fig. 6: Rotor model, demonstrating the parameter deviations ϵ, ξ and δl from a reference position

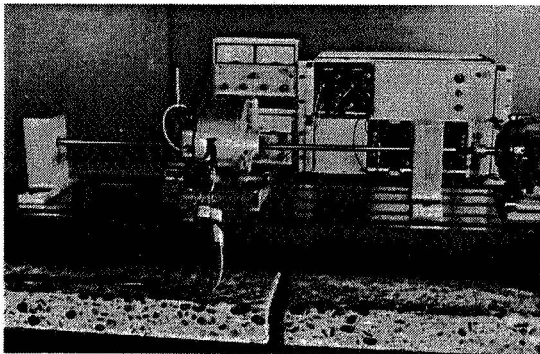


Fig. 7: Experimental setup

Vibration damping and spill-over effects.

A simple rotor model (Fig. 6) demonstrates the active damping of resonance vibrations (ref. 6). The experimental setup (fig. 7) consists of a conventionally supported, flexible rotor shaft with a disc in the "middle" of the shaft. The "exact" model for the rotor of figure 6 considers the imperfection parameters $\epsilon, \xi, \delta l$. Now the control design is based on a reduced-order model, taking only the displacements u_y, u_z into account. The motion of the "exact" rotor, however, will be affected by the coupling between translation and inclination of the disc. It is the imperfection parameter ϵ that causes observation spillover, and ξ provides control spillover. The eigenvalue shifts caused by these spillover effects are demonstrated in figure 8. The unmodelled modes can even become unstable. When actuator and sensor are collocated ($\epsilon = \xi$) then the "exact" model is stable even with the "simple" control. The calculations have been confirmed by experiments. Near the stability boundary however the above modeling was not sufficient: the small imperfections due to the phase/frequency response of the sensor had to be taken into account (ref. 7).

When the elastic rotor and the control are modelled according to the above rules, the active damper can reach good performance. Measurement results (fig. 9) demonstrate the considerable reduction of the resonance amplitudes for the experimental setup.

CONCLUSION

In order to control vibrations in flexible mechanical systems and to solve special suspension tasks it can be advantageous to use magnetic actuators. For the design of the multivariable control loop a suitable model of the mechanical system is derived. Starting from a FE-model of high order the reduced order model finally only retains the actuator and sensor coordinates and the modes considered to be important. In the control design the spillover aspects are discussed. A method for determining a control based on the reduced-order model and robust with respect to the number of unmodelled modes is demonstrated. Examples show the active suspension of a flexible beam, spillover effects, and measured resonance curves for an actively damped rotor running through its critical speed.

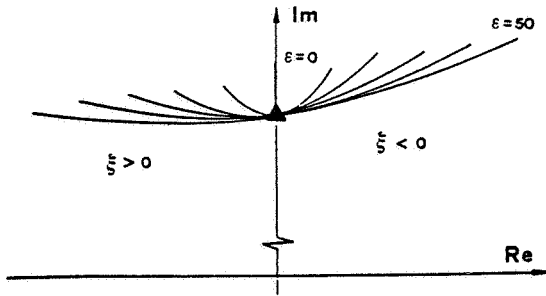


Fig. 8: Eigenvalue shift of the unmodelled modes depending on the parameters ϵ and ξ . Without control the eigenvalue is at \blacktriangle .

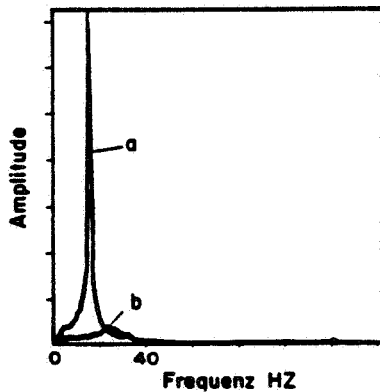


Fig. 9: Measured amplitude/frequency response, (a) uncontrolled, (b) controlled

REFERENCES

1. Habermann, H.: Le Palier Magnetique Actif "Actidyne". AGARD Conference Proc. No.323, Problems in Bearings and Lubrication, Ottawa, Canada, May 1982.
2. Schweitzer, G.; and Traxler, A.: Design of Magnetic Bearings. Internat. Symposium on Design and Synthesis, July 11-13, Tokyo, 1984.
3. Pietruszka, W.D.; and Wagner, N.: Aktive Beeinflussung des Schwingungsverhaltens eines magnetisch gelagerten Rotors. VDI Bericht Nr. 456, 1982.
4. Gondhalekar, V.; and Schweitzer, G.: Dynamics and Magnetic Control of a Micro-Gravity Platform. Report of the Institute of Mechanics, ETH Zürich, 1984/3.
5. Gondhalekar, V.; and Holmes, R.: Design of Electromagnetic Bearing for Vibration Control of Flexible Transmission Shaft. NASA Conf. Publ. 2338, 1984, p.351-365.
6. Salm, J.; and Schweitzer, G.: Modelling and Control of a Flexible Rotor with Magnetic Bearings. Conf. on Vibrations in Rotating Machinery, Institution of Mech. Eng., C277, York, 1984, p. 553-561.
7. Bucher, Ch.: Contributions to the Modelling of Flexible Structures for Vibration Control, Diss. ETH Zürich No. 7700, 1985.
8. Lin, J.G.: Closed-Loop Asymptotic Stability and Robustness Conditions for Large Space Systems with Reduced-Order Controllers. 20th IEEE Conference on Decision and Control, San Diego, 1981, p. 1497-1502.

ACTIVE MAGNETIC BEARINGS FOR OPTIMUM TURBOMACHINERY DESIGN

Jerry Hustak, R. Gordon Kirk, and Kenneth A. Schoeneck
Ingersoll-Rand Company
Phillipsburg, New Jersey 08865

The design and shop test results are given for a high speed eight stage centrifugal compressor supported by active magnetic bearings. A brief summary of the rotor dynamics analysis is presented with specific attention given to design considerations for optimum rotor stability. The concerns for retrofit of magnetic bearings in existing machinery are discussed with supporting analysis of a four stage centrifugal compressor. Recommendations are given on design and analysis requirements for successful machinery operation of either retrofit or new design turbomachinery.

INTRODUCTION

A decade ago new technology in the form of dry gas seals was introduced into the field of industrial turbomachinery design to minimize the capital, operating, and maintenance costs associated with seal oil systems (1). Today this type of sealing system is gaining widespread recognition because it has and is continuing to demonstrate its superior mechanical, performance, and economic features in certain applications. Now once again new technology in the form of active magnetic bearings (AMB) is being introduced into the marketplace for use on individual turbomachinery. The features of this technology when applied to turbocompressor design result in several economic, performance, and versatility improvements unavailable to the industry at the present time. Active magnetic bearings used in conjunction with dry gas seals and dry couplings now enable both the manufacturer and user to think in terms of oil-free centrifugal compressors, certainly a dramatic change from only ten years ago (2).

Patent activity on passive, active, and combination magnetic bearing systems spans 150 years. The bulk of the initial investigations centered on permanent magnetic systems because they were easy to fabricate. It was later shown, however, that a passive magnetic suspension for three axes of displacement is unstable; a theory that is still valid today. In 1969 Societe Europeenne de Propulsion (SEP), a French research firm, began investigating the characteristics of both passive and active magnetic suspension systems for a satellite flywheel application. In 1970 they developed a totally active magnetic suspension system for the COMSAT communications satellite. In 1976 SEP formed a new company Societe de Mecanique Magnetique (S2M) to further develop and commercially market active magnetic bearing (AMB) systems internationally (3,4).

DEVELOPMENT CENTRIFUGAL COMPRESSOR WITH AMB

Figure 1 is a view of an eight stage, horizontally-split, back-to-back centrifugal compressor equipped with magnetic radial and thrust bearings and gas seals on test at the authors' company (1980). The eight stage rotor housed inside the compressor, originally designed to run at 10,000 RPM (167 Hz) on hydrodynamic bearings,

has since operated successfully at speeds up to 13,000 RPM (217 Hz) on magnetic bearings. The compressor is shown attached to two closed loops constructed for the purpose of operating the rotor in a pressurized environment over a wide range of pressures and flows from choke to surge.

One unique feature of this compressor was the installation of the thrust and journal bearings located on the free end of the rotor directly into the gas (nitrogen) pressurized environment thereby eliminating the need for one shaft seal. To illustrate the concept of a nonlubricated centrifugal compressor a gas seal was chosen as the main shaft seal on the coupling end of the rotor. Table 1 summarizes some of the important design features of the eight stage back-to-back rotor while Figure 2 illustrates the appearance of the fully assembled test rotor.

Before power is applied to the bearings the rotor is supported on two auxiliary cage, dry lubricated ball bearings located in close proximity to the AMB. The clearance between the rotor and the inner race of the ball bearing is selected to prevent rotor contact with the AMB pole pieces or the internal seals of the compressor while the rotor is at rest or during an emergency shutdown. Typical radial clearances in the AMB, internal seals, and auxiliary bearing area are 0.012 in. (.3 mm), 0.010 in. (.254 mm), and 0.006 in. (.15 mm), respectively. When power is applied to the electronic controls the electromagnets levitate the rotor in the magnetic field and rotation of the driving source such as a motor or turbine can be started. The sensors and control system regulate the strength and direction of the magnetic fields to maintain exact rotor position by continually adjusting to the changing forces on the rotor. Should both the main and redundant features of the AMB fail simultaneously, the auxiliary bearings and rotor system are designed to permit safe deceleration.

The undamped critical speed map shown in Figure 3 compares the standard fluid film bearing/oil seal design to the magnetic bearing/gas seal design for the 8 stage development compressor. The magnetic bearing design increased the first rigid bearing mode by reducing the bearing span but decreased the second, third, and fourth modes due to the additional weight of the ferromagnetic journal sleeves and the larger diameter thrust collar. Superimposed on this map are the as measured stiffness and damping properties of the electromagnetic bearings as a function of rotor speed. For a design speed of 10,000 RPM (167 Hz), Figure 3 indicates the rotor would have to pass through three critical speeds and operate approximately 20% above the third critical and 40% below the fourth critical. Furthermore, since both the first and second criticals are rigid body modes only a significant response at approximately 8000 RPM (133 Hz) would be expected as the rotor passed through its third (free-free mode) critical. Subsequent unbalance forced response calculations verified these expectations with acceptable operation of the compressor to 14,000 RPM (233 Hz) (see Figures 4 and 5).

The damping required for optimum stability may be arrived at by construction of a Lund stability map (5) from the calculated damped critical speeds (5,6,7). For the 1st mode stiffness of 130,000 lb/in (22.8 N/ μ m), Figure 6 shows the movement of the eigenvalues as the bearing damping varies. Increased damping levels cause the first and second modes to become critically damped. The third mode increases in stability up to a point of 501 lb-sec/in (87.7 N-sec/ μ m) but then decreases as damping is increased further. Since the first and second modes become critically damped, a second study was undertaken to determine if the third mode would go unstable at its corresponding stiffness of 229,000 lb/in (40.1 N/ μ m). The results of that analysis are presented in Figure 7 which indicate the third mode becomes critically damped as the damping is increased while the 1st mode damping would be at an optimum for 645

lb-sec/in (112.9 N-sec/mm). The behavior of the 1st and 3rd modes, resulting from the increase in bearing stiffness, is similar to results presented by Lund (5). These results indicate that a level of 400-500 lb-sec/in (70 - 87.5 N-sec/mm) would be ideal for all modes up to and including the fourth.

The actual measured stiffness and damping characteristics for the magnetic bearing are given in Figure 8. Active magnetic bearings have an important difference when compared to conventional fluid film bearings. Typical preloaded five shoe tilt pad bearings have characteristics generated predominantly by operating speed, with little influence from non-synchronous excitations (8). The active magnetic bearing characteristics, shown in Figure 8, are dependent on the frequency of excitation regardless of operating speed. For a given stiffness value selected to minimize unbalance forced response, the damping characteristics at subsynchronous excitation frequencies can be specified to assure optimum stability (3, 4).

The test program outlined for the compressor was directed toward confirming the analytical predictions for the dynamic behavior of the rotor and experimentally demonstrating the reliability of the complete system under typical operating conditions. The fully assembled compressor was installed on the test stand and operated at a maximum discharge pressure of 600 psig (4.1 MPa) with speeds up to 13,000 RPM (217 Hz). The results for a decel as recorded at the bearing probe locations are given in Figures 9 and 10. The results are in general agreement with the predicted unbalance forced response results. Since the amount and location of the actual unbalance distributions are never known, the amplitude of each damped response is difficult to predict. The predicted peak response speeds are considered to be in good agreement with the test results.

DESIGN EVALUATION OF A FIELD RETROFIT

The economic advantages of gas seals and/or magnetic bearings has prompted interest in retrofit of existing units. For either retrofit or new machinery, attention must be given to placement of critical speeds for both main and back-up bearings, response sensitivity, and overall stability considerations. The preliminary design study for a 4 stage high speed centrifugal compressor will illustrate in more detail the parameters that must be considered for total system dynamic analysis. The basic design parameters for this rotor are indicated in the second column of Table 1.

The undamped critical speed map for the four stage compressor with dynamic stiffness values is shown in Figure 11. The magnetic bearing stiffness is positioned such that the compressor must pass through three critical speeds before reaching a maximum continuous operating speed of 14,500 RPM (241.7 Hz). Due to the rigid body nature of the second and third modes, the actual damped critical speeds will occur from the first and fourth modes as shown in Figures 13 and 14 at approximately 4300 (71.7 Hz) and 18,300 RPM (305 Hz) respectively. Figure 15 shows the Lund stability map using a constant first mode stiffness of 86,300 lb/in (15.1 N/ μ m) with variable damping values. The first forward mode typically goes unstable while the second and third modes become critically damped as the bearing damping is increased. For this compressor design, the first mode increases in stability as the damping increases up to 225 lb-sec/in (39.4 N-sec/mm) but then decreases as the damping is increased further. The damping value initially supplied, 140 lb-sec/in (24.5 N-sec/mm), should be increased by 61% based on the results of this analysis.

The optimum damping for stability was also calculated by an approximate method

using the modal mass, rigid bearing critical frequency, and actual bearing stiffness (see Table 1). The equation from Reference (9) can be written as follows (valid for high K ratios):

$$C_0 = 1.356 \times 10^{-4} N_{cr} \left\{ M_m + \frac{70417.7 K_B}{N_{cr}^2} \right\}$$

Example for 4-stage 1st mode:

$$\begin{aligned} C_0 &= 1.356 \times 10^{-4} \times (5423) \times (146 + (70417.7) \times (86300)/(5423)^2) \\ &= 259 \text{ lb-sec/in} \end{aligned}$$

This calculation gives an answer 15% higher than the actual optimum damping for this K ratio of 1.41.

Figure 16 shows a comparison of stability versus aerodynamic excitation between the conventional fluid film design and the magnetic bearing retrofit design. The increase in stability due to the magnetic bearings moves the log dec from near zero to a value of 1.41.

CONCLUSIONS AND RECOMMENDATIONS

The capability of an active magnetic bearing system to support a flexible turbo-compressor rotor and simultaneously influence its vibrations has been successfully demonstrated. During the 350 hours of accumulated operating time for the development compressor supported by magnetic bearings the following observations have been made:

1. The rotor behaved in a stable manner at all times when accelerating/decelerating through its first three critical speeds.
2. The rotor behaved in a stable manner while undergoing surge cycles at maximum discharge pressure.
3. The rotor was able to satisfy commonly accepted vibration amplitude and critical speed amplification criteria at all operating speeds up to 13,000 RPM (217 Hz). Speeds beyond this point were limited by impeller stress considerations.

The analysis of the two compressors has clearly shown the advantages of adjustable bearing stiffness and damping to achieve minimum response sensitivity and optimum stability. For example, the increase in stability from a log dec of approximately zero to 1.41 for the 4-stage compressor could not be accomplished by conventional fluid-film bearings.

The following recommendations can be made for the design and analysis of magnetic bearing suspension turbomachinery:

1. Bearing stiffness should be selected by evaluation of shaft stiffness ratio with typical placement at the beginning of the 3rd mode ramp on the undamped critical speed map.
2. Bearing damping should be specified to give the optimum growth factors, with consideration given to all modes below maximum operating speed.

3. Consideration must be given to the next mode above operating speed (typically the 4th mode) to assure adequate separation margins.

4. All clearances in the bearings and seals should be selected to avoid rotor/stator contact (i.e., rubs) for normal expected operating conditions.

5. The machinery must be engineered to give a minimum of 10% separation margin on any continuous operating speed for operation on the auxiliary bearings.

REFERENCES

1. Schoeneck, K.A. and Hornschuch, H., "Design Concept of a High Speed-High Pressure Ratio Centrifugal Compressor," ASME Paper 75-PET-4, Presented at Petroleum Mech. Engrg. Conf., Tulsa, OK, Sept. 1975.
2. Schoeneck, K.A., "The Application of Gas Seals and Magnetic Bearings to Centrifugal Compressors," Pacific Coast Gas Assoc. Transmission Conference, Spokane, WA, April 18-19, 1985.
3. Haberman, H., "The Active Magnetic Bearing Enables Optimum Damping of Flexible Rotors," ASME Paper 84-GT-117.
4. Haberman, H. and Brunet, M., "The Active Magnetic Bearing Enables Optimum Control of Machine Vibrations," ASME Paper 85-GT-22, Presented at Gas Turbine Conference, Houston, TX, March 18-21, 1985.
5. Lund, J.W., "Stability and Damped Critical Speeds of a Flexible Rotor in Fluid-Film Bearings," J. of Eng. for Industry, Trans. ASME, Series B, 96, No. 2, May (1974).
6. Bansal, P. and Kirk, R.G., "Stability and Damped Critical Speeds of Rotor-Bearing Systems," J. of Eng. for Industry, Trans. ASME, 98 Series B, No. 1, February (1976).
7. Kirk, R.G., "Stability and Damped Critical Speeds - How to Calculate and Interpret the Results," CAGI Technical Digest, Vol. 12, No. 2, 1980.
8. Wilson, B.W. and Barnett, "The Effect of Eigenvalue-Dependent Tilt Pad Bearing Characteristics on the Stability of Rotor-Bearing Systems", University of Virginia, Report No. UVA643092/MAES5/321, January, 1985.
9. Barrett, L.E., Gunter, E.J., and Allaire, P.E., "Optimum Bearing and Support Damping for Unbalance Response and Stability of Rotating Machinery, Trans. ASME, J. of Engr. for Power, 1978.

TABLE 1

CENTRIFUGAL COMPRESSOR DESIGN PARAMETERS AND NOMENCLATURE

<u>Parameter, Nomenclature, U.S. Units, (SI Units)</u>	<u>Eight Stage</u>	<u>Four Stage</u>
Operating Speed, N, RPM (Hz)	13000. (217.7)	14500. (241.7)
Total Weight, W, lb (N)	827. (3678)	278. (1237)
Bearing Span, , in. (mm)	49.97 (1269)	34.88 (886.0)
Shaft Length, , in. (mm)	74.90 (1902)	49.32 (1253)
Coupling End Overhang, , in. (mm)	12.00 (304.8)	7.28 (184.9)
Shaft Stiffness, Ks, lb/in (N/ μ m)	3.49E5 (61.1)	1.22E5 (21.4)
Bearing Stiffness @ MCOS, Kb, lb/in (N/ μ m)	3.65E5 (63.9)	1.60E5 (28.0)
Stiffness Ratio, K, Dim., (Dim.)	0.74 (0.74)	1.41 (1.41)
Mid-Span Diameter, , in. (mm)	4.88 (123.9)	3.00 (76.2)
Journal Diameter, , in. (mm)	7.38 (187.5)	3.66 (93.0)
First Rigid Bearing Critical, Ncr, RPM (Hz)	5551. (92.52)	5423. (90.38)
First Peak Response Speed, FPS1, RPM (Hz)	7700. (129.5)	4300. (71.67)
Second Peak Response Speed, FPS2, RPM (Hz)	16300. (271.7)	18300. (305.0)
First Mode Modal Mass, Mm, lbm (N)	399. (1775)	146. (649)
Bearing Stiffness @ N1, Kb1, lb/in (N/ μ m)	1.30E5 (22.8)	8.63E4 (15.1)
Optimum Damping (Ref. 9), Co, lb-sec/in (N-sec/ μ m)	524. (9.18E-2)	259. (4.54E-2)

NOTE: Values are given in both SI and U.S. customary units. The measurements and calculations were made in U.S. customary units.

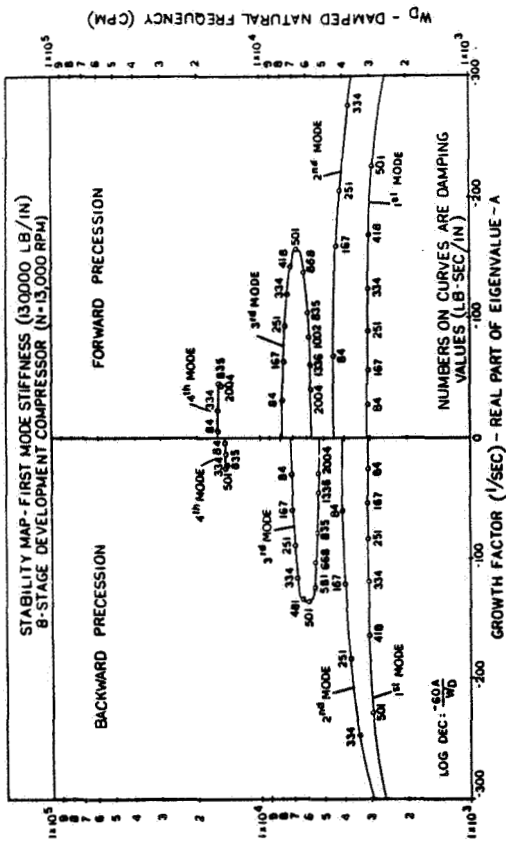


FIGURE 5

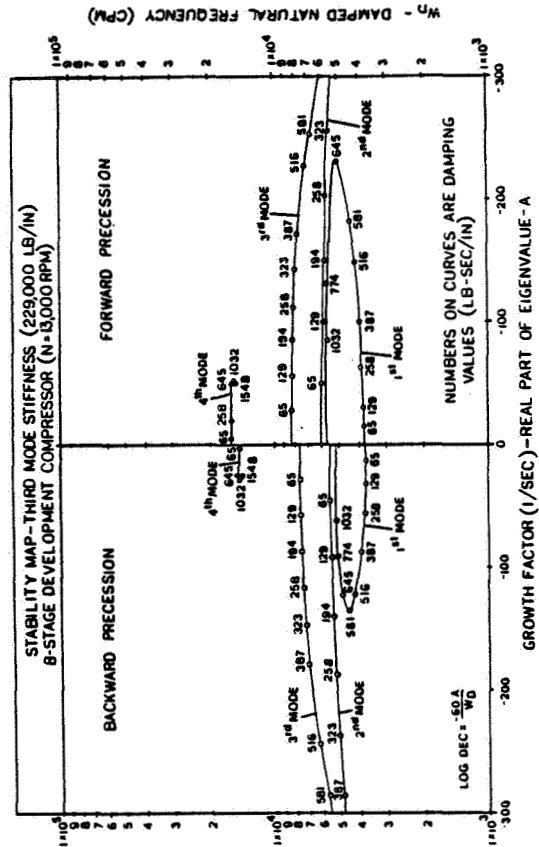


FIGURE 6

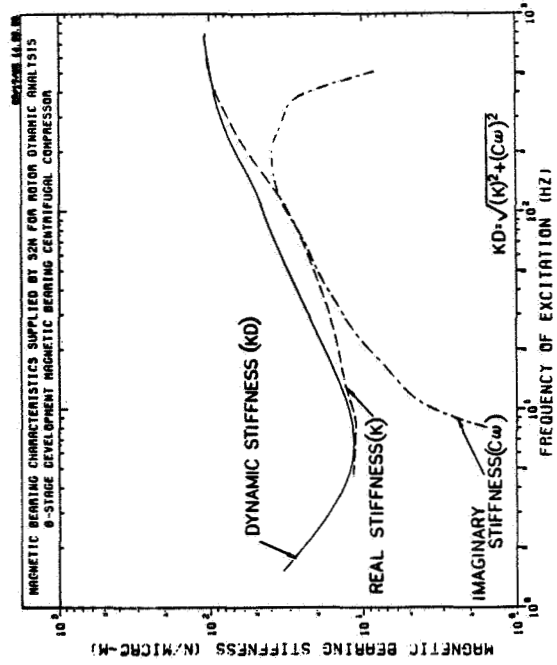


FIGURE 7

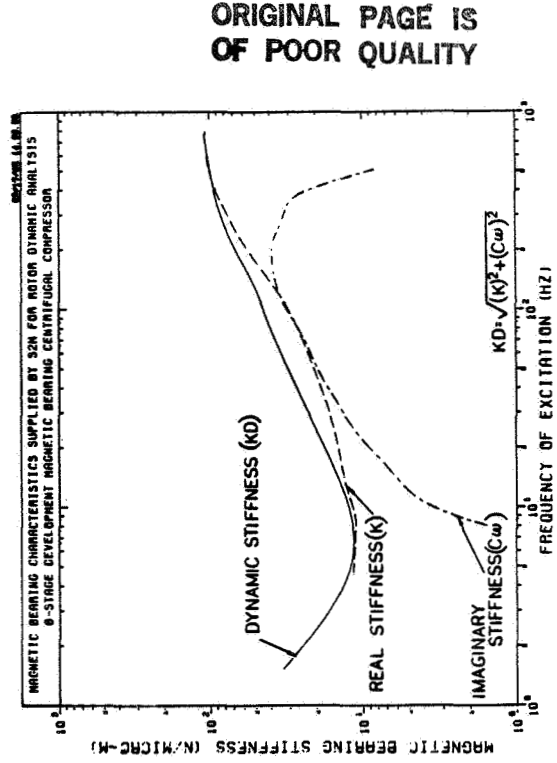


FIGURE 8

ORIGINAL PAGE IS
 OF POOR QUALITY

ORIGINAL PAGE IS
OF POOR QUALITY

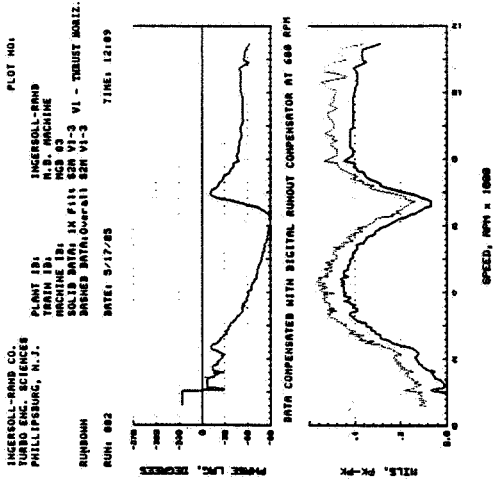


FIGURE 10

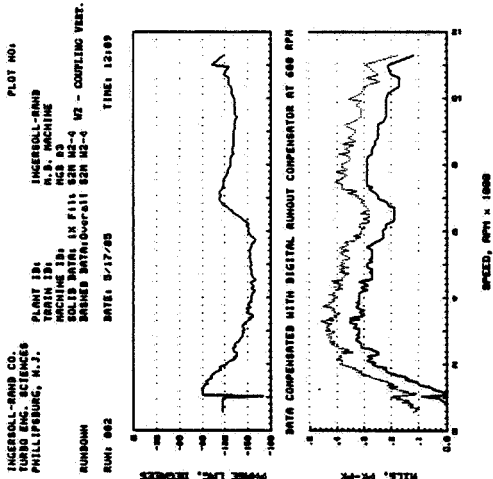


FIGURE 9

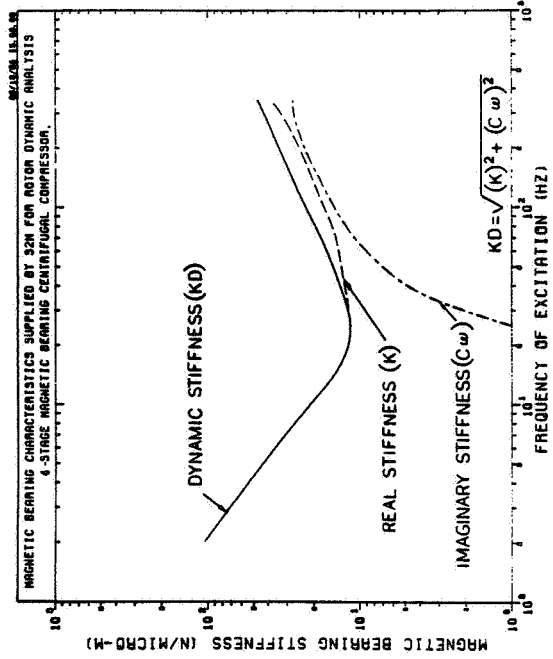


FIGURE 12

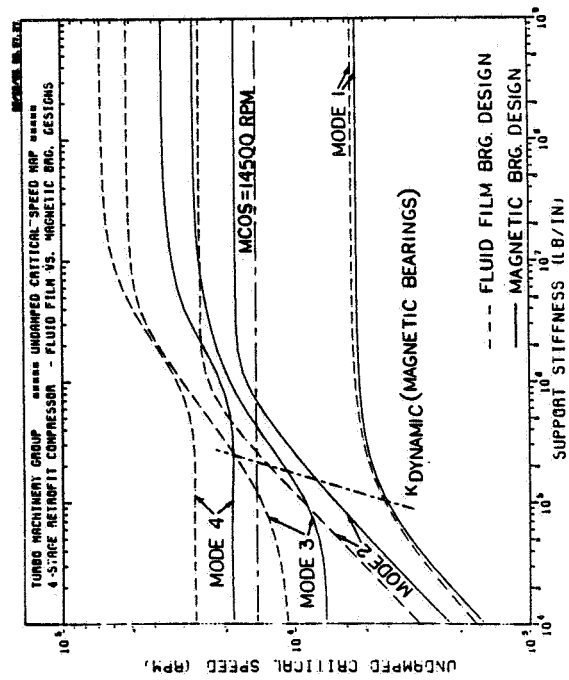


FIGURE 11

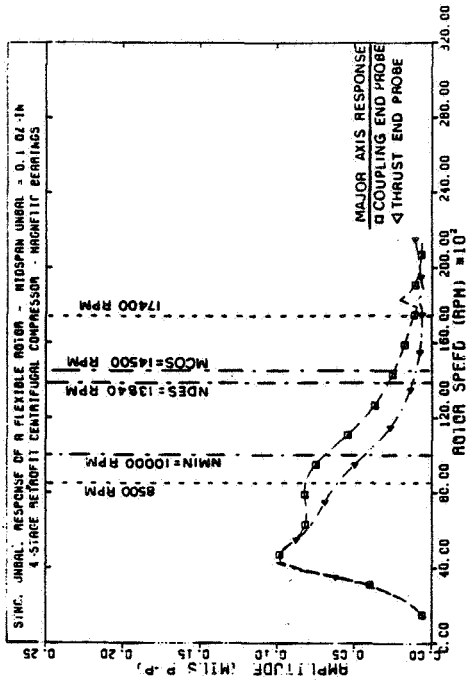


FIGURE 14

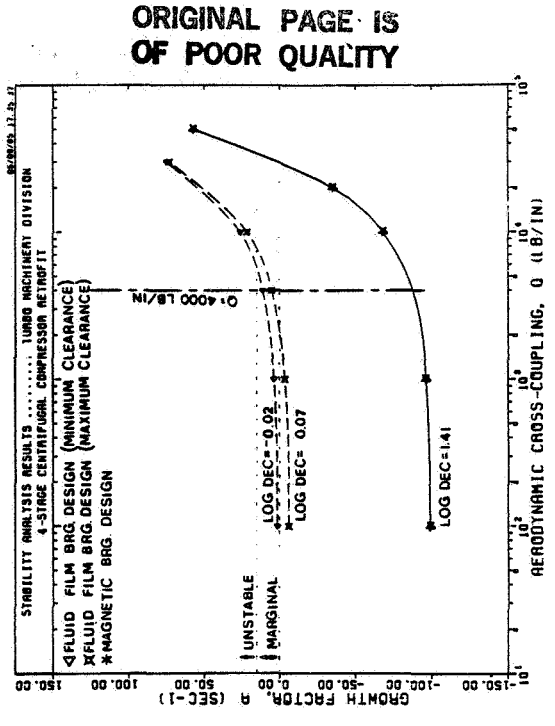


FIGURE 15

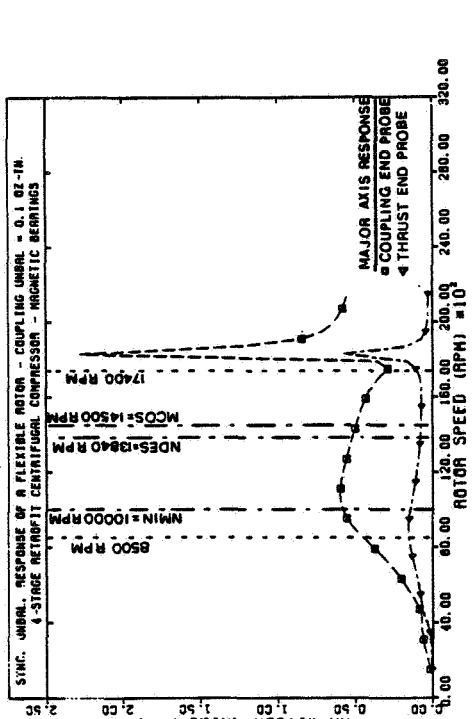


FIGURE 16

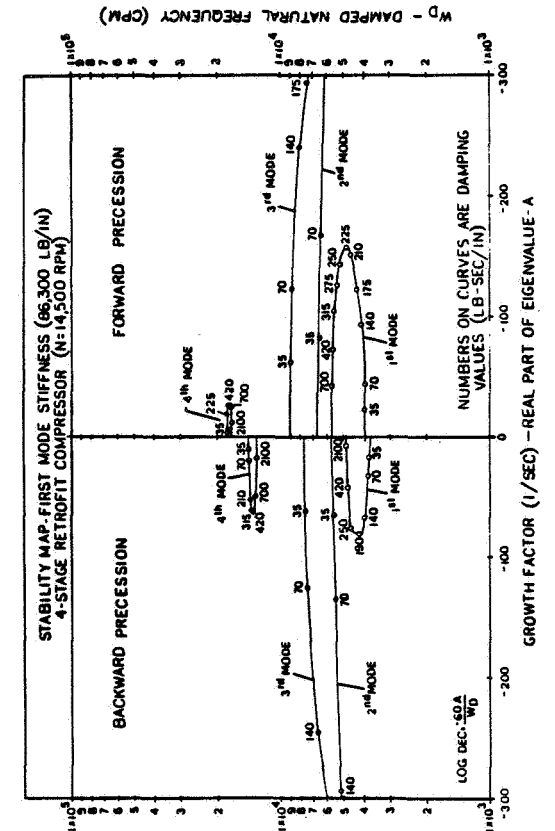


FIGURE 17

ORIGINAL PAGE IS
OF POOR QUALITY

ROTOR INTERNAL FRICTION INSTABILITY

Donald E. Bently and Agnes Muszynska
Bently Rotor Dynamics Research Corporation
Minden, Nevada 89423

Two aspects of internal friction affecting stability of rotating machines are discussed in this paper. The first role of internal friction consists of decreasing the level of effective damping during rotor subsynchronous and backward precessional vibrations caused by some other instability mechanisms. The second role of internal friction consists of creating rotor instability, i.e., causing self-excited subsynchronous vibrations. Experimental test results document both of these aspects.

1. INTRODUCTION

In rotating machines, damping effects are conventionally split into two categories: external and internal damping. The term "external" refers to the stationary elements and rotor environment, as they are "external" to the rotor. External damping is related to energy dissipation due to friction occurring between stationary and rotating elements, and/or fluid dynamic resistance in the rotor environment (mostly in fluid-lubricated bearings). External damping is also supplied by material damping of supports. External damping forces depend on the rotor absolute velocity of vibration, and their effect on the rotor vibration is usually welcome -- they provide stabilizing factors.

The term "internal" refers to the rotating elements, including the rotor itself. The same physical phenomena characterize internal and external damping. Internal damping forces are due to material damping in rotating and vibrating elements (mostly shafts) and friction between rotating parts (such as joint couplings and shrink-fitted disks on shafts). As internal damping occurs in the elements involved in rotating motion, the internal damping forces depend on relative velocity, i.e., on the difference between the absolute vibration velocity and the rotative speed. Thus the relative velocity may be "positive" (following absolute velocity when rotative speed is low) or "negative" (opposing absolute velocity when rotative speed is high). The corresponding internal damping forces can, therefore, act as a stabilizing (adding to the external damping to increase the total effective damping in the system) or a destabilizing factor (subtracting from the external damping to decrease the total effective damping of the system).

The term "damping" is traditionally related to the stabilizing effects created by the irreversible conversion of kinetic energy to heat. Being physically related to the same mechanism, rotor internal damping plays an additional role in rotating machines -- it opposes the external damping and actually transfers the rotational energy into vibrations. That is why the term "damping" does not fit well in this situation; by contrast, the term "internal friction" does not introduce ambiguity concerning stabilization.

Internal friction has been recognized as a cause of unstable rotor motion for more than 50 years [1-7]. Since the first description of internal friction-related in-

stability, many other rotor destabilizing factors have been identified, such as rub or fluid dynamic effects in fluid-flow machines and/or bearings and seals. The latter effects are much stronger than the internal friction effects and very often observed in the performance of rotating machines. They result in subsynchronous vibrations (rotative speed higher than vibrational frequency). Internal friction is now very seldom identified as a main cause of rotor unstable motion. However, internal friction plays a negative role by reducing the system-effective damping for forward subsynchronous and backward vibrations caused by other destabilizing factors.

In this paper two aspects of rotor internal friction are discussed: the first, a damping-reducing effect and the second, a cause of instability and self-excited vibrations. The experimental test results document both aspects.

2. ROTOR MODEL WITH INTERNAL FRICTION

To simplify the considerations, a symmetric rotor will be discussed. Dynamic behavior of a rotor in its lateral mode of vibrations is usually represented by a set of linear ordinary differential equations. For each mode, the set of equations reduces to two, which for a symmetric rotor can be presented in the form of one complex variable equation [8]:

$$M\ddot{z} + D\dot{z} + Kz + \frac{F(\dot{z} - j\omega z)}{|\Omega - \omega|} = 0, \quad z(t) = x(t) + jy(t), \quad \Omega \neq \omega, \quad j = \sqrt{-1} \quad (1)$$

where x, y are rotor horizontal and vertical deflections correspondingly, they describe the rotor precessional motion. M is the rotor mass; D is the external viscous damping coefficient; K is the rotor stiffness, including the shaft and pedestal stiffness. The rotor parameters M, D, K are generalized parameters corresponding to each separate mode; ω is rotative speed. The equation (1) may, in particular, describe rotor at its first mode. Eq.(1) contains frequency Ω of the resulting precessional motion, unknown a priori; $|\Omega - \omega|$ is the value of the shaft actual bending frequency. It has been introduced to the rotor model (1) following the way by which hysteretic damping is usually included in models of mechanical systems: a viscous damping coefficient is replaced by a product $K\eta/\Omega^*$, where K is stiffness coefficient, η is loss factor, and Ω^* represents the frequency of elastic element deformation. In the case of rotating shaft, the frequency of deformation is equal to a difference between rotative speed and frequency of precession. Note that for forward low frequency precessions, the frequency of shaft deformation is lower than rotative frequency. For backward precessions, the frequency of shaft deformation is a sum of rotative speed and frequency of precession. For circular synchronous precession ($\Omega = \omega$), the shaft is "frozen" into a fixed bow shape, so that internal friction does not act.

In Eq.(1) F (assumed positive) is internal friction function. For shaft material hysteretic damping F is constant and equal to $K\eta$. For the synchronous precession $F=0$. Generally, however, F can be a nonlinear function of z and \dot{z} [4, 6, 9].

For $F = \text{const}$ and Ω supposed constant, substituting $z = z_r e^{st}$, the eigenvalue problem of (1) yields four eigenvalues (satisfying the degrees of freedom of eq. (11))*:

$$s = -\delta \pm (1/\sqrt{2})[\sqrt{\delta^2 - K/M + \sqrt{\Delta}} \pm j\sqrt{K/M - \delta^2 + \sqrt{\Delta}}] \quad (2)$$

where

$$\delta = (D + F/|\Omega - \omega|)/(2M), \quad \Delta = (\delta^2 - K/M)^2 + F^2\omega^2/[M^2(\Omega - \omega)^2]$$

The real parts of (2) are non-positive, i.e., the system (1) is stable when $F^2\omega^2 M/K \leq (D|\Omega - \omega| + F)^2$ (3)

which for $\omega > 0$ yields the following conditions:

$$\begin{aligned} \text{For } \omega^2 < K/M & \text{ the rotor pure rotational motion is stable.} \\ \text{For } \omega^2 > K/M & \text{ it is stable only if } |F| \leq D|\Omega - \omega|/[w/\sqrt{K/M} - 1] \end{aligned} \quad (4)$$

At a threshold of stability, i.e., when $|F| = D|\Omega - \omega|/[w/\sqrt{K/M} - 1]$ the eigenvalues reduce to

$$s = \pm j\sqrt{K/M} \quad (5)$$

The rotor motion is purely periodic with the natural frequency determined by stiffness and mass (for the stable motion below the threshold of stability, the frequency is slightly lower than $\sqrt{K/M}$, due to damping).

If the stability condition is not satisfied and F exceeds the limits (4), then rotor pure rotational motion is unstable. The linear model (1) is not adequate anymore, as for high lateral deflections nonlinear factors become significant. Nonlinear factors eventually lead to a limit cycle of self-excited vibrations. The latter usually occur with the lowest natural frequency determined by the linear model, as the nonlinearities have very minor influence on frequency. With high amount of probability, the frequency Ω can be, therefore, equal to the rotor first natural frequency:

$$\Omega = \pm \sqrt{K_1/M_1} \quad (6)$$

*Solving the quadratic in s gives

$$s = -\left(\frac{D + \phi}{2M}\right) \pm \sqrt{\left(\frac{D + \phi}{2M}\right)^2 - \frac{K}{M} Fj \frac{\phi\omega}{M}}$$

Expanding $\sqrt{a + jb} = c + jd$ and solving for (c,d) gives

$$\pm \sqrt{a \pm jb} = \pm \frac{1}{\sqrt{2}} \left[\sqrt{a + \sqrt{a^2 + b^2}} \pm j \sqrt{-a + \sqrt{a^2 + b^2}} \right]$$

Substituting

$$a \equiv \left(\frac{D + \phi}{2M}\right)^2 - \frac{K}{M} \quad \text{and} \quad b \equiv \frac{\phi\omega}{M}$$

gives four roots:

$$s = -\left(\frac{D + \phi}{2M}\right) \pm \frac{1}{\sqrt{2}} \left[\sqrt{a + \sqrt{a^2 + b^2}} \pm j \sqrt{-a + \sqrt{a^2 + b^2}} \right]$$

where the index "1" refers to the first bending mode. If the model (1) describes the first mode, the stability condition (4) reduces to

$$|F| < D\sqrt{K_1/M_1} \equiv 2K_1\zeta_1 \quad (7)$$

where ζ_1 is the damping factor of the first mode. For the hysteretic damping, $F = K_1\eta_1$ and the inequality (7) yields

$$\eta_1 \leq 2\zeta_1 \quad (8)$$

i.e., for stability the shaft loss factor has to be lower than the double of external damping factor.

The modal approach to the rotor modelization permits evaluation of the stability conditions for several modes. For example, the inequality (4) for the i -th mode, (index "i") is:

$$|F| \leq D_i |\sqrt{K_1/M_1} - \omega| / [\omega/\sqrt{K_i/M_i} - 1] \quad (9)$$

Figure 1 illustrates the condition in which the same amount of internal friction may cause the first mode to be stable and the third mode unstable. This condition takes place when the modal damping ratio is sufficiently high, $D_1/D_3 > \sqrt{K_3/M_3}/\sqrt{K_1/M_1}$ and when the rotative speed exceeds a specific value, i.e.:

$$\omega > \frac{D_1/D_3 - 1}{D_1\sqrt{M_3/K_3}/D_3 - \sqrt{M_1/K_1}} \quad (10)$$

3. ROTOR EFFECTIVE DAMPING REDUCTION DUE TO INTERNAL FRICTION

Assume that the rotor performs steady nonsynchronous precessional, self-excited vibration with frequency Ω . This vibration occurs due to any instability mechanism (for instance, it may be oil whip). It means that the rotor motion can be presented in the form

$$z = Ae^{j\Omega t} \quad (11)$$

where A is an amplitude of the self-excited vibrations. Introducing (11) into (1) gives

$$-M\Omega^2 + Dj\Omega + K + F(\Omega - \omega)/|\Omega - \omega| = 0$$

The real part of this expression yields the frequency. The imaginary part relates to the system damping. The external damping term, $D\Omega$, is now completed by the term expressing internal friction:

$$D\Omega \rightarrow D\Omega + F(\Omega - \omega)/|\Omega - \omega|$$

or

$$D \rightarrow \begin{cases} D + F/\Omega & \text{for } \omega < \Omega \text{ (supersynchronous precession)} \\ D - F/\Omega & \text{for } \omega > \Omega \text{ (subsynchronous and backward precession)} \end{cases} \quad (12)$$

For supersynchronous precession internal friction adds to external damping and increases its level. For subsynchronous and backward precession, the internal friction reduces the level of "positive" stabilizing damping in the rotor system by the amount F/Ω . Taking into account that $\Omega = \sqrt{K/M}$, for subsynchronous precession the rotor effective damping factor decreases by the following amount:

$$\xi \rightarrow \xi - F/(2K) \quad (13)$$

It also means that the Amplification Factor Q increases:

$$Q \rightarrow Q/(1-FQ/K) \quad (14)$$

If, for instance, the Synchronous Amplification Factor is 5 and internal friction is due to shaft material hysteretic damping with loss factor $\eta = 0.06$ ($F=K\eta$), then the Subsynchronous Amplification Factor increases to 7.14 (the Supersynchronous Amplification Factor decreases to 3.85).

Note that the decrease of the "positive" external damping for rotor subsynchronous vibrations does not depend on the form of the function F (constant or displacement dependent).

In practical observations of rotating machine dynamic behavior, it has very often been noticed that subsynchronous vibrations are characterized by much higher amplitudes than any super-synchronous vibrations. There are many different causes of subharmonic vibrations in rotating machines. In each case, however, the role of internal friction opposing and decreasing the level of external, stabilizing damping is very important. Although not a primary cause of instability, internal friction often promotes subsynchronous vibrations and causes an increase of amplitudes. Figures 2, 3, and 4 illustrate dynamic responses of some unstable rotating machines. The self-excited, subsynchronous vibration amplitudes are much higher than amplitudes of synchronous and supersynchronous vibrations. More examples are given in [8].

The rotor model considered in this paper is symmetric; therefore, the synchronous precession is expected to be circular. In the case of circular synchronous precession at constant rotative speed, the bent shaft precesses "frozen" and is not a subject of periodic deformation. The internal friction does not act. The regular circular synchronous precession of real rotors very seldom occurs, however; usually nonsymmetry in the rotor and/or supporting system results in the elliptical synchronous precession. In this case, the bent shaft is not "frozen," but deforms with the frequency two times higher than the rotative speed. The internal friction then brings a "positive" effect: it adds to the external damping.

4. SELF-EXCITED VIBRATIONS DUE TO INTERNAL FRICTION

If in the equation (1), F is given in the form of a nonlinear function of the rotor radial displacement $|z|$, velocity of the radial displacement $d|z|/dt$ and relative angular velocity $\omega - \dot{\theta}$, [4,6] where

$$\theta(t) = \arctan [y(t)/x(t)], \quad |z| = \sqrt{x^2+y^2} \quad (15)$$

i.e., $F = F(|z|, d|z|/dt, \omega - \dot{\theta})$ then the rotor model (1) allows for the following particular solution

$$z(t) = B e^{j\Omega t} \quad (16)$$

where B and Ω are constant amplitude and frequency of the circular precessional self-excited vibrations correspondingly. They can be found from the following algebraic relation yielded by (1) and (16):

$$-M\Omega^2 + D j\Omega + K + jF(B, 0, \omega - \Omega)(\Omega - \omega)/|\Omega - \omega| = 0 \quad (17)$$

The nonlinear differential function F becomes nonlinear algebraic function.

Bolotin [9] quotes several forms of internal friction function F ; for instance, for a shrink-fitted disk on the shaft, the internal friction nonlinear function has the following form:

$$F(|z|, d|z|/dt, \omega - \dot{\theta}) = \frac{C_1 |z|^n}{C_2 + (\omega - \dot{\theta})^m} \quad (18)$$

where $C_1 > 0$, $C_2 > 0$, n , m are specific constant numbers. In case of the function (18) equation (17) for the first mode yields

$$\Omega = \sqrt{K_1/M_1}, \quad B = \{ [C_2 + (\omega - \sqrt{K_1/M_1})^m] D \sqrt{K_1/M_1} / C_1 \}^{1/n} \quad (19)$$

Since C_1 and C_2 are positive, the solution (16) with amplitude (19) exists for $\omega > \sqrt{K_1/M_1}$ only. This means that the self-excited vibrations (16) exist for sufficiently high rotative speed.

5. INTERNAL FRICTION EXPERIMENT

During balancing of the three-disk rotor rig (Fig. 5), an appearance of self-excited vibrations at the rotative speed above third balance resonance have been noticed (Fig. 6). The frequency of these self-excited vibrations exactly equals first natural frequency. The self-excited vibrations disappear for higher rotative speed. It was noted that when balancing weights, which affect the balance state for the third mode, were removed, causing a significant increase of the amplitude of the synchronous vibration at the third mode, the self-excited vibrations nearly disappeared (the amplitude decreased from 1.8 to 0.4 mils p/p, compare Figs. 6 and 8). It appeared that the energy from self-excited vibrations was transferred to the synchronous vibrations. Higher rotor deflection due to unbalance evidently caused some substantial modifications in the self-excitation mechanism.

Since there was no other obvious reason for the self-excitation, internal friction (of the shaft material and disk/shaft joints) was blamed for the appearance of these self-excited vibrations. To prove this supposition, an increase of the rotor internal friction was attempted. Half of the shaft was covered with a 4-mil-thick layer of damping material, commonly used for vibration control (acrylic adhesive ISD-112, 3M Company). Applied to the rotating shaft, the damping material increases the internal friction and magnifies the self-excitation effect. The expected result was confirmed: the amplitude of the self-excited vibrations increased from 0.4 to 0.7 mils p/p (compare Figs. 8 and 9).

The self-excited vibrations disappeared completely when the disks were eventually welded to the shaft, and the damping tape was removed.

The question of why the self-excited vibrations occur at the rotative speed ~ 7150 rpm and disappear in the higher range of speeds has not been answered. Nor was the internal damping function identified. The analysis presented in Section 2 gives, however, some indications that a nonlinear internal damping function may cause rotor instability in a limited range of rotative speeds. Figure 10 presents the stability chart for three modes.

6. CONCLUDING REMARKS

This paper discusses two important aspects of internal friction in rotating ma-

chines. Firstly, the internal friction in rotating elements causes a decrease of the amount of effective damping in the rotor system. This effective damping reduction occurs during rotor subsynchronous and backward precessional motion, which may be caused by any instability/self-excitation mechanism (such as rub or fluid flow dynamic forces). While usually not a primary cause of instability, internal friction promotes unstable motion and affects the value of self-excited vibration amplitudes.

Secondly, the internal friction occasionally is a major cause of rotor self-excited vibrations due to incorrect shrink fits, loosening of shrink fits by differential thermal growth, or by mechanical fatigue. Known for more than 50 years as a contributor to rotor instability, the internal friction analytical model has not, however, yet been adequately identified.

This paper documents experimentally these two aspects of internal friction in rotating machines and gives a qualitative description of the dynamic phenomena associated with rotor internal friction.

SYMBOLS

A,B	-- Amplitudes of self-excited vibrations	s	-- Eigenvalue
D	-- External damping coefficient	$z=x+jy$	-- Rotor radial deflection (x-horizontal, y-vertical)
F	-- Internal friction function	ξ	-- External damping factor
$j = \sqrt{-1}$		η	-- Loss factor
K,M	-- Rotor generalized (modal) stiffness and mass coefficients	θ	-- Angle of precessional motion
Q	-- Amplification Factor	ω	-- Rotative speed
		Ω	-- Angular speed of precession

REFERENCES

1. Newkirk, B. L.: Shaft Whipping. Gen. Elect. Rev., 27, 1924.
2. Kimball, A. L.: Internal Friction Theory of Shaft Whirling. Gen. Elect. Rev., 27, 1924.
3. Kimball, A. L.: Internal Friction as a Cause of Shaft Whirling. Phil., Mag., 49, 1925.
4. Tondl, A.: Some Problems of Rotor Dynamics. Prague, 1965.
5. Loewy, R. G., Piarulli, V. J.: Dynamics of Rotating Shafts. The Shock and Vibration Information Center, SVM-4, 1969.
6. Muszynska, A.: On Rotor Dynamics (Survey). Nonlinear Vibration Problems, 13, Warsaw 1972.
7. Bently, D.E.: The Re-excitation of Balance Resonance Regions by Internal Friction: Kimball Revised, Bently Nevada Corp. BNC-19, 1982.
8. Muszynska, A.: Rotor Instability. Senior Mechanical Engineering Seminar, Bently Nevada Corporation, Carson City, Nevada, June 1984.
9. Bolotin, V. V.: The Dynamic Stability of Elastic Systems (translated from Russian). Holden-Day Inc., San Francisco, 1964.
10. Wachel, J. C.: Rotordynamic Instability Field Problems. Rotordynamic Instability Problems in High-Performance Turbomachinery -- 1982, Proceedings of a Workshop Held at Texas A&M University, College Station, Texas, NASA CP 2250, May 1982.
11. Bonciani, L., Ferrara, P. L., Timori, A.: Aero-induced Vibrations in Centrifugal Compressors. Rotordynamic Instability Problems in High-Performance Turboma-

chinery, Proceedings of a Workshop held at Texas A&M University, College Station, Texas, NASA CP 2133, May 1980.

12. Muszynska, A.: Instability of the Electric Machine Rotors Caused by Irregularity of Electromagnetic Field. Bently Nevada Corporation, 1983.

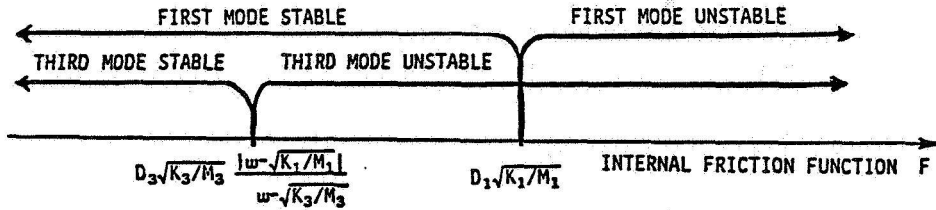


Figure 1. - Regions of stability for rotor first and third modes.

ORIGINAL PAGE IS
OF POOR QUALITY

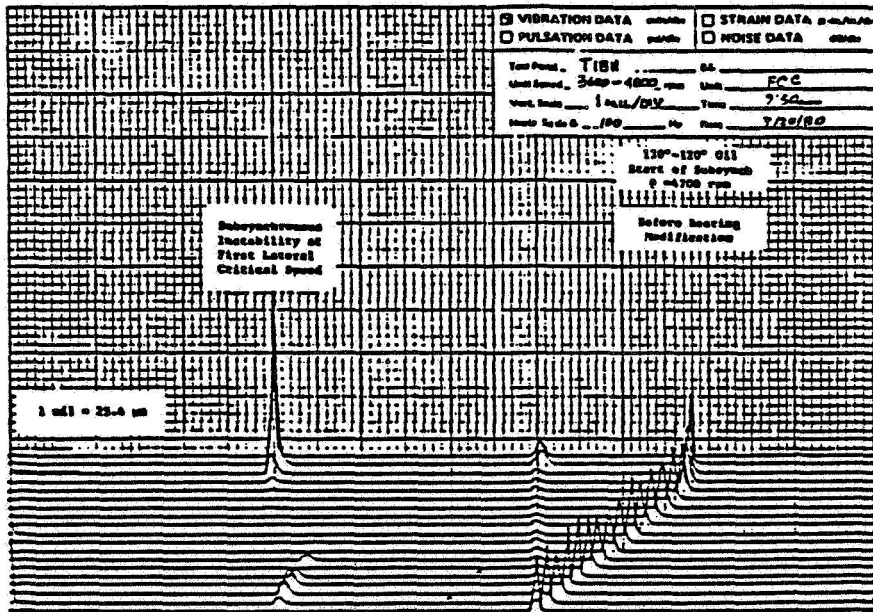


Figure 2. - Cascade spectrum of steam turbine vibrational response, indicating high subsynchronous vibrations. Data courtesy of J.C. Wachel [10].

ORIGINAL PAGE IS
OF POOR QUALITY

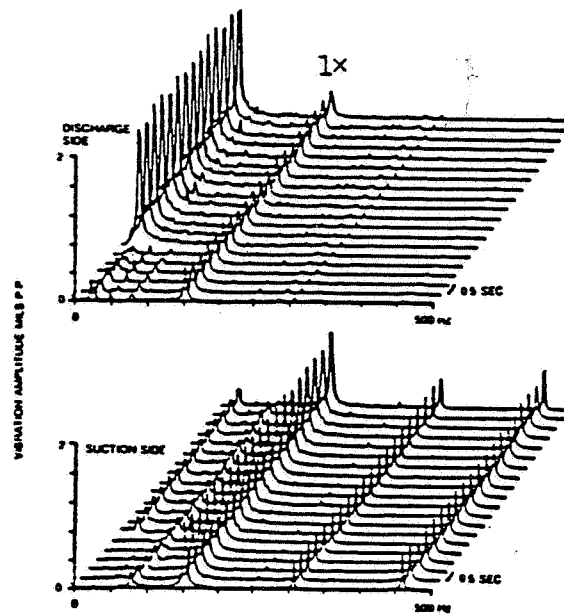


Figure 3. - Time histories of six-stage compressor at 9220 rpm. Subsynchronous vibrations due to destabilizing dynamic forces generated on last stage. Data courtesy of P.L. Ferrara [11].

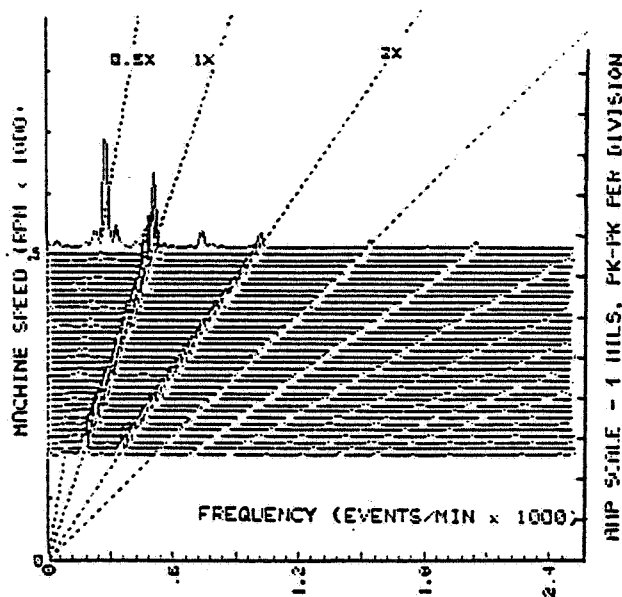


Figure 4. - Cascade plot of electric motor response during shutdown. At running speed of 510 rpm (below first balance resonance), high half-speed vibrations present due to electromagnetic field unbalance [12].

1. BASE PLATE
2. MOTOR
3. FLEXIBLE COUPLING
4. RIGID BEARING
5. KEYPHASOR DISK
6. X-Y NONCONTACTING PROBES
7. STEEL DISKS
8. STEEL SHAFT

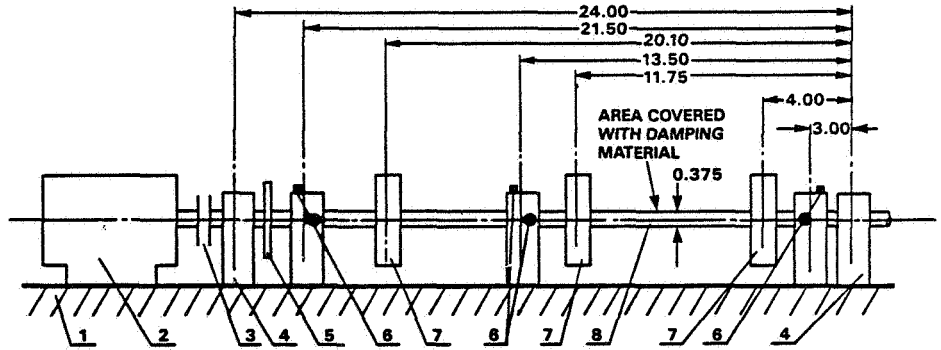


Figure 5. - Three-disk rotor rigidly supported. Disks attached to rotor by radial screws. (Dimensions are in inches.)

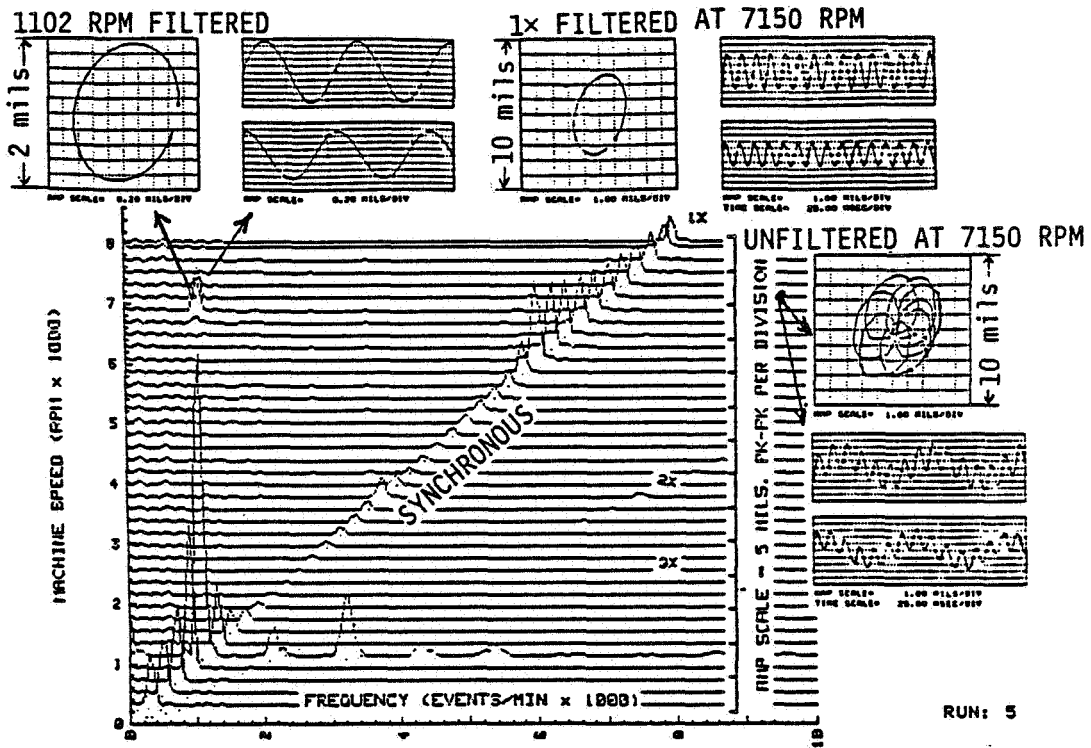


Figure 6. - Startup response of three-disk rotor measured at midspan position. Cascade spectrum and orbits indicate existence of subsynchronous self-excited vibrations.

ORIGINAL PAGE IS
OF POOR QUALITY

ORIGINAL PAGE IS
OF POOR QUALITY

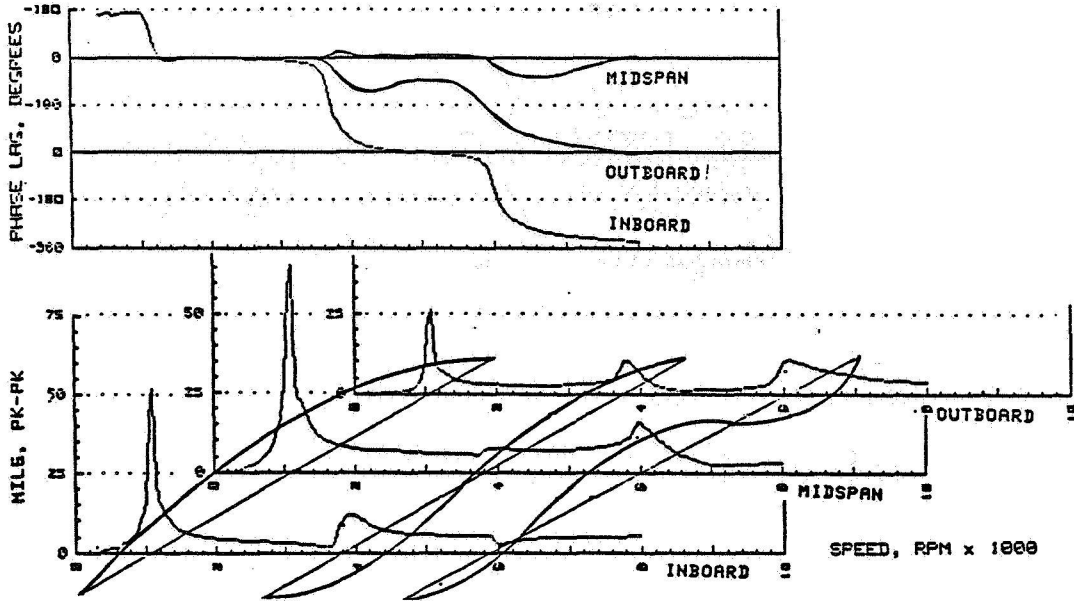


Figure 7. - Bode plots of 1X (synchronous) filtered rotor response and rotor mode shapes. Original state of unbalance.

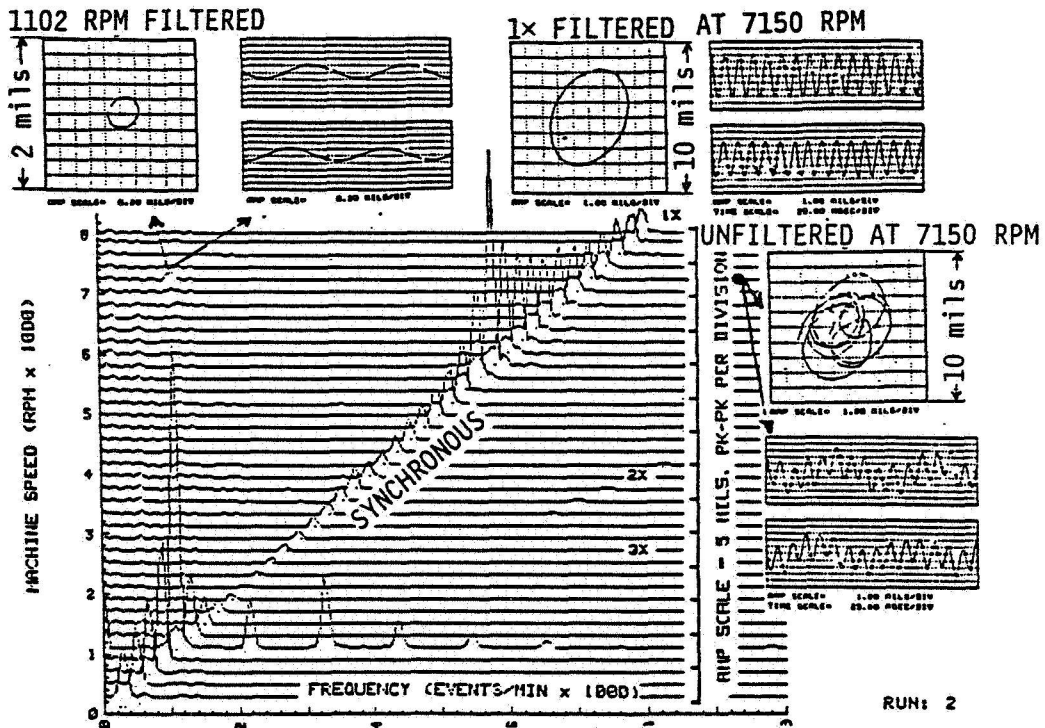


Figure 8. - Cascade spectrum and orbits of unbalanced shaft: Decrease of subsynchronous self-excited vibrations. Data from midspan position.

ORIGINAL PAGE IS
OF POOR QUALITY

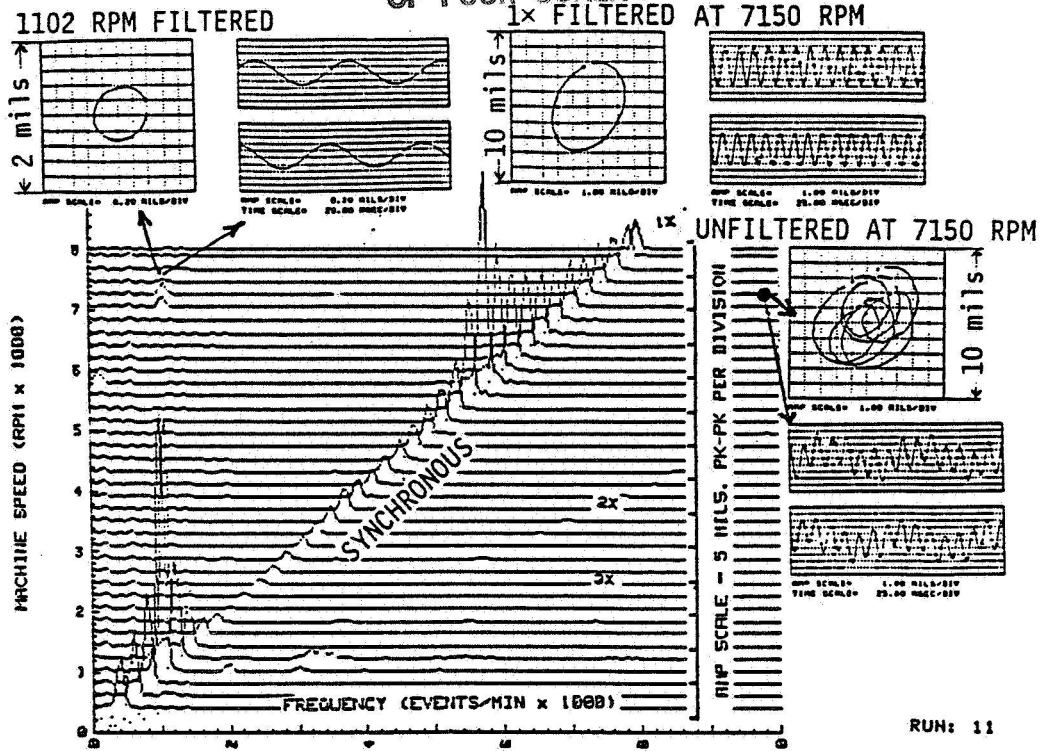


Figure 9. - Cascade spectrum and orbits of unbalanced rotor measured at midspan position. Shaft covered with damping material. Increase of subsynchronous self-excited vibrations.

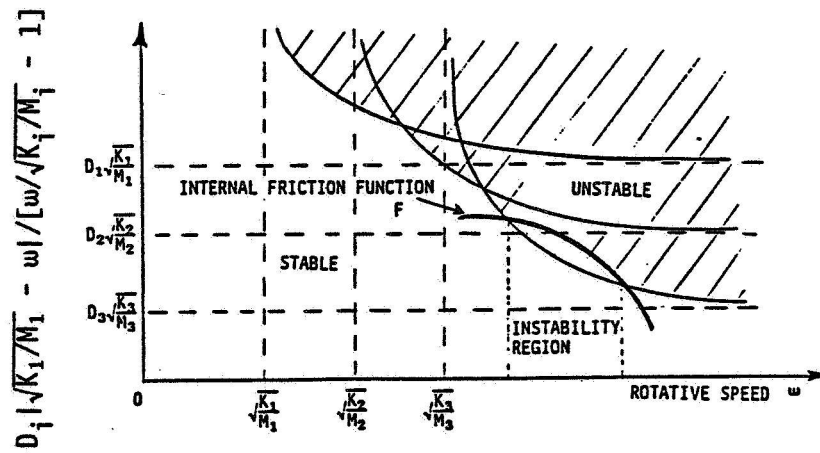


Figure 10. - Rotor stability chart for three modes (inequality (9)).

TOPPING TURBINE (103-JAT) ROTOR INSTABILITY IN 1150-STPD KELLOGG AMMONIA PLANTS

Richard Thomas
Agrico Chemical Company
Donaldsonville, Louisiana 70346

Agrico Chemical Company operates three nominal 1043 MeTPD (1150 STPD) Kellogg Ammonia Plants in the U.S.. In the Kellogg Ammonia Plant, the synthesis gas compressor train consists of two DeLaval steam turbines in tandem, one back pressure and one condensing, driving two Dresser-Clark barrel type centrifugal compressors. The back pressure or topping turbine operates at 10,343 kPa (1500 psig) inlet / 3792 kPa (550 psig) exhaust steam conditions while the condensing turbine operates at 3792 kPa (550 psig) inlet / 14 kPa (4" Hg) absolute exhaust steam conditions. The normal operating speed range is 10,400 - 10,700 rpm with a combined driver output of 20,507 kW (27,500 hp).

In two of Agrico's three plants, instabilities in the rotor / bearing system have been an ongoing problem. On occasion plant rates, i.e. machine speed, have been restricted in order to limit the exhaust end shaft relative vibration on the 103-JAT to a maximum value of 89 μ m (0.0035 in) peak to peak.

The purpose of this paper is to acquaint the reader with Agrico's experiences with exhaust end vibration and rotor instabilities on the 103-JAT topping turbine. The final conclusions arrived at in this paper were based on: 1) field acquired data both during steady state and transient conditions, 2) computer modeling of the rotor / bearing system, and 3) vibration data taken from a "control rotor" during a series of test runs in a high speed balancing machine from 0 to 110% of operating speed.

INTRODUCTION

A cross-sectional view of the 103-JAT is shown in Figure 1. The two stage rotor weighs 3585 N (806 lbf) and consists of bucketed wheels that are integral to the shaft. The steam end bearing journal diameter is 126.75 mm (4.990 in) while the exhaust end bearing journal has a diameter of 101.45 mm (3.994 in). The bearing span and shaft overall lengths are 137.16 cm (54.5 in) and 196.22 cm (77.25 in) respectively.

The turbine is coupled at both ends. The steam end is coupled to the condensing turbine via a Koppers size 2- $\frac{1}{2}$ / 3 class ACCS / RM gear coupling. The half weight of the coupling assembly mounted on the steam end of the 103-JAT is 115.65 N (26 lbf). At the exhaust end, the 103-JAT is coupled to the low pressure compressor through a Koppers size 4 class ACCS / RM gear coupling with a coupling half weight of 341.16 N (925 lbf).

VIBRATION HISTORY

During the period from 1974 through 1979, exhaust end journal bearing inspections usually showed wiped pads in the lower half of the bearing with some evidence of pounding of the babbitt material noted. In addition, it was not uncommon to see evidence of damage to the babbitted bearing oil seal as well. A general opinion during this time was that the pads were being damaged during shutdown of the topping turbine. However, data taken during a shutdown and subsequent startup of the 103-JAT in January, 1979 showed that in reality the pads were being damaged during the constant acceleration of the syn gas machine from slow roll to minimum governor rpm.

Consequently, in early 1980 a modified startup procedure was implemented. The new startup procedure called for a step acceleration of the 103-JAT. The 103-JAT would be accelerated from: slow roll to 2000 rpm, 2000 to 4000 rpm, 4000 to 6000 rpm, and finally 6000 to 8000 rpm. After each 2000 rpm increment a mandatory five minute minimum hold was utilized in order to allow the bearing pad temperatures to stabilize. A maximum allowable pad temperature of 120°C (250°F) was established with a mandatory shutdown required at 130°C (265°F). By bringing the turbine up to minimum governor in this manner, it was hoped that the effects of temperature and alignment changes from slow roll to operating speed would be minimized. This procedure has successfully been utilized in all three of Agrico's Kellogg Ammonia Plants since 1980. During startup with the modified procedure, the maximum pad temperatures are approximately 93°C (200°F) with the shaft experiencing a maximum excursion of 50 to 76 µm (0.002 to 0.003 in) outside of the bearing set clearance.

Typical exhaust end vertical and horizontal¹ spectra from the shaft proximity probes are shown in Figures 3 and 4. Strong $\frac{1}{2}x$ and $1x$ components, 24.4 µm (0.00096 in) and 63.5 µm (0.0025 in) respectively, are readily apparent with other minor multiples of $\frac{1}{2}x$ rpm also noted. During the period from 1980 to the present, some important points have been noted:

1. The $1x$ component begins to rapidly climb at speeds in excess of 10,200 rpm.
2. The $\frac{1}{2}x$ component tends to reduce in magnitude as more load is shifted to the 103-JAT from the condensing turbine.
3. The $\frac{1}{2}x$ component tends to increase in magnitude with increasing bearing clearance.
4. If the bearing clearance exceeds 0.203 mm (0.008 in), load shifting from the condensing turbine to the 103-JAT has little or no effect. However, removing load from the 103-JAT always made the $\frac{1}{2}x$ component increase in magnitude.
5. Within reasonable limits, imposed hot misalignment of the 103-JAT decreased the $\frac{1}{2}x$ component's magnitude.
6. The apparent translational balance resonance speed range is from approximately 5200 to 8000 rpm with the resonance peak at approximately 6800 rpm (figures 4 and 6).

¹Probe orientation on the 103-JAT is as follows: Facing the turbine from the steam end, with 0° coincidental with the positive x-axis on a Cartesian Coordinate System, and all angles measured in a CCW direction from 0°, vertical = 135°, horizontal = 45°.

7. The ends of the rotor are in phase (305° and 277° respectively) at the resonance amplitude at 6800 rpm (figures 5 and 7).
8. Between 8200 and 9200 rpm, the exhaust end suddenly goes out of phase with the steam end (figure 7).
9. Between 10,200 and 10,300 rpm the 1 x amplitude increases from $10.16\ \mu\text{m}$ (0.0004 in) to $38.1\ \mu\text{m}$ (0.0015 in) at the steam end and from $2.54\ \mu\text{m}$ (0.0001 in) to $25.40\ \mu\text{m}$ (0.001 in) at the exhaust end (figures 5 and 6). Also within this speed range, the $\frac{1}{2}$ x component suddenly appears at approximately $12.70\ \mu\text{m}$ (0.0005 in) at both ends of the rotor.
10. From 10,300 rpm to 10,560 rpm the exhaust end vibration increases to $23.88\ \mu\text{m}$ (0.00094 in) at $\frac{1}{2}$ x and $66.80\ \mu\text{m}$ (0.00263 in) at 1 x (figure 4).

ROTOR DYNAMICS ANALYSIS

The rotor / bearing system of the topping turbine was mathematically modeled as a series of lumped mass stations connected by elastic elements. Each mass station contains the mass and inertia properties for the discrete rotor segment that it represents. Included in the model, along with the mass station information, are the bearing support locations and the speed dependent properties of the oil film.¹

Figure 8 is a plot of the first three undamped critical speeds of the 103-JAT versus a nominal range of bearing stiffness values. Also plotted on this critical speed map are the bearing stiffness versus speed curves for the steam and exhaust ends. One can readily see that three out of the four principal stiffness curves intersect the third mode at the rotor speed of 10,500 rpm. Thus within the normal operating speed range, excitation of the third critical speed should be expected, especially in the horizontal plane. Tables 1 and 2 are a brief summarization of the data presented in figure 8.

So as not to readily excite the third mode within the normal operating speed range, the design of the bearings was modified. The main parameters of the redesign were:

1. The bearing stiffness would not be coincidental with the third mode at operating speed.
2. The bearing stiffness would be more nearly uniform between the steam and exhaust end bearings.
3. The bearing damping characteristics would be improved at operating speed.

The redesigned bearings were fabricated by Centritch Corporation and are designated internally by Agrico as the MOD-2 design. The MOD-2 bearing differs from the DeLaval standard bearings as listed in the following.

¹The computer modeling of the rotor was performed by Centritch Corporation of Houston, Texas.

STEAM END

	MOD-2	DeLaval
Pad Length	3.81 cm (1.50 in)	6.03 cm (2.373 in)
L/D	0.30	0.48
Preload	0.33	0.00
Orientation	Load Between Pads	Load On Pad
Adjustable Bearing Clearance	Yes	No
External Pressure Pad	Yes	No

EXHAUST END

	MOD-2	DeLaval
Pad Length	3.81 cm (1.50 in)	4.13 cm (1.625 in)
L/D	0.38	0.41
Preload	0.25	0.00
Orientation	Load Between Pad	Load On Pad
Adjustable Bearing Clearance	Yes	No
External Pressure Pad	Yes	No

The external pressure pads in the top half of both of the bearings were added in order to provide a secure fit between the bearings and turbine case during all phases of operation and thus reduce the possibility of generating a $\frac{1}{2}$ x vibration component.

The stiffness and damping coefficients for the MOD-2 bearing are summarized in Table 3 and 4 and depicted on the critical speed map as shown in figure 9. The principal stiffness curves all intersect the third mode in the 11,700 to 12,000 rpm range thus reducing the possibility of exciting this mode within the normal operating speed range of the turbine. Figures 10 through 12 depict the anticipated rotor mode shapes assuming an average support stiffness of 5.25×10^5 N/cm (3.00×10^5 lb_f/in).

CONTROL ROTOR TEST

A prototype version of the MOD-2 bearing was tested at DeLaval's repair shop in Houston, Texas. In order to duplicate as nearly as possible the actual rotor configuration, component balance coupling hubs were mounted on the control rotor. The control rotor was first run in the DeLaval bearings to establish a baseline (figure 13). The DeLaval bearings were replaced with the MOD-2 bearings and the control rotor was run for a second time (figure 14). Figures 15 and 16 compare the DeLaval and MOD-2 bearings on the same plot.

FIELD STARTUP

The MOD-2 bearings were installed in the 103-JAT topping turbine and field tested during the startup of the Ammonia Plant on May 15, 1985. Figures 17 and 18 are waterfall plots of the steam end vertical and horizontal probes. Figures 19 and 20 are waterfall plots of the exhaust end vertical and horizontal probes. In the 6000-6500 rpm range the additional harmonics in figure 18 and the frequency shift in figure 20 were caused by clipping of the input signal during the tape recording process.

The first observed critical speed occurred between 6200 and 6630 as summarized below:

STEAM END

Location	RPM	1 x (peak to peak)
61V (vertical)	6628	85.85 μm (0.00338 in)
63H (horizontal)	6628	95.25 μm (0.00375 in)

EXHAUST END

Location	RPM	1 x (peak to peak)
64V (vertical)	6224	73.15 μm (0.00288 in)
66H (horizontal)	6224	103.19 μm (0.00406 in)

A comparison of steady state data between the DeLaval and the MOD-2 bearings is listed below:

Location	DeLaval			MOD-2		
	rpm	$\frac{1}{2}$ x	1 x	rpm	$\frac{1}{2}$ x	1 x
61V	10,560	10.16 μm (0.00040 in)	15.24 μm (0.00060 in)	10,600	---	35.56 μm (0.0014 in)
63H	10,560	13.72 μm (0.00054 in)	32.51 μm (0.00128 in)	10,600	---	50.80 μm (0.0020 in)
64V	10,560	25.15 μm (0.00099 in)	59.18 μm (0.00233 in)	10,600	---	20.32 μm (0.0008 in)
66H	10,560	23.88 μm (0.00094 in)	66.80 μm (0.00263 in)	10,600	---	35.56 μm (0.0014 in)

CONCLUSIONS

The rotor dynamics study showed that the normal operating speed range was coincidental with the third undamped critical speed. Analysis of existing startup data supported the theory that the normal operating speed range falls within the domain of a resonance response region. In addition, analysis of startup and steady state data strongly suggested that the $\frac{1}{2}$ x mechanism was primarily due to loose bearings in the turbine case.

The MOD-2 bearings were offered as a possible solution to these two instability mechanisms. With the MOD-2 bearings in operation, the $\frac{1}{2}$ x instability is no longer present at either end of the turbine. At the same time, the overall exhaust end vibration levels have been reduced, on the average, by 68%, while the overall steam end vibration levels have remained approximately the same.

TABLE 1
ORIGINAL FIVE SHOE
TILT PAD BEARING COEFFICIENTS

STEAM END					
STIFFNESS (lb _f /in):	SPEED (RPM)				
	3719	6203	9869	10,500	12,374
K _{XX}	3.79x10 ⁶	4.81x10 ⁶	5.65x10 ⁶	5.71x10 ⁶	5.96x10 ⁶
K _{YY}	3.57x10 ⁵	2.78x10 ⁵	2.18x10 ⁵	2.11x10 ⁵	1.93x10 ⁵
DAMPING (lb _f -sec/in):					
C _{XX}	4.09x10 ²	3.87x10 ²	3.69x10 ²	3.68x10 ²	3.62x10 ²
C _{YY}	1.07x10 ³	6.98x10 ²	5.11x10 ²	5.01x10 ²	4.55x10 ²
EXHAUST END					
STIFFNESS (lb _f /in):	SPEED (RPM)				
	3246	6378	8513	10,500	11,112
K _{XX}	2.81x10 ⁶	4.34x10 ⁶	5.11x10 ⁶	5.68x10 ⁶	5.85x10 ⁶
K _{YY}	7.45x10 ⁵	5.48x10 ⁵	4.79x10 ⁵	4.33x10 ⁵	4.22x10 ⁵
DAMPING (lb _f -sec/in):					
C _{XX}	2.51x10 ²	2.34x10 ²	2.26x10 ²	2.21x10 ²	2.19x10 ²
C _{YY}	1.54x10 ³	7.87x10 ²	6.01x10 ²	5.02x10 ²	4.75x10 ²

TABLE 2
UNDAMPED CRITICAL SPEEDS
EXISTING TURBINE ROTOR
ORIGINAL BEARINGS

	HORIZONTAL PLANE	VERTICAL PLANE
FIRST CRITICAL	BETWEEN 940 AND 1200 RPM	BETWEEN 4500 AND 5600 RPM
SECOND CRITICAL	BETWEEN 1600 AND 2100 RPM	BETWEEN 6200 AND 7900 RPM
THIRD CRITICAL	9800 RPM	BETWEEN 10,000 AND 11,000 RPM

ORIGINAL PAGE IS
OF POOR QUALITY

TABLE 3
CENTRITECH MOD-2
TILT PAD BEARING COEFFICIENTS
STEAM END

STIFFNESS (lb _f /in):	SPEED (RPM)				
	3408	6289	7811	10,500	12,899
K _{XX}	2.87x10 ⁵	3.88x10 ⁵	4.12x10 ⁵	4.39x10 ⁵	4.91x10 ⁵
K _{YY}	4.50x10 ⁵	5.37x10 ⁵	5.37x10 ⁵	5.27x10 ⁵	5.78x10 ⁵
DAMPING (lb _f -sec/in):					
C _{XX}	8.35x10 ²	7.66x10 ²	7.06x10 ²	6.27x10 ²	5.70x10 ²
C _{YY}	10.60x10 ²	8.21x10 ²	8.21x10 ²	7.20x10 ²	6.71x10 ²

STIFFNESS (lb _f /in):	SPEED (RPM)				
	3353	5912	8928	10,500	11,349
K _{XX}	3.44x10 ⁵	3.16x10 ⁵	3.43x10 ⁵	4.71x10 ⁵	3.91x10 ⁵
K _{YY}	6.14x10 ⁵	5.10x10 ⁵	4.91x10 ⁵	6.13x10 ⁵	5.24x10 ⁵
DAMPING (lb _f -sec/in):					
C _{XX}	11.50x10 ²	8.48x10 ²	8.14x10 ²	7.59x10 ²	7.29x10 ²
C _{YY}	16.70x10 ²	10.80x10 ²	9.95x10 ²	8.85x10 ²	8.25x10 ²

TABLE 4
UNDAMPED CRITICAL SPEEDS
EXISTING TURBINE ROTOR
CENTRITECH MOD-2 BEARINGS

	HORIZONTAL PLANE	VERTICAL PLANE
FIRST CRITICAL	BETWEEN 4550 AND 4700 RPM	BETWEEN 5600 AND 5700 RPM
SECOND CRITICAL	BETWEEN 6700 AND 7600 RPM	BETWEEN 8200 AND 8400 RPM
THIRD CRITICAL	BETWEEN 11,700 AND 11,800 RPM	12,000 RPM

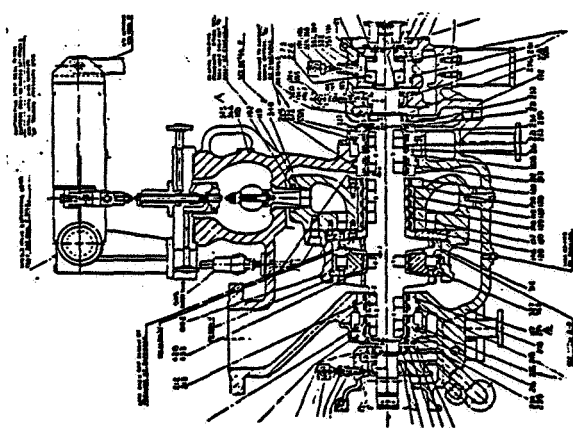


Figure 1

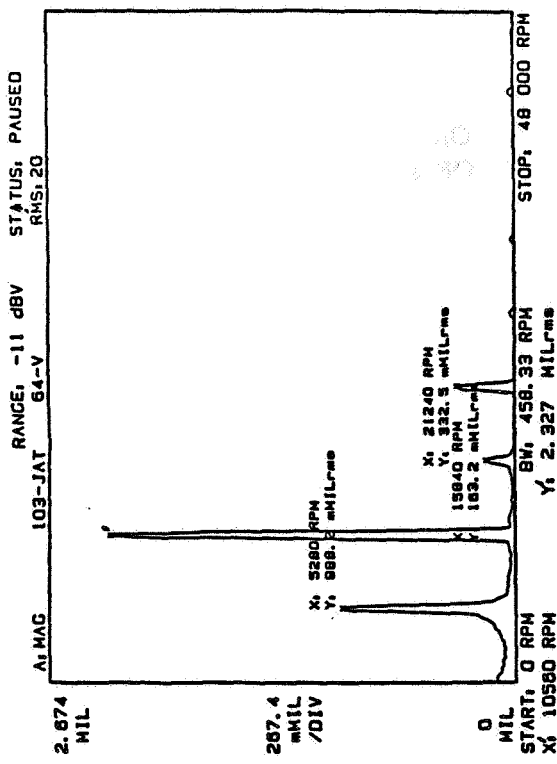


Figure 2

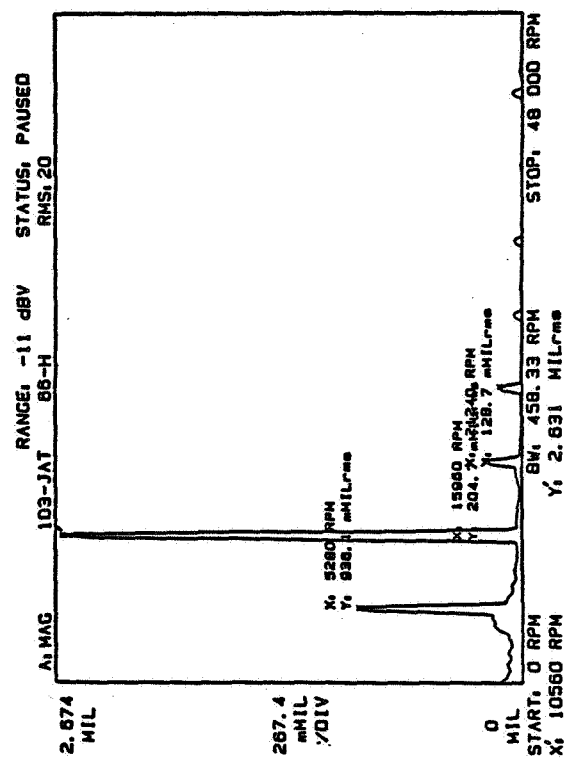


Figure 3

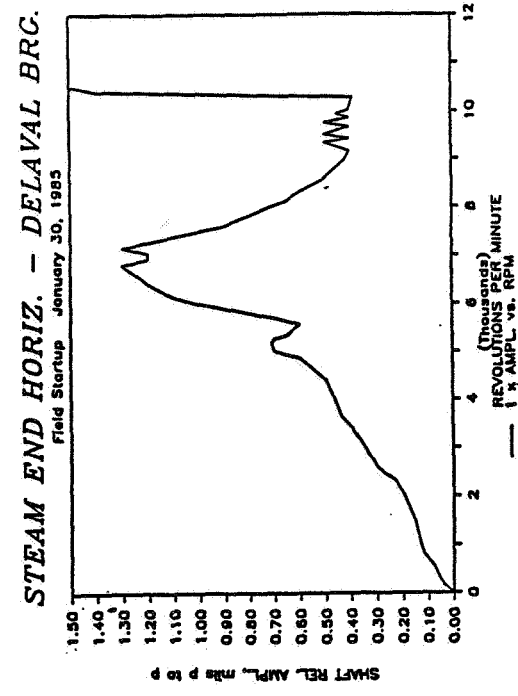


Figure 4

STEAM END HORIZ. - DELAVAL BRG.

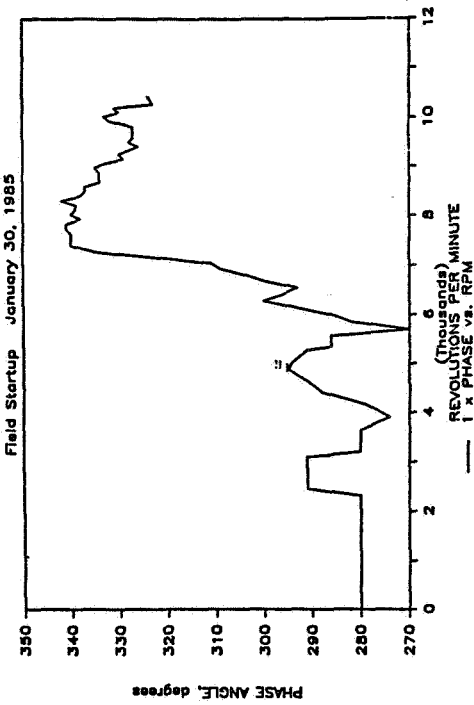
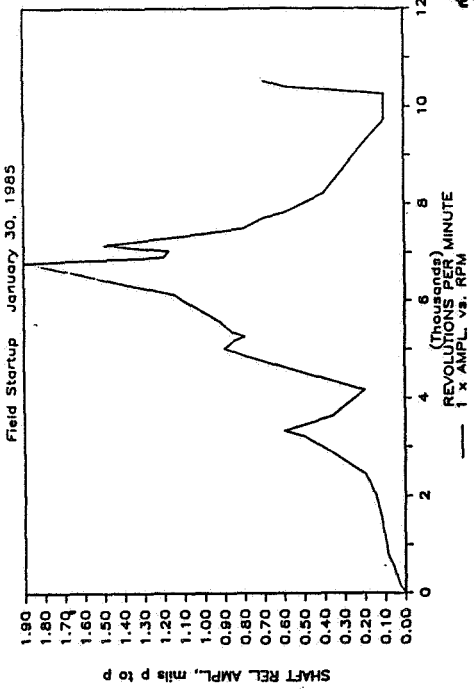


Figure 5

EXHAUST END HORIZ. - DELAVAL BRG.



ORIGINAL PAGE IS
OF POOR QUALITY

Figure 6

DE LAVAL 103 JAT STEAM TURBINE

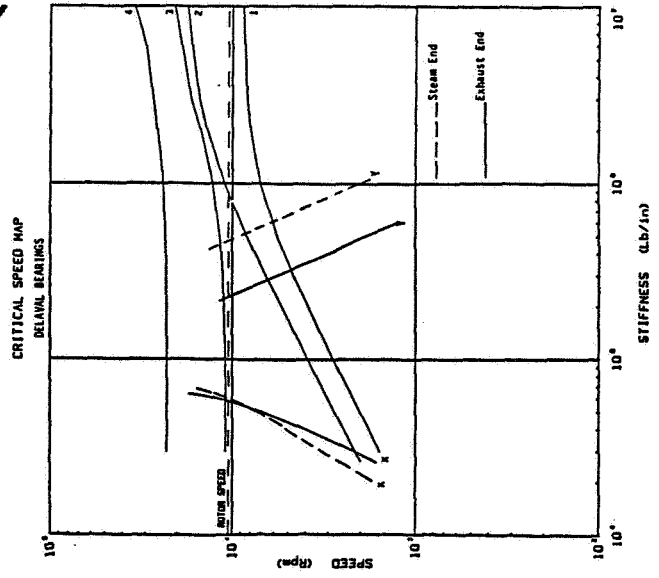


Figure 8

EXHAUST END HORIZ. - DELAVAL BRG.

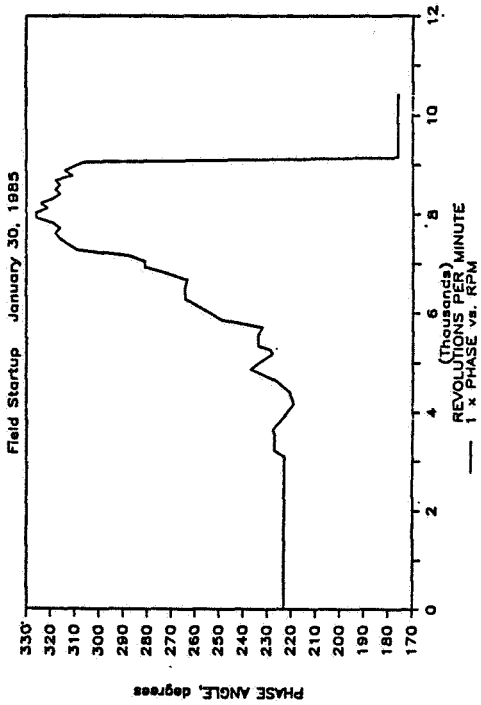


Figure 7

DE LAVAL 103 JAT STEAM TURBINE

CRITICAL SPEED MAP
CENTRITEC "MOD-2" BEARINGS

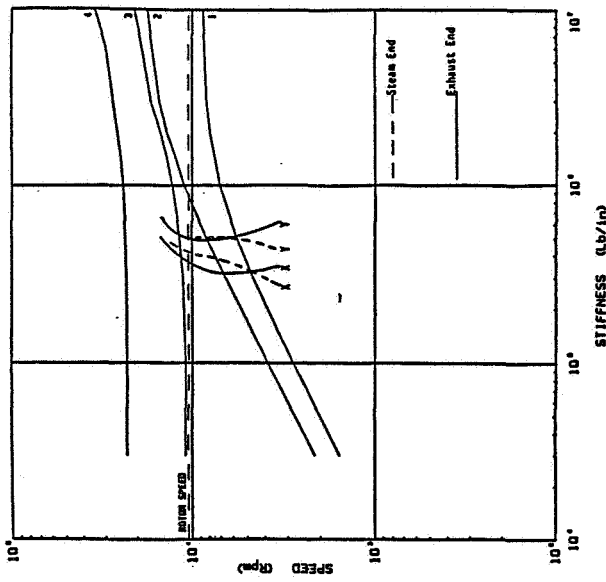


Figure 9

DE LAVAL 103 JAT STEAM TURBINE

SUPPORT STIFFNESS = .30E+08 LB/IN.
MODE SHAPE NO. 2 N = 6592 RPM

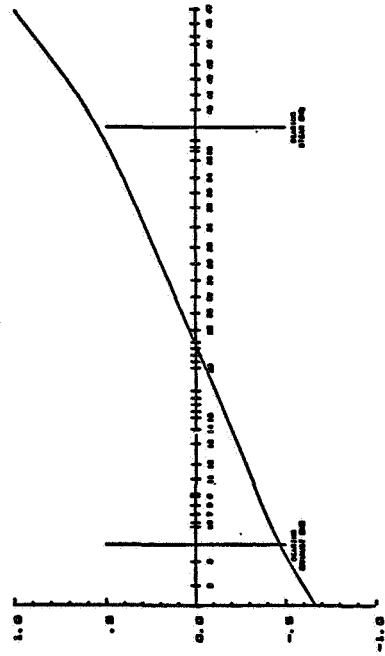


Figure 11

DE LAVAL 103 JAT STEAM TURBINE

SUPPORT STIFFNESS = .30E+08 LB/IN.
MODE SHAPE NO. 1 N = 4844 RPM

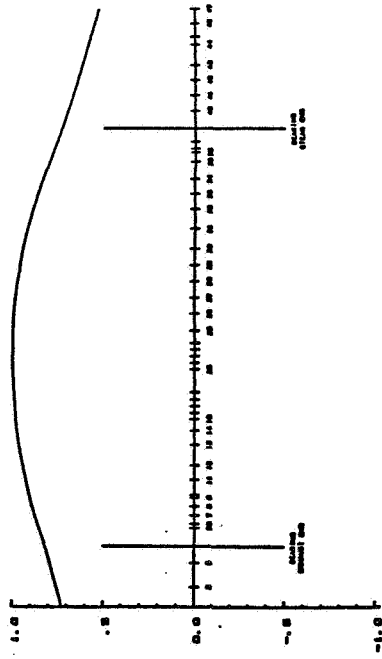


Figure 10

DE LAVAL 103 JAT STEAM TURBINE

SUPPORT STIFFNESS = .30E+08 LB/IN.
MODE SHAPE NO. 3 N = 11304 RPM

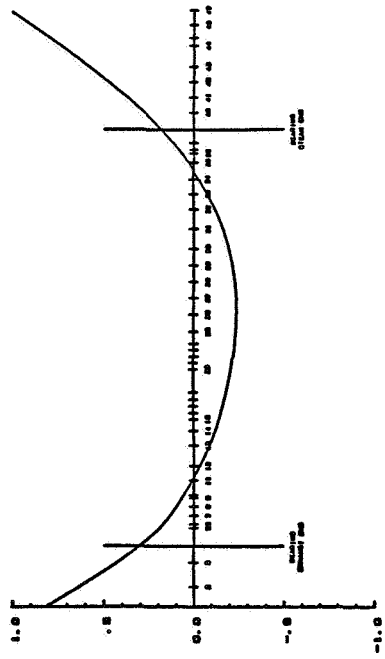


Figure 12

SE vs. EE, DELAVAL BRGS.

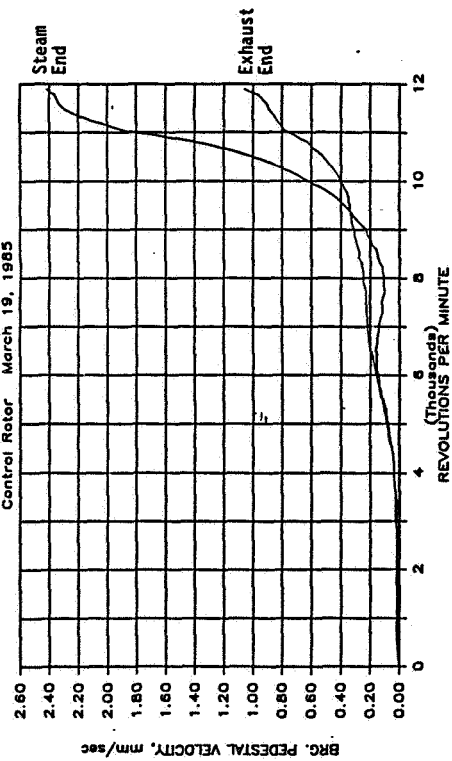


Figure 13

SE vs. EE, 'MOD-2" BRGS.

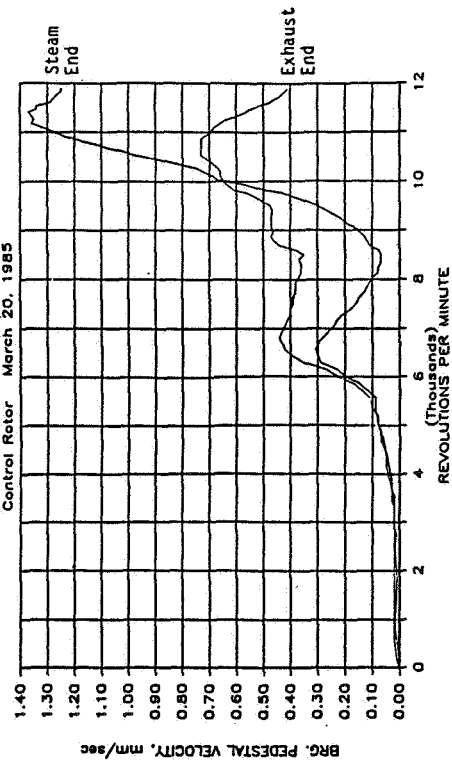


Figure 14

STEAM END - BRG. COMPARISON

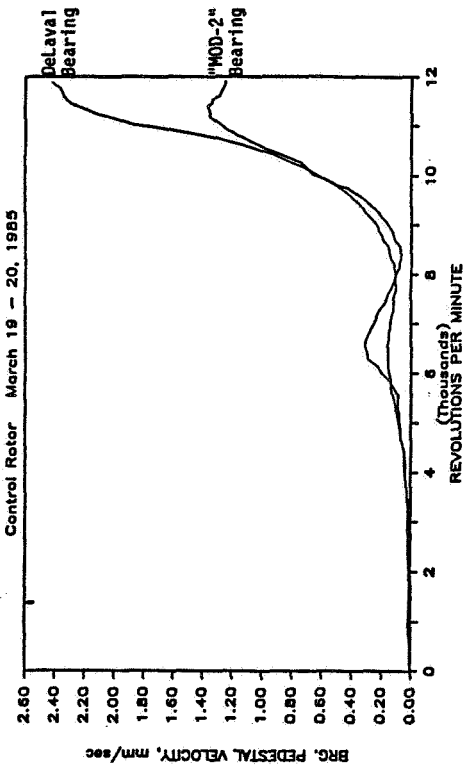


Figure 15

EXHAUST END - BRG. COMPARISON

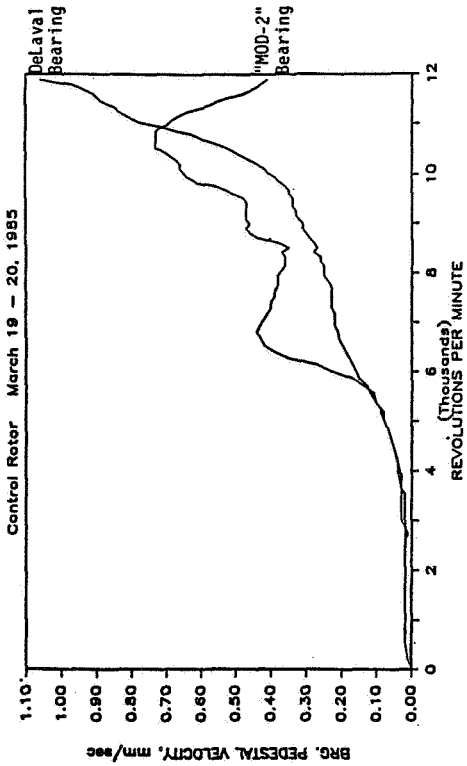


Figure 16

HYDRAULIC INDUCED INSTABILITY ON A VERTICAL SERVICE**WATER PUMP: CASE HISTORY**

**R.F. Bosmans
Bently Rotor Dynamics Research Corporation
Minden, Nevada 89423**

The case history contained in this paper provides insight toward the mechanical and hydraulic behavior of a vertical pump. It clearly demonstrates the need for measurements on the rotor at or near the impeller area.

INTRODUCTION

This case history reports the results of an analysis on a service water pump. This pump is typical of the water pumps used throughout the power generation industry. Although little is known of the mechanical behavior of vertical pumps because of difficulty in modeling the rotor system, recent developments in the application of submersible proximity transducers have made possible the measurement of pump dynamics under operating conditions.

The purpose of this study was to determine the proper selection and installation of vibration-monitoring transducers as well as to measure the effects of imbalance, misalignment, and hydraulics on the performance and reliability of vertical pumps. In addition, the cause of shaft failures on this pump was to be determined.

MACHINE DESCRIPTION

An outline drawing of this pump and motor is shown in figure 1. A number of shafts on this specific pump had failed in recent years for unknown reasons. The lower bearing consists of a grease-lubricated bronze bushing supported by the pump end bell. Intermediate "bearings," supported by the pump vertical column, are water lubricated and lined with scalloped rubber. This type of bearing is sometimes referred to as a "cutlass" bearing or bumper. The couplings between the shaft sections are rigid and transmit torque through two keys spaced 180° apart. For example, the transducer identified as DWD in figure 1 is located at the bottom bearing and is the west proximity probe. The rated pump performance is

- (1) Speed, 720 rpm
- (2) Horsepower, 1250 bhp
- (3) Rated flow, 30 000 gal/min
- (4) Rated differential pressure, 140 ft

This pump is one of three identical pumps connected to a common header. Flow is regulated by a control valve in the discharge piping of each pump.

TRANSDUCER SELECTION

Since very little information is available on the rotordynamic characteristics of this type of pump, proximity and velocity transducers were installed at each bearing and at the motor coupling. Locations are shown on the pump outline drawing. The transducers are identified by a three-letter code shown in the legend in figure 1. Transducers at locations C and D were below the river level and had to be water-proof. The transducer also had to be designed to provide mechanical protection and to survive the abrasive action of sand in the flowing water. Figure 2 is an outline drawing of the probe design used.

STATIC TESTING

The rotor system was tested experimentally for both lateral and torsional resonances. Testing was performed by suspending the instrument pump shaft, motor rotor, and pump impeller vertically and perturbing the assembly by striking it with an instrumented force hammer. The results of these tests, summarized in table 1 and figure 3, were correlated with data obtained in later field testing. The pump speed of 720 rpm dictated that the system would run above the second and below the third lateral balance resonance.

The first torsional resonance of the rotor occurs in the range 690 to 765 cpm. Since this range includes the running speed, torsional analysis was warranted. Strain gauges with telemetry were employed to measure shear strain. Values were extremely low - well below the fatigue limit - indicating a system well damped torsionally.

FIELD TESTING

The pump impeller was modified to allow the addition of balance weights to the impeller blades, without pulling the pump, by using a scuba diver to swim into the pump intake to add or remove weights. The pump impeller was then shop balanced to critical standards and installed in the pump case. The pump was assembled with the transducers mentioned earlier. Extreme care was taken to align the pump and motor. The axial position of the pump was set to the manufacturer's specification, establishing the clearance between the leading edge of the impeller and the casing.

IMBALANCE

The balance condition of the impeller was changed while holding the other variables constant. The amount of imbalance added, 80 oz-in, resulted in a centrifugal force equal to 84 lb. For a rotor weight of 1000 lb, this was 8.4 percent of the rotor weight.

Figures 4 and 5 show orbit and time-base plots of trial runs with and without the imbalance weight. These measurements were taken at the lower bearing (location D) and at location B. Note that the plots at the lower bearing (D) clearly show the effects of unbalance but the plots at the upper bearing (B) do not show a significant change.

MISALIGNMENT RESPONSE TESTING

The alignment between the motor shaft and the pump shaft was changed by adding a 0.010-in shim under one side of the motor. This resulted in an angular misalignment of approximately 2°. Radial offset is impossible with this type of coupling. Orbit and time-base plots of data at location B are shown in figure 6. The slight elliptical shape of the orbit on the second trial run indicates a preload caused by the misalignment. Spectrum plots of the same data (fig. 7) do not give strong indication of misalignment. Since the misalignment manifests itself as 1x vibration, no strong indication of traditional 2x misalignment is indicated on the spectrum plot. The preload was not as apparent at the bottom bearing, as expected.

HYDRAULIC RESPONSE TESTING

The pump was run with two different clearances between the leading edge of the impeller and the casing. Tests were conducted with design clearance of 0.043 in and excessive clearance of 0.200 in. The discharge pressure decreased by 20 psig with the increased impeller clearance, which is a good indication of the amount of recirculation and efficiency losses. With design clearance, spectrum plots of proximity probe data from the lower bearing showed strong subsynchronous response at 372 cpm (fig. 8). This frequency is the first lateral natural frequency (critical) of the pump shaft. When the clearance was increased, the subsynchronous vibration became less stable and occurred over a broader frequency range. As observed earlier with the balance response testing, the transducers located near the motor were unable to measure the subsynchronous activity on the impeller.

The hydraulic response testing determined that the excitation of the first balance resonance by the subsynchronous vibration was the cause of the recent shaft failure. These failures were diagnosed as bending fatigue failures by metallurgical analysis. However, several unanswered questions remained:

- (1) Why was the vibration higher with design clearance?
- (2) Why did the pumps operate without shaft failures until recently?
- (3) Why was the discharge pressure only 62 psig when rated pressure at present river level is 85 psig?

When maintenance records were researched, it was found that the start of shaft failures was preceded by a change in the supplier of the impellers. Recent impellers were not purchased from the original equipment manufacturer (OEM). The OEM has indicated that subtle changes in the blade attack angle could cause the reexcitation of the first lateral natural frequency (critical) because of vortex shedding.

CONCLUSIONS

Two major conclusions resulted from this testing:

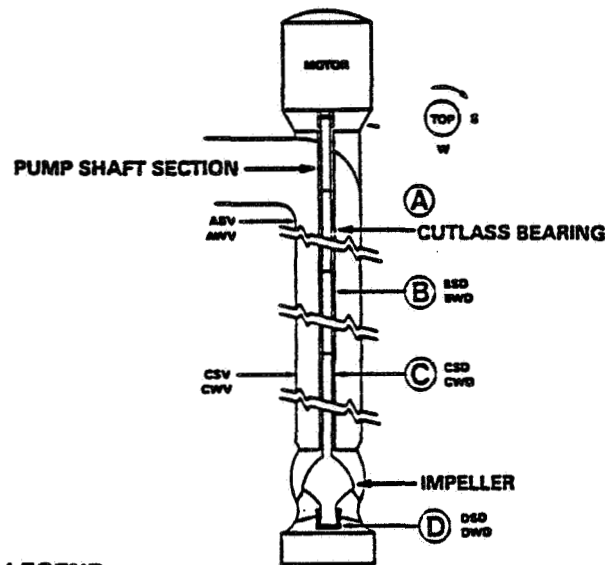
1. Long vertical pumps cannot be adequately monitored without measuring the motion of the shaft near the impeller. This pump was analyzed on many occasions by using transducers installed at location A. These casing transducers (velocity and

acceleration) failed to detect the large subsynchronous vibration occurring at the first balance resonant frequency of the shaft with the pump at running speed (720 rpm).

2. Hydraulic effects appear to be several orders of magnitude higher than imbalance and alignment effects. Any diagnostic effort should include the correlation of hydraulic data.

TABLE 1

ROTOR NATURAL FREQUENCIES (CPM)		
MODE	LATERAL	TORSIONAL
1	375	690
2	525	—
3	975	—
4	2325	—
5	3375	—
6	4275	—
7	5475	—
8	6600	—



LEGEND

- First Letter: Vertical location of measurement point (i.e., A, B, C, etc.)
- Second Letter: Horizontal location ("S" for south side of pump, "W" for west)
- Third Letter: Type of transducer ("D" for displacement proximity probe and "V" for velocity transducer)

Figure 1. - Vertical low-pressure service water pump.

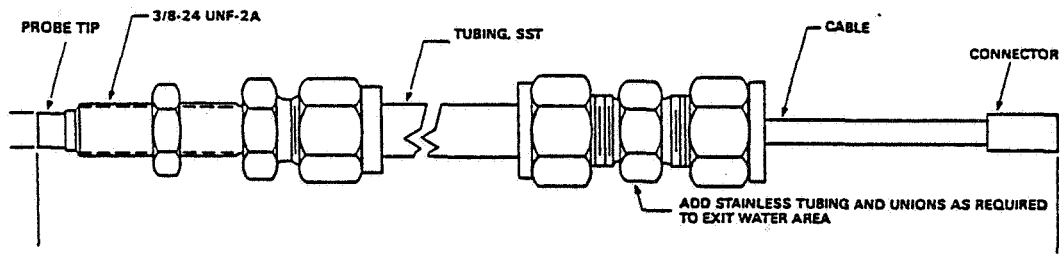


Figure 2. - Waterproof proximity probe transducer.

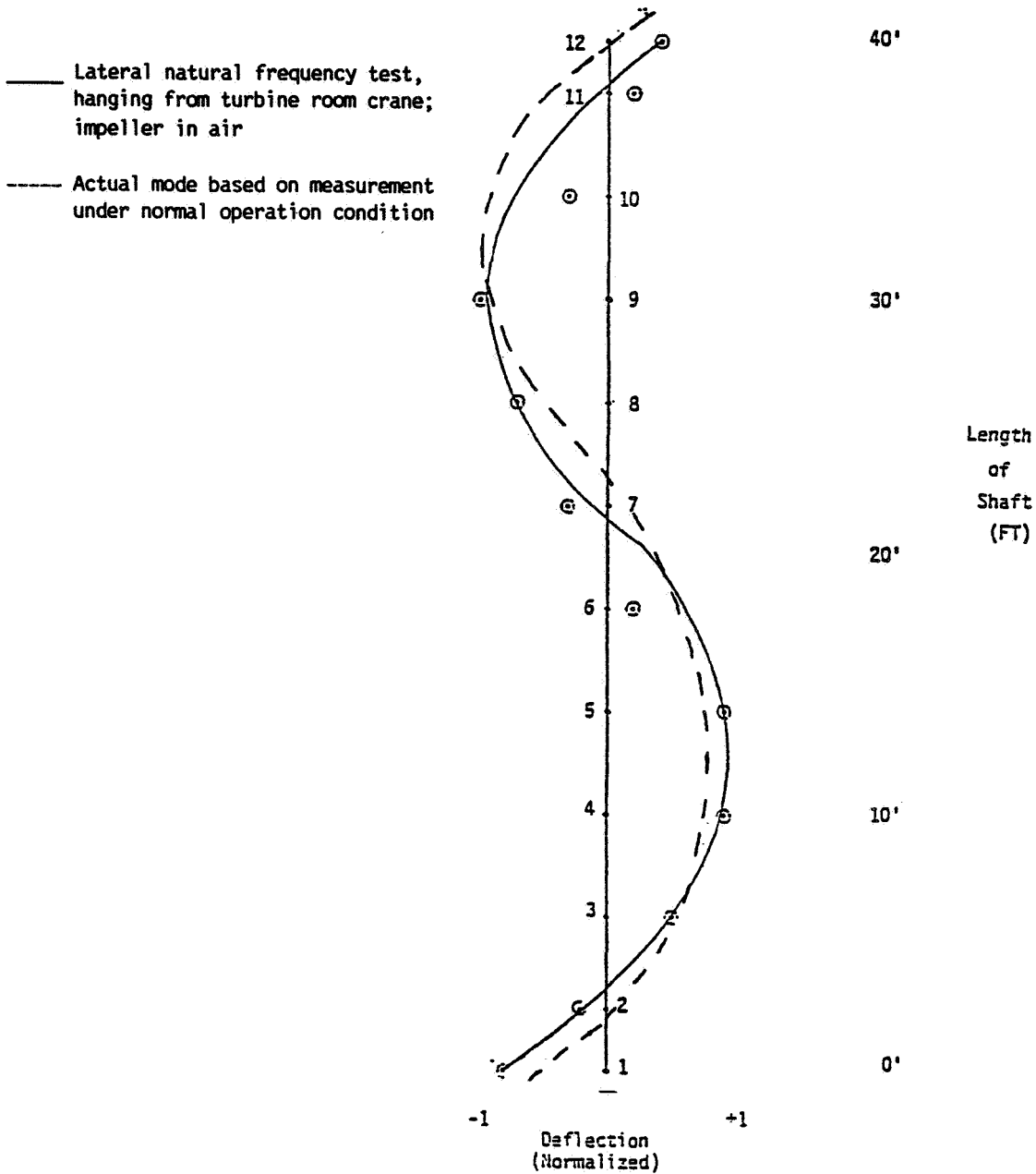


Figure 3. - Mode #2 at 525 cpm.

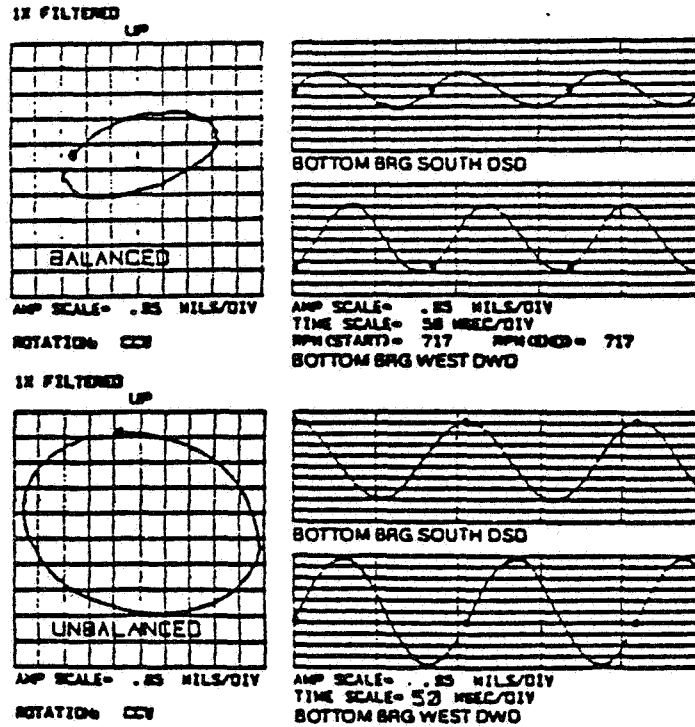


Figure 4. - Bottom-bearing orbit and time-base plots with and without imbalance weight.

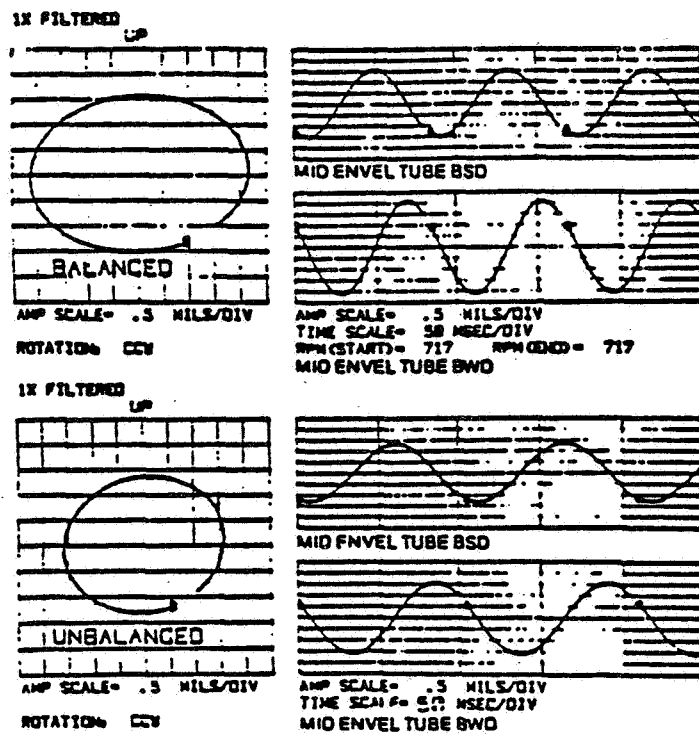


Figure 5. - Upper-bearing orbit and time-base plots with and without imbalance weight.

ORIGINAL PAGE IS
OF POOR QUALITY

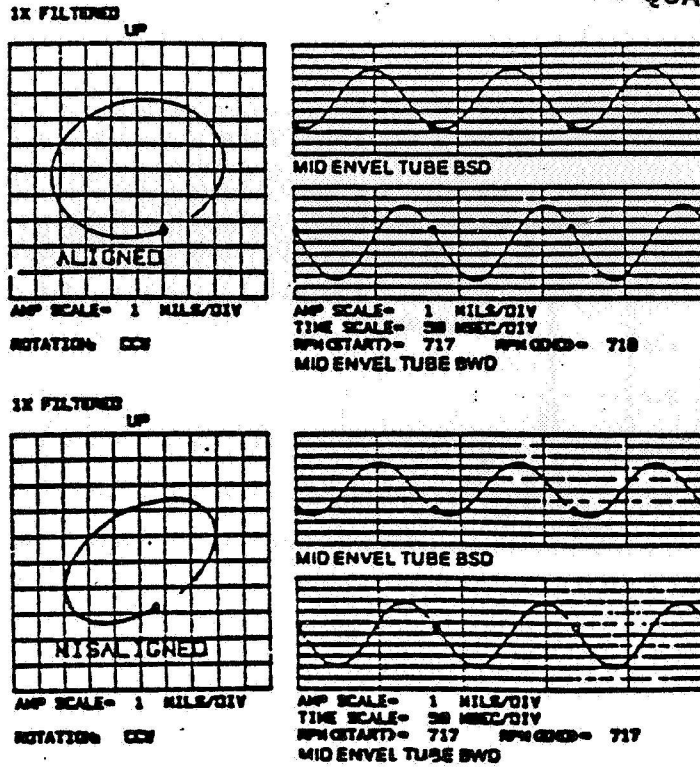


Figure 6. - Upper-bearing orbit and time-base plots with misalignment.

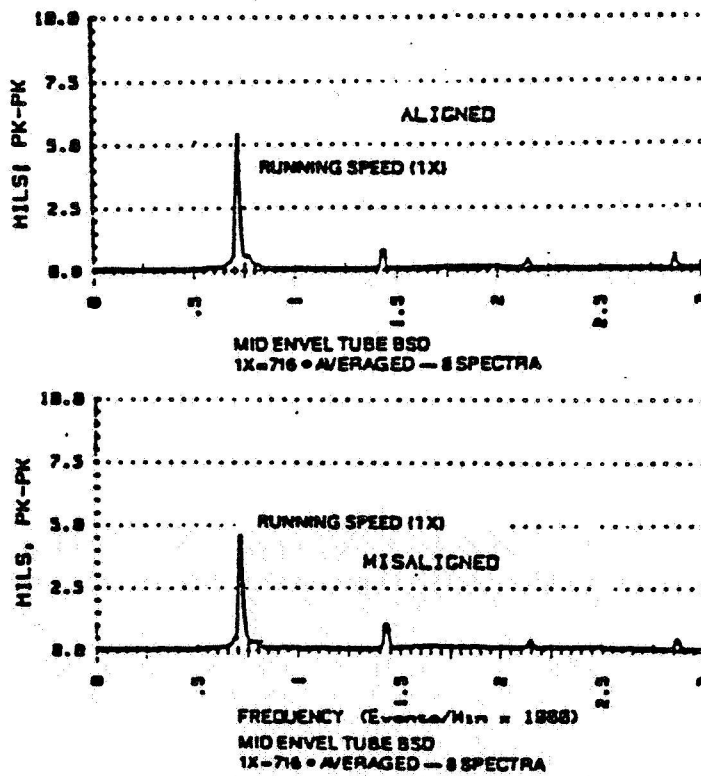


Figure 7. - Upper-bearing spectrum plots with misalignment.

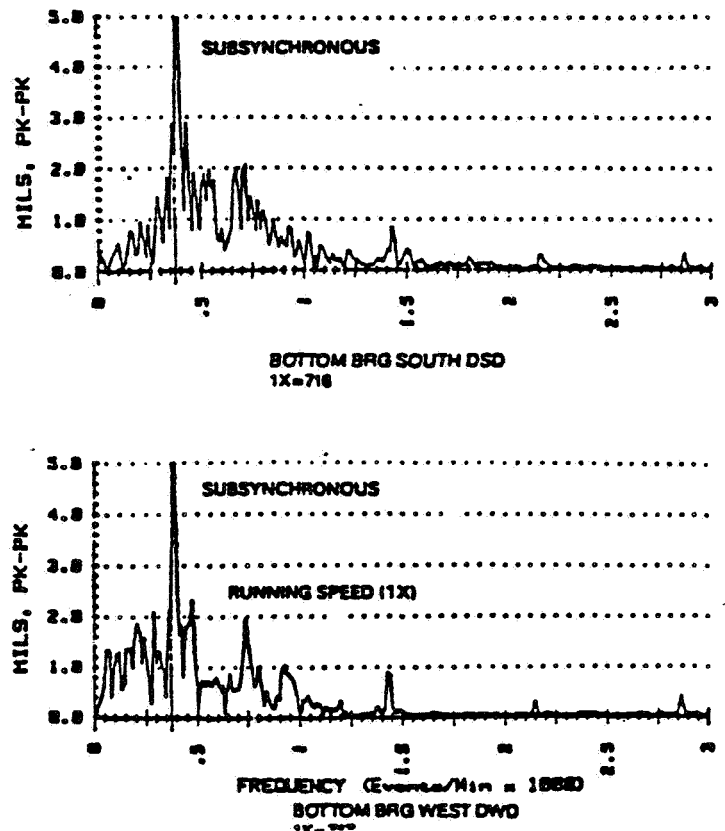


Figure 8. - Bottom-bearing spectrum plots showing subsynchronous vibration component.

C-5

AERODYNAMIC INSTABILITY: A CASE HISTORY

Robert C. Eisenmann
Machinery Diagnostics, Inc.
Minden, Nevada 89423

The identification, diagnosis, and final correction of complex machinery malfunctions typically require the correlation of many parameters such as mechanical construction, process influence, maintenance history, and vibration response characteristics. This paper reviews the progression of field testing, diagnosis, and final correction of a specific machinery instability problem. The case history presented in this paper addresses a unique low-frequency instability problem on a high-pressure barrel compressor. The malfunction was eventually diagnosed as a fluidic mechanism that manifested as an aerodynamic disturbance to the rotor assembly.

MECHANICAL CONFIGURATION

The machinery train consisted of an extraction steam turbine driving two barrel compressors. From a process standpoint the first two stages of compression were contained within the low-stage compressor. The third and fourth process stages were handled within the high-stage compressor. Each compression stage was equipped with interstage cooling and knockout drums. The initial design criteria called for a process stream rich in carbon dioxide. The actual composition of the gas consisted primarily of carbon dioxide (85.6 to 90.6 mol %) and water vapor (5 to 10 mol %).

The configuration of the high-stage rotor is presented in figure 1. The 10 wheels (5 per compression stage) were located back to back to minimize thrust load.

The compressor was equipped with 5-pad, tilt pad radial bearings and a traditional thrust arrangement. The unit exhibited an average first critical speed of 5100 rpm. Shop acceptance tests revealed normal behavior for each of the three machines. Hence up until the time of actual field commissioning there was no indication of a potential instability problem.

INITIAL FIELD STARTUP CHARACTERISTICS

During initial field startup with process gas the high-stage compressor wrecked. The general consensus of opinion was that the system was underdamped. To provide additional rotor damping, the original equipment manufacturer designed and retrofitted a set of squeeze-film damper bearings. This change proved successful, and the unit was easily brought up to normal operating speeds.

It appeared that most of the problems were over and the remainder of the plant startup could commence. However, when loading of the machine was attempted, shaft vibration levels increased dramatically. At discharge pressures of about 1500 psig a significant low-frequency excitation appeared. As discharge pressures were increased, the magnitude of the low-frequency vibration would likewise increase.

00108-001
Typical shaft response for this unit is shown in figure 2. Vibration amplitudes at running speed were approximately 1 mil, and most of the motion occurred at a frequency of 552 cpm. This motion was strongest on the coupling end bearing and somewhat lower on the outboard bearing. The shaft orbit was nearly circular with predominant motion at 552 cpm and a series of inside loops at running frequency. Under this set of operating conditions the rotor made almost 17 revolutions for every 1 cycle of the low-frequency excitation. This low-frequency vibration was audible on the compressor deck and the associated piping. In fact, the machine sounded more like a reciprocating engine than a centrifugal compressor. One of the workers claimed that it sounded like there was an "armadillo" in the piping.

INITIAL FIELD TEST RESULTS

A test program was established to run the machine during various conditions and to characterize the vibration response. The results of these preliminary tests are summarized as follows:

(1) The low-frequency vibration was present at significant amplitudes when discharge pressure exceeded 1500 psig and did not exist at discharge pressures below 1100 psig.

(2) The low-frequency vibration initially appeared at frequencies of 780 to 660 cpm and then shifted to a frequency of approximately 540 cpm as discharge pressure and temperature increased.

(3) The low-frequency vibration was measurable on the entire structure and the associated piping system.

(4) The concrete support structure did attenuate this motion, and the foundation below the baseplate was quiet.

(5) During startup and shutdown conditions the rotor system was well behaved and passed through its first critical in a normal fashion.

(6) There were no reciprocating machines in the immediate area that could influence this unit.

The initial test program confirmed the presence of this low-frequency vibration and tied down the fact that it was strongly related to discharge pressure. The initial test program did not provide any substantial clues as to the origin of the low-frequency vibration.

One suspicion was that there might be an excitation originating from the fourth-stage aftercooler. During one of the shutdowns the exchanger head was pulled, and a bundle of corrosion coupons was found bolted in place. That was the proverbial "armadillo" in the piping system. The coupons were removed and the machine restarted. At 1500 psig the low-frequency excitation reappeared; thus scratch the "armadillo" theory. Somewhat later the aftercooler was removed completely and replaced with a spool piece. Again no influence was found on the low-frequency action.

PRESSURE PULSATION TEST RESULTS

A second phase of field testing was then implemented. During these tests the shaft vibration was measured concurrently with the dynamic pressure pulsation at the fourth-stage discharge flange. The significant results of this test are summarized in figure 3. From these data it is apparent that a strong relationship must exist between low-frequency shaft vibration, dynamic pressure pulsation, and discharge conditions.

After following several other blind alleys, we established a test plan to make a series of dynamic pressure pulsation measurements throughout the high-stage piping system. Figure 4 shows the approximate location of available test points A to J, corresponding to the casing drain at the third-stage suction all the way through the fourth-stage discharge piping. During this test the compressor exhibited a low-frequency vibration at 558 cpm (fig. 5). The measurements revealed that under this condition the third stage (points A, B, and C) did not exhibit the low-frequency activity, and neither did the suction of the fourth stage (point D). However, the fourth-stage casing drain (point E) and the fourth-stage discharge piping (points F to J) did reveal a definite pressure pulsation at 558 cpm.

These same data were observed in another manner (fig. 6) by plotting dynamic pressure pulsation amplitudes versus distance from the fourth-stage discharge flange. This showed that the magnitude of the pressure pulsation decayed rapidly as a function of discharge pipe length. Since the low-frequency excitation did not appear on the suction nozzle to this stage, it was concluded that the exciting force was internal to the compressor and probably located between the fourth-stage suction and discharge flange.

After many hours of discussion with the original equipment manufacturer it was generally agreed that the rotating assembly could not generate the type of frequency measured. Since everything on the rotor system appeared to be normal, the next step was to begin examining the entire machine drawing set for anything that was different from traditional design. During this review someone mentioned the balance port at both the third and fourth-stage discharge nozzles. This balance port consisted of a rectangular passage that connected one side of the discharge nozzle with the other side of the nozzle (fig. 7). The passage was an integral part of the casing and was intended as a means to pressure balance each discharge nozzle.

From this discussion it was decided (1) to plug both ends of each balance port, (2) to hand grind the surface in contour with the nozzle, and (3) to provide a drilled weep hole in one side. After return to the plant site it was confirmed that a balance port did exist. Running a piece of wire through the hole on one side confirmed that the balance port was a circumferential passage that connected both sides of each discharge nozzle.

BEHAVIOR AFTER MODIFICATIONS

The unit came up smoothly through the first critical and reached normal operating speed without any problem. This time the machine came up to 1500 psi, then 1600 psi, without the low-frequency excitation. Finally the compressor was fully loaded, and the previously encountered vibration at 540 or 660 cpm did not appear. Figure 8 is representative of the final condition of this machine at 9340 rpm and a discharge pressure of 2150 psig.

Note that running speed motion was decreased to amplitudes of 0.13 mil vertically and 0.09 mil horizontally. This was due to refinement of compressor rotor balance during the course of this project. There are two minor components at 900 and 2580 cpm that appeared at amplitudes of 0.04 and 0.06 mil, respectively. These components were considered to be nondestructive and were later found to be associated with the stiffness of the O-rings installed with the squeeze-film dampers.

As part of the overall testing program X-Y shaft proximity probes were installed on the floating squeeze-film bearing housing to observe shaft motion relative to the housing. In addition, the standard X-Y shaft probes were mounted on the case and provided a measurement of shaft motion with respect to the case. The 1X vectors from both sets of probes are presented in figure 9.

From this plot of shaft motion with respect to the case and the bearing, the vector difference must be the motion of the squeeze-film bearing housing with respect to the case. Hence the squeeze-film housing was moving and providing the necessary additional system damping.

CONCLUSIONS

This unusual problem was corrected by plugging the discharge nozzle balance ports. The low-frequency vibration and the pressure pulsation in the fourth-stage discharge were eliminated. However, it is difficult to verify the exact nature of the specific physical mechanism and the associated forcing function. This uncertainty is due to a lack of knowledge of the accurate fluid properties of the process gas stream plus insufficient documentation of flow characteristics during the execution of field tests.

Sometime after the conclusion of this project one opinion was that the balance port passage acted as an acoustic resonator (open at both ends). On the basis of the passage length and the estimated sonic velocity, the fundamental acoustic resonant frequency was approximately related to the measured low-frequency excitation. Another opinion was that the measured frequency was related to a vortex shedding phenomenon as the discharge flow passed across the rectangular balance port passages. In either case a more rigorous examination of the specific flow characteristics would be required to gain a proper understanding of this fluid-related excitation.

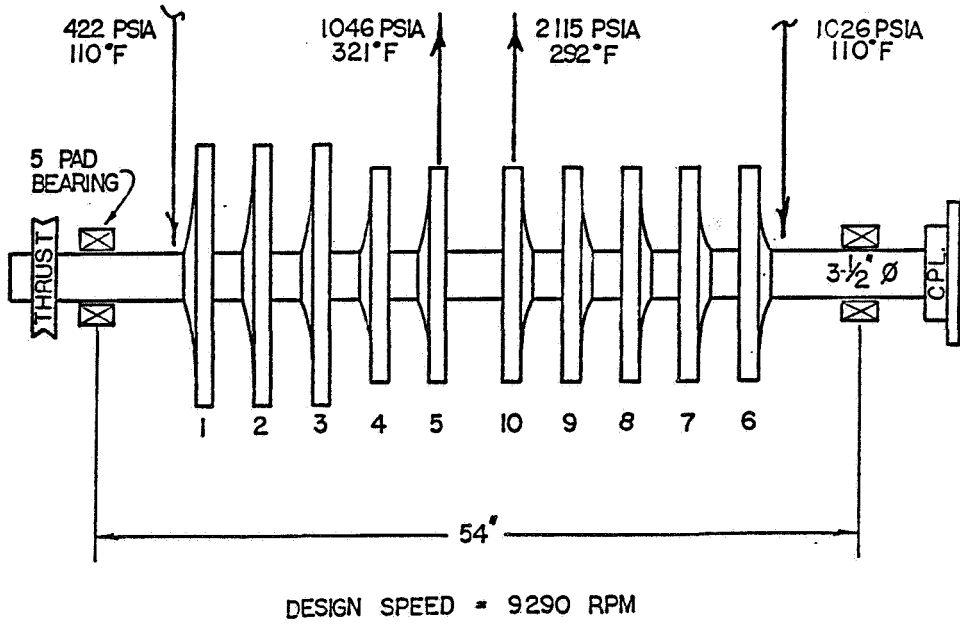


Figure 1. - Ten-stage rotor configuration.

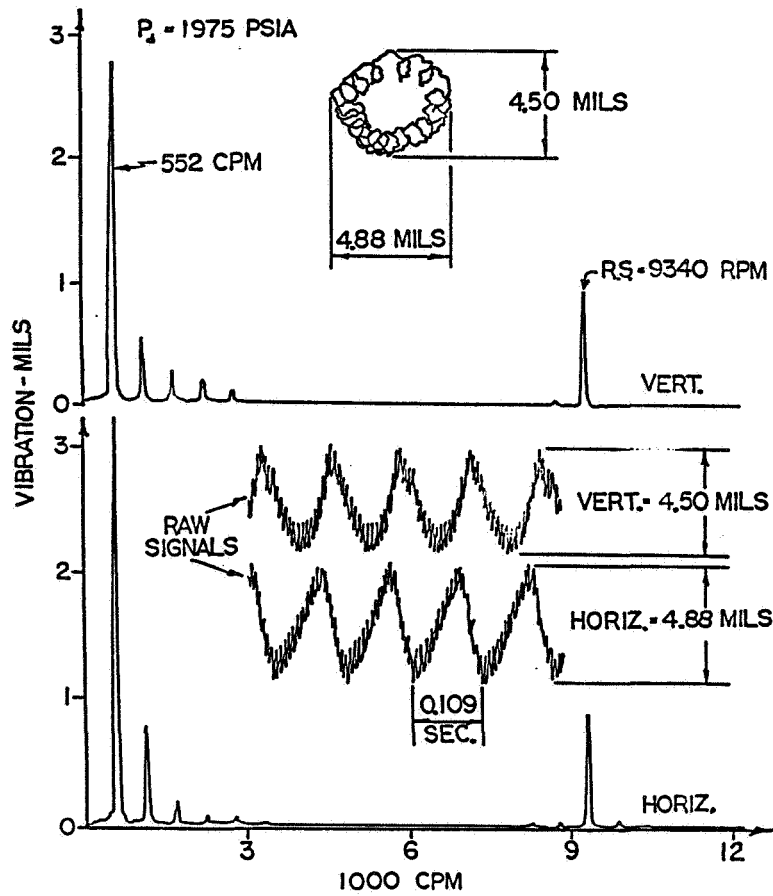


Figure 2. - Initial coupling-end shaft vibration.

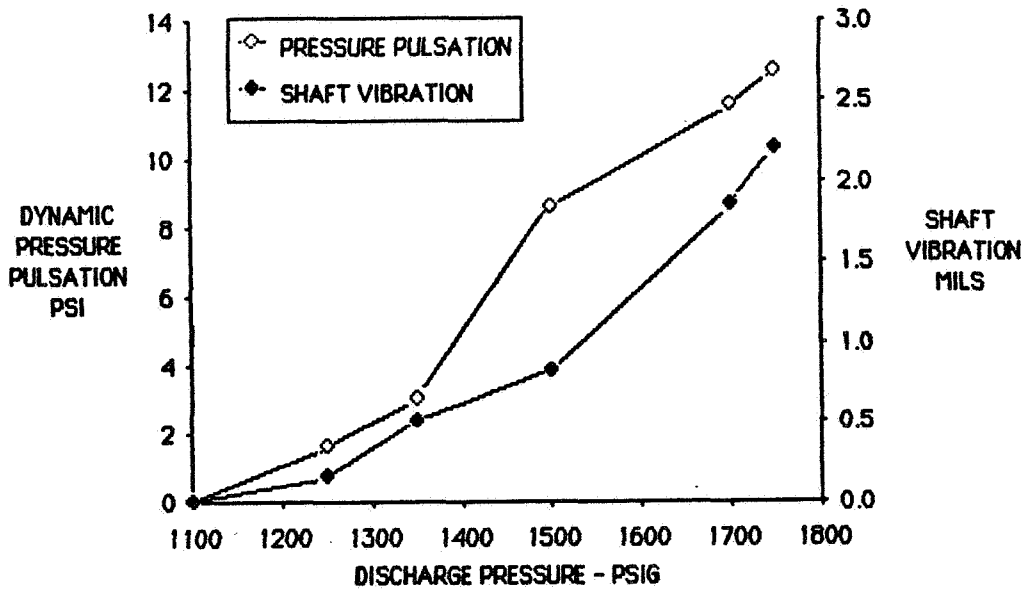


Figure 3. - Pressure pulsation and vibration versus discharge pressure.

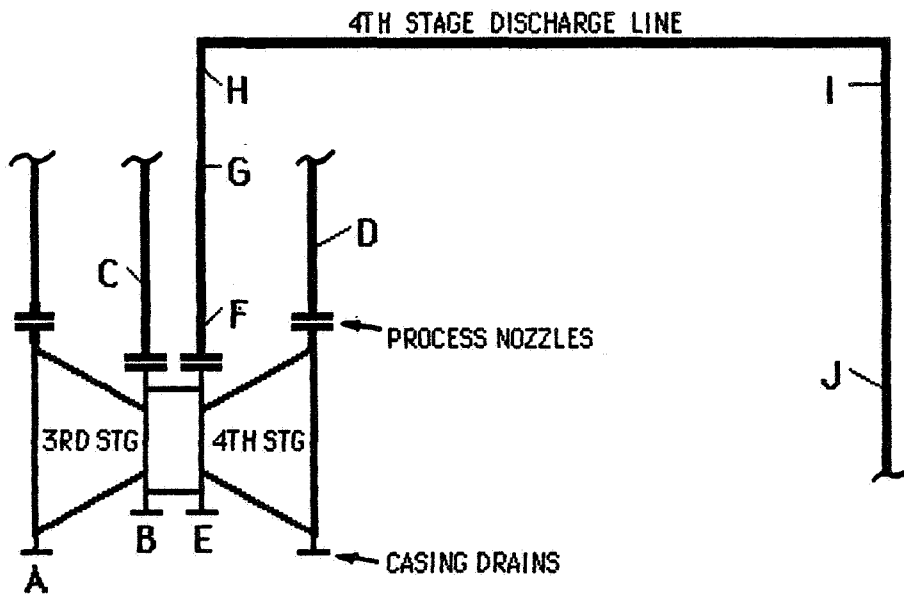


Figure 4. - Location of pressure pulsation transducers.

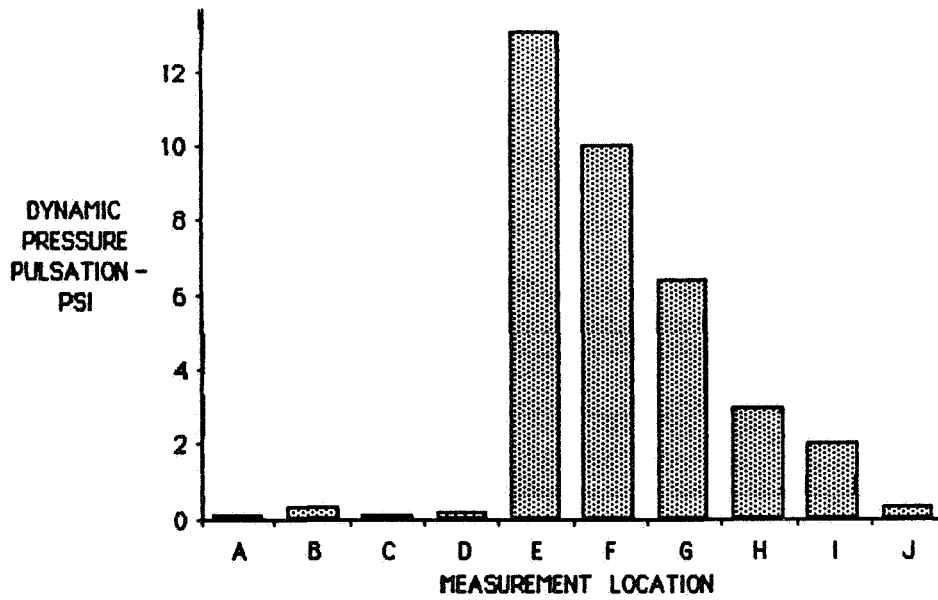


Figure 5. - Dynamic pressure pulsation at 558 cpm.

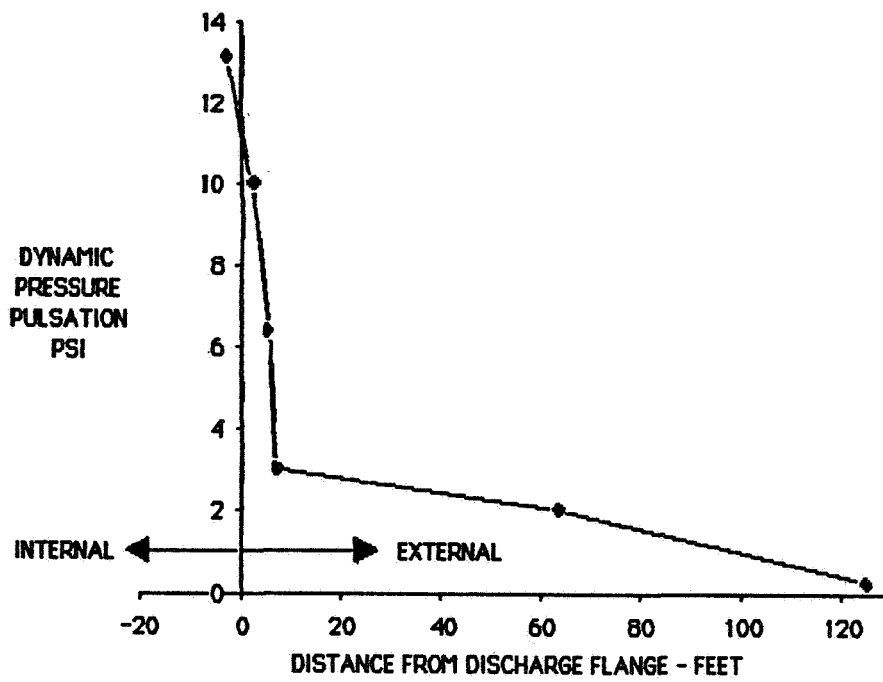


Figure 6. - Pressure pulsation with respect to discharge pipe length.

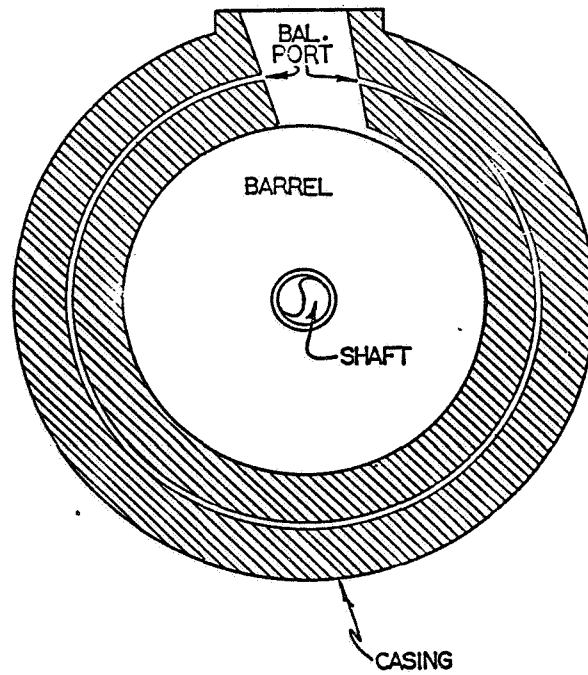


Figure 7. - Cross section through discharge nozzle.

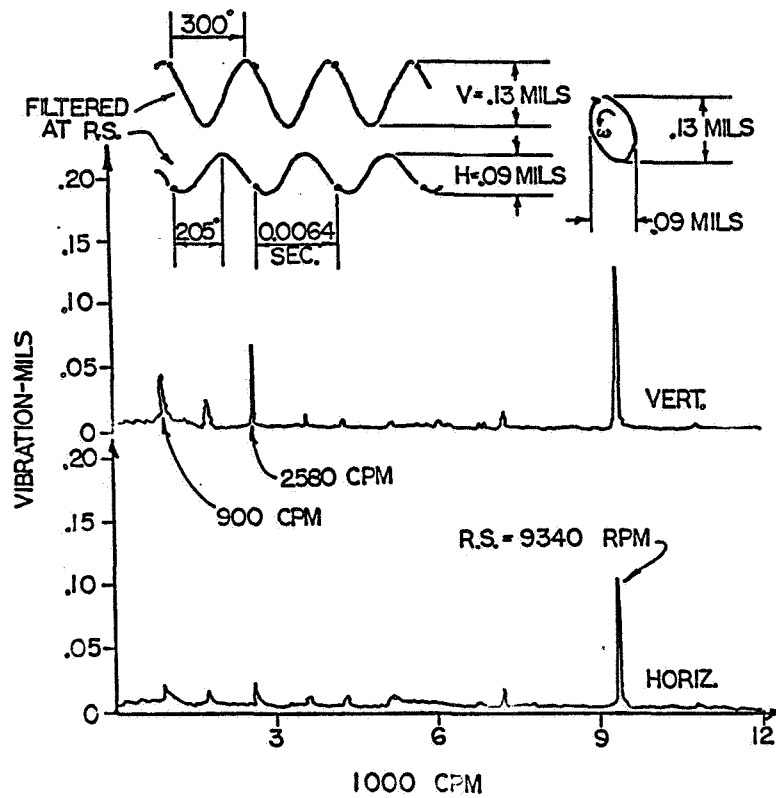


Figure 8. - Final coupling-end shaft vibration.

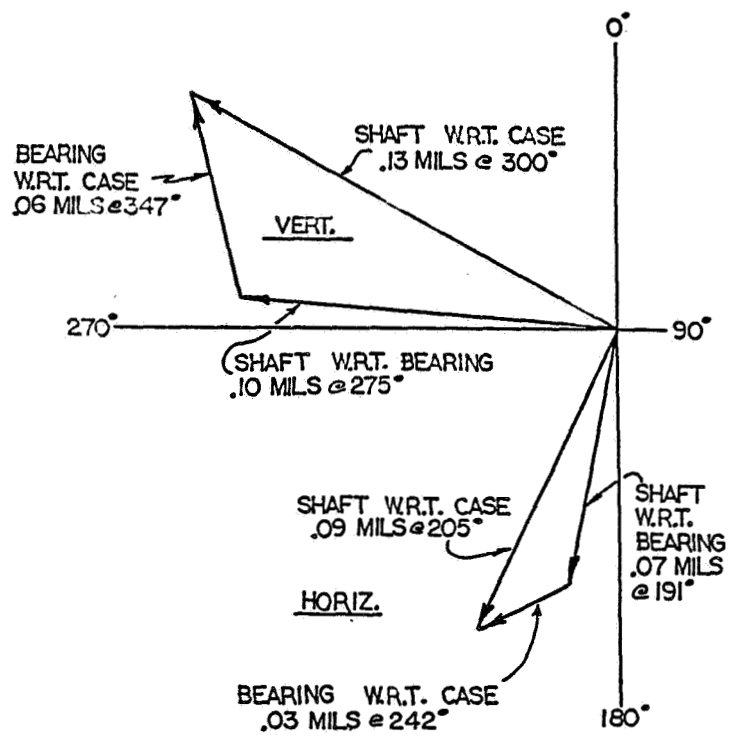


Figure 9. - Relative motion of coupling-end bearing.

REMARKS ON ROTOR STABILITY (A CONTRIBUTION TO DISCUSSION DURING SYMPOSIUM ON INSTABILITY IN ROTATING MACHINERY)

E. Krämer
Technical University of Darmstadt
Darmstadt, Federal Republic of Germany

The remarks refer to two subjects:

1. Influence of nonlinear factors in fluid-lubricated bearings on rotor vibrations. (Figures 1 through 8)
2. Computation of threshold of stability for systems with multiple degrees of freedom. (Figures 9 and 10)

Notes on the first subject are taken from [1]. The thesis [1] is written in German; therefore, it is useful to present here some major contributions from this publication. The reason for this investigation was to learn more about the influence of tilting pad bearings on vertical rotors. The eigenvalues, the stability threshold, the response on the Heaviside-function and the unbalance response were calculated for a rigid rotor, a Jeffcott rotor and for the finite element model of a real rotor. The comparison of the linear and nonlinear calculations shows the limits of the linear calculations.

The second contribution is suppose to show, that the model of the Jeffcott rotor is not sufficient in most practical cases to determine the stability threshold. This is known since some years, when computed results were compared with the behavior of real machines. That's why a program was developed, which is roughly described in the following:

Finite Element Program "MADYN"

Bar elements, rigid bodies, journal fluid-lubricated bearings. Elements may be arbitrarily located and orientated in space. Free matrices for special cases. Maximum 2000 degrees of freedom.

Computations

Eigenvalues (complex), eigenvectors, harmonically forced vibrations, transient vibrations, earthquake excitation, random vibrations.

Procedures

Householder, Hessenberg, Inverse Vector Iteration, Complex Gauss, Modal Analysis (right-hand and left-hand eigenvectors), step by step methods.

Developed at the Institute of Machine Dynamics of the Technical University of Darmstadt during 1972-1982 (leader of the project: H. D. Klement, Ph.D.).

As an example fig. 10 shows the real part of the eigenvalue, determining the stability threshold of the turbogenerator shown in fig. 9 as a function of the rotational speed. A positive real part means that the rotor is unstable. It can be seen that the threshold depends to a high extent on how the foundation was taken into account for the calculation.

Final remark:

My opinion about instability problems in rotating machinery is that the most efficient way to solve them is to consider both analytical computations and measurement results.

When computation is not used, very limited insight to the problem is gained. On the other hand, without measurements one cannot learn about the dynamic behavior of real machines. Both, measurements and computations, are necessary. An intelligent comparison and correlation of measurement and computational results will certainly positively contribute to the increased knowledge of the causes of instability in rotating machinery.

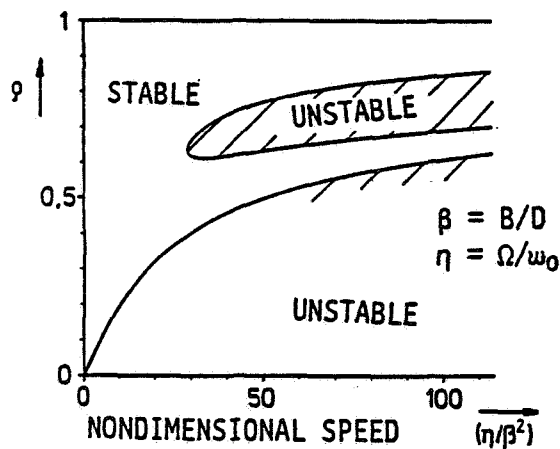


Figure 1. Stability map for a rigid shaft with circular fluid-lubricated bearings. η/β^2 is nondimensional speed, ρ is eccentricity ratio.

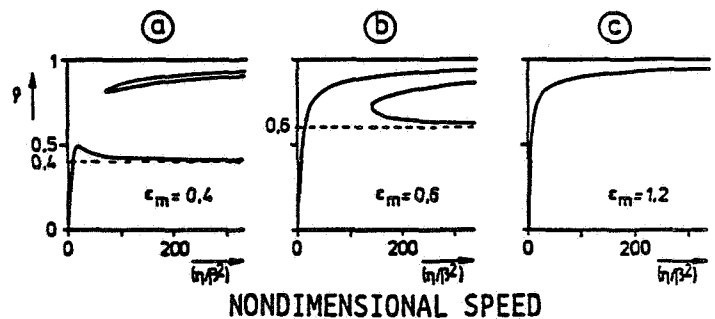


Figure 2. Radius of shaft orbit versus rotative speed. Possible cases. Rigid shaft. Zero static load. ϵ_m = mass eccentricity/clearance.

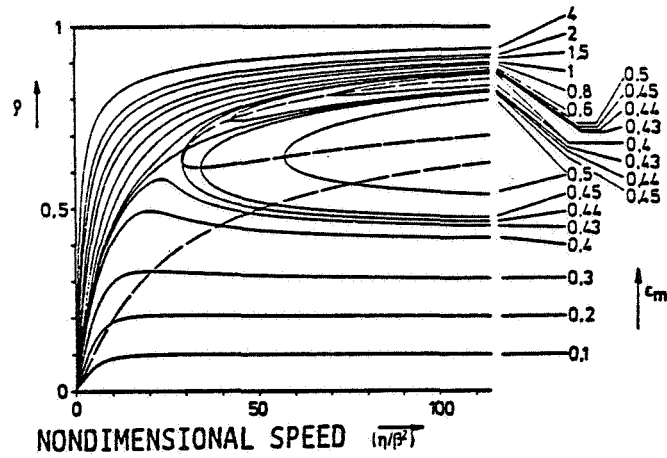


Figure 3. Details of the cases presented in Figure 2.

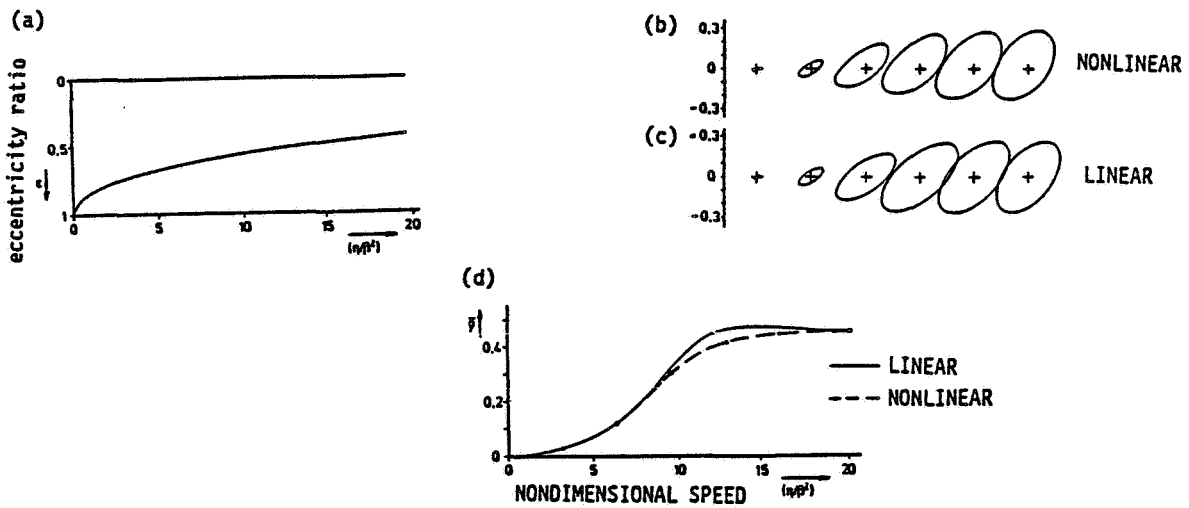


Figure 4. Orbits of a rigid shaft versus rotative speed. Circular fluid-lubricated bearings. Effect of unbalance ($\epsilon = 0.2$) and static force. (a) Location of orbit center, (b) Orbits (nonlinear), (c) Orbits (linear), (d) Mean orbit radius.

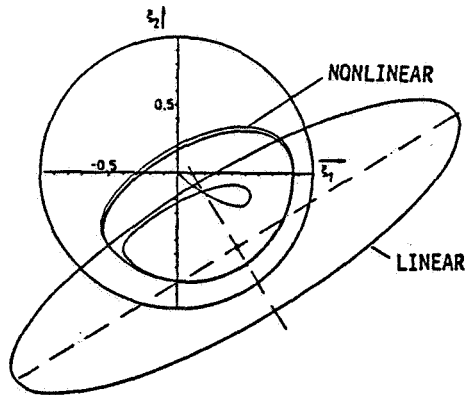


Figure 5. Orbit of a rigid shaft with unbalance and static force. Comparison between the results yielded by linear and nonlinear models.

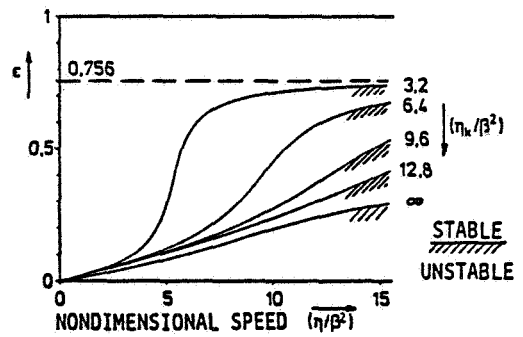


Figure 6. Stability chart for elastic shafts with circular fluid-lubricated bearings. Static position of shaft center.

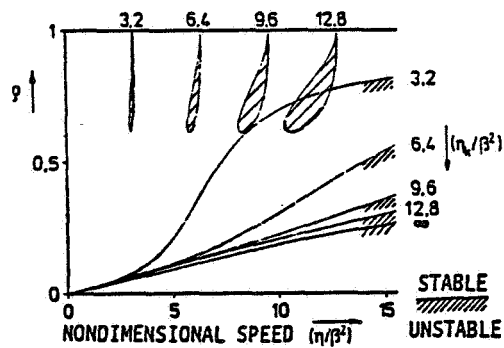


Figure 7. Stability chart for elastic shafts with fluid-lubricated bearings. The shaft center moves on a circular concentric path with relative radius ρ .

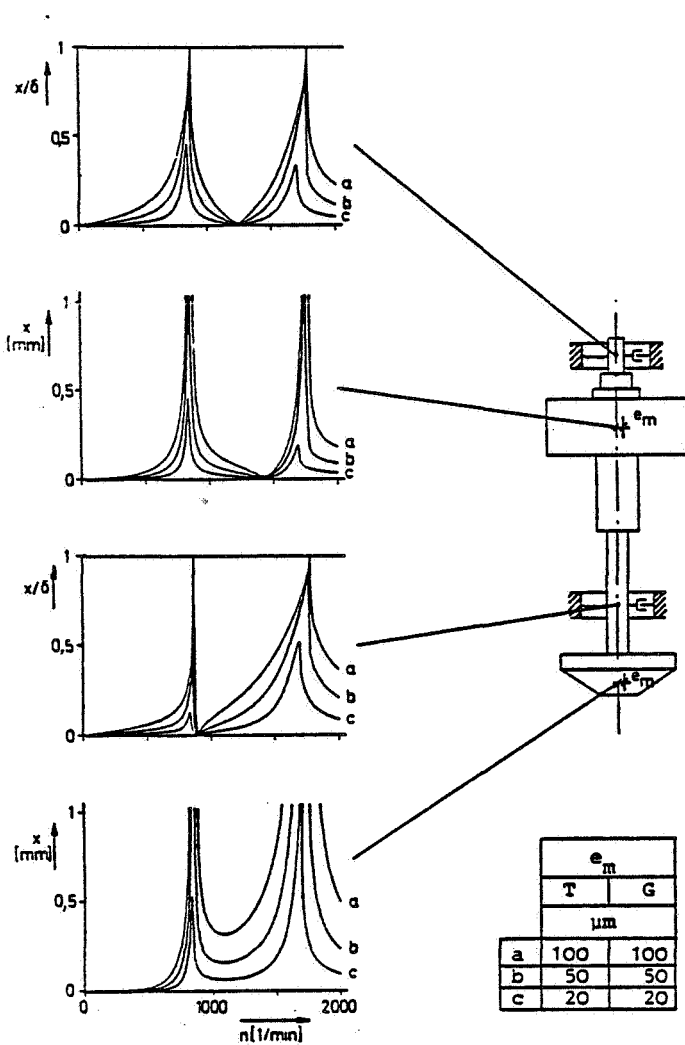


Figure 8. Amplitudes of a 200 MW pump turbine. Results of computation for nonlinear cases a, b, c, corresponding to various amounts of unbalance.

DEGREES OF FREEDOM:

ROTOR = 148
 FOUNDATION = 112
 TOTAL = 260

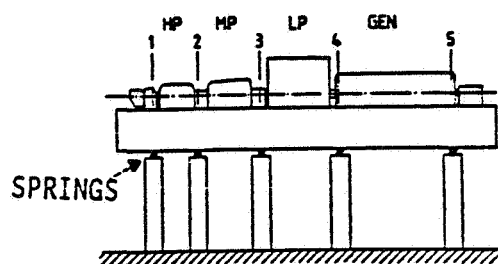


Figure 9. 350 MW turbogenerator. Model: Shaft and foundation have 260 degrees of freedom (condensed). Length = 32 m.

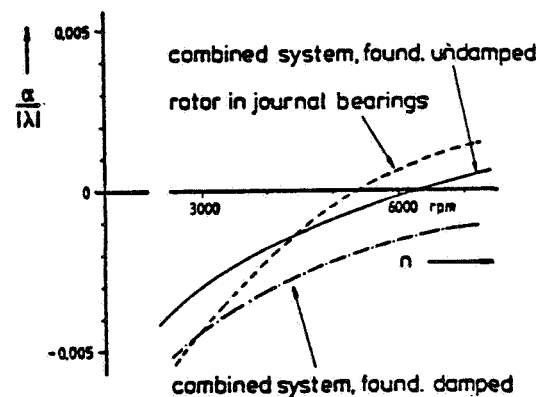


Figure 10. Oil whip instability of system presented in Figure 9 for different models of foundation. Real part of eigenvalue determines stability threshold.

EIGENVALUES AND STABILITY PROBLEMS OF ROTORS

Zbigniew Walczyk
 Polish Academy of Sciences
 80-952 Gdańsk, Fiszera 14, Poland

The essential theoretical results of the application of a developed transfer matrix method to the free transverse vibration of a rotor are shown. Gyroscopic and shear effects, rotary inertia, and external and internal damping as well as the influence of sleeve bearings and rotor supports are taken into consideration. The eigenvalues of the motion equations of the rotor are searched by using a modified determinant method.

INTRODUCTION

An essential feature of the presented method is the application of transfer matrices to uniform and flexible continuous elements of a rotor. These elements are assumed to be the basic elements of the rotor. The motion equations of the remaining rotor elements (rigid discs or complex continuous elements) can be obtained by a suitable modification of the motion equations of the basic rotor element. In this case, quantitative properties of the basic rotor element ought to be the same as in the case when these different rotor elements coexist altogether in a real rotor. In particular, the quantitative properties of the spectrum (set of eigenvalues) of the motion equations of the rotor are preserved.

The first part of the paper is devoted to solving the motion equation of the basic elements and rotor support construction in transfer matrix form. Subsequently, a numerical method of eigenvalues of the motion equations of the whole rotor and its support construction is explained. The final part of the paper contains the analysis of the spectrum of the basic element, which is treated as a simple rotor.

A very similar transfer matrix method was successfully applied to solve the forced vibration of the real rotors of an energy plant turboset (ref. 1). The computer program designed for computation of rotor forced vibration makes possible the evaluation of the critical speeds of the rotor (i.e., speed of resonance peak) with high numerical accuracy and stability. The recently created free rotor vibration computer program, which is based on the method presented in the paper, has the same properties.

SYMBOLS

$Oxyz, O\xi\eta z$	inertial and rotating coordinate systems (fig. 1)
ρ, E, G, b_i	density, Young's and shear moduli, coefficient of internal damping, respectively
R, A, I, β	radius, area, moment of inertia, and shear coefficient of rotor cross section, respectively
b_e	coefficient of external damping

L	length of rotor element
Ω	rotational speed of rotor
Ω_F	angular frequency of exciting force
λ	eigenvalue, $\gamma + j\omega$
$g(z,t); f(z)$	complex rotor dynamic deflection and static deflection, respectively
$G(z)$	free vibration mode of rotor
ϕ	complex rotor cross-section rotary angle
M, T	complex internal bending moment and shearing force
m, q	complex intensity of bending moment and complex continuous load of rotor
$\mu, \nu, \kappa, \Lambda, B$	parameters of motion equation (3)
u, ζ	complex displacement of bearing oil film and support
$C^{XX}, C^{XY}, C^{YX}, C^{YY}$ $\lambda^{XX}, \lambda^{XY}, \lambda^{YX}, \lambda^{YY}$	elastic and damping hydrodynamic characteristics of bearing oil film
$\Delta^{XX}, \Delta^{XY}, \Delta^{YX}, \Delta^{YY}$	dynamic influence coefficients of rotor supports
R	reaction of support
$\{w\}$	complex state vector of rotor cross section, $\text{col}\{G, \phi^*, M, T\}$
$\{G(z)\}$	auxiliary vector of rotor cross section, $\text{col}\{G(z), G'(z), G''(z), G'''(z)\}$
$\{\tilde{w}\}$	real state vector of rotor cross section, $\text{col}\{K_e\{w\}, m\{w\} \}$
$D_k; \tilde{D}_k$	complex and real transfer matrix of rotor element
$H_k; \tilde{H}_k$	complex and real transfer matrix of rotor support and bearing (support construction)
$B; \tilde{B}$	complex and real transfer matrix throughout rotor with fulfilled boundary conditions at both ends of rotor; $\dim B = 2 \times 2$; $\dim \tilde{B} = 4 \times 4$
δ	complex characteristic determinant, $\det B$
$\tilde{\delta}$	real characteristic determinant, $\det \tilde{B}$
$\tilde{B}_G; \tilde{\delta}_G = \det \tilde{B}_G$	general real transfer matrix and its determinant throughout rotor with fulfilled boundary conditions at both ends of rotor; $\dim \tilde{B}_G = 8 \times 8$

β_n	shape number of vibration mode of simple rotor, $n\pi/L$
g_e	acceleration of gravity
t	time
$j^2 = -1$	imaginary unit
e	base of natural logarithm
n	natural number

The physical vector quantities are described by complex variables. Their components on axes Ox and Oy or ($O\xi$ and $O\eta$) establish the real and imaginary parts of these variables, respectively.

Superscription

$()^*$	quantity connected only with rotor bending
$()^{**}$	quantity connected only with rotor shearing
$()'$	derivative with respect to time t
$()'_z$	derivative with respect to z coordinate
$()^-$	complex conjugate quantity
$()^+; ()^-$	quantities connected with right or left side of rotor cross section

Subscription

$k, k+1$	indices of both element ends
cr	critical values of parameters
$()_+; ()_-$	quantities connected with vibrations when their angular speeds are $+\omega$ and $-\omega$, respectively

FREE MOTION OF UNIFORM CONTINUOUS ROTOR ELEMENT

Using the technical theory of bending of beams and taking into consideration the sign convention of components of vector quantities shown in figure 1, the following basic equations are obtained:

$$\left. \begin{aligned}
 T' &= -q; & M' + m &= -jT \\
 M &= jEIg^{**}; & \phi^* &= jg^{*'}; & \phi^{**} &= jg^{**'} \\
 T &= \frac{AG}{\beta} g^{**'}; & g &= g^* + g^{**}; & \phi &= \phi^* + \phi^{**}
 \end{aligned} \right\} \quad (1)$$

and

$$\left. \begin{aligned} q &= -\rho A \ddot{g} = b_e \dot{g} \\ m &= I b_i (\Omega g^{*''''} + j g^{*''''}) - I \rho (2\Omega \dot{g}^{*'} + j \ddot{g}^{*'}) \end{aligned} \right\} \quad (2)$$

In these expressions, the shear effect is taken according to Timoshenko's theory and the internal damping according to the theory of Voight-Kelvin. After elimination of quantities connected only with pure bending and shearing, the final form of the motion equation can be obtained:

$$\begin{aligned} \kappa B \ddot{g}'' + \kappa B (\mu - 2j\Omega) \dot{g}'' + (1 - 2j\Omega \kappa \mu B) \ddot{g} + \mu g - \nu B \dot{g}'' + [(j\Omega \nu - \Lambda - \nu \mu) B - \kappa] \dot{g}'' \\ + [(j\Omega \nu - \Lambda) B \mu + 2j\Omega \kappa] \dot{g}'' + \nu g'''' + (\Lambda - j\Omega \nu) g'''' = 0 \end{aligned} \quad (3)$$

where

$$\mu = \frac{b_e}{A \rho}; \quad \nu = \frac{I b_i}{A \rho}; \quad \kappa = \frac{I}{A}; \quad \Lambda = \frac{EI}{A \rho}; \quad B = \beta \frac{\rho}{G} \quad (4)$$

Solution of equation (3) can be predicted as

$$g(z, t) = e^{\lambda t} G(z) \quad (5)$$

After applying solution (5) to equation (3) the equation of vibration modes is obtained:

$$W G''''(z) + V G''(z) + U G(z) = 0 \quad (6)$$

where

$$\left. \begin{aligned} W &= \nu \lambda + \Lambda - j\Omega \nu \\ V &= -\nu B \lambda^3 + [(j\Omega \nu - \Lambda - \nu \mu) B - \kappa] \lambda^2 + [(j\Omega \nu - \Lambda) B \mu + 2j\Omega \kappa] \lambda \\ U &= \kappa B \lambda^4 + \kappa B (\mu - 2j\Omega) \lambda^3 + (1 - 2j\Omega \kappa \mu B) \lambda^2 + \mu \lambda \end{aligned} \right\} \quad (7)$$

Differential equation (6) can be solved by using a known method, and its solution has the form

$$G(z) = \sum_{i=1}^9 c_i e^{r_i z} \quad (8)$$

where c_i are complex constants and r_i are complex roots of the following biquadratic equation:

$$W r^4 + V r^2 + U = 0 \quad (9)$$

If a dependence between auxiliary vectors $\{G(z)\}$ at both element ends ($z = 0$; $z = L$) is searched, the constants c_i can be eliminated:

$$\{G\}_{k+1} = RER^{-1}\{G\}_k \quad (10)$$

where

$$\{G\}_{k+1} = \{G(L)\}$$

$$\{G\}_k = \{G(0)\}$$

and

$$E = \text{diag} \left[e^{r_1 L}; e^{r_2 L}; e^{r_3 L}; e^{r_4 L} \right]; \quad R = \begin{bmatrix} 1 & 1 & 1 & 1 \\ r_1 & r_2 & r_3 & r_4 \\ r_1^2 & r_2^2 & r_3^2 & r_4^2 \\ r_1^3 & r_2^3 & r_3^3 & r_4^3 \end{bmatrix}$$

In order to obtain the transfer matrix, a dependence between the auxiliary vector $\{G(z)\}$ and the state vector $\{w\}$ has to be estimated. This dependence can be expressed by a matrix Γ , namely

$$\{w\} = \Gamma \{G(z)\} \quad (12)$$

Elements of the matrix Γ can be obtained by using equations (1) and (2):

$$\Gamma = \begin{bmatrix} 1 & 0 & 0 & 0 \\ 0 & \chi_1 & 0 & \chi_2 \\ \chi_3 & 0 & \chi_4 & 0 \\ 0 & \chi_5 & 0 & \chi_6 \end{bmatrix} \quad (13)$$

and

$$\chi_1 = j \left(1 - \frac{B}{A\rho} \right) \chi_5$$

$$\chi_2 = -j \frac{B}{A\rho} \chi_6$$

$$\chi_3 = -jEIB(\lambda^2 + \mu\lambda)$$

$$\chi_4 = jEI$$

$$\chi_5 = \alpha \{ \kappa(\lambda^2 - 2j\Omega\lambda) + B(\lambda^2 + \mu\lambda)[\Lambda + v(\lambda - j\Omega)] \}$$

$$\chi_6 = -\alpha[\Lambda + v(\lambda - j\Omega)]$$

$$\alpha = A\rho[1 + B\kappa(\lambda^2 - 2j\Omega\lambda)]^{-1}$$

Applying equation (12) to equation (10), we can obtain the form of the complex transfer matrix of the considered rotor element:

$$D_k = \Gamma R E R^{-1} \Gamma^{-1} \quad (14)$$

Although in many papers the motion equation has less complicated form, our equation (3) follows from accepted assumptions and mathematical transformation. If damping forces are neglected ($\nu = \mu = 0$), equation (3) has the well-known form demonstrated by Timoshenko (ref. 2), Dimentberg (ref. 3), and Tondl (ref. 4). Additionally, the state vector of rotor cross section has to contain the rotary angle ϕ^* , which is connected only with pure bending. This dependence on ϕ^* complicates the form of equation (13). Such an approach allows us to satisfy the continuity conditions at common boundary cross sections of two adjacent rotor elements and to obtain the transfer matrix throughout the rotor by multiplying transfer matrices of successive rotor elements and supports. Note that only if the shear and gyroscopic effects as well as internal damping are omitted ($B = \kappa = \mu = 0$) does the matrix (13) reduce to the widely known form:

$$\Gamma = \text{diag}[1; j; jEI; -EI] \quad (15)$$

TRANSFER MATRIX OF ROTOR BEARING AND SUPPORT

The basic system of the motion equations of rotor support construction becomes

For bearing oil film reaction:

$$R = Cu + \tilde{C}\tilde{u} + Au + \tilde{A}\tilde{u} \quad (16)$$

$$\left. \begin{aligned} C &= \frac{1}{2} \left[\left(c^{xx} + c^{yy} \right) + j \left(c^{yx} - c^{xy} \right) \right]; & A &= \frac{1}{2} \left[\left(\lambda^{xx} + \lambda^{yy} \right) + j \left(\lambda^{yx} - \lambda^{xy} \right) \right] \\ \tilde{C} &= \frac{1}{2} \left[\left(c^{xx} - c^{yy} \right) + j \left(c^{yx} + c^{xy} \right) \right]; & \tilde{A} &= \frac{1}{2} \left[\left(\lambda^{xx} - \lambda^{yy} \right) + j \left(\lambda^{yx} + \lambda^{xy} \right) \right] \end{aligned} \right\} \quad (17)$$

For support displacement:

$$\zeta = \Delta R + \tilde{\Delta}\tilde{R} \quad (18)$$

$$\Delta = \frac{1}{2} \left[\left(\Delta^{xx} + \Delta^{yy} \right) + j \left(\Delta^{yx} - \Delta^{xy} \right) \right]; \quad \tilde{\Delta} = \frac{1}{2} \left[\left(\Delta^{xx} - \Delta^{yy} \right) + j \left(\Delta^{yx} + \Delta^{xy} \right) \right] \quad (19)$$

For forced equilibrium and displacement continuity:

$$G = \zeta + u \quad \text{and} \quad R = T^+ - T^- \quad (20)$$

The hydrodynamic characteristics of a bearing oil film can be obtained as the gradients of oil forces at the static balance point and are calculated by using a linear perturbation method to the Reynolds equation. Only in one case can the elements of the transfer matrix of supports be expressed by complex variables without using any complex conjugate quantities. It takes place when support construction has no couplings ($\tilde{C} = \tilde{A} = \tilde{\Delta} = 0$); then the transfer matrix of support has the form:

$$\tilde{D}_k = \begin{bmatrix} \tilde{D}_{k+} & 0 \\ 0 & \tilde{D}_{k-} \end{bmatrix} \quad (26)$$

where

$$\tilde{D}_{k\alpha} = \begin{bmatrix} \text{Re}D_{k\alpha} & -\text{Im}D_{k\alpha} \\ \text{Im}D_{k\alpha} & \text{Re}D_{k\alpha} \end{bmatrix}$$

and

$$\alpha = + \text{ or } -$$

The matrix D_{k+} is analogous with matrix (14); however, matrix D_{k-} is obtained from matrix (14) by replacing λ by λ . Transfer through rotor elements or rotor supports can be described by using real matrix (26) or (23) and the following real state vector of rotor cross sections:

$$\{W\} = \text{col} \{ \{\tilde{w}\}_+; \{\tilde{w}\}_- \} \quad (27)$$

EIGENVALUES AND MOTION STABILITY

The transfer matrix through the rotor is obtained as the consequent product of transfer matrices of rotor elements and supports. The characteristic matrix is obtained from the transfer matrix through the rotor by inserting an appropriate set of boundary conditions. Let us consider three cases:

(1) The rotor support construction has no couplings: The characteristic matrix (denoted as B) is obtained in complex form, and its characteristic determinant is complex:

$$\delta = \det B \quad (28)$$

(2) The rotor support construction has no couplings: The characteristic matrix (denoted as \tilde{B}) is obtained in real form, and it is related to matrix B in the following manner:

$$\tilde{B} = \begin{bmatrix} \text{Re}B & -\text{Im}B \\ \text{Im}B & \text{Re}B \end{bmatrix} \quad (29)$$

The determinant of matrix \tilde{B} is real:

$$\tilde{\delta} = \det \tilde{B} \quad (30)$$

(3) The rotor support construction has couplings: The characteristic matrix (denoted as \tilde{B}_G) is obtained in real form by using real matrices (23) and (26), and its determinant is real:

$$\delta_G = \det B_G \quad (31)$$

The following relations are valid for these three determinants:

$$\tilde{\delta} = \delta \bar{\delta} \quad (32)$$

$$\tilde{\delta}_G = \tilde{\delta}^2 + \psi \quad (33)$$

Expression (32) results in widely known properties of determinants. Equation (33) is obtained in the same way as (32). The quantity ψ is connected with couplings of the rotor support construction. As the degree of support construction anisotropy is increased, the value of ψ decreases and the following quantities are the measure of the support anisotropy:

$$C^{xx} - C^{yy}, C^{yx} + C^{xy}; \lambda^{xx} - \lambda^{yy}, \lambda^{yx} + \lambda^{xy}; \Delta^{xx} - \Delta^{yy}, \Delta^{yx} + \Delta^{xy}$$

In real turbine construction these quantities usually have values such that the determinant $\tilde{\delta}_G$ is positive (known by performing several numerical calculations). It is evident that the determinant $\tilde{\delta}$ is positive.

These conclusions are useful in the numerical computations of eigenvalues (roots of characteristic determinants). As the real determinants are always positive, they can vanish only in places where their local minima in the complex $\lambda = \gamma + j\omega$ plane are observed because the determinants can be considered as the continuous functions of two real variables γ and ω . Computing results given in technical papers (e.g., refs. 5 and 6) point out that eigenvalues are located relatively far from one another. Besides the subspaces of spectrum plane (complex plane of eigenvalues) in which real determinants can decrease monotonically to their minimal values are relatively large. This remark probably explains why Lund's gradient method (ref. 6) as well as Muller's quadratic approximation technique can be successfully applied without any hard restrictions concerning starting points for the iteration procedure. These properties also permit us to use with success the bisection method alternately applied to both real arguments (γ, ω) of the real determinants $\tilde{\delta}_G$ or $\tilde{\delta}$. A very important problem, whether each determinant minimum is its zero, has not been theoretically solved, and one can answer this question by the numerical verification of an appropriate eigenvector mode of free vibration.

The procedure for computing the minimal values of a real determinant can be simultaneously used to evaluate so-called critical speeds of resonance peak. The real determinant $\tilde{\delta}_G$ is a function of three arguments: $\tilde{\delta}_G = \tilde{\delta}_G(\gamma, \omega, \Omega)$. The critical speeds of resonance peak are calculated under assumptions $\gamma = 0$ and $\omega = \Omega_F$ and are determined by the following condition:

$$\tilde{\delta}_G(0, \Omega_F, \Omega) = \min \quad (34)$$

where $\Omega_F = \pm\Omega, \pm 2\Omega, \pm 3\Omega$, etc.; usually $\Omega_F = \Omega$. From the theory of the linear dynamical systems it is known that any minimum of expression (34) is connected with a certain critical speed of resonance peak.

We can obviously compute only a finite number of eigenvalues. Therefore the stability problem of rotor motion, based on investigation of the real parts of eigenvalues, can be solved partially because the full spectrum of the rotor motion equation always contains an infinite number of elements. In further consideration an example is presented when stable and unstable modes of rotor free vibration exist simultaneously (see case 3.1 next section).

BASIC ROTOR ELEMENT AS A SIMPLE ROTOR

In this section, in order to examine some interesting properties of the spectrum of the rotor motion equations, the single rotor element is treated as a simple rotor. Consider a rotor simply supported on its ends by a rigid support structure. This is equivalent to the following boundary conditions:

$$g(0,t) = g(L,t) = 0 \quad \text{and} \quad M(0,t) = M(L,t) = 0 \quad (35)$$

From equation (12) and matrix (13) these conditions take the form:

$$G(0) = G(L) = 0; \quad \chi_3 G(0) + \chi_4 G''(0) = 0; \quad \chi_3 G(L) + \chi_4 G''(L) = 0 \quad (36)$$

The equations (36) point out that

$$G(z) = G_0 \sin \beta_n z \quad (37)$$

can be chosen as a mode function. Substituting expression (37) into the motion equation (3) gives the complex determinant δ in the expanded form:

$$\begin{aligned} \delta = \kappa B \lambda^4 + \left[(\mu - 2j\Omega)\kappa + v\beta_n^2 \right] B \lambda^3 + \left\{ [(\Lambda - j\Omega v + \mu v)B + \kappa] \beta_n^2 \right. \\ \left. + (1 - 2j\Omega\kappa\mu B) \right\} \lambda^2 + \mu + \left\{ [(\Lambda - j\Omega v)\mu B - 2j\Omega\kappa] \beta_n^2 + v\beta_n^4 \right\} \lambda \\ + (\Lambda - j\Omega v) \beta_n^4 \end{aligned} \quad (38)$$

The roots of complex determinants δ and $\bar{\delta}$ establish the eigenvalue spectrum. Additionally, the roots of determinant δ are located symmetrically to the roots of determinant $\bar{\delta}$, and the real axis is the axis of symmetry.

In general, the determinant (38) has four complex roots for each parameter β_n . Further some particular cases of the physical model of the simple rotor are considered.

Case 1. $\Omega \equiv 0$ (no rotating rotor): The determinant (38) has only real coefficients. Therefore each spectrum element is a root of determinant δ and determinant $\bar{\delta}$ as well. The rotor motion is not coupled. The motion in planes Oxz and Oyz can be executed independently.

Case 2. $B \equiv 0$ (no shear effect): The number of roots of determinant (38) decreases twice.

Case 3. $\omega = 0$; $\lambda = \gamma$ (critical damping): Substituting the above assumptions into expression (38), we obtain two real equations, for which the dependence among three parameters γ , v , μ can be investigated.

Case 3.1. $\omega = 0$ and $B \equiv 0$: In this case the equations take the form:

$$\left. \begin{aligned} (1 + \kappa \beta_n^2) \gamma^2 + \mu (+ v \beta_n^4) \gamma + \Lambda \beta_n^4 &= 0 \\ 2\kappa \gamma + v \beta_n^2 &= 0 \end{aligned} \right\} \quad (39)$$

A dependence among three critical parameters is given by

$$\left. \begin{aligned} \gamma_{cr} &= - \frac{v_{cr} \beta_n^2}{2\kappa} \\ v_{cr} &= \kappa \left\{ \mu_{cr} \pm \left[\mu_{cr}^2 - 4\Lambda (1 - \kappa \beta_n^2) \beta_n^4 \right]^{1/2} \right\} \left[(1 - \kappa \beta_n^2) \beta_n^2 \right]^{-1} \end{aligned} \right\} \quad (40)$$

The quantity v_{cr} is positive when the expression $(1 - \kappa \beta_n^2)$ is positive (independently of the quantity μ_{cr}). However, v_{cr} has only real values if

$$\mu_{cr} > \left[2 \Lambda (1 - \kappa \beta_n^2) \right]^{1/2} \beta_n^2 \quad (41)$$

For any given rotor size L, R we can determine a value n_0 such that for $n > n_0$ the expression $(1 - \kappa \beta_n^2)$ becomes negative. Thus rotor motion with modes $n > n_0$ is given by

$$n_0 > \frac{2L}{\pi R} \quad (42)$$

which depends on the geometrical parameters of the rotor.

The next two cases concern the estimations of the spectrum limits. The results are equivalent to the necessary conditions. To find these estimations, one should assume that the variable λ is finite.

Case 4. $n \rightarrow \infty$ or $\beta_n \rightarrow \infty$ (mode order increases): In this case the spectrum is limited and the boundary values of the parameters satisfy the following equation:

$$v \lambda^\infty + (\Lambda - j \Omega v) = 0, \text{ or } \gamma^\infty = - \frac{\Lambda}{v} \text{ and } \omega^\infty = \Omega \quad (43)$$

The spectrum is limited only by the internal damping; when $v \equiv 0$, the spectrum is unlimited. The limit of the damped critical speed is equal to the rotor speed Ω .

Case 5. $\Omega \rightarrow \infty$ (rotor speed increases): The characteristic equation takes the form:

$$2\kappa B (\lambda^\infty)^3 + B (2\kappa \mu + v \beta_n^2) (\lambda^\infty)^2 + (B v \mu + 2\kappa) \beta_n^2 \lambda^\infty + v \beta_n^4 = 0 \quad (44)$$

The coefficients of equation (44) are real, and it has real roots or one real and two complex roots. Therefore the spectrum is limited.

Case 5.1. $\Omega \rightarrow \infty$ and $\nu \equiv 0$ (without internal damping): From equation (44) follows the next limiting conditions:

$$\lambda^\infty = 0 \quad \text{or} \quad \lambda^\infty = -\frac{1}{2} \mu \pm \left[\left(\frac{1}{2} \mu \right)^2 - \beta \frac{2}{n} B^{-1} \right]^{1/2} \quad (45)$$

The limitation (45) points out that the "bending motion" of the rotor is impossible as ($\lambda^\infty = 0$). Only "shearing motion" of the rotor is possible. In this limiting case the rotor shear motion can be either periodic or aperiodic. The critical parameter of external damping is given by

$$\mu_{cr}^\infty = 2\beta B^{-1/2} \quad (46)$$

Case 5.2. $\Omega \rightarrow \infty$ and $B \equiv 0$: The limiting conditions can be expressed as

$$\gamma^\infty = -\frac{\nu \beta^2}{2\kappa} \quad \text{and} \quad \omega^\infty = 0 \quad (47)$$

If the internal damping is neglected ($\nu = 0$), then $\lambda^\infty = 0$ and no rotor motion is possible.

From these results it follows that the internal damping taken according to the hypothesis of Voight-Kelvin has a significant influence on the critical and limiting parameters of motion of the rotor. Additionally, internal damping of this type can lead to the unstable aperiodic motion of the rotor. The spectrum of the rotor motion equations always has an infinite number of elements. Damping of the bearing oil film has the same character as the external damping of the rotor, and it should not affect the quantitative results.

CENTER OF ROTOR MOTION

Usually the line of the rotor motion center is a line of static rotor displacement under its weight. However, in the considered physical model, the motion center has an additional component in horizontal direction caused by the internal damping. The equation of the motion center is given by

$$(\Lambda - j\Omega\nu)f'''' = j\zeta e \quad (48)$$

This additional component increases simultaneously with the speed of the rotor. These conclusions are important because the hydrodynamic characteristics of the bearings of a multisupported rotor (statically indeterminate) should be calculated after solving the static problem for the whole rotor, where a misalignment of the bearings has to be taken into consideration. When the multisupported rotor and its supporting construction are relatively rigid, the static effect of the bearing oil film should be taken into consideration. Although that static problem is non-linear, it can be solved by the method of successive linear iterations (ref. 7).

REFERENCES

1. Walczyk, Z.: The Influence of Shearing Forces on Critical Speeds of Rotors of Energy-Plant Machines. Reports of IFFM PAS, Gdańsk, No.: 20/885/77 and 108/1004/81. (In Polish.)
2. Timoshenko, S.: Vibration Problems in Engineering. D. Van Nostrand, 1956.
3. Dimentberg, F.M.: Flexural Vibrations of Rotating Shafts. Publ. of SAS, Moscow, 1959.
4. Tondl, A.: Some Problems of Rotor Dynamic. Publ. House of CAS, Prague, 1965.
5. Bansal, P.N.; and Kirk, R.G.: Stability and Damped Critical Speeds of Rotor-Bearing Systems. Journal of Engineering for Industry, Nov. 1975.
6. Lund, J.W.: Stability and Damped Critical Speeds of a Flexible Rotor in Fluid-Film Bearings. Journal of Engineering for Industry, May 1974.
7. Walczyk, Z.: Forced Vibrations and Motion Stability of Multisupported Turbine Rotors. Report of IFFM PAS, Gdańsk 1976. (In Polish.)

CHANGES OF INSTABILITY THRESHOLDS OF ROTOR DUE TO BEARING MISALIGNMENTS

Helmut Springer and Horst Ecker
Technical University of Vienna
Vienna, Austria

Edgar J. Gunter
University of Virginia
Charlottesville, Virginia 22901

In this paper the influence of bearing misalignment upon the dynamic characteristics of statically indeterminate rotor bearing systems is investigated. Both bearing loads and stability speed limits of a rotor may be changed significantly by magnitude and direction of bearing misalignment. The useful theory of short journal bearings is introduced and simple analytical expressions, governing the misalignment problem, are carried out. Polar plots for the bearing load capacities and stability maps, describing the speed limit in terms of misalignment, are presented. These plots can be used by the designer to estimate deviations between calculation and experimental data due to misalignment effects.

INTRODUCTION

Bearing misalignment and initial shaft bow may considerably change the dynamic characteristics of a rotor bearing system. In general, bearing misalignment and shaft bow represent imperfections of a system with unknown amount which cannot be predicted exactly by the designer. Therefore, a qualitative analysis, investigating the influence of bow and misalignment upon vibration amplitudes, dynamic bearing loads, and stability, etc., of a rotor, might be useful. Also significant deviations between experimental data and theoretical calculations of a rotor bearing system may be caused by bearing misalignments, for example. In this case an error estimation between experiment and calculation, considering the above mentioned imperfections, is necessary.

It is well known from the literature that beside static and dynamic unbalance of a rotor a residual shaft bow may be considered as an additional external force that is exciting the rotor with constant amplitude independent of the speed. If a linearized (first order) analysis is applicable to a system then initial shaft bow and unbalance do not change the stability characteristics of the rotor. In other words, no interactions between self-excited shaft whirl and external excitation can be described by a linear approach; for example, see reference 1. Therefore, in this paper the response of unbalance and shaft bow is not considered, since, in a first order sense, it does not change the onset of instability of the rotor.

Gasch has shown in his paper, see reference 2, that in a statically indeterminate rotor bearing system the static bearing loads depend upon the speed of the shaft because of nonlinear hydrodynamic bearing characteristics. Nasuda and Hori, reference 3, investigated the influence of journal bearing misalignment upon the stability characteristics. They determined so-called "contour stability maps" for a two-mass and four-bearing rotor.

In this paper the theory of short journal bearings is used, see reference 4, in order to calculate bearing loads, bearing stiffness and damping coefficients, and stability thresholds of a flexible rotor in terms of bearing misalignment. Both, magnitude and direction of the misalignment vector of a bearing are varied and ranges of high and low sensitivity of the stability limit can be observed.

NOMENCLATURE

[A]	dynamical matrix ($1/s^2$)	L	bearing length (m)
b	magnitude of initial shaft bow (m)	λ	misalignment attitude angle (direction of misalignment with respect to vertical x-axis) (rad)
β	phase angle of initial shaft bow (rad)	m	magnitude of misalignment (m)
C	radial bearing clearance (m)	m_x, m_y	misalignment components in x- and y-direction, resp. (m)
[C _B]	bearing damping matrix (Ns/m)	[M]	mass matrix (kg)
[C _E]	external damping matrix (Ns/m)	μ	dynamic viscosity of bearing lubricant (Ns/m^2)
[C _I]	internal damping matrix (Ns/m)	N^+	stability speed limit (Hz)
ϵ	bearing eccentricity to clearance ratio	ω	angular speed of shaft (1/s)
η	horizontal shaft displacement to clearance ratio	ψ	shaft center attitude angle (rad)
{F _O }	external static load (N)	R	radius of the shaft at a bearing station (m)
{F _B }	dynamic bearing load (N)	S = $\frac{\mu\omega L^3 R}{4\pi C^2 F_{Bo}}$	Sommerfeld number
{F _{Bo} }	static bearing load capacity (N)	σ	eigenvalue (1/s)
ϕ	bearing load attitude angle (rad)	t	time (s)
[I]	identity matrix	{U}	unbalance vector (kgm)
[K _B]	bearing stiffness matrix (N/m)	W	total weight of the rotor (N)
[K _I]	stiffness matrix due to internal damping (N/m)	{z}	shaft displacement vector (m)
[K _S]	shaft stiffness matrix (N/m)	{u}	eigenvector
κ	misalignment to clearance ratio		
ξ	vertical shaft displacement to clearance ratio		

Subscripts

B bearing
 f,l first and last bearing station, respectively
 j station number ($1 \leq j \leq n$)
 n total number of shaft stations
 o static load conditions
 x,y vertical and horizontal direction, respectively

Superscripts

T transposition of a matrix or column vector

Brackets

{ } column vector
 [] matrix
 () function of

EQUATIONS OF MOTION

Various definitions of bearing misalignments can be introduced for a rotor-bearing system. For example, in figure 1, lateral displacements of the bearings are measured with respect to a line that is connecting the centers of the outer bearings (i.e. first and last bearing). Beside lateral bearing misalignment slope misalignment of the bearing axis may occur in practice but is neglected in this paper. Also slope deviations between shaft axis and bearing axis are not considered in this investigation. Therefore, at least three bearings have to be present in order to get a statically indeterminate system that exhibits misalignment effects.

Initial shaft bow, for example, can be measured in a "non-assembled" strain-free configuration of the shaft where shaft centers and bearing centers at the first and the last bearing station coincide, see figure 1. In general, for an n-stations shaft the lateral misalignment vector is defined as

$$\{m\} = \{0, \dots, 0, m_{f+1} \cos \lambda_{f+1}, \dots, m_{1-1} \cos \lambda_{1-1}, 0, \dots, 0\} \\ \{0, \dots, 0, m_{f+1} \sin \lambda_{f+1}, \dots, m_{1-1} \sin \lambda_{1-1}, 0, \dots, 0\}^T \quad (1)$$

The magnitude of misalignment m_j for a "no-bearing" station j is defined to zero. Initial shaft bow is given by

$$\{b(t)\} = \{b_1 \cos(\omega t + \beta_1), \dots, 0, \dots, b_j \cos(\omega t + \beta_j), \dots, 0, \dots, b_n \cos(\omega t + \beta_n)\} \\ \{b_1 \sin(\omega t + \beta_1), \dots, 0, \dots, b_j \sin(\omega t + \beta_j), \dots, 0, \dots, b_n \sin(\omega t + \beta_n)\}^T \quad (2)$$

in terms of the shaft rotational angle ωt , see figure 1. If internal and external damping forces are considered and gyroscopic forces are neglected then the equations of motion of the rotor-bearing system can be written in the form

$$[M]\{\ddot{z}\} + [C_E + C_I]\{\dot{z}\} + [K_S + K_I]\{z\} = \\ = \{F_o\} + [K_S]\{b(t)\} + \omega^2\{U(t)\} + \{F_B(\{z-m\}, \{\dot{z}\}, \omega)\} \quad (3)$$

where $\{z\} = \{x_1, \dots, x_n | y_1, \dots, y_n\}^T$ is a column vector containing lateral (vertical and horizontal) displacements of the shaft at n stations, see reference 1. A Taylor-expansion of equation (3) with respect to the nonlinear bearing forces $\{F_B\}$ is convergent if the static preload $\{F_0\}$ is sufficiently high compared with unbalance and shaft bow excitation forces. Under this assumption an expansion leads to

$$[K_S + K_I]\{z_0\} - \{F_{B0}(\{z_0 - m\}, \{0\}, \omega)\} - \{F_0\} = \{0\} \quad (4)$$

and

$$\begin{aligned} [M]\{\ddot{z}_1\} + [C_E + C_I + C_B(\{m\}, \omega)]\{\dot{z}_1\} + [K_S + K_I(\omega) + K_B(\{m\}, \omega)]\{z_1\} = \\ = [K_S]\{b(t)\} + \omega^2\{U(t)\} \end{aligned} \quad (5)$$

with $\{z\} = \{z_0\} + \{z_1(t)\}$ being the "first order" solution of equation (3). The stationary part $\{z_0\} = \{z_0(\{F_0\}, \{m\}, \omega)\}$ of this solution is evaluated from the nonlinear system equations (4), with $\omega = \text{const.} \neq 0$ being the angular speed of the shaft. The stability of $\{z_0\}$ is governed by the linear system of differential equations (5) with initial shaft bow and unbalance being set to zero.

Note that first order stiffness and damping characteristics of the bearings, $[C_B]$ and $[K_B]$ respectively, depend upon the stationary solution $\{z_0(\{F_0\}, \{m\}, \omega)\}$. Therefore, the rotor's stability limit depends upon bearing misalignment $\{m\}$ and is not influenced by the shaft bow $\{b\}$ as long as the above expansion converges.

BEARING CHARACTERISTICS

Static load capacity

The static load capacity $\{F_{B0}\}$ of the bearings is evaluated by employing the theory of short journal bearings, see reference 4 and figure 2. For a single bearing, located at station j , the static bearing load components in the vertical x - and the horizontal y -direction can be written in the form

$$\begin{Bmatrix} F_{Box} \\ F_{Boy} \end{Bmatrix} = \frac{\omega(\mu L^3 R)}{2C^2} \begin{Bmatrix} \xi_{oj}^{-\kappa_j} \cos \lambda_j & | & -\eta_{oj} + \kappa_j \sin \lambda_j \\ \hline \eta_{oj}^{-\kappa_j} \sin \lambda_j & | & \xi_{oj}^{-\kappa_j} \cos \lambda_j \end{Bmatrix} \begin{Bmatrix} \frac{-2\varepsilon_{oj}}{(1-\varepsilon_{oj}^2)^2} \\ \hline \frac{\pi}{2(1-\varepsilon_{oj}^2)^{3/2}} \end{Bmatrix} \quad (6)$$

where

$$\varepsilon_{oj} = \sqrt{(\xi_{oj}^{-\kappa_j} \cos \lambda_j)^2 + (\eta_{oj}^{-\kappa_j} \sin \lambda_j)^2} \quad (7)$$

is the local bearing eccentricity ratio at station j and $\xi_{oj} = x_{oj}/C_j$, $\eta_{oj} = y_{oj}/C_j$, and $\kappa_j = m_j/C_j$ are local static shaft displacement and bearing misalignment to bearing clearance ratios, respectively. Substituting equation (6) for each bearing into

equation (4) yields a nonlinear system of relations to be solved numerically for the static displacement vector $\{z_0\} = \{x_{01}, \dots, x_{0n} | y_{01}, \dots, y_{0n}\}^T$.

Bearing stiffness and damping characteristics

Once the stationary solution of the rotor at $\omega = \text{const.} \neq 0$ is determined for a given misalignment $\{m\}$, local bearing stiffness and damping matrices can easily be evaluated for a bearing at station j from

$$[K_{Bj}] = \frac{\omega}{2} \left(\frac{\mu L^3 R}{C^3} \right)_j [T_j] \begin{bmatrix} \frac{4\epsilon_{oj}(1+\epsilon_{oj}^2)}{(1-\epsilon_{oj}^2)^3} & \frac{\pi}{2(1-\epsilon_{oj}^2)^{3/2}} \\ -\frac{\pi(1+2\epsilon_{oj}^2)}{2(1-\epsilon_{oj}^2)^{5/2}} & \frac{2\epsilon_{oj}}{(1-\epsilon_{oj}^2)^2} \end{bmatrix} [T_j]^T \quad (8)$$

and

$$[C_{Bj}] = \frac{1}{2} \left(\frac{\mu L^3 R}{C^3} \right)_j [T_j] \begin{bmatrix} \frac{\pi(1+2\epsilon_{oj}^2)}{(1-\epsilon_{oj}^2)^{5/2}} & \frac{-4\epsilon_{oj}}{(1-\epsilon_{oj}^2)^2} \\ \frac{-4\epsilon_{oj}}{(1-\epsilon_{oj}^2)^2} & \frac{\pi}{(1-\epsilon_{oj}^2)^{3/2}} \end{bmatrix} [T_j]^T \quad (9)$$

respectively, with $\epsilon_{oj} \neq 0$ and

$$[T_j] = \frac{1}{\epsilon_{oj}} \begin{bmatrix} \xi_{oj}^{-\kappa_j} \cos \lambda_j & -\eta_{oj}^{+\kappa_j} \sin \lambda_j \\ \eta_{oj}^{-\kappa_j} \sin \lambda_j & \xi_{oj}^{-\kappa_j} \cos \lambda_j \end{bmatrix} \quad (10)$$

being an orthogonal transformation matrix between a local r-t-reference frame of the bearing j and the global x-y-system, see figure 2. As an example, in figure 3a and 3b, respectively, dimensionless first order stiffness and damping coefficients for the short journal bearing are shown in terms of the Sommerfeld number. The load attitude angle ϕ is chosen to be zero in this example, i.e. the direction of the static load coincides with the global (vertical) x-axis. For any other arbitrary load direction equations (8) and (9) have to be applied.

STABILITY

After substituting the local bearing stiffness and damping matrices into the global matrices of equation (5) the corresponding eigenvalue problem

$$[A - \sigma I] \{u\} = \{0\} \quad (11)$$

can be solved for σ as a function of the rotor angular speed ω and the bearing misalignment vector $\{m\}$. The dynamical matrix $[A]$ is of dimension $2n \times 2n$ and is given by

$$[A(\{m\}, \omega)] = \left[\begin{array}{c|c} [0] & [I] \\ \hline -[M]^{-1}[K_S + K_I(\omega)] & -[M]^{-1}[C_E + C_I] \\ -[M]^{-1}[K_B(\{m\}, \omega)] & -[M]^{-1}[C_B(\{m\}, \omega)] \end{array} \right] \quad (12)$$

EXAMPLE

Figure 4 shows a symmetric five stations rotor with three short journal bearings and two major masses mounted on a flexible shaft. The data for this rotor are listed in Table 1. The center bearing of the system may be misaligned with respect to the outer bearings by m_x and m_y in a vertical and horizontal direction, respectively. The numerical calculations for this example were carried out on the main frame computer CDC-CYBER 170/730 of the Technical University of Vienna, Austria. The nonlinear equation solver ZSPOW and the eigenvalue solver EIGRF of the IMSL-computer library were used.

Figure 5 shows the static load ratio of the center bearing in terms of the shaft speed. The horizontal misalignment m_y is kept zero while the vertical misalignment m_x is varied. It can be seen that each curve in figure 5 approaches the stability threshold at a certain speed of the rotor. The bearing load gradient is high at low speeds and decreases with increasing speed. The stability threshold is increasing with increasing misalignment above $12 \mu\text{m}$ and below $-5 \mu\text{m}$ in this example. In general, the center bearing load ratio in figure 5 is increasing with increasing speed except within a small range of misalignments between $(-30 \mu\text{m} \leq m_x \leq -15 \mu\text{m})$ at low speeds. A similar diagram can be drawn for the outer bearing load ratios. Note that these bearing load characteristics might change with changes in the shaft bending stiffness and the bearing clearances. Also, in practice, the misalignment attitude angle λ is unknown and different from zero. Therefore, the influence of both $m_x \neq 0$ and $m_y \neq 0$ upon bearing loads and stability limits has to be studied.

Figure 6 shows polar plots for the bearing load ratios with the rotor speed kept constant at $N=200$ Hz. Curves of constant magnitudes of misalignment are drawn in a plane where the polar angle indicates the direction of misalignment (attitude angle λ) and the radius is the bearing load ratio, i.e. at constant radii the bearing loads are constant and at constant polar angles the ratio m_y/m_x is constant. At zero misalignment the load ratios of both center and outer bearings are constant. Hence, the curves

$m=0$ represent circles with constant bearing loads. For increasing magnitudes of misalignment the bearing load ratios change substantially with the direction of misalignment λ . For example, if a misalignment of $10\ \mu\text{m}$ is present in the system, (i.e. 40% of the center bearing clearance or $1/24000$ of the outer bearing span) then the center bearing load ratio varies between 0.2 at $\lambda=25^\circ$ and 1.09 at $\lambda=225^\circ$. A corresponding change for the outer bearing can be seen on the right hand side of figure 6.

It is to expect that for misalignment directions that cause low bearing loads in the system the stability speed limit of the rotor is decreased also. This can be observed from figure 7, showing a polar plot of the stability limits of the present rotor. The polar angle in this diagram again indicates the direction of misalignment λ while the radius now is the stability speed limit. Curves of constant misalignment magnitudes are drawn in the figure. For low misalignments up to $m=12\ \mu\text{m}$ and for attitude angles of about $\lambda=20^\circ$ and $\lambda=220^\circ$ the stability limits tip down significantly. For example, if $m=10\ \mu\text{m}$, then the stability limit of the rotor changes between $N^+=275\ \text{Hz}$ and $N^+=365\ \text{Hz}$. Within the ranges of ($180^\circ \leq \lambda \leq 250^\circ$) and ($0 \leq m \leq 12\ \mu\text{m}$) a high sensitivity of the stability speed limit with respect to the direction of misalignment can be observed.

Stability maps and polar plots as discussed above give a complete information to the designer and make it possible for him to estimate misalignment effects upon the stability thresholds and the bearing load capacities of a given rotor.

CONCLUSION

The theory of short journal bearings makes it possible to formulate the misalignment problem of statically indeterminate rotor bearing systems in a simple and easy manner. The numerical effort to carry out bearing loads and stability limits in terms of misalignment is comparatively low even for a multi-station rotor supported by a multi-bearing system. There are a number of good and reliable algorithms available in various computer libraries to solve the governing equations of the problem. Since magnitude and direction of bearing misalignment are never exactly known in a real system the above presented theory is sufficiently accurate for practical applications and can be used by the designer in order to make a good estimation on whether or not a certain amount of bearing misalignment might dynamically endanger or damage a rotating machinery. Also the above results may explain deviations between experimental data and predictions where misalignment effects were not included.

REFERENCES

1. Springer, H., Ecker, H., Gunter, E.J.: Nonlinear Unbalance Response and Stability Thresholds of a Warped Multimass Rotor in Misaligned Bearings. Proceedings of Third Int. Conf. on Vibrations in Rotating Machinery. The Inst. of Mech. Eng., London, 1984, p.499-506.
2. Gasch, R.: Berechnung der Lagerlasten mehrfach gleitgelagerter Rotoren unter Berücksichtigung des nichtlinearen Verhaltens des Ölfilms. Konstruktion, 22, 1970, p.229-235 (in German).

ORIGINAL PAGE IS
OF POOR QUALITY

DIMENSIONLESS BEARING STIFFNESS AND DAMPING CHARACTERISTICS
FOR THE SHORT JOURNAL BEARING
(Load attitude angle $\phi = 0^\circ$)

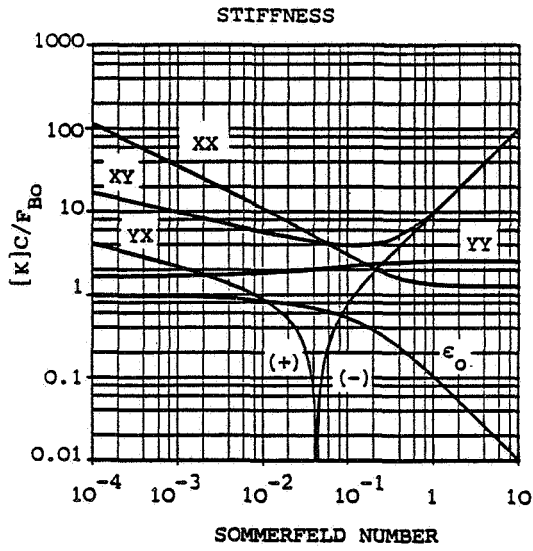


Figure 3a.

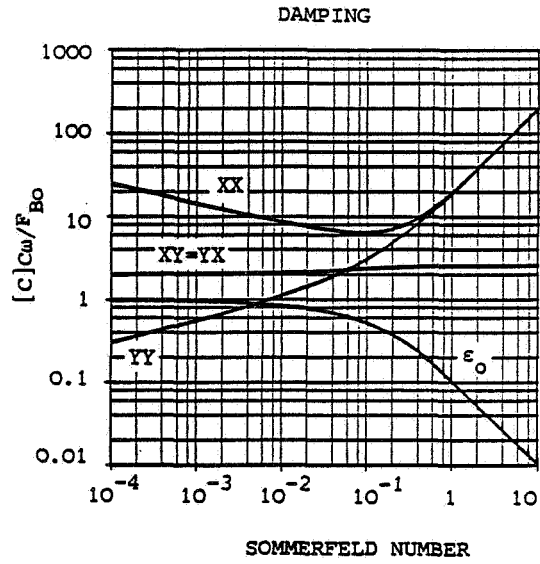


Figure 3b.

SYMMETRIC ROTOR BEARING SYSTEM
WITH MISALIGNMENT

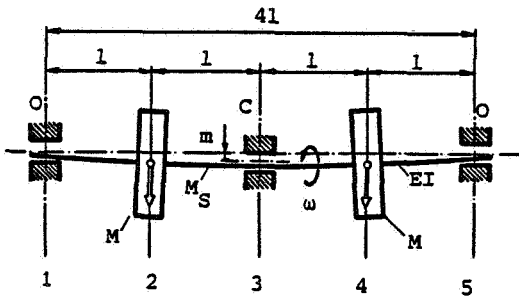


Figure 4.

CENTER BEARING LOAD RATIO VS.
SHAFT SPEED FOR VARIOUS VERTICAL
MISALIGNMENTS m_x

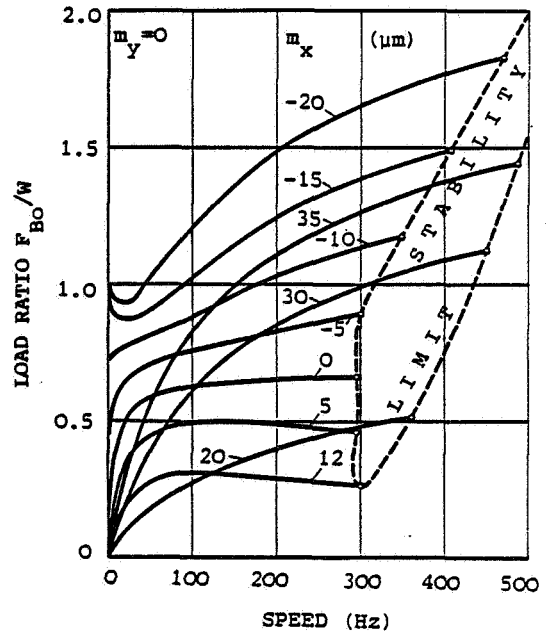


Figure 5.

BEARING LOAD RATIOS F_B/W IN TERMS OF MISALIGNMENT ATTITUDE
 ANGLE λ AND MISALIGNMENT MAGNITUDE M
 (Rotor speed $N = 200$ Hz)

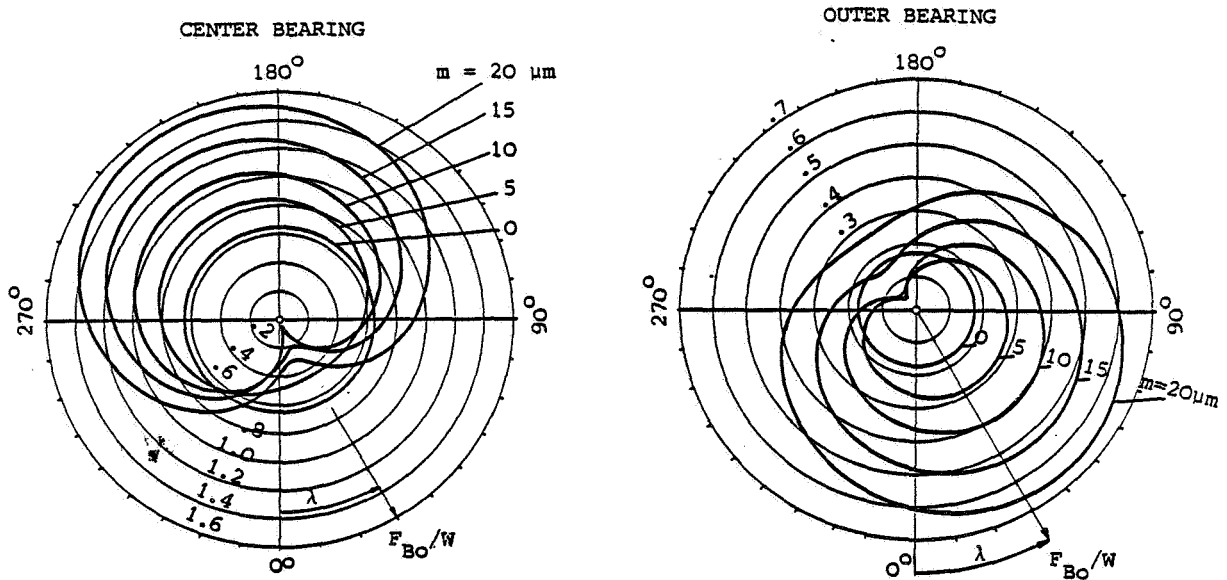


Figure 6.

STABILITY SPEED LIMITS N^+ IN
 TERMS OF MISALIGNMENT ATTITUDE
 ANGLE λ AND MISALIGNMENT MAGNI-
 TUDE M

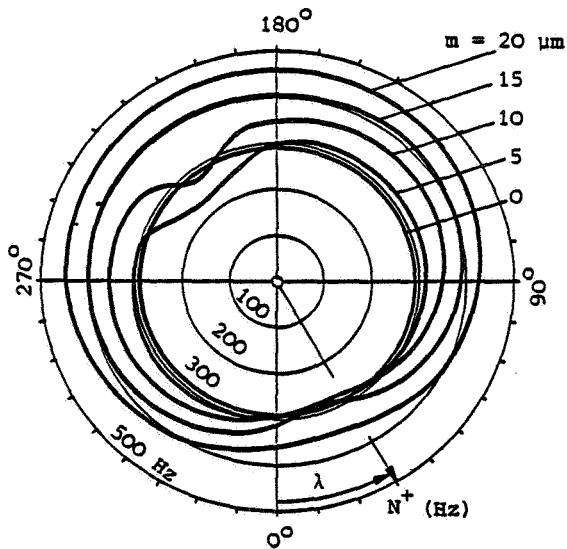


Figure 7.

DATA OF THE ROTOR BEARING SYSTEM
 AS SHOWN IN FIGURE 4

Total mass of the rotor	16.8 kg	
Shaft bending stiffness	3350 Nm ²	
Outer bearing span	240 mm	
BEARING DATA	CENTER	OUTER
Length	15 mm	7.5 mm
Diameter	25 mm	12.5 mm
Radial clearance	25 micrometers	15 micrometers
Lubricant viscosity	0.01 Ns/m ²	

Table 1.

**DEMONSTRATION OF VARIOUS ROTOR INSTABILITIES (EXHIBIT OF BENTLY ROTOR DYNAMICS
RESEARCH CORPORATION LABORATORY RIGS AT SYMPOSIUM ON INSTABILITY
IN ROTATING MACHINERY)**

**Agnes Muszynska
Bently Rotor Dynamics Research Corporation
Minden, Nevada 89423**

The following papers describe the operation of rotor rigs used at the symposium exhibit to demonstrate various instability phenomena occurring in rotating machines. The instability phenomena demonstrated included oil whirl/whip (fig. 1), antiscrub (fig. 2), rub (fig. 3), loose rotating parts (fig. 4), water-lubricated bearing instabilities (fig. 5), and cracked shaft (fig. 6). The rotor rigs were also used to show corrective measures for preventing instabilities. Vibrational response data from the rigs were taken with modern, computerized instrumentation.

The rotor nonsynchronous perturbation rig demonstrated modal identification techniques for rotor/bearing systems (fig. 7). Computer-aided data acquisition and presentation, using the dynamic stiffness method, makes it possible to identify rotor and bearing parameters for low modes.

The shaft mode demonstrator (fig. 8) presented the amplified modal shape line of the shaft excited by inertia forces of unbalance (synchronous perturbation). The first three bending modes of the shaft can be demonstrated.

The user-friendly software, "Orbits," presented a simulation of rotor precessional motion that is characteristic of various instability phenomena.

The data presentation demonstration used data measured on a turbine-driven compressor train as an example of how computer-aided data acquisition and presentation assists in identifying rotating machine malfunctions.

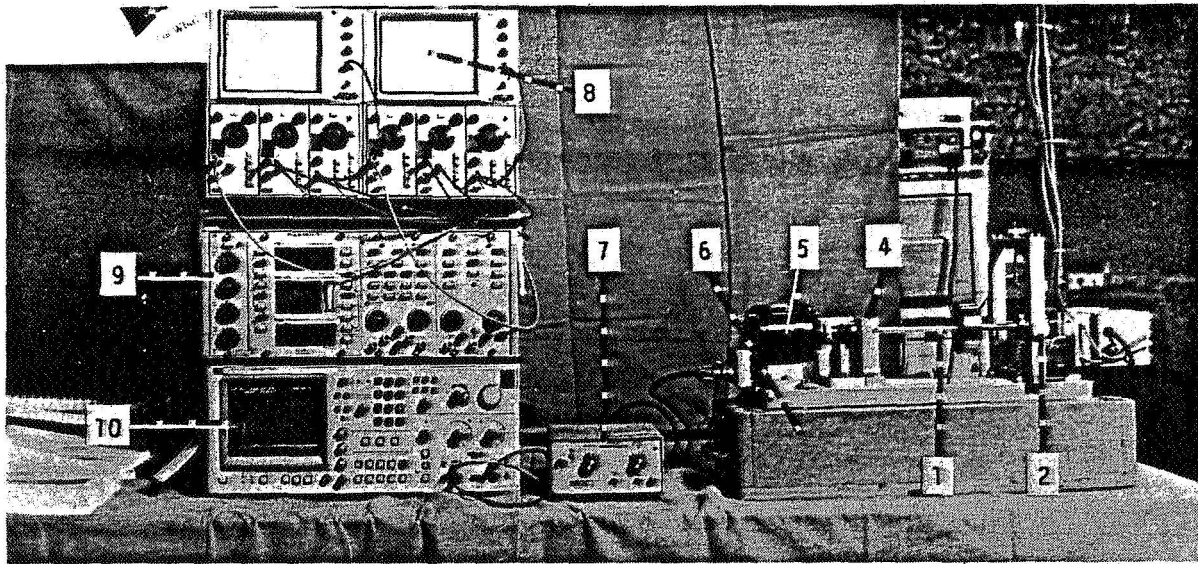


Figure 1. Oil Whirl/Whip Demonstration. 1 -- Rotor, 2 -- Oil Lubricated Cylindrical bearing, 3 -- Oil Tank, 4 -- Rigid Bearing, 5 -- Electric Motor, 6 -- Concrete Base, 7 -- Speed Controller, 8 -- Oscilloscope, 9 -- Digital Vector Filter DVF 2, 10 -- Spectrum Analyzer.

ORIGINAL PAGE IS
OF POOR QUALITY

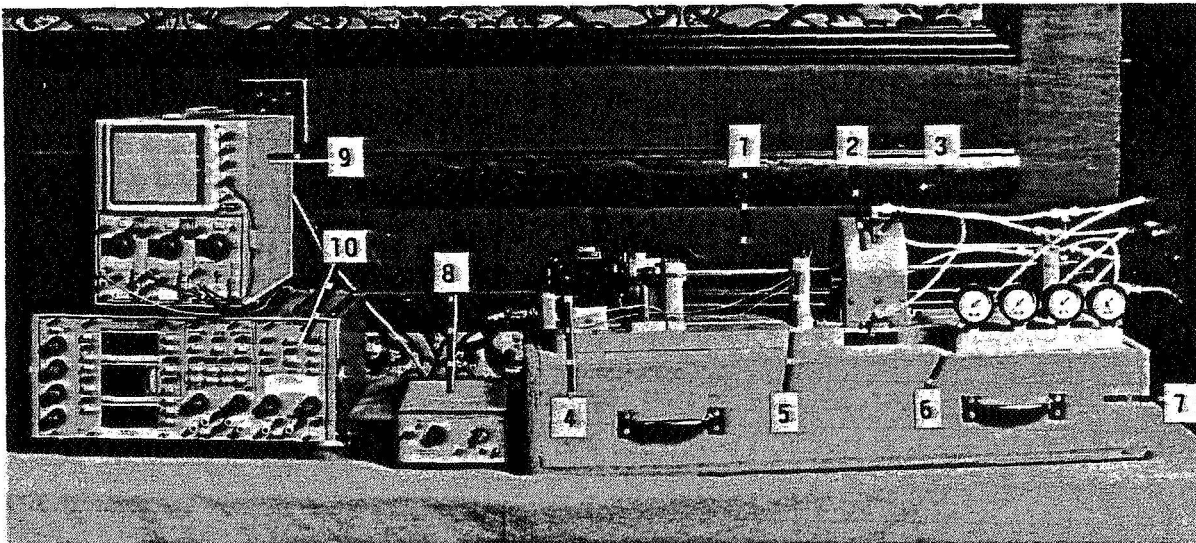


Figure 2. Anti-Swirl Demonstrator. 1 -- Rotor, 2 -- Seal, 3 -- Air Jet, 4 -- Electric Motor, 5 -- Proximity Probes, 6 -- Manometers, 7 -- Concrete Base, 8 -- Speed Controller, 9 -- Oscilloscope, 10 -- Digital Vector Filter DVF 2.

ORIGINAL PAGE IS
OF POOR QUALITY

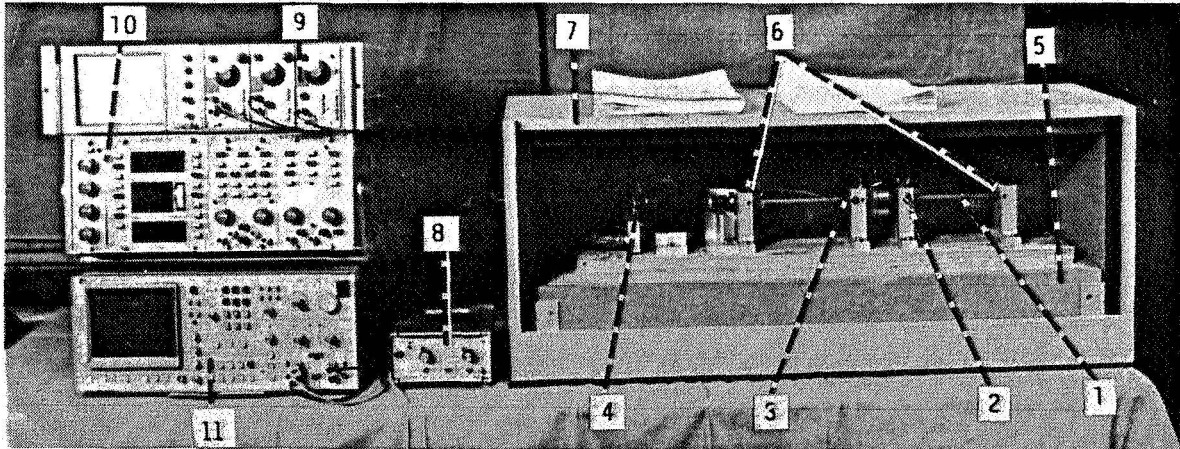


Figure 3. Partial Rotor-to-Stator Rub Demonstration. 1 -- Shaft, 2 -- Brass Screw Generating Rub, 3 -- X-Y Displacement Proximity Probes, 4 -- Electric Motor, 5 -- Concrete Base, 6 -- Rigid Bearings, 7 -- Acoustic Insulation Box, 8 -- Speed Controller, 9 -- Oscilloscope, 10 -- Digital Vector Filter DVF 2, 11 -- Spectrum Analyzer.

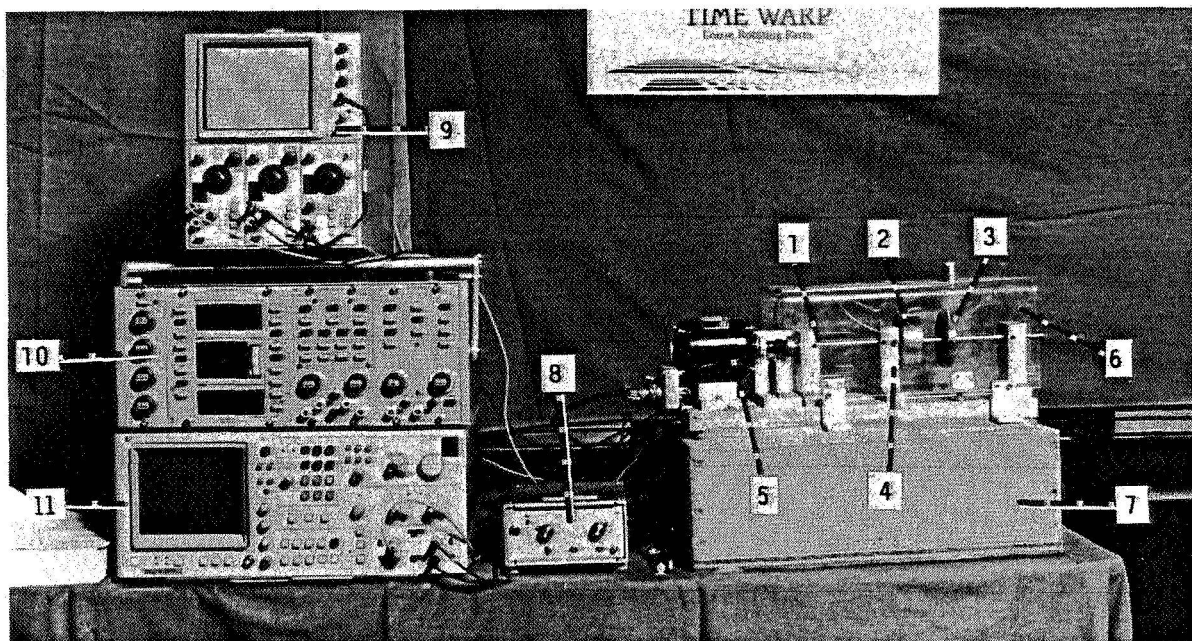


Figure 4. Loose Rotating Part Instability Demonstration. 1 -- Rotor, 2 -- Fixed Disk, 3 -- Loose Disk, 4 -- X-Y Displacement Proximity Probes, 5 -- Electric Motor, 6 -- Protection Guard, 7 -- Concrete Base, 8 -- Speed Controller, 9 -- Oscilloscope, 10 -- Digital Vector Filter DVF 2, 11 -- Spectrum Analyzer.

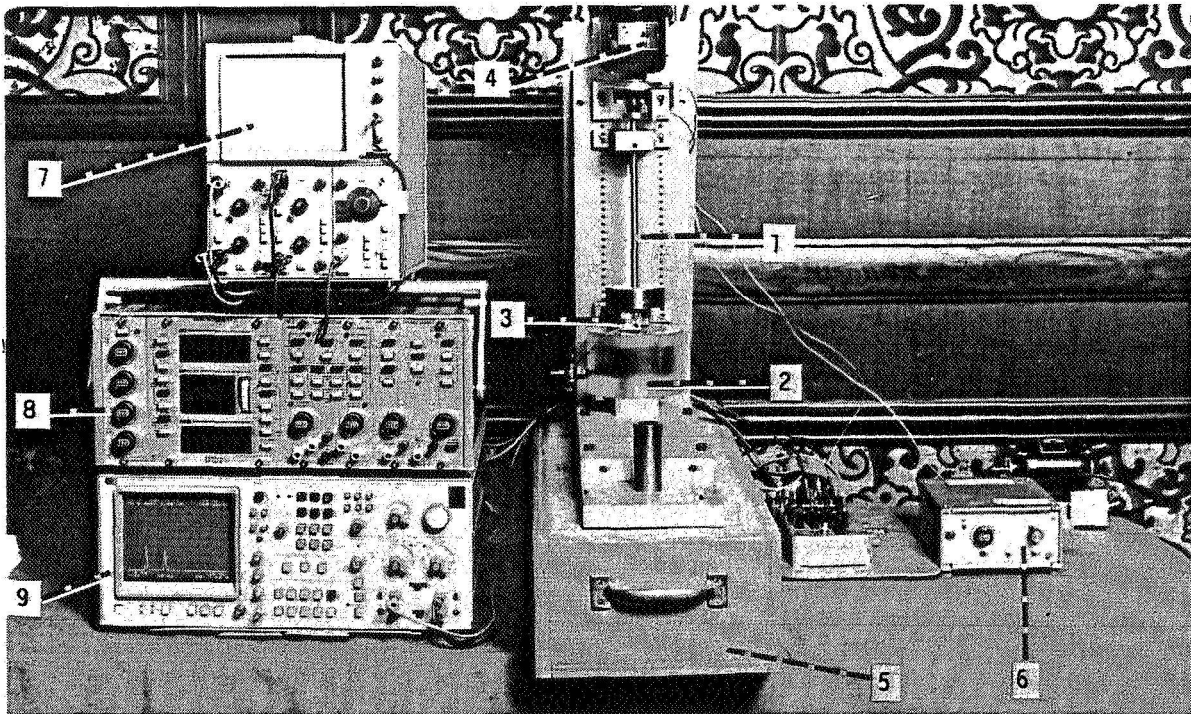


Figure 5. Rotor with Rubber-Lined Water-Lubricated Bearing Demonstrating Instabilities in Fluid Flow Machines. 1 -- Rotor, 2 -- Rubber-Lined Water-Lubricated Bearing, 3 -- X-Y Displacement Proximity Probes, 4 -- Electric Motor, 5 -- Concrete Base, 6 -- Speed Controller, 7 -- Oscilloscope, 8 -- Digital Vector Filter DVF 2, 9 -- Spectrum Analyzer.

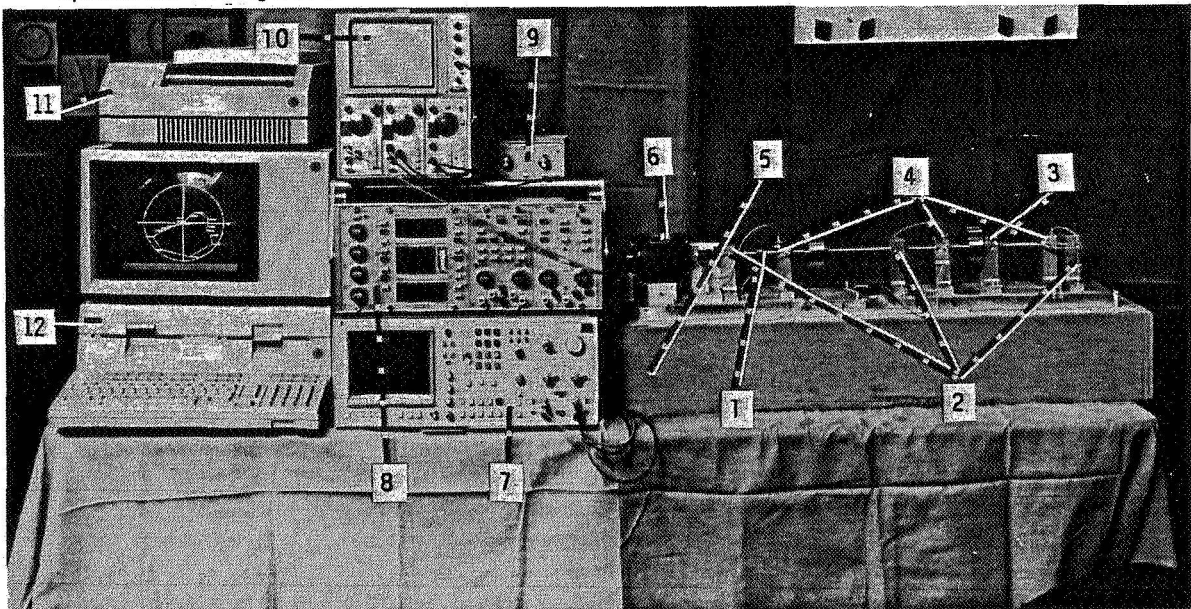


Figure 6. Cracked Shaft Demonstrator. 1 -- Rotor, 2 -- Bearings, 3 -- Safety Guard, 4 -- X-Y Displacement Non-contacting Probes, 5 -- Concrete Base, 6 -- Electric Motor, 7 -- Spectrum Analyzer, 8 -- Digital Vector Filter DVF 2, 9 -- Speed Controller, 10 -- Oscilloscope, 11 -- Printer/Plotter, 12 -- Hewlett Packard 9836C Computer.

ORIGINAL PAGE IS
OF POOR QUALITY

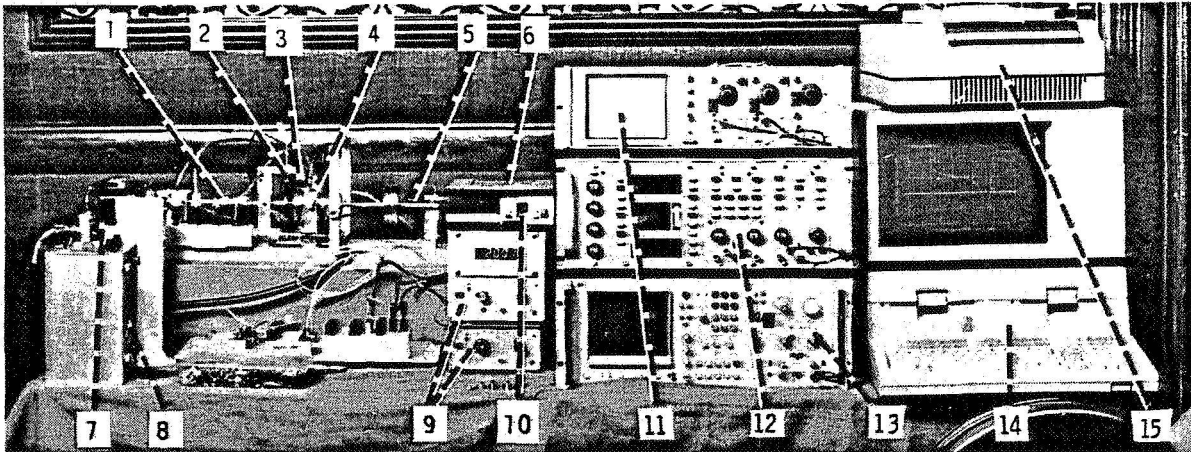


Figure 7. Laboratory Rig Demonstrating Identification of Rotor/Bearing Parameters by Perturbation Testing. 1 -- Perturbation Rotor, 2 -- Keyphasor Probe, 3 -- Oil Lubricated Bearing, 4 -- X-Y Proximity Probes, 5 -- Main Rotor, 6 -- Main Electric Motor, 7 -- Perturbation Electric Motor, 8 -- Pressure Controller, 9 -- Speed Controller, 10 -- Thermometer, 11 -- Oscilloscope, 12 -- Digital Vector Filter DVF 2, 13 -- Spectrum Analyzer, 14 -- Hewlett Packard 9836C Computer, 15 -- Printer/Plotter

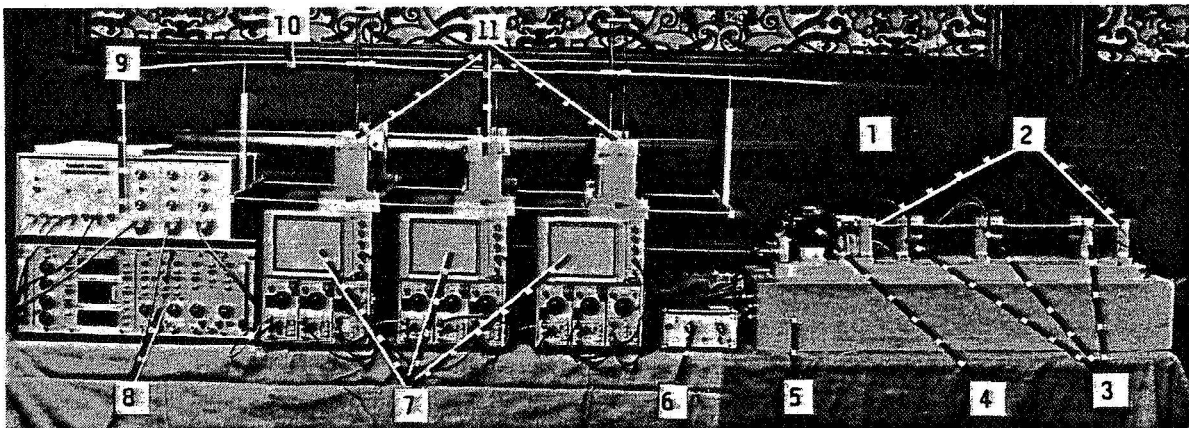


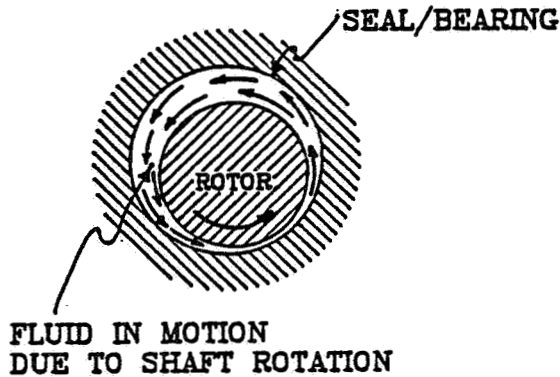
Figure 8. Shaft Bow Mode Demonstrator. 1 -- Rotor with Three Disks, 2 -- Rigid Bearings, 3 -- X-Y Proximity Probes, 4 -- Electric Motor, 5 -- Concrete Base, 6 -- Speed Controller, 7 -- Oscilloscope, 8 -- Digital Vector Filter DVF 2, 9 -- Amplifier, 10 -- Elastic Rod Demonstrating Shaft Bow, 11 -- Servomechanism Translating 1v Amplitudes and Frequencies (Polar Coordinates) of the Vertical Signals into Vertical and Horizontal Motion (Cartesian Coordinates) of the Rod Supports.

09868

WHIRL/WHIP DEMONSTRATION

Robert Grissom
Bently Nevada Corporation
Minden, Nevada 89423

Fluid flow in bearings and seals, set in motion by shaft rotation (Figure 1), generates dynamic forces which may result in a well-recognized instability known as whirl and whip. These are lateral, forward precessional, self-excited, subsynchronous vibrations in which the amplitude may vary from very small to nearly the limit of the bearing or seal clearances. Oil whirl in lubricated bearings, in particular, typically occurs at somewhat less than half rotative speed. As the rotative speed increases, the frequency relationship remains constant until the whirl frequency approaches the first balance resonance. Now the whirl is smoothly replaced by whip at a nearly constant frequency asymptotically approaching first balance resonance, independent of increasing rotative speed. Changes in bearing/seal radial loading can permit, prevent, or eliminate this instability.



SOURCE OF INSTABILITY!

Figure 1. - Bearing/seal fluid-generated instability.

OBJECTIVE

The oil whirl/whip rig demonstrates the effects of fluid dynamic forces generated by the rotating shaft. At low rotative speeds, this produces changes of the journal static equilibrium position within the bearing. The demonstrator shows the relationship between any load direction and the average journal equilibrium position (attitude angle) (Figure 2). At higher rotative speeds, the instability threshold is observed as a function of unidirectional radial load, unbalance, and rotor configuration.

PRECEDING PAGE BLANK NOT FILMED

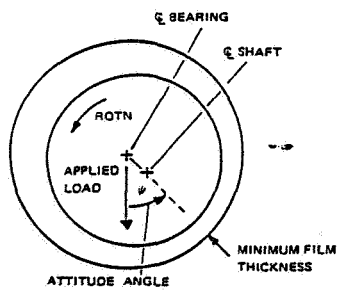


Figure 2. - Attitude angle between load direction and average journal equilibrium position.

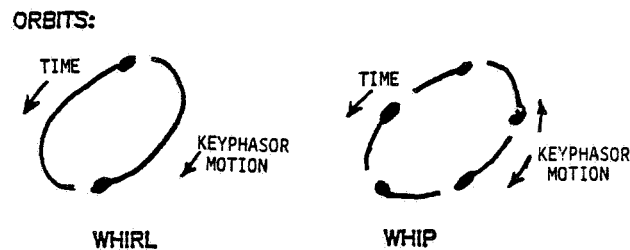


Figure 3. - Oscilloscope presentation of oil whirl and oil whip orbital motion (vibration precession) of journal, combined with once-per-turn reference (keyphasor) signal. Keyphasor marks may move forward or backward relative to time depending on ratio of vibration frequency to rotative speed.

speed.

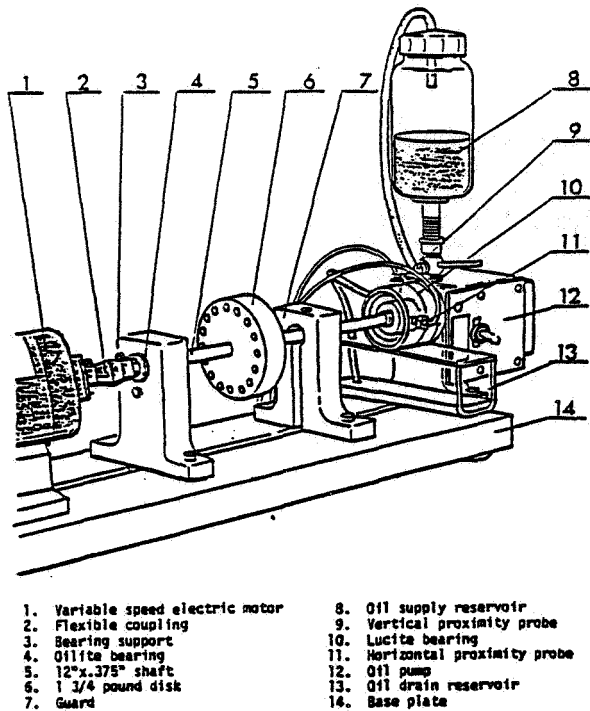
The fixed relationship between oil whirl frequency and rotative speed, as well as the transition to oil whip at a frequency slightly below the first balance resonance frequency, may be observed on the oscilloscope (Figure 3) and spectrum analyzer. Note the distinctive oscilloscope orbit pattern of the two Keyphasor marks slowly rotating counter to time direction (stroboscopic effect) during oil whirl and the multiple Keyphasor marks during oil whip (variable frequency ratios).

ROTOR RIG

The rotor rig consists of a single disk rotor supported in an Oilite (oil impregnated, sintered bronze) bearing at the inboard end and an oil lubricated Lucite journal bearing at the outboard end. The journal is 0.980" in diameter with 0.006" to 0.013" diametrical clearance. Oil is gravity fed through an axial groove (Figure 4).

The disk may be positioned anywhere along the shaft to modify the stiffness. Radial loading of the journal bearing may be controlled with horizontal and vertical springs or a nylon stick (Figure 5).

The rotor is driven by a variable speed (0-12,000 rpm) electric motor through a flexible coupling.



- | | |
|----------------------------------|--------------------------------|
| 1. Variable speed electric motor | 8. Oil supply reservoir |
| 2. Flexible coupling | 9. Vertical proximity probe |
| 3. Bearing support | 10. Lucite bearing |
| 4. Oilite bearing | 11. Horizontal proximity probe |
| 5. 12"x.375" shaft | 12. Oil pump |
| 6. 1 3/4 pound disk | 13. Oil drain reservoir |
| 7. Guard | 14. Base plate |

ORIGINAL PAGE IS
OF POOR QUALITY

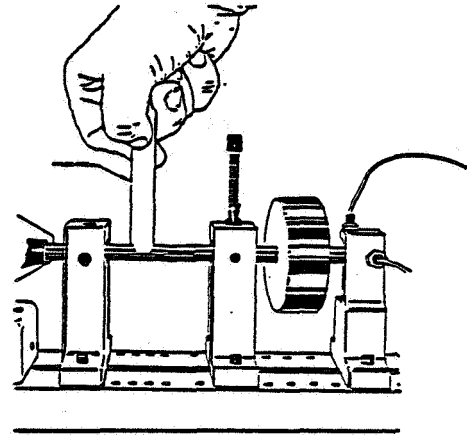


Figure 4. - Rotor rig for demonstrating oil whirl/whip. Figure 5. - Application of preload with nylon stick.

INSTRUMENTATION

X-Y proximity probes located at the journal bearing provide position and vibration information for the orbit and time base display on the oscilloscope. The Digital Vector Filter (DVF 2), an automatic or manually tuned bandpass filter, displays rotative speed, amplitude, and phase. An FFT spectrum analyzer generates a frequency domain display.

MEASUREMENT PARAMETERS

The parameters of interest are:

- Rotor equilibrium position and vibration measured at the journal.
- Average oil swirling ratio, λ .
- Oil whip frequency.
- Direction of vibration precession.
- Change in threshold of stability with changes in disk position and unbalance (two additional stability thresholds).
- Relative radial load changes (magnitude and direction) to stabilize or destabilize system.

RESULTS

Figures 6 through 15 illustrate the transition from whirl to whip and the effect of unbalance force on the whirl threshold. The vibration mode shape for whirl and whip and variations in stability threshold with rotor configuration are also shown.

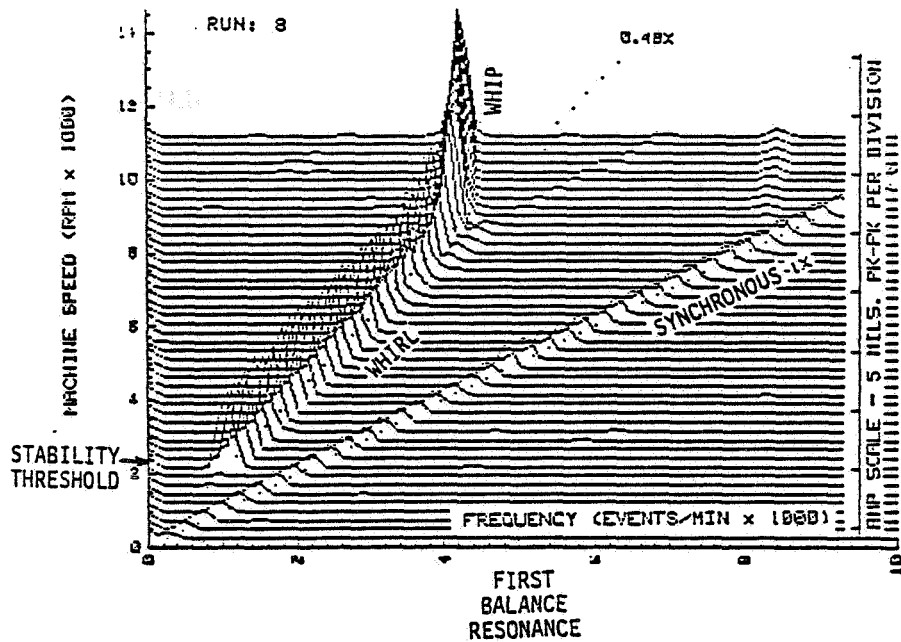


Figure 6. - Cascade spectrum of vertical vibration response during startup with well-balanced rotor.

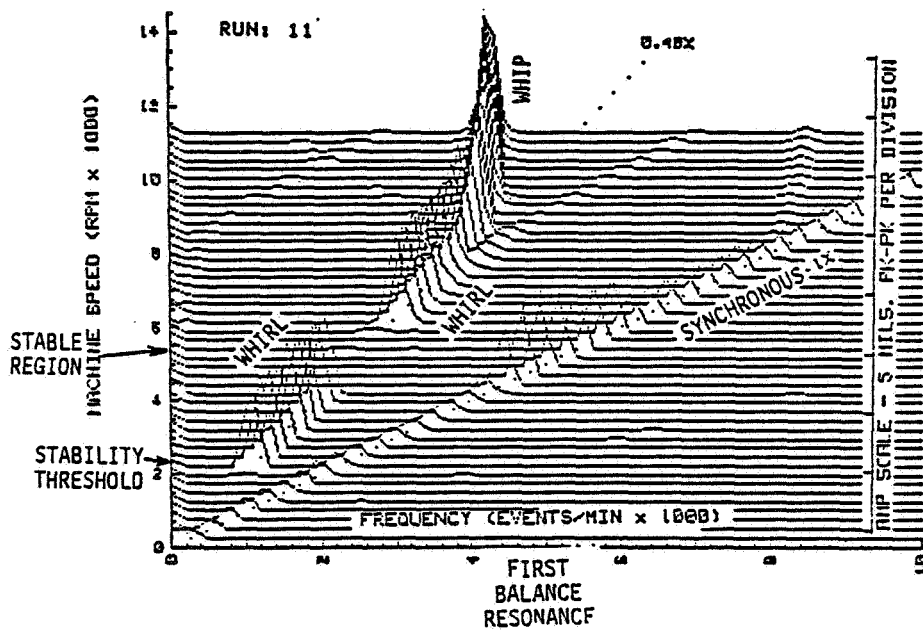


Figure 7. - Cascade spectrum of vertical vibration response during startup with moderately unbalanced rotor. Note stable region for synchronous vibrations associated with increased unbalance vibration.

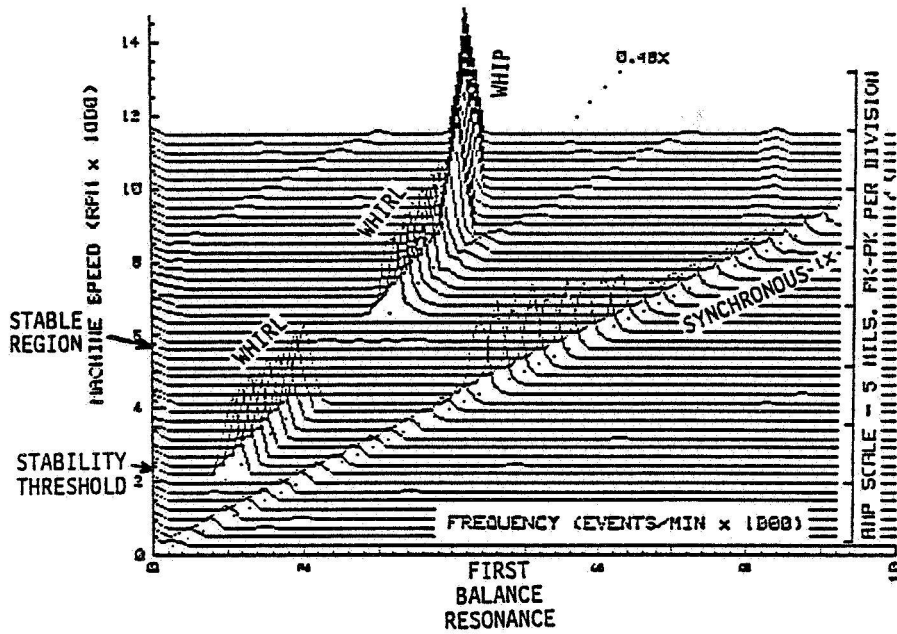
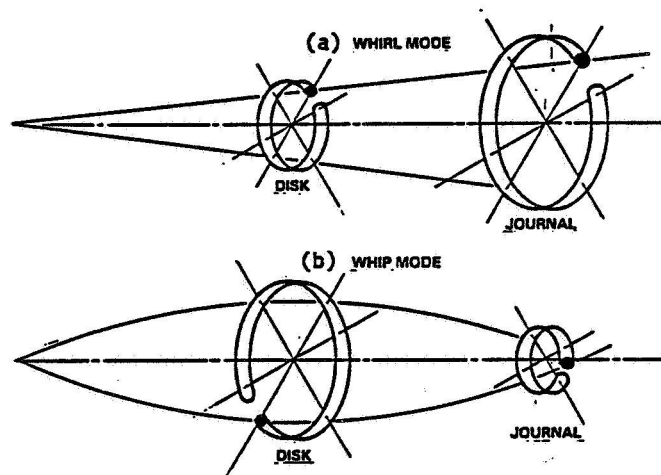


Figure 8. - Cascade spectrum of vertical vibration response during startup with more severely unbalanced rotor. Note expanded stable region of synchronous vibrations.



(a) Whirl mode - disk and journal motion in phase.
(b) Whip mode - journal motion 90° ahead of disk motion.

Figure 9. - Rotor modes revealed by perturbation testing.

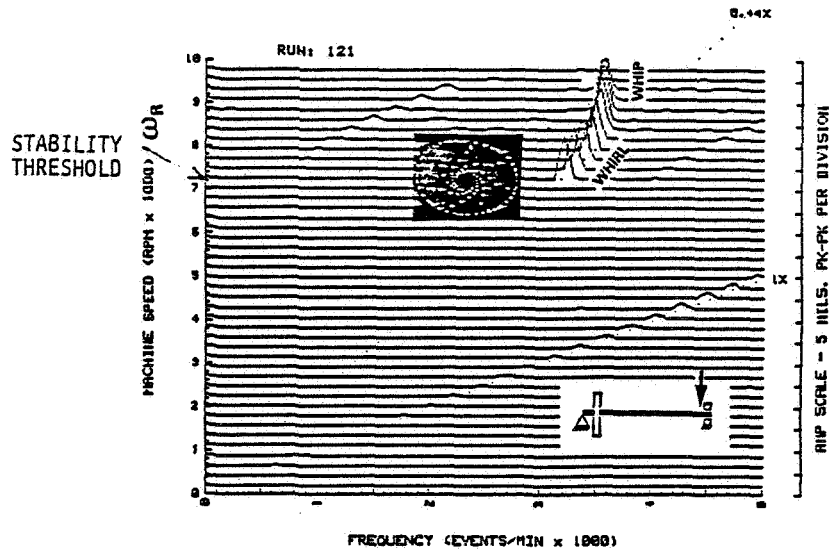


Figure 10. - Cascade spectrum of main rotor runup vertical vibration response and oil whirl inception measured at oil bearing position. Disk located next to motor.

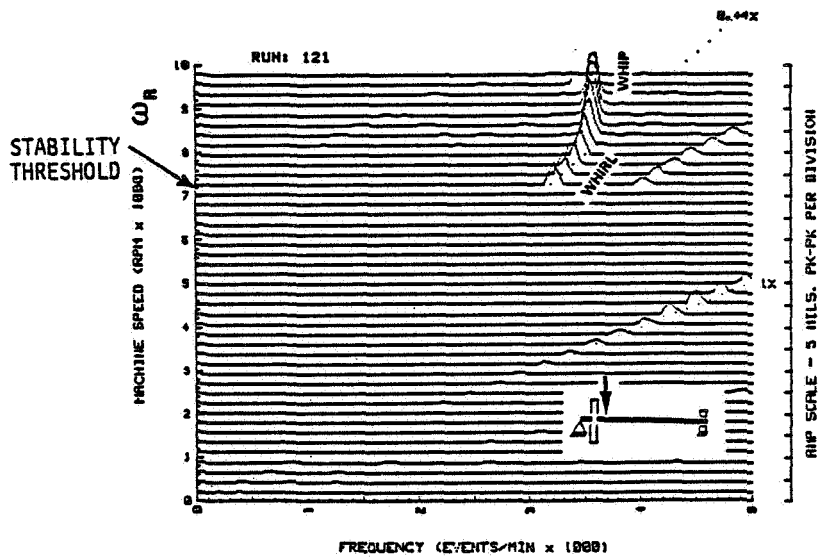


Figure 11. - Cascade spectrum of main rotor runup vertical vibration response measured at disk position. Disk located next to motor.

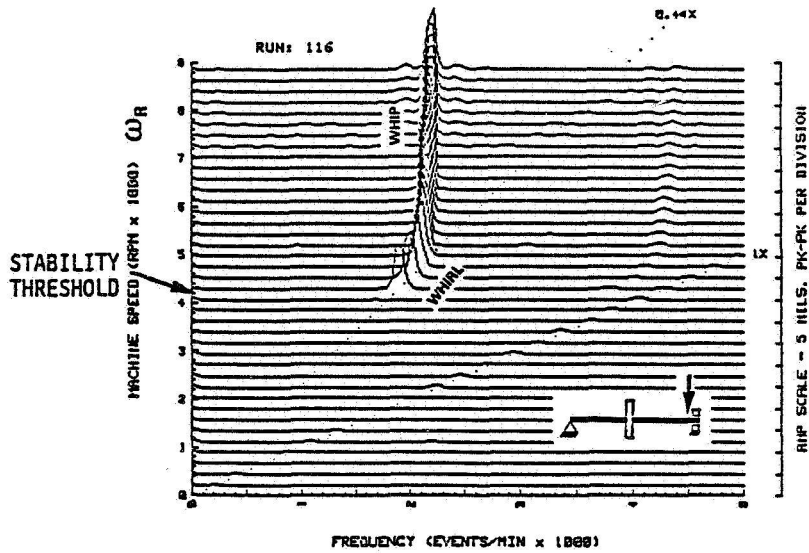


Figure 12. - Cascade spectrum of main rotor runup vertical vibration response measured at oil bearing position. Disk located at shaft midspan.

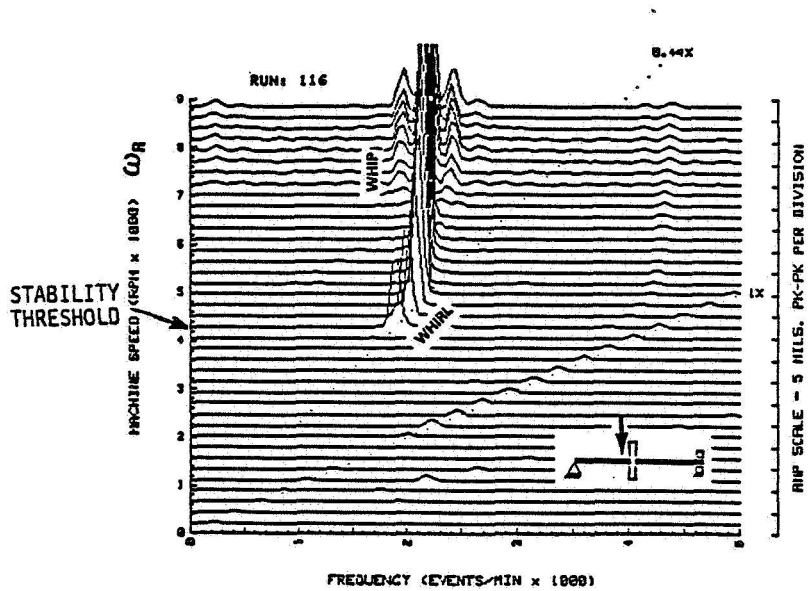


Figure 13. - Cascade spectrum of main rotor runup vertical vibration response measured at disk position. Disk located at shaft midspan.

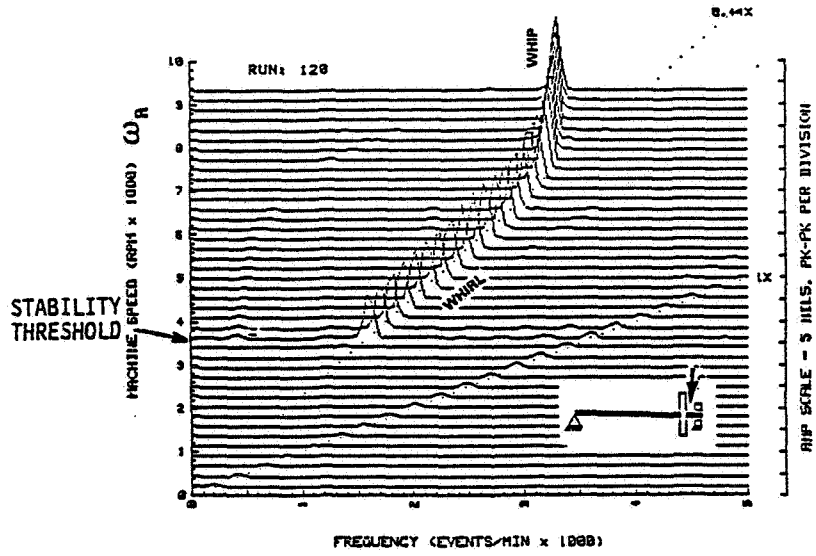


Figure 14. - Cascade spectrum of main rotor runup vertical vibration response measured at bearing position. Disk located next to oil bearing.

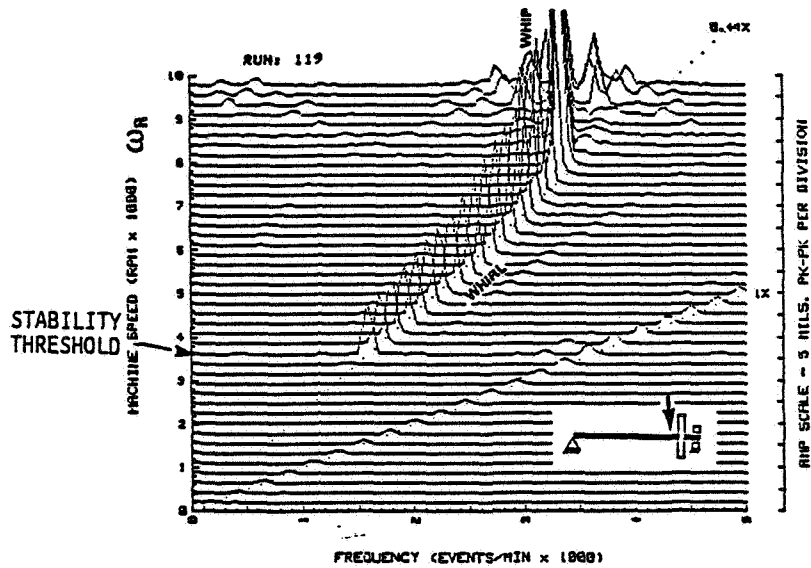


Figure 15. - Cascade spectrum of main rotor runup vertical vibration response measured at disk position. Disk located next to oil bearing. Compare stability threshold versus disk position of figures 10, 12, and 14.

ANTI-SWIRLING DEMONSTRATION

Agnes Muszynska
Bently Rotor Dynamics Research Corporation
Minden, Nevada 89423

Fluid in bearings and seals, involved in motion due to shaft rotation and generating fluid dynamic forces, represents the well-recognized source of instability known as whirl and whip (Figure 1). It is characterized by shaft forward circular precession at subsynchronous frequency. Control of the flow pattern in the bearing/seal clearance may enhance the stability.

OBJECTIVE

The rotor system demonstrates the dynamic effect of perturbation of the flow pattern in a seal gap by blowing compressed air in the rotor tangential direction. This effect results in shifting the rotor threshold of stability to a higher value of rotative speed when the air jet direction opposes rotation, and to a lower value of rotative speed when the air jet direction coincides with rotation. This effect implies that an unstable rotor can be stabilized by blowing air in the direction opposite to rotation. This technique is known as anti-swirl (Figure 2).

ROTOR SYSTEM CONFIGURATION

The system consists of a slender shaft, rigidly supported, carrying a mid-span disk. The stator models a seal with 10 mils radial clearance and 5.4×10^{-3} clearance-to-radius ratio (Figure 3).

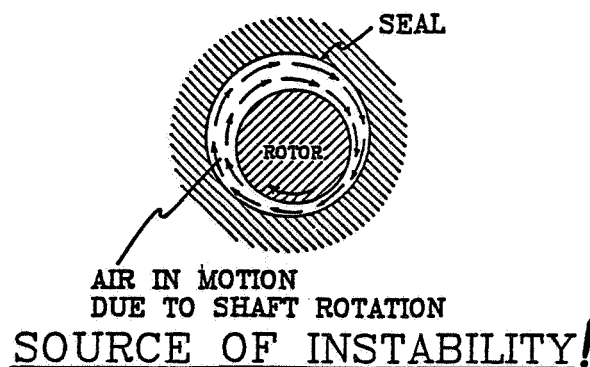
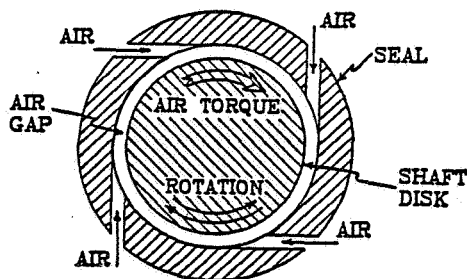


Figure 1. - Bearing/seal fluid-generated instability.



- AIR FLOW IN THE DIRECTION OF SHAFT ROTATION CAUSES DESTABILIZING EFFECT.
- AIR FLOW AGAINST THE DIRECTION OF SHAFT ROTATION CAUSES STABILIZING EFFECT (BREAKS THE ROTATION-INDUCED FLOW PATTERN).

Figure 2. - Anti-swirling technique (in setup, it is much easier to change rotation direction than to reverse air jets for demonstration of anti-swirling effect).

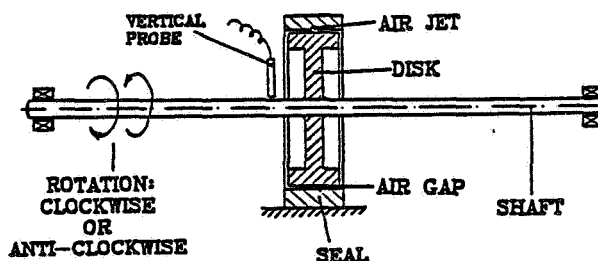


Figure 3. - Anti-swirling demonstration rig.

Four air jets with on/off valves are located tangentially to the disk (Figure 2). Rotative speed of the driving motor is variable in the range 0 to 12,000 rpm. The shaft can be rotated either clockwise or counterclockwise. The system is supplied with a speed controller and an air compressor.

INSTRUMENTATION

Two eddy current proximity probes mounted next to the disk allow monitoring of the rotor vertical and horizontal displacements. A Keyphasor probe gives phase and rotative speed measurements. Oscilloscope serves for continuous observation of the vibration pattern.

RESULTS

Results are given in the form of cascade spectra for several values of the supplied air pressure and both directions of rotation. The graphs indicate the different thresholds of stability.

ORIGINAL PAGE IS
OF POOR QUALITY

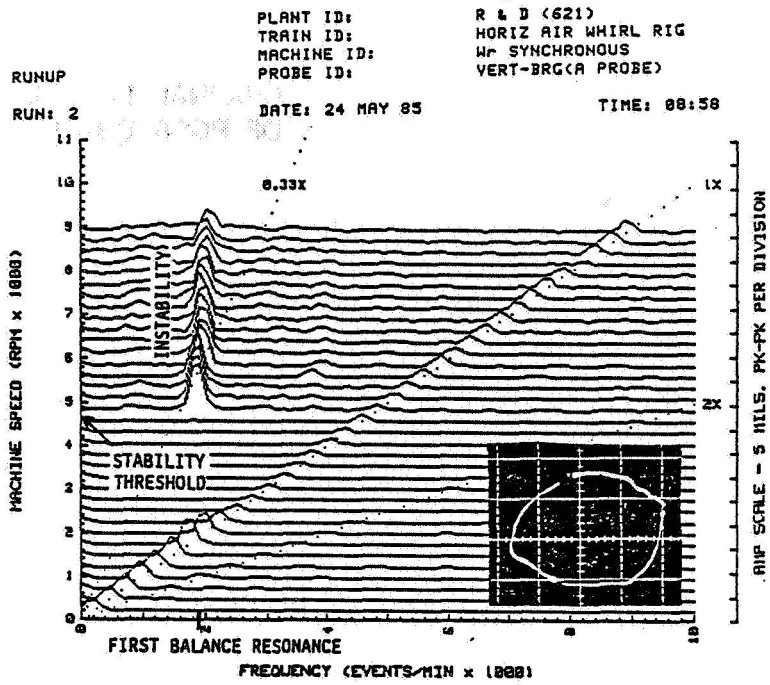


Figure 4. - Cascade spectrum of rotor original response and orbit at 6000 rpm. Threshold of stability, ~4800 rpm.

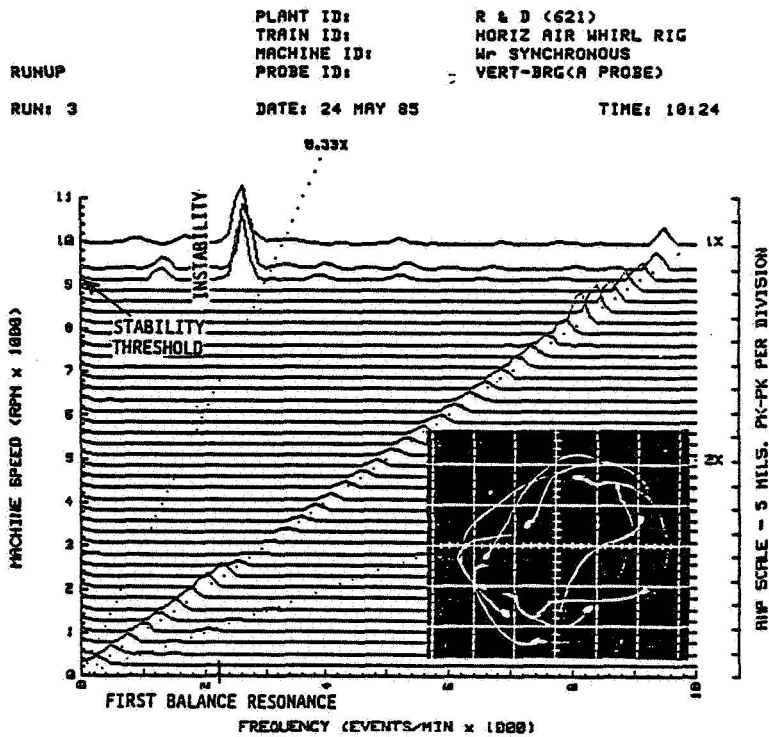


Figure 5. - Cascade spectrum of rotor response for 9-psi pressure (jets against rotation) and orbit at 9500 rpm. Threshold of stability, ~9100 rpm: anti-swirl effect.

ORIGINAL PAGE IS
OF POOR QUALITY

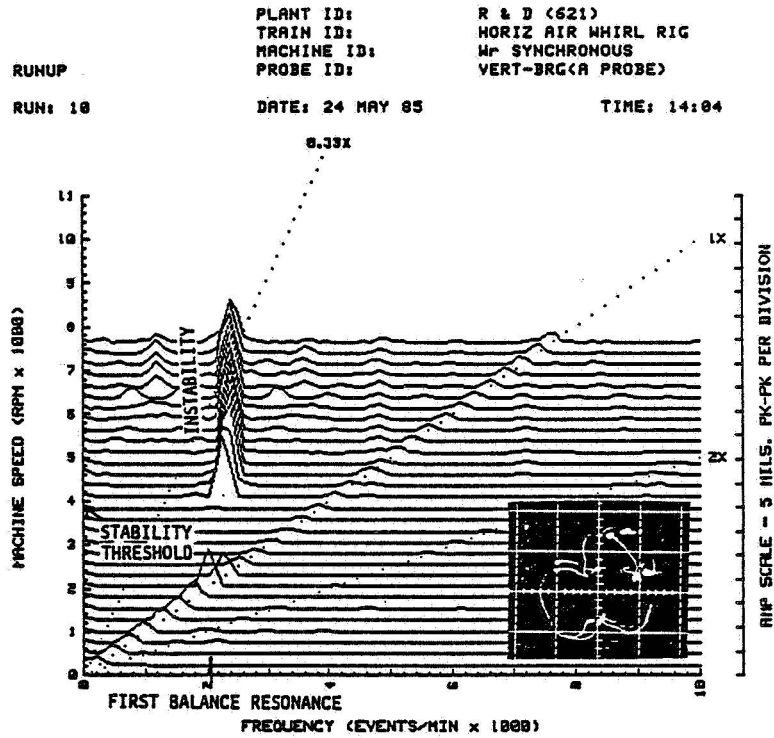


Figure 6. - Cascade spectrum of rotor response for 9-psi pressure (jets in direction of rotation) and orbit at 7500 rpm. Threshold of stability, ~4050 rpm.

PARTIAL ROTOR-TO-STATOR RUB DEMONSTRATION

Robert Grissom
 Bently Nevada Corporation
 Minden, Nevada 89423

A rotor radial rub typically occurs in seals or at a blade tip or shroud when there is insufficient clearance, high vibration, or the shaft equilibrium position has been displaced to effectively limit the clearance (eccentricity).

There are two extreme cases of radial rubs: full annular rub; when the rotor maintains continuous contact with the seal, etc., and a partial rub; when the contact occurs during a fraction of the precession period (Fig. 1). They both involve similar physical phenomena such as friction and modification of stiffness. In partial rubs with consecutive impacts, a significant average value of radial force is generated. This results in shaft average displacement in the direction opposite the rub location.

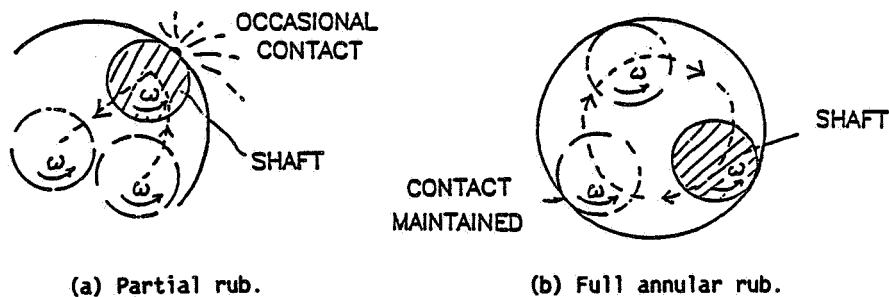


Figure 1. - Two distinct rub regimes.

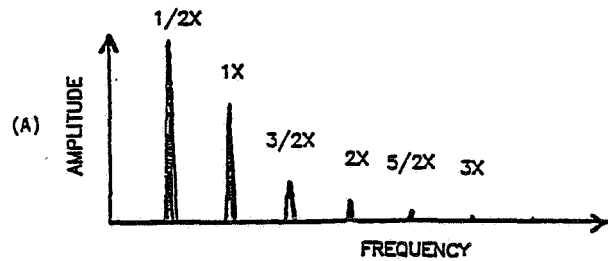
OBJECTIVE

The rotor rig demonstrates the characteristics of a partial lateral rub of varying severity and location. These characteristics include:

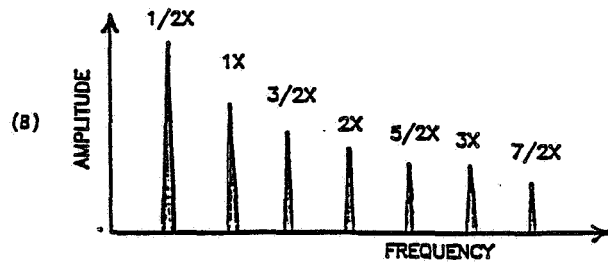
- Subharmonic components as a function of rotative speed/first balance resonance ratio and radial force (Fig. 2)
- Higher harmonic content as a function of severity (Fig. 3)
- Increased average rotor stiffness resulting in increased first balance resonance speed
- Change in overall orbital pattern as a sum of the unbalance response ($1\times$) and subharmonic response ($1/n\times$) (Fig. 4)

When:	
$\omega < 2\omega_r$	result is 1x
$\omega \geq 2\omega_r$	result is 1x OR 1/2x
$\omega \geq 3\omega_r$	result is 1x OR 1/2x OR 1/3x
$\omega \geq 4\omega_r$	result is 1x OR 1/2x OR 1/3x OR 1/4x
← HIGHER RADIAL FORCE	

Figure 2. - Subharmonic content of rub signal as a function of rotative speed ω and radial force (ω_r is first balance resonance speed.)



(a) Light rub - harmonics attenuate quickly.



(b) Heavy rub - rich frequency spectrum (sharp impacts, friction, and other nonlinearities).

Figure 3. - Harmonic content of rub signals.

- ORBITS --- POWERFUL TOOL

- NUMBER OF $K\phi$ INDICATES 1X, 1/2X, 1/3X... RUB
- EXTERNAL LOOPS IN ORBITS INDICATE REVERSE REBOUNDED MOTION
- UNFILTERED ORBIT SHAPES INDICATE RADIAL POSITION OF RUBBING PLACE



- FILTERED ORBITS: 1X + 1/2X



- COMPLEX ORBIT SHAPE: PARTIAL RUB, SEVERAL LOCATIONS

Figure 4. - Orbital pattern characteristics, including keyphasor (once-per-turn reference signal), of a partial rub.

ROTOR RIG

The rotor rig consists of a rigidly supported long, flexible single disk shaft rotating in Oilite (oil impregnated, sintered bronze) bushings, driven by a variable speed (0-12,000 rpm) electric motor through a flexible coupling. Vertical and horizontal brass screws are used to initiate the rub (Fig. 5).

INSTRUMENTATION

X-Y proximity probes mounted at the disk provide shaft vibration data to an oscilloscope for time base and orbit presentations, and to a Digital Vector Filter (DVF 2) for bandpass filtering, speed, and phase data. An FFT spectrum analyzer is used to generate the frequency domain presentation.

MEASUREMENT PARAMETERS

First balance resonance speed (ω_r) measured with the help of spectrum analyzer (e.g., impulse testing). Time domain, orbital pattern and frequency domain for harmonic content of vibration signal measured at rotative speeds of:

- Less than $2\omega_r$
- At $2\omega_r$
- Between $2\omega_r$ and $3\omega_r$
- Above $3\omega_r$

Direction of precession of orbital components filtered at synchronous ($1\times$) speed and $1/n\times$ frequency evaluated with the help of the oscilloscope.

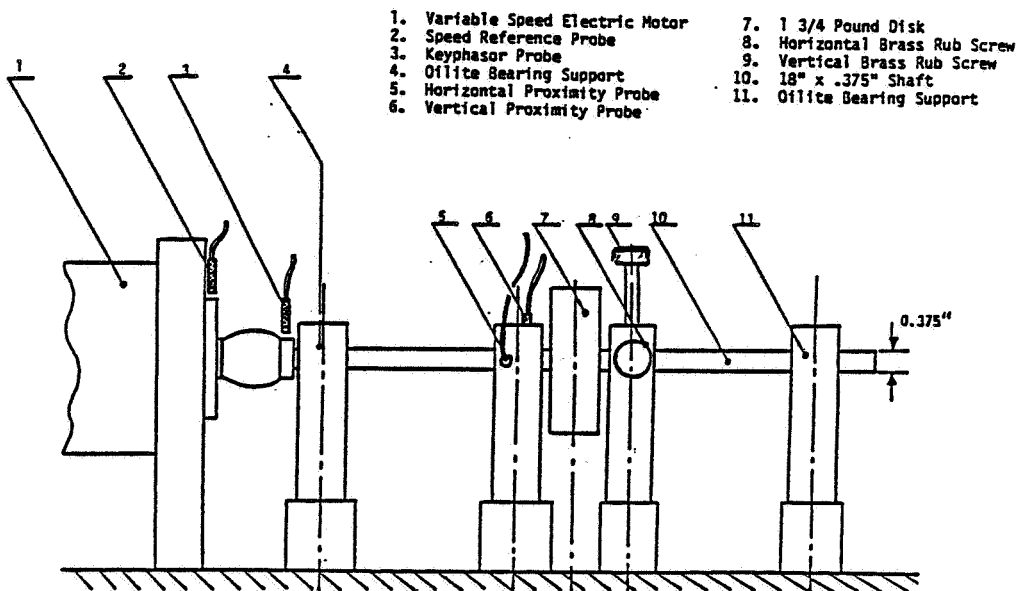


Figure 5. - Rotor rig for partial rub demonstration.

RESULTS

ORIGINAL PAGE IS
OF POOR QUALITY

Results are given in the form of cascade spectra and orbit plots including 1x and 1/nx orbit components in Figures 6 and 7.

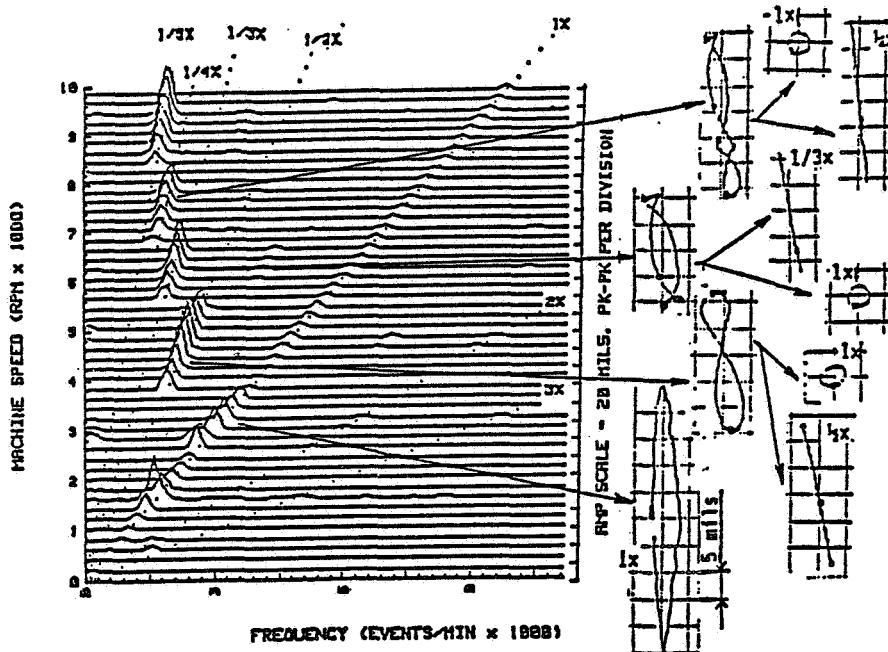


Figure 6. - Cascade spectrum and oscilloscope orbit patterns of light rubs, producing primarily subharmonic frequency components.

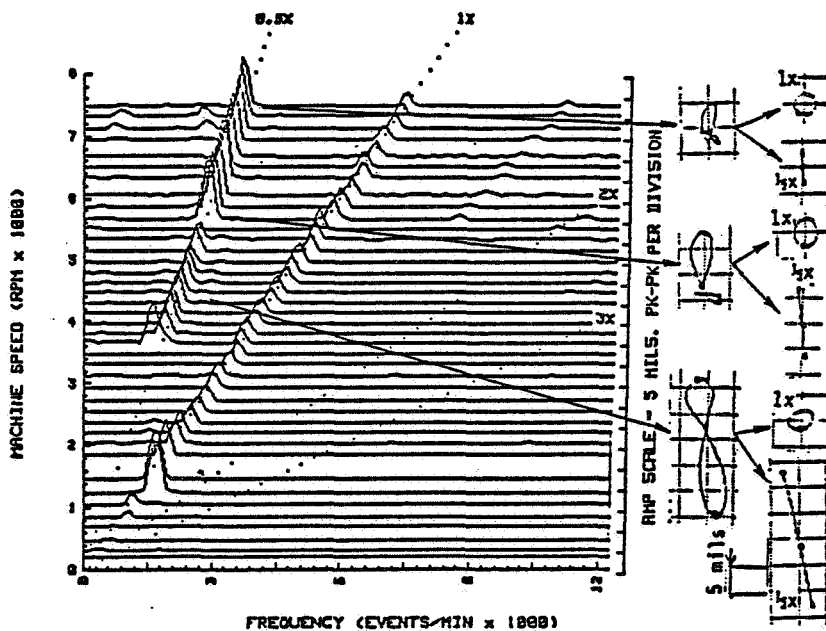


Figure 7. - Cascade spectrum and oscilloscope orbit patterns of rub with higher radial force.

ROTOR INSTABILITY DUE TO LOOSE ROTATING PART

Agnes Muszynska
Bently Rotor Dynamics Research Corporation
Minden, Nevada 89423

Loosening of a rotating part from its fixed position on the shaft or a part of the stator which comes loose and begins to turn with the rotor represents very frequent machinery malfunction. The loose part becomes involved in rotative motion mostly due to dry or fluid friction, and thus its motion is very erratic. The loose part can also move axially along the shaft. Detachment of the rotating part causes changes in the rotor balance state. Most often this results in higher unbalance. During steady-state operation the effect of a loose rotating part can manifest itself through beat vibration. It can be diagnosed by observing periodic changes of amplitude and phase of the synchronous response. During start-up (or shutdown) a loose rotating part carrying some amount of unbalance may manifest its dynamic action in the form of subsynchronous vibrations, very similar to those of other instabilities.

OBJECTIVE

The objective of this demonstration is to observe the effect of a loose rotating part (fixed, however, in the axial direction) under both steady-state (rotor constant speed) and transient (rotor start-up or shutdown) operation. The dynamic response depends very much on the amount of damping in the system: lubrication of the loose part/shaft surfaces and addition/elimination of aerodynamic drag blades, mounted on the loose disk, significantly change the rotor response.

ROTOR SYSTEM

The system consists of a shaft carrying a fixed disk and another "loose" disk mounted on the shaft with a rolling element bearing (Fig. 1). Both disks can be forced to rotate together when they are mechanically attached, or the second ("loose") disk can rotate freely on the shaft, when the attachment is cut off. The "loose" disk can be allowed to start its free rotation at any chosen rotor speed. Four, three, or two air drag blades of various sizes can be mounted on the "loose" disk to introduce an external resistance torque.

INSTRUMENTATION

Two eddy current noncontacting proximity probes mounted in X-Y configuration next to the loose disk allow monitoring of the rotor vertical and horizontal displacements. A Keyphasor® probe gives phase and rotative speed measurements. Oscilloscope serves for continuous observation of the vibration pattern. Spectrum Analyzer yields amplitude/frequency relationship for the vibration signals.

ORIGINAL PAGE IS
OF POOR QUALITY

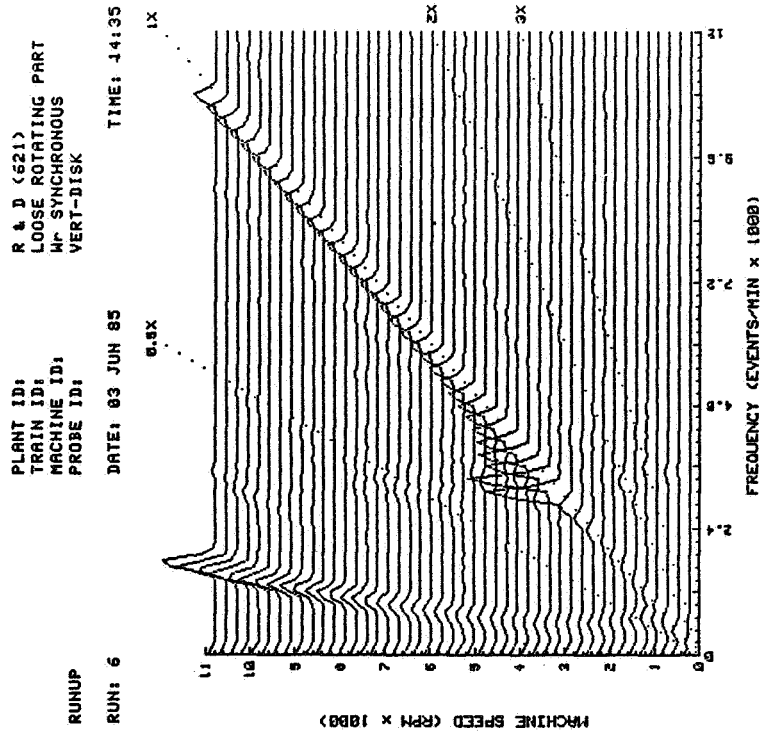


Figure 6. - Cascade spectrum for three-blade loose-disk rotor startup response. Frequency of subsynchronous vibrations caused by loose disk, $\sim 1/6X$.

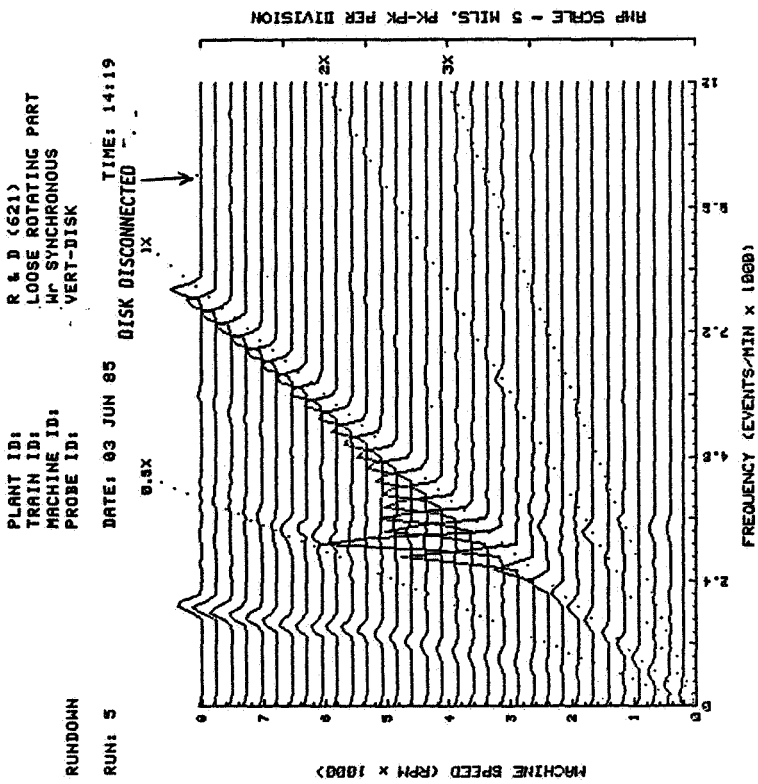
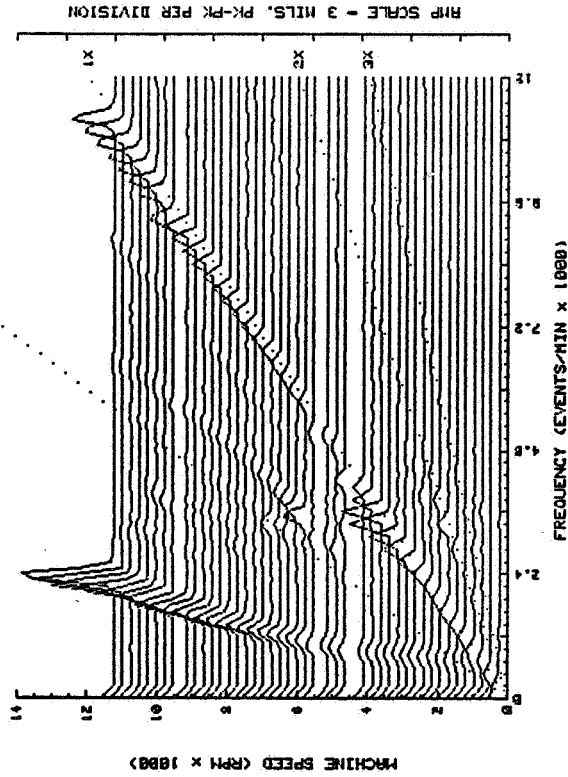


Figure 5. - Cascade spectrum of rotor response during shutdown. Four-blade disk disconnected from main rotor at rotative speed (8000 rpm). Frequency of subsynchronous vibrations caused by loose disk, $\sim 1/4X$.

PLANT ID: R & D (621)
 TRAIN ID: LOOSE ROTATING PART
 MACHINE ID: M- SYNCHRONOUS
 PROBE ID: VERT-DISK
 RUNUP
 RUN: 9
 DATE: 03 JUN 85
 TIME: 17:07
 0.5X



ORIGINAL PAGE IS OF POOR QUALITY

Figure 8. - Cascade spectrum for two-blade, loose disk rotor startup response. Frequency of subsynchronous vibrations caused by loose part, $\sim 1/5X$; frequency of additional subsynchronous vibrations, $\sim 3/5X$; amplitude becomes significantly high when rotative speed reaches double first balance resonance.

PLANT ID: R & D (621)
 TRAIN ID: LOOSE ROTATING PART
 MACHINE ID: M- SYNCHRONOUS
 PROBE ID: VERT-DISK
 RUNDOWN
 RUN: 7
 DATE: 03 JUN 85
 TIME: 15:57
 0.5X

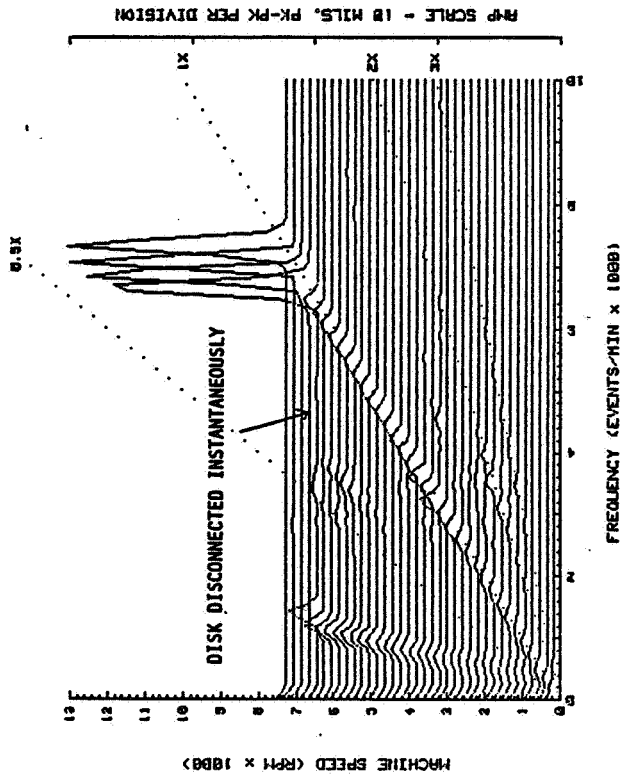


Figure 7. - Cascade spectrum of rotor response during shutdown. Three-blade disk disconnected from main rotor at rotative speed (6500 rpm). Frequency of subsynchronous vibrations caused by loose disk, $\sim 1/6X$.

PLANT ID: R & D (621)
 TRAIN ID: LOOSE ROTATING PART
 MACHINE ID: HP SYNCHRONOUS
 PROBE ID: VERT-DISK

RUN: 10

DATE: 01 MAR 00

TIME: 00:15

0.1X

1X

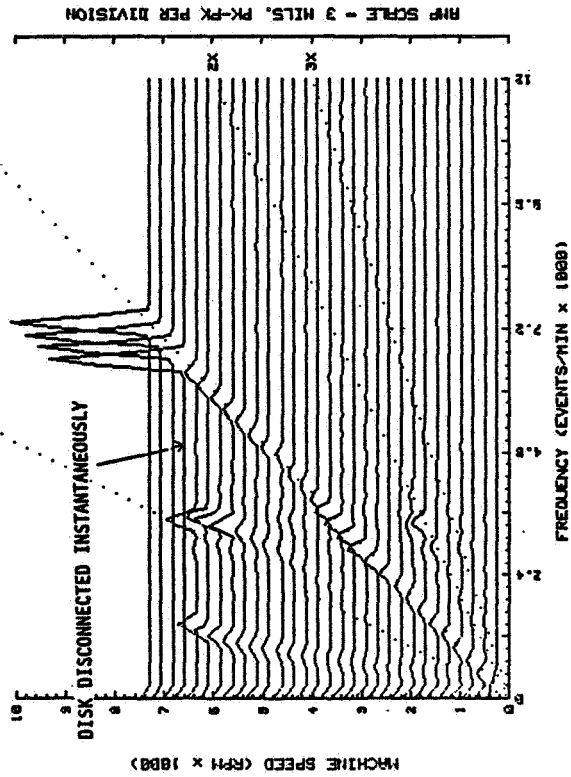


Figure 9. - Cascade spectrum of rotor response during shutdown. Two-blade disk disconnected from main rotor at rotative speed (6500 rpm). Frequencies of subsynchronous vibration caused by loose disk, $\sim 1/4X$ and $3/5X$. Latter meets first balance resonance frequency.

PLANT ID: R & D (621)
 TRAIN ID: LOOSE ROTATING PT.
 MACHINE ID: HP SYNCHRONOUS
 PROBE ID: VERT-BRGCA PROBE

RUN: 3

DATE: 31 MAY 85

TIME: 12:57

0.1X

1X

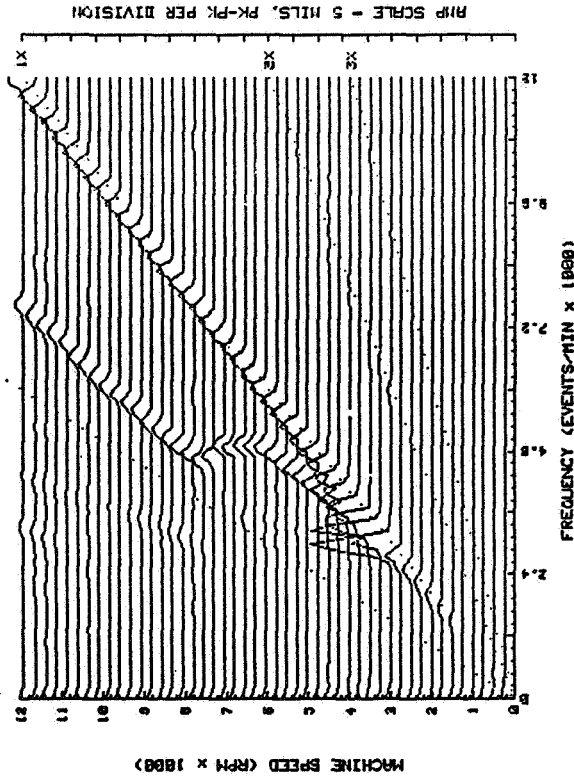


Figure 10. - Cascade spectrum for two-blade, loose-disk rotor startup response. Subsynchronous vibrations with variable frequency caused by loose part (probably due to variable friction/damping conditions at shaft/loose disk surface). Blades half size of those in previous tests (lower air drag).

ORIGINAL PAGE IS
OF POOR QUALITY

RUNDOWN
RUN: 2
PLANT ID: R & D (621)
TRAIN ID: LOOSE ROTATING PT.
MACHINE ID: W/ SYNCHRONOUS
PROBE ID: VERT-BRG(A PROBE)
DATE: 31 MAY 85
TIME: 11:15

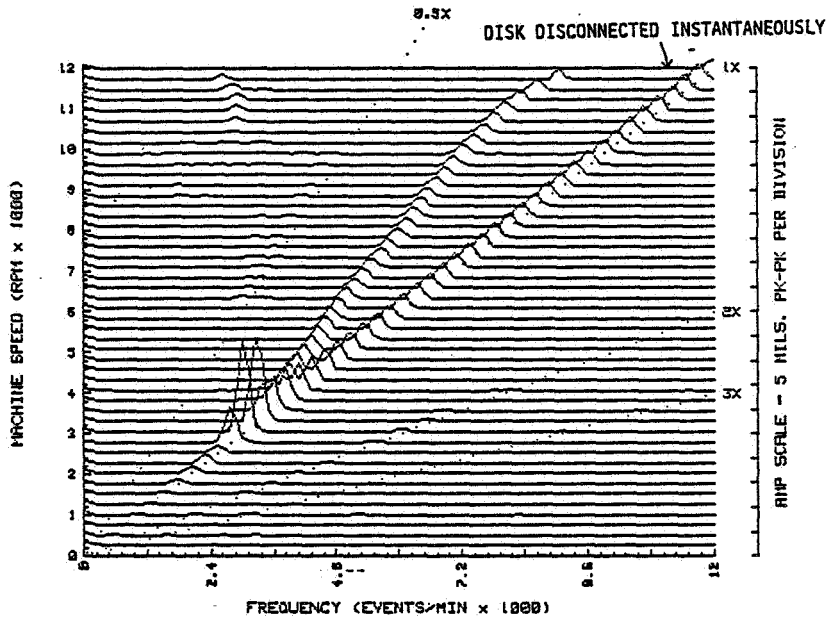


Figure 11. - Cascade spectrum of rotor response during shutdown. Two-blade disk disconnected from main rotor at rotative speed (11 900 rpm). Frequency of subsynchronous vibrations caused by loose disk first sharply, then slowly, decreasing. At first balance resonance speed subsynchronous vibrations disappear. Blades half size of those in previous tests (lower air drag).

INSTABILITY IN HYDRAULIC MACHINES DEMONSTRATION RIG

**Agnes Muszynska
Bently Rotor Dynamics Research Corporation
Minden, Nevada**

**M.J. Braun
University of Akron
Akron, Ohio 44325**

In fluid-flow machines, the working fluid involved in rotative motion due to shaft rotation significantly modifies the rotor synchronous response. This can result in the rotor maintaining the high vibration amplitude that occurs at resonance over an extended rotative speed range. The phase changes in this range are typically very small. The fluid may also create rotor instability, i.e., subsynchronous self-excited vibrations, when the rotative speed is sufficiently high. This rotor instability is often rub-related and increases with higher rotor unbalance. (Opposite to other types of instability such as oil whirl/whip, internal friction, etc.)

OBJECTIVE

The rotor rig demonstrates typical dynamic behavior of hydraulic machines. At lower speeds the effect of amplitude/phase mentioned above is noticeable; at higher speeds the subsynchronous instability occurs.

ROTOR RIG

The rig consists of a vertical single disk rotor and supported in one rigid and one 10-segment rubber-lined, water-lubricated bearing (Fig. 1 and 2).

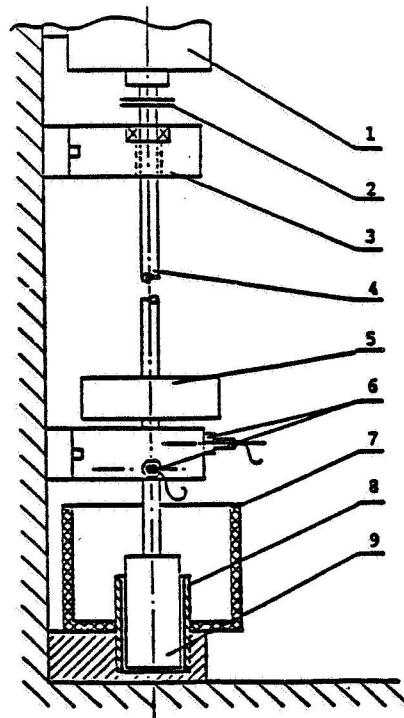
INSTRUMENTATION

Two pairs of x-y eddy current proximity probes and one Keyphasor® probe connected to the oscilloscope allow monitoring rotor vibrations at the water bearing and next to the disk. The rotative speed may be varied from 0 to 12,000 rpm.

RESULTS

The results are presented in a form of cascade spectrum, orbit, as well as Bodé & polar plots of the synchronous (1x) response (Figures 3, 4 and 5).

ORIGINAL PAGE IS
OF POOR QUALITY



1. MOTOR
2. COUPLING
3. RIGID BEARING HOUSING
4. SHAFT
5. DISK
6. PROXIMITY PROBES
7. WATER CONTAINER
8. 3/4" DIAMETER RUBBER-LINED BEARING
9. SHAFT JOURNAL

Figure 1. - Vertical rotor rig supported by rubber-lined, water-lubricated bearing.

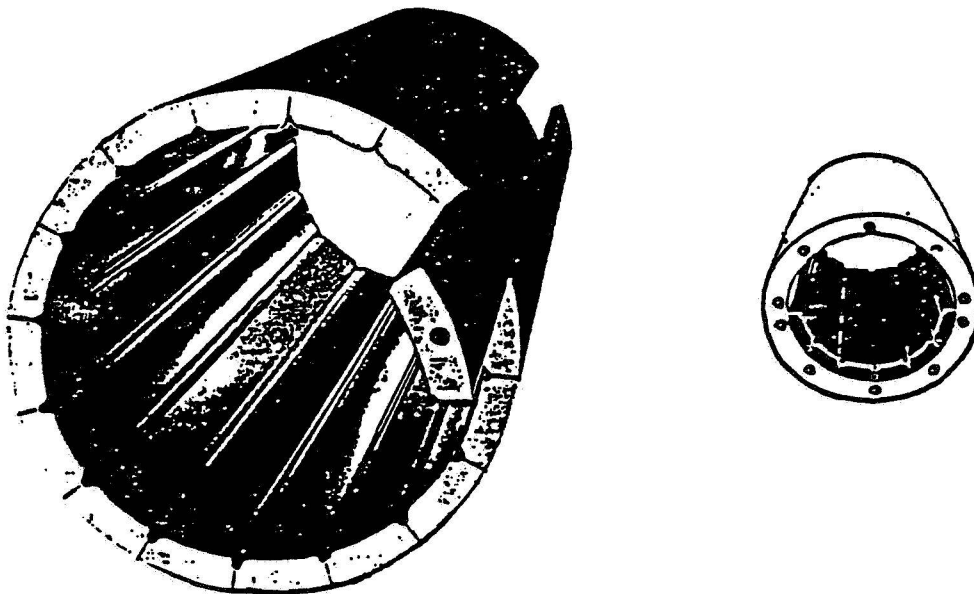


Figure 2. - Rubber-lined, water-lubricated bearing.

PLANT ID: R & D (621)
 TRAIN ID: VERT WATER WHIRL RIG
 MACHINE ID: M₁ SYNCHRONOUS
 PROBE ID: HORIZ-BRG(3) PROBE
 RUNUP
 RUN: 1
 DATE: 21 MAY 85
 TIME: 01:18

ORIGINAL PAGE IS
OF POOR QUALITY

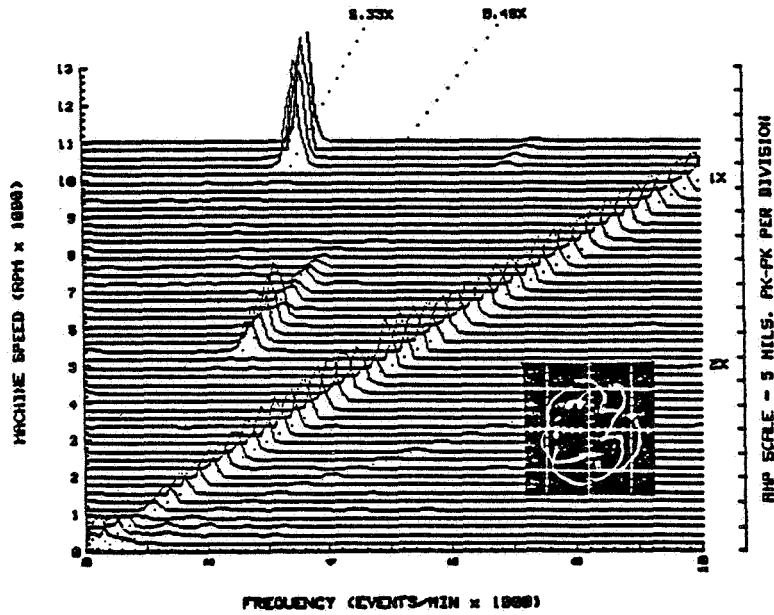


Figure 3. - Cascade spectrum of unbalanced rotor radial response and orbit at 10 500 rpm.

PLANT ID: R & D (621)
 TRAIN ID: VERT WATER WHIRL RIG
 MACHINE ID: M₁ SYNCHRONOUS
 PROBE ID: HORIZ-BRG(3) PROBE
 RUNUP
 RUN: 2
 DATE: 21 MAY 85
 TIME: 01:53

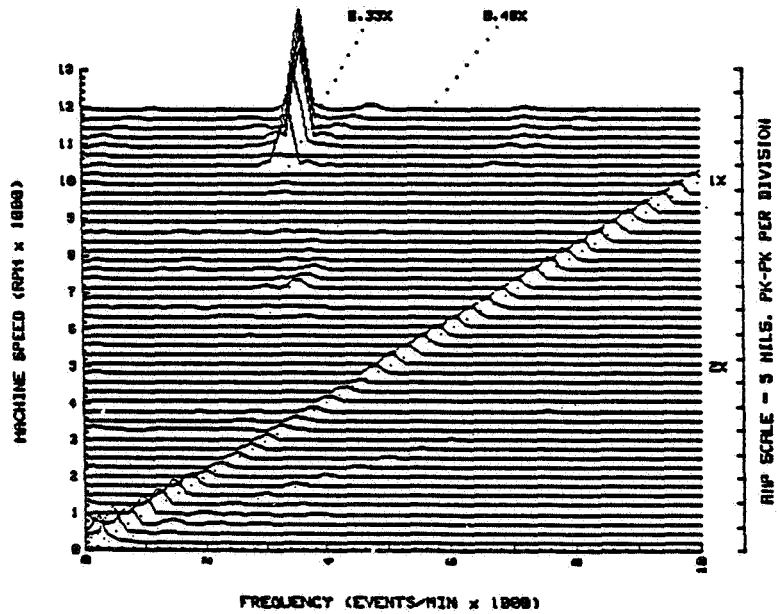


Figure 4. - Cascade spectrum at balanced rotor radial response.

ORIGINAL PAGE IS
OF POOR QUALITY

BENTLY NEVADA CORP.
MINDEN, NEVADA

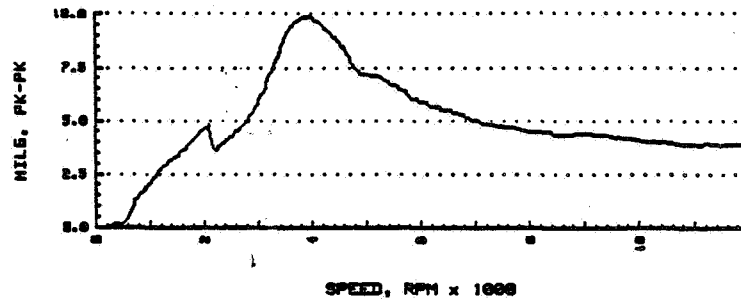
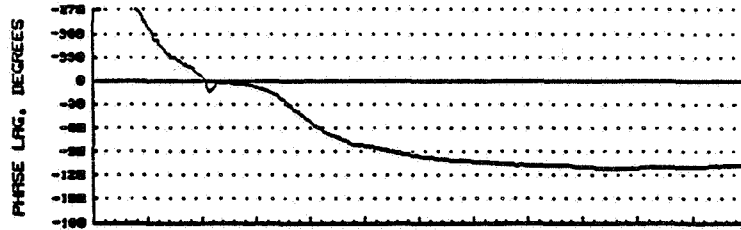
PLANT ID: R & D (621)
TRAIN ID: VERT WATER WHIRL RIG
MACHINE ID: W/ SYNCHRONOUS
SOLID DATA: Comp VERT-BRG(A PROBE)

RUNUP

RUN: 3

DATE: 21 MAY 85

TIME: 02:19



BENTLY NEVADA CORP.
MINDEN, NEVADA

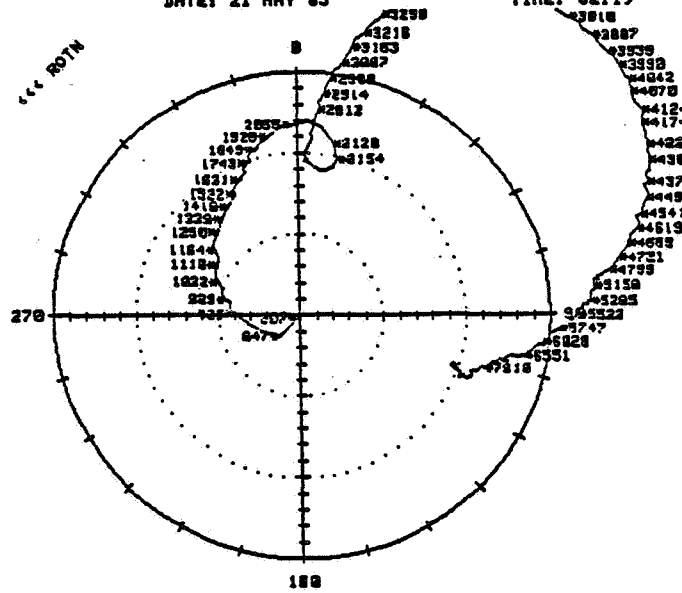
PLANT ID: R & D (621)
TRAIN ID: VERT WATER WHIRL RIG
MACHINE ID: W/ SYNCHRONOUS
SOLID DATA: Comp VERT-BRG(A PROBE)

RUNUP

RUN: 3

DATE: 21 MAY 85

TIME: 02:19



FULL SCALE AMP = 6 MILS, PK-PK AMP PER DIV = .4 MILS, PK-PK

Figure 5. - Bode and polar plots of rotor synchronous (1X) response. Graphs indicate existence of low-frequency structural resonance.

CRACKED ROTOR DEMONSTRATION

R.F. Bosmans
Bently Rotor Dynamics Research Corporation
Minden, Nevada 89423

Rotating elements in turbomachinery are exposed to a number of concurrent forcing functions. These forces may result in large displacements and vibrations of the rotor. If the forces are periodic and very high, the rotor will experience high induced stress levels with a large number of cycles. Any combination of high stress/low number of cycles or low stress/high number cycles may cause a fatigue failure within the rotor, initiated by a crack in the rotor at a site of the highest stress level. Typically, this occurs in areas such as coupling keyways or other shaft lateral locations experiencing stress concentrations.

The onset of a crack in the rotor system introduces an immediate asymmetry in the rotor geometry. This asymmetry modifies the stiffness properties of the rotor. The stiffness in the plane of the crack is much softer than the axis perpendicular to the crack. If the rotor operates in the horizontal plane, a unique forcing function occurs. The force of gravity acts perpendicular downward on the rotor. Each time the crack (soft axis) is exposed to this force of gravity, the rotor will deflect some additional amount. For a singular crack site on the rotor, the soft axis will be exposed to gravity forces twice for each revolution of the rotor. This introduces a vibration component which has a frequency value of twice (2X) rotor speed in the rotor response. It can be measured with the use of proximity transducers and quantified with the help of an oscilloscope observing shaft centerline motion and/or a spectrum analyzer.

If this malfunction is observed over some RPM range of operation, a secondary effect can manifest. Since the rotor is experiencing a strong 2X vibration component, when the rotor speed is exactly one half the frequency of a system resonance, that resonance will be excited. Amplitudes of the 2X component will increase, inducing further stresses and ultimately crack propagation. Repeated operation in these areas will cause the rotor to ultimately fracture. This transient behavior can best be observed with oscilloscope, spectrum cascade, and 2X POLAR PLOTS. For the rotor operation speed exceeding 1/2 first balance resonance, each start-up and shutdown, the machine will cause a transient high vibration level.

OBJECTIVE

The purpose of this demonstration is to observe the behavior of a rotor with a single crack. This will be presented in oscilloscope orbits, 2X POLAR PLOTS, and spectrum cascade diagrams. Crack detection must be observed in all three formats and monitored over a period of time or start-ups. The change in the 2X behavior pattern provides an early warning

that a crack potentially exists and that it is likely propagating toward total rotor fracture.

ROTOR SYSTEM

The demonstration rotor system (FIG. 1) contains the following:

- A) Variable speed drive motor with speed controller
- B) Flexible Coupling
- C) Three bronze oilite bearings
- D) Two mass disks located between bearings
1 & 2 and 2 & 3

The rotor system is operated over a speed range from 0 - 5000 RPM. This range permits excitation of two balance resonances and two resonances of the from the 2X vibration component. The rotor contains a radial crack of approximately 25% shaft penetration. The crack is located between bearings 2 & 3. Speed is controlled with a special speed control module which determines maximum speed and rate of acceleration. During the start-up, the oscilloscope and spectrum analyzer are the primary instruments used for visual observation. The oscilloscope presentation will indicate a large internal loop on the orbit when the 2X vibration excites the balance resonance. The spectrum display will show the 1X and 2X components over the entire operating range. The dynamic motion data will be processed through the HP computer with ADRE software for 2X POLAR plots and spectrum cascade diagrams (FIG.'s 2, 3, & 4).

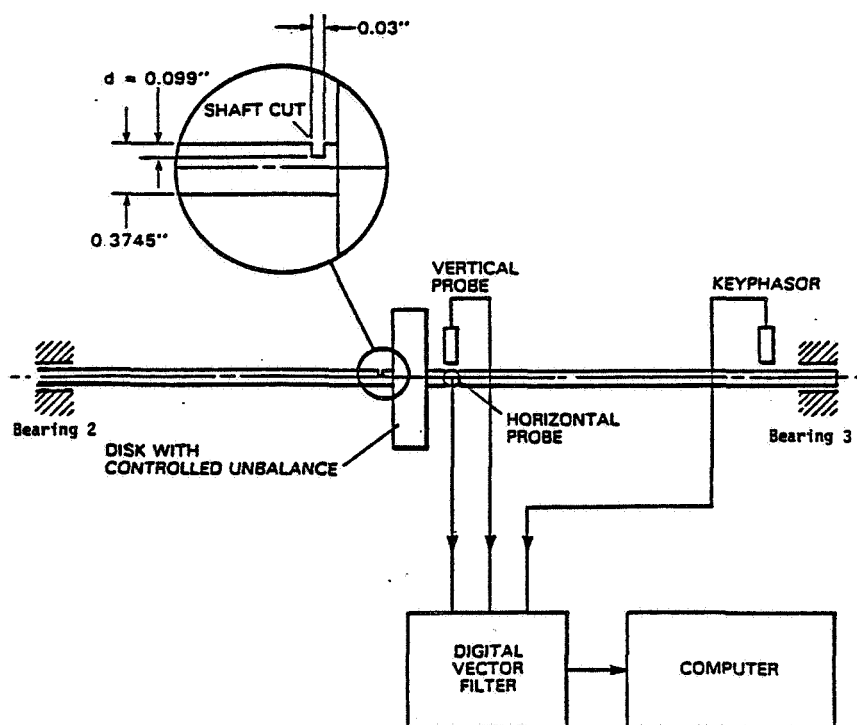


Figure 1.- Rotor system with "cracked" shaft simulated by saw cut.

INSTRUMENTATION

The system behavior is captured with proximity transducers located between bearing 1 & 2 and 2 & 3. The output of these transducers can be observed on the oscilloscope for shaft centerline motion studies. In addition, a DVF2 and spectrum analyzer are connected directly to an HP9836 computer operating on ADRE software. The DVF2 is configured with its internal tracking filter locked in to the 2X vibration component. This permits presentation of 2X POLAR PLOTS with the use of ADRE software. The spectrum analyzer and ADRE software permits presentation of spectrum cascade plots over the operating speed range. The 2X polar plots (FIG. 3) indicates the resonance response of the system due to the forcing function of 2X dynamic motion behavior. The spectrum cascade plot (FIG. 4) indicates the response of the 1X and 2X vibration over the entire operating speed range.

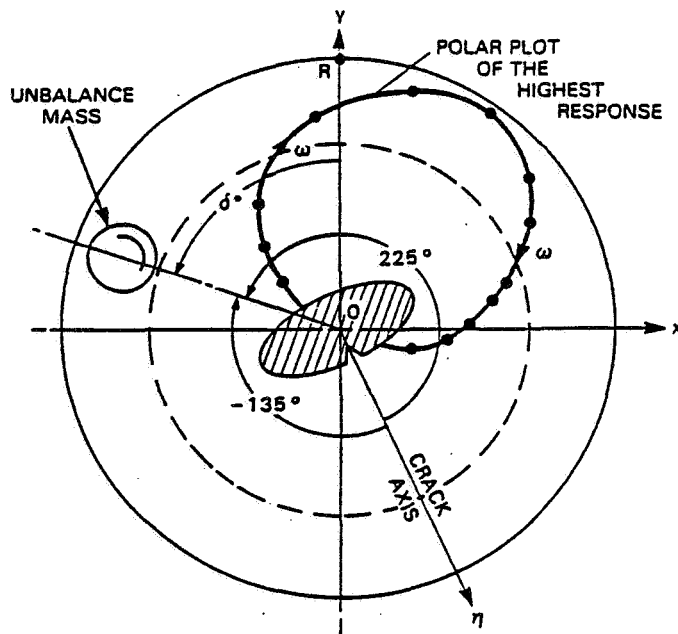
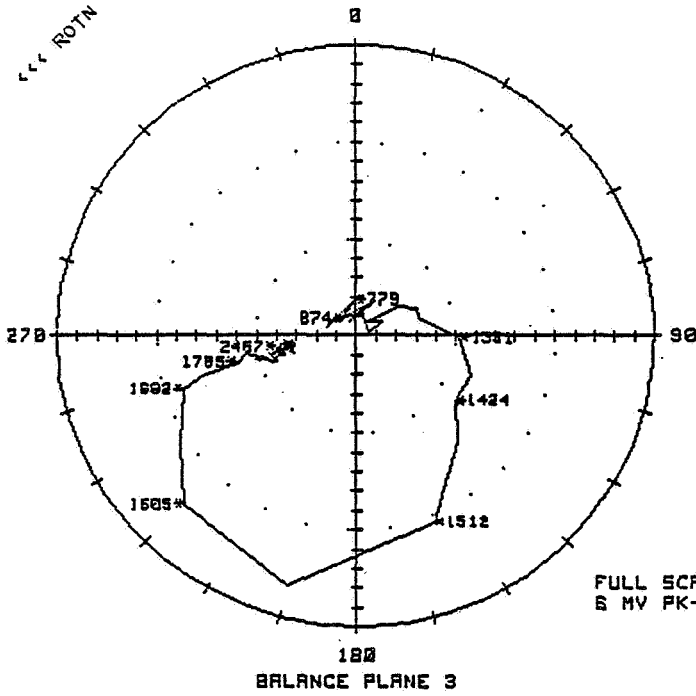


Figure 2.- 1X polar plot of cracked rotor response.

SUMMARY

Observing cracked rotor behavior in these three plot formats provides early warning of cracked rotor condition. Monitoring this behavior over a period of time provides insight toward rate of propagation of a crack and will prevent catastrophic rotor fracture. The 1X and 2X components must be monitored as vectors i.e. AMPLITUDE & PHASE have to be acquired at each rotative speed. Any change in behavior must be quantified as vectors. These vectors can be plotted within a POLAR diagram and a range of "normal" behavior established. Significant vectoral deviation from the acceptable range of values provides warning of cracked rotor activity.



ORIGINAL PAGE IS
OF POOR QUALITY

PLANT ID: CRACKED SHAFT DEMO
 TRAIN ID: 1
 MACHINE ID: 2X
 SOLID DATA: VERT OUTB 2X

DATE: 1 Mar 1968 TIME: 00:47:05

Figure 3.- 2X polar plot of cracked rotor response.

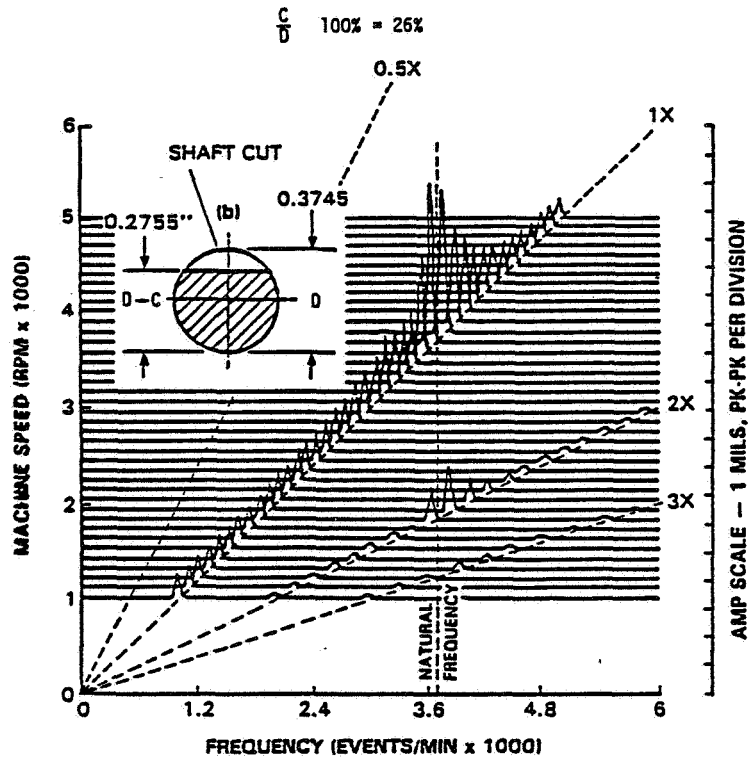


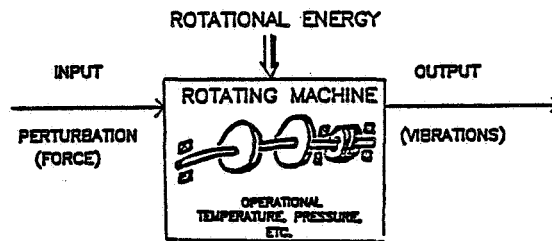
Figure 4.- Spectrum cascade diagram of cracked rotor response.

ROTOR/BEARING SYSTEM DYNAMIC STIFFNESS MEASUREMENTS

BY NONSYNCHRONOUS PERTURBATION

Agnes Muszynska
Bently Rotor Dynamics Research Corporation
Minden, Nevada 89423

Sweep perturbation testing as used in Modal Analysis when applied to a rotating machine has to take into consideration the machine dynamic state of equilibrium at its operational rotative speed. This stands in contrast to a static equilibrium of nonrotating structures (Fig. 1). The rotational energy has a significant influence on rotor dynamic characteristics. The best perturbing input for rotating machines is a forward or reverse rotating, circular force applied directly to the shaft (Fig. 2).



ADVANTAGES OF PERTURBATION BY USING A ROTATIONAL HARMONIC FORCE

- PERTURBATION BY CONTROLLED UNBALANCE IS EASY TO GENERATE, CONTROL AND MEASURE
- CIRCULAR PERTURBATION IN THE PLANE PERPENDICULAR TO SHAFT AXIS PROVIDES THE BEST ROTOR BEHAVIOR INSIGHT
- CIRCULAR PERTURBATION CAN BE APPLIED TO THE ROTOR IN FORWARD OR REVERSE DIRECTION (RELATIVE TO SHAFT ROTATION)

Figure 1. - Perturbation technique for rotating machines.

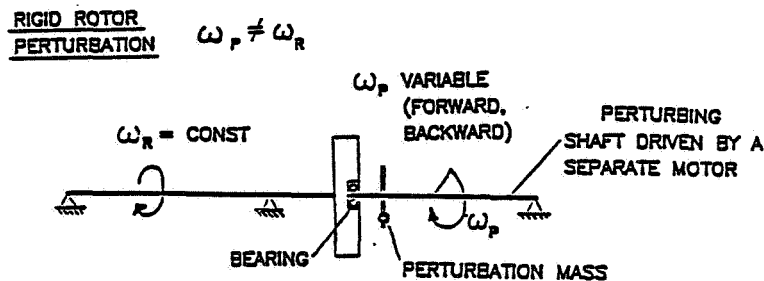


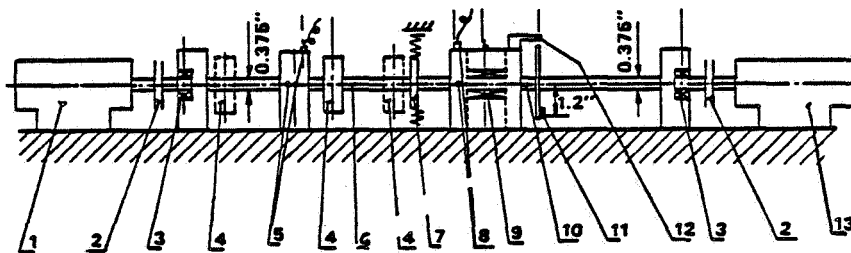
Figure 2. - Nonsynchronous perturbation of rotating machine through auxiliary perturbing shaft with controlled unbalance.

OBJECTIVE

Determination of Dynamic Stiffness Characteristics of the rotor bearing system by nonsynchronous perturbation of a symmetric rotating shaft supported in one relatively rigid and one oil lubricated bearing.

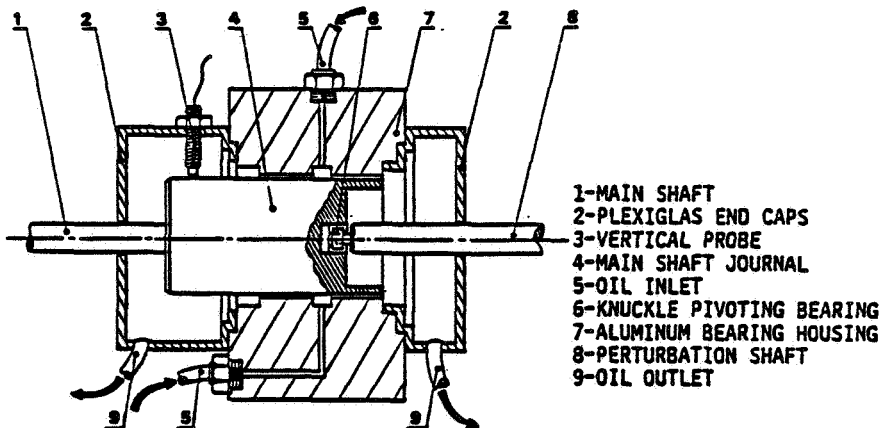
EXPERIMENTAL ROTOR RIG

The experimental rotor system consists of the main shaft rotating at constant angular speed (ω_p) and the auxiliary shaft generating a rotating perturbing force with sine-sweep variable frequency (ω_p). This force is applied to the main journal (Figs. 3 and 4).



1-MAIN ROTOR; 2-FLEXIBLE COUPLINGS; 3-RIGID SUPPORTS WITH PIVOTING BEARINGS; 4-DISK WITH THREE OPTIONAL POSITIONS ON THE SHAFT; 5-HORIZONTAL AND VERTICAL NONCONTACTING PROBES; 6-MAIN SHAFT; 7-ROTOR WEIGHT BALANCING SPRINGS; 8-HORIZONTAL AND VERTICAL PROBES; 9-OIL LUBRICATED BEARING; 10-PERTURBATION SHAFT; 11-PERTURBATION UNBALANCE MASS; 12-KEYPHASOR PROBE; 13-PERTURBATION MOTOR

Figure 3. - Rotor rig for perturbation testing.



1-MAIN SHAFT
2-PLEXIGLAS END CAPS
3-VERTICAL PROBE
4-MAIN SHAFT JOURNAL
5-OIL INLET
6-KNUCKLE PIVOTING BEARING
7-ALUMINUM BEARING HOUSING
8-PERTURBATION SHAFT
9-OIL OUTLET

Figure 4. - Oil bearing used for perturbation testing.

INSTRUMENTATION

Primary instruments:

- Four eddy current proximity probes for measuring the journal and disk horizontal and vertical displacements
- Keyphasor narrow beam optical probe for phase measurements
- Digital Vector Filter for filtering $1\times$ response during perturbation testing
- Spectrum analyzer for yielding amplitude/frequency spectra of nonperturbed rotor runs
- Oscilloscope for continuous observation of the rotor motion
- Hewlett Packard 9836 computer with Bently Nevada software for data acquisition, storage, reduction, analytical computation and displays.

Peripheral instruments:

- Speed controllers for rotation and perturbation frequency
- Oil supply system including filter and pressure control
- Oil heating/cooling device
- Three thermometers (at oil inlet, outlet and in bearing housing).

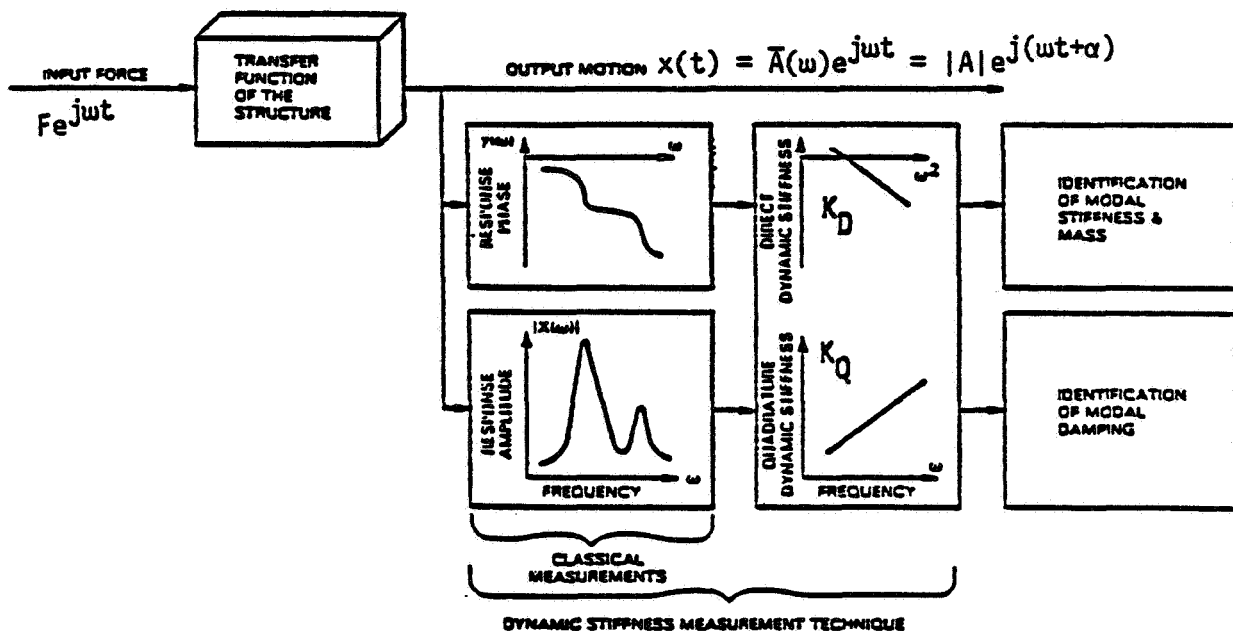


Figure 5. - Dynamic stiffness measurement technique by perturbation testing.

HINTS TO MAINTAIN DATA ACCURACY

- Rigid rotor support, concrete foundations, rigid auxiliary fixtures (elimination of additional degrees of freedom).
- Balanced rotor system.
- Balanced perturbation system, with precisely known perturbation imbalance introduced later.
- Rotor centered in the test bearing by adjustment of the external supporting springs for all deliberately centered tests.

- Control of oil temperature at the bearing to $\pm 1^\circ\text{C}$.
- Accurate control of constant rotative speed ω_R .
- Slow ramp of the perturbation speed.

EXPERIMENTAL PARAMETERS

- Main rotor rotational speed: 0 (squeeze film test) 500, 1000, 1500, 2000, 2500, 3000, 3500, 4000 rpm.
- Perturbation speed range: -6000 to 6000 rpm (minus indicates reverse direction).
- Perturbation imbalance masses: $m_p = 0.75, 2.35, \text{ and } 7$ grams.
(Low mass was used for better evaluation of resonant amplitudes; high mass was used to increase the sensitivity in the out-of-resonance regions.)
- Perturbation radius: $r_p = 1.2''$ (0.03 m)
- T-10 oil density = 794 kg/m^3
- Oil temperature: 80°F (26.7°C)
- Corresponding oil dynamic viscosity: $7.25 \times 10^{-6} \text{ lbs s/in}^2$ (50 c poise).
- Oil pressure: 3 psi (20684 Pa). The bearing is center fed and has two-directional axial flow. A circumferential oil feed groove and relatively low, well controlled pressure enable a uniform axial pressure to be maintained in the bearing.
- Main steel shaft weight (including aluminum journal): 0.614 lbs.
- Perturbation aluminum shaft weight: 0.181 lbs.
- Disk weight: 1.79 lbs (disk mass $4.64 \times 10^{-3} \text{ lbs s}^2/\text{in} = 0.81 \text{ kg}$).
- Aluminum bearing radial clearance: $0.0075''$ ($190 \mu\text{m}$).
- Bearing length: $0.5''$ (0.013 m)
- Bearing diameter: $1.0''$ (0.0254 m)
- Bearing radial clearance to radius ratio: 0.015.

RESULTS (Example)

The perturbation testing yields response data in form of vibration amplitude and phase, which are eventually used to obtain Direct and Quadrature Dynamic Stiffness characteristics of the rotor/bearing system. The latter permits the identification of the system modal stiffness, mass and damping.

The results of the perturbation tests are presented in Figures 6 through 10 in the form of Bodé plots, polar plots, and Dynamic Stiffness versus perturbation speed plots.

ORIGINAL PAGE IS
OF POOR QUALITY

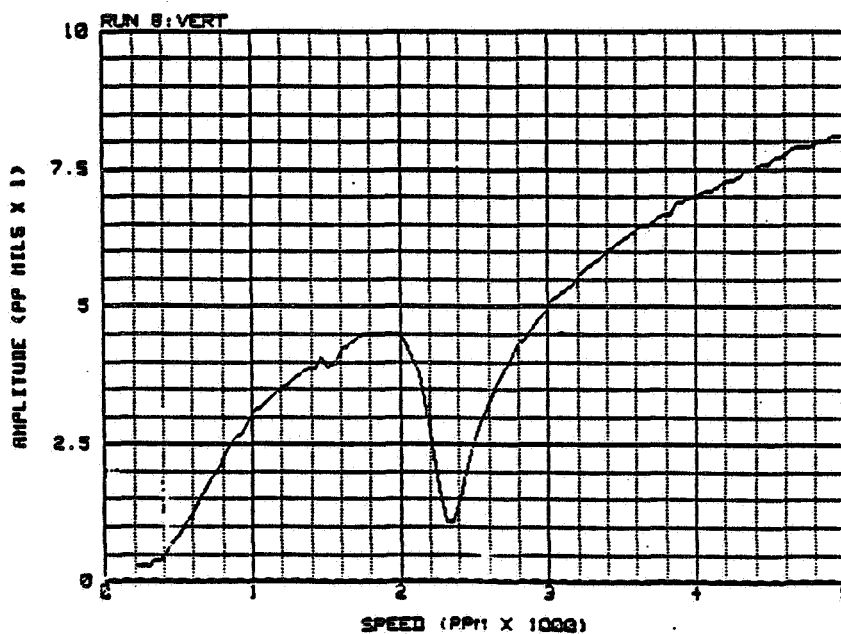
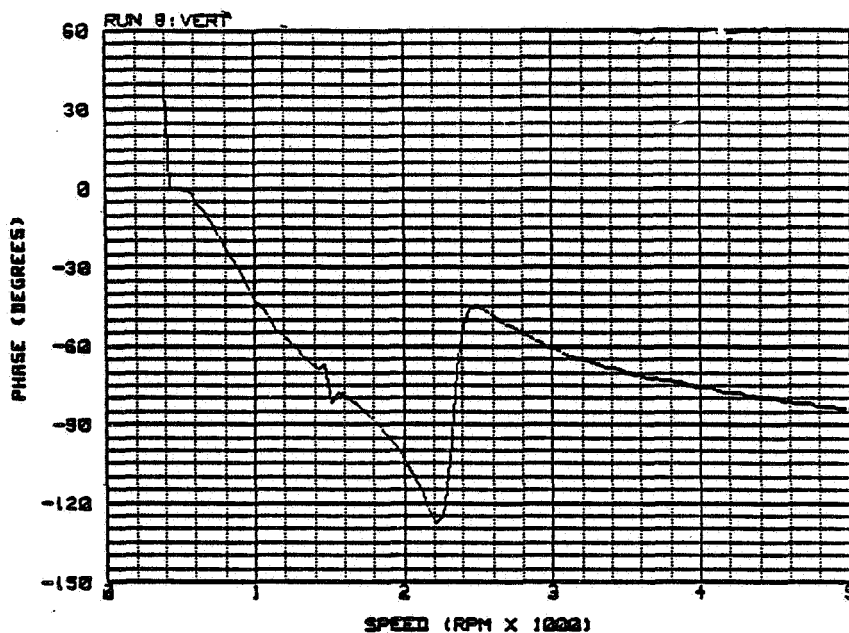


Figure 6. - Journal phase and amplitude of vertical response. Rotative speed, 1500 rpm; m_p , 1.6 g; T, 80 °F; forward perturbation.

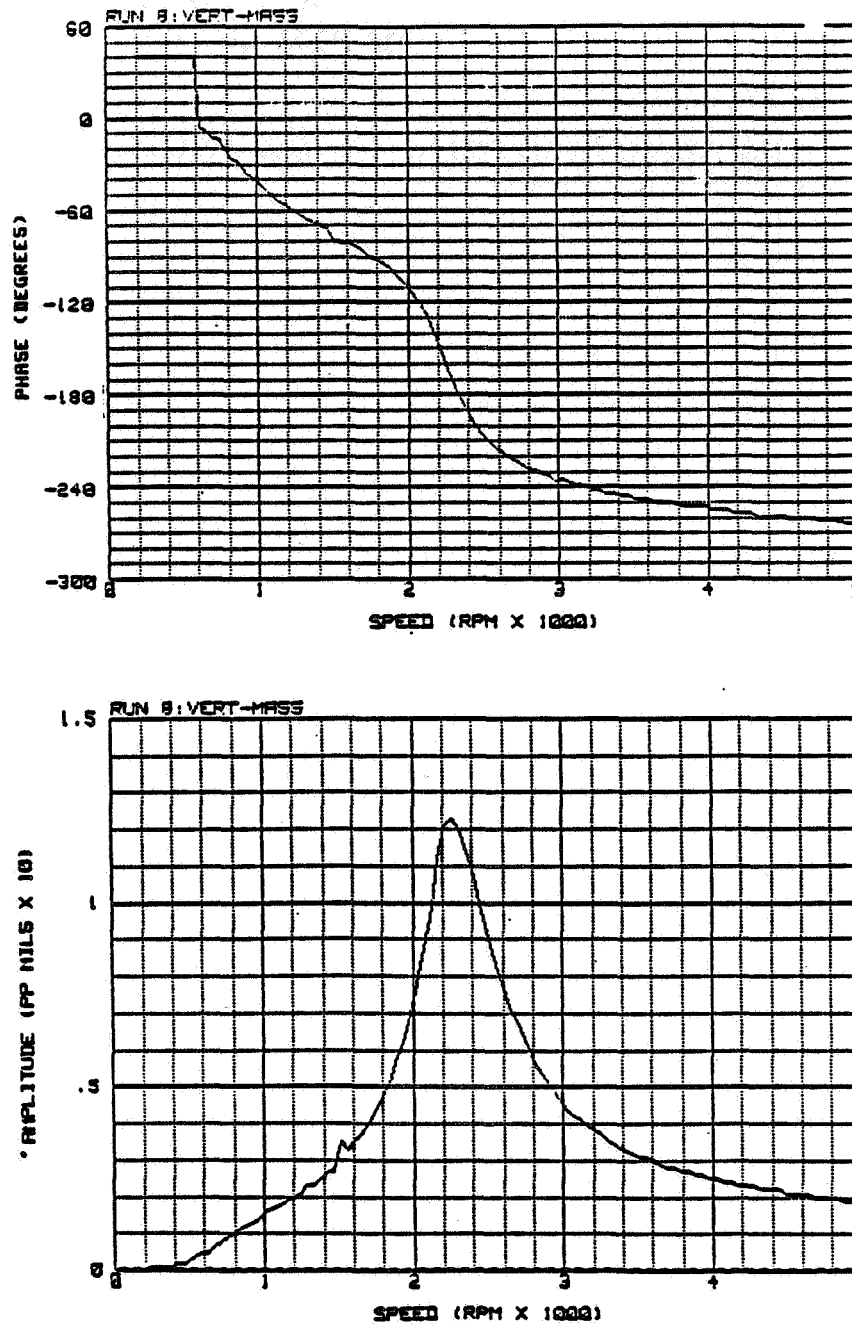


Figure 7. - Disk phase and amplitude of vertical response (parameters same as in fig. 6).

ORIGINAL PAGE IS
OF POOR QUALITY

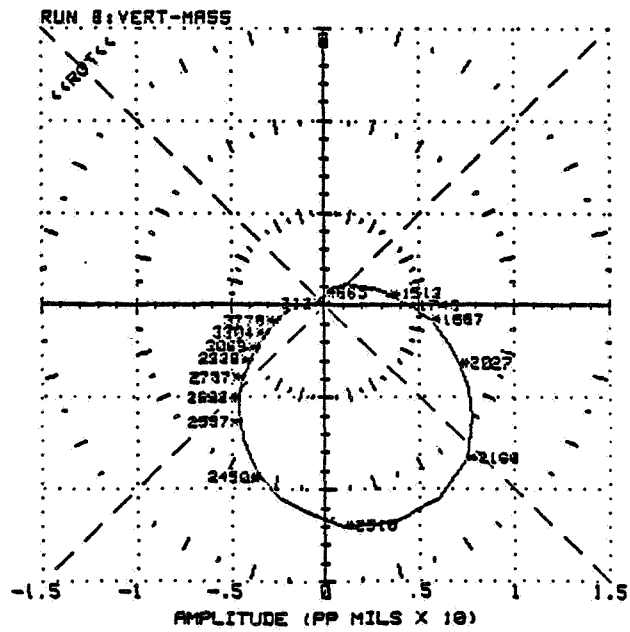
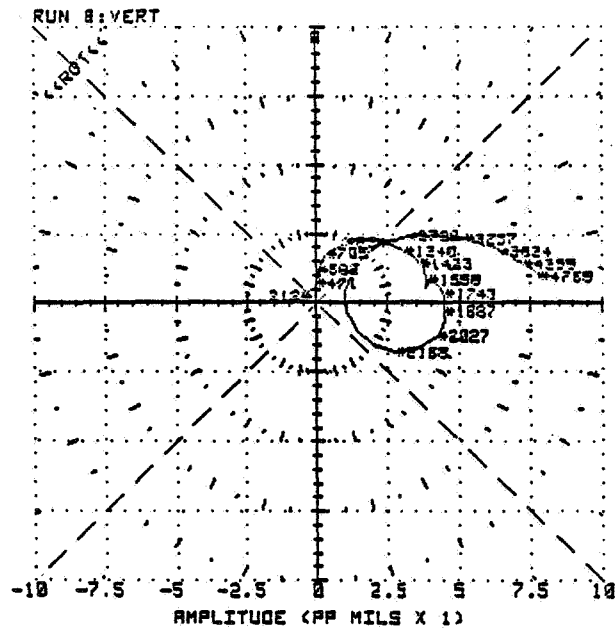


Figure 8. - Journal and disk response in form of polar plots (parameters same as in fig. 6).

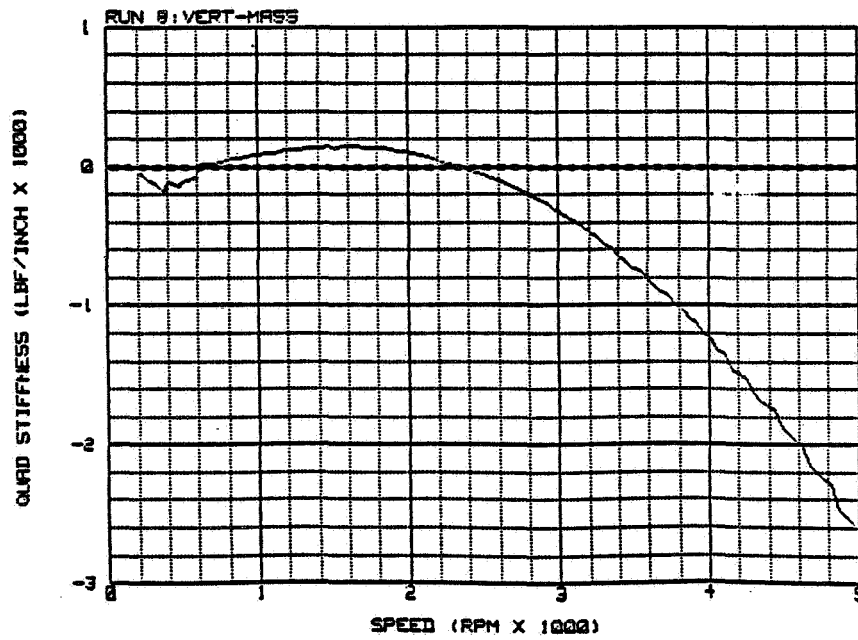
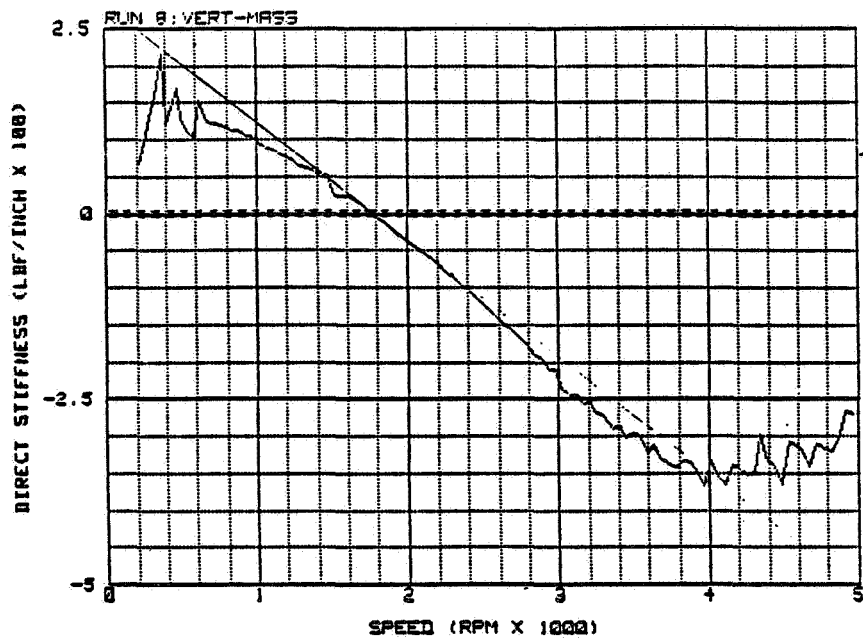


Figure 9. - Rotor/bearing dynamic stiffnesses (journal) (parameters same as in fig. 6).

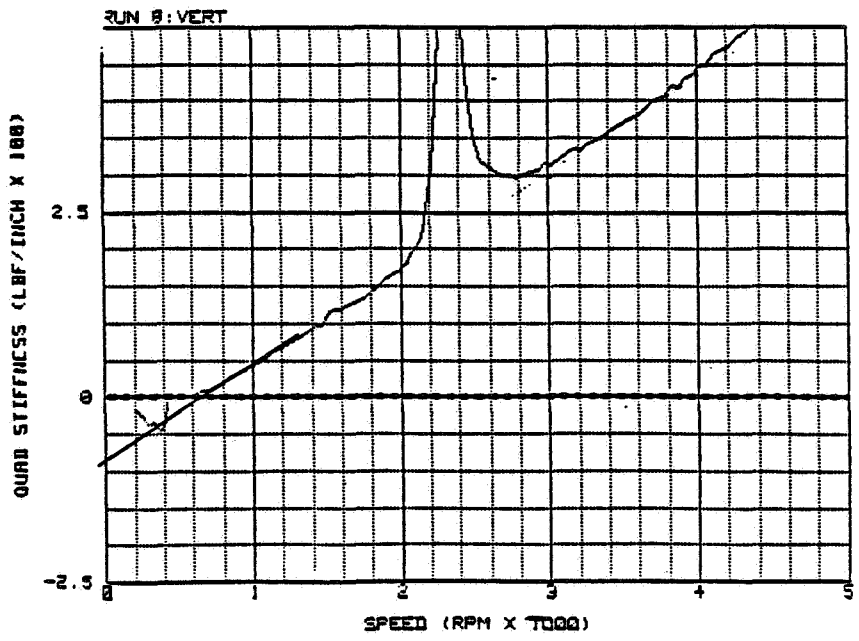
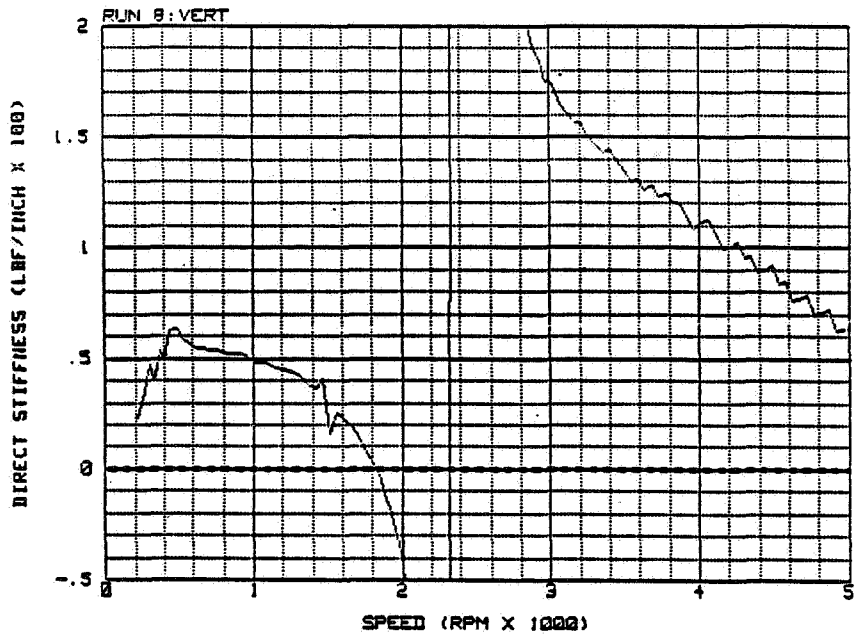


Figure 10. - Rotor/bearing dynamic stiffness (disk) (parameters same as in fig. 6).

REFERENCES

1. Muszynska, A.: Dynamic Stiffness Measurements for Better Mechanical System Identification. Bently Nevada Corporation, Paper presented at EPRI-Nuclear Power Division Pump Workshop, Toronto, Canada, August 1982.
2. Muszynska, A.: Application of the Perturbation Method to Rotating Machines. BNC Senior Mechanical Engineering Seminar, Carson City, NV, June 1984.
3. Bently, D.E., Muszynska, A., Olas, A.: Identification of the Parameters of a Rotor with the Strong Gyroscopic Effect by Perturbation Testing, Bently Nevada Corporation, 1984.
4. Bently, D.E., Muszynska, A.: Stability Evaluation of Rotor/Bearing System by Perturbation Tests, Rotordynamic Instability Problems in High Performance Turbomachinery, Proc. of a Workshop, Texas A&M University, College Station, TX, 1982.
5. Bently, D.E., Muszynska, A.: Oil Whirl Identification by Perturbation Test. Advances in Computer-aided Bearing Design, ASME/ASLE Lubrication Conference, Washington, DC, October 1982.
6. Bently, D.E., Muszynska, A.: Perturbation Tests of Bearing/Seal for Evaluation of Dynamic Coefficients. Symposium on Rotor Dynamical Instability, Summer Annual Conference of the ASME Applied Mechanics Division, Houston, TX, June 1983.
7. Bently, D.E., Muszynska, A.: Perturbation Study of Rotor/Bearing System : Identification of the Oil Whirl and Oil Whip Resonances. Tenth Biennial ASME Design Engineering Division Conference on Mechanical Vibration and Noise, Cincinnati, OH, September 1985.
8. Bently, D.E., Muszynska, A.: The Dynamic Stiffness Characteristics of High Eccentricity Ratio Bearings and Seals by Perturbation Testing. Workshop on Rotordynamic Instability Problems in High Performance Turbomachinery, Texas A&M University, May 1984.

SHAFT MODE SHAPE DEMONSTRATION

Robert Grissom
Bently Nevada Corporation
Minden, Nevada 89423

The dynamic response of a rotating machine is directly influenced by its geometric configuration and all aspects of the rotor construction. These determine two significant parameters, mass distribution and stiffness, which yield a spectrum of natural frequencies and mode shapes. The mode shapes can be presented as "snapshots" of the characteristic amplitude/phase response patterns of the shaft, due to the major forcing function of unbalance, at different rotative speeds (Figure 1).

OBJECTIVE

To demonstrate the three shaft mode shapes of the rotor rig using the Shaft Mode Demonstrator and oscilloscopes. The synchronous (1X) amplitude and phase of the rotor vibration in the vertical direction from several points along the shaft is displayed on corresponding points of the demonstrator. Unfiltered vibration from vertical and horizontal probe pairs is displayed on the oscilloscopes in orbit format for a dynamic presentation of the mode shape.

ROTOR RIG

The rotor rig consists of a flexible, three-disk rotor supported in relatively rigid, oil impregnated, sintered bronze bearings. The disks are symmetrically placed on the shaft, which is driven by a variable speed (0-12,000 rpm) electric motor through a flexible coupling.

INSTRUMENTATION

The instrumentation consists of x-y proximity probes mounted next to each disk observing shaft vibration, and a Keyphasor probe for speed and phase measurement. The Shaft Mode Demonstrator, a three-channel vector filter, measures the 1X phase and amplitude at each vertical probe, and converts it from polar to cartesian format to drive the servo-controlled x-y positioners at each display location. The plastic shaft presents an amplified version of the shaft mode "snapshot." Oscilloscopes display the corresponding orbit (shaft precessional motion).

MEASUREMENT PARAMETERS

Vertical IX amplitude and phase at each measurement location as a function of rotative speed. Corresponding orbital motion. Relative amplitude/phase and phase change at each location through the three balance resonance speeds.

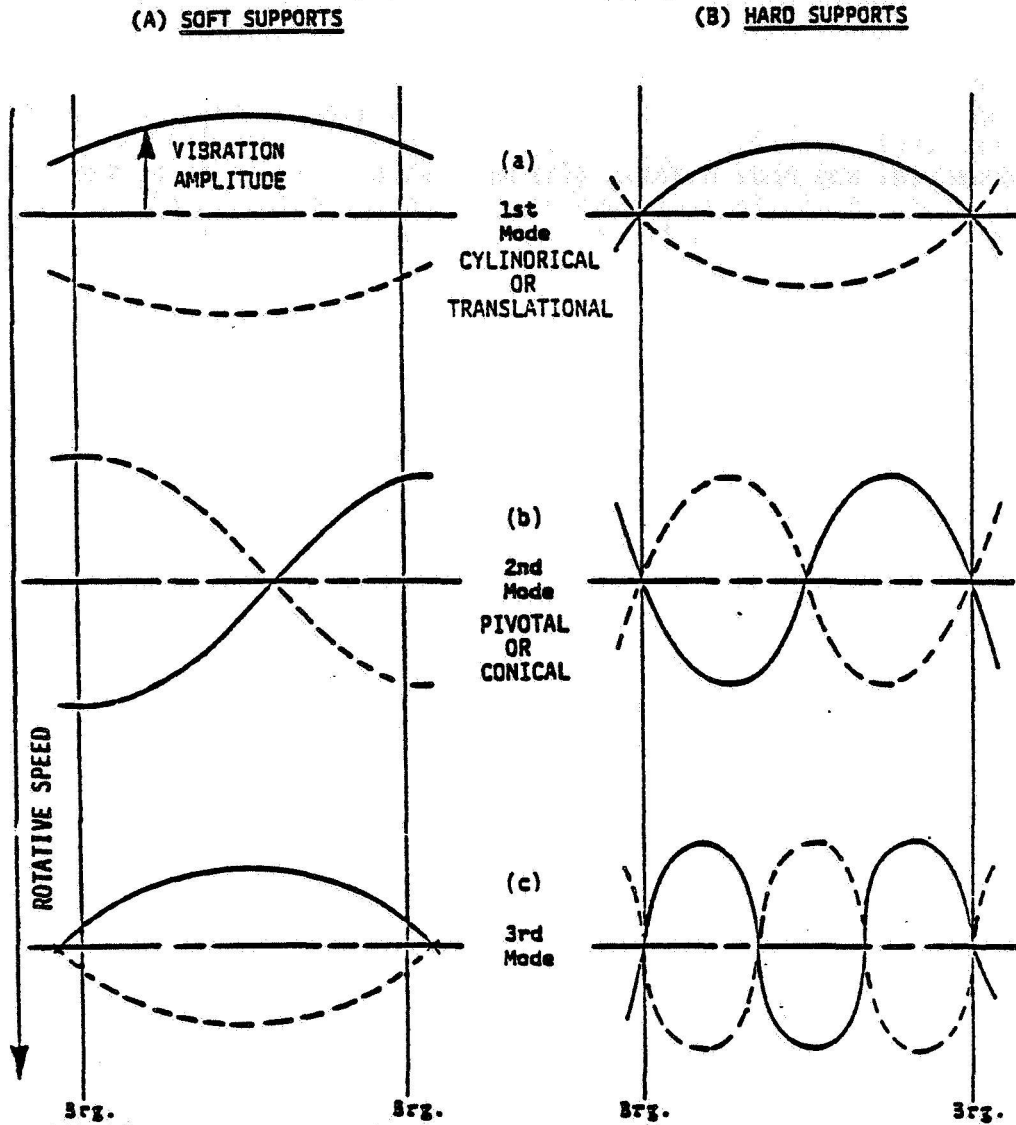


Figure 1. Modal shapes of a shaft in soft supports (A) and hard supports (B).

ORBITS - COMPUTER SIMULATION

Agnes Muszynska
Bently Rotor Dynamics Research Corporation
Minden, Nevada 89423

In rotating machinery dynamics an orbit (Lissajous curve) represents the dynamic path of the shaft centerline motion during shaft rotation and resulting precession. The orbit can be observed with an oscilloscope connected to XY proximity probes. The orbits can also be simulated by a computer.

OBJECTIVE

The software for HP computer simulates orbits for two cases:

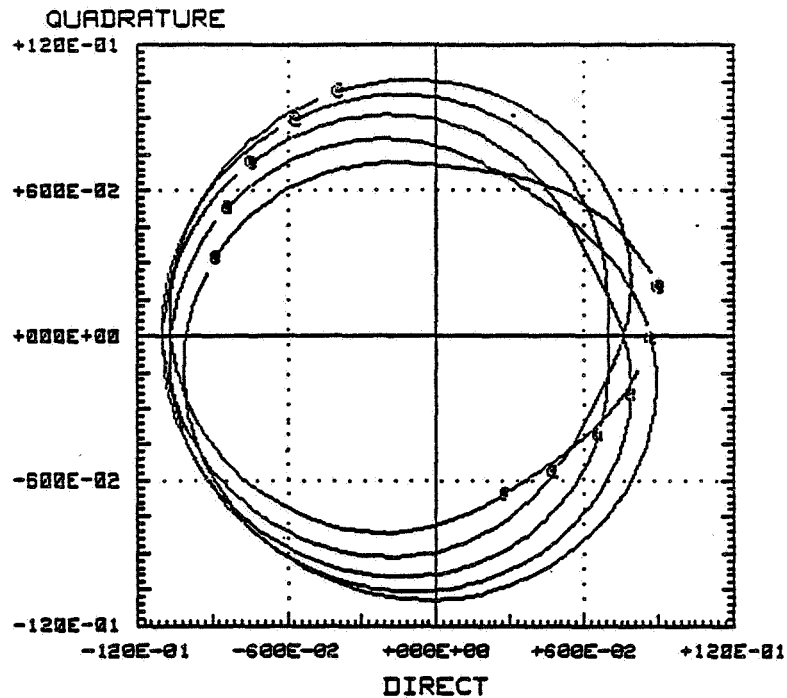
- (1) Symmetric orbit with four frequency components with different radial amplitudes and relative phase angles.
- (2) Nonsymmetric orbit with two frequency components with two different vertical/horizontal amplitudes and two different relative phase angles.

Each orbit carries a Keyphasor mark (one-per-turn reference). The frequencies, amplitudes, and phase angles, as well as number of time steps for orbit computation, have to be chosen and introduced to the computer by the user.

The orbit graphs can be observed on the computer screen. Hard copies are available from the corresponding plotter.

RESULTS

Figures 1 through 5 give the examples of the computer-generated orbits, simulating various rotating machine malfunctions.



**** DATA ****

```

1.) AX1 : HORIZONTAL AMPLITUDE OF THE 1ST COMPONENT ***** 2
2.) AY1 : VERTICAL AMPLITUDE OF THE 1ST COMPONENT ***** 2
3.) AX2 : HORIZONTAL AMPLITUDE OF THE 2ND COMPONENT ***** 9
4.) AY2 : VERTICAL AMPLITUDE OF THE 2ND COMPONENT ***** 9
5.) ALPX1 : HORIZONTAL PHASE ANGLE OF THE 1ST COMPONENT [DEG] ***** 90
6.) ALPY1 : VERTICAL PHASE ANGLE OF THE 1ST COMPONENT [DEG] ***** 90
7.) ALPX2 : HORIZONTAL PHASE ANGLE OF THE 2ND COMPONENT [DEG] ***** 0
8.) ALPY2 : VERTICAL PHASE ANGLE OF THE 2ND COMPONENT [DEG] ***** 0
9.) OME1 : FREQUENCY OF THE 1ST COMPONENT [RAD/SEC] ***** 100
10.) OME2 : FREQUENCY OF THE 2ND COMPONENT [RAD/SEC] ***** 48
11.) NMAX : NUMBER OF 'TIME'-STEPS ***** 900

```

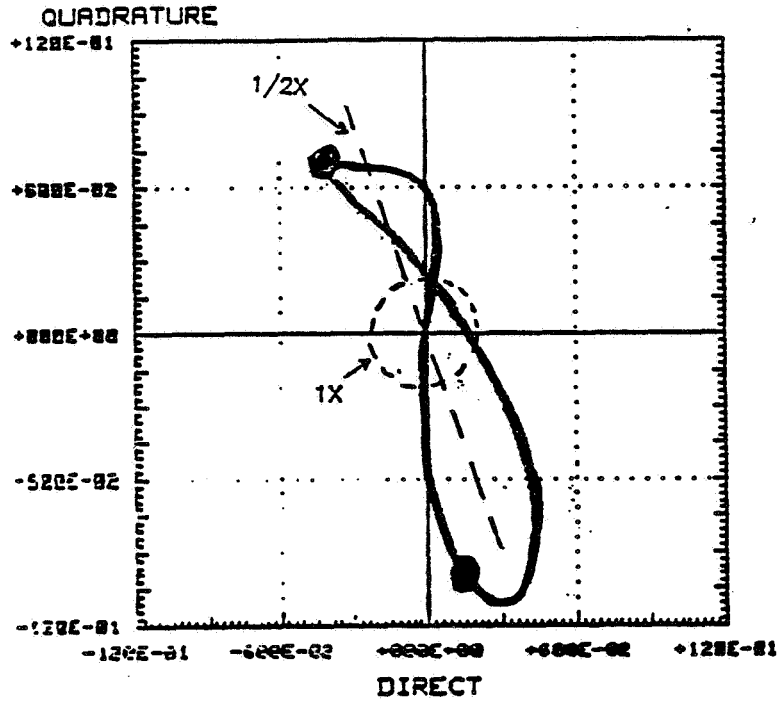
**** ROTOR ORBITAL MOTION ****

$$x = \langle Ax1 \rangle \cos(\omega_1 t + \alpha_{px1}) + \langle Ax2 \rangle \cos(\omega_2 t + \alpha_{px2})$$

$$y = \langle Ay1 \rangle \sin(\omega_1 t + \alpha_{py1}) + \langle Ay2 \rangle \sin(\omega_2 t + \alpha_{py2})$$

Figure 1. - Orbit simulating oil whirl.

ORIGINAL PAGE IS
OF POOR QUALITY



**** DATA ****

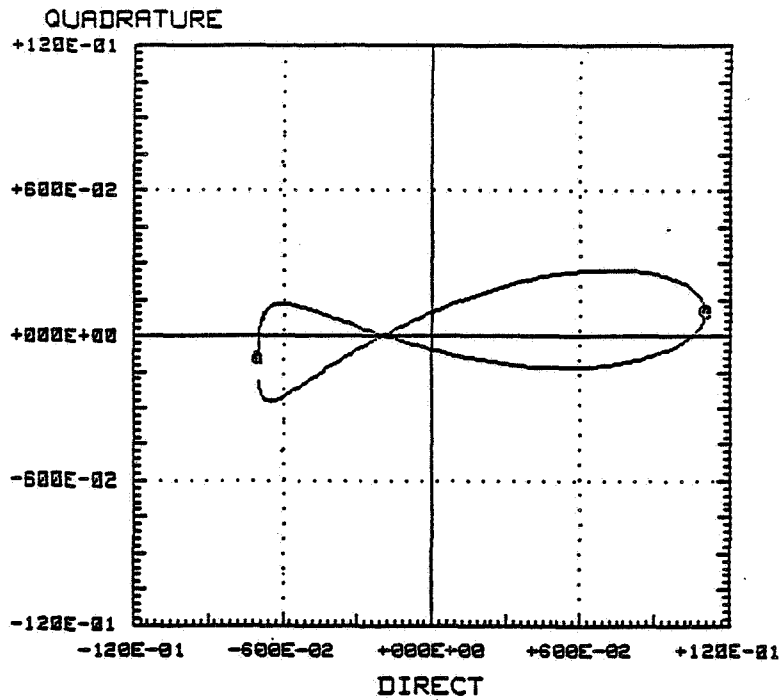
1.)	AX1	:	HORIZONTAL AMPLITUDE OF THE 1ST COMPONENT *****	2
2.)	AY1	:	VERTICAL AMPLITUDE OF THE 1ST COMPONENT *****	2
3.)	AX2	:	HORIZONTAL AMPLITUDE OF THE 2ND COMPONENT *****	3
4.)	AY2	:	VERTICAL AMPLITUDE OF THE 2ND COMPONENT *****	9
5.)	ALPX1	:	HORIZONTAL PHASE ANGLE OF THE 1ST COMPONENT [DEG] *****	225
6.)	ALPY1	:	VERTICAL PHASE ANGLE OF THE 1ST COMPONENT [DEG] *****	225
7.)	ALPX2	:	HORIZONTAL PHASE ANGLE OF THE 2ND COMPONENT [DEG] *****	20
8.)	ALPY2	:	VERTICAL PHASE ANGLE OF THE 2ND COMPONENT [DEG] *****	290
9.)	OME1	:	FREQUENCY OF THE 1ST COMPONENT [RAD/SEC] *****	100
10.)	OME2	:	FREQUENCY OF THE 2ND COMPONENT [RAD/SEC] *****	-50
11.)	NMAX	:	NUMBER OF 'TIME'-STEPS *****	300

**** ROTOR ORBITAL MOTION ****

$$x = (Ax1)\cos(\omega_1 + \alpha_{px1}) + (Ax2)\cos(\omega_2 + \alpha_{px2})$$

$$y = (Ay1)\sin(\omega_1 + \alpha_{py1}) + (Ay2)\sin(\omega_2 + \alpha_{py2})$$

Figure 2. - Orbit simulating vertical partial rotor-to-stator rub.



**** DATA ****

```

1.) AX1 : HORIZONTAL AMPLITUDE OF THE 1ST COMPONENT ***** 2
2.) AY1 : VERTICAL AMPLITUDE OF THE 1ST COMPONENT ***** 2
3.) AX2 : HORIZONTAL AMPLITUDE OF THE 2ND COMPONENT ***** 9
4.) AY2 : VERTICAL AMPLITUDE OF THE 2ND COMPONENT ***** 1
5.) ALPX1 : HORIZONTAL PHASE ANGLE OF THE 1ST COMPONENT [DEG] ***** 0
6.) ALPY1 : VERTICAL PHASE ANGLE OF THE 1ST COMPONENT [DEG] ***** 0
7.) ALPX2 : HORIZONTAL PHASE ANGLE OF THE 2ND COMPONENT [DEG] ***** 0
8.) ALPY2 : VERTICAL PHASE ANGLE OF THE 2ND COMPONENT [DEG] ***** 90
9.) OME1 : FREQUENCY OF THE 1ST COMPONENT [RAD/SEC] ***** 100
10.) OME2 : FREQUENCY OF THE 2ND COMPONENT [RAD/SEC] ***** -50
11.) NMAX : NUMBER OF 'TIME'-STEPS ***** 300

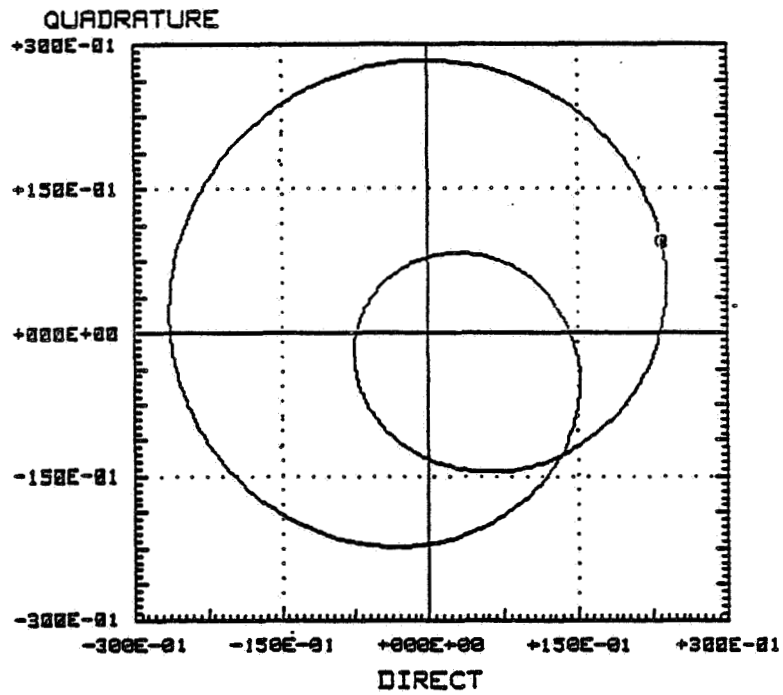
```

**** ROTOR ORBITAL MOTION ****

$$x = (Ax1)\cos(\omega_1 t + \alpha_{x1}) + (Ax2)\cos(\omega_2 t + \alpha_{x2})$$

$$y = (Ay1)\sin(\omega_1 t + \alpha_{y1}) + (Ay2)\sin(\omega_2 t + \alpha_{y2})$$

Figure 3. - Orbit simulating horizontal partial rotor-to-stator rub.



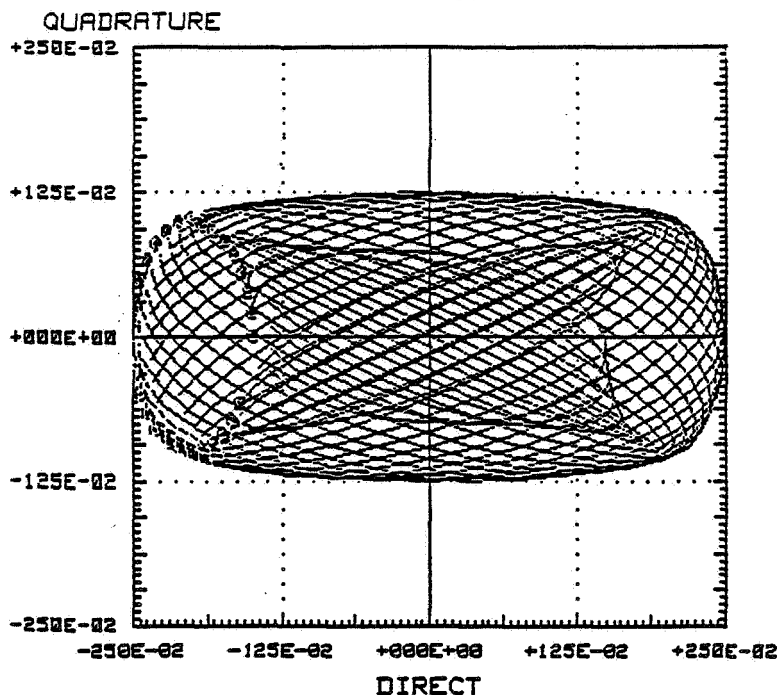
$$z = \underbrace{(10) \exp(j(50t+70))}_{\substack{\uparrow \\ \text{FIRST COMPONENT IS SYNCHRONOUS}}} + (18) \exp(j(100t+0)) + (1) \exp(j(150t+0)) \\ + (1) \exp(j(200t+0))$$

FIRST COMPONENT IS SYNCHRONOUS

ROTOR ORBITAL MOTION

Figure 4. - Orbit simulating cracked shaft.

ORIGINAL PAGE IS
OF POOR QUALITY



**** DATA ****

1.)	AX1	:	HORIZONTAL AMPLITUDE OF THE 1ST COMPONENT *****	-2
2.)	AY1	:	VERTICAL AMPLITUDE OF THE 1ST COMPONENT *****	-.25
3.)	AX2	:	HORIZONTAL AMPLITUDE OF THE 2ND COMPONENT *****	.5
4.)	AY2	:	VERTICAL AMPLITUDE OF THE 2ND COMPONENT *****	1
5.)	ALPX1	:	HORIZONTAL PHASE ANGLE OF THE 1ST COMPONENT [DEG] *****	0
6.)	ALPY1	:	VERTICAL PHASE ANGLE OF THE 1ST COMPONENT [DEG] *****	180
7.)	ALPX2	:	HORIZONTAL PHASE ANGLE OF THE 2ND COMPONENT [DEG] *****	0
8.)	ALPY2	:	VERTICAL PHASE ANGLE OF THE 2ND COMPONENT [DEG] *****	180
9.)	OME1	:	FREQUENCY OF THE 1ST COMPONENT [RAD/SEC] *****	100
10.)	OME2	:	FREQUENCY OF THE 2ND COMPONENT [RAD/SEC] *****	97
11.)	NMAX	:	NUMBER OF 'TIME'-STEPS *****	900

**** ROTOR ORBITAL MOTION ****

$$x=(Ax1)\cos(\omega_1t+\alpha_{px1})+(Ax2)\cos(\omega_2t+\alpha_{px2})$$

$$y=(Ay1)\sin(\omega_1t+\alpha_{py1})+(Ay2)\sin(\omega_2t+\alpha_{py2})$$

Figure 5. - Orbit simulating rotor instability.

DATA PRESENTATION TECHNIQUES FOR ROTATING MACHINERY MALFUNCTION DIAGNOSIS

Thomas Spettel
Bently Rotor Dynamics Research Corporation
Minden, Nevada 89423

Modern industrial processes demand operation of rotating machinery over a wide range of pressures, temperatures, and flow rates. This variety of operating conditions dictates a similarly large distribution of machinery types and mechanical configurations. Although the variables involved are extensive, a common focal point appears when reliability and mechanical integrity are discussed. In all cases, it is economically favorable to evaluate the on-stream mechanical condition of the process machinery. Furthermore, when problems do appear, the early detection and diagnosis of the malfunction is not only desirable, but often mandatory. In the pursuit of parameters to accurately assess mechanical condition, the measurement of machine vibration characteristics has consistently proven to be a powerful tool.

Successful vibration measurement and analysis requires that the vibration signals must be reduced to hard copy data for engineering evaluation. The format utilized for data presentation can enhance the information, yielding a direct identification of the occurring mechanism.

Baseline steady-state data is excellent for documentation of vibration signals at normal operating conditions. Assuming that a set of initial data was acquired with the machinery in a good state of repair, any future changes or deterioration in mechanical condition can be easily compared to the baseline information. Often this type of comparison will yield sufficient information for evaluation of the problem. However, many malfunctions require the analysis of transient data in order to identify the malfunction.

Steady-state data formats consist of:

- Time Base Waveform
- Orbit
- Spectrum

Transient data formats consist of

- Polar
- Bodé
- Cascade

OBJECTIVE

Our objective is to demonstrate the use of the above formats to diagnose a machine malfunction. A turbine-driven compressor train is chosen as an example. The machine train outline drawing is shown as Figure 1.

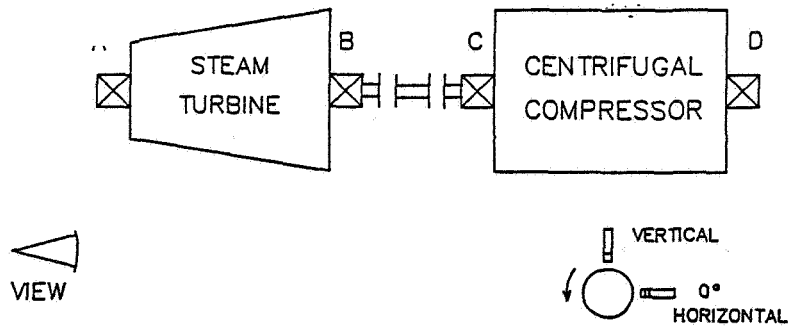


Figure 1. - Machine outline drawing.

Vibration data taken during start-up from the X-Y proximity probes at the "C" bearing has been stored in digitized form in the computer. The ADRE® transient software will be used to produce Bodé, Polar, and Cascade plots from the horizontal transducer. Copies of these plots are given as Figures 2 through 5.

ANALYSIS

Observation of the filtered synchronous amplitude and phase information on the Bodé (Figure 2) indicates that the synchronous vibration amplitudes are low and that the first balance resonance occurs in the region from 4750 to 7000 rpm.

The polar plot (Figure 3) confirms this data.

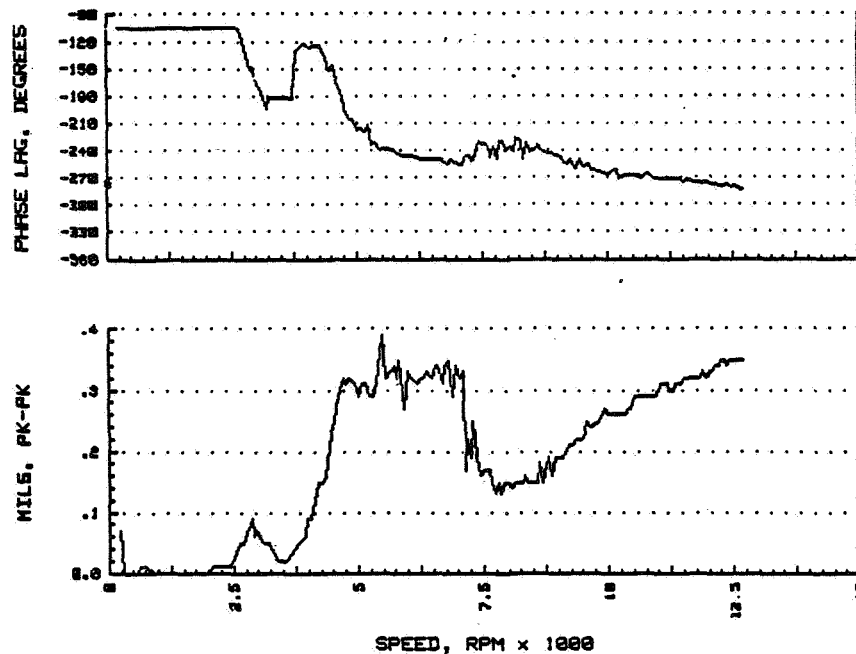


Figure 2. - Bodé plot of compressor inboard horizontal response.

ORIGINAL PAGE IS
OF POOR QUALITY

The cascade plot (Figure 5) presents the same start-up data in the frequency domain format. Analysis of this data indicates that vibration occurs at a frequency of approximately 50% of running speed from 5,000 rpm to 8,000 rpm. After 8,000 rpm, the vibration frequency "locks-in" at 4,200 cpm and no longer increases with an increase of running speed.

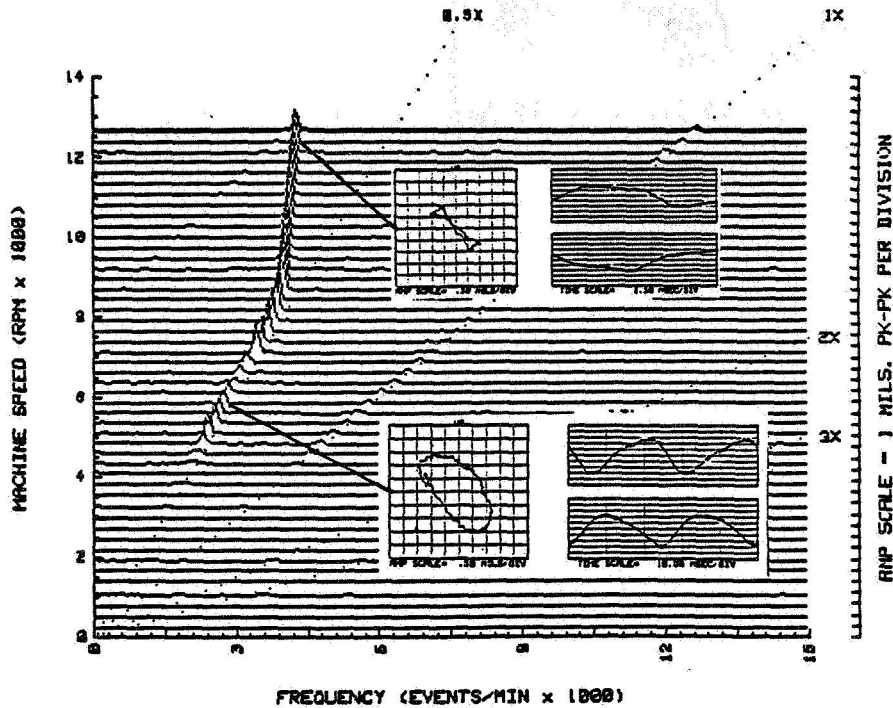


Figure 5. - Cascade spectrum plots of compressor inboard horizontal response.

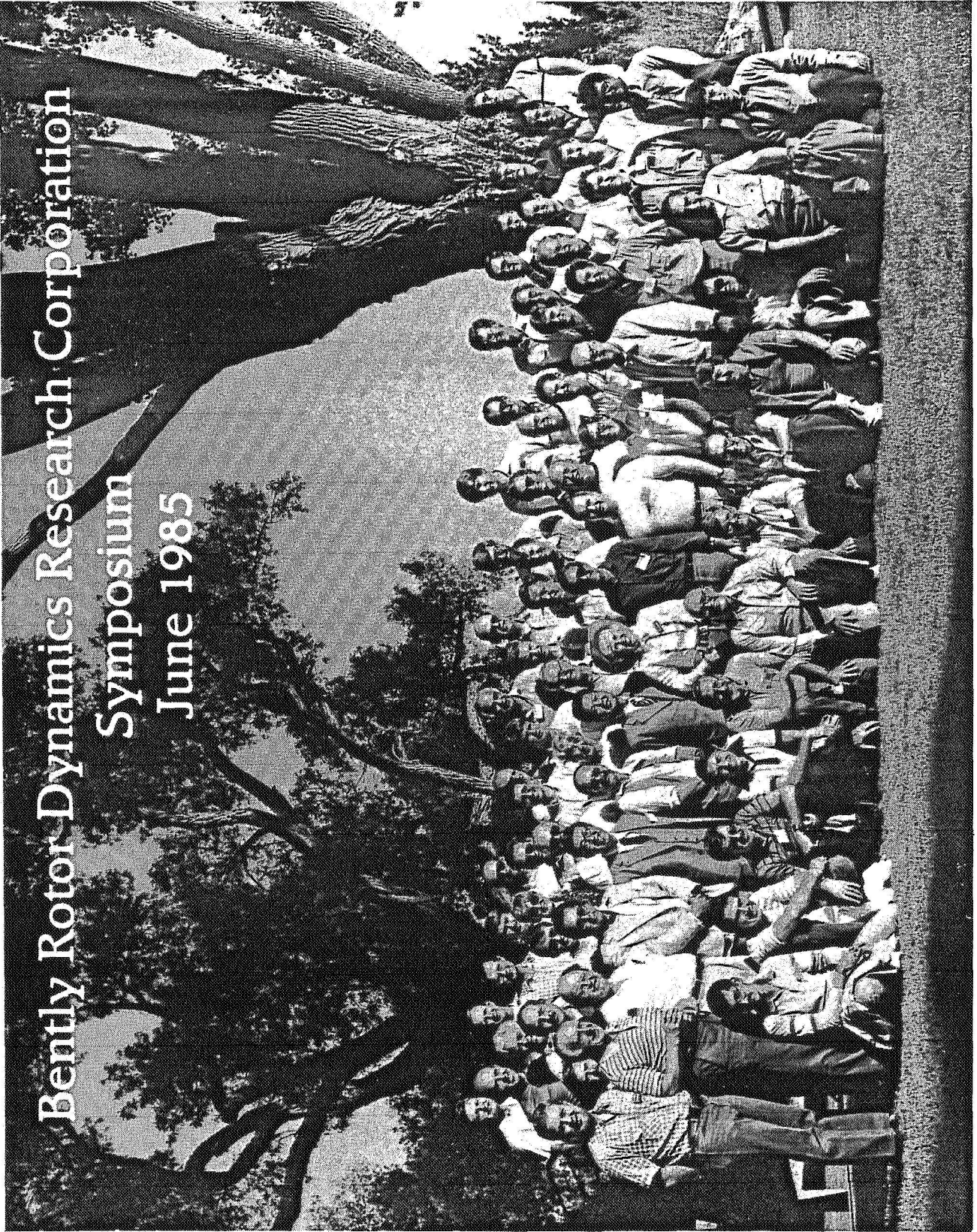
The orbit plots taken at 5,000 rpm and 12,600 rpm, superimposed on the cascade plot, show the characteristic multiple keyphasor per revolution associated with "oil whirl" and "oil whip," respectively.

CONCLUSION

It is apparent that a wide variety of data presentation techniques are available to the machinery diagnostician. Since mechanical malfunctions have a tendency to disguise themselves with side effects and misleading disturbances, it is essential that the acquired data be reviewed in every reasonable manner prior to forming a conclusion. Failure to perform this additional work will commit the machinery diagnostician to a life of treating symptoms rather than identifying and solving the basic problems.

ORIGINAL PAGE IS
OF POOR QUALITY

Bently Rotor Dynamics Research Corporation
Symposium
June 1985



1. Report No. NASA CP-2409	2. Government Accession No.	3. Recipient's Catalog No.	
4. Title and Subtitle Instability in Rotating Machinery		5. Report Date December 1985	
		6. Performing Organization Code	
7. Author(s)		8. Performing Organization Report No. E-2652	
		10. Work Unit No.	
9. Performing Organization Name and Address National Aeronautics and Space Administration Lewis Research Center Cleveland, Ohio 44135		11. Contract or Grant No.	
		13. Type of Report and Period Covered Conference Publication	
12. Sponsoring Agency Name and Address National Aeronautics and Space Administration Washington, D.C. 20546		14. Sponsoring Agency Code	
		15. Supplementary Notes	
16. Abstract The Instability in Rotating Machinery Symposium was sponsored by the Bently Rotor Dynamics Research Corporation and held in Carson City, Nevada, June 10-14, 1985. The proceedings contains 45 papers on a wide range of subjects including flow-generated instabilities in fluid-flow machines, cracked-shaft detection, case histories of instability phenomena in compressors, turbines, and pumps, vibration control in turbomachinery (including anti-swirl techniques), and the simulation and estimation of destabilizing forces in rotating machines. The symposium was held to serve as an update on the understanding and control of rotating machinery instability problems between the biennial workshops sponsored by Texas A&M University.			
17. Key Words (Suggested by Author(s)) Rotordynamics Turbomachinery Instability		18. Distribution Statement Unclassified - unlimited STAR Category 37	
19. Security Classif. (of this report) Unclassified	20. Security Classif. (of this page) Unclassified	21. No. of pages 479	22. Price* A21

**National Aeronautics and
Space Administration
Code NIT-4**

**Washington, D.C.
20546-0001**

**Official Business
Penalty for Private Use, \$300**

**SPECIAL FOURTH CLASS MAIL
BOOK**

**Postage and Fees Paid
National Aeronautics and
Space Administration
NASA-451**



NASA

**POSTMASTER: If Undeliverable (Section 158
Postal Manual) Do Not Return**
